MEMBRANE AND CYTOSKELETON MECHANICS

EDITED BY: Yuan Lin and Ying Li
PUBLISHED IN: Frontiers in Physics and Frontiers in Molecular Biosciences

frontiers Research Topics

frontiers

ISSN 1664-8714
ISBN 978-2-88974-366-7
DOI 10.3389/978-2-88974-366-7

About Frontiers

Frontiers is more than just an open-access publisher of scholarly articles: it is a pioneering approach to the world of academia, radically improving the way scholarly research is managed. The grand vision of Frontiers is a world where all people have an equal opportunity to seek, share and generate knowledge. Frontiers provides immediate and permanent online open access to all its publications, but this alone is not enough to realize our grand goals.

Frontiers Journal Series

The Frontiers Journal Series is a multi-tier and interdisciplinary set of open-access, online journals, promising a paradigm shift from the current review, selection and dissemination processes in academic publishing. All Frontiers journals are driven by researchers for researchers; therefore, they constitute a service to the scholarly community. At the same time, the Frontiers Journal Series operates on a revolutionary invention, the tiered publishing system, initially addressing specific communities of scholars, and gradually climbing up to broader public understanding, thus serving the interests of the lay society, too.

Dedication to Quality

Each Frontiers article is a landmark of the highest quality, thanks to genuinely collaborative interactions between authors and review editors, who include some of the world's best academicians. Research must be certified by peers before entering a stream of knowledge that may eventually reach the public - and shape society; therefore, Frontiers only applies the most rigorous and unbiased reviews.
Frontiers revolutionizes research publishing by freely delivering the most outstanding research, evaluated with no bias from both the academic and social point of view. By applying the most advanced information technologies, Frontiers is catapulting scholarly publishing into a new generation.

What are Frontiers Research Topics?

Frontiers Research Topics are very popular trademarks of the Frontiers Journals Series: they are collections of at least ten articles, all centered on a particular subject. With their unique mix of varied contributions from Original Research to Review Articles, Frontiers Research Topics unify the most influential researchers, the latest key findings and historical advances in a hot research area! Find out more on how to host your own Frontiers Research Topic or contribute to one as an author by contacting the Frontiers Editorial Office: frontiersin.org/about/contact

MEMBRANE AND CYTOSKELETON MECHANICS

Topic Editors:
Yuan Lin, The University of Hong Kong, SAR China
Ying Li, University of Connecticut, United States

Citation: Lin, Y., Li, Y., eds (2022). Membrane and Cytoskeleton Mechanics. Lausanne: Frontiers Media SA. doi: 10.3389/978-2-88974-366-7

Table of Contents

frontiers in Physics

EDITORIAL
published: 04 January 2022
doi: 10.3389/fphy.2021.827025

Editorial: Membrane and Cytoskeleton Mechanics

Yuan Lin[1]* *and Ying Li*[2]

[1]Department of Mechanical Engineering, The University of Hong Kong, Hong Kong, China, [2]Department of Mechanical Engineering and Polymer Program, Institute of Materials Science, University of Connecticut, Storrs, CT, United States

Keywords: cell membrane, cytoskeleton, cell mechanics, modeling, experiment, cell biophysics

Editorial on the Research Topic

Membrane and Cytoskeleton Mechanics

As two main structural components of a cell, the lipid bilayer membrane [1] and cytoskeleton [2] are responsible for stabilizing the cell shape as well as playing key roles in different cellular functions. For example, important processes like cell migration [3–6], division [7, 8], and embryo development [9, 10] are all driven by internal forces generated within the cytoskeleton. In addition, various mechano-sensitive proteins in the membrane allow cells to probe their microenvironment and perform functions such as mechano-transduction [11, 12] and volume regulation [13, 14]. For these reasons, extensive efforts have been devoted in the past few decades to elucidating key factors dictating the mechanical response of the lipid membrane and cytoskeleton [15–18] as well as connecting them to the capability of cells to perform biological duties or the progression of diseases such as cancer [19] and malaria [20]. This research topic intends to present a collection of substantial advances made in this field recently.

The paper by Burgos-Bravo et al. shows that proteoglycan receptor Syndecan-4 can form a ternary complex with $\alpha_V\beta_3$ integrin and the neuronal protein Thy-1, increase the lifetime of Thy-1 – $\alpha_V\beta_3$ integrin binding, modulate their mechano-transduction function, and eventually result in faster neurite retraction and suppressed neurite outgrowth under pro-inflammatory conditions.

The paper by Ricketts et al. focuses on how ionic conditions influence the rearrangement of networks of actin and microtubules. Specifically, the authors show that the bulk contraction of both actin and actin-microtubule networks increases when Mg^{2+} concentrations varies from 2 to 20 mM. Interestingly, actin networks begin to contract at lower Mg^{2+} concentrations and shorter times than actin-microtubule networks. These results shed light on how varying environmental conditions can dynamically tune the morphology of the cytoskeleton without the help of motor proteins.

The paper by Bashirzadeh et al. discusses how the properties of actin crosslinkers and surrounding confinement geometry regulate the formation of actin bundles and bundle networks. Specifically, depending on the size of giant unilamellar vesicles (GUVs) encapsulating actin and concentration of fascin, a short crosslinker, straight F-actin bundles, or crosslinked bundle networks can be formed. In addition, the authors also show that the presence of a long crosslinker, α-actinin, impacts fascin-induced GUV shape changes and significantly impairs the formation of filopodia-like protrusions.

The paper by Dasanna et al. presents how the contrast/ratio of viscosities between RBC cytosol and blood plasma affects the shape and dynamics of RBCs via mesoscopic hydrodynamics simulations. Interestingly, it is found that distinct RBC shapes, including tumbling cells, parachutes, and tank-treading slippers, can all appear depending on the values of viscosity contrast, flow rate, and tube diameter. Furthermore, the authors demonstrate that the tumbling-to-slipper transition, as well as the size of the parachute region, is strongly affected by viscosity contrast.

The paper by Galluzzi et al. discusses the influence of photothermal effects of fluorescent dyes on the mechanical response and stability of membranes. Specifically, the authors show a 30 min laser

OPEN ACCESS

Edited and reviewed by:
Ralf Metzler,
University of Potsdam, Germany

***Correspondence:**
Yuan Lin
ylin@hku.hk

Received: *01 December 2021*
Accepted: *09 December 2021*
Published: *04 January 2022*

Citation:
Lin Y and Li Y (2022) Editorial: Membrane and Cytoskeleton Mechanics. Front. Phys. 9:827025. doi: 10.3389/fphy.2021.827025

irradiation, with intensity similar to that in a typical confocal scanning microscopy experiment, is enough to trigger a ~40% decrease in the breakthrough force of the stained phospholipid bilayer membrane along with a ~30% reduction in its apparent elastic modulus, highlighting the importance of considering such effect when using, for example, atomic force-fluorescence correlative microscopy to investigate the deformability and permeability of cell membranes.

The paper by Schmidt and Kierfeld proposes a chemomechanical model of microtubule dynamics on the dimmer level. By taking into account the attachment/detachment and hydrolysis of tubulin dimers, the deformation of protofilaments, and the rupture/formation of lateral bonds between them, the authors show the model is computationally efficient to capture repeated catastrophes and rescues at realistic tubulin concentrations and hydrolysis rates, as well as gain insight into microscopic structural features triggering these events.

The paper by Chen et al. discusses the organization of F-actin and viscoelasticity distribution in migrating cells in response to pH changes in the microenvironment. In particular, by using multifrequency atomic force microscopy (AFM) with amplitude modulation-frequency modulation (AM–FM), the authors show that, unlike the randomly distributed F-actin and the homogeneous viscoelasticity at the normal pH level, living Huh-7 cancer cells with the reduced pH level of 6.5 exhibits highly oriented and organized F-actin along the lamellipodium direction coupled with a spatial gradient both in elasticity and viscosity of the cell.

The paper by Castaneda et al. reviews recent progress on understanding how different environmental factors contribute to actin bundle assembly, organization, and mechanics. Specifically, the effects of macromolecular crowding, cation interactions, and actin-crosslinking proteins on F-actin bundling, higher-ordered structure formation, and mechanical response of the resulting network are discussed in detail.

The paper by Leong et al. presents coarse-grained molecular dynamics models of spike proteins in SARS-CoV-2 coronavirus and angiotensin-converting enzyme 2 (ACE2) receptor proteins to study the endocytosis of the virus under physiologically relevant spatial and temporal scales. The coarse-grained molecular simulations show that, during their interaction with the ACE2 receptors, the spike proteins adopt bent configurations because of their unique flexibility, which facilitates their attachment to the host cell membrane, compared with rigid spikes.

The paper by Mierke reviews the current understanding of the bidirectional mechanical interplay between cells and their microenvironment. Specifically, it points out how, on the one hand, the intracellular cytoskeletal architecture and, on the other hand, the matrix architecture contribute to cellular stiffness or contractility and thereby determines the emergence of a distinct migration mode of cells. In addition, it also discusses whether universal hallmarks of the migratory phenotype can be defined.

The paper by Strychalski presents a 3D dynamic computational model for describing cell blebbing where membrane locally detaches from the actin cortex, resulting in a pressure-driven flow of the cytosol and membrane expansion. In particular, bleb expansion dynamics under different initiation mechanisms are analyzed. Furthermore, the author also discusses the influence of treating the cytoplasm as a viscous fluid or as a poroelastic material on blebs' shape and growing speed.

AUTHOR CONTRIBUTIONS

This Editorial was prepared jointly by YLin and YLi.

REFERENCES

1. Alberts B. *Molecular Biology of the Cell*. 4th ed. New York: Garland Science (2002).
2. Fletcher DA, Mullins RD. Cell Mechanics and the Cytoskeleton. *Nature* (2010) 463:485–92. doi:10.1038/nature08908
3. Theriot JA, Mitchison TJ. Actin Microfilament Dynamics in Locomoting Cells. *Nature* (1991) 352:126–31. doi:10.1038/352126a0
4. Lin Y, Shenoy VB, Hu B, Bai L. A Microscopic Formulation for the Actin-Driven Motion of Listeria in Curved Paths. *Biophysical J* (2010) 99:1043–52. doi:10.1016/j.bpj.2010.06.001
5. Mogilner A, Oster G. Force Generation by Actin Polymerization II: The Elastic Ratchet and Tethered Filaments. *Biophysical J* (2003) 84:1591–605. doi:10.1016/s0006-3495(03)74969-8
6. Lin Y. Mechanics Model for Actin-Based Motility. *Phys Rev E Stat Nonlin Soft Matter Phys* (2009) 79:021916. doi:10.1103/PhysRevE.79.021916
7. Heng Y-W, Koh C-G. Actin Cytoskeleton Dynamics and the Cell Division Cycle. *Int J Biochem Cel Biol* (2010) 42:1622–33. doi:10.1016/j.biocel.2010.04.007
8. Brust-Mascher I, Civelekoglu-Scholey G, Kwon M, Mogilner A, Scholey JM. Model for Anaphase B: Role of Three Mitotic Motors in a Switch from Poleward Flux to Spindle Elongation. *Proc Natl Acad Sci* (2004) 101:15938–43. doi:10.1073/pnas.0407044101
9. Lardennois A, Pásti G, Ferraro T, Llense F, Mahou P, Pontabry J, et al. An Actin-Based Viscoplastic Lock Ensures Progressive Body-axis Elongation. *Nature* (2019) 573:266–70. doi:10.1038/s41586-019-1509-4
10. Fang C, Wei X, Shao X, Lin Y. Force-mediated Cellular Anisotropy and Plasticity Dictate the Elongation Dynamics of Embryos. *Sci Adv* (2021) 7:eabg3264. doi:10.1126/sciadv.abg3264
11. Humphrey JD, Dufresne ER, Schwartz MA. Mechanotransduction and Extracellular Matrix Homeostasis. *Nat Rev Mol Cel Biol* (2014) 15:802–12. doi:10.1038/nrm3896
12. Engler AJ, Sen S, Sweeney HL, Discher DE. Matrix Elasticity Directs Stem Cell Lineage Specification. *Cell* (2006) 126:677–89. doi:10.1016/j.cell.2006.06.044
13. Hui TH, Kwan KW, Chun Yip TT, Fong HW, Ngan KC, Yu M, et al. Regulating the Membrane Transport Activity and Death of Cells via Electroosmotic Manipulation. *Biophysical J* (2016) 110:2769–78. doi:10.1016/j.bpj.2016.05.011
14. Yellin F, Li Y, Sreenivasan VKA, Farrell B, Johny MB, Yue D, et al. Electromechanics and Volume Dynamics in Nonexcitable Tissue Cells. *Biophysical J* (2018) 114:2231–42. doi:10.1016/j.bpj.2018.03.033
15. Evans E, Heinrich V, Ludwig F, Rawicz W. Dynamic Tension Spectroscopy and Strength of Biomembranes. *Biophysical J* (2003) 85:2342–50. doi:10.1016/s0006-3495(03)74658-x
16. Lin Y, Wei X, Qian J, Sze KY, Shenoy VB. A Combined Finite Element-Langevin Dynamics (FEM-LD) Approach for Analyzing the Mechanical Response of Bio-Polymer Networks. *J Mech Phys Sol* (2014) 62:2–18. doi:10.1016/j.jmps.2013.06.006
17. Onck PR, Koeman T, van Dillen T, van der Giessen E. Alternative Explanation of Stiffening in Cross-Linked Semiflexible Networks. *Phys Rev Lett* (2005) 95:178102. doi:10.1103/physrevlett.95.178102

18. Wei X, Zhu Q, Qian J, Lin Y, Shenoy VB. Response of Biopolymer Networks Governed by the Physical Properties of Cross-Linking Molecules. *Soft Matter* (2016) 12:2537–41. doi:10.1039/c5sm02820e
19. Cross SE, Jin Y-S, Rao J, Gimzewski JK. Nanomechanical Analysis of Cells from Cancer Patients. *Nat Nanotech* (2007) 2:780–3. doi:10.1038/nnano.2007.388
20. Suresh S, Spatz J, Mills JP, Micoulet A, Dao M, Lim CT, et al. Connections between Single-Cell Biomechanics and Human Disease States: Gastrointestinal Cancer and Malaria. *Acta Biomater* (2005) 1:15–30. doi:10.1016/j.actbio.2004.09.001

Conflict of Interest: The authors declare that the research was conducted in the absence of any commercial or financial relationships that could be construed as a potential conflict of interest.

Publisher's Note: All claims expressed in this article are solely those of the authors and do not necessarily represent those of their affiliated organizations, or those of the publisher, the editors and the reviewers. Any product that may be evaluated in this article, or claim that may be made by its manufacturer, is not guaranteed or endorsed by the publisher.

frontiers in Molecular Biosciences

ORIGINAL RESEARCH
published: 29 September 2020
doi: 10.3389/fmolb.2020.582257

Application of Force to a Syndecan-4 Containing Complex With Thy-1–$\alpha_V\beta_3$ Integrin Accelerates Neurite Retraction

*Francesca Burgos-Bravo[1,2,3], Samuel Martínez-Meza[1,2], Andrew F. G. Quest[1,2], Christian A. M. Wilson[3] and Lisette Leyton[1,2]**

[1] Laboratory of Cellular Communication, Center for Studies on Exercise, Metabolism and Cancer, Institute of Biomedical Sciences, Santiago, Chile, [2] Advanced Center for Chronic Diseases, Facultad de Medicina, Universidad de Chile, Santiago, Chile, [3] Single Molecule Biochemistry and Mechanobiology Laboratory, Department of Biochemistry and Molecular Biology, Facultad de Ciencias Químicas y Farmacéuticas, Universidad de Chile, Santiago, Chile

OPEN ACCESS

Edited by:
Yuan Lin,
The University of Hong Kong,
Hong Kong

Reviewed by:
Xueying Shao,
The University of Hong Kong,
Hong Kong
Kyle Miller,
Michigan State University,
United States

***Correspondence:**
Lisette Leyton
lleyton@med.uchile.cl;
lisetteleyton@gmail.com

Specialty section:
This article was submitted to Biophysics, a section of the journal Frontiers in Molecular Biosciences

Received: 11 July 2020
Accepted: 25 August 2020
Published: 29 September 2020

Citation:
Burgos-Bravo F, Martínez-Meza S, Quest AFG, Wilson CAM and Leyton L (2020) Application of Force to a Syndecan-4 Containing Complex With Thy-1–$\alpha_V\beta_3$ Integrin Accelerates Neurite Retraction. Front. Mol. Biosci. 7:582257. doi: 10.3389/fmolb.2020.582257

Inflammation contributes to the genesis and progression of chronic diseases, such as cancer and neurodegeneration. Upregulation of integrins in astrocytes during inflammation induces neurite retraction by binding to the neuronal protein Thy-1, also known as CD90. Additionally, Thy-1 alters astrocyte contractility and movement by binding to the mechano-sensors $\alpha_V\beta_3$ integrin and Syndecan-4. However, the contribution of Syndecan-4 to neurite shortening following Thy-1–$\alpha_V\beta_3$ integrin interaction remains unknown. To further characterize the contribution of Syndecan-4 in Thy-1-dependent neurite outgrowth inhibition and neurite retraction, cell-based assays under pro-inflammatory conditions were performed. In addition, using Optical Tweezers, we studied single-molecule binding properties between these proteins, and their mechanical responses. Syndecan-4 increased the lifetime of Thy-1–$\alpha_V\beta_3$ integrin binding by interacting directly with Thy-1 and forming a ternary complex (Thy-1–$\alpha_V\beta_3$ integrin + Syndecan-4). Under *in vitro*-generated pro-inflammatory conditions, Syndecan-4 accelerated the effect of integrin–engaged Thy-1 by forming this ternary complex, leading to faster neurite retraction and the inhibition of neurite outgrowth. Thus, Syndecan-4 controls neurite cytoskeleton contractility by modulating $\alpha_V\beta_3$ integrin mechano-receptor function. These results suggest that mechano-transduction, cell-matrix and cell-cell interactions are likely critical events in inflammation-related disease development.

Keywords: cell–cell adhesion, single-molecule analysis, trimolecular adhesion complex, mechano-sensor, mechano-transduction, inflammation, cell adhesion molecules

Abbreviations: bFGF, basic fibroblast growth factor; CAD, Cath.a-differentiated; CNS, central nervous system; CSPG, chondroitin sulfate proteoglycans; FA, focal adhesions; FGFR, fibroblast growth factor receptor; Hase III, heparitinase III; HBD, heparan binding domain; Hep, heparin; HS, heparan sulfate; HSPG, heparan sulfate proteoglycans; pN, piconewton; TMB, 3,3′,5,5′-tetramethylbenzidine; TNF, tumor necrosis factor.

INTRODUCTION

Cell–cell adhesion is initiated by the interaction in "trans" of membrane receptors located on opposing cell surfaces. An example of such heterophilic interactions is that mediated by the glycosyl-phosphatidylinositol (GPI)-anchored adhesion protein Thy-1 (expressed on many cells including neurons, fibroblasts, thymocytes and cancer cells) with integrins, such as $\alpha_V\beta_3$ on astrocyte and $\alpha_5\beta_1$ on human melanoma cells (Herrera-Molina et al., 2013). These transmembrane mechano-receptors are well known to connect extracellular matrix ligands to the cytoskeleton to promote cell adhesion, contractility, and migration. However, association also occurs between oligomerized, preassembled Thy-1 complexes and integrin clusters located on adjacent cell surfaces (Hagood, 2019; Leyton et al., 2019). For example, under inflammatory conditions in the CNS, $\alpha_V\beta_3$ integrin clustering, and the intracellular signaling cascade initiated in astrocytes by neuronal Thy-1 binding, leads to the assembly of focal adhesions (FA) and cell motility (Kong et al., 2013; Lagos-Cabré et al., 2017). Alternatively, $\alpha_V\beta_3$ integrin binding to Thy-1 complexes on an adjacent cell (the neuron), triggers neurite retraction or inhibition of neurite outgrowth (Herrera-Molina et al., 2012; Maldonado et al., 2017). Another example is the binding of melanoma integrins to the Thy-1-expressing cytokine-activated endothelium, which increases endothelial cell contractility (Schubert et al., 2013). In this case, cell contraction results in extravasation of cancer cells through the blood vessel wall, an important event for establishing secondary tumors (Bendas and Borsig, 2012). These examples underscore the importance of studying the effect of forces generated by alterations in cytoskeletal tension on the cell responses mediated by Thy-1–integrin association.

Bonds supporting protein-protein interactions respond to mechanical forces in three manners, force might (i) accelerate bond dissociation (slip bond); (ii) slow down dissociation (catch bond); or (iii) maintain bond lifetime (ideal bond) (Dembo et al., 1988; Zhu, 2014). Molecular force spectroscopy is a technique employed to characterize the effect of force on these interactions, and is used to obtain information concerning bond strength, the energy landscape of the dissociation process and the lifetime of bimolecular interactions (Yuan et al., 2000; Stangner et al., 2013).

In a recent study, binding of Thy-1-coated beads to the purified $\alpha_5\beta_1$ integrin ectodomain was shown to exhibit a slip bond behavior (non-stiffening bond). Additionally, when the Thy-1-beads were challenged with $\alpha_5\beta_1$ integrin expressed in K562 cells, a "dynamic catch" behavior was observed, that is the slip bond changed to a catch bond (stiff bond) and then reverted back to slip bond behavior, as the force applied increased (Fiore et al., 2014). In these experiments, antibodies against $\alpha_5\beta_1$ integrin only partially blocked the interactions, suggesting the participation of other adhesive components in the bead-cell model. This led to the discovery of the heparan sulfate proteoglycan Syndecan-4 as the missing protein component that, by forming a tri-molecular complex with Thy-1 and the integrin, changes the stiffness of the bonds involved under mechanical stimulation.

Interestingly, the bi-directional signaling described by our group studying neuron-astrocyte interactions under pro-inflammatory conditions, induced for instance by traumatic brain injury or neurodegenerative diseases was shown to require similar components. That is, Thy-1 binding to $\alpha_V\beta_3$ integrin in astrocytes requires Syndecan-4 to induce FA turnover and forward cell motility in reactive astrocytes (Avalos et al., 2009; Kong et al., 2013). Thy-1-stimulated astrocyte migration is an essential response of this glial cell to reach and repair the damage zone (Lagos-Cabré et al., 2017). Alternatively, $\alpha_V\beta_3$ integrin binding to Thy-1 on neurons leads to neurite retraction (Herrera-Molina et al., 2012; Maldonado et al., 2017), an early response of axons to injury required to remove at a small-scale damaged axonal connections, to stabilize the affected neuronal network and to initiate the repairing processes (Houle and Tessler, 2003; Luo and O'Leary, 2005). However, a role for Syndecan-4 in the $\alpha_V\beta_3$ integrin-induced alteration of the neuronal actin-myosin cytoskeleton has not been reported.

Thus, the physical properties and the biological significance underlying the formation of the tri-molecular complex in neuron-astrocyte interactions were studied. To this end, bond behavior under force was analyzed using optical miniTweezers in combination with various cell-based assays. Here, we report that Thy-1–$\alpha_V\beta_3$ integrin binding, and the neuronal responses elicited downstream of this interaction are modulated by Syndecan-4 association. In addition, and contrary to the dynamic catch model previously reported (Fiore et al., 2014), we found that Syndecan-4 does not change the slip bond properties of the Thy-1–$\alpha_V\beta_3$ integrin interaction, but rather stabilizes the interaction between these two proteins, thereby potentiating the integrin effect in neurons. Importantly, only reactive astrocytes induced these outcomes in neurons, suggesting that inflammatory conditions are required to favor the ternary complex formation. These studies yield important insights to how inflammation affects neuronal architecture inducing changes in mechano-transduction that will contribute to neurodegeneration.

MATERIALS AND METHODS

Antibodies and Reagents

Immunoblot analysis of astrocyte cell lysates was performed using antibodies, including anti-β_3 integrin (AB2984; Millipore), anti-Δ-heparan sulfate (3G10; Seikagaku), anti β actin (A5060; Sigma-Aldrich), and secondary horseradish peroxidase-conjugated goat anti-mouse (074-1806) or anti-rabbit (074-1516) IgG polyclonal secondary antibodies from KPL. Anti-Syndecan-4 (sc-12766; Santa Cruz) was used to detect the recombinant Syndecan-4-Fc. Goat polyclonal antibody anti-rat β_3 integrin (sc-6627; Santa Cruz) and rabbit polyclonal anti-rat β_1 integrin (sc-8978; Santa Cruz) were used as blocking antibodies in the co-culture assays. Reagents used in this work were: Heparin (H-3400; Sigma-Aldrich), Heparitinase III from *Flavobacterium heparinum* EC 4.2.2.8 (H-8891; Sigma-Aldrich), Cell TrackerTM Green 5-chloromethyl fluorescein diacetate dye

(C2925; Invitrogen) for monitoring living cells. The cell Line Nucleofector Kit (VCA-1003; Lonza) was used to transfect the astrocytes in the Nucleofector Device, X-treme GENE HP DNA Transfection Reagent (06-366 244 01; Roche) for HEK293T cell transfection, 1-Step Ultra TMB (3,3′,5,5′-tetramethylbenzidine) ELISA substrate (34028; Thermo Scientific), recombinant human bFGF protein (PH-G0266; Gibco), bovine serum albumin fraction V protease- and immunoglobulin-free (BSA-50; Rockland), protein A-sepharose from *Staphylococcus aureus* (P-3391; Sigma) and protein G-polystyrene beads (3.1 and 2.1 μm; Spherotech).

Cell Cultures

CAD cells (Cath.a-differentiated) were used as a neuronal model to study neuronal process outgrowth (Qi et al., 1997; Li et al., 2007). CAD cells were grown in DMEM/F12 medium (Gibco, United States) supplemented with 8% of fetal bovine serum (FBS HyClone, Canada) and morphological and functional differentiation of CAD cells was induced by serum deprivation for 24 h in DMEM/F12 supplemented with 50 ng/ml of sodium selenite (S5261; Sigma-Aldrich) as reported (Herrera-Molina et al., 2012). The astrocyte cell line DITNC1 was maintained in RPMI 1640 medium (Gibco) with 5% FBS (HyClone, United States) and 0.1 mM 2-mercaptoethanol (Gibco). Primary astrocytes were derived from mixed glial cell cultures recovered from cortices of 2-day-old rats (P2) (bioethical protocol approved by the biothical committe of the Universidad de Chile) and cultured with DMEM/F12 medium supplemented with 10% FBS (Biological Industries) as previously described (Lagos-Cabré et al., 2017). HEK293T cells used to produce recombinant $\alpha_V\beta_3$-Fc and Syndecan-4-Fc proteins were grown in DMEM/High-glucose medium supplemented with 10% FBS (Hyclone, Canada). All cells were maintained with 1% penicillin-streptomycin solution on standard tissue culture dishes in a humidified atmosphere of 5% CO_2 and 37°C.

Recombinant Fc-Tagged Proteins

Purified Thy-1-Fc wild-type, Thy-1(RLE)-Fc mutant for the integrin-binding site, Thy-1(AEAAA)-Fc mutant for the HBD, as well as human TRAIL-R2-Fc fusion proteins were obtained as previously reported (Schneider, 2000; Leyton et al., 2001). Recombinant $\alpha_V\beta_3$-Fc integrin, possessing the ectodomain of the heterodimeric protein and the Fc portion of the human immunoglobulin IgG1, was secreted into serum-free cell culture media of transiently transfected HEK293T cells and purified as previously published (Burgos-Bravo et al., 2018). A similar experimental strategy was used to produce the Fc-tagged protein of Syndecan-4 (Syndecan-4-Fc), where the extracellular domain of the human proteoglycan at the C terminus was fused to the Fc tag. Here, HEK293T cells were transfected with the Syndecan-4-Fc expression plasmid using the X-treme GENE HP DNA transfection reagent according to the manufacturer's instructions (Roche). After 2 days in culture, serum-free medium containing soluble Syndecan-4-Fc was recovered, filtered and stored at -20°C. Commercially purified human Syndecan (ectodomain)-4-Fc was used for optical tweezers experiments.

Characterization of Syndecan-4-Fc Functionality

HS chains on the recombinant Syndecan-4-Fc protein were characterized by the electrophoretic mobility of Syndecan-4-Fc after treatment with Heparitinase (Hase III), which removes the HS chains from the core protein. Syndecan-4-Fc was first precipitated from the serum-free medium obtained from HEK293T transfected cells, by incubating for 1 h at 4°C, with an excess of protein A-sepharose beads. Then, the solution was centrifuged (3000 $g \times 5$ min) and the precipitate contained the Syndecan-4-Fc protein (Precipitated; **Figure 2B**), while the medium was depleted of the fusion protein (Depleted; **Figure 2B**). All samples were digested for 3 h at 37°C with 0.5 mU Hase III and resuspended in the digestion buffer (20 mM Tris-HCl, pH 7.4 containing 50 mM NaCl and 2 mM $CaCl_2$). As controls, undigested samples were also prepared by incubating them only with the digestion buffer. Samples were then boiled for 5 min in Laemmli buffer (2% SDS, 10% Glycerol, 62.5 mM Tris-HCl, pH 6.8, 5% β-mercaptoethanol and 0.01% bromophenol blue), separated by 10% SDS-PAGE gels, transferred onto nitrocellulose membrane (Millipore) and blocked in 5% w/v non-fat, dry milk in TBS containing 0.1% Tween-20. Immunoblots were analyzed by incubation of membranes with anti-Syndecan-4 antibodies (1:2000, Santa Cruz) for 1 h at room temperature. Membranes were then washed and incubated with horseradish peroxidase-conjugated goat anti-mouse IgG (1:3000, KPL) for 1 h at room temperature. The peroxidase activity was revealed with a chemiluminescence kit (Pierce, Thermo Scientific). The functionality of Syndecan-4-Fc was tested by enzyme-linked immunosorbent assay (ELISA). First, bFGF (1 μg/ml) or BSA (1 μg/ml; control) were immobilized overnight in a 96-well plate (Maxisorp, Nunc) at 4°C. Then, serum-free medium containing Syndecan-4-Fc protein as well as TRAIL-R2-Fc protein (Fc-tagged protein control) were added to wells and incubated for 2 h at 37°C. To detect Syndecan-4-Fc/bFGF binding, HRP-coupled goat anti-human IgG1 antibodies and the chromogenic TMB substrate were used according to manufacturer's instructions (Thermo Scientific).

Neurite Outgrowth Assay

DITNC1 cells (5×10^5 cells/cm^2) or primary astrocytes (3×10^5 cells/cm^2) were seeded and grown to 90% confluency on 8-well glass bottom plates. To induce a pro-inflammatory environment, rat primary astrocytes were stimulated with 10 ng/ml of TNF for 48 h. Astrocyte monolayers were treated with Hase III (0.5 mU) for 3 h at 37°C in serum-free medium to study whether heparin sulfate chains were involved in neurite outgrowth inhibition. In other experiments, astrocyte Syndecan-4 was silenced using siRNA against exons 3 and 4, as reported (Avalos et al., 2009). Control siRNA (siCTRL) was used to confirm specificity. Astrocytes were fixed with 4% p-formaldehyde for 30 min at room temperature and washed with abundant PBS containing 5 mM glycine. Then, fixed monolayers were incubated with anti-β_3 integrin antibody (5 μg/ml) during 1 h at 37°C to block β_3 or β_1-containing heterodimeric integrins in the astrocyte surface, respectively. Next, cell tracker green-labeled CAD cells

(5×10^4 cells/cm^2) were added to the astrocyte monolayer and maintained in co-culture for 24 h. In some experiments, CAD cells were pre-incubated with Heparin (400 μg/ml) for 30 min at room temperature to block astrocyte surface HS chain binding. The next day, cells were washed with PBS and morphological differentiation of CAD cells (i.e., neurite outgrowth) was induced in serum-free medium for 24 h. Images of living cells were acquired using a FV10i confocal microscope (Olympus Corp., Tokyo, Japan) equipped with UPLSAPO 60X/1.35 water immersion objective. CAD cells were analyzed using NeuronJ plug-in for ImageJ software as was previously reported (Herrera-Molina et al., 2012; Maldonado et al., 2017). The length of processes was measured and expressed in μm. CAD cells were considered morphologically differentiated when presenting at least one neurite longer or equal to 15 μm. The number of varicosities per neuronal process was also used to characterize differentiated CAD cells.

Neurite Retraction Assay

CAD cells (5×10^4 cells/cm^2) were seeded in 24-well plastic plates and grown in serum-containing DMEME/F12 medium overnight to reach 60% confluency. Then, morphological differentiation was induced in serum-free medium for 24 h as indicated before. CAD cells with established neurites (i.e., with neuronal processes) were incubated with serum-free medium containing $\alpha_V\beta_3$-Fc integrin (one tenth of the total volume), in the absence or presence of different volumes of Syndecan-4-Fc-containing medium at 37°C. Control cells were incubated with Fc-tagged depleted medium, which was obtained by overnight incubation with an excess of protein A-sepharose beads. In other experiments, medium-containing $\alpha_V\beta_3$-Fc protein was pre-incubated with Protein-A (2 μg) and added to morphologically differentiated CAD cells. Neurite length changes were recorded after 5, 10, 20, and 40 min of exposure to Syndecan-4-Fc and/or $\alpha_V\beta_3$-Fc-containing supernatant using a Disk Scanning Unit-IX81 Spinning disk confocal microscope (Olympus Corp.). The neuronJ plug-in was used to quantify neurite length over time.

Immunoblotting Analysis

For immunoblot analysis of DITNC1 cells or primary astrocytes, cells were washed with ice-cold PBS and lysed with ice-cold lysis buffer (150 mM NaCl, 0.1% SDS, 0.25% sodium deoxycholate,1% Triton-X100, in 50 mM Tris-HCl pH, 7.0) supplemented with protease and phosphatase inhibitors (1 mM sodium orthovanadate, 2 μg/ml antipain, 1 μg/ml leupeptin, 10 μg/ml benzamidine and 1 mM PMSF). Protein extracts (30 μg) were mixed with Laemmli buffer, boiled for 5 min, electrophoretically separated on 10% SDS-PAGE and transferred to nitrocellulose membranes (Millipore). For Syndecan-4 detection, protein extracts were first digested with Heparitinase III (0.5 mU) for 3 h at 37°C and then mixed with Laemmli buffer. The membranes were blocked with TBS-T 5% fat-free milk and subsequently incubated with anti-Δ-heparan sulfate (1:2500; Seikagaku), anti-β_3 integrin (1:3000; Millipore), or anti-β-actin (1:3000; Sigma-Aldrich) antibodies for 1 h at room temperature, followed by the appropriate horseradish peroxidase-conjugated secondary antibodies. In all cases, peroxidase activity was revealed with the chemiluminescence kit (Pierce, Thermo Scientific). Immunoblot quantification was performed by measuring band intensity using ImageJ software and normalized to the loading control (β actin).

Optical Tweezers and Force Measurement Protocols

To characterize the mechanical properties of the Thy-1-dependent interactions, a miniTweezers device was used as a single-molecule force transducer instrument (Smith et al., 2003), using a stiffness of 0.1 pN/nm. All binding experiments were performed in Hepes buffer (10 mM Hepes, pH 7.4) containing 100 mM NaCl and 1 mM $MgCl_2$ at 25°C, using a microchamber with a glass micropipette as reported (Burgos-Bravo et al., 2018). Protein G-coated polystyrene beads were used to attach the Fc-tagged proteins at a femtomolar concentration (description in **Figure 1A**). In order to characterize the rupture forces required to dissociate the Thy-1-Fc-dependent interactions and determine the adhesion frequency between Thy-1-Fc (wild-type and mutants) and Syndecan-4-Fc, a force-ramp assay was performed pulling the optically trapped bead at a constant force-loading rate (10 pN/s) as described (Burgos-Bravo et al., 2018). The rupture force histograms were obtained with at least 120 binding events per four pairs of freshly prepared beads and normalized for the total number of approaching-retraction cycles (i.e., when both protein-coated beads are put in contact to promote the protein-protein interaction and then are separated at a constant rate to dissociate the binding). These histograms contain rupture forces associated to non-specific binding events of Thy-1-Fc (**Figure 1B**, Thy-1/buffer condition), however, for comparison studies, we assumed that these non-specific interactions of lower affinity were affecting each histogram in similar magnitude, mainly in the low range of force values. The bin size was calculated using Scott's rule (Scott, 1979). For the adhesion frequency assay, events with and without binding were characterized to calculate an adhesion frequency in at least 50 approach-retraction cycles carried out per 4–5 pairs of different beads. The lifetime of each bond (Thy-1-Fc–Syndecan-4-Fc, Thy-1-Fc–$\alpha_V\beta_3$-Fc or Thy-1–$\alpha_V\beta_3$-Fc + Syndecan-4-Fc) was determined using the constant-force assay, in which the optically trapped bead is placed in close proximity of the other bead to promote bond formation and then quickly subjected to a ramp force (<1 s) at a constant value (constant forces applied here were: 10, 20, 30, 40, and 50 pN) until the interaction is dissociated. The bond lifetime was measured as the time from when the force reached the desired level until the instant the binding was disrupted (**Figure 1C**). At each constant force condition, a collection of lifetime data was obtained and plotted as a function of the constant force. The Bell model:

$$\tau\,(F) = \tau^0 e^{\left(\frac{x^{\ddagger}F}{k_B T}\right)}$$

was used to describe the effect of force on bond lifetime, where τ^0 is the lifetime in the absence of force, $x^{\ddagger}$ is the distance to the transition state, F is the force applied to the bond, k_B is the Boltzmann′s constant, and T is the absolute temperature. The Bell model predicts that the time that both proteins interact

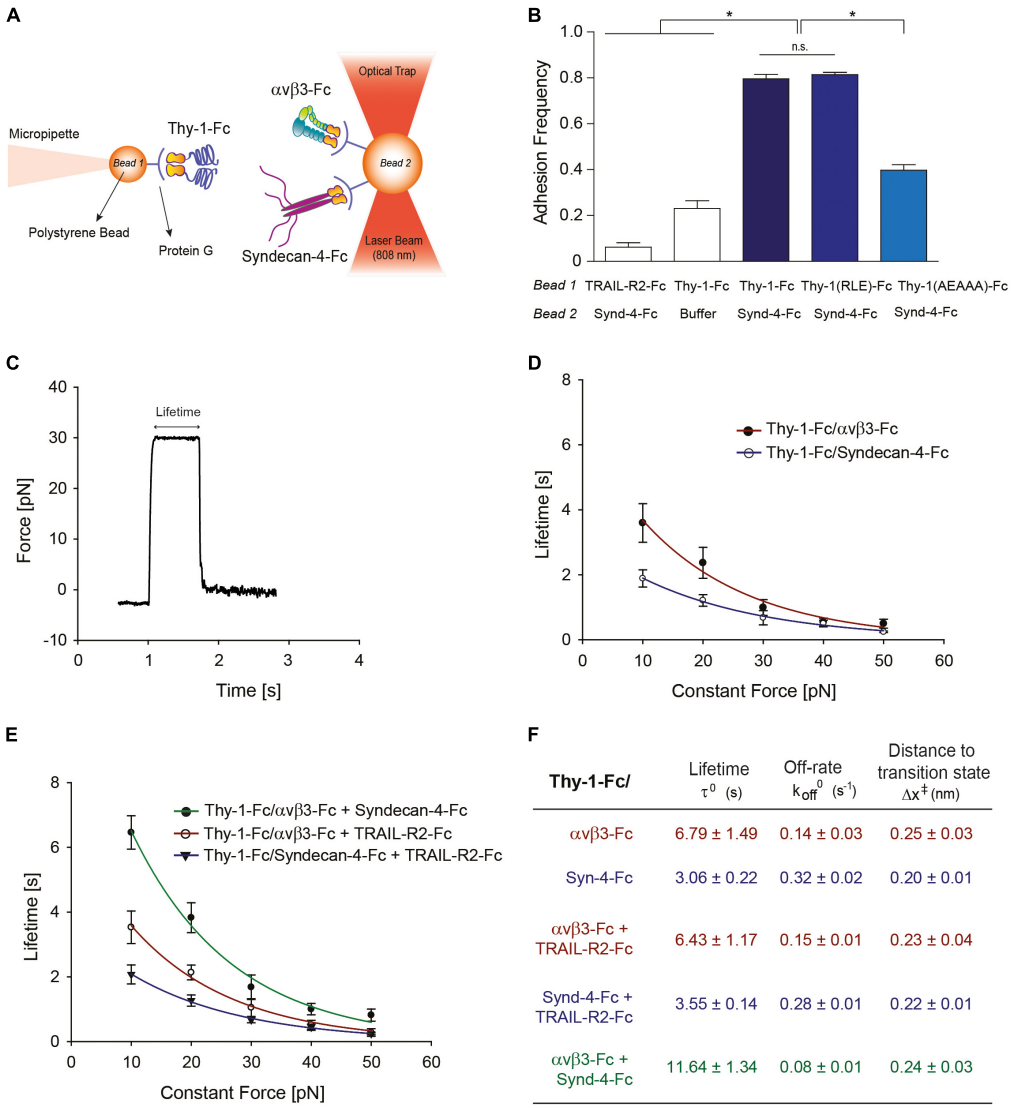

F

Thy-1-Fc/	Lifetime τ^0 (s)	Off-rate k_{off}^0 (s^{-1})	Distance to transition state $\Delta x^{\ddagger}$ (nm)
αvβ3-Fc	6.79 ± 1.49	0.14 ± 0.03	0.25 ± 0.03
Syn-4-Fc	3.06 ± 0.22	0.32 ± 0.02	0.20 ± 0.01
αvβ3-Fc + TRAIL-R2-Fc	6.43 ± 1.17	0.15 ± 0.01	0.23 ± 0.04
Synd-4-Fc + TRAIL-R2-Fc	3.55 ± 0.14	0.28 ± 0.01	0.22 ± 0.01
αvβ3-Fc + Synd-4-Fc	11.64 ± 1.34	0.08 ± 0.01	0.24 ± 0.03

FIGURE 1 | Characterization at the single-molecule level reveals that Syndecan-4 increases the lifetime of the Thy-1–$\alpha_V\beta_3$ integrin binding by forming a ternary complex. **(A)** Scheme of the assay using miniTweezers. Two different sizes of protein G-coated beads were used; the smaller bead (Bead 1; 2.1 μm) contained purified Thy-1-Fc and was attached to a micropipette by suction; the larger bead (Bead 2; 3.1 μm) containing the $\alpha_V\beta_3$-Fc, Syndecan-4-Fc or both molecules, was trapped by a laser beam and held in the focus of the microscope (Figure adapted from Burgos-Bravo et al., 2018. https://doi.org/10.1091/mbc.E17-03-0133). **(B)** Adhesion frequency of Syndecan-4 (Synd-4-Fc) with TRAIL-R2-Fc (control protein), wild-type Thy-1-Fc, Thy-1(RLE)-Fc mutated in the integrin binding-site, and Thy-1-(AEAAA)-Fc mutated in the heparin binding domain, was assessed using force-ramp assays at a loading rate of 10 pN/s. The total number of binding events in at least 50 approaching-retraction cycles per 4–5 pairs of beads were measured. Non-specific interactions were evaluated using Thy-1-Fc- and Hepes buffer-treated beads (Buffer). Data are expressed as the mean ± SEM (*$p < 0.05$; n.s. non-significant, assessed by Mann–Whitney's test). **(C)** Representative force-time trace obtained by force-constant assay at 30 pN between Thy-1-Fc and Syndecan-4-Fc. The force is ramped to and sustained at a constant force until the interaction is disrupted. **(D)** Lifetime of bi-molecular Thy-1-Fc interactions with Syndecan-4-Fc (Thy-1-Fc/Syndecan-4-Fc) or $\alpha_V\beta_3$-Fc integrin (Thy-1-Fc/$\alpha_V\beta_3$-Fc) as a function of the constant force. **(E)** Lifetime of tri-molecular Thy-1-Fc interactions with $\alpha_V\beta_3$-Fc integrin and Syndecan-4-Fc (Thy-1-Fc/$\alpha_V\beta_3$-Fc + Syndecan-4-Fc) plotted versus constant force. As a control for the tri-molecular interactions, lifetime data were evaluated for Thy-1-Fc binding with TRAIL-R2-Fc in the presence of Syndecan-4-Fc (Thy-1-Fc/Syndecan-4-Fc + TRAIL-R2-Fc) or $\alpha_V\beta_3$-Fc integrin (Thy-1-Fc/$\alpha_V\beta_3$-Fc + TRAIL-R2-Fc). Lifetime data plotted against constant forces were fitted to the Bell model (see Materials and Methods) to calculate the unbinding parameters at zero force for each interaction **(F)**, including lifetime (τ^0), off-rate constants (k_{off}^0; inversely related to the lifetime), and the distance to the transition state ($\Delta x^{\ddagger}$). Lifetime data in **(D,E)** are expressed as the mean ± SEM from at least 60 binding events obtained using 3 pairs of different beads. Force-ramp and constant-force results were analyzed by a Matlab program.

decreases exponentially with force (Bell, 1978) and was used due to non-deviation from linearity in the force-dependent lifetime plot. Both force-ramp and constant-force data were processed with Matlab using the "Tweezers Analysis" program developed by Jesse Dill in the laboratories of Carlos Bustamante and Susan Marqusee (Dill, 2012) to estimate rupture force values, lifetime and binding/non-binding event data for each condition evaluated.

Statistical Analysis

Data are expressed as the mean ± standard error of the mean (SEM) from $n = 3$ or more independent experiments. Results were compared by non-parametric unpaired, one-tailed Mann–Whitney analysis using GraphPad Prism 5 software, as was previously reported (Herrera-Molina et al., 2012; Maldonado et al., 2017). Statistical significance is indicated in each figure.

RESULTS

Characterization at the Single-Molecule Level Reveals that Syndecan-4 Increases the Lifetime of the Thy-1–$\alpha_V\beta_3$ Integrin Binding by Forming a Ternary Complex

Our prior results suggest the existence of a tri-molecular complex in the neuron-astrocyte cell-cell adhesion model, which involves Thy-1, Syndecan-4 and the $\alpha_V\beta_3$ integrin (Avalos et al., 2009; Kong et al., 2013). Considering that not only the $\alpha_V\beta_3$ integrin, but also Syndecan-4 acts as a mechano-receptor in other cells (Bellin et al., 2009), we first investigated the mechanical response of these Thy-1-dependent interactions either as bi-molecular binding between Thy-1–Syndecan-4 and Thy-1–$\alpha_V\beta_3$ integrin, or tri-molecular binding Thy-1–$\alpha_V\beta_3$ integrin + Syndecan-4. To this end, we purified Fc-tagged recombinant proteins and employed the optical miniTweezers instrument to characterize the interactions between fusion proteins by molecular force spectroscopy (**Figure 1A**).

We used optical tweezers experiments at a dilution that ensures detection of single binding events to obtain evidence for a direct interaction between Thy-1 and Syndecan-4 (Burgos-Bravo et al., 2018). The two fusion proteins were attached to different size polystyrene beads coated with protein G; Thy-1-Fc was bound to the smaller bead attached to a micropipette, while Syndecan-4-Fc was attached to the bigger bead trapped with a laser beam (**Figure 1A**). As we previously reported for the Thy-1–$\alpha_V\beta_3$ integrin interaction, the probability of adhesion between two proteins is estimated from the frequency of adhesion events in a sequence of approaching-retraction cycles between both beads (Burgos-Bravo et al., 2018). Therefore, we performed an adhesion frequency assay using the force-ramp strategy to study binding specificity. Higher adhesion frequencies of Syndecan-4 with Thy-1-Fc wild type [Thy-1(RLD)-Fc] compared to the control conditions with TRAIL-R2-Fc receptor (TRAIL-R2-Fc) or beads without proteins (Buffer) were observed (**Figure 1B**). TRAIL-R2-Fc is an Fc-tagged protein that serves as a negative control in all our functional assays (Maldonado et al., 2017; Lagos-Cabré et al., 2018).

The Thy-1-Fc mutated in the integrin-binding site [Thy-1(RLE)-Fc] (Hermosilla et al., 2008) showed a similar binding frequency as the wild type Thy-1, ruling out the participation of this domain in the interaction with Syndecan-4 (**Figure 1B**). Conversely, Thy-1-Fc mutated in the heparin-binding domain [HBD, Thy-1(AEAAA)-Fc] (Avalos et al., 2009; Kong et al., 2013) showed a lower binding frequency with Syndecan-4-Fc (**Figure 1B**). These results are consistent with the rupture force distribution profiles obtained for each individual interaction, where similar peak rupture forces for the interaction between Syndecan-4-Fc and both Thy-1-Fc wild type and Thy-1(RLE)-Fc were observed (**Supplementary Figures S1A,B**). As expected, a different rupture force histogram was obtained for the binding of the proteoglycan Syndecan-4 and Thy-1(AEAAA)-Fc mutated in the HBD (**Supplementary Figure S1C**). These results are indicative of a direct interaction between Syndecan-4 and Thy-1 and the involvement of the Thy-1 HBD in the binding between these two proteins.

A constant-force strategy was implemented with the optical tweezers to characterize the mechanical response of the Thy-1-dependent interactions. Here, once the beads are in contact, the force is quickly ramped to and held at a desired constant force until the interaction is disrupted. Thus, the bond lifetime is determined as the time that it takes to dissociate the bond at a given constant force (Marshall et al., 2003). A representative force-time trace obtained for the interaction between Thy-1-Fc and Syndecan-4-Fc is shown in **Figure 1C**. Using this methodology, we then measured the bond lifetime for each bi-molecular interaction (Thy-1-Fc–Syndecan-4-Fc and Thy-1-Fc–$\alpha_V\beta_3$-Fc; **Figure 1D**) and the tri-molecular interaction (Thy-1-Fc–$\alpha_V\beta_3$-Fc + Syndecan-4-Fc; **Figure 1E**) at different constant forces, between 10 and 50 pN, and plotted bond lifetime as a function of constant force. The lifetime data were then fitted by applying the Bell model (Bell, 1978) (see section Materials and Methods). As predicted by the Bell's equation, **Figure 1D** shows that force accelerates the dissociation of both bi-molecular interactions, indicative of slip bond behavior. These mechanical responses were corroborated by plotting the force-dependent lifetime data on a logarithmic scale (**Supplementary Figure S1D**). Using this model, we characterized the kinetic parameters of the unbinding process for each set of bi-molecular binding events in the absence of force (**Figure 1F**). A significant difference in the mechanical response is observed at forces lower than 10 pN, where the calculated bond lifetime values are lower for the interaction of Thy-1 with the proteoglycan Syndecan-4. The result suggests that this interaction is disrupted more rapidly than Thy-1–$\alpha_V\beta_3$ integrin binding at forces lower than 10 pN. The higher bond lifetime at zero force that was found for Thy-1–$\alpha_V\beta_3$ integrin binding ($\tau^0 = 6.79 \pm 1.49$ s) compared to that of Thy-1–Syndecan-4 ($\tau^0 = 3.06 \pm 0.22$ s) suggests that in the absence of mechanical forces, the Thy-1–$\alpha_V\beta_3$ integrin interaction is more stable than that of Thy-1–Syndecan-4. In addition, a similar distance to the transition state value was characterized for both interactions (∼0.2 nm; **Figure 1F**), suggesting that despite the differences found in the mechanical responses for each bi-molecular interaction, the nature of these bonds is similar.

We also studied the mechanical response of Thy-1-dependent binding in the presence of both astrocytic proteins, Syndecan-4 and $\alpha_V\beta_3$ integrin. As a control for binding specificity, we first evaluated the force-dependent lifetime in the presence of the TRAIL-R2-Fc protein (i.e., Thy-1-Fc–Syndecan-4-Fc + TRAIL-R2-Fc and Thy-1-Fc–$\alpha_V\beta_3$-Fc + TRAIL-R2-Fc; **Figure 1E**). Under these conditions, the mechanical response and the bond lifetime at zero force were similar to those characterized for each

bi-molecular Thy-1–$\alpha_V\beta_3$ and Thy-1–Syndecan-4 association (**Figure 1D**). These findings confirm that the mechanical response observed depends on the specific interaction mediated by Thy-1 and its ligands and not on the addition of another component to the system. Interestingly, when the constant-force assay was performed using Thy-1-Fc and $\alpha_V\beta_3$ integrin + Syndecan-4, we found that force accelerated the dissociation of these molecules (**Figure 1E** and **Supplementary Figure S1E**). However, at forces between 0 and 20 pN, the binding lifetime was higher for the tri-molecular complex than for the bi-molecular Thy-1-dependent interactions (**Figure 1E**). Similarly, the bond lifetime at zero force in the presence of $\alpha_V\beta_3$ integrin and Syndecan-4 increased to 11.64 ± 1.34 s (**Figure 1F**), when compared to those τ^0 values calculated for the bi-molecular binding. These results indicate that both astrocytic proteins, $\alpha_V\beta_3$ integrin and Syndecan-4, stabilize and enhance binding parameters of Thy-1-dependent interactions in the absence of force.

Syndecan-4 Accelerates Neurite Retraction Promoted by the $\alpha_V\beta_3$ Integrin

Our laboratory has shown that the Thy-1–$\alpha_V\beta_3$ integrin + Syndecan-4 association triggers signals in astrocytes to promote cell movement (Avalos et al., 2009; Kong et al., 2013). On the other hand, $\alpha_V\beta_3$ integrin binding to Thy-1 in neurons induces neurite retraction (Herrera-Molina et al., 2012; Maldonado et al., 2017). In the latter case, the integrin acts as a ligand rather than a receptor. Thus, we next determined whether the ternary Thy-1–$\alpha_V\beta_3$ + Syndecan-4 complex acts bi-directionally playing a role in both astrocyte migration and the contraction of the neuronal processes (**Figure 2A**).

To answer this question, we used Syndecan-4-Fc fusion protein obtained in the supernatant of transiently transfected HEK293T cells (i.e., serum-free medium containing Syndecan-4-Fc; see section "Materials and Methods"). First, we demonstrated the functionality of Syndecan-4-Fc protein: (1) the protein contains heparan sulfate chains as shown by Heparitinase treatment and immunoblot analysis (**Figure 2B**); (2) Syndecan-4-Fc binds to human basic Fibroblast Growth Factor (bFGF) in an ELISA (**Figure 2C**), as expected based on the reported existence of an interaction between bFGF and the heparan sulfate chains of Syndecan-4 (Allen et al., 2001; Horowitz et al., 2002). As a negative control, bFGF was incubated with a different Fc-tagged protein (TRAIL-R2-Fc). We observed an increment in the oxidation of the chromogenic substrate TMB, as compared to the other control conditions, when the supernatant containing Syndecan-4-Fc was incubated with bFGF (**Figure 2C**). These results are indicative of the presence of heparan sulfate chains with ligand binding properties in Syndecan-4-Fc.

We then tested the contribution of Syndecan-4-Fc to neurite retraction induced by $\alpha_V\beta_3$-Fc integrin. To this end, morphologically differentiated neuron-like CAD cells (i.e., CAD cells with at least 15 μm neuronal processes; see section "Materials and Methods") were incubated with serum-free HEK293T medium containing the two fusion proteins Syndecan-4-Fc and $\alpha_V\beta_3$-Fc. Then, morphological changes on CAD cells were recorded (**Supplementary Figure S2**) and neurite length was quantified (**Figure 2D**) as described in our previous publications (Herrera-Molina et al., 2012; Maldonado et al., 2017). Neurite retraction reportedly occurs after 20 min of incubation with $\alpha_V\beta_3$-Fc, and this effect is maintained for at least 40 min of stimulation with the integrin (Maldonado et al., 2017). Thus, the effect of $\alpha_V\beta_3$-Fc on neurite retraction in the presence of Syndecan-4-Fc at different time points (0–40 min) was tested. When differentiated CAD cells were incubated with Syndecan-4-Fc (inverted purple triangle), neurite length did not change over time (**Figure 2D** and **Supplementary Figure S2**). As expected, $\alpha_V\beta_3$-Fc (green circle) promoted a significant retraction of neurites at 20 and 40 min of incubation. Interestingly, when CAD cells were incubated with $\alpha_V\beta_3$-Fc and Syndecan-4-Fc (ratio 1:1), a significant reduction in neurite length was observed after 5 min (orange diamond) (**Figure 2D** and **Supplementary Figure S2**). One possibility to explain the accelerated neurite contraction is that Syndecan-4 might be facilitating the clustering of integrin and thus, of Thy-1. If this were the case, the addition of Protein A [Protein A favors cross-linking of the Fc-fusion proteins (Moks et al., 1986)] in the absence of Syndecan-4, should induce aggregation of $\alpha_V\beta_3$-Fc, and thus a similar response. Indeed, we observed that incubation of CAD cells with $\alpha_V\beta_3$-Fc pre-treated with Protein A induced neurite retraction after already 5 min (blue triangle, **Figure 2D**), thus accelerating the effect of $\alpha_V\beta_3$-Fc, just as observed when $\alpha_V\beta_3$-Fc and Syndecan-4-Fc were added together. We additionally tested the effect of the concentration of Syndecan-4 on the retraction process at 40 min of incubation, by adding $\alpha_V\beta_3$-Fc and Syndecan-4-Fc at different ratios to differentiated CAD cells. $\alpha_V\beta_3$-Fc in the absence of Syndecan-4-Fc induced a reduction in neurite length (green bar), compared to the condition without any fusion proteins (gray bar, **Figure 2E**). Interestingly, neurite retraction promoted by $\alpha_V\beta_3$-Fc integrin was not significantly modified by the addition of Syndecan-4-Fc at any dilution at this time point (purple bars, **Figure 2E**). These results agree with those shown in **Figure 2D**, where no differences in neurite retraction induced by $\alpha_V\beta_3$-Fc in the presence or absence of Syndecan-4-Fc were found at 40 min. Altogether, the results suggest that although Syndecan-4 interacts directly with Thy-1, recombinant Syndecan-4-Fc by itself has no effect on neuronal CAD cell extensions. However, Syndecan-4 increases the speed at which neurite retraction is promoted by $\alpha_V\beta_3$-Fc integrin, suggesting that the proteoglycan Syndecan-4 acts as a co-ligand for Thy-1.

The Inhibitory Effect of Astrocytes on Neurite Extension Requires Syndecan-4

We next evaluated whether the neuronal response triggered by $\alpha_V\beta_3$ integrin plus Syndecan-4 also occurs in cell-to-cell communication. As a control, neurite outgrowth was induced in CAD cells seeded in a tissue culture dish. Here, neurons extended processes longer than 60 μm (CAD/Plate) (**Figures 3A,B**). Such growth was largely inhibited (3-fold) when CAD cells were cultured over a monolayer of fixed DITNC1 astrocytes, which are known to express both $\alpha_V\beta_3$ integrin (Kong et al., 2013) and Syndecan-4 (Avalos et al., 2009) (CAD/DITNC1) (**Figures 3A,B**).

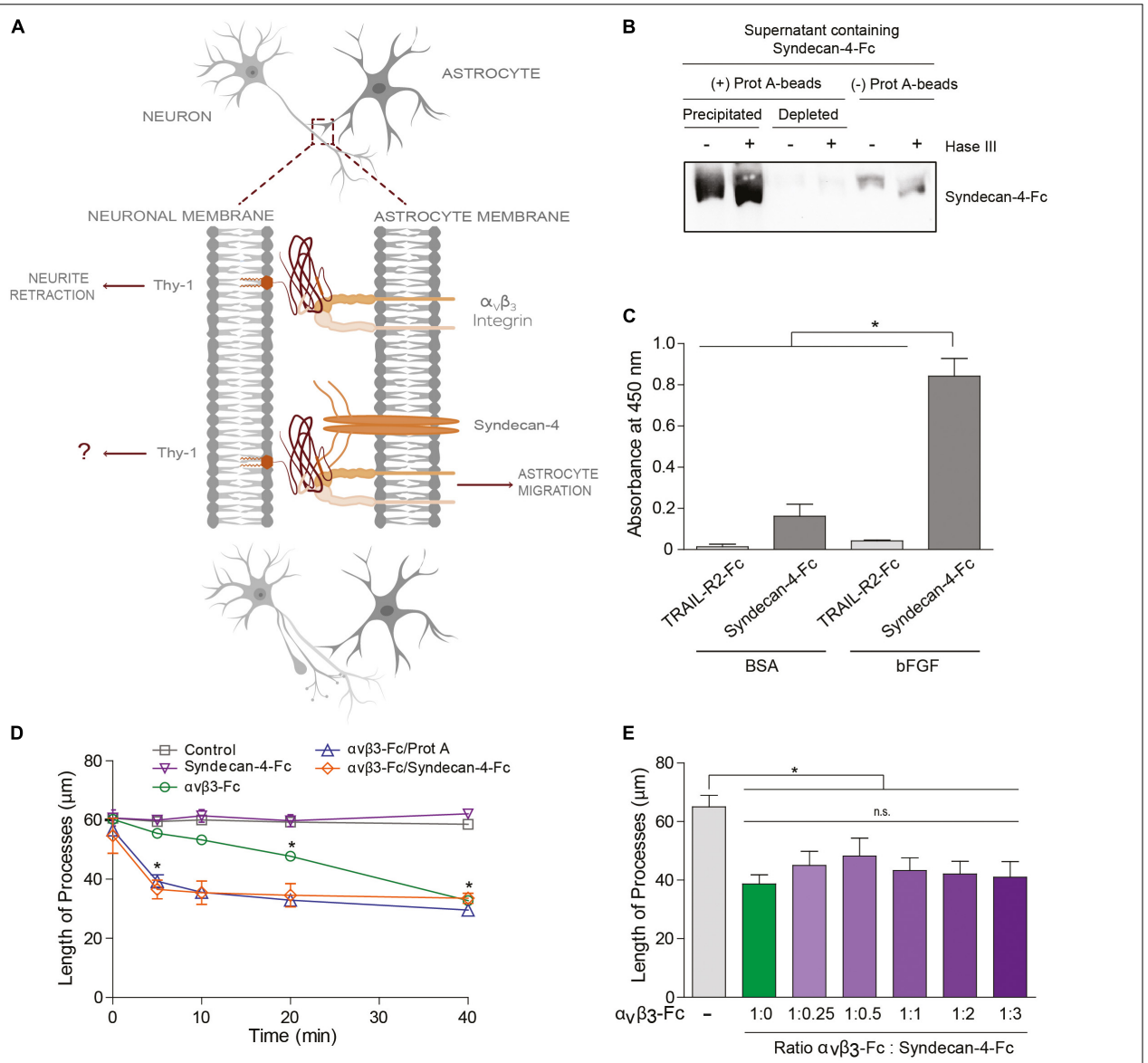

FIGURE 2 | Syndecan-4 accelerates neurite retraction promoted by the $\alpha_V\beta_3$ integrin. **(A)** Thy-1–$\alpha_V\beta_3$ integrin binding induces cell signaling events resulting in the retraction of neuronal processes. On the other hand, Thy-1–$\alpha_V\beta_3$ integrin + Syndecan-4 association promotes astrocyte migration. Here, the effect of Syndecan-4 on $\alpha_V\beta_3$ integrin-induced neurite retraction was tested. **(B)** Serum-free medium containing Syndecan-4-Fc fusion protein was incubated (+) or not (–) with an excess of protein-A-sepharose beads and then centrifuged to obtain a precipitated Syndecan-4-Fc-protein-A-sepharose complex and Syndecan-4-depleted supernatant, respectively. All these samples were treated (+) or not (–) with Heparitinase III, separated by SDS-PAGE and analyzed by immunoblotting with anti-Syndecan-4 antibodies. **(C)** A microplate coated with human bFGF (1 µg/ml) or BSA (1 µg/ml) was incubated with serum-free medium containing Syndecan-4-Fc or TRAIL-R2-Fc (control Fc-protein), followed by incubation with anti-Fc-HRP conjugated antibody. Specific binding was measured in a colorimetric method with TMB substrate solution (Absorbance at 450 nm). **(D)** Quantification of the neurite length of differentiated CAD cells (1×10^5 cells/cm^2) over a 24-well plate after 5, 10, 20, and 40 min of incubation with control medium (without fusion proteins), Syndecan-4-Fc or $\alpha_V\beta_3$-Fc in serum-free medium, $\alpha_V\beta_3$-Fc/Protein-A, or $\alpha_V\beta_3$-Fc/Syndecan-4-Fc (ratio 1:1). **(E)** Quantification of the neurite length of differentiated CAD cells over a 24-well plate (1×10^5 cells/cm^2) after 40 min incubation with serum-free medium containing $\alpha_V\beta_3$-Fc (1:10 of the total volume, 100 µl) in the absence or presence of different volumes of serum-free medium containing Syndecan-4-Fc. In **(D,E)** the neurites of at least 100 cells were measured per condition by using NeuronJ plug-in for ImageJ. In all graphs, data are expressed as the mean ± SEM ($n = 3$; *$p < 0.05$; n.s. non-significant, assessed by Mann–Whitney's test). In **(D)** *$p < 0.05$ compared to the control situation at the respective times analyzed.

To test the contribution of Syndecan-4 heparin sulfate groups in neurite outgrowth inhibition, the monolayer of DITNC1 astrocytes was pre-treated with heparitinase III (Hase III) (Levy-Adam et al., 2008). The reduction in neurite extension was not as pronounced when CAD cells were cultured over heparitinase-treated astrocytes (CAD/DITNC1 + Hase III; neurite length ~35 µm) (**Figures 3A,B**). Interestingly, treatment with the antibody against β_3 integrin showed an effect similar to the

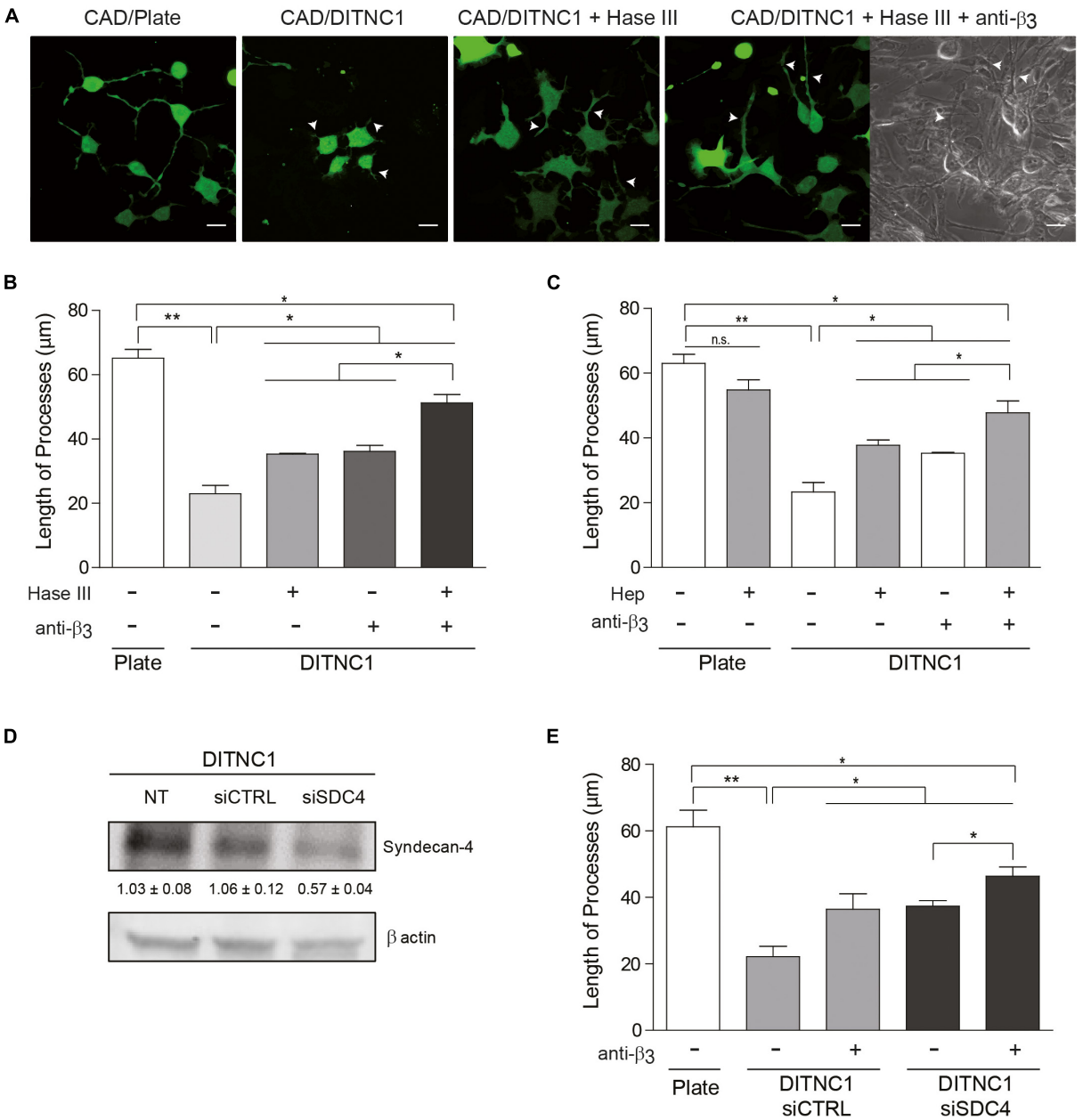

FIGURE 3 | The inhibitory effect of astrocytes on neurite extension requires Syndecan-4. Cell tracker green-labeled CAD cells (5×10^4 cells/cm^2) were seeded onto a plate or co-cultured on top of a fixed-monolayer of DITNC1 astrocytes. Neurite extension was then induced by serum deprivation for 24 h (1×10^5 cells/cm^2). To evaluate the participation of heparan sulfate chains in the inhibition of neurite outgrowth, DITNC1 cells were pre-treated with Heparitinase III (Hase III; 0.5 mU; 3 h at 37°C) or pre-incubated with Heparin (Hep; 400 μg/ml; 30 min). To block $\alpha_V\beta_3$-integrin, astrocytes were incubated with anti-β_3 integrin antibodies (anti-β_3; 5 μg/ml; 1 h; 37°C). **(A)** Representative microphotographs of different conditions. Quantification of neurite length (μm) after **(B)** Hase III treatment or **(C)** Hep incubation. **(D)** siRNA silencing of Syndecan-4 protein in whole cell lysates. DITNC1 cells that were either non-transfected (NT), transfected with siRNA control (siCTRL) or with siRNA targeting Syndecan-4 (siSDC4) were evaluated by immunoblotting. Actin was used as a loading control. The band intensities were quantified by ImageJ software and normalized to actin. **(E)** Quantification of neurite length (μm) after Syndecan-4 silencing. For each quantification **(B,C,E)**, neurites of at least 100 cells per condition were evaluated by using NeuronJ plug-in for ImageJ. Arrowheads in **(A)** indicate neurites growing over the DITNC1 astrocytes. In all graphs data are expressed as mean ± SEM ($n = 3$; *$p < 0.05$; **$p < 0.01$; n.s. non-significant, assessed by Mann–Whitney's test).

heparitinase treatment. Then, when the astrocyte monolayer was incubated with heparitinase together with the antibody against β_3 integrin (CAD/DITNC1 + Hase + anti-β_3; neurite length ~52 μm), neurite length increased compared to the condition without any astrocyte pre-treatment (CAD/DITNC1 ~22 μm) or with individual pre-treatments (~35 μm, **Figures 3A,B**). In addition to the length of processes, we characterized morphological differentiation of CAD cells, defined by the

presence of at least one neurite of ≥15 μm in length (**Supplementary Figure S3A**). When CAD cells were seeded onto a tissue culture dish, ∼80% of the cells differentiated. Alternatively, only ∼19% developed such extended processes over a monolayer of DITNC1 astrocytes. However, the percentage of differentiated cells increased after heparitinase treatment (∼50%). As expected, this effect was enhanced when β_3 integrin was also blocked (∼62%). Another indicator of morphological differentiation is the number of varicosities along CAD processes (**Supplementary Figure S3B**). Here, results similar to those shown in **Figure 3B** and **Supplementary Figure S3A** were obtained. Heparitinase pre-treatment also prevented the reduction of varicosities induced by the astrocyte monolayer. Therefore, the ability of DITNC1 astrocytes to block neurite extension requires Syndecan-4. Importantly, considering that a fixed monolayer of cells was used as a substrate to differentiate the CAD cells, the effects observed can be attributed exclusively to membrane-bound rather than soluble factors.

Considering that Thy-1 interacts directly with sulfated glycans, such as heparin (Hueber et al., 1992), a second strategy was to pre-incubate CAD cells with heparin. In this case, heparin should compete with Syndecan-4 heparan sulfate chains for the Thy-1 HBD. Neurite extension was not affected when CAD cells were pre-incubated with heparin and seeded directly onto a tissue culture dish (CAD + Hep/Plate) (**Figure 3C** and **Supplementary Figure S4**); however, inhibition of neurite outgrowth was observed when CAD cells were cultured over astrocytes (CAD/DITNC1) (**Figure 3C**). In addition, an increase in process outgrowth was observed when CAD cells were pre-incubated with heparin (CAD + Hep/DITNC1), or when the DITNC1 cell monolayer was treated with anti-β_3 integrin antibodies. These effects were potentiated by the combined addition of heparin and anti-β_3 integrin antibodies (CAD + Hep/DITNC1 + anti-β_3) (**Figure 3C**). The results obtained with heparitinase and heparin treatments suggest that astrocyte heparan sulfate proteoglycans (HSPG) are required to inhibit CAD cell neurite outgrowth induced by Thy-1. To confirm the specific involvement of Syndecan-4 in the neuronal response, we used two different small interference RNA (siRNA) against exons 3 and 4 (Avalos et al., 2009) to silence Syndecan-4 in DITNC1 astrocytes. Immunoblot analysis revealed a 50% reduction in the levels of the proteoglycan after siRNA transfection (siSDC4), compared to the non-transfected (NT) cells or to those transfected with a siRNA control (siCTRL) (**Figure 3D**). To evaluate whether inhibition of neurite outgrowth depends on astrocytic Syndecan-4, CAD cells were co-cultured over a monolayer of DITNC1 with silenced Syndecan-4, and then neurite extension was induced by serum deprivation. Quantification of neurite length showed a process extension of ∼60 μm in the control condition. In contrast, for DITNC1 astrocytes transfected with siCTRL, neurite length was only ∼21 μm (**Figure 3E**). This reduction in neurite length was attenuated when β_3 integrin was blocked with an anti-β_3 integrin antibody (∼38 μm). A similar effect was observed when CAD cells were seeded over astrocytes transfected with siRNA targeting Syndecan-4 (∼39 μm). Interestingly, when β_3 integrin was blocked in Syndecan-4 knock down astrocytes, neurite length increased (∼45 μm) (**Figure 3E**). These findings indicate that inhibition of neurite outgrowth mediated by Thy-1 depends on the combined action of $\alpha_V\beta_3$ integrin and Syndecan-4 present on the surface of astrocytes.

Primary Astrocytes Under Pro-inflammatory Conditions Inhibit Neurite Outgrowth in an $\alpha_V\beta_3$ Integrin- and Syndecan-4-Dependent Manner

Primary astrocytes reportedly display growth promoting properties that favor neurite extension (Hama et al., 2004). Interestingly, astrocytes from adult individuals do not express $\alpha_V\beta_3$ integrin (Ellison et al., 1998); however, under pathological conditions associated with inflammation, astrocytes adopt a reactive phenotype and upregulate the expression of $\alpha_V\beta_3$ integrin (Gladson and Cheresh, 1991; Ellison et al., 1998; Del Zoppo and Milner, 2006) and Syndecan-4 (Iseki et al., 2002; Okuyama et al., 2013; Lagos-Cabré et al., 2017). Our previous results indicate that primary astrocytes treated with pro-inflammatory cytokines increment protein levels of $\alpha_V\beta_3$ integrin and Syndecan-4 *in vitro* and become reactive astrocytes (Lagos-Cabré et al., 2017, 2018). Therefore, we tested the hypothesis that cytokine-treated astrocytes should inhibit neurite outgrowth in a co-culture assay with CAD cells. Immunoblot analysis of primary astrocytes treated with TNF (+TNF) confirmed the presence of elevated levels of $\alpha_V\beta_3$ integrin and Syndecan-4 in such astrocytes compared to the control condition (−TNF) (**Figure 4A**). For CAD cells seeded over a monolayer of TNF-treated astrocytes, process extension decreased compared to the control condition without cytokines (**Figure 4B** and **Supplementary Figure S5**). Neurite outgrowth under pro-inflammatory conditions (i.e., in the presence of TNF) increased when primary astrocytes were pre-treated with anti-β_3 integrin antibodies or heparitinase to block Syndecan-4. Moreover, the combined treatment (+Hase; +anti-β_3) lead to an even greater increase in neurite extension, reaching essentially the same values as in the absence of TNF (**Figure 4B** and **Supplementary Figure S5**). To evaluate the specific role of Syndecan-4 on the inhibition of neurite outgrowth, co-culture assays were employed utilizing primary astrocytes in which the proteoglycan Syndecan-4 was silenced. In the absence or presence of TNF, protein levels of Syndecan-4 after transfection with siRNA against Syndecan-4 (siSDC4) remained low compared to the non-transfected (NT) cells or those transfected with an siRNA control (siCTRL) (**Figure 4C**). CAD cells in serum-free medium grew long processes over primary astrocytes transfected with siCTRL, whereas neurite outgrowth was decreased by the addition of TNF (**Figure 4D** and **Supplementary Figure S6**). This inhibition was partially prevented when β_3-integrin was blocked with specific antibodies (+TNF; +anti-β_3; siCTRL). On the other hand, when CAD cells were seeded over astrocytes transfected with siSDC4, in the absence of pro-inflammatory conditions (−TNF; siSDC4), neurite length was similar to that observed in the transfection control condition (−TNF; siCTRL). Interestingly, when primary astrocytes transfected with siSDC4 were treated with TNF, extension of neurites was inhibited (+TNF; siSDC4), compared to control condition without TNF (−TNF; siSDC4);

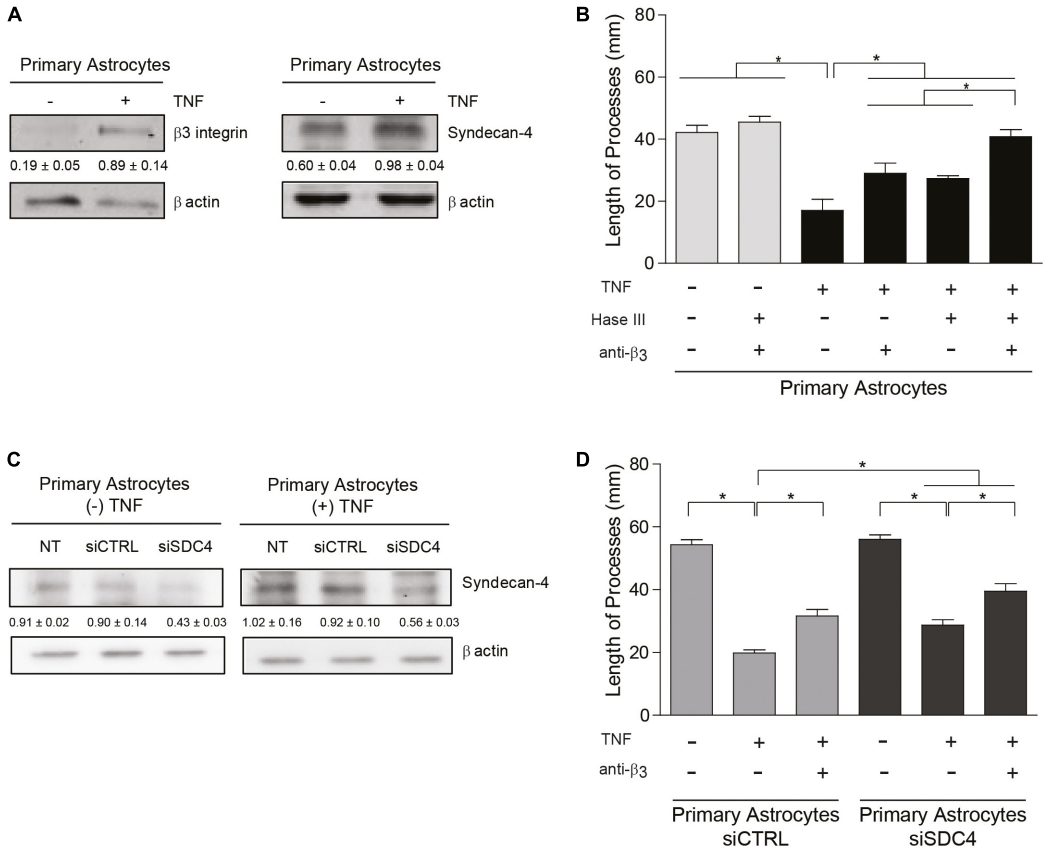

FIGURE 4 | Primary astrocytes under pro-inflammatory conditions inhibit neurite outgrowth in an $\alpha_V\beta_3$ integrin- and Syndecan-4-dependent manner. **(A,C)** Protein levels of β_3 integrin and Syndecan-4 in primary astrocytes treated or not with TNF were evaluated by immunoblotting. Actin was used as a loading control. The band intensities were quantified by ImageJ software and normalized to actin. **(B,C)** CAD cells (5×10^4 cells/cm^2) were seeded on top of a monolayer of primary astrocytes pre-treated or not with TNF (10 ng/ml; 48 h) and neurite extension was induced by serum deprivation. Primary astrocytes were **(B)** pre-treated with Heparitinase (Hase III; 0.5 mU) for 3 h at 37°C or **(D)** transfected with siRNA against Syndecan-4 (siSDC4) to evaluate heparan sulfate chains and Syndecan-4 participation in the inhibition of neurite outgrowth, respectively. To block $\alpha_V\beta_3$ integrin, astrocytes were also incubated with anti-β_3 integrin antibodies (5 μg/ml; 1 h; 37°C). **(B,D)** Quantification of neurite length (μm) in co-culture assays. Neurites of at least 100 CAD cells per condition were evaluated by using NeuronJ plug-in for ImageJ. Data are expressed as mean ± SEM ($n = 3$; $^*p < 0.05$, assessed by Mann–Whitney's test).

however, such inhibition was not as pronounced as that induced by astrocytes transfected with siCTRL under pro-inflammatory conditions (+TNF; siCTRL) (**Figure 4D** and **Supplementary Figure S6**). In addition, when β_3 integrin was blocked in primary astrocytes with silenced Syndecan-4 and treated with TNF, a significant recovery in neurite extension was observed (+TNF; +anti-β_3; siSDC4). These results indicate that under pro-inflammatory conditions the combined action of the surface molecules $\alpha_V\beta_3$ integrin and Syndecan-4 in astrocytes promotes inhibition of CAD cell neurite extension. In conclusion, under pathophysiological conditions, where astrocytes are exposed to an inflammatory environment, neurite retraction is promoted in a Syndecan-4-dependent manner.

DISCUSSION

Signals exchanged between neurons and astrocytes regulate the cytoskeleton of both cells suggesting a bi-directional flow of information between the two cell types (Herrera-Molina et al., 2013; Leyton et al., 2019). In our present study, results obtained at a single molecule level using molecular force spectroscopy indicate that Thy-1 interacts directly with Syndecan-4. We also show that the proteoglycan Syndecan-4 forms a ternary complex with Thy-1 and $\alpha_V\beta_3$ integrin increasing the Thy-1–$\alpha_V\beta_3$ integrin bond lifetime, even when exposed to mechanical stress. In a cellular context, the role of Syndecan-4 in this ternary complex is important because it increases the speed of the neuronal responses. This neuronal outcome is facilitated under inflammatory conditions due to the increased expression of Syndecan-4 (Iseki et al., 2002; Properzi et al., 2008) and $\alpha_V\beta_3$ integrin (Ellison et al., 1998, 1999; Lagos-Cabré et al., 2017).

The ternary molecular complex described here (Thy-1–$\alpha_V\beta_3$ + Syndecan-4) differs from that reported by Barker's group (Thy-1–$\alpha_5\beta_1$ + Syndecan-4) with respect to the integrin heterodimer involved, the biological context, and also the manner in which force regulates bond dissociation (Fiore et al., 2014). The $\alpha_5\beta_1$ integrin ternary complex formed mediates adhesion

between activated endothelium and melanoma cells, while the complex containing $\alpha_V\beta_3$ integrin is involved in neuron-to-astrocyte bi-directional communication. The bi-molecular Thy-1–$\alpha_5\beta_1$ integrin bond behaves as a slip bond when force is applied, but when Syndecan-4 is present, a tri-phasic slip-catch-slip behavior is observed implying that force abruptly increases bond strength (Fiore et al., 2014). Although other authors have described a catch bond behavior at forces around 5–10 pN for other ternary complexes, such as that formed by Cadherin-Catenin-Actin (Buckley et al., 2015), Fiore's findings revealed a catch bond behavior at forces between 20 and 35 pN for the ternary complex. Here, we demonstrate that both bi-molecular complexes formed by Thy-1 (i.e., Thy-1–$\alpha_V\beta_3$ integrin and Thy-1–Syndecan-4) have slip bond characteristics, as the bond lifetime decreases with forces between 10 and 50 pN (**Figure 1D**). Also, the absolute values of lifetime in the absence of force suggest a weaker interaction, and therefore a lower relative binding affinity between Thy-1 and Syndecan-4 than with $\alpha_V\beta_3$ integrin, which might reflect Thy-1 binding to heparan sulfate chains rather than a protein-protein interaction. Indeed, such differences in affinities have also been described for the fibronectin-dependent interactions with either Syndecan-4 or $\alpha_5\beta_1$ integrin. There too, the binding to the proteoglycan is of lower affinity (Kennelly et al., 2019).

The lifetime values are consistent with the responses in neurons (e.g., neurite retraction) triggered by the astrocyte proteins: $\alpha_V\beta_3$ integrin induces a significant retraction of neuronal processes, while the proteoglycan Syndecan-4 does not promote any morphological changes (**Figure 2D**). The slip bond behavior found for both bi-molecular interactions coincides with the mechanical characterization described for Thy-1–$\alpha_5\beta_1$ binding (Fiore et al., 2014) as well as for FGF with the HSPG (Sevim et al., 2017). Moreover, we found that the ternary complex (Thy-1–$\alpha_V\beta_3$ integrin + Syndecan-4) is more stable in terms of force-dependent lifetime than each binary complex. The presence of both astrocyte proteins increases the time that Thy-1-dependent interactions last, both in the absence of force ($\sim$11.7 s) as well as when force is applied (e.g., $\sim$4 s at 20 pN). This extended lifetime is consistent with the enhanced and faster neuronal effect promoted by the $\alpha_V\beta_3$ integrin in the presence of Syndecan-4, suggesting that the proteoglycan stabilizes the Thy-1–$\alpha_V\beta_3$ interaction, thereby accelerating its specific biological functions.

In contrast to the mechanical response reported by Barker's group, the Thy-1–$\alpha_V\beta_3$ integrin + Syndecan-4 complex dissociates more rapidly under force, indicating that the slip bond properties are retained, and that the nature of the integrin as well as its biological function is what defines how Thy-1-dependent interactions are regulated by external forces. In this context, the $\alpha_5\beta_1$ integrin determines adhesion strength and is involved in cell adhesion maturation processes (Roca-Cusachs et al., 2012; Fiore et al., 2014). Alternatively, the $\alpha_V\beta_3$ integrin acts as a mechano-transducer by providing a connection to the cytoskeleton (Roca-Cusachs et al., 2009) and triggering downstream events required for cell migration. Altogether, these findings permit hypothesizing that when Syndecan-4 is present, Thy-1–$\alpha_5\beta_1$ bond (catch) resists higher forces to form strong and stable adhesion complexes, whereas the Thy-1–$\alpha_V\beta_3$-bond (slip) is transient and less resistant to mechanical forces facilitating force sensing and mechano-transduction.

In a cellular context, the stimulation of neurons expressing Thy-1 on their surface, with a combination of soluble $\alpha_V\beta_3$ integrin and Syndecan-4 proteins ($\alpha_V\beta_3$-Fc and Syndecan-4-Fc), accelerates neurite retraction when compared with stimulation of Thy-1 with only $\alpha_V\beta_3$ integrin. Interestingly, such accelerated retraction is also seen for neurons stimulated with $\alpha_V\beta_3$ integrin in a multivalent format (with Protein A) (Herrera-Molina et al., 2012). These results can be explained assuming that Syndecan-4 induces structural changes in $\alpha_V\beta_3$ integrin to favor more efficient interactions between Thy-1 and the $\alpha_V\beta_3$ integrin, thereby promoting $\alpha_V\beta_3$ integrin clustering and activation. In support of this idea, Syndecan-1–$\alpha_V\beta_3$ integrin interaction reportedly stimulates integrin binding to fibronectin, not only by bringing the two molecules together, but also by inducing integrin activation (Beauvais et al., 2004). Intriguingly, the effect of Syndecan-1 requires that the proteoglycan is ligand-engaged, favoring the possibility that conformational changes and/or clustering of Syndecan-1 are required to induce integrin activation. In this context, the association of the Syndecan-1 ectodomain with $\alpha_V\beta_3$ integrin provides a docking surface to incorporate the growth factor receptor IGF1R into the complex and promote IGFR1 kinase activity that depends on Syndecan-1 clustering. Then, in turn, activated IGF1R induces changes in the cytoplasmic protein Talin, which promotes integrin activation (Beauvais and Rapraeger, 2010). Therefore, Syndecan-dependent integrin activation is attributable to both molecular clustering and changes in cytoplasmic signaling.

The inhibition of morphological neuronal differentiation induced by the engagement of Thy-1 in cell-cell association requires the collective action of $\alpha_V\beta_3$ integrin and Syndecan-4 expressed in reactive astrocytes. Accordingly, Syndecan-4 downregulation or the blockade of HS chains with Hase III or Hep, all favor neuronal differentiation and neurite outgrowth. However, when β_3 integrin is blocked by antibodies, and Syndecan-4 is treated with Hase III or Hep at the same time, neuronal differentiation is promoted to levels where process extension, number of processes, and number of varicosities are similar to, but still significantly lower than those observed in the control samples. These results reveal that although $\alpha_V\beta_3$ integrin and Syndecan-4 are important for Thy-1-dependent inhibition of neuronal differentiation, additional molecules or the protein core of Syndecan-4 (not affected by Hase III or Hep treatments) likely also contribute to inhibition of neurite outgrowth. Indeed, for CSPGs both the protein core and the chondroitin sulfate chains are known to independently inhibit axonal regeneration (Bandtlow and Zimmermann, 2000; Asher et al., 2001). In contrast, little information is available concerning the regulation and function of astrocytic HSPGs in response to brain pathological conditions. Nevertheless, HS moieties of Syndecan-4 are important to mediate the integrin-independent interaction of Thy-1 with Syndecan-4. This is supported by the optical tweezers results revealing that Thy-1-Syndecan-4 interaction requires the HBD of Thy-1 and does not depend on

the presence of the $\alpha_V\beta_3$ integrin binding domain (RLD) or the occurrence of Thy-1-integrin interaction.

Moreover, HSPGs reportedly act as potential "scaffolds" that bring together two proteins to favor their interaction, and thus regulate where and when signaling events begin (Xu and Esko, 2014). An example of this is the interaction of FGF with its receptor (FGFR), where Syndecan-4 acts as a co-receptor (Carey, 1997). In this case, although the FGF/FGFR binding is of high affinity, the interaction with Syndecan-4 and the subsequent signaling events are amplified in the presence of HS chains (Sperinde and Nugent, 2000). Moreover, the formation of a ternary complex FGF/FGFR/Syndecan-4 has been reported to reduce the dissociation constant (k_{off}; or increases the lifetime) of the FGF/FGFR interaction, increase the primary ligand-receptor affinity and favor the activation of FGFR at low concentrations of the ligand (Nugent and Edelman, 1992; Forsten-Williams et al., 2005). This data is consistent with the function established for Syndecan-4 in this study, where we report that the HSPG facilitates neuronal retraction and is required for inhibition of neurite outgrowth mediated by Thy-1–$\alpha_V\beta_3$ integrin association.

Considering a CNS physio-pathological context, our results suggest that under inflammatory conditions- where both astrocytic $\alpha_V\beta_3$ and Syndecan-4 protein levels are increased - the ternary complex formed by Thy-1–$\alpha_V\beta_3$ integrin + Syndecan-4 promotes more stable neuron-astrocyte association (i.e., extended lifetime compared to bi-molecular Thy-1-dependent interactions). Consequently, the effects triggered by these adhesion proteins, such as neurite retraction, are enhanced. However, mechanical cues from the surrounding environment exerted on the Thy-1-$\alpha_V\beta_3$ integrin + Syndecan-4 complex regulate these cellular processes by stimulating rapid bond dissociation between the molecules. On the other hand, under physiological conditions, when both $\alpha_V\beta_3$ integrin and Syndecan-4 are expressed at low levels (Lagos-Cabré et al., 2017), bi-molecular interactions are more likely to occur. Thus, the faster bond dissociation of these complexes, with or without mechanical forces, makes stimulation of retraction of neuronal processes unlikely. Therefore, Syndecan-4 appears to play a key role in modulating the speed of neuronal responses under pathological conditions (**Figure 5**), in agreement with the rapid axon retraction observed *in vivo* (Houle and Tessler, 2003) and *in vitro* (Shao et al., 2019).

Here, we studied morphological neuronal changes stimulated by cell-cell communication between neurons and astrocytes through the cell adhesion molecules, Thy-1, $\alpha_V\beta_3$ integrin and Syndecan-4. It has also been reported that cell-extracellular matrix interactions play a key role in the regulation of neuronal process retraction (Ahmad et al., 2000; Franze et al., 2009; Shao et al., 2019), as well as in the contraction of other cell types (Okamoto et al., 1998). In our neurite retraction assays, CAD cells were seeded directly over standard tissue culture dishes without additional treatments (e.g., poly-L-lysine). Thus, further investigation is required to decipher how the magnitude of neurite retraction resulting from neuron-to-astrocyte communication is affected by the strength of the adhesion between neurons and the extracellular matrix.

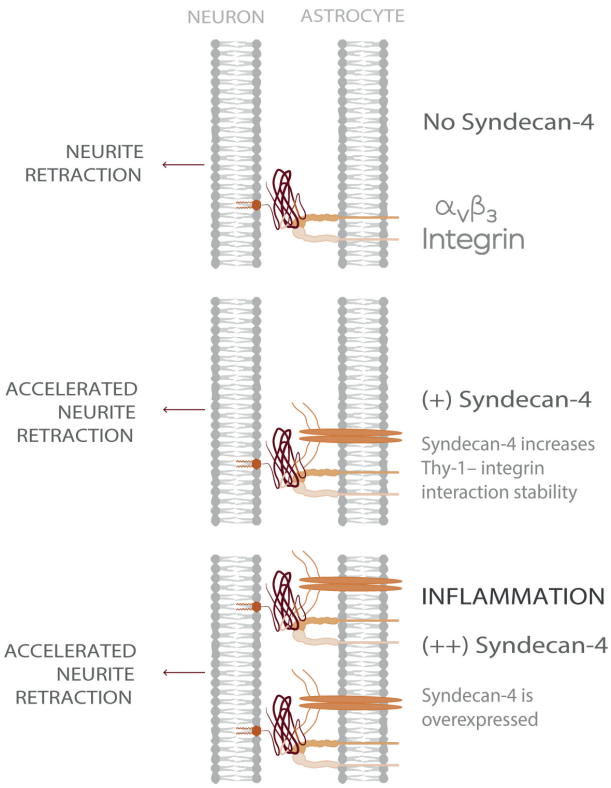

FIGURE 5 | Model showing Syndecan-4 as a key player in neuron-astrocyte interactions under inflammation accelerating axonal retraction. The illustrated behavior is particularly relevant under inflammatory conditions where the expression of both Syndecan-4 and $\alpha_V\beta_3$ integrin increase on astrocytes and exacerbate the detrimental effects of Thy-1–$\alpha_V\beta_3$ integrin association, on neurons.

Retraction of neuronal processes is also driven by mechanical tension produced by the active contraction of the actomyosin cytoskeleton (Kranenburg et al., 1997; Govek et al., 2005; Maldonado et al., 2017). Our prior results demonstrate that the engagement of astrocytic $\alpha_V\beta_3$ integrin with Thy-1 on the surface of neurons triggers specific RhoA-dependent signaling pathways through a preformed membrane complex between Thy-1, the transmembrane protein CBP and the non-receptor tyrosine kinase Src, that drives actomyosin cytoskeleton contraction and, consequently, leads to neurite retraction (Herrera-Molina et al., 2012; Maldonado et al., 2017). Results shown here indicate that Syndecan-4 accelerates the effect of integrin-engaged Thy-1 by interacting directly with the neuronal protein, suggesting that this proteoglycan may also modulate the reported signaling pathway; however, this interesting possibility needs to be confirmed in future experiments.

We describe a Thy-1–$\alpha_V\beta_3$ + Syndecan-4 ternary complex, which is crucial in determining the Thy-1-dependent response of neurons to astrocytes under inflammation-related diseases in the CNS. In this tri-molecular complex, Syndecan-4 is identified as an enhancer of $\alpha_V\beta_3$ integrin effect in neurite contractility likely by stabilizing Thy-1–$\alpha_V\beta_3$ interaction, even when exposed

to mechanical forces. Considering that both Syndecan-4 and $\alpha_V\beta_3$ integrin are upregulated in astrocytes by pro-inflammatory cytokines, our results indicate that under pathological conditions (inflammation), protein expression ultimately determines the formation, as well as the different properties and functions, of the Thy-1–$\alpha_V\beta_3$ integrin + Syndecan-4 ternary complex (**Figure 5**). Therefore, our research provides new insights towards understanding how inflammation contributes to neurodegeneration and how mechanical stimuli regulate unbinding properties of adhesion proteins occurring during neuron-to-astrocyte communication.

DATA AVAILABILITY STATEMENT

All datasets generated for this study are included in the article/**Supplementary Material**.

ETHICS STATEMENT

The animal use and care protocol was reviewed and approved by Comité de Bioética de Animales, Facultad de Medicina, Universidad de Chile, Protocol #CBA0790-FMUCH.

AUTHOR CONTRIBUTIONS

FB-B: conceptualization, investigation, data curation, preparation of all data, figures, and text. SM-M: investigation, methodology, and preparation of figures. AQ: formal data analysis, funding acquisition, and writing—review and editing. CW: visualization, methodology, data curation, formal analysis, and writing—review and editing. LL: conceptualization, formal data analysis, funding acquisition, project administration, work supervision, and writing—review and editing. All authors contributed to the article and approved the submitted version.

FUNDING

This study was supported by the Comisión Nacional de Investigación Científica y Tecnológica: Francesca Burgos-Bravo, 21130008; Fondo Nacional de Desarrollo Científico y Tecnológico (FONDECYT): Andrew F. G. Quest, 1130250; 1170925; Fondo Nacional de Desarrollo Científico y Tecnológico (FONDECYT): Lisette Leyton, 1150744; 1200836; Fondo de Financiamiento de Centros de Investigación en Áreas Prioritarias: Andrew F. G. Quest, Lisette Leyton, 15130011; Fondo Nacional de Desarrollo Científico y Tecnológico (FONDECYT): Christian A. M. Wilson, 1181361. The funders had no role in study design, data collection and interpretation, or the decision to submit the work for publication.

ACKNOWLEDGMENTS

We thank Steven B. Smith from Steven B. Smith Engineering for helping in miniTweezers construction.

SUPPLEMENTARY MATERIAL

The Supplementary Material for this article can be found online at: https://www.frontiersin.org/articles/10.3389/fmolb.2020.582257/full#supplementary-material

REFERENCES

Ahmad, F. J., Hughey, J., Wittmann, T., Hyman, A., Greaser, M., and Baas, P. W. (2000). Motor proteins regulate force interactions between microtubules and microfilaments in the axon. *Nat. Cell Biol.* 2, 276–280. doi: 10.1038/35010544

Allen, B. L., Filla, M. S., and Rapraeger, A. C. (2001). Role of heparan sulfate as a tissue-specific regulator of FGF-4 and FGF receptor recognition. *J. Cell Biol.* 155, 845–857. doi: 10.1083/jcb.200106075

Asher, R. A., Morgenstern, D. A., Moon, L. D. F., and Fawcett, J. W. (2001). Chondroitin sulphate proteoglycans: inhibitory components of the glial scar. *Prog. Brain Res.* 132, 611–619. doi: 10.1016/S0079-6123(01)32106-4

Avalos, A. M., Valdivia, A. D., Muñoz, N., Herrera-Molina, R., Tapia, J. C., Lavandero, S., et al. (2009). Neuronal Thy-1 induces astrocyte adhesion by engaging syndecan-4 in a cooperative interaction with αvβ3 integrin that activates PKCα and RhoA. *J. Cell Sci.* 122, 3462–3471. doi: 10.1242/jcs.034827

Bandtlow, C. E., and Zimmermann, D. R. (2000). Proteoglycans in the developing brain: new conceptual insights for old proteins. *Physiol. Rev.* 80, 1267–1290. doi: 10.1152/physrev.2000.80.4.1267

Beauvais, D. M., Burbach, B. J., and Rapraeger, A. C. (2004). Syndecan1 regulates αvβ3 and αvβ5 integrin activation during angiogenesis and is blocked by synstatin, a novel peptide inhibitor. *J. Cell Biol.* 206, 171–181. doi: 10.1084/jem.20081278

Beauvais, D. M., and Rapraeger, A. C. (2010). Syndecan-1 couples the insulin-like growth factor-1 receptor to inside-out integrin activation. *J. Cell Sci.* 123, 3796–3807. doi: 10.1242/jcs.067645

Bell, G. I. (1978). Models for the specific adhesion of cells to cells. *Science* 200, 618–627. doi: 10.1126/science.347575

Bellin, R. M., Kubicek, J. D., Frigault, M. J., Kamien, A. J., Steward, R. L. Jr., Barnes, H. M., et al. (2009). Defining the role of syndecan-4 in mechanotransduction using surface-modification approaches. *Proc. Natl. Acad. Sci .U.S.A.* 106, 22102–22107. doi: 10.1073/pnas.0902639106

Bendas, G., and Borsig, L. (2012). Cancer cell adhesion and metastasis: selectins, integrins, and the inhibitory potential of heparins. *Int. J. Cell Biol.* 2012, 676–731. doi: 10.1155/2012/676731

Buckley, C. D., Tan, J., Anderson, K. L., Hanein, D., Volkmann, N., Weis, W. I., et al. (2015). The minimal cadherin-catenin complex binds to actin filaments under force. *Science* 346, 1–22. doi: 10.1126/science.1254211

Burgos-Bravo, F., Figueroa, N. L., Casanova-Morales, N., Quest, A. F. G., Wilson, C. A. M., and Leyton, L. (2018). Single-molecule measurements of the effect of force on Thy-1/αvβ3-integrin interaction using nonpurified proteins. *Mol. Biol. Cell* 29, 326–338. doi: 10.1091/mbc.E17-03-0133

Carey, D. J. (1997). Syndecans: Multifunctional cell-surface co-receptors. *Biochem. J.* 327, 1–16. doi: 10.1042/bj3270001

Del Zoppo, G. J., and Milner, R. (2006). Integrin-Matrix Interactions in the Cerebral Microvasculature. *Arter. Thromb. Vasc. Biol.* 26, 1966–1975. doi: 10.1161/01.ATV.0000232525.65682.a2

Dembo, M., Torney, D. C., Saxman, K., and Hammer, D. (1988). The reaction-limited kinetics of membrane-to-surface adhesion and detachment. *Proc. R. Soc. B Biol. Sci.* 234, 55–83. doi: 10.1098/rspb.1988.0038

Dill, J. (2012). *Struts, Springs and Crumple Zones: Protein Structures under Force*. Doctoral dissertation, University of California at Berkeley, Berkeley, CA.

Ellison, J. A., Barone, F. C., and Feuerstein, G. Z. (1999). Matrix remodeling after stroke: de novo expression of matrix proteins and integrin receptors. *Ann. N. Y. Acad. Sci.* 890, 204–222. doi: 10.1111/j.1749-6632.1999.tb07996.x

Ellison, J. A., Velier, J. J., Spera, P., Jonak, Z. L., Wang, X., Barone, F. C., et al. (1998). Osteopontin and its integrin receptor αvβ3 are upregulated during formation of the glial scar after focal stroke. *Stroke* 29, 1698–1707. doi: 10.1161/01.STR.29.8.1698

Fiore, V. F., Ju, L., Chen, Y., Zhu, C., and Barker, T. H. (2014). Dynamic catch of a Thy-1–α5β1 + syndecan-4 trimolecular complex. *Nat. Commun.* 5:4886. doi: 10.1038/ncomms5886

Forsten-Williams, K., Chua, C. C., and Nugent, M. A. (2005). The kinetics of FGF-2 binding to heparan sulfate proteoglycans and MAP kinase signaling. *J. Theor. Biol.* 233, 483–499. doi: 10.1016/j.jtbi.2004.10.020

Franze, K., Gerdelmann, J., Weick, M., Betz, T., Pawlizak, S., Lakadamyali, M., et al. (2009). Neurite branch retraction is caused by a threshold-dependent mechanical impact. *Biophys. J.* 97, 1883–1890. doi: 10.1016/j.bpj.2009.07.033

Gladson, C. L., and Cheresh, D. A. (1991). Glioblastoma expression of vitronectin and the αvβ3 integrin. Adhesion mechanism for transformed glial cells. *J. Clin. Invest.* 88, 1924–1932. doi: 10.1172/JCI115516

Govek, E., Newey, S. E., and Van Aelst, L. (2005). The role of the Rho GTPases in neuronal development. *Genes Dev.* 19, 1–49. doi: 10.1101/gad.1256405.and

Hagood, J. S. (2019). Thy-1 as an integrator of diverse extracellular signals. *Front. Cell Dev. Biol.* 7:26. doi: 10.3389/fcell.2019.00026

Hama, H., Hara, C., Yamaguchi, K., and Miyawaki, A. (2004). PKC signaling mediates global enhancement of excitatory synaptogenesis in neurons triggered by local contact with astrocytes. *Neuron* 41, 405–415. doi: 10.1016/S0896-6273(04)00007-8

Hermosilla, T., Muñoz, D., Herrera-Molina, R., Valdivia, A., Muñoz, N., Nham, S.-U., et al. (2008). Direct Thy-1/αVβ3 integrin interaction mediates neuron to astrocyte communication. *Biochim. Biophys. Acta* 1783, 1111–1120. doi: 10.1016/j.bbamcr.2008.01.034

Herrera-Molina, R., Frischknecht, R., Maldonado, H., Seidenbecher, C. I., Gundelfinger, E. D., Hetz, C., et al. (2012). Astrocytic αvβ3 integrin inhibits neurite outgrowth and promotes retraction of neuronal processes by clustering Thy-1. *PLoS One* 7:e34295. doi: 10.1371/journal.pone.0034295

Herrera-Molina, R., Valdivia, A., Kong, M., Alvarez, A., Cárdenas, A., Quest, A. F. G., et al. (2013). Thy-1-interacting molecules and cellular signaling in Cis and Trans. *Int. Rev. Cell Mol. Biol.* 305, 163–216. doi: 10.1016/B978-0-12-407695-2.00004-4

Horowitz, A., Tkachenko, E., and Simons, M. (2002). Fibroblast growth factor–specific modulation of cellular response by syndecan-4. *J. Cell Biol.* 157, 715–725. doi: 10.1083/jcb.200112145

Houle, J. D., and Tessler, A. (2003). Repair of chronic spinal cord injury. *Exp. Neurol.* 182, 247–260. doi: 10.1016/S0014-4886(03)00029-3

Hueber, A. O., Pierres, M., and He, H. T. (1992). Sulfated glycans directly interact with mouse Thy-1 and negatively regulate Thy-1 mediated adhesion of thymocytes to thymic epithelial cells. *J. Immunol.* 148, 3692–3699.

Iseki, K., Hagino, S., Mori, T., Zhang, Y., Yokoya, S., Takaki, H., et al. (2002). Increased syndecan expression by pleiotrophin and FGF receptor-expressing astrocytes in injured brain tissue. *Glia* 39, 1–9. doi: 10.1002/glia.10078

Kennelly, T. M., Li, Y., Cao, Y., Qwarnstrom, E. E., and Geoghegan, M. (2019). Distinct binding interactions of α5β1-integrin and proteoglycans with fibronectin. *Biophys. J.* 117, 688–695. doi: 10.1016/j.bpj.2019.07.002

Kong, M., Muñoz, N., Valdivia, A., Alvarez, A., Herrera-Molina, R., Cárdenas, A., et al. (2013). Thy-1-mediated cell–cell contact induces astrocyte migration through the engagement of αVβ3 integrin and syndecan-4. *Biochim. Biophys. Acta* 1833, 1409–1420. doi: 10.1016/j.bbamcr.2013.02.013

Kranenburg, O., Poland, M., Gebbink, M., Oomen, L., and Moolenaar, W. H. (1997). Dissociation of LPA-induced cytoskeletal contraction from stress fiber formation by differential localization of RhoA. *J. Cell Sci.* 2427, 2417–2427.

Lagos-Cabré, R., Alvarez, A., Kong, M., Burgos-Bravo, F., Cárdenas, A., Rojas-Mancilla, E., et al. (2017). αVβ3 integrin regulates astrocyte reactivity. *J. Neuroinflammat.* 14, 1–13. doi: 10.1186/s12974-017-0968-5

Lagos-Cabré, R., Brenet, M., Díaz, J., Pérez, R., Pérez, L., Herrera-Molina, R., et al. (2018). Intracellular Ca^{2+} increases and connexin 43 hemichannel opening are necessary but not sufficient for Thy-1-induced astrocyte migration. *Int. J. Mol. Sci.* 19:2179. doi: 10.3390/ijms19082179

Levy-Adam, F., Feld, S., Suss-Toby, E., Vlodavsky, I., and Ilan, N. (2008). Heparanase facilitates cell adhesion and spreading by clustering of cell surface heparan sulfate proteoglycans. *PLoS One* 3:e2319. doi: 10.1371/journal.pone.0002319

Leyton, L., Díaz, J., Martínez, S., Palacios, E., Pérez, L. A., and Pérez, R. D. (2019). Thy-1 / CD90 a bidirectional and lateral signaling scaffold. *Front. Cell Dev. Biol.* 7:132. doi: 10.3389/fcell.2019.00132

Leyton, L., Schneider, P., Labra, C. V., Ruegg, C., Hetz, C. A., Quest, A. F. G., et al. (2001). Thy-1 binds to integrin β_3 on astrocytes and triggers formation of focal contact sites. *Curr. Biol.* 11, 1028–1038. doi: 10.1016/S0960-9822(01)00262-7

Li, Y., Hou, L. X.-E., Aktiv, A., and Dahlström, A. (2007). Studies of the central nervous system-derived CAD cell line, a suitable model for intraneuronal transport studies? *J. Neurosci. Res.* 85, 2601–2609. doi: 10.1002/jnr.21216

Luo, L., and O'Leary, D. D. M. (2005). Axon retraction and degeneration in development and disease. *Annu. Rev. Neurosci.* 28, 127–156. doi: 10.1146/annurev.neuro.28.061604.135632

Maldonado, H., Calderon, C., Burgos-Bravo, F., Kobler, O., Zuschratter, W., Ramirez, O., et al. (2017). Astrocyte-to-neuron communication through integrin-engaged Thy-1/CBP/Csk/Src complex triggers neurite retraction via the RhoA/ROCK pathway. *Biochim. Biophys. Acta* 1864, 243–254. doi: 10.1016/j.bbamcr.2016.11.006

Marshall, B. T., Long, M., Piper, J. W., Yago, T., McEver, R. P., and Zhu, C. (2003). Direct observation of catch bonds involving cell-adhesion molecules. *Nature* 423, 190–193. doi: 10.1038/nature01605

Moks, T., Abrahmsen, L., Nilsson, B., Hellman, U., Sjoquist, J., and Uhlen, M. (1986). Staphylococcal protein A consists of five IgG-binding domains. *Eur. J. Biochem.* 156, 637–643. doi: 10.1111/j.1432-1033.1986.tb09625.x

Nugent, M. A., and Edelman, E. R. (1992). Kinetics of basic fibroblast growth factor binding to its receptor and heparan sulfate proteoglycan: a mechanism for cooperativity. *Biochemistry* 31, 8876–8883. doi: 10.1021/bi00152a026

Okamoto, H., Nakamori, S., Mukai, M., and Shinkai, K. (1998). Down-regulation of focal adhesion kinase, pp125 FAK, in endothelial cell retraction during tumor cell invasion. *Clin. Exp. Metastasis* 16, 243–252. doi: 10.1023/a:1006544925878

Okuyama, E., Suzuki, A., Murata, M., Ando, Y., Kato, I., Takagi, Y., et al. (2013). Molecular mechanisms of syndecan-4 upregulation by TNF-α in the endothelium-like EAhy926 cells. *J. Biochem.* 154, 41–50. doi: 10.1093/jb/mvt024

Properzi, F., Lin, R., Kwok, J., Naidu, M., van Kuppevelt, T. H., ten Dam, G. B., et al. (2008). Heparan sulphate proteoglycans in glia and in the normal and injured CNS: expression of sulphotransferases and changes in sulphation. *Eur. J. Neurosci.* 27, 593–604. doi: 10.1111/j.1460-9568.2008.06042.x

Qi, Y., Wang, J. K. T., McMillian, M., and Chikaraishi, D. M. (1997). Characterization of a CNS cell line, CAD, in which morphological differentiation is initiated by serum deprivation. *J. Neurosci.* 17, 1217–1225. doi: 10.1523/JNEUROSCI.17-04-01217.1997

Roca-Cusachs, P., Gauthier, N. C., Del Rio, A., and Sheetz, M. P. (2009). Clustering of α5β1 integrins determines adhesion strength whereas αvβ3 and talin enable mechanotransduction. *Proc. Natl. Acad. Sci. U.S.A.* 106, 16245–16250. doi: 10.1073/pnas.0902818106

Roca-Cusachs, P., Iskratsch, T., and Sheetz, M. (2012). Finding the weakest link: exploring integrin-mediated mechanical molecular pathways. *J. Cell Sci.* 125, 3025–3038. doi: 10.1242/jcs.095794

Schneider, P. (2000). Production of recombinant TRAIL and TRAIL receptor: Fc chimeric proteins. *Meth. Enzym.* 322, 325–345. doi: 10.1016/S0076-6879(00)22031-4

Schubert, K., Gutknecht, D., Köberle, M., Anderegg, U., and Saalbach, A. (2013). Melanoma cells use Thy-1 (CD90) on endothelial cells for metastasis formation. *Am. J. Pathol.* 182, 266–276. doi: 10.1016/j.ajpath.2012.10.003

Scott, D. W. (1979). On optimal and data-based histograms. *Biometrika* 66, 605–610. doi: 10.1093/biomet/66.3.605

Sevim, S., Ozer, S., Jones, G., Wurzel, J., Feng, L., Fakhraee, A., et al. (2017). Nanomechanics on FGF-2 and heparin reveal slip bond characteristics with pH dependency. *ACS Biomater. Sci. Eng.* 3, 1000–1007. doi: 10.1021/acsbiomaterials.6b00723

Shao, X., You, R., Hui, T. H., Fang, C., Gong, Z., Yan, Z., et al. (2019). Tension- and adhesion-regulated retraction of injured axons. *Biophys. J.* 117, 193–202. doi: 10.1016/j.bpj.2019.06.011

Smith, S. B., Cui, Y., and Bustamante, C. (2003). Optical-trap force transducer that operates by direct measurement of light momentum. *Methods Enzymol.* 361, 134–162. doi: 10.1016/S0076-6879(03)61009-8

Sperinde, G. V., and Nugent, M. A. (2000). Mechanisms of fibroblast growth factor 2 Intracellular processing: a kinetic analysis of the role of heparan sulfate proteoglycans. *Biochemistry* 39, 3788–3796. doi: 10.1021/bi992243d

Stangner, T., Wagner, C., Singer, D., Angioletti-Uberti, S., Gutsche, C., Dzubiella, J., et al. (2013). Determining the specificity of monoclonal antibody HPT-101 to tau-peptides with optical tweezers. *ACS Nano* 7, 11388–11396. doi: 10.1021/nn405303u

Xu, D., and Esko, J. D. (2014). Demystifying heparan sulfate–protein interactions. *Annu. Rev. Biochem.* 83, 129–157. doi: 10.1146/annurev-biochem-060713-035314

Yuan, C., Chen, A., Kolb, P., and Moy, V. T. (2000). Energy landscape of streptavidin–biotin complexes measured by atomic force microscopy. *Biochemistry* 39, 10219–10223. doi: 10.1021/bi992715o

Zhu, C. (2014). Mechanochemitry: a molecular biomechanics view of mechanosensing. *Ann. Biomed. Eng.* 42, 388–404. doi: 10.1007/s10439-013-0904-5

Conflict of Interest: The authors declare that the research was conducted in the absence of any commercial or financial relationships that could be construed as a potential conflict of interest.

frontiers in Molecular Biosciences

BRIEF RESEARCH REPORT
published: 09 November 2020
doi: 10.3389/fmolb.2020.610277

Confinement Geometry Tunes Fascin-Actin Bundle Structures and Consequently the Shape of a Lipid Bilayer Vesicle

*Yashar Bashirzadeh[1], Nadab H. Wubshet[1] and Allen P. Liu[1,2,3,4]**

[1] Department of Mechanical Engineering, University of Michigan, Ann Arbor, MI, United States, [2] Department of Biomedical Engineering, University of Michigan, Ann Arbor, MI, United States, [3] Department of Biophysics, University of Michigan, Ann Arbor, MI, United States, [4] Cellular and Molecular Biology Program, University of Michigan, Ann Arbor, MI, United States

Depending on the physical and biochemical properties of actin-binding proteins, actin networks form different types of membrane protrusions at the cell periphery. Actin crosslinkers, which facilitate the interaction of actin filaments with one another, are pivotal in determining the mechanical properties and protrusive behavior of actin networks. Short crosslinkers such as fascin bundle F-actin to form rigid spiky filopodial protrusions. By encapsulation of fascin and actin in giant unilamellar vesicles (GUVs), we show that fascin-actin bundles cause various GUV shape changes by forming bundle networks or straight single bundles depending on GUV size and fascin concentration. We also show that the presence of a long crosslinker, α-actinin, impacts fascin-induced GUV shape changes and significantly impairs the formation of filopodia-like protrusions. Actin bundle-induced GUV shape changes are confirmed by light-induced disassembly of actin bundles leading to the reversal of GUV shape. Our study contributes to advancing the design of shape-changing minimal cells for better characterization of the interaction between lipid bilayer membranes and actin cytoskeleton.

Keywords: actin, fascin, membrane deformation, encapsulation, giant unilamellar lipid vesicles

OPEN ACCESS

Edited by:
Yuan Lin,
The University of Hong Kong, Hong Kong

Reviewed by:
Feng-Ching Tsai,
Institut Curie, France
Ellen Hyeran Kang,
University of Central Florida, United States

***Correspondence:**
Allen P. Liu
allenliu@umich.edu

Specialty section:
This article was submitted to Biophysics, a section of the journal Frontiers in Molecular Biosciences

Received: *25 September 2020*
Accepted: *20 October 2020*
Published: *09 November 2020*

Citation:
Bashirzadeh Y, Wubshet NH and Liu AP (2020) Confinement Geometry Tunes Fascin-Actin Bundle Structures and Consequently the Shape of a Lipid Bilayer Vesicle. Front. Mol. Biosci. 7:610277. doi: 10.3389/fmolb.2020.610277

INTRODUCTION

Dynamics of actin filaments are coordinated to form different networks that regulate cellular functions by supporting and remodeling the plasma membrane (Fletcher and Mullins, 2010; Stricker et al., 2010), generating driving forces for cell motility and cell division, facilitating cell adhesion to extracellular matrix (Burridge et al., 1990), and spatially organizing cellular machineries (Matsudalra, 1991; Pollard and Borisy, 2003; Pollard and Cooper, 2009). The dynamic organization of actin networks is regulated by a number of accessory proteins that coordinate actin polymerization/de-polymerization and crosslink actin filaments to one another, to other cytoskeletal components, and to cellular membranes. Actin crosslinkers organize actin filaments into bundles and networks, and each type of actin crosslinker has specific attributes to regulate actin organization and subsequently cellular functionality (Matsudalra, 1991; Tseng et al., 2002), including cell locomotion. Given the diversity in crosslinkers and architecture of actin networks, it is important to understand how the assembly of actin networks induces morphological changes of cells and how multiple crosslinkers orchestrate cellular shape changes.

During cell motility, two distinct structures are formed at the leading edge of the cell: filopodia and lamellipodia. Filopodia is a protrusive organelle that together with lamellipodia drives cellular motility, particularly by functioning as a sensor to the external environment (Ridley et al., 2003; Adams, 2004). The prominent actin crosslinker in filopodia is fascin (Yamashiro et al., 1998). Fascin is a small crosslinker that forms linear, closely packed bundles from parallel filaments that, under specific circumstances, dynamically remodels the plasma membrane through the formation of filopodia (Otto et al., 1979; Small, 1988; Lewis and Bridgman, 1992; Svitkina et al., 2003). Prior *in vitro* reconstitution works have shown the mechanism of filopodia formation and the role of fascin as an actin filament crosslinker forming stiff linear actin bundles (Vignjevic et al., 2003; Yang et al., 2013). Using *in vitro* reconstitution on functionalized beads and supported lipid bilayers, research has demonstrated the transition of actin filaments from dendritic networks to bundled networks by the recruitment of fascin as actin filaments elongate (Haviv et al., 2006; Vignjevic et al., 2006; Lee et al., 2010). Furthermore, reconstituted dendritic actin networks on the surface of giant unilamellar vesicles (GUVs) have been shown to spontaneously generate filopodia-like protrusions that deform membranes in the absence of fascin (Liu et al., 2008; Simon et al., 2019). Moreover, research has also delved into how two crosslinkers, fascin and α-actinin, concurrently generate force to form filopodia and its subsequent effect in enhancing the mechanical response of the cell (Tseng et al., 2005). Recently, it was also demonstrated that the size of fascin and α-actinin allows them to self-sort *in vitro* when forming actin bundles by inhibiting the recruitment of one another (Winkelman et al., 2016).

Although actin crosslinkers such as fascin have been well-studied using various reconstitution assays previously, it remains unclear how different actin crosslinkers individually and synergistically construct actin bundle structures that generate forces to induce membrane deformation. Encapsulation of actin and accessory proteins inside membrane-enclosed systems such as GUVs allow for studying the orchestration of actin networks and their interaction with the lipid membrane in a cell-like compartment without the involvement of complex cell signaling pathways (Bashirzadeh and Liu, 2019). Encapsulated actin crosslinkers such as fascin, α-actinin, and filamin assemble actin into diverse structures (Honda et al., 1999; Abkarian et al., 2011; Bashirzadeh et al., 2020; Litschel et al., 2020). These structures have been shown to induce diverse GUV morphological changes (Honda et al., 1999; Limozin and Sackmann, 2002; Abkarian et al., 2011; Tsai and Koenderink, 2015; Litschel et al., 2020), and the shape changes were recently shown to be reversible by light-induced actin bundle disassembly (Litschel et al., 2020). Recent advances in encapsulation methods have been shown to be effective in generating GUVs encapsulating functional proteins (Majumder et al., 2019; Litschel et al., 2020). Reconstitution of actin networks inside GUVs has shown motor protein-induced membrane deformation by contracting membrane-associated actin cortex and rings (Maan et al., 2018; Litschel et al., 2020), but examples of such cellular reconstitution studies remain limited.

By confining actin polymerization and bundling process in GUVs, here we studied the formation of actin structures by fascin and their interaction with the lipid membrane. We found that membrane deformation patterns were correlated to the concentration of fascin. In addition, small GUVs increased bundle-bundle proximity, fascin-induced crosslinking at the GUV center, and the formation of protrusions akin to filopodia. Actin bundle-induced deformations could be reversed by actin de-polymerization using exposure to light. Light-induced actin bundle disassembly and restorative property of deformed membranes are further characterized as a function of actin bundle architecture. Moreover, we co-encapsulated fascin and α-actinin at different concentration ratios and studied changes in membrane deformation as a function of GUV size and GUV shape restoration in comparison to fascin alone. Our results highlight the feasibility of the confinement of a mixture of biopolymer networks for studying cytoskeleton-membrane interactions and cellular shape changes.

MATERIALS AND METHODS

Preparation of Proteins and Reagents

We purified actin from rabbit skeletal muscle acetone powder (Pel-Freez Biologicals) as described previously (Pardee and Aspudich, 1982) or purchased it from Cytoskeleton Inc, United States. ATTO 488 actin was purchased from Hypermol Inc, Germany. α-Actinin was purchased from Cytoskeleton Inc. We purified fascin from *E. coli* as Glutathione-S-Transferase (GST) fusion protein. For purification, BL21(DE3) *E. coli* cells was transformed with pGEX-4T-3 (GE Healthcare) containing the coding sequences of fascin. Cells were grown at 37°C while shaking at 220 rpm until the OD_{600} reached 0.5–0.6. Protein expression was induced with 0.1 mM IPTG and cell culture was incubated at 24°C for 8 h. Cells were harvested by centrifugation at 4,000 × g for 15 min and washed with PBS once. Pellets were stored at −80°C until the day of purification. Cell pellets were resuspended in lysis buffer (20 mM K-HEPES pH 7.5, 100 mM NaCl, 1 mM EDTA, 1 mM PMSF) and ruptured by sonication. Cell lysates were centrifuged at 75,000 × g for 25 min and supernatants were loaded on a GSTrap FF 1 mL column (GE Healthcare) using an AKTA Start purification system (GE Healthcare) at a flow rate of 1 mL/min. The column was washed with 15 mL washing buffer (20 mM K-HEPES pH 7.5, 100 mM NaCl) and the protein was eluted with 5 mL elution buffer (washing buffer + 10 mM reduced L-glutathione). Purified fascin was dialyzed against 1 L PBS twice for 3 h and once overnight at 4°C. Protein concentration was calculated by UV absorption using predicted molar extinction coefficients (ExPasy) of 110,700 $M^{-1}cm^{-1}$. Proteins were concentrated with Centricon filters (Merck-Millipore) when needed and/or diluted to a final concentration of 1 mg/mL in PBS.

Generation of GUVs

We modified continuous droplet interface crossing encapsulation (cDICE) technique for robust encapsulation in GUVs of various sizes (Abkarian et al., 2011; Bashirzadeh et al., 2020; Litschel et al.,

2020). Briefly, a custom 3D-printed chamber is mounted on a benchtop stir plate and rotated at 1,200 rpm. An outer solution of 200 mM glucose (matched to the osmolarity of the inner solution) is pipetted into the chamber. Then, the lipid mixture (∼70% DOPC, 30% cholesterol, and a trace concentration of fluorescent lipid) in a mixture of silicone oil and mineral oil (4:1) is added. The lipid-oil solution forms an interface at the oil–water interface. Inner solution containing 5 μM actin including 10% ATTO 488 actin in polymerization buffer containing 50 mM KCl, 2 mM $MgCl_2$, 0.2 mM $CaCl_2$, and 4.2 mM ATP in 15 mM Tris, pH 7.5 and 5% OptiPrep, 0.25–2.5 μM fascin and/or 0.5–1.5 μM α-actinin were added into 700 μL of the lipid–oil mix and droplets were generated by pipetting up and down. GUVs were then generated by dispensing the droplets into the cDICE chamber. A lipid bilayer is formed when a second layer of lipid is acquired as the droplets cross the lipid/oil-outer solution interface.

Bulk Fascin-Actin Bundle Assay

Five micrometers of monomeric actin with different concentrations of fascin were added to the actin polymerization buffer containing the same amounts buffer, salts, and ATP as those used for encapsulation experiments. Thirty minutes after polymerization and bundling at room temperature, Acti-stain 488 phalloidin was added (instead of using ATTO 488 actin) to stabilize actin bundles.

Imaging and Image Processing

Following cDICE, GUVs were transferred to a 96-well plate for imaging. OptiPrep in the inner solution increases GUV density and accelerates sedimentation of GUVs onto the bottom of well plate. For imaging actin bundles in bulk, the solution containing actin bundles was confined between a cover slip and glass slide. All samples were imaged at least 1 hour after actin polymerization and bundling. An Olympus IX-81 inverted microscope equipped with a spinning disk confocal (Yokogawa CSU-X1), AOTF-controlled solid-state lasers (Andor Technology), and an iXON3 EMCCD camera (Andor Technology) was used for microscopy. Images were magnified by an oil immersion 60×/1.4 NA objective lens mounted on the microscope. Images were acquired by MetaMorph software (Molecular Devices). Fluorescence images of actin and lipids were taken with 488 nm and 561 nm laser excitation, respectively. Z-stack fluorescence confocal image sequence of lipids and actin were taken with a z-step size of 0.5 μm.

Images were processed using ImageJ/Fiji (Schindelin et al., 2012; Schneider et al., 2012; Litschel et al., 2020), SOAX (Xu et al., 2014, 2015), and MATLAB routines (Bashirzadeh et al., 2020). 3D images were created using 3D Project command in ImageJ/Fiji. Skeletonized bundles were generated by SOAX source code (Xu et al., 2014, 2015) following image-processing of z-stack image sequences using ImageJ/Fiji, complemented with the plugin Squassh (Rizk et al., 2014) from the MOSAIC ToolSuite update site (Litschel et al., 2020). MATLAB routines were developed to reconstruct generated SOAX text files as a USCF Chimera marker file, include a colormap for z coordinates, and save file as.cmm format for 3D visualization in USCF Chimera (Pettersen et al., 2004).

Data Analysis

Actin bundle phenotypes and GUV shape changes were characterized from z-stack actin and lipid images. The diameter of a GUV was measured by line scan from GUV images. The percentages and probabilities of mid-plane bundle formation, network formation, filopodia-like protrusions, and GUV shape changes (membrane deformation and/or filopodia-like protrusions) were obtained by their count divided by the total number of GUVs with actin bundles (i.e. GUVs encapsulating fluorescent actin monomers with no sign of bundling activity were not counted). We calculated the persistence length of fascin-actin bundles using the skeletonized images of actin bundles by measuring their orientational correlation function as described previously (Bashirzadeh et al., 2020). Persistence length values are shown as average ± standard error of the mean of the data at each fascin concentration.

For probability and percentage measurements at least 2 independent experiments were conducted for each condition indicated. The reported p values are two-tail, unpaired two-sample student t-test assuming unequal variances.

RESULTS

Actin Bundling by Fascin Reshapes GUVs to Different Geometries Yet Reversible by Light

We first encapsulated actin and fascin in actin polymerization buffer into GUVs to observe F-actin bundling activity in a membrane-enclosed environment. Fascin formed rigid actin bundles some of which were non-protrusive yet deformed the membrane while others were rigid enough to protrude into the membrane and formed long filopodia-like structures (**Figure 1**). Stabilized GUVs deformed by fascin bundles were restored to their spherical resting shape due to actin bundle disassembly under prolonged exposure to 488 nm light (**Figure 1**). In the absence of actin, prolonged light exposure has no impact on vesicle shapes at all. This confirms that bundle elongations act as the driving force for GUV shape changes, and they support and stabilize deformed GUVs. Although bundle disassembly under light exposure was accompanied by GUV shape reversal, the absence of bundle-membrane interactions in filopodia-like membrane protrusions and disassembly of actin filaments in their interior destabilized the now actin-free protruded membrane. After the disassembly of actin bundles, all GUVs maintained their spherical shape without rupturing (**Supplementary Video S1**).

GUV Size-Dependent Amalgamation of Fascin-Bundles Contribute to Protrusion

In order to test the influence of confinement geometry on actin bundling by fascin and interaction of bundles, we encapsulated fascin and actin at different molar ratios in a large population of GUVs with varying sizes. Fascin-bundles appeared as either

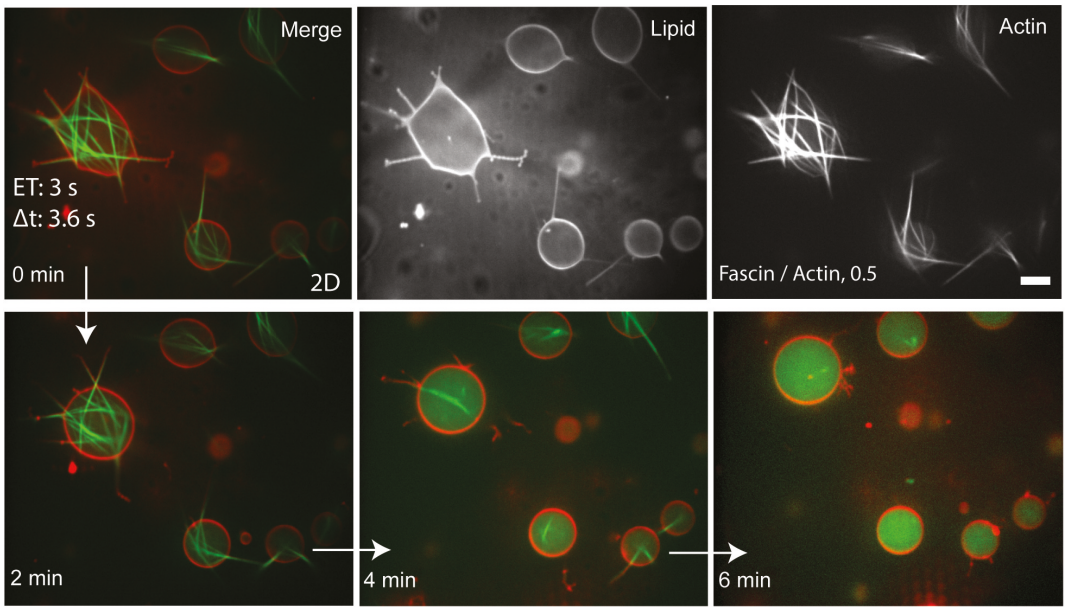

FIGURE 1 | Actin **(top right)**, lipid **(top middle)**, and merged **(top left)** confocal images of actin bundles which assembled to deform GUVs and formed long filopodia-like membrane protrusions. Application of 488 nm light at high exposure times (3 s) resulted in the disassembly of actin bundles and reversal of GUV shape without affecting the integrity of the lipid bilayer. Images were captured at 1 frame/3.6 s. Fascin/actin, 0.5 (M/M). Scale bar, 10 μm.

networks or a single bundle in GUVs (**Figure 2**). At fascin / actin molar ratio of 0.5, fascin-bundles in small GUVs (7–16 μm diameter) mostly appeared as long bundles at the GUV midplane which protrude into the membrane to form long filopodia-like structures from both ends of the bundle. Bundles were straight and their lengths were consistent with those observed in bulk, some spanning beyond GUV diameter (**Supplementary Figure 1**) (Claessens et al., 2008; Breitsprecher et al., 2011). We find that fascin-to-actin molar ratio determines bundle length in our encapsulated system, as opposed to the concentration of actin and fascin in bulk experiments (Claessens et al., 2008). At fascin/actin molar ratio of 0.5 and 0.1, actin bundles in most GUVs appeared as an amalgamation of several actin bundles changing GUV shape from spheres to spindles (**Figures 2A,B**). Some GUVs, however, deformed into irregular shapes by crimped or protruded actin bundles the majority of which had lengths well above GUV diameter (**Figures 2A,B**). The majority of single bundles aligned horizontally with respect to the GUV surface and localized at the GUV equatorial plane. Actin localization was often more intense at the locus of membrane protrusion in GUVs (**Figures 2C,D**) which could possibly be an indication of membrane-induced actin bundling to facilitate protrusion (Liu et al., 2008). By decreasing fascin concentration to a molar ratio of 0.05, we rarely observed single bundles. Rather, the majority of actin bundles appeared to be forming networks in small GUVs (7–16 μm diameter) (**Figure 2E**).

Analyzing GUV populations at three fascin molar ratios showed that indeed, the probability of the formation of a single actin bundle in small (7–16 μm diameter) GUVs was high (0.75) at fascin-to-actin ratios of 0.5 and 0.1 while network formation probability was high (0.8 and 0.92, respectively) in large (>16 μm diameter) GUVs at the same fascin molar ratios (**Figure 3A**). Increased fascin-mediated interaction between actin filaments being bundled in a small volume increase the chance of actin to merge into a single bundle. The balance of forces in and on GUVs possibly positions single bundles in the GUV equatorial plane. The resistance of long packed bundles against bending under the influence of membrane curvature could also contribute to the merging of actin bundles at the GUV mid-plane. Such resistance, described in terms of bundle persistence length, is highly influenced by crosslinker type and concentration (Claessens et al., 2006a; Takatsuki et al., 2014). The persistence length of encapsulated fascin-actin bundles were indeed increased from 53 ± 12 μm to 173 ± 41 μm by increasing fascin molar ratio from 0.05 to 0.5 which is significantly greater than the F-actin persistence length (∼14–17 μm) (**Figure 3B**) (Le Goff et al., 2002). Such increase is consistent with an increase in persistence length of fascin-actin bundles in bulk and motility assays values from ∼20 μm at molar ratio of 0.05 to ∼150 μm at molar ratio of 0.5 (Takatsuki et al., 2014). The increase in persistence length is an indication of the effect of encapsulation in merging nearby actin bundles with high flexural rigidity. Encapsulation of actin networks has also been shown to increase network stiffness by diminishing filament fluctuations (Claessens et al., 2006b). We found no relationship between the length and persistence length of the encapsulated actin bundles. While high persistence length of the elongated fascin-actin bundles favors merging and protrusion at the mid-plane of small GUVs, lowering fascin concentration and consequently bundle persistence length can induce the formation of kinked actin bundle structures around GUV periphery. Fascin at a molar ratio of 0.5 induced large-scale membrane shape changes in all small GUVs (**Figure 3C**),

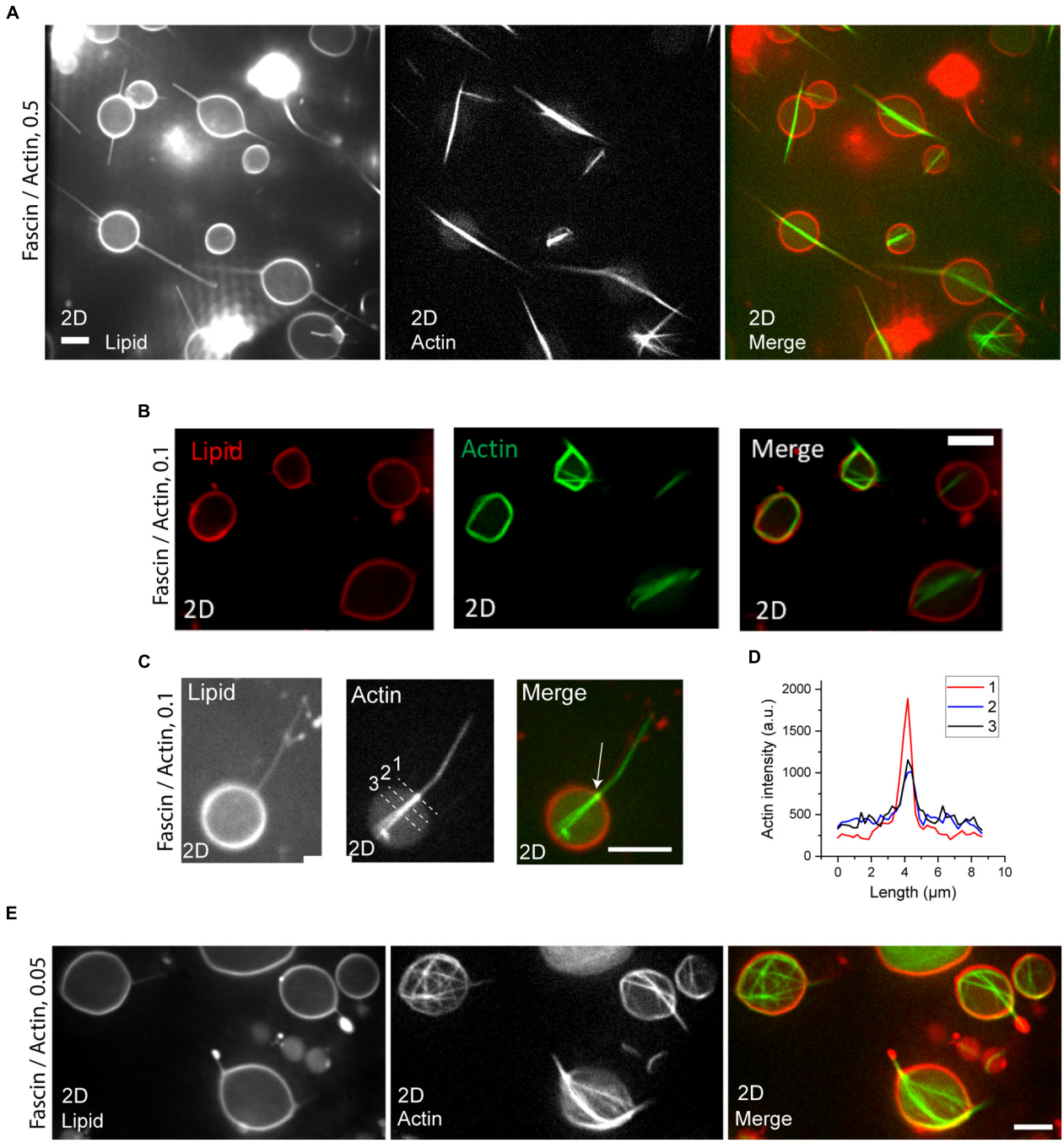

FIGURE 2 | (A,B) Actin (left), lipid (middle), and merged (right) confocal images of actin bundles in small GUVs (diameter < 16 μm) at fascin concentrations of 2.5 μM **(A)** and 0.5 μM **(B)**. Actin, 5 μM. Scale bars, 10 μm. **(C)** Actin (left), lipid (middle), and merged (right) confocal images of a protruding actin bundle with aggregated actin at the point of initiation of membrane protrusion (arrow) at fascin concentration of 0.5 μM. **(D)** Actin fluorescence intensity profile across the dashed lines in **(C)**. **(E)** Actin (left), lipid (middle), and merged (right) confocal images of actin bundles in small GUVs (diameter < 16 μm) at a fascin concentration of 0.25 μM. Actin, 5 μM. Scale bar, 10 μm.

the majority of which had at least one filopodia-like membrane protrusion (**Figure 3D**). Fascin concentration here was high enough to induce GUV shape changes in all large GUVs with the majority of them appearing to have filopodia-like protrusions (not statistically analyzed). At a low fascin concentration, smaller portion of GUVs changed shape as expected due to lower bundle rigidity (Takatsuki et al., 2014) (**Figures 3C,D**). The schematic in **Figure 3E** illustrates bundle-bundle interactions at high fascin concentrations in small GUVs that could lead to the formation of a single bundle with increased rigidity at the

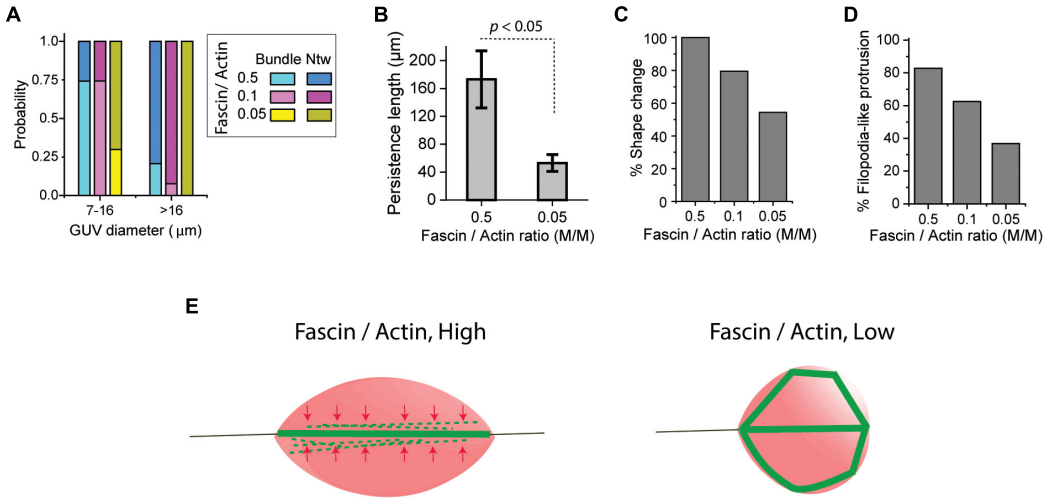

FIGURE 3 | (A) Probability of the formation of a single actin bundle (Bundle) or networks (Ntw) in small GUVs (7–16 μm diameter) and large GUVs (>16 μm diameter) at actin concentration of 5 μM with different fascin concentrations indicated. Number of GUVs >30 per experiment per category; ≥2 independent experiments per fascin concentration. **(B)** The persistence length of actin bundles at two fascin concentrations. Actin, 5 μM; >18 bundles in 6 GUVs across two independent experiments were analyzed per fascin concentration. Error bar represents standard error of the mean. **(C)** The percentage of small GUVs (7–16 μm diameter) with shape changes (deform and/or protrude) by fascin-actin bundles at various fascin concentrations indicated. Number of GUVs > 30 per experiment per category; ≥2 independent experiments per fascin concentration. **(D)** The percentage of small GUVs (7–16 μm diameter) with filopodia-like membrane protrusions by fascin-actin bundles at different fascin concentrations indicated. Actin concentration is 5 μM. Number of GUVs > 30 per experiment per category; ≥2 independent experiments per fascin concentration. **(E)** Schematic representation of the formation of single actin bundles at high fascin concentrations (left) and actin bundle structures around the membrane at low fascin concentrations (right) in small GUVs (7–16 μm diameter). Small geometry of confinement increases the interaction of fascin-bundled actin filaments at high fascin concentrations to merge into a stiff protruding bundle at the GUV mid-plane. These bundles cause GUVs to deform into spindle-like vesicles with filopodia-like protrusions.

GUV midplane thereby contributing to membrane protrusion. At low fascin concentrations, low persistence length and the absence of bundle-bundle interactions result in bundle buckling and/or bending around the membrane to form peripheral actin bundle structures.

Fascin-Induced Filopodia-Like Protrusions Are Abrogated in the Presence of α-Actinin

To explore how the flexibility of actin bundles can influence their interaction at the midplane of GUVs and subsequent GUV shape changes, we sought to co-encapsulate fascin and α-actinin with actin in GUVs. The persistence length of encapsulated α-actinin-actin bundles is lower than the persistence length of fascin-actin bundles measured here (Takatsuki et al., 2014; Bashirzadeh et al., 2020). This causes α-actinin-actin bundles to bend around the membrane and merge into an actin ring in cell-sized GUVs in order to minimize their elastic energy (Miyazaki et al., 2015) (**Supplementary Figure 2A**). Bending also increases the chance of actin bundle-membrane interactions and colocalization of actin filaments with the membrane (**Supplementary Figure 2B**). Encapsulation of fascin, α-actinin, and actin in GUVs caused a portion of actin bundles to bend at the GUV periphery (**Figure 4A**) some of which resulted in local (**Figure 4B**) or large-scale (**Figure 4C**) membrane deformations by forming an actin meshwork around the periphery (**Figure 4D**, arrow). Reversal of the GUV shape to its original spherical shape under exposure to 488 nm light was observed similar to that observed in the presence of fascin-only bundled actin (**Figure 1**, **Supplementary Figures 3A–C**, and **Supplementary Videos 2–4**). This confirmed that fascin-α-actinin actin bundles drove GUV shape changes and applied lateral forces to deform GUVs. Higher α-actinin concentration required higher exposure time indicating that the presence of α-actinin can suppress bundle disassembly under light exposure (**Supplementary Figure 3D** and **Supplementary Video 5**). This was confirmed by the observation that α-actinin-actin networks do not disassemble by 488 nm light (**Supplementary Figure 3E** and **Supplementary Video 6**). Further investigations are required to examine the influence of light on association/dissociation rate and bundling ability of α-actinin and fascin.

Although fascin-α-actinin-actin bundles could often deform GUVs, only around half of small (7–16 μm diameter) GUVs changed shape in the presence of α-actinin and fascin both at a molar ratio of 0.1. This was significantly lower compared to the number of GUVs deformed by fascin-actin bundles at a fascin molar ratio of 0.1 (50% < 80%) (**Figure 4E**). The portion of small GUVs which changed shape further decreased by increasing α-actinin molar ratio from 0.1 to 0.3 (37% < 50%) (**Figure 4E**). The majority of fascin-actin bundles at fascin molar ratio of 0.1 induced filopodia-like membrane–protrusions (62.5%) in small GUVs more than two-third of which was by protrusion of single bundles at the GUV midplane (**Figure 4F**). Addition of α-actinin at molar ratio of 0.1 abrogated the formation

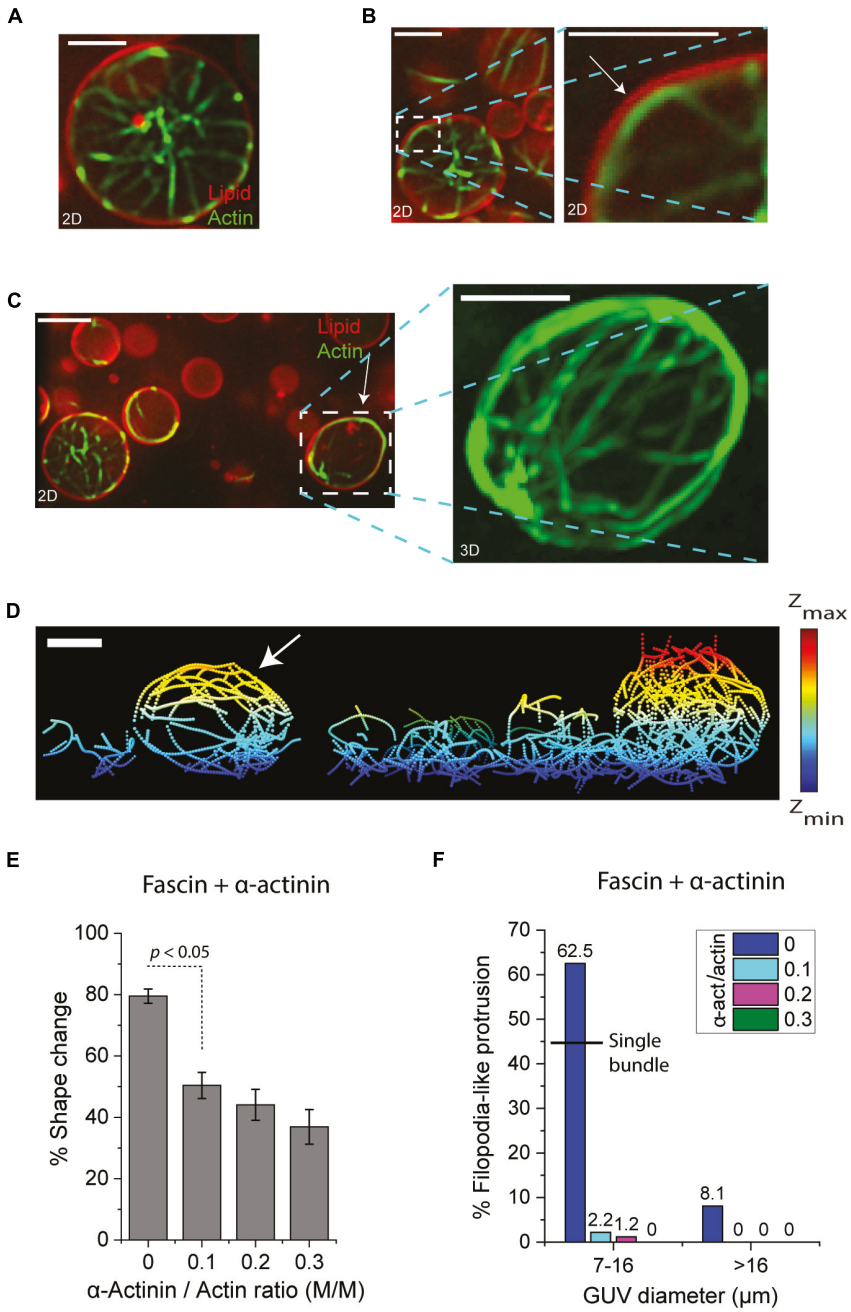

FIGURE 4 | (A–C) Representative confocal merged images (actin:green, lipid:red) of GUVs encapsulating actin bundles in the presence of fascin and α-actinin. Actin bundles in the lumen of large GUVs do not deform GUVs **(A)**. Localized actin bundles **(B)** and meshwork **(C)** at or around the periphery deform GUVs (arrows). Fascin/actin, 0.1 (M/M). α-actinin/actin, 0.1 (M/M). Scale bars, 10 μm. **(D)** Skeletonized image of encapsulated actin bundles in **(C)**. Actin meshwork in the deformed GUV is indicated by arrow. Scale bar, 10 μm. **(E)** The percentage of small GUVs (7–16 μm diameter) with shape changes by fascin-actin bundles without and with α-actinin at various concentrations. Fascin/actin, 0.1 (M/M). Actin, 5 μM. Error bars indicate standard error of the mean. Number of GUVs > 30 per experiment per category; three independent experiments per category. **(F)** The percentage of GUVs with filopodia-like membrane protrusions formed by fascin-actin bundles without and with α-actinin at various concentrations in small (7–16 μm diameter) and large (>16 μm diameter) GUVs. The black line indicates the probability of filopodia-like protrusion in small GUVs encapsulating a single actin bundle. Fascin/actin, 0.1 (M/M). Actin, 5 μM. Number of GUVs > 30 per experiment per category; three independent experiments per category.

of fascin-induced filopodia-like membrane protrusions (2.2%) (**Figure 4F**). No filopodia-like structures were observed by increasing α-actinin concentration to a molar ratio of 0.3. Similar trend was observed in large GUVs. However, filopodia-like protrusions by fascin-actin bundles were also significantly lower in large (>16 μm diameter) GUVs than small (7–16 μm

diameter) GUVs (8.1% < 62.5%) (**Figure 4F**). These results underscore the influence of actin crosslinkers and possibly a crosslinker competition mechanism for actin bundling on bundle persistence length and consequently GUV shape changes.

DISCUSSION

By cellular reconstitution of actin and actin crosslinking proteins in GUVs, we could recapitulate diverse membrane morphologies. We showed that both confinement geometry and crosslinker concentration influence bundle–bundle and bundle–membrane interactions in confinement thereby determining actin bundle architecture and GUV shape. These results highlight the influence of cell size and density of actin crosslinking proteins on the interaction of actin cytoskeleton and plasma membrane in small scale and the overall cellular structure in a larger scale. We speculate that depletion effects in small volume increase the chance of non-specific attractions between filaments and bundles which contribute to ATP hydrolysis-dependent actin polymerization and fascin-mediated bundling (Marenduzzo et al., 2006a,b; Miyazaki et al., 2015). We showed that high fascin concentration significantly contributed to the amalgamation of actin bundles into one protruding unit in small GUVs. Bundle persistence length was shown to sharply increase by increasing the concentration of fascin. Hence, our observations suggest that GUV size and fascin concentration both contribute to fascin-mediated filopodia-like protrusions by increasing the chance of actin bundles interacting with one another in a confined environment. Our results are in agreement with the formation of packed fascin-actin bundles which remain straight at the tip of protrusion (Tsai and Koenderink, 2015). It has been suggested that membrane elasticity can contribute to actin bundle assembly and protrusion of branched actin networks at the membrane (Liu et al., 2008). This model and occasional aggregation of straight bundles in protrusion sites suggest a mechanism by which membrane protrusion is facilitated through a feedback mechanism where flexible lipid bilayer and fascin both contribute to protrusion at the bundle-membrane interface.

External control over bundle disassembly and the consequent reversal of GUV shape by light exposure reported here can lay the foundation for numerous studies on membrane morphology and the mechanics of network–membrane complex in membrane-encapsulated biopolymer networks. One future approach could be light-induced localized disassembly of reconstituted actin bundles and branched actin networks by targeted photo-illumination (Linsmeier et al., 2016). This will enable direct observation of actin-membrane interactions upon actin network disassembly in only selected regions of interest. By cellular reconstitution of membrane-associated actin networks in the presence of fascin and network disassembly by targeted illumination, one can study the dynamics of assembly/disassembly in filopodia-like structures, which can provide insights into the understanding of transition/remission from lamellipodia to filopodia in reconstituted networks (Haviv et al., 2006) and in living cells.

Our findings revealed that fascin-mediated filopodia-like protrusions in cell-sized GUVs were suppressed in the presence of α-actinin. We have shown recently that actin bundles are more likely to undergo transient interactions with the bilayer at high α-actinin concentrations (Bashirzadeh et al., 2020). Hence, the bending of encapsulated α-actinin-actin bundles and their interaction with the membrane is expected to be responsible for the inhibition of protrusion. Supported by coarse-grained simulations, bulk and motility reconstitution assays have demonstrated spontaneous sorting and domain formation of fascin and α-actinin in a crosslinker size-dependent manner (Winkelman et al., 2016; Freedman et al., 2019). As protein sorting is expected to contribute to the formation of filopodia by fascin-bundles, the mechanism of inhibition of membrane spikes in the presence of α-actinin remains an open question. Visualizing fluorescently labeled crosslinkers in actin bundles can potentially reveal the existence of such mechanism.

DATA AVAILABILITY STATEMENT

The raw data supporting the conclusions of this article will be made available by the authors, without undue reservation.

AUTHOR CONTRIBUTIONS

YB and AL designed the experiments. YB and NW conducted the experiments. YB analyzed the experimental data. YB, NW, and AL prepared purified proteins. YB developed the data processing methods. YB, NW, and AL wrote the manuscript. All authors discussed the results and commented on the manuscript.

FUNDING

This work was supported by the National Science Foundation (NSF) under Grant No. CBET-1844132 to AL. AL also acknowledges support from NSF MCB-1817909 and MCB-1935265.

ACKNOWLEDGMENTS

We thank Petra Schwille, Thomas Litschel, and Giovanni Cardone of the MPI-Biochemistry for providing FIJI image processing tools.

SUPPLEMENTARY MATERIAL

The Supplementary Material for this article can be found online at: https://www.frontiersin.org/articles/10.3389/fmolb.2020.610277/full#supplementary-material

REFERENCES

Abkarian, M., Loiseau, E., and Massiera, G. (2011). Continuous droplet interface crossing encapsulation (cDICE) for high throughput monodisperse vesicle design. *Soft. Matter.* 7, 4610–4614. doi: 10.1039/c1sm05239j

Adams, J. C. (2004). Fascin protrusions in cell interactions. *Trends Cardiovasc. Med.* 14, 221–226. doi: 10.1016/j.tcm.2004.06.002

Bashirzadeh, Y., and Liu, A. P. (2019). Encapsulation of the cytoskeleton: towards mimicking the mechanics of a cell. *Soft. Matter.* 15, 8425–8436. doi: 10.1039/c9sm01669d

Bashirzadeh, Y., Redford, S. A., Lorpaiboon, C., Groaz, A., Litschel, T., Schwille, P., et al. (2020). Actin crosslinker competition and sorting drive emergent GUV size-dependent actin network architecture. *bioRxiv* [Preprint]. doi: 10.1101/2020.10.03.322354

Breitsprecher, D., Koestler, S. A., Chizhov, I., Nemethova, M., Mueller, J., Goode, B. L., et al. (2011). Cofilin cooperates with fascin to disassemble filopodial actin filaments. *J. Cell Sci.* 124, 3305–3318. doi: 10.1242/jcs.086934

Burridge, K., Nuckolls, G., Otey, C., Pavalko, F., Simon, K., and Turner, C. (1990). Actin—membrane interaction in focal adhesions. *Cell Diff. Dev.* 32, 337–342. doi: 10.1016/0922-3371(90)90048-2

Claessens, M. M., Bathe, M., Frey, E., and Bausch, A. R. (2006a). Actin-binding proteins sensitively mediate F-actin bundle stiffness. *Nat. Mater.* 5, 748–753. doi: 10.1038/nmat1718

Claessens, M. M., Tharmann, R., Kroy, K., and Bausch, A. (2006b). Microstructure and viscoelasticity of confined semiflexible polymer networks. *Nat. Phys.* 2, 186–189. doi: 10.1038/nphys241

Claessens, M. M. A. E., Semmrich, C., Ramos, L., and Bausch, A. (2008). Helical twist controls the thickness of F-actin bundles. *Proc. Natl. Acad. Sci. U.S.A.* 105, 8819–8822. doi: 10.1073/pnas.0711149105

Fletcher, D. A., and Mullins, R. D. (2010). Cell mechanics and the cytoskeleton. *Nature* 463, 485–492.

Freedman, S. L., Suarez, C., Winkelman, J. D., Kovar, D. R., Voth, G. A., Dinner, A. R., et al. (2019). Mechanical and kinetic factors drive sorting of F-actin cross-linkers on bundles. *Proc. Natl. Acad. Sci. U.S.A.* 116, 16192–16197. doi: 10.1073/pnas.1820814116

Haviv, L., Brill-Karniely, Y., Mahaffy, R., Backouche, F., Ben-Shaul, A., Pollard, T. D., et al. (2006). Reconstitution of the transition from lamellipodium to filopodium in a membrane-free system. *Proc. Natl. Acad. Sci. U.S.A.* 103, 4906–4911. doi: 10.1073/pnas.0508269103

Honda, M., Takiguchi, K., Ishikawa, S., and Hotani, H. (1999). Morphogenesis of liposomes encapsulating actin depends on the type of actin-crosslinking. *J. Mol. Biol.* 287, 293–300. doi: 10.1006/jmbi.1999.2592

Le Goff, L., Hallatschek, O., Frey, E., and Amblard, F. (2002). Tracer studies on f-actin fluctuations. *Phys. Rev. Lett.* 89:258101.

Lee, K., Gallop, J. L., Rambani, K., and Kirschner, M. W. (2010). Self-assembly of filopodia-like structures on supported lipid bilayers. *Science* 329, 1341–1345. doi: 10.1126/science.1191710

Lewis, A. K., and Bridgman, P. C. (1992). Nerve growth cone lamellipodia contain two populations of actin filaments that differ in organization and polarity. *J. Cell Biol.* 119, 1219–1243. doi: 10.1083/jcb.119.5.1219

Limozin, L., and Sackmann, E. (2002). Polymorphism of cross-linked actin networks in giant vesicles. *Phys. Rev. Lett.* 89:168103.

Linsmeier, I., Banerjee, S., Oakes, P. W., Jung, W., Kim, T., and Murrell, M. P. (2016). Disordered actomyosin networks are sufficient to produce cooperative and telescopic contractility. *Nat. Commun.* 7, 1–9.

Litschel, T., Kelley, C. F., Holz, D., Koudehi, M. A., Vogel, S. K., Burbaum, L., et al. (2020). Reconstitution of contractile actomyosin rings in vesicles. *bioRxiv* [Preprint]. doi: 10.1101/2020.06.30.180901v1

Liu, A. P., Richmond, D. L., Maibaum, L., Pronk, S., Geissler, P. L., and Fletcher, D. A. (2008). Membrane-induced bundling of actin filaments. *Nat. Phys.* 4, 789–793. doi: 10.1038/nphys1071

Maan, R., Loiseau, E., and Bausch, A. R. (2018). Adhesion of active cytoskeletal vesicles. *Biophys. J.* 115, 2395–2402. doi: 10.1016/j.bpj.2018.10.013

Majumder, S., Wubshet, N., and Liu, A. P. (2019). Encapsulation of complex solutions using droplet microfluidics towards the synthesis of artificial cells. *J. Micromech. Microeng.* 29:083001. doi: 10.1088/1361-6439/ab2377

Marenduzzo, D., Finan, K., and Cook, P. R. (2006a). The depletion attraction: an underappreciated force driving cellular organization. *J. Cell Biol.* 175, 681. doi: 10.1083/jcb.200609066

Marenduzzo, D., Micheletti, C., and Cook, P. R. (2006b). Entropy-driven genome organization. *Biophys. J.* 90, 3712–3721. doi: 10.1529/biophysj.105.077685

Matsudalra, P. (1991). Modular organization of actin crosslinking proteins. *Trends Biochem. Sci.* 16, 87–92. doi: 10.1016/0968-0004(91)90039-x

Miyazaki, M., Chiba, M., Eguchi, H., Ohki, T., and Ishiwata, S. I (2015). Cell-sized spherical confinement induces the spontaneous formation of contractile actomyosin rings in vitro. *Nat. Cell Biol.* 17, 480–489. doi: 10.1038/ncb3142

Otto, J. J., Kane, R. E., and Bryan, J. (1979). Formation of filopodia in coelomocytes: localization of fascin, a 58,000 dalton actin cross-linking protein. *Cell* 17, 285–293. doi: 10.1016/0092-8674(79)90154-5

Pardee, J. D., and Aspudich, J. (1982). *[18] Purification of Muscle Actin, in Methods in Enzymology*. Amsterdam: Elsevier, 164–181.

Pettersen, E. F., Goddard, T. D., Huang, C. C., Couch, G. S., Greenblatt, D. M., Meng, E. C., et al. (2004). UCSF Chimera—A visualization system for exploratory research and analysis. *J. Comput. Chem.* 25, 1605–1612. doi: 10.1002/jcc.20084

Pollard, T. D., and Borisy, G. G. (2003). Cellular motility driven by assembly and disassembly of actin filaments. *Cell* 112, 453–465. doi: 10.1016/s0092-8674(03)00120-x

Pollard, T. D., and Cooper, J. A. (2009). Actin, a central player in cell shape and movement. *Science* 326, 1208–1212. doi: 10.1126/science.1175862

Ridley, A. J., Schwartz, M. A., Burridge, K., Firtel, R. A., Ginsberg, M. H., Borisy, G., et al. (2003). Cell migration: integrating signals from front to back. *Science* 302, 1704–1709. doi: 10.1126/science.1092053

Rizk, A., Paul, G., Incardona, P., Bugarski, M., Mansouri, M., Niemann, A., et al. (2014). Segmentation and quantification of subcellular structures in fluorescence microscopy images using Squassh. *Nat. Protoc.* 9, 586–596. doi: 10.1038/nprot.2014.037

Schindelin, J., Arganda-Carreras, I., Frise, E., Kaynig, V., Longair, M., Pietzsch, T., et al. (2012). Fiji: an open-source platform for biological-image analysis. *Nat. Methods* 9, 676–682. doi: 10.1038/nmeth.2019

Schneider, C. A., Rasband, W. S., and Eliceiri, K. W. (2012). NIH Image to ImageJ: 25 years of image analysis. *Nat. Methods* 9, 671–675. doi: 10.1038/nmeth.2089

Simon, C., Kusters, R., Caorsi, V., Allard, A., Abou-Ghali, M., Manzi, J., et al. (2019). Actin dynamics drive cell-like membrane deformation. *Nat. Phys.* 15, 602–609. doi: 10.1038/s41567-019-0464-1

Small, J. (1988). The actin cytoskeleton. *Electron Microsc. Rev.* 1, 155–174.

Stricker, J., Falzone, T., and Gardel, M. L. (2010). Mechanics of the F-actin cytoskeleton. *J. Biomech.* 43, 9–14. doi: 10.1016/j.jbiomech.2009.09.003

Svitkina, T. M., Bulanova, E. A., Chaga, O. Y., Vignjevic, D. M., Kojima, S.-I., Vasiliev, J. M., et al. (2003). Mechanism of filopodia initiation by reorganization of a dendritic network. *J. Cell Biol.* 160, 409–421. doi: 10.1083/jcb.200210174

Takatsuki, H., Bengtsson, E., and Månsson, A. (2014). Persistence length of fascin-cross-linked actin filament bundles in solution and the in vitro motility assay. *Biochim. Biophys. Acta Gen. Subj.* 1840, 1933–1942. doi: 10.1016/j.bbagen.2014.01.012

Tsai, F.-C., and Koenderink, G. H. (2015). Shape control of lipid bilayer membranes by confined actin bundles. *Soft. Matter.* 11, 8834–8847. doi: 10.1039/c5sm01583a

Tseng, Y., Kole, T. P., Lee, J. S., Fedorov, E., Almo, S. C., Schafer, B. W., et al. (2005). How actin crosslinking and bundling proteins cooperate to generate an enhanced cell mechanical response. *Biochem. Biophys. Res. Commun.* 334, 183–192. doi: 10.1016/j.bbrc.2005.05.205

Tseng, Y., Schafer, B. W., Almo, S. C., and Wirtz, D. (2002). Functional synergy of actin filament cross-linking proteins. *J. Biol. Chem.* 277, 25609–25616. doi: 10.1074/jbc.m202609200

Vignjevic, D., Kojima, S.-I., Aratyn, Y., Danciu, O., Svitkina, T., and Borisy, G. G. (2006). Role of fascin in filopodial protrusion. *J. Cell Biol.* 174, 863–875. doi: 10.1083/jcb.200603013

Vignjevic, D., Yarar, D., Welch, M. D., Peloquin, J., Svitkina, T., and Borisy, G. G. (2003). Formation of filopodia-like bundles in vitro from a dendritic network. *J. Cell Biol.* 160, 951–962. doi: 10.1083/jcb.200208059

Winkelman, J. D., Suarez, C., Hocky, G. M., Harker, A. J., Morganthaler, A. N., Christensen, J. R., et al. (2016). Fascin-and α-actinin-bundled networks contain intrinsic structural features that drive protein sorting. *Curr. Biol.* 26, 2697–2706. doi: 10.1016/j.cub.2016.07.080

Xu, T., Vavylonis, D., and Huang, X. (2014). 3D actin network centerline extraction with multiple active contours. *Med. Image Anal.* 18, 272–284. doi: 10.1016/j.media.2013.10.015

Xu, T., Vavylonis, D., Tsai, F.-C., Koenderink, G. H., Nie, W., Yusuf, E., et al. (2015). SOAX: a software for quantification of 3D biopolymer networks. *Sci. Rep.* 5:9081.

Yamashiro, S., Yamakita, Y., Ono, S., and Matsumura, F. (1998). Fascin, an actin-bundling protein, induces membrane protrusions and increases cell motility of epithelial cells. *Mol. Biol. Cell.* 9, 993–1006. doi: 10.1091/mbc.9.5.993

Yang, S., Huang, F.-K., Huang, J., Chen, S., Jakoncic, J., Leo-Macias, A., et al. (2013). Molecular mechanism of fascin function in filopodial formation. *J. Biol. Chem.* 288, 274–284. doi: 10.1074/jbc.m112.427971

Conflict of Interest: The authors declare that the research was conducted in the absence of any commercial or financial relationships that could be construed as a potential conflict of interest.

frontiers in Physics

BRIEF RESEARCH REPORT
published: 09 November 2020
doi: 10.3389/fphy.2020.596699

Triggering Cation-Induced Contraction of Cytoskeleton Networks via Microfluidics

*Shea N. Ricketts[1], Pawan Khanal[1], Michael J. Rust[2], Moumita Das[3], Jennifer L. Ross[4] and Rae M. Robertson-Anderson[1]**

[1]Department of Physics and Biophysics, University of San Diego, San Diego, CA, United States, [2]Department of Molecular Genetics and Cell Biology, University of Chicago, Chicago, IL, United States, [3]School of Physics and Astronomy, Rochester Institute of Technology, Rochester, NY, United States, [4]Department of Physics, Syracuse University, Syracuse, NY, United States

The dynamic morphology and mechanics of the cytoskeleton is determined by interacting networks of semiflexible actin filaments and rigid microtubules. Active rearrangement of networks of actin and microtubules can not only be driven by motor proteins but by changes to ionic conditions. For example, high concentrations of multivalent ions can induce bundling and crosslinking of both filaments. Yet, how cytoskeleton networks respond in real-time to changing ion concentrations, and how actin-microtubule interactions impact network response to these changing conditions remains unknown. Here, we use microfluidic perfusion chambers and two-color confocal fluorescence microscopy to show that increasing magnesium ions trigger contraction of both actin and actin-microtubule networks. Specifically, we use microfluidics to vary the Mg^{2+} concentration between 2 and 20 mM while simultaneously visualizing the triggered changes to the overall network size. We find that as Mg^{2+} concentration increases both actin and actin-microtubule networks undergo bulk contraction, which we measure as the shrinking width of each network. However, surprisingly, lowering the Mg^{2+}concentration back to 2 mM does not stop or reverse the contraction but rather causes both networks to contract further. Further, actin networks begin to contract at lower Mg^{2+} concentrations and shorter times than actin-microtubule networks. In fact, actin-microtubule networks only undergo substantial contraction once the Mg^{2+} concentration begins to lower from 20 mM back to 2 mM. Our intriguing findings shed new light on how varying environmental conditions can dynamically tune the morphology of cytoskeleton networks and trigger active contraction without the use of motor proteins.

Keywords: cytoskeleton, microfluidics, actin, microtubules, microscopy

OPEN ACCESS

Edited by:
Yuan Lin,
The University of Hong Kong, Hong Kong

Reviewed by:
Xinpeng Xu,
Guangdong Technion-Israel Institute of Technology (GTIIT), China
Taeyoon Kim,
Purdue University, United States

****Correspondence:***
Rae M. Robertson-Anderson
randerson@sandiego.edu

Specialty section:
This article was submitted to Biophysics, a section of the journal Frontiers in Physics

Received: *20 August 2020*
Accepted: *28 September 2020*
Published: *09 November 2020*

Citation:
Ricketts SN, Khanal P, Rust MJ, Das M, Ross JL and Robertson-Anderson RM (2020) Triggering Cation-Induced Contraction of Cytoskeleton Networks via Microfluidics. Front. Phys. 8:596699. doi: 10.3389/fphy.2020.596699

INTRODUCTION

The cytoskeleton, a dynamic network of filamentous proteins, enables cells to maintain shape and structure while carrying out a wide range of processes such as cell proliferation, migration and division. To enable such diverse processes and structural properties, cytoskeletal networks readily rearrange in response to changing environmental conditions (ions, nucleotide-triphosphates, and crowding) and interactions with accessory proteins. Two of the principle constituents of the cytoskeleton are thin semiflexible actin filaments, ~7 nm wide with a persistence length of

l_p ~ 10 μm, and thicker rigid microtubules, ~25 nm wide with l_p ~ 1 mm [1, 2]. Both filaments are also polyelectrolytes with an average linear charge density of 4 e/nm for actin filaments and 280 e/μm for microtubules [3–5]. Actin filaments serve primary roles in migratory processes, cellular contraction and maintaining cellular polarity while microtubules organize and maintain axonal branching, intracellular trafficking and mitotic spindle orientation during cellular division [6–10]. Further, interactions between actin and microtubules play critical roles in essential dynamic processes including directed cell migration, neuronal growth, cellular wound healing, cortical flow, and cellular division [11–16].

Active reorganization of cytoskeleton networks is typically driven by ATP-consuming motor proteins including myosin and kinesin. *In vitro* actin-myosin networks are shown to be contractile, while purified microtubule-kinesin networks form extensile liquid crystal networks [17–19]. However, due to the polyelectrolyte nature of both actin and microtubules, changes to the ionic conditions of the network environment can also trigger rearrangements in actin and microtubule networks. For example, high concentrations of Mg^{2+} ions have been shown to induce bundling and crosslinking of actin filaments [20–23] and microtubules [24, 25] via counterion crossbridges. Increasing Mg^{2+} concentration has also been shown to promote higher order structure formation in both actin and microtubule networks *in vitro* and *in vivo* [26–31].

We previously showed that the mechanical response of actin networks depended strongly on the Mg^{2+} concentration. Specifically, actin networks polymerized at Mg^{2+} concentrations of 2–52 mM exhibited an increase in network stiffness, nonlinear force response, elasticity and relaxation timescales with increasing Mg^{2+} concentration. We showed that this increase in the mechanical response arose from small-scale counterion-enabled crosslinking and bundling of actin filaments that occurred for Mg^{2+} concentrations ≥10 mM Mg^{2+}. Surprisingly, despite dramatic changes in mechanical behavior, the mesoscopic changes to network morphology and architecture were relatively small in nature [22].

While varying Mg^{2+} concentration has been shown to impact both actin and microtubules, no studies have investigated the effects of Mg^{2+} on composite actin-microtubule networks. Moreover, how dense cytoskeleton networks dynamically morph from one state to another as ion concentration changes remains unknown. To address these open questions, we use microfluidic perfusion chambers to slowly vary the Mg^{2+} concentration between 2 and 20 mM while imaging the triggered changes in actin and actin-microtubule networks using two-color confocal microscopy. Specifically, we characterize how the bulk network size changes as we vary the Mg^{2+} concentration from low (2 mM) to high (20 mM) and back to low (2 mM). We show that increasing the Mg^{2+} concentration triggers bulk contraction of both actin networks and actin-microtubule networks. However, when subsequently lowering the concentration from 20 to 2 mM Mg^{2+} both actin and actin-microtubule networks surprisingly continue contracting rather than re-expanding or stopping contraction. Moreover, as we describe here within, while both networks contract, there are marked differences in the contraction rate and characteristics for actin vs. actin-microtubule networks.

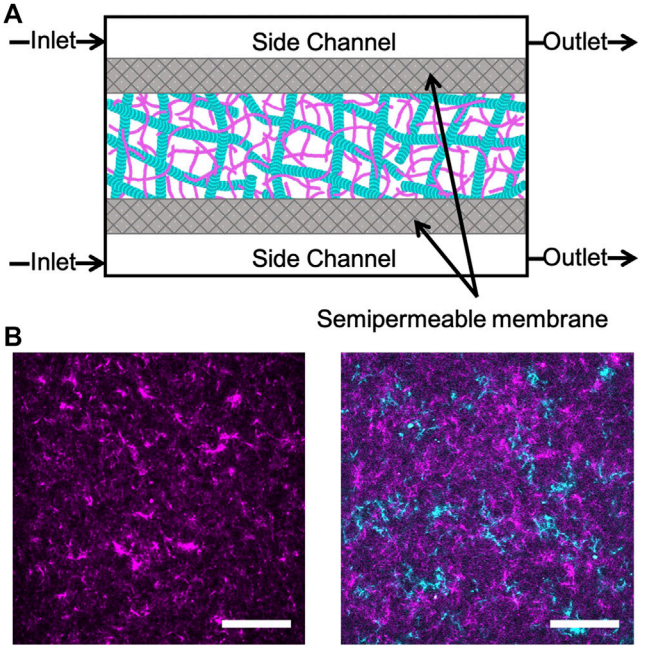

FIGURE 1 | Experimental approach to triggering cation-induced contraction of cytoskeleton networks. **(A)** Cartoon of microfluidic device comprised of three channels separated by two semipermeable membranes (gray). The device has a central chamber containing the sample and two side channels used for buffer exchange. Buffer is pulled into the inlet and out of the outlet through capillary tubing using a syringe pump. The flow rate is set to allow for passive diffusion of buffer into the sample chamber as it flows from inlet to outlet. **(B)** Two-color laser scanning confocal images of an actin network **(left)** and an equimolar actin-microtubule network **(right)** where actin is magenta and microtubules are cyan. Scale bar is 50 μm.

METHODS

Sample Preparation

Rabbit skeletal actin and Alexa-568-labeled actin were purchased from Cytoskeleton (AKL99) and Thermofisher (A12374) and stored at −80°C in Ca buffer [2 mM Tris (pH 8.0), 0.2 mM ATP, 0.5 mM DTT, 0.1 mM $CaCl_2$]. Porcine brain tubulin and rhodamine-labeled tubulin were purchased from Cytoskeleton (T240, TL590M) and stored at −80°C in PEM-100 (100 mM PIPES (pH 6.8), 2 mM $MgCl_2$, and 2 mM EGTA). Both actin and actin-microtubule networks were formed at a fixed concentration of 5.8 μM total protein concentration and included a fraction of labeled protein to image networks (**Figure 1**). Actin networks were polymerized from 3.9 μM unlabeled actin monomers and 2 μM labeled actin monomers in PEM-100 with 2 mM ATP. Equimolar actin-microtubule networks were prepared by polymerizing 2.4 μM actin monomers, 0.5 μM labeled actin monomers, 2 μM tubulin dimers and 0.9 μM labeled tubulin dimers in PEM-100 with 2 mM ATP, 2 mM GTP, and 5 μM Taxol. By including a small fraction of labeled monomers in the solution prior to network polymerization, rather than doping in pre-formed labeled filaments, we are able to directly visualize the network structure and morphology rather than relying on tracer

filaments to report the structure [32]. However, the caveat to this technique is that individual filaments cannot be resolved as each filament is too sparsely labeled and the network is too dense (<1 μm mesh size). As such, the networks in **Figure 1** show structure but not individual filaments. To reduce photobleaching, oxygen scavenging agents (4.5 μg/ml glucose, 0.005% β-mercaptoethanol, 4.3 μg/ml glucose oxidase, 0.7 μg/ml catalase) were included. For both network types, the final solution was mixed and pipetted into the central channel of the microfluidic sample chamber (**Figure 1**) and incubated at 37°C for 30 min prior to further microfluidic assembly (described below). We have shown these networks to be isotropic and stable for up to ~48 h [33]. As such, we do not expect filament orientation or sample aging to play a role in our results.

Microfluidics

The construction of the microfluidic device shown in **Figure 1** is adapted from techniques in Ref. 34 and Ref. 35. The microfluidic sample chamber is formed from a coverslip, a glass microscope slide, and parafilm. The coverslip and glass slide were washed thoroughly with deionized water, acetone, and isopropanol and then plasma cleaned for 30 min. A mixture of 0.5% TMSPMA in isopropanol was baked onto the coverslip and glass slide at 80°C for 2 h. The slide and coverslip were washed with isopropanol and ethanol and left to air dry. To assemble the sample chamber and create a flow cell, the slide, coverslip, and parafilm spacer were placed on a 60°C plate to allow the parafilm to melt and fuse the slide and coverslip together.

The flow cell was filled with a 50:1 mixture of polyethylene glycodiacrylate (PEG-DA) and photoinitiator, 2-hydroxy-2-methylpropiophenone, diluted to 10% in 10 mM Tris-HCl, then exposed to UV through a custom photomask to form two semipermeable membranes of crosslinked PEG-DA. The flow cell was immediately flushed with DI to remove the un-linked PEG-DA solution. This process results in three channels separated by two semipermeable membranes: one central channel for holding the sample and two side channels to enable buffer exchange via diffusion. The flow cell was flushed with 5% Tween (in PEM-100) followed by PEM-100.

The sample was pipetted into the central channel and the side channels were filled with the original polymerization buffer consisting of PEM-100, 2 mM ATP and 2 mM GTP (only for actin-microtubule networks). The flanking side channels were then connected to capillary tubing (74/95 mm inner/outer diameter, Incom) at both ends. The sides of the device were sealed with epoxy to completely enclose the sample within the central chamber and the capillary tubing in the side channels. The capillary tubes were connected to separate Tygon tubing (Cole Parmer Tygon tubing AAD02091- CP, 0.010/0.030 inches inner/outer diameter) before sealing all tubing with epoxy. The Tygon tubing on the inlet side of the microfluidic device was prefilled with the original polymerization buffer. We included 2 μM fluorescein salt in the original polymerization buffer as a proxy to measure ion concentration. To enable buffer exchange, the outlet Tygon tubes were connected to a digitally controlled syringe pump and the inlet Tygon tubing was inserted into the desired buffer reservoir. When the syringe pump is turned on, buffer is pulled into the side channels from the reservoir at a flow rate of 3 μl/min to enable buffer exchange within the sample chamber via passive diffusion through the semipermeable membranes.

The microfluidic experiment took place over the course of 3 h. In the first 10 min, the pump remained off in order to equilibrate the system. We then pumped in the fluorescein-polymerization buffer for 30 min to achieve simultaneous flow at an equal flow rate. After 30 min of pumping the fluorescein-polymerization buffer we switched the reservoir to the buffer containing PEM-100, 20 mM $MgCl_2$, 2 mM ATP and 2 mM GTP (only for actin-microtubule networks). This buffer did not contain fluorescein. We pumped this buffer through for 90 min before switching back to the fluorescein-polymerization buffer and pumping for 50 min.

Confocal Imaging

A Nikon A1R laser scanning confocal microscope with a 4× objective and QImaging QICAM CCD camera was used to collect time-series of labeled cytoskeletal networks and buffer channels. The low magnification objective enabled us to visualize the entire network to determine bulk morphological changes triggered by buffer exchange. It also allowed us to view the entire device in a single field of view to characterize the rate of buffer exchange and to correlate the network activity with Mg^{2+} concentration. The microscope is outfitted with 488 nm and 561 nm lasers and simultaneously records separate images for each laser channel. As such, we are able to separately visualize the cytoskeleton network in the sample chamber (568 nm laser channel) and the intensity of fluorescein dye in the side channels and sample chamber (488 nm laser channel). Time-series of 512 × 512 images (6.215 μm/pixel) in each channel were recorded for 3 h with each image taken every minute. Time-series from the network channel and fluorescein channel were analyzed separately using custom written Matlab code to determine network width and corresponding Mg^{2+} concentration.

RESULTS

We use microfluidic perfusion chambers and two-color confocal microscopy to measure the bulk structural changes induced in cytoskeletal networks in response to continuous variation of Mg^{2+} concentration (**Figure 1**, Methods). We prepare entangled actin networks and co-entangled actin-microtubule networks using previously established protocols [32, 33]. We polymerize networks within home-built microfluidic chambers to enable subsequent variation of Mg^{2+} concentration, via passive diffusion, without disrupting the network of polymerized filaments.

Once networks are formed in microfluidic chambers, each 170 min experiment proceeds as follows (depicted in **Figure 2**). For the first 30 min, we pump the original 2 mM Mg^{2+} polymerization buffer through the device, allowing for passive diffusion of the buffer into the network (Phase I). This phase serves as a control to ensure that we achieve simultaneous flow with equal flow rate through both side channels. After 30 min we change the buffer to include 20 mM Mg^{2+} (Phase II). After 90 min of 20 mM Mg^{2+} buffer flow (t = 120 min), we reintroduce the original 2 mM Mg^{2+} polymerization buffer (Phase III).

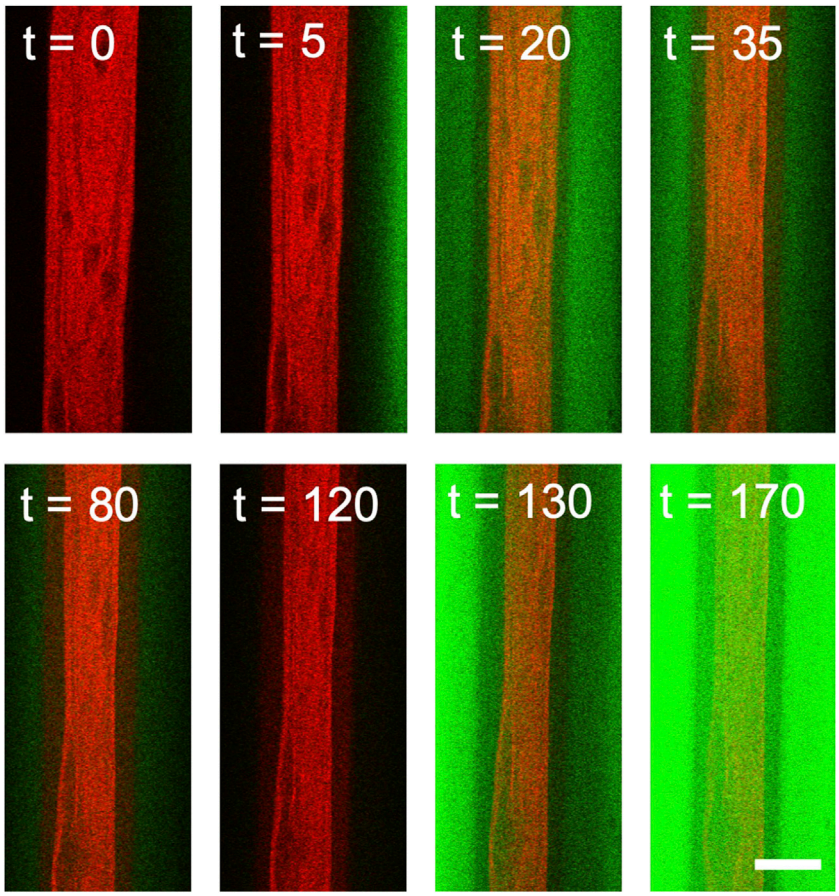

FIGURE 2 | Two-color confocal imaging of actin network undergoing contraction triggered by variation in Mg^{2+} concentration. Two-color laser scanning confocal images of an actin network (red) as the Mg^{2+} concentration slowly varies from 2 mM (green) to 20 mM (black) and back to 2 mM (green). Fluorescein in the 2 mM Mg^{2+} buffer (but not in the 20 mM Mg^{2+} buffer) is used to quantify the Mg^{2+} concentration as a function of time. Because it takes ~5 min for the buffer from the reservoir to enter the sample channel, the buffer channels in the first few images are black despite being at 2 mM Mg^{2+}. At t = 30 min, the 20 mM Mg^{2+} solution is introduced, which is seen as the green signal intensity decaying to black. At t = 120 min, the 2 mM Mg^{2+} solution is reintroduced, viewed as increasing intensity in the green channel. Scale bar is 500 μm and time is in minutes.

Because buffer exchange occurs via passive diffusion, the ion concentration in the network sample chamber does not instantaneously change when we switch buffers. Thus, to determine the Mg^{2+} concentration as a function of time during the experiment we include fluorescein dye in the 2 mM Mg^{2+} buffer. We determine the relative ion concentration, which increases from 2 to 20 mM, by monitoring the decay of the fluorescein intensity. When we reintroduce the 2 mM Mg^{2+} buffer we use the fluorescein intensity once again to measure ion concentration as it decreases from 20 mM to 2 mM Mg^{2+} (**Figures 2**, **3**). We simultaneously image the cytoskeleton network as shown in **Figure 2**.

We find that both actin and actin-microtubule networks contract as the ion concentration increases, shown by the shrinking width of the material over the course of the experiment (**Figures 2–4**). The extent of contraction over the full course of the experiment is similar for both networks, with both widths shrinking to ~13% of their initial width (**Figure 4**).

Due to the ability to control the concentration of the ions with the perfusion chamber, we can identify three phases of ion concentration resulting in changes in the network organization. Phase I is the time when buffer is flowed through the chamber, but the ionic strength of the buffer is constant. Phase II is the time frame when we increase the ion concentration. Phase III is when we return to the original buffer conditions.

As shown in **Figure 3**, during Phase I, the widths of both actin and actin-microtubule networks remain fairly stable, as expected as the environmental conditions are not changing significantly. The only difference between the polymerization buffer pumped in vs. the polymerization buffer the networks were formed in is the lack of the oxygen scavenging system and Taxol.

In Phase II, as Mg^{2+} concentration increases from 2 to 20 mM, actin and actin-microtubule networks both contract but the contraction dynamics are markedly different for the two network types. Actin networks contract at a nearly constant rate of ~4 μm/min, reaching 28 ± 10% of their initial width (**Figure 3**). Conversely, the width of actin-microtubule networks remains stable for the majority of this phase, only starting to contract after ~70 min of the 90 min phase, and reaching 68 ± 5% of the initial width (**Figures 3**, **4**).

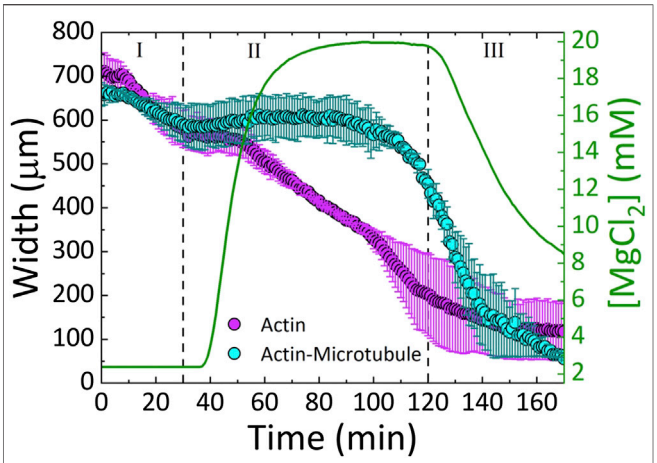

FIGURE 3 | Actin and actin-microtubule networks contract in response to continuous variation of Mg^{2+} concentration. The average width (left axis) of the actin network samples (magenta) and actin-microtubule network samples (cyan) as a function of time. The Mg^{2+} concentration (right axis) is also plotted (green line) as a function of time. The three phases of the experiment (I-III) are separated by dashed lines: I) 2 mM Mg^{2+} solution (original polymerization buffer) diffuses through the sample for 30 min II) exchange to 20 mM Mg^{2+} buffer is initiated and proceeds until 120 min III) 2 mM Mg^{2+} buffer is reintroduced for 50 min.

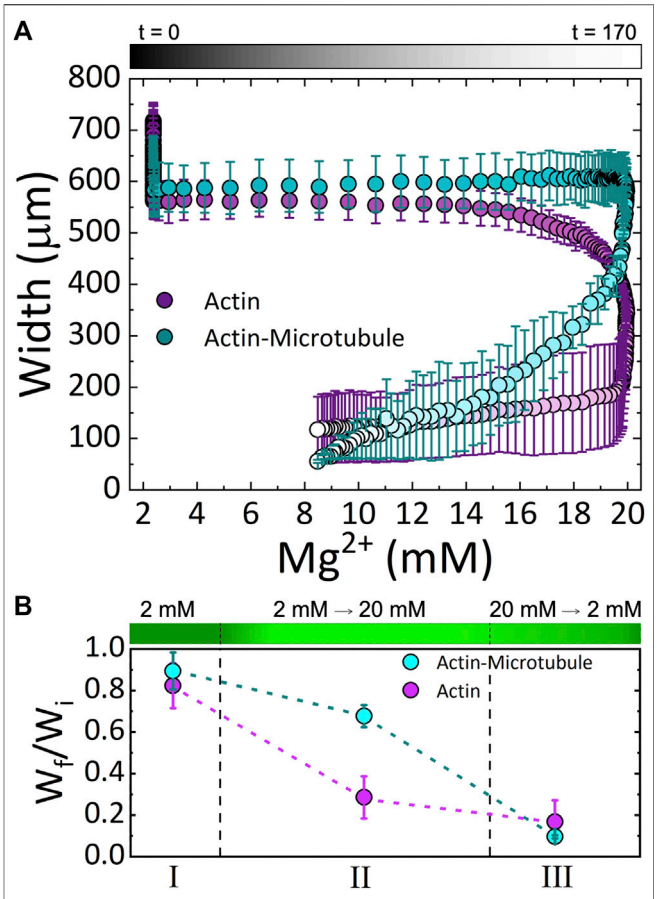

FIGURE 4 | Cytoskeleton networks exhibit network-dependent contraction in response to both increasing and decreasing Mg^{2+} concentration **(A)** The average width of actin network samples (magenta) and actin-microtubule network samples (cyan) as a function of Mg^{2+} concentration. Experimental time is indicated in the symbol gradient coloring where t = 0 is cyan and magenta and t = 170 is light cyan and magenta. **(B)** The fractional amount of contraction measured for each Phase (I, II, III; described in the text), computed by W_f/W_i where W_i is the width at the beginning of the experiment and W_f is the width at the end of the corresponding Phase. The dashed lines separating the three Phases approximate the relative length of time of each phase. The corresponding Mg^{2+} concentration is depicted as a gradient with dark to light green indicating 2 to 20 mM Mg^{2+}.

In Phase III, when we reintroduce the original 2 mM Mg^{2+} buffer, we surprisingly find that both networks continue to contract rather than re-expand or stabilize. The rate of contraction for the actin network is slowed appreciably during this phase and appears to be approaching a steady-state width, contracting by only 11% during this phase (**Figures 3**, **4B**). However, the rate of contraction for the actin-microtubule network actually increases during this phase, dropping by 88% at a nearly constant contraction rate of ~7 μm/min over the course of the 50 min phase (t = 120 min to t = 170 min, **Figure 3**).

These results can be seen more readily in **Figure 4A** in which we plot the width for both networks as a function of Mg^{2+} concentration. The color gradient indicates the experimental time that correlates with the given Mg^{2+} concentration. As shown, actin networks begin to noticeably contract when the Mg^{2+} concentration reaches ~12 mM. Noticeable contraction of actin networks continues as the Mg^{2+} concentration increases to 20 mM, with the most dramatic contraction happening between ~18 and 20 mM Mg^{2+}. Conversely, actin-microtubule networks appear to remain relatively stable as Mg^{2+} concentration increases to ~20 mM, yet undergo dramatic contraction as the concentration drops from 20 to ~17 mM. While the contraction of actin-microtubule networks slows as the Mg^{2+} concentration is lowered further, they continue to exhibit more substantial contraction than actin networks during this phase.

Figure 4B summarizes our findings for the three Phases of our experiment and highlights the key results: 1) both actin networks and actin-microtubule networks undergo significant bulk contraction in response to increasing Mg^{2+} concentration; 2) both networks continue to contract even as the Mg^{2+} concentration is lowered back to the original concentration; and 3) the onset of contraction is delayed for actin-microtubule networks in comparison to actin networks.

We note that in both networks the main period of contraction, in which a constant negative slope is observed in **Figure 3**, exhibits the smallest standard deviation among different samples (**Figures 3**, **4**). This small error demonstrates the reproducibility of Mg^{2+}-driven contraction. The regions with larger standard deviation, at the beginning and end of the experiments, represent variations in the initial and final widths of the different samples, likely arising from small differences in the semipermeable membranes of each microfluidic chamber (**Figure 1**). Slight differences in membrane thickness and pore size impact the width of the central sample channel and the rate of buffer exchange, which in turn alter the initial and final network widths.

DISCUSSION

Previous studies have shown that the charge screening from divalent Mg^{2+} cations are sufficient to enable bundling, crosslinking and reorientation of actin and microtubules *in vitro* and *in vivo* [26, 36, 37]. The onset of contraction for actin networks, occurring at ~12 mM Mg^{2+} (**Figure 4**), is consistent with the previously shown critical concentration of ~10 mM Mg^{2+} needed to induce actin bundling and crosslinking [21, 22]. As such, our results suggest that this self-association can trigger bulk contraction of dense cytoskeleton networks. If the networks are highly entangled, as they are here, as each filament begins to associate with its nearest neighbor the filament pulls with it other surrounding filaments that it is entangled with, resulting in overall contraction of a fully connected network.

We can also understand this contraction process by considering the entropic cost of trapping the Mg^{2+} cations between neighboring filaments [38, 39]. At low Mg^{2+} concentrations, the cations between two filaments are in an energetically favorable state (near negatively charged surfaces), and the filaments repel each other due to the cloud of positive ions surrounding them (and repelling each other). Squeezing the two filaments together would lower the entropy of the "trapped" ions and is thus avoided. This effect is similar to an osmotic pressure difference that drives water between the filaments to try to balance the concentration of cations near and far from filament surfaces [38, 40, 41]. However, as the cation concentration increases this osmotic pressure difference is lowered and then reversed as the concentration of cations in bulk increases. Thus, water flows out of the region between filaments into the bulk, driving the filaments together. The net result is overall network contraction as the cation concentration increases. It is important to note that this depletion-like effect is driven by thermal fluctuations of the filaments. Namely, thermal fluctuations that drive the filaments together, and thus push the water out, are preferred. As such, the timescale for this contraction process depends on the relaxation timescales of the filaments.

The more counterintuitive and surprising result is that contraction continues when we lower the Mg^{2+} concentration by reintroducing the original 2 mM Mg^{2+} polymerization buffer (Phase III). While Phase II contraction is largely driven by the free energy minimization of the cations, as we describe above, we interpret the Phase III contraction as arising from the free energy minimization of the filamentous network. Namely, as filaments are pulled toward each other and linked together by cation crossbridges, the initial configuration is not the most entropically favorable in terms of their configuration. There are likely mechanical stresses on the filaments that were pulled together by the increasing ion concentration. Thus, the filaments will rearrange and reorient to relieve this stress and increase their configurational entropy, even when the cation concentration is reduced. Because the relaxation timescales of entangled actin networks such as these can be as long as minutes to hours, [33, 42–44] this can indeed be a slow process. The fact that this process leads to contraction rather than re-expansion suggests that the cation crossbridges that form between filaments at high Mg^{2+} concentration are quite strong. Further, there is no obvious driving force, analogous to the entropic force that drives the filaments together, that would force the filaments apart. Finally, there are theoretical predictions that suggest that thermal Casimir forces may play a role in electrolyte solutions confined by surfaces (which in this case are the filaments) and in biopolymer networks [45, 46]. This force, arising from thermal fluctuations in the ionic concentration near filaments leads to an attractive force between filaments, similar to the van der Waals interaction [47]. This effect may also play a role in the Phase III contraction.

The question remains as to why the actin-microtubule networks exhibit contraction dynamics that are so distinct from actin networks. Namely, actin-microtubule networks require more Mg^{2+} cations (~20 mM Mg^{2+}) for the onset of contraction than actin networks, and the most pronounced contraction occurs only after the ion concentration starts to drop (**Figure 4**). Microtubules are much stiffer than actin, with a ~100× larger persistence length, and are also comprised of more proteins per unit length. The result then of replacing half of the molar protein concentration of the actin network with tubulin is that the network is stiffer and the mesh size of the network is ~2× larger [33]. In addition, the relaxation dynamics of the actin-microtubule network are slower as the microtubules relax and reorient over much longer timescales than actin [33].

The longer relaxation times could explain the delay in contraction triggered by increasing Mg^{2+} concentration due to the time needed for the actin-microtubule network to rearrange and reorient in response to the triggered attraction. The increased mesh size of the actin-microtubule network could also delay the depletion-like self-association of filaments. As the spacing between filaments trapping the cations is larger, more thermal fluctuations (and thus longer time) and/or a stronger entropic force (dictated by the cation concentration difference between the bulk and in between filaments) would be required for neighboring filaments to be driven together by the osmotic-like depletion of water between the filaments. As such, a higher Mg^{2+} concentration and longer time would be needed to induce contraction, just as we see in **Figures 3** and **4**. Just as the actin-microtubule network is harder to start contracting, the composite would also be more difficult to stop contracting, as if it had an inertial response to the ions. Thus, we see a delay in the contraction, and the most significant contraction only occurring once the ion concentration begins to drop (**Figure 4**). Interestingly, while the contraction is delayed in actin-microtubule composites compared to actin networks, once contraction begins the rate is ~2× faster than for actin networks. This faster contraction, is most likely due to their larger mesh size. While the composites require higher Mg^{2+} concentration and more time for thermal fluctuations to move neighboring filaments close enough to each other to allow for depletion-driven contraction, once the filaments reach this point they can move together more rapidly because there are fewer steric constraints (entanglements) restricting their motion. Namely, the empty voids in the mesh that filaments can freely move through are larger than in actin networks. While actin filaments are more flexible and can thus more readily respond to depletion forces, their smaller network mesh size (i.e., higher entanglement density, smaller empty voids) prevents the filaments from moving as quickly together as in the actin-microtubule composites.

Finally, the shift that actin-microtubule composites exhibit at ~140 min (in Phase III) from relatively fast contraction (~13 μm/min) to slower contraction of ~3 μm/min (**Figure 3**) may indicate

a shift from contraction triggered by the osmotic-like force from the cations (albeit delayed) to the slow rearrangement of filaments to increase their configurational entropy. We expect that if we delayed the onset of Phase III (lowering of Mg^{2+} concentration) that rapid contraction of actin-microtubule networks would still occur at the same experimental time, governed by the intrinsic relaxation timescale of the network. However, we expect that the shift to slower contraction that occurs in Phase III would occur proportionally later, as it is determined by a shift to configurational entropy maximization that can only occur after the network has been in the presence of low ion concentration for a long enough time. In future work we will more fully explore these hypotheses by varying the times over which the networks are exposed to high and low cation concentrations as well as the maximum Phase II cation concentration.

We chose to focus our study on Mg^{2+} due to its importance in physiological processes such as actin and microtubule polymerization and myosin-driven actin contraction [1, 2, 17, 33, 48]. We expect that other divalent ions, such as Ca^{2+}, would produce similar results for polyelectrolytes with similar charge densities as actin and microtubules [23]. However, previous studies examining cation-driven bundling of actin have shown that monovalent ions are not able to induce substantial actin self-association [23, 38]. Further, while Mg^{2+} promotes actin polymerization and stabilizes filamentous actin, Ca^{2+} can destabilize actin filaments and promote depolymerization, which could negatively impact contractile behavior [33].

We have previously shown that actin-microtubule composites exhibit increasing stiffness, mesh size and heterogeneity as the ratio of microtubules to actin is increased [33]. In future work, we will explore the dependence of Mg^{2+}-triggered contraction on this ratio. We expect our results to smoothly vary between the two cases we present here as we vary this ratio. While the networks we have studied do not have any crosslinking proteins present, we plan to incorporate actin and microtubule crosslinkers and determine their impact on the results. Based on our previous microrheology measurements on crosslinked actin-microtubule composites [49, 50], we expect to measure a more complicated dependence of crosslinker type and concentration on the contraction behavior.

CONCLUSION

We have presented an experimental approach that combines diffusion-controlled microfluidics with two-color fluorescence confocal microscopy to measure bulk morphological changes to cytoskeletal networks triggered by increasing and decreasing concentrations of magnesium ions. We show that both actin networks as well as actin-microtubule networks undergo bulk contraction triggered by increasing Mg^{2+} concentration. The contraction dynamics are highly dependent on the network type, with actin-microtubule networks exhibiting a substantially delayed response relative to actin networks. We also show that both networks continue to contract during subsequent lowering of Mg^{2+} concentration, which we attribute to slow network rearrangement to maximize the configurational entropy of the filaments. Our results demonstrate unexpected ways in which the cytoskeleton can dynamically morph and contract in response to environmental stimuli, and how the varying mechanical and structural properties of actin and microtubules can tune the characteristics of this dynamic response.

DATA AVAILABILITY STATEMENT

The raw data supporting the conclusions of this article will be made available by the authors, without undue reservation.

AUTHOR CONTRIBUTIONS

SR conduced microscopy and microfluidic experiments, analyzed and interpreted data, and wrote the manuscript. PK optimized microfluidic experiments and conducted microscopy and microfluidic experiments. MR helped analyze and interpret data. MD helped analyze and interpret data. JR analyzed and interpret data. RA designed and guided experiments, analyzed and interpreted data, and wrote the manuscript.

FUNDING

This research was funded by a William M. Keck Foundation Research Grant (awarded to RA, JR, MD, and MR) and a National Institutes of Health R15 Award (National Institute of General Medical Sciences Award No. R15GM123420, awarded to RA).

ACKNOWLEDGMENTS

We thank C. Currie for work in preparing samples and analyzing data.

REFERENCES

1. Cooper GM, Hausman R. *The cell* 2nd ed. Sunderland, MA: Sinauer Associates (2000)
2. Wen Q, Janmey PA, Polymer physics of the cytoskeleton. *Curr Opin Solid State Mater Sci* (2011) **15**:177–82. doi:10.1016/j.cossms.2011.05.002
3. Sanders LK, Xian W, Guáqueta C, Strohman MJ, Vrasich CR, Luijten E, et al. Control of electrostatic interactions between F-actin and genetically modified lysozyme in aqueous media. *Proc Natl Acad Sci USA* (2007) **104**:15994–9. doi:10.1073/pnas.0705898104
4. Tuszyński J, Portet S, Dixon J, Luxford C, Cantiello H. Ionic wave propagation along actin filaments. *Biophys J* (2004) **86**:1890–903. doi:10.1016/S0006-3495(04)74255-1
5. Kim T, Kao MT, Hasselbrink EF, Meyhöfer E. Nanomechanical model of microtubule translocation in the presence of electric fields, *Biophys J* (2008) **94**: 3880–92. doi:10.1529/biophysj.107.112755
6. Le Clainche C, Carlier MF. Regulation of actin assembly associated with protrusion and adhesion in cell migration. *Physiol Rev* (2008) **88**:489–513. doi:10.1152/physrev.00021.2007
7. Janmey PA. Creating a niche in the cytoskeleton: actin reorganization by a protein kinase. *Proc Natl Acad Sci USA* (2001) **98**:14745–7. doi:10.1073/pnas.011601598

8. Dent EW, Kalil K, Axon branching requires interactions between dynamic microtubules and actin filaments. *J Neurosci* (2001) **21**:9757–69. doi:10.1523/jneurosci.21-24-09757.2001
9. Gross SP. Hither and yon: a review of bi-directional microtubule-based transport. *Phys Biol* (2004) **1**:R1. doi:10.1088/1478-3967/1/2/r01
10. Lopez BJ, Valentine MT. Molecular control of stress transmission in the microtubule cytoskeleton. *Biochim Biophys Acta Mol Cell Res* (2015) **1853**: 3015–24. doi:10.1016/j.bbamcr.2015.07.016
11. Rodriguez OC, Schaefer AW, Mandato CA, Forscher P, Bement WM, Waterman-Storer CM. Conserved microtubule-actin interactions in cell movement and morphogenesis. *Nat Cell Biol* (2003) **5**:599–609. doi:10.1038/ncb0703-599
12. Salmon WC, Adams MC, Waterman-Storer CM, Dual-wavelength fluorescent speckle microscopy reveals coupling of microtubule and actin movements in migrating cells. *J Cell Biol* (2002) **158**:31–7. doi:10.1083/jcb.200203022
13. Schaefer AW, Kabir N, Forscher P. Filopodia and actin arcs guide the assembly and transport of two populations of microtubules with unique dynamic parameters in neuronal growth cones. *J Cell Biol* (2002) **158**:139–52. doi:10.1083/jcb.200203038
14. Mandato CA, Bement WM. Actomyosin transports microtubules and microtubules control actomyosin recruitment during Xenopus oocyte wound healing. *Curr Biol* (2003) **13**:1096–105. doi:10.1016/s0960-9822(03)00420-2
15. Waterman-Storer CM, Salmon ED. Actomyosin-based retrograde flow of microtubules in the lamella of migrating epithelial cells influences microtubule dynamic instability and turnover and is associated with microtubule breakage and treadmilling. *J Cell Biol* (1997) **139**:417–434. doi:10.1083/jcb.139.2.417
16. Silverman-Gavrila R, Forer A. Evidence that actin and myosin are involved in the poleward flux of tubulin in metaphase kinetochore microtubules of crane-fly spermatocytes. *J Cell Sci* (2000) **113**:597–609.
17. Murrell MP, Gardel ML. F-actin buckling coordinates contractility and severing in a biomimetic actomyosin cortex. *Proc Natl Acad Sci USA* (2012) **109**:20820–20825. doi:10.1073/pnas.1214753109
18. Foster PJ, Fürthauer S, Shelley MJ, Needleman DJ. Active contraction of microtubule networks. *Elife* (2015) **4**:e10837. doi:10.7554/elife.10837
19. Sanchez T, Chen DTN, DeCamp SJ, Heymann M, Dogic Z. Spontaneous motion in hierarchically assembled active matter. *Nature* (2012) **491**:431–4. doi:10.1038/nature11591
20. Tang JX, Janmey PA. The polyelectrolyte nature of F-actin and the mechanism of actin bundle formation. *J Biol Chem* (1996) **271**:8556–63. doi:10.1074/jbc.271.15.8556
21. Huber F, Strehle D, Käs J. Counterion-induced formation of regular actin bundle networks. *Soft Matter* (2012) **8**:931–6. doi:10.1039/c1sm06019h
22. Gurmessa B, Francis M, Rust MJ, Das M, Ross JL, Robertson-Anderson RM. Counterion crossbridges enable robust multiscale elasticity in actin networks. *Phys Rev Res* (2019) **1**:013016. doi:10.1103/physrevresearch.1.013016
23. Castaneda N, Zheng T, Rivera-Jacquez HJ, Lee HJ, Hyun A, Balaeff A, et al. Cations modulate actin bundle mechanics, assembly dynamics, and structure. *J Phys Chem B* (2018) **122**:3826–35. doi:10.1021/acs.jpcb.8b00663
24. Needleman DJ, Ojeda-Lopez MA, Raviv U, Miller HP, Li Y, Song C, et al. Ion specific effects in bundling and depolymerization of taxol-stabilized microtubules. *Faraday Dis* (2013) **166**:31–45. doi:10.1039/c3fd00063j
25. Safinya CR, Chung PJ, Song C, Li Y, Miller HP, Choi MC, et al. Minireview - microtubules and tubulin oligomers: shape transitions and assembly by intrinsically disordered protein tau and cationic biomolecules. *Langmuir* (2019) **35**:15970–8. doi:10.1021/acs.langmuir.9b02208
26. Needleman DJ, Ojeda-Lopez MA, Raviv U, Miller HP, Wilson L, Safinya CR. From the cover: higher-order assembly of microtubules by counterions: from hexagonal bundles to living necklaces. *Proc Natl Acad Sci USA* (2004) **101**: 16099–103. doi:10.1073/pnas.0406076101
27. Needleman DJ, Jones JB, Raviv U, Ojeda-Lopez MA, Miller HP, Li Y, et al. Supramolecular assembly of biological molecules purified from bovine nerve cells: from microtubule bundles and necklaces to neurofilament networks. *J Phys Condens Matter* (2005) **17**:S3225. doi:10.1088/0953-8984/17/45/005
28. Wang C, Li J, Yuan M. Salt tolerance requires cortical microtubule reorganization in arabidopsis. *Plant Cell Physiol* (2007) **48**:1534–47. doi:10.1093/pcp/pcm123
29. Deshpande S, Pfohl T. Hierarchical self-assembly of actin in micro-confinements using microfluidics. *Biomicrofluidics* (2012) **6**:034120. doi:10.1063/1.4752245
30. Janmey PA, Slochower DR, Wang YH, Wen Q, Cēbers A. Polyelectrolyte properties of filamentous biopolymers and their consequences in biological fluids. *Soft Matter* (2014) **10**:1439–49. doi:10.1039/c3sm50854d
31. Huber F, Strehle D, Schnauß J, Käs J. *New J Phys* (2015) **17**:043029. doi:10.1088/1367-2630/17/4/043029
32. Ricketts SN, Gurmessa B, Robertson-Anderson RM. Microscale mechanics of plug-and-play in vitro cytoskeleton networks. *Parasitology and microbiology research*. London, UK: IntechOpen (2019).
33. Ricketts SN, Ross JL, Robertson-Anderson RM. Co-entangled actin-microtubule composites exhibit tunable stiffness and power-law stress relaxation. *Biophys J* (2018) **115**:1055–67. doi:10.1016/j.bpj.2018.08.010
34. Park CY, Jacobson DR, Nguyen DT, Willardson S, Saleh OA. A thin permeable-membrane device for single-molecule manipulation. *Rev Sci Instrum* (2016) **87**:014301. doi:10.1063/1.4939197
35. Gurmessa BJ, Bitten N, Nguyen DT, Saleh OA, Ross JL, Das M, et al. Triggered disassembly and reassembly of actin networks induces rigidity phase transitions. *Soft Matter* (2019) **15**:1335–44. doi:10.1039/c8sm01912f
36. Schnauß J, Händler T, Käs J. Semiflexible biopolymers in bundled arrangements. *Polymers* (2016) **8**:274. doi:10.3390/polym8080274
37. Tang JX, Wong S, Tran PT, Janmey PA. Counterion induced bundle formation of rodlike polyelectrolytes. *Ber Bunsen Ges Phys Chem* (1996) **100**:796–806. doi:10.1002/bbpc.19961000620
38. Nelson P. *Biological physics* New York, NY: WH Freeman (2004)
39. Gelbart WM, Bruinsma RF, Pincus PA, Parsegian VA, DNA-Inspired electrostatics. *Phys Today* (2000) **53**:38–44. doi:10.1063/1.1325230
40. Israelachvili JN. *Intermolecular and surface forces*. San Diego, CA: Academic press (2015)
41. Safran S. *Statistical thermodynamics of surfaces, interfaces, and membranes*. Boca Raton, FL: CRC Press (2018)
42. Semmrich C, Larsen RJ, Bausch AR. Nonlinear mechanics of entangled F-actin solutions. *Soft Matter* (2008) **4**:1675–80. doi:10.1039/b800989a
43. Liu J, Gardel M, Kroy K, Frey E, Hoffman BD, Crocker JC, et al. *Phys Rev Lett* (2006) **96**:118104. doi:10.1103/physrevlett.96.118104
44. Gurmessa B, Fitzpatrick R, Falzone TT, Robertson-Anderson RM. Entanglement density tunes microscale nonlinear response of entangled actin. *Macromolecules* (2016) **49**:3948–55. doi:10.1021/acs.macromol.5b02802
45. Lee AA, Hansen JP, Bernard O, Rotenberg B. Casimir force in dense confined electrolytes. *Mol Phys* (2018) **116**:3147–3153. doi:10.1080/00268976.2018.1478137
46. Kachan D, Kachan D. *Equilibrium & nonequilibrium fluctuation effects in biopolymer networks*. [PhD dissertation]. Los Angeles(CA): *University of California, Los Angeles* (2014)
47. Kardar M, Golestanian R. The "friction" of vacuum, and other fluctuation-induced forces. *Rev Mod Phys* (1999) **71**:1233. doi:10.1103/revmodphys.71.1233
48. Lee G, Rust MJ, Das M, McGorty RJ, Ross JL, Robertson-Anderson RM. Myosin-driven actin-microtubule networks exhibit self-organized contractile dynamics. *bioRxiv* (2020)
49. Ricketts SN, Francis ML, Farhadi L, Rust MJ, Das M, Ross JL, et al. Varying crosslinking motifs drive the mesoscale mechanics of actin-microtubule composites. *Sci Rep* (2019) **9**:1–12. doi:10.1038/s41598-019-49236-4
50. Francis ML, Ricketts SN, Farhadi L, Rust MJ, Das M, Ross JL, et al. Non-monotonic dependence of stiffness on actin crosslinking in cytoskeleton composites. *Soft Matter* (2019) **15**:9056–65. doi:10.1039/c9sm01550g

Conflict of Interest: The authors declare that the research was conducted in the absence of any commercial or financial relationships that could be construed as a potential conflict of interest.

frontiers in Molecular Biosciences

ORIGINAL RESEARCH
published: 06 May 2021
doi: 10.3389/fmolb.2021.669361

Unveiling a Hidden Event in Fluorescence Correlative Microscopy by AFM Nanomechanical Analysis

Massimiliano Galluzzi[1], Bokai Zhang[2,3,4], Han Zhang[2,5], Lingzhi Wang[6], Yuan Lin[7,8], Xue-Feng Yu[1], Zhiqin Chu[9] and Jiangyu Li[2,10]**

[1]Materials Interfaces Center, Shenzhen Institutes of Advanced Technology, Chinese Academy of Sciences, Shenzhen, China, [2]Shenzhen Key Laboratory of Nanobiomechanics, Shenzhen Institutes of Advanced Technology, Chinese Academy of Sciences, Shenzhen, China, [3]DGene (Dongjin Big Health (Shenzhen)) Co., Ltd., Shenzhen, China, [4]BenHealth Biopharmaceutical (Shenzhen) Co., Ltd., Shenzhen, China, [5]State Key Laboratory of Traction Power, Southwest Jiaotong Univerisity, Chengdu, China, [6]Department of Electrical and Electronic Engineering, The University of Hong Kong, Hong Kong, [7]Department of Mechanical Engineering, The University of Hong Kong, Hong Kong, [8]Advanced Biomedical Instrumentation Centre, Shatin, Hong Kong, [9]Department of Electrical and Electronic Engineering, Joint Appointment with School of Biomedical Sciences, The University of Hong Kong, Hong Kong, [10]Department of Materials Science and Engineering, Southern University of Science and Technology, Shenzhen, China

OPEN ACCESS

Edited by:
Srabanti Chaudhury, Indian Institute of Science Education and Research, Pune, India

Reviewed by:
Andrea Alessandrini, University of Modena and Reggio Emilia, Italy
Ivan Lopez-Montero, Complutense University of Madrid, Spain

***Correspondence:**
Zhiqin Chu
zqchu@eee.hku.hk
Jiangyu Li
jy.li1@siat.ac.cn

Specialty section:
This article was submitted to Biophysics, a section of the journal Frontiers in Molecular Biosciences

Received: 18 February 2021
Accepted: 22 April 2021
Published: 06 May 2021

Citation:
Galluzzi M, Zhang B, Zhang H, Wang L, Lin Y, Yu X-F, Chu Z and Li J (2021) Unveiling a Hidden Event in Fluorescence Correlative Microscopy by AFM Nanomechanical Analysis. Front. Mol. Biosci. 8:669361. doi: 10.3389/fmolb.2021.669361

Fluorescent imaging combined with atomic force microscopy (AFM), namely AFM-fluorescence correlative microscopy, is a popular technology in life science. However, the influence of involved fluorophores on obtained mechanical information is normally underestimated, and such subtle changes are still challenging to detect. Herein, we combined AFM with laser light excitation to perform a mechanical quantitative analysis of a model membrane system labeled with a commonly used fluorophore. Mechanical quantification was additionally validated by finite element simulations. Upon staining, we noticed fluorophores forming a diffuse weakly organized overlayer on phospholipid supported membrane, easily detected by AFM mechanics. The laser was found to cause a degradation of mechanical stability of the membrane synergically with presence of fluorophore. In particular, a 30 min laser irradiation, with intensity similar to that in typical confocal scanning microscopy experiment, was found to result in a ~40% decrease in the breakthrough force of the stained phospholipid bilayer along with a ~30% reduction in its apparent elastic modulus. The findings highlight the significance of analytical power provided by AFM, which will allow us to "see" the "unseen" in correlative microscopy, as well as the necessity to consider photothermal effects when using fluorescent dyes to investigate, for example, the deformability and permeability of phospholipid membranes.

Keywords: atomic force microscopy, correlative fluorescence microscopy, biomembrane, fluorophore, hybrid phospholipids

INTRODUCTION

Fluorescence microscopy is one of the most often used imaging techniques in biology and material science (Lichtman and Conchello, 2005; Shashkova and Leake, 2017), and this is dictated by efficient staining agents with ability to bind on target while maintaining fluorescence. The high-specificity of fluorophores is relative to the interaction force between those label agents and target biomolecules.

While process of measurement requires to minimize the perturbation of system under investigation, a strong (for example covalent (Luitz et al., 2017)) label-target interaction can produce an opposite effect. Complementary investigations are essential to unveil the influence of fluorescent tags, as well as to understand the targeting quality and uniformity.

A peculiar way enabled by atomic force microscopy (AFM), is to investigate the mechanical properties in biological system through quantitatively measuring viscoelastic modifications (Nautiyal et al., 2018; Garcia, 2020; Zhou et al., 2021). Considering the versatility of AFM in biology, it is significant to integrate such platform with optics, the so-called correlative microscopy (Zhou et al., 2021). With such a combination, the mechanical quantities and biochemical events can be simultaneously investigated with high spatial-temporal resolution. This will provide new insights into biological processes, but previous studies also suggested the used fluorophores could have huge impact on the targeted biomolecules during visualization (Luitz et al., 2017; Cosentino et al., 2019). Highly desirable now is to understand the underlying cross-talk between the two techniques, especially in a quantitative manner.

For our study we selected one of the most studied bio-systems, represented by phospholipid bilayers as a model system mimicking real cell membrane (Eeman and Deleu, 2010; Redondo-Morata et al., 2020). Furthermore, the modeled biomembranes can be flexibly reconstructed to facilitate surface techniques for investigation of mechanical properties such as AFM (Stetter et al., 2016; Müller et al., 2020; Redondo-Morata et al., 2020), and molecular dynamic simulations (Hofsäß et al., 2003; Leeb and Maibaum, 2018). This is significant since the biomembrane is the most critical interface between the living organisms and the external environment, while mechanical properties are correlated with its stability (Alessandrini and Facci, 2012; Beedle et al., 2015; Balleza et al., 2019; Mescola et al., 2020).

In current work, we perform an AFM-fluorescence correlative microscopy study on a model system consisting of biomembrane (DOPC bilayer) interacting with a commonly used hydrophobic molecule, Nile red (Ira and Krishnamoorthy, 1998; Jain and Das, 2006; Kurniasih et al., 2015; Levitt et al., 2015; Halder et al., 2018), having high efficacy staining intracellular neutral lipid droplets and phospholipid cell membranes. Very recently, Zhanghao et al. (Zhanghao et al., 2020) used Nile red to perform single-cell super-resolution lipidomic resolving the membrane morphology, polarity, and phase of cell membrane and subcellular organelles. Lipid order in outer leaflet of bacterial membrane was investigated with high-sensitivity fluorescent probe based on Nile red (Bogdanov et al., 2020). Therefore, the investigation of mechanical properties of membrane in physiological conditions will be essential to determine a cross-talk induced by fluorescent optical microscopy. Our obtained results are well-validated by direct comparison of AFM single force spectra with finite element simulations (FEM) based on AFM topography. We compare the cases of model system with or without laser irradiation, and show different degrees of mechanical modifications. Moreover, we used our routine on a hybrid system composed by DOPC + Nile red before aqueous micellization, again highlighting the synergistic effect of laser and fluorophore in modifying fluidity and stability of lipid-based membranes.

MATERIALS AND METHODS

Phospholipid Bilayer Preparation and Red Nile

The phospholipid molecules (dioleoyl phosphatidylcholine (DOPC) from Sigma-Aldrich, St. Louis, MO) were initially dissolved in a chloroform solution at a concentration of 10 mg/ml. The dried lipids (0.1 mg) were rehydrated in PBS (phosphate buffer saline) maintaining 0.5 mg/ml concentration, the final solution increases turbidity due to formation of micelles. The ionic strength of PBS is necessary to shield effectively the electrostatic repulsive interaction between the negatively charged mica surface and phospholipids heads (Reviakine and Brisson, 2000; Richter and Brisson, 2005; Indrieri et al., 2008). The lipids solution is vortexed and sonicated for 10 min. The effect of sonication was to break bigger multi-layered vesicles, favoring the formation of smaller single-layered vesicles. After sonication, the solution containing the lipids is deposited on a freshly cleaved mica surface in the amount of 40 µl with 2 min incubation time. The deposition protocol proceeds with the elimination of deposition buffer by spin coating at 5000 rpm for 2 min. We found that spin coating was the best methodology to control the quantity of single bilayers on mica substrate, achieving repeatability. Finally, the sample was rehydrated in PBS to perform AFM measurement in fluid environment using the imaging buffer. In this work, PBS was utilized to mimic closer physiological conditions. Importantly, the supported bilayers can be stabilized by the higher ionic strength on mica (therefore it is easier to find bilayers during microscopy). Moreover, the electrostatic interaction is shielded by ionic strength. The "unshielded" electrostatic interaction in liquid (described by DLVO theory) is increasing uncertainty during contact point determination. The overall procedure was tested several times in order to ensure repeatability.

Nile Red (N1142, Invitrogen, Carlsbad, CA) was firstly dissolved in DMSO at a concentration of 10 mg/ml, then the solution was further diluted to a final concentration of 2.5 µg/ml in PBS, which was applied as the imaging buffer. CellTracker Deep Red (C34565, Thermo Fisher Scientific, Waltham, MA) and HOECHST (33,342, Thermo Fisher Scientific) were dissolved in PBS with concentrations of 25 µg/ml and 2.5 µg/ml, respectively.

Laser Installation and Alignment

To simulate the confocal microscope environment to the maximum extent, we installed the 532 nm laser (green) to the optical microscopy (Eclipse Ti2, Nikon, Tokyo, Japan) as the light source for the excitation of Nile Red and CellTracker Deep Red, while 480 nm laser (blue) was used for HOECHST. In brief, a front-surface mirror was placed on the stage of the microscopy, the installed laser was adjusted to focus onto the reflective surface using the 40X objective lanes. Then filter settings were selected to allow some of the reference laser to be bounced back through the

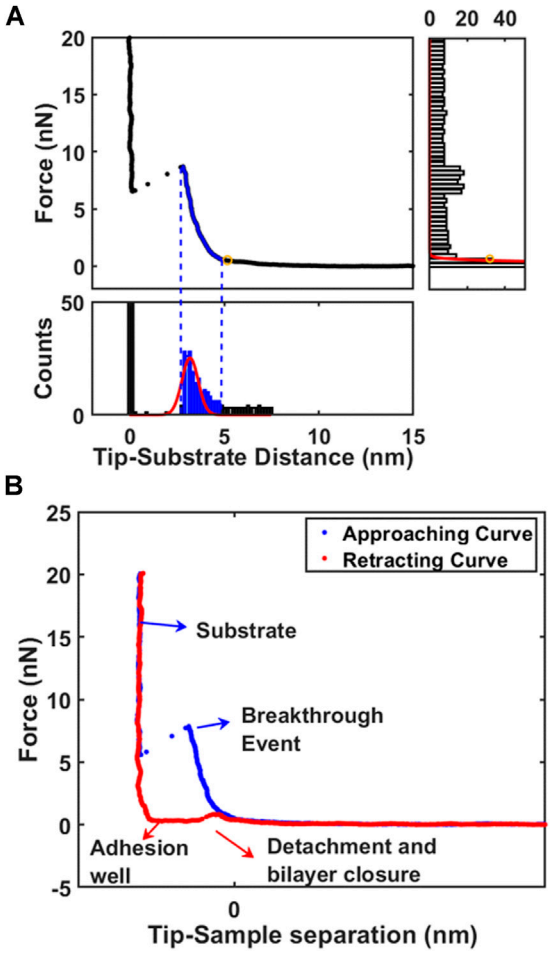

FIGURE 1 | The analysis of supported phospholipid bilayers. **(A)** Working principle of algorithm to identify automatically the contact point on first layer by decomposition of force curve (FC) with X-Y histograms. **(B)** Typical force curve (approaching and retracting) acquired on phospholipid bilayer highlighting important positions.

microscopy optical train and out through the external coupling port. After alignment, the laser power intensity is adjusted by the controller. In our case, 10.1 mW power intensity was set to obtain a final output power intensity of 35.4 mW/μm^2. More details on this calculation are collected in Supporting Information, **Supplementary Figure SI1**.

AFM Force Spectroscopy

AFM force spectroscopy experiments were performed with MFP 3DBio (Asylum Research, Goleta, CA) mounting short-wide SNL probes (Bruker, Billerica, MA) with nominal elastic constant k = 0.5 N/m, nominal radius R = 10 nm, allowing to cover force interaction range from 10–10^4 pN. The elastic constant of cantilever was calibrated by thermal tuning with built-in procedure in air and in water leading to consistent results of elastic constant as k = 0.42 N/m. We used the environmental control unit to keep the temperature constant at 30°C, slightly higher than room temperature to allow the system to re-equilibrate in case of thermal modification induced by AFM operation and laser application.

During AFM force spectroscopy, the probe approaches vertically the phospholipid bilayer recording the interaction force in function of probe-surface position. The first visible nanomechanical parameter is related to the quantitative determination of the breakthrough event, i.e. the force threshold indicative of AFM probe penetrating the lipid layer, also confirming its existence (Butt et al., 2005; Redondo-Morata et al., 2020). Raw morphology from integrated software is representative of mica substrate, neglecting layers breaking during force curves. For each sample, a series of force volume mapping at 64 × 64 resolution was performed insisting on the same area but using different conditions (dye injection and/or laser application) in different macroscopic positions to improve the statistical reliability of the experiments.

Data Analysis

Data analysis was performed in MATLAB (The MathWorks, Natick, MA) environment with custom routine functions. Analysis is firstly focused in converting raw force curves from Deflection Voltage (V) vs. Piezo Travel Distance (nm) into Force (nN) vs. Tip-substrate separation (nm)(Butt et al., 2005). To this purpose, optical lever sensitivity Zsens (nm/V) is calculated from contact part when probe reached the substrate after breaking through the layer, while spring constant is used to finally convert in Force.

After conversion, the tip-sample contact point must be determined to consider the morphology of soft biomembranes (Galluzzi et al., 2018). As first approach, the force axis is binned resulting in a well-defined peaked histogram indicating non-contact region (right part of **Figure 1A**). To avoid considering electrostatic interactions, the low-force morphology is reconstructed individuating contact point above 0.3 nN. The second approach is focused in finding the layer near the substrate by binning the distance axis. While the peak correspondent to zero distance is representing the substrate, the second peak represents the nearest layer (bottom part of **Figure 1A**). Gaussian fitting is employed to find automatically the peaks for all force curves in force volume. The second approach is particularly powerful to exclude long-range electrostatic interactions or loosely bounded contaminants on surface of phospholipid bilayer. Using the peak correspondent to first layer facing the substrate, the contact point and breakthrough force can be retrieved easily as left and right extremes of Gaussian fitting. After contact with surface, AFM probe starts to compress the bilayer until the indentation reaches circa 2.5 nm, at which point the elastic energy of the deformed bilayer overcomes the energetic cost of forming a hole and the tip penetrates the bilayer reaching the substrate in a breakthrough event (**Figure 1B**). (Garcia-Manyes et al., 2005; Das et al., 2010; Garcia-Manyes and Sanz, 2010) The breakthrough force is a parameter representing the mechanical stability to vertical compressive loads. After reaching the maximum force setpoint, the tip reverses the motion and retracts from surface allowing to measure the force necessary to detach from surface and close the hole in phospholipid bilayer (red curve in **Figure 1B**).

The first layer topography map is obtained from difference between contact point and substrate, so that thickness map (from h parameter) is equivalent to standard morphology. The contact part of force curve between contact point and F_{break} is then used for mechanical analysis. Considering the typical probe radius can be approximated by sphere which radius is larger than indentation length (usually 2 nm for our system), we consider standard Hertz model with the correction for finite thickness to describe a system composed by a thin elastic layer supported on solid substrate (Garcia-Manyes and Sanz, 2010; Garcia-Manyes et al., 2005; Das et al., 2010). For the elastic contribution, we implement the theoretical model represented in second term of **Eq 1**: (Dimitriadis et al., 2002; Stetter et al., 2016)

$$F = \frac{4}{3}\frac{E\sqrt{R}}{(1-\nu^2)}\delta^{3/2}\left[1 + 1.133\chi_S + 1.283\chi_S^2 + 0.769\chi_S^3 + 0.0975\chi_S^4\right];\ \chi_S = \frac{\sqrt{R\delta}}{h} \quad (1)$$

Where F is the applied force, δ the indentation, ν the Poisson's ratio, E the effective Young's Modulus of the lipid bilayer, and R the radius of the spherical probe and the adimensional parameter $\chi_S = \sqrt{R\delta/h}$. Poisson ratio for lipid bilayers is close to 0.5, with relative deviations about 3%. (Terzi et al., 2019) For a single measurement, the error σ associated with the mean thickness, F_{break} or Young's modulus of the membrane is calculated taking into account the propagated uncertainty in calibration procedure and the width of histogram distribution correspondent to a single measurement. We highlight that quantification of mechanical parameters is difficult or hardly reproducible, because the geometry of apex of sharp probe is unknown or irregular, moreover the choice of probe geometry and correspondent model is causing largest differences in the interpretation of the data. (Eid et al., 2021) Here we simplify using a probe with apex approximated as a sphere with nominal radius R = 10 nm, moreover we managed to use the very same probe for all experiments and performing comparisons relative to control specimen. Between different experiments AFM probe was cleaned by gentle flux of ethanol.

FEM Simulations

A 2D-axisymmetric numerical model was developed to study indentation on a supported phospholipid bilayer with a spherical indenter, mimicking AFM experiments as closely as possible. The total size of bilayer was 1 um in lateral dimension (radius) and 5 nm layer supported on 500 nm thick mica (can be considered as thin slab supported on semi-infinite substrate). The radius of the spherical indenter was set as in AFM experiments, R = 10 nm. During deformation, the left boundary, representing the symmetry axis, was allowed to move only vertically, while the bottom boundary was constrained to move horizontally. The right and top boundaries were not constrained, except when indenter is contacting the top objects (surface or inclusions): the contact area was restricted to follow the indenter contour ensuring hard contact between the indenter and the sample. Material properties for substrate (mica), and indenter (silicon) are required as input parameters in the modeling and set as $E_{substrate}$ = 3.3 GPa, $\nu_{substrate}$ = 0.34, E_{Si} = 160 GPa, ν_{Si} = 0.22. These hard materials have Young's moduli several orders of magnitude larger (GPa range) than phospholipid bilayers (usually in the MPa range (Jacquot et al., 2014; Stetter et al., 2016)) in this study, showing negligible deformations. Young's moduli of phospholipid bilayer were directly measured by AFM indentation experiments. A methodological study, comparing AFM indentation and FEM model was recently published by our group (Tang et al., 2018; Tang et al., 2019).

Stress and deformation fields (example is reproduced in **Supplementary Figure SI2**) produced by indenter approaching vertically are directly converted in Force (nN) vs. Indentation (nm) to be compared with AFM approaching force curves.

An array of simulation was generally built variating a single unknown quantity around the most probable value guessed from AFM morphology and mechanical analysis (Thickness and corrected Young's Modulus). FEM model can be designed tuning the slip/friction at the interface between thin layer and substrate: 2 extreme conditions are represented by perfect bound (zero slip) and perfect loose (free slip). Although the deformation pattern at the interface at zero and free slip can be qualitatively similar, only quantitative analysis through AFM comparison can distinguish the proper behavior at the interface.

RESULTS AND DISCUSSION

The Issues in AFM-combined Fluorescence Correlative Microscopy

The commonly integrated fluorescence microscopy, especially the confocal laser scanning microscopy (CLSM), raises the concern of photochemistry effects induced by tightly focused laser beam, particularly in the presence of dye molecules. Whether these photochemical effects can affect the mechanical properties becomes critical, but difficult to detect. **Figure 2** represents the schematic of experimental setup used in current study, to perform laser fluorescent microscopy co-localized with atomic force microscopy. Before all the experiments, laser alignment on AFM probes was achieved as explained in Materials and Methods. We ensured that intrinsic noise during force spectroscopy was not modified during laser application.

When exposed in dry air, a progressive bending of the probe was observed presumably due to local heating induced by intensely focused green laser. However, such effect became negligible when the probe was immersed in water with temperature controlled at 30 °C. Also, we noticed that global thermal output remains constant even after 1 h of green (or blue) laser irradiation, showing that excitation laser is not influencing (with 0.1°C resolution) the global temperature of cell dish containing 2 ml PBS.

Standard laser confocal scanning microscopy setup was then adopted where laser spot was focused on surface through microscopy objective, so that local power density of laser was enhanced. In **Supplementary Figure SI1** we show the schematic of laser focused application, along with calculation of laser power

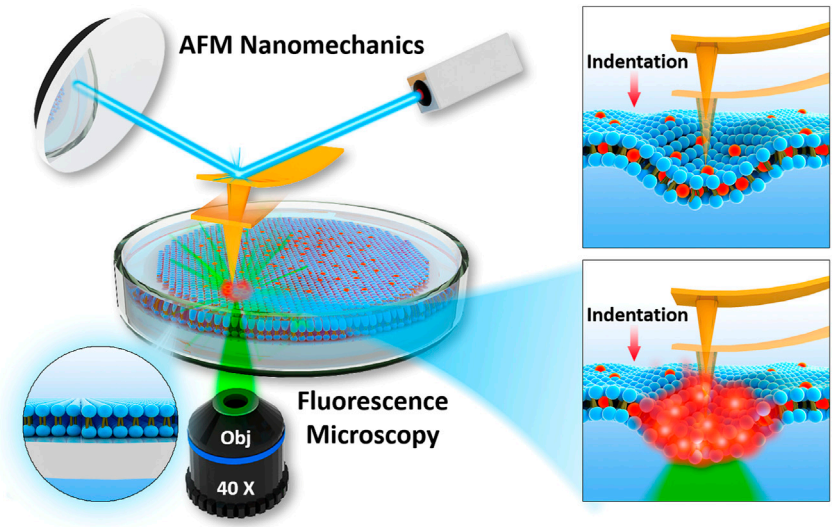

FIGURE 2 | Schematics of integration of AFM with fluorescence microscopy used to determine nanomechanics of phospholipid bilayers interacting with fluorophore and focused laser light.

density. All experiments involving green laser excitation were maintained at the same output power measured directly on sample stage as P = 10.1 mW. Laser beam was focused onto sample surface with a 40X objective lens finally leading to a local power density around 35.4 mW/μm^2 (see Supporting Information, section: Focusing the laser for more details).

AFM Mechanical Imaging of Phospholipid Bilayers

DOPC phospholipid bilayers were deposited on mica and AFM measurements were performed as described in Materials and Methods. As an example, we showed a typical AFM mechanical investigation by indenting a mica substrate partially covered by DOPC bilayers in **Figure 3**. Between contact point and breakthrough event, the contact part was fitted using **Eq. 1** in order to retrieve the Young's modulus value after finite thickness correction (Dimitriadis et al., 2002). As shown in **Figure 3A**, the fitting curve follows the experimental data resulting in a final modulus of 153 ± 8 MPa. Following the generic mechanical approach and using simple Hertz model derivation, Young's modulus results in 406 ± 7 MPa, largely overestimating the modulus due to the hard substrate contribution. In addition, we built an array of FEM simulations (**Supplementary Figure SI2**) using same thickness of experimental data (5 nm), different Young's moduli values and free to slip boundary conditions (as expected from fluid-phase DOPC). In **Figure 3A** the simulated indentation curves are overlapped to data and **Eq. 1** fit showing that finite thickness correction is a good approximation and necessary to extract quantitative mechanical properties.

In our experiments, DOPC supported bilayers on mica were investigated by repeating single force spectroscopy events along a regular matrix, forming a Force Volume (FV). This approach is finally leading to property maps and corresponding histograms of distributed values to improve the statistic reliability. As an example, in **Figure 3B** we show the overlay of breakthrough force map on 3D morphology while highlighting the pixel/force spectroscopy grid. The values obtained during control test analysis (shown in **Table 1**) were in agreement with values found in literature (Das et al., 2010; Garcia-Manyes and Sanz, 2010; Alessandrini and Facci, 2012).

Our FV measurement approach was compared with morphology by tapping mode in liquid using photothermal actuation. While tapping mode morphology in **Supplementary Figure SI3A** is qualitatively similar to FV morphology (**Supplementary Figure SI3B**), the quantification shows underestimation of thickness as Δh = 1.4 nm (compare **Supplementary Figures SI3D,SI3E**). Tapping mode on soft layer is exerting an average non-negligible force, causing a compression not easy to evaluate without force curve approach. We highlight that such compression can be exploited in advanced nanomechanical approaches, such as bimodal AMFM, in order to measure Young's modulus with high-resolution, as well to correct the morphology adding indentation (Al-Rekabi and Contera, 2018; Liu et al., 2020).

Before introducing Nile red as fluorophore, several control experiments were performed to benchmark selected physical stimulations. Firstly, the influence of continuous measurements was investigated by scanning in FV mode for 3 h on an area (70 μm × 70 μm). Comparing the first and last measurements, no significant differences were detected (see **Table 1**). In particular, such experiment shows that the formation of holes is reversible and the area of layers is large enough to minimize erosion at the edges. Such reversible character is clearly shown when vertical forces (for example in retracting curve of **Figure 1B**) decrease below the threshold required to reform the bilayer. Considering that laser irradiation can have a photothermal effect, we measured the

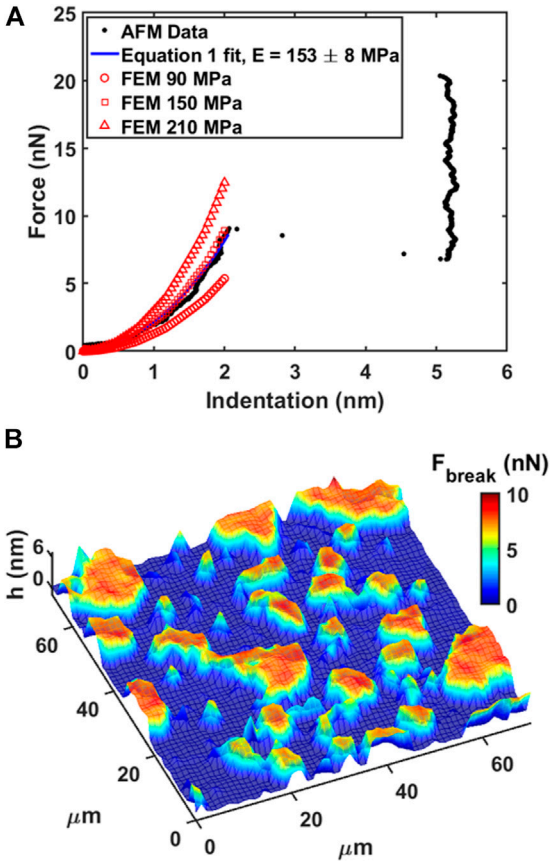

FIGURE 3 | Force spectroscopy and force volume on phospholipid bilayer. **(A)** Force vs. Indentation with fitting of **Eq. 1** and FEM simulated curves overlapped. **(B)** 3D Map representation of 64 × 64 force volume grid by overlapping breakthrough force color map on morphology. Low 'h' thickness (blue color) represents substrate, while higher 'h' thickness (red color) represents the bilayer.

mechanical properties of DOPC bilayers gradually increasing temperature of AFM cell up to 41°C. A series of breakthrough maps of phospholipid after temperature increase are shown in **Supplementary Figure SI4**, showing a slight decrease of F_{break} up to −15%. This is well-documented, as thermal energy decreases the stability of repulsive steric forces in hydrophobic lipid tails. Vertical shrinking and decrease of breakthrough forces was evidenced by Leonenko et al. on phospholipid bilayers including DOPC at 60°C (Leonenko et al., 2004).

Finally, we investigated the effect of laser power focusing the beam on phospholipid bilayer area by maintaining a power density of 35.4 mW/μm^2 for 30 min. In **Supplementary Figure SI5**, we compared DOPC control sample with the situation after irradiation, showing only slight decrease of breakthrough forces at −12%. The numerical data are shown in **Table 1**. In order to avoid systematic uncertainty in model and tip radius determination, we present the final results of all experiments considering control. It is interesting that effect of laser irradiation focused below the probe is similar to environmental cell heating, although no modification of temperature was detected. This behavior is expected to be enhanced when fluorophores, excited by laser light, are employed.

Revealing the Influence of Fluorophore and Laser Irradiation

Nile red fluorophore, which has the excitation and emission wavelength at 552 and 636 nm respectively, was dispersed in a solution of DMSO/PBS (1:5) prior injection in AFM liquid cell. Considering a volume of 2 ml, we obtained a final concentration of 2.5 μg/ml Nile red and 2.5% solution of DMSO to ensure dispersion in water. Previous studies suggest that the influence of DMSO at a concentration of 2.5% is negligible on phospholipid structure (Hughes et al., 2012; Cheng et al., 2015), moreover we used the standard procedure employed to stain living cells (Rumin et al., 2015).

AFM measurements were performed after 20 min equilibration upon injection of Nile red. Considering the control DOPC (**Figures 4A–C**), **Figure 4A** shows the first layer thickness analysis obtained from force curves (typical example in **Figure 4C**) using the procedure described in Material and Methods, focusing on bilayer near substrate. **Figure 4B** is the morphology obtained by detecting an interaction probe-sample with force F = 0.3 nN, showing good overlap with optimized first-layer morphology of **Figure 4A**. Quantification through histogram is parallelly reported in **Figures 5A,B**. After injection of Nile red, morphology of first layer is unchanged (**Figure 4D**) while an increase of thickness is detected in **Figure 4E** (searching contact point with a low force as F = 0.3 nN) and confirmed quantitatively in **Figure 4D**. The increase of thickness is relative to oscillations in force curves before contact with first DOPC layer as shown in **Figure 4F**. With low-force sensitivity, AFM probe is able to detect a weakly bounded overlayer on top of DOPC bilayer. This is suggesting that Nile red molecules are attracted to DOPC bilayer, showing not-negligible interaction and forming weakly bounded aggregates. After injection of Nile red, the force curves on clean substrate are same as control substrate, showing that Nile red molecules are not forming stable interactions with mica surface, as well excluding that surface of probe has contaminations.

After irradiating for 20 min the area under the probe with green laser at 35.4 mW/μm^2, AFM investigation was performed in the same region, shown in **Figures 4G–I**. Interestingly, the amount of overlayer detected in **Figure 4H** decreases noticeably (if compared to **Figure 4E**), as highlighted in area selected in blue circles. The quantification shown in **Figures 5D,F** confirms a decrease of coverage of overlayer aggregates from 17.2% to 10.9% peak area. Probably, focusing the laser for several minutes can cause an increase of the mobility of Nile red molecules, leading to displacement of weakly bounded surface aggregates. More dramatic changes are affecting the force curves, evidently decreasing the breakthrough forces (highlighted with green circles in **Figure 4**) as shown in **Figure 4I** in comparison with **Figures 4C,F**.

The nanomechanical analysis is evidencing modifications related to stability and elasticity. Considering the control

TABLE 1 | Summary of experimental setting parameters and obtained mechanical properties. For each experiment we show the percentual variability of selected conditions in comparison with control.

Condition	Thickness (nm)	Breakthrough (nN)	Young's modulus (MPa)	Adhesion (pN)
Control	4.67 ± 0.53	7.13 ± 0.73	157 ± 22	74 ± 11
Time 3 h	4.48 ± 0.65	7.28 ± 0.98	152 ± 34	47 ± 5
	−4%	2%	−3%	-36%
Control	4.62 ± 0.46	8.67 ± 1.12	169 ± 27	89 ± 11
T = 41°C	4.41 ± 0.34	7.53 ± 0.69	153 ± 22	101 ± 19
	−4%	−15%	−10%	11%
Control	4.85 ± 0.63	7.68 ± 0.64	149 ± 30	30 ± 5
Laser green	4.72 ± 0.54	6.89 ± 0.48	144 ± 31	31 ± 6
	−3%	−12%	−3%	3%
Control	4.44 ± 0.47	7.43 ± 0.66	161 ± 43	80 ± 21
NR 2.5 µg/ml	4.39 ± 0.65	7.97 ± 0.75	157 ± 51	474 ± 189
Laser green	4.20 ± 0.66	4.49 ± 0.56	111 ± 36	428 ± 145
	−1% | −6%	7% | −40%	−3% | −31%	492% | 435%
Hybrid DOPC+NR	4.64 ± 1.21/10.1 ± 1.2	9.25 ± 0.62	219 ± 34	112 ± 45
Laser green	5.07 ± 1.14/9.44 ± 1.04	7.43 ± 1.17	122 ± 27	97 ± 47
	9% | −6%	−20%	−44%	−13%

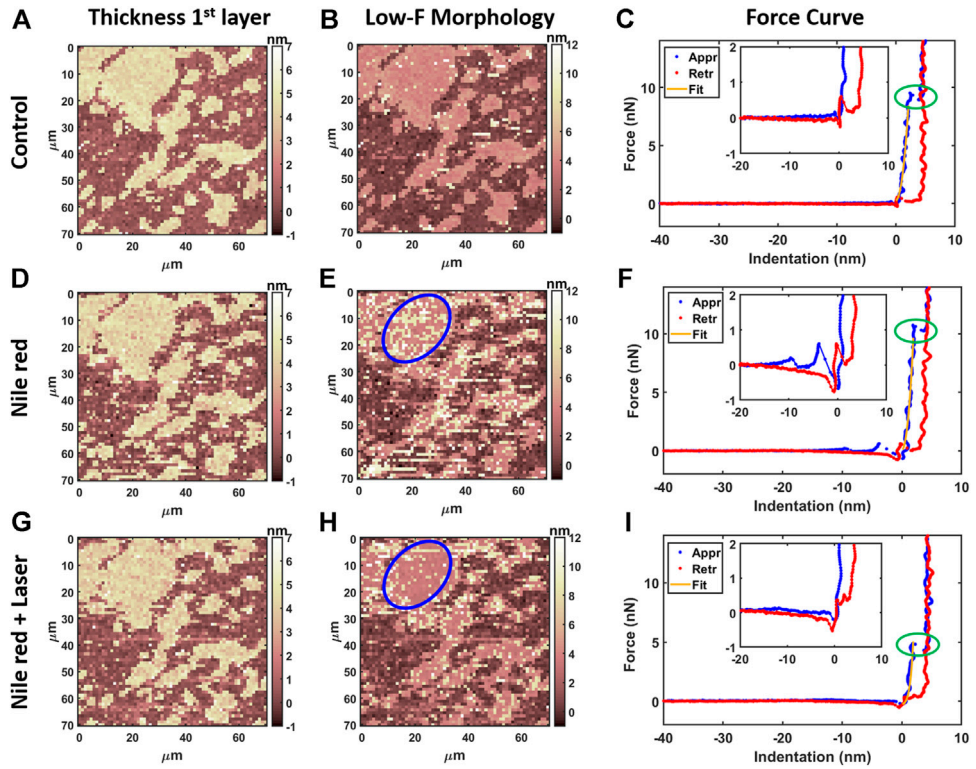

FIGURE 4 | Results of morphological analysis of DOPC partially covering mica using 64x64 force curves. **(A)** Thickness map of first layer and substrate, **(B)** low-force (F < 0.3 nN) morphology and **(C)** examples of approaching (Appr) and retracting (Retr) force curves with fit from **Eq. 1** on control DOPC bilayer. Inset represents a zoom near contact point. With the same order of DOPC control **(A–C)**, DOPC after 30 min incubation with 2.5 ug/ml Nile red with DMSO at 2.5% **(D–F)**, and after irradiating probe region with 35.4 mW/µm^2 laser **(G–I)**. Blue circles in panel e and h are representative of an area where overlayer recedes after laser application. Green ovals in panels **C**, **F**, i highlight breakthrough events.

DOPC, we show the maps for breakthrough force required to break the DOPC bilayer in **Figure 6A**, the Young's Modulus in **Figure 6B** and the adhesion force between probe and layer in **Figure 6C**. **Figure 7** shows the quantification through histogram relative to **Figure 6**, while data are presented and compared in **Table 1**. For instance, after adding Nile red to the solution, the adhesion increases noticeably in agreement with the presence of a weakly bound overlayer that can trap the AFM probe after closing

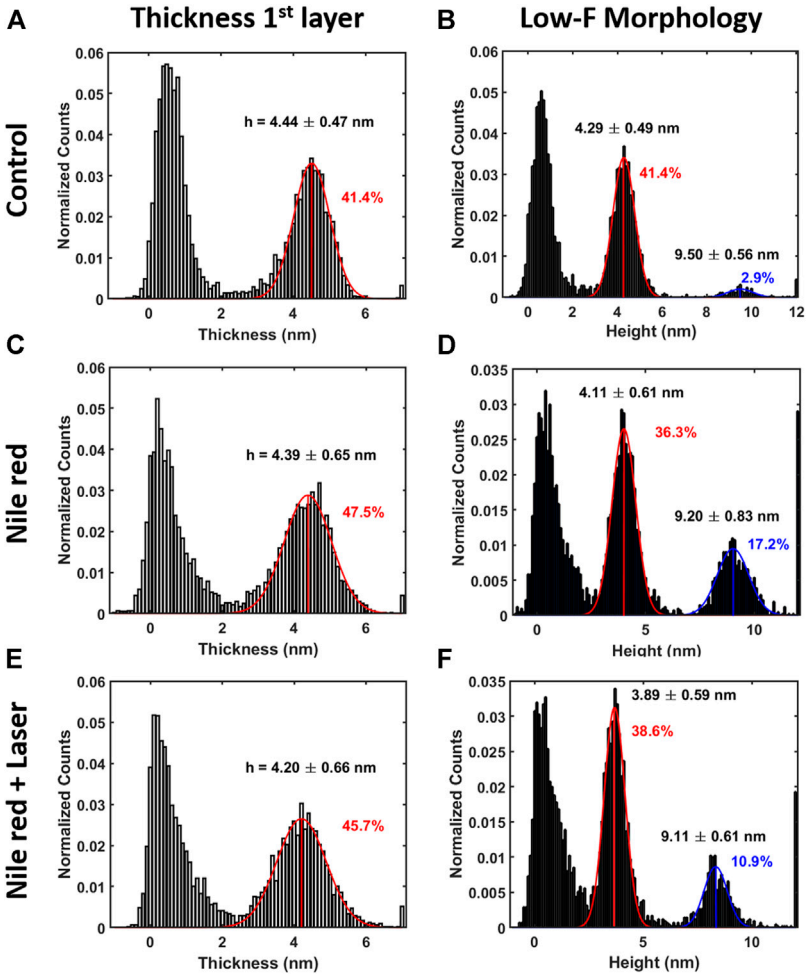

FIGURE 5 | Quantification with histograms and Gaussian fit relative to morphological analysis. **(A)** Thickness histogram of first layer and substrate, **(B)** low-force (F < 0.3 nN) morphology histogram for control DOPC. Same order of histogram of DOPC after 30 min incubation with 2.5ug/ml Nile red with DMSO at 2.5% **(C,D)**, and after irradiating probe region with 35.4 mW/μm^2 laser **(E,F)**. Gaussian fitting and average are depicted for first (red color) and additional layers (blue color), while percentages are indicative of area coverage (events falling in under the fit curve). Counts of vertical axis are normalized on total number of traces (4096).

the layer during the retract phase (see adhesion map **Figures 6F,I** compared with control **Figure 6C**). Also in agreement with idea of weakly bounded overlayer of Nile red, the breakthrough force threshold slightly increases, in fact, similar to multilayer structures, more force is required to displace laterally the overlayer before final breakthrough event (Relat-Goberna et al., 2017).

After 30 min laser irradiation, the effect on layer mechanics is very noticeable, exhibiting a decrease of force required to breakthrough (−40%, **Figures 6G**, **7A,G** decrease of Young's modulus (−31%, **Figures 6H**, **7H**). The synergic effect of fluorophore and laser may be an indication of laser energy absorption by Nile red, subsequent relaxation (part of incident energy dissipated non-radiatively) and final decrease of ordering/stability reflected by mechanics of DOPC phospholipid layer.

The experiments of DOPC bilayer interacting with Nile red and green laser were repeated, maintaining the same conditions but changing AFM probe. In this case, the value of radius may have large errors leading to different absolute values in breakthrough force and Young's modulus.

Particularly, the experiment was performed 3 times showing the same behavior. While morphological analysis shows negligible modifications, breakthrough force has slight increase after adding Nile red and noticeable decrease after laser application. An overlayer is visualized from force curves after staining, while disappearing after laser application. The two additional independent experiments using different probes are in supporting information respectively in **Supplementary Figures SI6, SI7**, while data are collected in **Supplementary Table SI1**.

Increasing Concentration of Nile Red

To further explore the combined effect of amphiphilic fluorophore Nile red and laser on DOPC bilayer, we produced a hybrid structure by mixing 10 mg/ml DOPC with 2.5 μg/ml Nile red in chloroform before dispersing in water. While in previous

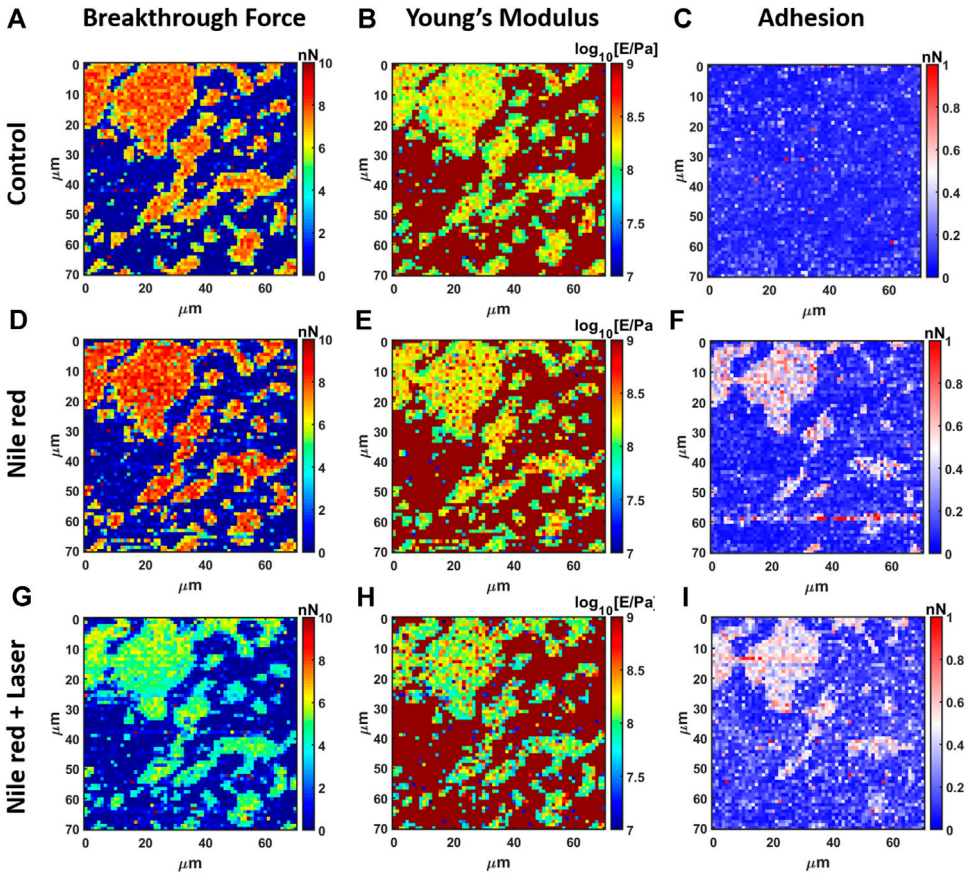

FIGURE 6 | Results of mechanical analysis of DOPC partially covering mica using force curves. **(A)** Breakthrough force map of first layer, **(B)** Young's Modulus map and **(C)** adhesion map on control DOPC bilayer. With the same order of DOPC control **(A–C)**, DOPC after 30 min incubation with 2.5 ug/ml Nile red with DMSO at 2.5% **(D–F)**), and after irradiating probe region with 35.4 mW/μm^2 green laser **(G–I)**.

experiments we experience interaction of Nile red at the most exterior phospholipid leaflet, the objective is to produce a hybrid system including Nile red homogeneously in both leaflets. After chloroform evaporation and rehydration in PBS, hybrid liposomes in solution are red indicating Nile red is incorporated in apolar lipidic environment. Nile red is blue/purple in a polar environment such as water and quickly aggregating. Compared with previous experiments where same concentration of Nile red is dispersed in PBS, we expect the effective quantity of Nile red within the hybrid system is higher.

After deposition on mica, AFM morphology shows DOPC + Nile red hybrids formed irregular, fragmented layers (oppositely to pure DOPC) and double bilayers were often encountered, as shown in **Supplementary Figure SI8**. In average, the breakthrough force is higher than pure DOPC single layer, as expected from multilayer systems showing the layer near the substrate exhibiting higher stability (see **Supplementary Figure SI8B** for map and **Supplementary Figure SI8C** examples of force curves on single or double bilayer). After several measurements, we have evidenced that double bilayer of hybrid structure is the most stable. It may be possible that Nile Red molecules added before micellization in water can favor the formation and stabilization of multilayer structures.

Laser is causing large delamination of layers and reorganization of material. The hybrid structure is becoming very movable, while the probe is probably influencing the displacement of layers by lateral drags. **Supplementary Figures SI9D,SI9E** show the layers broken and certain amorphous accumulation near the scan area border (evidenced by red circles). By comparing the quantification through histograms in **Supplementary Figure SI9**, the second bilayer almost disappears and the first greatly reduces in dimensions. The breakthrough force and Young's modulus decrease about −20% and −44%, respectively in comparison with control. When mixed before micellization in water, we speculate a stronger interaction between hydrophobic Nile red and core of lipid tails.

DOPC Interacting with Other Dyes

The investigation of model membrane interacting with different dyes and lasers is important to understand how much the synergy between dye excitation and mechanical modifications can be generalized.

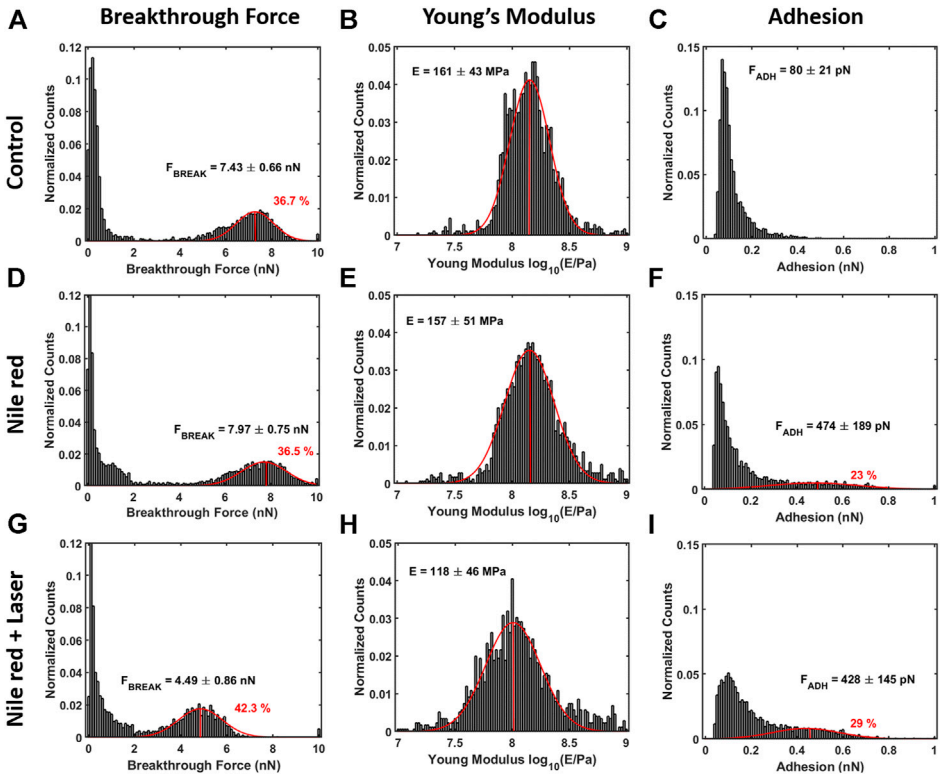

FIGURE 7 | Quantification with histograms and Gaussian fit relative to mechanical analysis. **(A)** Breakthrough force histogram of first layer, **(B)** Young's Modulus histogram and **(C)** adhesion histogram on control DOPC bilayer. With the same order of DOPC control **(A–C)**, DOPC after 30 min incubation with 2.5ug/ml Nile red with DMSO at 2.5% **(D–F)**), and after irradiating probe region with 35.4 mW/μm^2 green laser **(G–I)**. Gaussian fitting and average are depicted for first and additional layers, while percentages are indicative of area coverage (events falling in under the fit curve). The peaks around zero breakthrough force in **(A,D,G)** reflect the fact that some parts of the mica surface were not covered by DOPC bilayer. Counts of vertical axis are normalized on total number of traces (4096).

For example, we performed AFM nanomechanical experiments on DOPC membrane interacting with different dyes and lasers. If not stated otherwise we always use the experimental conditions described in Material and Methods.

First, we used CytoTracker deep red, a staining agent, to visualize cytosol for the purpose of tracking cells' movements. This dye is more hydrophilic than Nile Red; not specific for cell membrane, but membrane permeable. Therefore, in a model system such as supported bilayer with staining solution always in contact, a certain interaction was expected. Using operative concentration of 2.5 μg/ml no modification was evidenced. Only increasing concentration 10 times (25 μg/ml) a decrease of breakthrough force was showed similarly to Nile red. The corresponding results are shown in **Supplementary Table S2**; **Supplementary Figure SI10**.

Secondly, we used HOECHST, a common staining agent for DNA molecules in order to visualize nucleus in confocal measurements. The dye is amphiphilic, not specific for cell membrane but permeable. Here, using operative staining concentration of 2.5 μg/ml we noticed a large deposit forming on top of DOPC layer causing difficulties in AFM measurement. The thickness doubled the breakthrough force, while the adhesion force increased 100 times, evidencing a complex of DOPC/dye molecules strongly attracting AFM probe. The laser application (same power as in main text but blue color) was dramatic, removing all material from surface within 1 min. The corresponding results are shown in **Supplementary Table S2**; **Supplementary Figure SI1**, in particular we show adhesion signal as the most significant.

Hydrophilic molecules require higher concentration to modify the membrane, while we speculate that they can have more influence on their target (proteins in cytosol). Amphiphilic molecules such as HOECHST can have more effect on membrane (especially after long time of continuous interaction). For this reason, standard protocols for HOECHST staining are requiring to remove excess of dye by washing after short time (15 min).

Finally, we highlight that the effects we observed here are dependent on the nature of the system. While a general photooxidation is expected when using focused laser, the intensity of mechanical modifications depends on the interaction between dye molecules and biological target, therefore additional investigations using confocal AFM mechanics could help in determining which system should be treated with more care.

DISCUSSION

Fluorescence microscopy, especially the laser confocal scan microscopy, raises the concern of biologically relevant modifications induced by irradiated laser, particularly in the presence of dye molecules. Whether these effects can affect the mechanical properties becomes critical for membrane integrity during live measurements. Hidden events in standard fluorescence microscopy can be detected by implementing optomechanical correlative microscopy analysis. Firstly, by controlling the applied force during analysis, we detected Nile red fluorophores forming weakly bounded composite structures on top of phospholipid layer near substrate. Weakly bounded layer is visible in force oscillation in **Figure 4F** as well increase of adhesion force during retracting. These oscillations are also detected by AFM force spectroscopy when weakly bounded molecular electrolytes are attracted to solid surface electrode (Sakai et al., 2015; Cui et al., 2016; Griffin et al., 2016). In this framework, phospholipid mixtures were investigated using rhodamine-based phospholipid as fluorescent probe to visualized raft structures (Ayuyan and Cohen, 2006). Excitation of fluorophore induced photooxidation of DOPC in a three component lipid mixture, evidenced by the formation of large raft-like structures. While a substantial amount of DOPC may be converted in lipid peroxides easily visible by fluorescence microscopy, mechanical properties were never investigated. Nanomechanics by AFM was used in this work to unveil modification not easily detected during fluorescence microscopy. In fact, we revealed that the degradation of mechanical properties of model phospholipid membranes is driven by synergic presence of bounded fluorophores and focused laser irradiation. Similar to modification induced by temperature rise (Leonenko et al., 2004; Garcia-Manyes et al., 2005), we expect laser energy transfer between fluorophores and biomembranes is at the base of this modification. Instead, it was evidenced that fluorescence intensity is decreasing dependent with temperature increase for DOPC and Nile red system (Halder et al., 2018). Such effect was explained as temperature related increase of flexibility and consequent water penetration, leading to partial Nile red quenching. Beside quenching, we expect the modification of mechanical properties induced by combined action of laser and fluorophore will lead to additional deterioration of fluorescence performance. Conversely, the possibility to tailor fluorescence and photothermal relaxations for near-infrared fluorophores was recently explored by Gao et al. (Gao et al., 2019) In particular, fluorescence imaging can enhance intraoperative guidance, at the same time allowing photothermal ablation therapy for cancer lesions. In confocal experiments, the signal/noise ratio can be improved by increasing the quantity of staining agent or laser light intensity. While this strategy is proven effective, photo quenching is often encountered, moreover, we now highlight how the structural equilibrium of phospholipids can break upon irradiation if relative quantity of fluorophore is high. As shown in the hybrid system, photothermal energy conversion may be responsible for degradation of mechanical properties and increased mobility stressed by relatively higher quantity of accumulated Nile red. Similar behavior (increased mobility and fluidity, displacement of layers during measurements) are observed when using cationic surfactants strongly interacting with lipid tails (Lima et al., 2013; Redondo-Morata et al., 2014).

CONCLUSION

This work highlights the analytical power provided by AFM to obtain subtle yet important information, which are otherwise hard to detect, in correlative microscopy as well as the necessity in taking photothermal effects into account when using fluorophores in examining the behavior of cell membranes. Indeed, a synergistic effect of focused laser and Nile red fluorophore interacting with DOPC model membrane was detected by AFM nanomechanics, showing remarkable decrease of stability and elasticity of supported bilayers. This effect is comparable to that caused by elevated temperature, suggesting the critical role of local heat transfer (within the membrane) induced by excitation/relaxation of Nile red fluorophores in this process. The equilibrium between radiative (fluorescence) and non-radiative (lattice vibrations) relaxations is worth investigating in order to evaluate the extent of prospective applications when using multi-modal nanoparticles able to switch fluorophore and photothermal characteristics. Our results are accompanied by a robust and reliable methodology to implement correlative AFM mechanics and optical microscopy, as well a routine of custom data analysis. While we investigate phospholipid bilayers influenced by excited Nile red, the scope of application of this methodology can be extended to other biosystems where synergic action of fluorophore and laser may play important role in nanomechanical modifications.

DATA AVAILABILITY STATEMENT

The raw data supporting the conclusions of this article will be made available by the authors, without undue reservation.

AUTHOR CONTRIBUTIONS

ZC, JL and MG initiated the project and designed the experiments. MG and BZ prepared the samples. BZ and LW implemented the correlative microscope and installed the laser. MG performed the AFM experiments. HZ performed the finite element simulations. YL, MG and JL conducted the data analysis. MG, BZ, YL and ZC wrote the manuscript. All authors discussed the results of the study.

FUNDING

Authors acknowledge the financial support from the National Natural Science Foundation of China (No. 21950410518 and 32071318), Shenzhen Basic Research Project (No.

JCYJ20190807163007525), SIAT Innovation Program for Excellent Young Researchers (No. Y8G032), Chinese Academy of Sciences President's International Fellowship Initiative (No. 2019PM0006), the leading talents of Guangdong province (2016LJ06C372) and Key-Area Research and Development Program of Guangdong Province (2018B010109009). ZC acknowledges financial support from the HKSAR Research Grants Council (RGC) General Research Fund (GRF, No. 14306117), Early Career Scheme (ECS, No. 27202919) and HKU Start-Up Grant, Small Equipment Grant (No. 102009812).

SUPPLEMENTARY MATERIAL

The Supplementary Material for this article can be found online at: https://www.frontiersin.org/articles/10.3389/fmolb.2021.669361/full#supplementary-material

REFERENCES

Al-Rekabi, Z., and Contera, S. (2018). Multifrequency AFM Reveals Lipid Membrane Mechanical Properties and the Effect of Cholesterol in Modulating Viscoelasticity. *Proc. Natl. Acad. Sci. USA* 115 (11), 2658–2663. doi:10.1073/pnas.1719065115

Alessandrini, A., and Facci, P. (2012). Nanoscale Mechanical Properties of Lipid Bilayers and Their Relevance in Biomembrane Organization and Function. *Micron* 43 (12), 1212–1223. doi:10.1016/j.micron.2012.03.013

Ayuyan, A. G., and Cohen, F. S. (2006). Lipid Peroxides Promote Large Rafts: Effects of Excitation of Probes in Fluorescence Microscopy and Electrochemical Reactions during Vesicle Formation. *Biophysical J.* 91 (6), 2172–2183. doi:10.1529/biophysj.106.087387

Balleza, D., Alessandrini, A., and Beltrán García, M. J. (2019). Role of Lipid Composition, Physicochemical Interactions, and Membrane Mechanics in the Molecular Actions of Microbial Cyclic Lipopeptides. *J. Membr. Biol* 252 (2), 131–157. doi:10.1007/s00232-019-00067-4

Beedle, A. E., Williams, A., Relat-Goberna, J., and Garcia-Manyes, S. (2015). Mechanobiology - Chemical Origin of Membrane Mechanical Resistance and Force-dependent Signaling. *Curr. Opin. Chem. Biol.* 29 (Suppl. C), 87–93. doi:10.1016/j.cbpa.2015.09.019

Bogdanov, M., Pyrshev, K., Yesylevskyy, S., Ryabichko, S., Boiko, V., Ivanchenko, P., et al. (2020). Phospholipid Distribution in the Cytoplasmic Membrane of Gram-Negative Bacteria Is Highly Asymmetric, Dynamic, and Cell Shape-dependent. *Sci. Adv.* 6 (23), eaaz6333. doi:10.1126/sciadv.aaz6333

Butt, H.-J., Cappella, B., and Kappl, M. (2005). Force Measurements with the Atomic Force Microscope: Technique, Interpretation and Applications. *Surf. Sci. Rep.* 59 (1), 1–152. doi:10.1016/j.surfrep.2005.08.003

Cheng, C.-Y., Song, J., Pas, J., Meijer, L. H. H., and Han, S. (2015). DMSO Induces Dehydration Near Lipid Membrane Surfaces. *Biophysical J.* 109 (2), 330–339. doi:10.1016/j.bpj.2015.06.011

Cosentino, M., Canale, C., Bianchini, P., and Diaspro, A. (2019). AFM-STED Correlative Nanoscopy Reveals a Dark Side in Fluorescence Microscopy Imaging. *Sci. Adv.* 5 (6), eaav8062. doi:10.1126/sciadv.aav8062

Cui, T., Lahiri, A., Carstens, T., Borisenko, N., Pulletikurthi, G., Kuhl, C., et al. (2016). Influence of Water on the Electrified Ionic Liquid/Solid Interface: A Direct Observation of the Transition from a Multilayered Structure to a Double-Layer Structure. *J. Phys. Chem. C* 120 (17), 9341–9349. doi:10.1021/acs.jpcc.6b02549

Das, C., Sheikh, K. H., Olmsted, P. D., and Connell, S. D. (2010). Nanoscale Mechanical Probing of Supported Lipid Bilayers with Atomic Force Microscopy. *Phys. Rev. E* 82 (4 Pt 1), 041920. doi:10.1103/PhysRevE.82.041920

Dimitriadis, E. K., Horkay, F., Maresca, J., Kachar, B., and Chadwick, R. S. (2002). Determination of Elastic Moduli of Thin Layers of Soft Material Using the Atomic Force Microscope. *Biophysical J.* 82 (5), 2798–2810. doi:10.1016/s0006-3495(02)75620-8

Eeman, M., and Deleu, M. (2010). From Biological Membranes to Biomimetic Model Membranes. *Biotechnologie Agronomie Societe Et Environnement* 14 (4), 719–736.

Eid, J., Greige-Gerges, H., Monticelli, L., and Jraij, A. (2021). Elastic Moduli of Lipid Membranes: Reproducibility of AFM Measures. *Chem. Phys. Lipids* 234, 105011. doi:10.1016/j.chemphyslip.2020.105011

Galluzzi, M., Tang, G., Biswas, C. S., Zhao, J., Chen, S., and Stadler, F. J. (2018). Atomic Force Microscopy Methodology and AFMech Suite Software for Nanomechanics on Heterogeneous Soft Materials. *Nat. Commun.* 9 (1), 3584. doi:10.1038/s41467-018-05902-1

Gao, S., Wei, G., Zhang, S., Zheng, B., Xu, J., Chen, G., et al. (2019). Albumin Tailoring Fluorescence and Photothermal Conversion Effect of Near-Infrared-II Fluorophore with Aggregation-Induced Emission Characteristics. *Nat. Commun.* 10 (1), 2206. doi:10.1038/s41467-019-10056-9

Garcia, R. (2020). Nanomechanical Mapping of Soft Materials with the Atomic Force Microscope: Methods, Theory and Applications. *Chem. Soc. Rev.* 49, 5850–5884. doi:10.1039/D0CS00318B

Garcia-Manyes, S., Oncins, G., and Sanz, F. (2005a). Effect of Ion-Binding and Chemical Phospholipid Structure on the Nanomechanics of Lipid Bilayers Studied by Force Spectroscopy. *Biophysical J.* 89 (3), 1812–1826. doi:10.1529/biophysj.105.064030

Garcia-Manyes, S., Oncins, G., and Sanz, F. (2005b). Effect of Temperature on the Nanomechanics of Lipid Bilayers Studied by Force Spectroscopy. *Biophysical J.* 89 (6), 4261–4274. doi:10.1529/biophysj.105.065581

Garcia-Manyes, S., and Sanz, F. (2010). Nanomechanics of Lipid Bilayers by Force Spectroscopy with AFM: A Perspective. *Biochim. Biophys. Acta (Bba) - Biomembranes* 1798 (4), 741–749. doi:10.1016/j.bbamem.2009.12.019

Griffin, L. R., Browning, K. L., Clarke, S. M., Smith, A. M., Perkin, S., Skoda, M. W. A., et al. (2016). Direct Measurements of Ionic Liquid Layering at a Single Mica-Liquid Interface and in Nano-Films between Two Mica-Liquid Interfaces. *Phys. Chem. Chem. Phys.* 19 (1), 297–304. doi:10.1039/c6cp05757h

Halder, A., Saha, B., Maity, P., Kumar, G. S., Sinha, D. K., and Karmakar, S. (2018). Lipid Chain Saturation and the Cholesterol in the Phospholipid Membrane Affect the Spectroscopic Properties of Lipophilic Dye Nile Red. *Spectrochimica Acta A: Mol. Biomol. Spectrosc.* 191, 104–110. doi:10.1016/j.saa.2017.10.002

Hofsäß, C., Lindahl, E., and Edholm, O. (2003). Molecular Dynamics Simulations of Phospholipid Bilayers with Cholesterol. *Biophysical J.* 84 (4), 2192–2206. doi:10.1016/s0006-3495(03)75025-5

Hughes, Z. E., Mark, A. E., and Mancera, R. L. (2012). Molecular Dynamics Simulations of the Interactions of DMSO with DPPC and DOPC Phospholipid Membranes. *J. Phys. Chem. B* 116 (39), 11911–11923. doi:10.1021/jp3035538

Indrieri, M., Suardi, M., Podestà, A., Ranucci, E., Ferruti, P., and Milani, P. (2008). Quantitative Investigation by Atomic Force Microscopy of Supported Phospholipid Layers and Nanostructures on Cholesterol-Functionalized Glass Surfaces. *Langmuir* 24 (15), 7830–7841. doi:10.1021/la703725b

Iraand Krishnamoorthy, G. (1998). Probing the Dynamics of Planar Supported Membranes by Nile Red Fluorescence Lifetime Distribution. *Biochim. Biophys. Acta* 1414 (1-2), 255–259. doi:10.1016/s0005-2736(98)00157-6

Reviakine, I., and Brisson, A.: Formation of Supported Phospholipid Bilayers from Unilamellar Vesicles Investigated by Atomic Force Microscopy. *Langmuir*, 16(4), 1806–1815. (2000). doi:10.1021/La9903043

Jacquot, A., Francius, G., Razafitianamaharavo, A., Dehghani, F., Tamayol, A., Linder, M., et al. (2014). Morphological and Physical Analysis of Natural Phospholipids-Based Biomembranes. *PLOS ONE* 9 (9), e107435. doi:10.1371/journal.pone.0107435

Jain, B., and Das, K. (2006). Fluorescence Resonance Energy Transfer between DPH and Nile Red in a Lipid Bilayer. *Chem. Phys. Lett.* 433 (1-3), 170–174. doi:10.1016/j.cplett.2006.11.050

Kurniasih, I. N., Liang, H., Mohr, P. C., Khot, G., Rabe, J. P., and Mohr, A. (2015). Nile Red Dye in Aqueous Surfactant and Micellar Solution. *Langmuir* 31 (9), 2639–2648. doi:10.1021/la504378m

Leeb, F., and Maibaum, L. (2018). Spatially Resolving the Condensing Effect of Cholesterol in Lipid Bilayers. *Biophysical J.* 115 (11), 2179–2188. doi:10.1016/j.bpj.2018.10.024

Leonenko, Z. V., Finot, E., Ma, H., Dahms, T. E. S., and Cramb, D. T. (2004). Investigation of Temperature-Induced Phase Transitions in DOPC and DPPC Phospholipid Bilayers Using Temperature-Controlled Scanning Force Microscopy. *Biophysical J.* 86 (6), 3783–3793. doi:10.1529/biophysj.103.036681

Levitt, J. A., Chung, P.-H., and Suhling, K. (2015). Spectrally Resolved Fluorescence Lifetime Imaging of Nile Red for Measurements of Intracellular Polarity. *J. Biomed. Opt.* 20 (9), 096002. doi:10.1117/1.JBO.20.9.096002

Lichtman, J. W., and Conchello, J.-A. (2005). Fluorescence Microscopy. *Nat. Methods* 2 (12), 910–919. doi:10.1038/nmeth817

Lima, L. M. C., Giannotti, M. I., Redondo-Morata, L., Vale, M. L. C., Marques, E. F., and Sanz, F. (2013). Morphological and Nanomechanical Behavior of Supported Lipid Bilayers on Addition of Cationic Surfactants. *Langmuir* 29 (30), 9352–9361. doi:10.1021/la400067n

Liu, M., Xie, S., Wei, L., Galluzzi, M., Li, Y., Wang, Q., et al. (2020). Quantitative Functional Imaging of VO2 Metal-Insulator Transition through Intermediate M2 Phase. *Acta Materialia* 195, 720–727. doi:10.1016/j.actamat.2020.06.014

Luitz, M. P., Barth, A., Crevenna, A. H., Bomblies, R., Lamb, D. C., and Zacharias, M. (2017). Covalent Dye Attachment Influences the Dynamics and Conformational Properties of Flexible Peptides. *PLOS ONE* 12 (5), e0177139. doi:10.1371/journal.pone.0177139

Mescola, A., Ragazzini, G., and Alessandrini, A. (2020). Daptomycin Strongly Affects the Phase Behavior of Model Lipid Bilayers. *J. Phys. Chem. B* 124, 8562–8571. doi:10.1021/acs.jpcb.0c06640

Müller, D. J., Dumitru, A. C., Lo Giudice, C., Gaub, H. E., Hinterdorfer, P., Hummer, G., et al. (2020). Atomic Force Microscopy-Based Force Spectroscopy and Multiparametric Imaging of Biomolecular and Cellular Systems. *Chem. Rev.* doi:10.1021/acs.chemrev.0c00617

Nautiyal, P., Alam, F., Balani, K., and Agarwal, A. (2018). The Role of Nanomechanics in Healthcare. *Adv. Healthc. Mater.* 7 (3), 1700793. doi:10.1002/adhm.201700793

Redondo-Morata, L., Giannotti, M. I., and Sanz, F. (2014). Structural Impact of Cations on Lipid Bilayer Models: Nanomechanical Properties by AFM-Force Spectroscopy. *Mol. Membr. Biol.* 31 (1), 17–28. doi:10.3109/09687688.2013.868940

Redondo-Morata, L., Losada-Pérez, P., and Giannotti, M. I. (2020). "Lipid Bilayers: Phase Behavior and Nanomechanics," in *Membrane Biomechanics*. Editor L. Irena and T. Andreea (Cambridge, MA: Elsevier), 1–55. doi:10.1016/bs.ctm.2020.08.005

Relat-Goberna, J., Beedle, A. E. M., and Garcia-Manyes, S. (2017). The Nanomechanics of Lipid Multibilayer Stacks Exhibits Complex Dynamics. *Small* 13 (24), 1700147. doi:10.1002/smll.201700147

Richter, R. P., and Brisson, A. R. (2005). Following the Formation of Supported Lipid Bilayers on Mica: a Study Combining AFM, QCM-D, and Ellipsometry. *Biophysical J.* 88 (5), 3422–3433. doi:10.1529/biophysj.104.053728

Rumin, J., Bonnefond, H., Saint-Jean, B., Rouxel, C., Sciandra, A., Bernard, O., et al. (2015). The Use of Fluorescent Nile Red and BODIPY for Lipid Measurement in Microalgae. *Biotechnol. Biofuels* 8 (1), 42. doi:10.1186/s13068-015-0220-4

Sakai, K., Okada, K., Uka, A., Misono, T., Endo, T., Sasaki, S., et al. (2015). Effects of Water on Solvation Layers of Imidazolium-type Room Temperature Ionic Liquids on Silica and Mica. *Langmuir* 31 (22), 6085–6091. doi:10.1021/acs.langmuir.5b01184

Shashkova, S., and Leake, M. C. (2017). Single-molecule Fluorescence Microscopy Review: Shedding New Light on Old Problems. *Biosci. Rep.* 37 (4). doi:10.1042/bsr20170031

Stetter, F. W. S., Hyun, S.-H., Brander, S., Urban, J. M., Thompson, D. H., and Hugel, T. (2016). Nanomechanical Characterization of Lipid Bilayers with AFM-Based Methods. *Polymer* 102, 326–332. doi:10.1016/j.polymer.2015.11.038

Tang, G., Galluzzi, M., Biswas, C. S., and Stadler, F. J. (2018). Investigation of Micromechanical Properties of Hard Sphere Filled Composite Hydrogels by Atomic Force Microscopy and Finite Element Simulations. *J. Mech. Behav. Biomed. Mater.* 78, 496–504. doi:10.1016/j.jmbbm.2017.10.035

Tang, G., Galluzzi, M., Zhang, B., Shen, Y.-L., and Stadler, F. J. (2019). Biomechanical Heterogeneity of Living Cells: Comparison between Atomic Force Microscopy and Finite Element Simulation. *Langmuir* 35 (23), 7578–7587. doi:10.1021/acs.langmuir.8b02211

Terzi, M. M., Deserno, M., and Nagle, J. F. (2019). Mechanical Properties of Lipid Bilayers: a Note on the Poisson Ratio. *Soft Matter* 15 (44), 9085–9092. doi:10.1039/C9SM01290G

Zhanghao, K., Liu, W., Li, M., Wu, Z., Wang, X., Chen, X., et al. (2020). High-dimensional Super-resolution Imaging Reveals Heterogeneity and Dynamics of Subcellular Lipid Membranes. *Nat. Commun.* 11 (1), 5890. doi:10.1038/s41467-020-19747-0

Zhou, G., Zhang, B., Tang, G., Yu, X.-F., and Galluzzi, M. (2021). Cells Nanomechanics by Atomic Force Microscopy: Focus on Interactions at Nanoscale. *Adv. Phys. X* 6, 1866668. doi:10.1080/23746149.2020.1866668

Conflict of Interest: BZ was employed by the companies DGene (Dongjin Big Health (Shenzhen)) Co., Ltd, and BenHealth Biopharmaceutical (Shenzhen) Co., Ltd.

The remaining authors declare that the research was conducted in the absence of any commercial or financial relationships that could be construed as a potential conflict of interest.

frontiers in Physics

ORIGINAL RESEARCH
published: 11 May 2021
doi: 10.3389/fphy.2021.666913

Importance of Viscosity Contrast for the Motion of Erythrocytes in Microcapillaries

*Anil K. Dasanna, Johannes Mauer, Gerhard Gompper and Dmitry A. Fedosov**

Theoretical Physics of Living Matter, Institute of Biological Information Processing and Institute for Advanced Simulation, Forschungszentrum Jülich, Jülich, Germany

The dynamics and deformation of red blood cells (RBCs) in microcirculation affect the flow resistance and transport properties of whole blood. One of the key properties that can alter RBC dynamics in flow is the contrast λ (or ratio) of viscosities between RBC cytosol and blood plasma. Here, we study the dependence of RBC shape and dynamics on the viscosity contrast in tube flow, using mesoscopic hydrodynamics simulations. State diagrams of different RBC dynamical states, including tumbling cells, parachutes, and tank-treading slippers, are constructed for various viscosity contrasts and wide ranges of flow rates and tube diameters (or RBC confinements). Despite similarities in the classification of RBC behavior for different viscosity contrasts, there are notable differences in the corresponding state diagrams. In particular, the region of parachutes is significantly larger for $\lambda = 1$ in comparison to $\lambda = 5$. Furthermore, the viscosity contrast strongly affects the tumbling-to-slipper transition, thus modifying the regions of occurrence of these states as a function of flow rate and RBC confinement. Also, an increase in cytosol viscosity leads to a reduction in membrane tension induced by flow stresses. Physical mechanisms that determine these differences in RBC dynamical states as a function of λ are discussed.

Keywords: red blood cell, channel flow, cell shape, cell dynamics, cell deformation, mesoscopic simulation

OPEN ACCESS

Edited by:
Ying Li,
University of Connecticut, United States

Reviewed by:
Aurora Hernandez-Machado,
University of Barcelona, Spain
Paolo Malgaretti,
Helmholtz Institute Erlangen-Nürnberg, Germany
Zhangli Peng,
University of Notre Dame, United States

****Correspondence:***
Dmitry A. Fedosov
d.fedosov@fz-juelich.de

Specialty section:
This article was submitted to Biophysics, a section of the journal Frontiers in Physics

Received: *11 February 2021*
Accepted: *06 April 2021*
Published: *11 May 2021*

Citation:
Dasanna AK, Mauer J, Gompper G and Fedosov DA (2021) Importance of Viscosity Contrast for the Motion of Erythrocytes in Microcapillaries. Front. Phys. 9:666913. doi: 10.3389/fphy.2021.666913

1. INTRODUCTION

Microvascular blood flow is essential for the homeostasis of organism tissues, as it transports nutrients and waste products and mediates various physiological processes. This research field has received enormous attention directed at understanding complex microvascular transport and regulation [1–5]. Blood is a liquid tissue whose major cellular component is erythrocytes or red blood cells (RBCs) which constitute about 45% of blood volume. A healthy RBC has a biconcave shape with a diameter of 6–8 μm and thickness of 2 μm [6]. The RBC membrane consists of a lipid bilayer and spectrin network (cytoskeleton) attached to the inside of the bilayer [7]. These structures supply cell deformability and durability, as RBCs have to frequently pass capillaries with a diameter comparable to the RBC size. The ability of RBCs to deform is vital for microvascular perfusion, as an increased membrane rigidity is generally associated with pathological conditions [8, 9] such as sickle-cell anemia [10] and malaria [11, 12].

One of the important steps toward understanding microvascular blood flow is a detailed description of RBC behavior in microcapillaries. Early experiments [13–15] have shown that RBCs passing through small vessels either deform into cup-like parachute shapes at the vessel

center or assume elongated slipper shapes at an off-center position. A number of more recent microfluidic experiments [16–20] have systematically studied and confirmed these observations and suggested a connection between RBC elasticity and its shape in flow. From the physics point of view, it is interesting to understand how such shapes develop and which cell and flow properties determine their stability. First simple axisymmetric models of RBCs flowing in microvessels [21] have demonstrated the ability of RBCs to attain parachute and bullet-like (in very narrow vessels) shapes due to the stresses exerted by fluid flow. Two dimensional (2D) simulations of fluid vesicles mimicking RBCs have shown that cell behavior in microcapillary flow is quite complex [22–27]. In addition to the parachute and slipper shapes, snaking dynamics (a periodic cell swinging around the tube center) at low flow rates and a region of co-existing parachutes and slippers at high flow rates were reported [24, 25]. These 2D simulations have also demonstrated that the transition between parachute and slipper shapes can be triggered by changes in flow rate or RBC membrane elasticity. This transition can be characterized by the distance between the cell's center-of-mass and the channel center, which has been shown to have a similar behavior as a pitchfork bifurcation [23]. Nevertheless, it is still not fully clear why the parachute-to-slipper transition takes place.

Three dimensional (3D) simulations of RBCs flowing in microchannels [28–34] have confirmed the existence of stable slippers in 3D. Despite some similarities between the results obtained from 2D and 3D simulations, RBC dynamics in microchannels is inherently three dimensional, so that the results from 2D simulations are at most qualitative. For instance, 3D simulations have shown the existence of a dynamic state of RBC tumbling at a radial position away from the tube center [29, 34]. In fact, the transition from tumbling to slipper state with increasing flow rate is reminiscent of the well-known tumbling-to-tank-treading transition of RBCs in simple shear flow [35–38]. Furthermore, recent experiments on RBCs in flow within square microchannels have found a tumbling trilobe state at large flow rates and low confinements [34]. Such trilobe dynamics has so far only been reproduced in simulations of RBCs in simple shear flow, and occurs at large shear rates and for large enough viscosity contrasts λ defined as the ratio between viscosities of RBC cytosol and suspending medium [39, 40], with $\lambda \gtrsim 3.5$.

Most of the current simulation studies assume for simplicity the viscosity contrast of unity, even though the average physiological value of λ is about five [41, 42]. The viscosity contrast is an important parameter that significantly affects RBC behavior in simple shear flow [39, 40, 43–45]. However, it remains unclear whether the viscosity contrast is equally important for RBC dynamics in microcapillary flow. Therefore, we focus on the effect of λ on RBC dynamical states in tube flow. Several state diagrams of RBC dynamics, including snaking, tumbling, tank-treading slipper, and parachute, are presented for different viscosity contrasts, tube diameters, and flow rates. Even though the dynamical states are similar for $\lambda = 1$ and $\lambda = 5$, there are differences in flow conditions at which they appear. In particular, the region of tumbling dynamics for $\lambda = 5$ expands toward larger flow rates in comparison to $\lambda = 1$, since an increased dissipation inside the cell suppresses membrane tank-treading in favor of tumbling motion. Furthermore, the region of parachute shapes is larger for $\lambda = 1$ than that for $\lambda = 5$. A larger viscosity inside the RBC also leads to a decrease in membrane tension for the same flow conditions. Physical mechanisms that determine these differences in dynamical state diagrams for various viscosity contrasts are discussed.

2. MODELS AND METHODS

2.1. Red Blood Cell Model

A RBC is modeled as a triangulated surface with $N_v = 3,000$ vertices, N_e edges, and N_f triangular faces [28, 46–48]. The total potential energy of the system is given by

$$V = V_{\text{in-plane}} + V_{\text{bend}} + V_{\text{area}} + V_{\text{vol}}. \tag{1}$$

The term $V_{\text{in-plane}}$ represents an in-plane elastic energy as [47, 48]

$$V_{\text{in-plane}} = \sum_{i=1}^{N_e} \frac{k_B T \ell_m \left(3x_i^2 - 2x_i^3\right)}{4p\,(1 - x_i)} + \sum_{i=1}^{N_e} \frac{k_p}{\ell_i}, \tag{2}$$

where the first term is an attractive worm-like chain potential and the second term is a repulsive potential with a strength coefficient k_p. In the attractive potential, p is the persistence length, ℓ_i is the extension of edge i, ℓ_m is the maximum edge extension, and $x_i = \ell_i/\ell_m$.

The second term in Equation (1) corresponds to bending resistance of the membrane,

$$V_{\text{bend}} = \sum_{i=1}^{N_e} \kappa_b \left(1 - \cos(\theta_i - \theta_0)\right), \tag{3}$$

where κ_b is the bending coefficient, θ is the angle between two neighboring faces, and θ_0 is the spontaneous angle. Equation (3) is a basic discretization of the Helfrich bending energy [49], which is acceptable for RBCs as their dynamics and deformation are primarily governed by shear-elastic properties. Other discretizations of the Helfrich energy are also available [50, 51].

The last two terms in Equations (1), V_{area}, and V_{vol}, represent surface area and volume constraints given by

$$V_{\text{area}} = \frac{k_a (A - A_0)^2}{2A_0} + \sum_{i=1}^{N_f} \frac{k_d \left(A_i - A_i^0\right)^2}{2A_i^0}, \tag{4}$$

$$V_{\text{vol}} = \frac{k_v (V - V_0)^2}{2V_0},$$

where k_a, k_d, and k_v are local area, total surface area and volume constraint coefficients, respectively. A_i^0, A_0, and V_0 are local area of individual faces, total surface area and total volume of the RBC, respectively. Note that the membrane viscosity is omitted in the employed RBC model for simplicity.

2.2. Modeling Hydrodynamic Flow

Fluid flow is modeled by the smoothed dissipative particle dynamics (SDPD) method which is a Lagrangian discretization of the Navier-Stokes equations [52, 53]. The SDPD fluid consists of N fluid particles which interact through conservative (C), translational dissipative (D), rotational dissipative (R), and random forces ($\sim$). The forces between particles i and j are given by,

$$\mathbf{F}^{\mathrm{C}}_{ij} = \left(\frac{p_i}{\rho_i^2} + \frac{p_j}{\rho_j^2}\right) F_{ij}\mathbf{r}_{ij}, \tag{5}$$

$$\mathbf{F}^{\mathrm{D}}_{ij} = -\gamma_{ij}\left(\mathbf{v}_{ij} + \left(\mathbf{v}_{ij}\cdot\mathbf{e}_{ij}\right)\mathbf{e}_{ij}\right), \tag{6}$$

$$\mathbf{F}^{\mathrm{R}}_{ij} = -\gamma_{ij}\frac{\mathbf{r}_{ij}}{2}\times(\boldsymbol{\omega}_i + \boldsymbol{\omega}_j), \tag{7}$$

$$\tilde{\mathbf{F}}_{ij} = \sigma_{ij}\left(d\overline{\mathcal{W}}^{\mathrm{S}}_{ij} + \frac{1}{3}tr[d\mathcal{W}_{ij}]\mathbb{1}\right)\cdot\frac{\mathbf{e}_{ij}}{dt}, \tag{8}$$

where $\mathbf{r}_i$, $\mathbf{v}_i$, and $\boldsymbol{\omega}_i$ are the particle position, velocity, and angular velocity, and $\mathbf{r}_{ij} = \mathbf{r}_i - \mathbf{r}_j$, $\mathbf{v}_{ij} = \mathbf{v}_i - \mathbf{v}_j$, and $\mathbf{e}_{ij} = \mathbf{r}_{ij}/|\mathbf{r}_{ij}|$. $\rho_i = \sum_{j[i]} m_j W_{ij}$ is the particle density, where the sum runs over the particle i and its neighbors within a smoothing length (or cutoff radius) h, m_i is the particle mass, and $W_{ij} = W(r_{ij})$ is the smoothing kernel represented by the Lucy function [54]

$$W(r) = \frac{105}{16\pi h^3}\left(1 + 3\frac{r}{h}\right)\left(1 - \frac{r}{h}\right)^3. \tag{9}$$

The function F_{ij} is calculated from W_{ij} as $\nabla_i W_{ij} = -\mathbf{r}_{ij}F_{ij}$. The particle pressure p_i is defined as $p_i = p_0(\rho_i/\rho_0)^\alpha - b$, where ρ_0 is the reference density and the parameters p_0, α, and b control fluid compressibility, and can be freely selected [55]. $tr[d\mathcal{W}_{ij}]$ is the trace of matrix of independent Wiener increments $d\mathcal{W}_{ij}$ and $d\overline{\mathcal{W}}^{\mathrm{S}}_{ij}$ is the traceless symmetric part. The dissipative $\gamma_{ij} = 20\eta F_{ij}/(7\rho_i\rho_j)$ and random σ_{ij} force coefficients are related as $\sigma_{ij} = 2\sqrt{k_{\mathrm{B}}T\gamma_{ij}}$ where η is the dynamic viscosity, k_{B} is the Boltzmann constant, and T is temperature. dt is the time step.

The solvent inside the RBC (cytosol) is separated from outside fluid (plasma) by the membrane. The number density of fluid particles is set to $n = 12$ (per unit volume in model units) for both cytosol and plasma, providing a good resolution for fluid flow inside and outside the RBC. The reference density is set to $\rho_0 = mn$ with $m = 1$. Solid walls are modeled by frozen SDPD particles. Fluid-membrane interactions have two contributions: (*i*) fluid particles bounce back from the membrane surface and (*ii*) the dissipative force coefficient between fluid particles and membrane vertices is set such that no-slip boundary conditions are attained. Note that the conservative force for fluid-membrane interactions is turned off. Fluid particles are also reflected back at the solid wall. In addition, an adaptive shear force is added to fluid particles near the wall to ensure no-slip boundary conditions [56].

2.3. Simulation Setup and Parameters

Poiseuille flow with a single RBC suspended in a viscous fluid inside a cylindrical tube of length $L = 50\ \mu$m is simulated. The tube axis is aligned with the flow direction along the x axis. Diameter of the tube $D = 2R$ determines RBC confinement as $\chi = D_r/D$, where $D_r = \sqrt{A_0/\pi}$ is the effective RBC diameter. To generate flow, a force f is applied on every solvent particle, representing a pressure gradient $\Delta P/L = f\cdot n$ with the pressure drop ΔP along the tube length.

In simulations, cell properties correspond to average characteristics of a healthy RBC with a membrane area $A_0 = 133\ \mu\mathrm{m}^2$, cell volume $V_0 = 93\ \mu\mathrm{m}^3$, shear modulus $\mu = 4.8\ \mu$N/m, and bending rigidity $\kappa = 70\ k_{\mathrm{B}}T = 3\times10^{-19}$ J [6, 57–59]. This leads to $D_r = 6.5\ \mu$m ($D_r = 6.5$ in model units) and a RBC reduced volume of $V^* = 6V_0/\left(\pi D_r^3\right) \approx 0.64$. Note that the stress-free shape of a RBC elastic network (Equation 2) is assumed to be an oblate spheroid with a reduced volume of 0.96. The biconcave shape of a RBC with $V^* = 0.64$ is obtained by deflating the stress-free spheroid with a reduced volume of 0.96. Furthermore, the energy unit $k_{\mathrm{B}}T$ is selected to be $k_{\mathrm{B}}T = 0.2$ in simulations, corresponding to a physiological temperature of 37° C.

To characterize different flow conditions, several non-dimensional parameters are employed

(i) Reynolds number $Re = \rho\bar{\dot{\gamma}}D_r^2/\eta$ is the ratio of inertial and viscous forces, where ρ is the mass density, $\bar{\dot{\gamma}} = \bar{v}/D = Dfn/(32\eta)$ is the average (or pseudo) shear rate, and η is the external fluid viscosity. In all simulations, $Re \leq 0.3$.

(ii) $\lambda = \eta_i/\eta_o$ is the viscosity contrast between internal (cytosol) and external (plasma) fluids. The average value of λ under physiological conditions is $\lambda = 5$ [41, 42].

(iii) $\dot{\gamma}^* = \bar{\dot{\gamma}}\cdot\tau$ is the dimensionless shear rate that characterizes flow strength. τ is the RBC relaxation time given by $\tau = \eta D_r/\mu$.

To keep Reynolds number low enough (i.e., $Re \leq 0.3$), in most simulations $\dot{\gamma}^*$ is controlled by varying η instead of changing the flow rate for a fixed viscosity.

2.4. Dynamical Characteristics and Membrane Tension

To analyze dynamical properties of a flowing RBC, the gyration tensor

$$T_{ij} = \frac{1}{N}\sum_{n=1}^{N}\left(r_{n,i} - r_{c,i}\right)\cdot\left(r_{n,j} - r_{c,j}\right) \tag{10}$$

is employed, where i and j denote x, y, or z, $\mathbf{r}_n$ is the position of membrane vertex n, and $\mathbf{r}_c$ is the center of mass of the RBC. Then, the eigenvalues ξ_i of the gyration tensor T_{ij} characterize RBC deformation. The eigenvector that corresponds to the smallest eigenvalue is used to define the orientational axis of the cell. Orientation angle θ_1 of the RBC is defined as the angle between its orientational axis and the flow direction. The eigenvalues are also used to compute cell asphericity $\mathcal{O}$, which characterizes its deviation from a spherical shape

$$\mathcal{O} = \left[(\xi_1 - \xi_2)^2 + (\xi_2 - \xi_3)^2 + (\xi_3 - \xi_1)^2\right]/\left(2R_g^4\right), \tag{11}$$

where $R_g^2 = \xi_1 + \xi_2 + \xi_3$.

To calculate local membrane tension G_i at vertex i, virial stress is used as

$$G_i = -\frac{1}{2a_i}\sum_{j(i)} \mathbf{r}_{i,j} \cdot \mathbf{F}_{i,j}, \tag{12}$$

where a_i is the vertex area computed as one third of a sum of all face areas adjacent to vertex i, $j(i)$ represents all neighboring vertices connected to i by an edge, and $\mathbf{r}_{i,j}$ and $\mathbf{F}_{i,j}$ are position and force vectors at the edge (i, j), respectively. Note that the in-plane elastic energy, bending potential, surface area, and volume constraints can contribute to the membrane tension. The kinetic energy contribution to tension is omitted, as it is very small under a significant membrane stretching in flow.

3. RESULTS

In microcapillary flow, RBCs are known to exhibit different dynamical states, including snaking, tumbling, tank-treading, and parachute [15, 17, 20, 24, 25, 29, 34]. Snaking is characterized by a periodic swinging in RBC orientation around the tube axis [24, 25, 29]. Tumbling is an off-axis rigid-body-like rotation, similar to RBC tumbling in simple shear flow [37, 40, 60]. Tank-treading is represented by membrane rotation with a nearly fixed cell orientation, which also occurs in simple shear flow at low enough λ [37, 40, 61]. The tank-reading state of a RBC in microcapillary flow is also often referred to as slipper. Finally, parachute is a stable stomatocyte-like RBC deformation in the tube center. These dynamical states depend on RBC mechanical properties (e.g., shear modulus, bending rigidity, viscosity contrast), cell confinement, and the flow rate. Here, we primarily focus on how the viscosity contrast affects these dynamical states for a wide range of RBC confinements and flow rates.

3.1. Dynamic State Diagram

Figure 1 presents dynamic state diagram for the viscosity contrast $\lambda = 5$ and different χ and $\dot{\gamma}^*$ values. The representative snapshots of tumbling, tank-treading, and parachute states are also displayed (see **Supplementary Movies 1–3**). The snaking state exhibits minimal deformation and appears at very low shear rates $\dot{\gamma}^* \lesssim 0.01$ for all confinements χ. The tumbling state occurs for small confinements and moderate shear rates. As the shear rate increases, a tumbling RBC transits into a tank-treading state. The critical shear rate, at which the tumbling-to-tank-treading transition takes place, depends on χ and increases with increasing confinement. For large enough confinements and shear rates, the RBC adopts a parachute shape which exhibits least dynamics out of all observed states. Note that the classification of different states becomes difficult close to the transition boundaries, because the RBC may exhibit complex deformations. Therefore, these boundaries are approximate and intended to provide a visual guidance.

To understand the effect of viscosity contrast on dynamical states of the RBC in microcapillary flow, the state diagrams for $\lambda = 1$ and $\lambda = 3$ are shown for comparison in **Figure 2**. As the viscosity contrast is decreased from $\lambda = 5$ to $\lambda = 1$, the parachute region widens toward smaller confinement values. This is a surprising result considering the fact that an increase in viscosity contrast suppresses tank-treading in simple shear flow [39, 40], which will be discussed later. The tumbling-to-tank-treading transition shifts toward larger shear rates as the viscosity contrast is increased from $\lambda = 1$ to $\lambda = 5$. This result is consistent with our expectations that an increase in internal viscosity leads to increased fluid stresses inside the RBC, suppressing membrane tank-treading. A similar observation has also been made in the context of adhered malaria-infected RBCs (iRBCs) under flow, such that an increase in viscosity contrast suppresses iRBC crawling at the surface and results in iRBC flipping or its complete detachment [62]. Note that the snaking state remains nearly unchanged by the viscosity contrast.

3.2. Dynamical Characteristics

To examine differences in dynamical characteristics of RBCs with a change in viscosity contrast, multiple dynamical measures which uniquely characterize each state are computed. **Figure 3** presents time evolution of the orientation angle θ_1 and asphericity $\mathcal{O}$ for two different flow conditions ($\chi = 0.35$ & $\dot{\gamma}^* = 0.076$; $\chi = 0.44$ & $\dot{\gamma}^* = 0.1$) and viscosity contrasts $\lambda = 1$ and $\lambda = 5$. For the case with $\chi = 0.35$ and $\dot{\gamma}^* = 0.076$ in **Figures 3A,B**, the RBC tank-treads for $\lambda = 1$, whereas it tumbles for $\lambda = 5$. In an idealized tank-treading state with only membrane rotation and without cell deformation, both θ_1 and $\mathcal{O}$ should remain constant. However, a moderate periodic deformation and oscillatory orientation swinging is observed in **Figure 3A** for $\lambda = 1$. For the tumbling state in **Figure 3B** with $\lambda = 5$, membrane deformation is significantly reduced, and the orientation angle spans a much wider range, indicating whole-cell flipping. For the case with $\chi = 0.44$ and $\dot{\gamma}^* = 0.1$ in **Figures 3C,D**, $\lambda = 1$ results in a parachute state with nearly constant θ_1 and $\mathcal{O}$, while $\lambda = 5$ leads to a tank-treading state with variations in θ_1 and $\mathcal{O}$ resembling those in **Figure 3A**. Interestingly, the frequency of the variations in θ_1 and $\mathcal{O}$ for $\lambda = 5$ in **Figure 3D** is significantly smaller than that for $\lambda = 1$ in **Figure 3A**, even though the shear rate is larger for $\lambda = 5$. This means that an increased internal viscosity slows down membrane dynamics in microcapillary flow due to an increased dissipation, which is consistent with the results of a study on discocyte (fluid) vesicles for various viscosity contrasts and membrane viscosities [63].

Another difference in **Figures 3A,D** for the tank-treading state is that the amplitude of oscillations in cell orientation angle is larger for $\lambda = 5$ than for $\lambda = 1$. Note that, a RBC at large enough viscosity contrasts ($\lambda \gtrsim 3.5$) in an unbounded shear flow does not exhibit tank-treading, but shows a rotational dynamics [40]. In the microchannel, the tank-treading motion of a RBC for $\lambda = 5$ is facilitated by cell confinement [64]. Therefore, the aforementioned tendency of the RBC at $\lambda = 5$ for rotation likely results in the larger amplitude of oscillations in the orientation angle in comparison to that for $\lambda = 1$.

3.3. Membrane Tension

It is interesting to take a look at the effect of viscosity contrast on local membrane tension, as it might be important for the

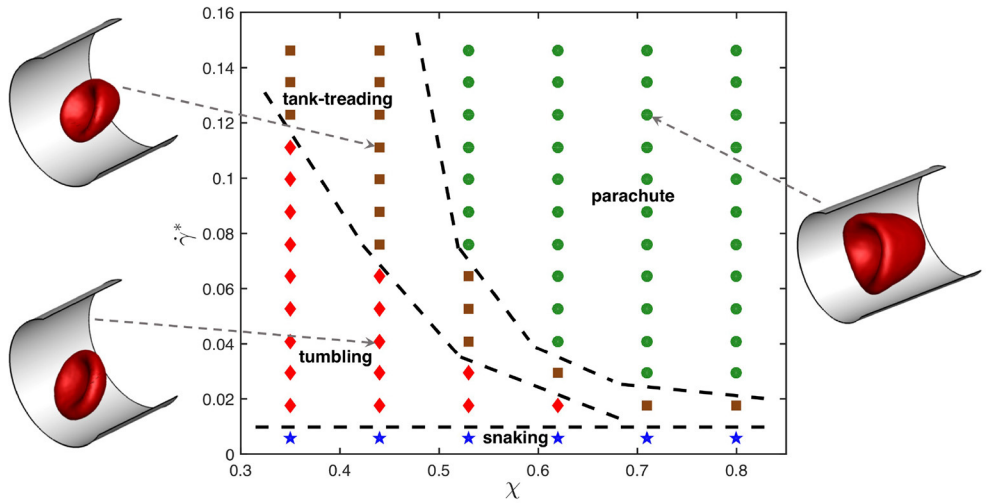

FIGURE 1 | State diagram for $\lambda = 5$ showing different dynamical states of the RBC for various confinement ratios χ and non-dimensional shear rates $\dot{\gamma}^*$. The states include snaking (blue stars), tumbling (red diamonds), tank-treading (brown squares), and parachute (green circles). Dashed lines separating regions with different states are drawn for visual guidance. Representative snapshots for tumbling, tank-treading, and parachute states are also displayed.

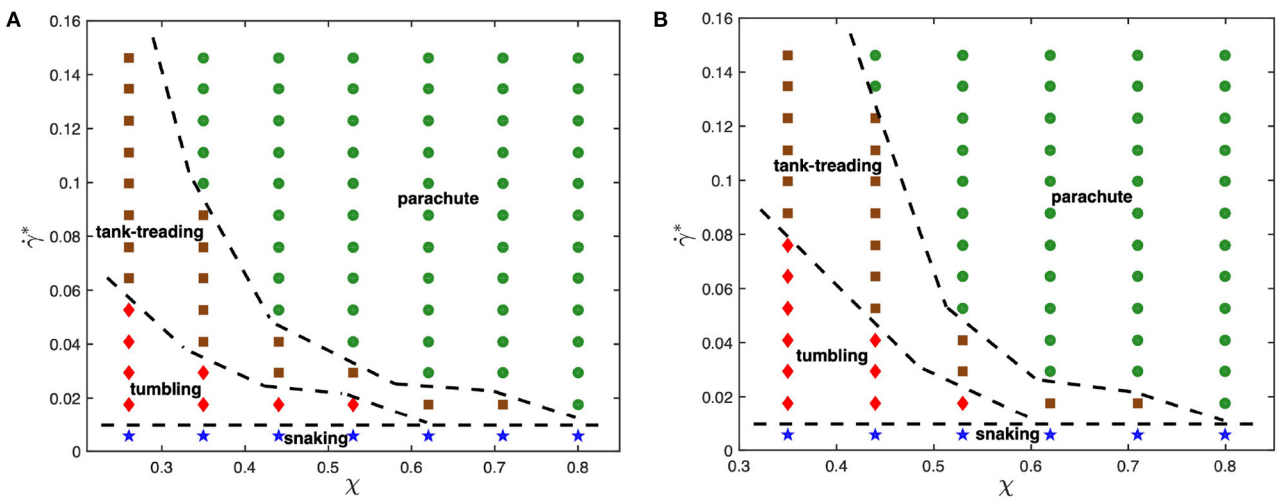

FIGURE 2 | State diagrams for viscosity contrasts **(A)** $\lambda = 1$ and **(B)** $\lambda = 3$ with snaking (blue stars), tumbling (red diamonds), tank-treading (brown squares), and parachute (green circles) states. Dashed lines separating regions with different states are drawn for visual guidance.

activation of mechano-sensitive channels within the membrane [65, 66]. **Figure 4A** shows the distribution of local tension G for a parachute shape normalized by the shear modulus μ. The local tension G is calculated using Equation (12), where all contributions from model potentials in Equation (1) are considered, even though the in-plane elastic-energy term supplies the maximum contribution to G. The concave part of the parachute shape has a significantly lower tension than the convex front of the RBC exposed to strong fluid stresses. The tension distribution for tumbling and tank-treading RBCs has a qualitatively similar trend, in which the frontal part of the cell has larger tension than the back portion. However, for tumbling and tank-treading states, local tension fluctuates in accord with the discussed RBC dynamics, while for the parachute state, temporal tension changes are generally small.

Figure 4B presents tension $\bar{G}$ averaged over the RBC surface as a function of $\dot{\gamma}^*$ for two different viscosity contrasts $\lambda = 1$ and $\lambda = 5$. The average tension increases with the shear rate $\dot{\gamma}^*$ in an almost linear fashion for both viscosity contrasts. Interestingly, $\lambda = 5$ generally leads to a lower tension in comparison with $\lambda = 1$, which is consistent with a previous numerical investigation [67] showing that the maximum tension increases with the flow rate and decreases with increasing viscosity contrast. For $\lambda = 5$, there is a jump in tension at approximately $\dot{\gamma}^* \simeq 0.065$ that corresponds to the tank-treading-to-parachute transition as shown in **Figure 1**. Note that such jump is not present for $\lambda = 1$.

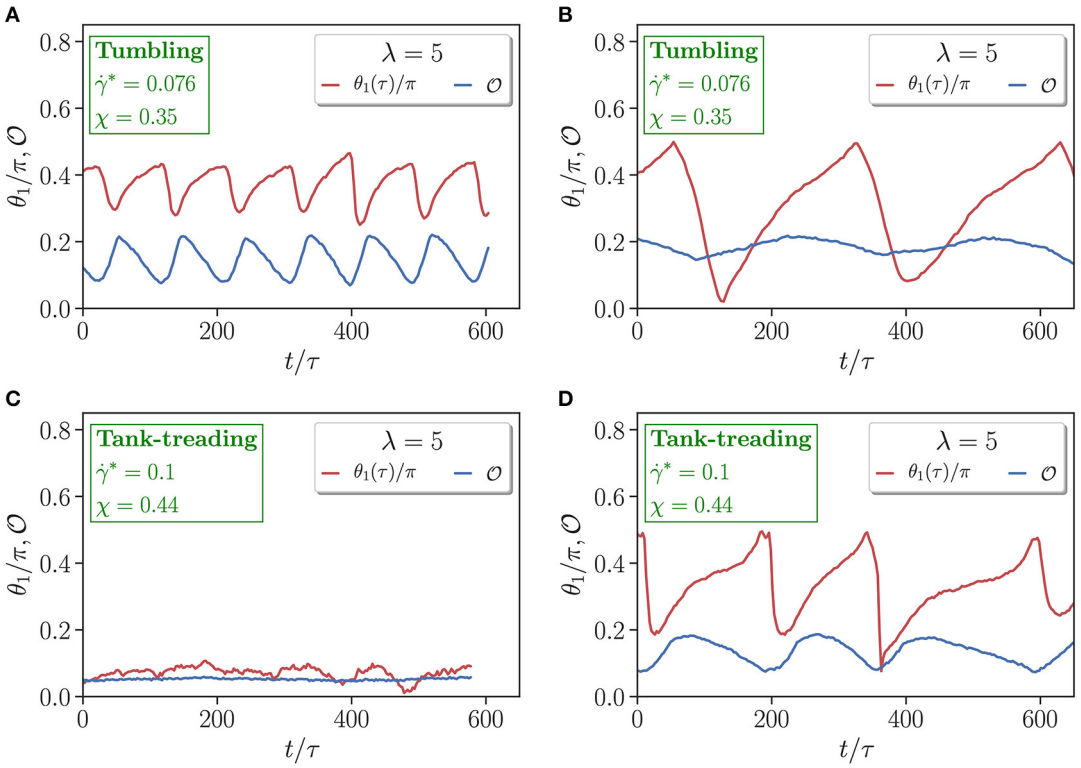

FIGURE 3 | Comparison of time-dependent cell orientation θ_1 and asphericity $\mathcal{O}$ for **(A,C)** $\lambda = 1$ and **(B,D)** $\lambda = 5$. Two flow conditions are selected, including **(A,B)** $\chi = 0.35$ and $\dot{\gamma}^* = 0.076$, and **(C,D)** $\chi = 0.44$ and $\dot{\gamma}^* = 0.1$. Both **(A,D)** represent tank-treading states, whereas **(B)** corresponds to a tumbling state and **(C)** to a parachute state.

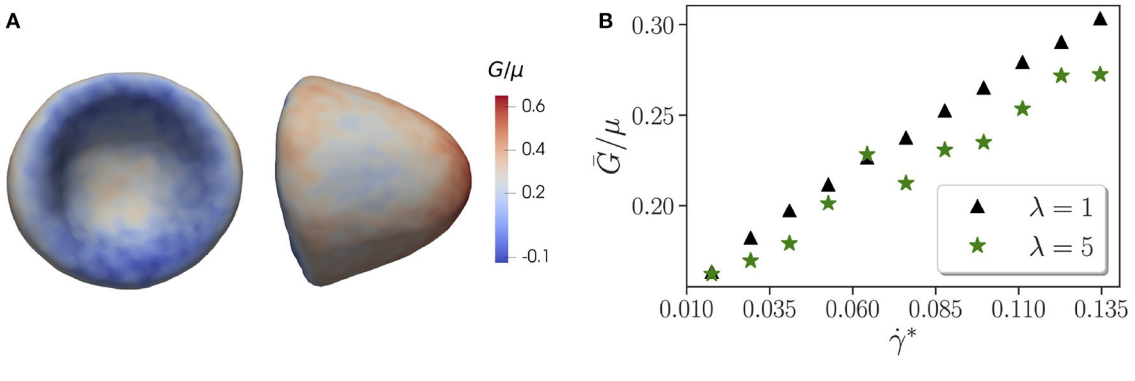

FIGURE 4 | Membrane tension. **(A)** Side and front views of the parachute shape with a local tension G indicated by the color code and normalized by the shear modulus μ. Here, $\lambda = 5$, $\chi = 0.71$, and $\dot{\gamma}^* = 0.076$. **(B)** Average tension $\bar{G}/\mu$ of the whole RBC as a function of non-dimensional shear rate $\dot{\gamma}^*$. Here, the confinement is fixed at $\chi = 0.53$. The data are shown for two different viscosity contrasts $\lambda = 1$ and $\lambda = 5$. A jump in tension for $\lambda = 5$ at $\dot{\gamma}^* \simeq 0.065$ corresponds to the tank-treading-to-parachute transition.

An average tension of about $\bar{G} = 10^{-6}$ N/m (or $\bar{G}/\mu \approx 0.2$) is comparatively large. For example, in a recent study on sculpting of lipid vesicles by enclosed active particles [68], complex vesicle shapes have been observed for floppy vesicles with a tension of about 10^{-8} N/m, while a high membrane tension of about 10^{-5} N/m completely suppresses any vesicle shape changes. Apart from the average tension, it is also instructive to look at the maximum tension $G_{\max} = \max\{G_i\}$ for different χ and $\dot{\gamma}^*$. As expected, $G_{\max}$ increases with increasing shear rate. For $\lambda = 5$, the maximum tension at $\chi = 0.62$ is $G_{\max}/\mu = 0.7$ for $\dot{\gamma}^* = 0.053$ and $G_{\max}/\mu = 0.77$ for $\dot{\gamma}^* = 0.076$ (both are parachute states). For a given shear rate, an increase in confinement results in elevation of $G_{\max}$, e.g., for $\dot{\gamma}^* = 0.053$, $G_{\max}/\mu = 0.64$ for $\chi = 0.35$ (tumbling state) and $G_{\max}/\mu = 0.7$ for $\chi = 0.62$

(parachute state). These trends are similar for $\lambda = 1$. However, differences in G_{max} with respect to the viscosity contrast are rather small, indicating that external fluid stresses mainly govern the membrane tension. The magnitudes of maximal tension from our simulations are consistent with the values reported in [67].

4. DISCUSSION AND CONCLUSIONS

In our study, we have focused on the effect of viscosity contrast λ on RBC dynamic states in microcapillary flow. State diagrams with different dynamic states, such as snaking, tumbling, tank-treading, and parachute, have been constructed for several λ values and wide ranges of non-dimensional shear rates $\dot{\gamma}^*$ and confinements χ. Our central result is that there are significant changes in the state diagram when the viscosity contrast is decreased from $\lambda = 5$ to $\lambda = 1$. In particular, the region of stable parachutes becomes larger and expands toward lower confinements with decreasing λ. This result seems to be in contradiction to the fact that a large viscosity inside the RBC dampens membrane dynamics and hence, should suppress the dynamic tank-treading state [39, 40]. To verify the robustness of our simulation predictions, we have performed simulations with a consecutive change in the viscosity contrast for several conditions where parachutes are stable for $\lambda = 1$ and tank-treading is stable for $\lambda = 5$. Thus, after reaching a stable parachute state for $\lambda = 1$, the viscosity contrast is instantaneously switched to $\lambda = 5$, leading to the tank-treading state. Then, switching back to $\lambda = 1$ brings the initially tank-treading RBC to the parachute state. Furthermore, a larger parachute region for $\lambda = 1$ than that for $\lambda = 5$ has also been observed in 2D simulations of vesicles [24, 25].

To reconcile this seeming contradiction, physical mechanisms that govern the parachute-to-tank-treading transition in tube flow have to be uncovered. A study based on 2D simulations of vesicles in an unbounded parabolic flow [23] suggests that the parachute-to-slipper transition can be described well by a pitchfork bifurcation and that a slipper shape provides a higher flow efficiency for 2D RBC-like vesicles. In particular, there is a lag between the vesicle velocity and the imposed parabolic flow in the parachute state, which is proposed to trigger this instability. This lag increases as the parachute conforms less with the parabolic flow profile for decreasing flow rate or increasing bending rigidity of the vesicle. Unfortunately, this argument has not been connected in any way to the viscosity contrast or internal cell dissipation. From existing experimental and simulation studies [15, 17, 20, 24, 25, 29, 34], it is clear that the parachute state requires large enough flow rates, such that flow stresses in the tube center are sufficient to deform the RBC into a parachute shape. Therefore, only when a RBC conforms well enough to the flow profile, the parachute state is stable. Nevertheless, the change in the parachute-to-slipper transition for different λ cannot be attributed to differences in the parachute shape (or conformity with the flow), as we have not found substantial differences in parachute shapes for different viscosity contrasts. The insensitivity of the parachute shape to λ is likely due to the fact that a non-dynamic parachute state of the RBC depends primarily on its elastic properties, and is nearly independent of internal dissipation.

Our hypothesis is that membrane dynamics is also important for parachute stability at the tube center. As the parachute-to-tank-treading transition is approached, a perturbation (e.g., due to cell diffusion) in RBC position from the tube center leads to the asymmetry in fluid-flow stresses which pull the RBC away from the center and set the membrane into a tank-treading-like motion. A slight motion of the membrane in the parachute state is observed in our simulations, as the RBC is never perfectly symmetric and is often located slightly away from the tube center. For $\lambda = 1$, the membrane can rotate faster than in case of $\lambda = 5$, and therefore, the mismatch between local membrane motion and fluid flow is smaller, resulting in reduced local fluid stresses that pull the RBC away from the center. For $\lambda = 5$, the local fluid stresses on the RBC are larger due to slow membrane tank-treading, leading to the destabilization of parachute shape at larger confinements in comparison to $\lambda = 1$.

Another important difference in the state diagrams for $\lambda = 1$ and $\lambda = 5$ is that the tumbling-to-tank-treading transition occurs at larger shear rates for $\lambda = 5$ than for $\lambda = 1$. This can be explained by the fact that an increased dissipation inside the RBC for $\lambda = 5$ suppresses tank-treading motion and delays the transition in terms of $\dot{\gamma}^*$. In fact, in simple shear flow, the tank-treading state does not exist for $\lambda = 5$ [39, 40]. For microcapillary flow, RBC tank-treading becomes possible at $\lambda = 5$ due to the confinement which can trigger the tumbling-to-tank-treading transition even when cell dimensions are smaller than the distance between two walls [64]. For a large enough vessel diameter, it is plausible to expect that the tank-treading state should disappear for $\lambda = 5$, as local flow conditions should closely resemble simple shear flow at the scale of RBC size. For instance, recent microfluidic experiments in a square channel [34] have reported the existence of rotating trilobe shapes at low confinements and high flow rates, which are consistent with RBC shapes in simple shear flow at $\lambda = 5$ [39, 40].

Membrane tension must be directly related to mechano-transduction as the RBC membrane contains many mechano-sensitive channels [65, 66]. We have shown that an increase in the viscosity contrast lowers the membrane tension. A high viscosity of the cytosol provides a large dissipation, reducing membrane tension. Furthermore, the maximum tension increases with increasing shear rate $\dot{\gamma}^*$ and confinement χ. Several experimental studies show that flow stresses can change RBC biochemical properties. For instance, when RBCs pass through small constrictions, they release ATP which can participate in vasodilation signaling [69, 70]. Furthermore, a recent investigation [71] reports that when RBCs pass through small constrictions, the mechano-sensitive channels (e.g., Piezo1 and Gardos channels) that participate in RBC volume control become activated. The relevance of membrane tension has also been demonstrated for malaria disease, such that an increased RBC membrane tension in the Dantu blood group significantly reduces the invasion of RBCs by malaria parasites, which is a protective mechanism from malaria infection [72].

DATA AVAILABILITY STATEMENT

The raw data supporting the conclusions of this article will be made available by the authors, without undue reservation.

AUTHOR CONTRIBUTIONS

AD and JM performed simulations and analyzed the data. GG and DF designed the research. DF supervised the project. All authors discussed the results and wrote the manuscript.

SUPPLEMENTARY MATERIAL

The Supplementary Material for this article can be found online at: https://www.frontiersin.org/articles/10.3389/fphy.2021.666913/full#supplementary-material

REFERENCES

1. Popel AS, Johnson PC. Microcirculation and hemorheology. *Annu Rev Fluid Mech.* (2005) 37:43–69. doi: 10.1146/annurev.fluid.37.042604.133933
2. Lipowsky HH. Microvascular rheology and hemodynamics. *Microcirculation.* (2005) 12:5–15. doi: 10.1080/10739680590894966
3. Pries AR, Secomb TW. Blood flow in microvascular networks. In: Tuma RF, Duran WN, Ley K, editors, *Handbook of Physiology, The Cardiovascular System, Microcirculation*. San Diego, CA: Academic Press (2008). p. 3–36.
4. Secomb TW. Blood flow in the microcirculation. *Annu Rev Fluid Mech.* (2017) 49:443–61. doi: 10.1146/annurev-fluid-010816-060302
5. Gompper G, Fedosov DA. Modeling microcirculatory blood flow: current state and future perspectives. *WIREs Syst Biol Med.* (2016) 8:157–68. doi: 10.1002/wsbm.1326
6. Evans EA, Skalak R. *Mechanics and Thermodynamics of Biomembranes.* Boca Raton, FL: CRC Press, Inc. (1980).
7. Discher DE, Mohandas N, Evans EA. Molecular maps of red cell deformation: hidden elasticity and *in situ* connectivity. *Science.* (1994) 266:1032–5. doi: 10.1126/science.7973655
8. Diez-Silva M, Dao M, Han J, Lim CT, Suresh S. Shape and biomechanical characteristics of human red blood cells in health and disease. *MRS Bull.* (2010) 35:382–8. doi: 10.1557/mrs2010.571
9. Tomaiuolo G. Biomechanical properties of red blood cells in health and disease towards microfluidics. *Biomicrofluidics.* (2014) 8:051501. doi: 10.1063/1.4895755
10. Kaul DK, Fabry ME, Windisch P, Baez S, Nagel RL. Erythrocytes in sickle cell anemia are heterogeneous in their rheological and hemodynamic characteristics. *J Clin Invest.* (1983) 72:22–31.
11. Cranston HA, Boylan CW, Carroll GL, Sutera SP, Williamson JR, Gluzman IY, et al. Plasmodium falciparum maturation abolishes physiologic red cell deformability. *Science.* (1984) 223:400–3. doi: 10.1126/science.6362007
12. Fedosov DA, Caswell B, Suresh S, Karniadakis GE. Quantifying the biophysical characteristics of Plasmodium-falciparum-parasitized red blood cells in microcirculation. *Proc Natl Acad Sci USA.* (2011) 108:35–9. doi: 10.1073/pnas.1009492108
13. Skalak R, Branemark PI. Deformation of red blood cells in capillaries. *Science.* (1969) 164:717–9. doi: 10.1126/science.164.3880.717
14. Gaehtgens P, Dührssen C, Albrecht KH. Motion, deformation, and interaction of blood cells and plasma during flow through narrow capillary tubes. *Blood Cells.* (1980) 6:799–812.
15. Bagge U, Branemark PI, Karlsson R, Skalak R. Three-dimensional observations of red blood cell deformation in capillaries. *Blood Cells.* (1980) 6:231–7.
16. Tomaiuolo G, Preziosi V, Simeone M, Guido S, Ciancia R, Martinelli V, et al. A methodology to study the deformability of red blood cells flowing in microcapillaries *in vitro*. *Ann Ist Super Sanita.* (2007) 43:186–92.
17. Tomaiuolo G, Simeone M, Martinelli V, Rotoli B, Guido S. Red blood cell deformation in microconfined flow. *Soft Matter.* (2009) 5:3736–40. doi: 10.1039/b904584h
18. Guido S, Tomaiuolo G. Microconfined flow behavior of red blood cells *in vitro*. *C R Phys.* (2009) 10:751–63. doi: 10.1016/j.crhy.2009.10.002
19. Abkarian M, Faivre M, Stone HA. High-speed microfluidic differential manometer for cellular-scale hydrodynamics. *Proc Natl Acad Sci USA.* (2006) 103:538–42. doi: 10.1073/pnas.0507171102
20. Abkarian M, Faivre M, Horton R, Smistrup K, Best-Popescu CA, Stone HA. Cellular-scale hydrodynamics. *Biomed Mater.* (2008) 3:034011. doi: 10.1088/1748-6041/3/3/034011
21. Secomb TW, Skalak R, Özkaya N, Gross JF. Flow of axisymmetric red blood cells in narrow capillaries. *J Fluid Mech.* (1986) 163:405–23. doi: 10.1017/S0022112086002355
22. Secomb TW, Styp-Rekowska B, Pries AR. Two-dimensional simulation of red blood cell deformation and lateral migration in microvessels. *Ann Biomed Eng.* (2007) 35:755–65. doi: 10.1007/s10439-007-9275-0
23. Kaoui B, Biros G, Misbah C. Why do red blood cells have asymmetric shapes even in a symmetric flow? *Phys Rev Lett.* (2009) 103:188101. doi: 10.1103/PhysRevLett.103.188101
24. Kaoui B, Tahiri N, Biben T, Ez-Zahraouy H, Benyoussef A, Biros G, et al. Complexity of vesicle microcirculation. *Phys Rev E.* (2011) 84:041906. doi: 10.1103/PhysRevE.84.041906
25. Tahiri N, Biben T, Ez-Zahraouy H, Benyoussef A, Misbah C. On the problem of slipper shapes of red blood cells in the microvasculature. *Microvasc Res.* (2013) 85:40–5. doi: 10.1016/j.mvr.2012.10.001
26. Aouane O, Thiébaud M, Benyoussef A, Wagner C, Misbah C. Vesicle dynamics in a confined Poiseuille flow: from steady state to chaos. *Phys Rev E.* (2014) 90:033011. doi: 10.1103/PhysRevE.90.033011
27. Lázaro GR, Hernández-Machado A, Pagonabarraga I. Rheology of red blood cells under flow in highly confined microchannels: I. Effect of elasticity. *Soft Matter.* (2014) 10:7195–206. doi: 10.1039/C4SM00894D
28. Noguchi H, Gompper G. Shape transitions of fluid vesicles and red blood cells in capillary flows. *Proc Natl Acad Sci USA.* (2005) 102:14159–64. doi: 10.1073/pnas.0504243102
29. Fedosov DA, Peltomäki M, Gompper G. Deformation and dynamics of red blood cells in flow through cylindrical microchannels. *Soft Matter.* (2014) 10:4258–67. doi: 10.1039/C4SM00248B
30. Ye T, Phan-Thien N, Khoo BC, Lim CT. Dissipative particle dynamics simulations of deformation and aggregation of healthy and diseased red blood cells in a tube flow. *Phys Fluids.* (2014) 26:111902. doi: 10.1063/1.4900952
31. Fedosov DA, Noguchi H, Gompper G. Multiscale modeling of blood flow: from single cells to blood rheology. *Biomech Model Mechanobiol.* (2014) 13:239–58. doi: 10.1007/s10237-013-0497-9
32. Ye T, Shi H, Peng L, Li Y. Numerical studies of a red blood cell in rectangular microchannels. *J Appl Phys.* (2017) 122:084701. doi: 10.1063/1.5000357
33. Guckenberger A, Kihm A, John T, Wagner C, Gekle S. Numerical-experimental observation of shape bistability of red blood cells flowing in a microchannel. *Soft Matter.* (2018) 14:2032–43. doi: 10.1039/C7SM02272G
34. Reichel F, Mauer J, Nawaz AA, Gompper G, Guck J, Fedosov DA. High-throughput microfluidic characterization of erythrocyte shapes and mechanical variability. *Biophys J.* (2019) 117:14–24. doi: 10.1016/j.bpj.2019.05.022
35. Fischer TM. Shape memory of human red blood cells. *Biophys J.* (2004) 86:3304–13. doi: 10.1016/S0006-3495(04)74378-7
36. Skotheim JM, Secomb TW. Red blood cells and other nonspherical capsules in shear flow: oscillatory dynamics and the tank-treading-to-tumbling transition. *Phys Rev Lett.* (2007) 98:078301. doi: 10.1103/PhysRevLett.98.078301
37. Abkarian M, Faivre M, Viallat A. Swinging of red blood cells under shear flow. *Phys Rev Lett.* (2007) 98:188302. doi: 10.1103/PhysRevLett.98.188302

38. Dupire J, Socol M, Viallat A. Full dynamics of a red blood cell in shear flow. *Proc Natl Acad Sci USA*. (2012) 109:20808–13. doi: 10.1073/pnas.1210236109
39. Lanotte L, Mauer J, Mendez S, Fedosov DA, Fromental JM, Claveria V, et al. Red cells' dynamic morphologies govern blood shear thinning under microcirculatory flow conditions. *Proc Natl Acad Sci USA*. (2016) 113:13289–94. doi: 10.1073/pnas.1608074113
40. Mauer J, Mendez S, Lanotte L, Nicoud F, Abkarian M, Gompper G, et al. Flow-induced transitions of red blood cell shapes under shear. *Phys Rev Lett*. (2018) 121:118103. doi: 10.1103/PhysRevLett.121.118103
41. Cokelet GR, Meiselman HJ. Rheological comparison of hemoglobin solutions and erythrocyte suspensions. *Science*. (1968) 162:275–77. doi: 10.1126/science.162.3850.275
42. Wells R, Schmid-Schönbein H. Red cell deformation and fluidity of concentrated cell suspensions. *J Appl Physiol*. (1969) 27:213–7. doi: 10.1152/jappl.1969.27.2.213
43. Yazdani AZK, Bagchi P. Phase diagram and breathing dynamics of a single red blood cell and a biconcave capsule in dilute shear flow. *Phys Rev E*. (2011) 84:026314. doi: 10.1103/PhysRevE.84.026314
44. Sinha K, Graham MD. Dynamics of a single red blood cell in simple shear flow. *Phys Rev E*. (2015) 92:042710. doi: 10.1103/PhysRevE.92.042710
45. Cordasco D, Yazdani A, Bagchi P. Comparison of erythrocyte dynamics in shear flow under different stress-free configurations. *Phys Fluids*. (2014) 26:041902. doi: 10.1063/1.4871300
46. Gompper G, Kroll DM. Triangulated-surface models of fluctuating membranes. In: Nelson DR, Piran T, Weinberg S, editors. *Statistical Mechanics of Membranes and Surfaces,* 2nd Edn. Singapore: World Scientific (2004). p. 359–426.
47. Fedosov DA, Caswell B, Karniadakis GE. A multiscale red blood cell model with accurate mechanics, rheology, and dynamics. *Biophys J*. (2010) 98:2215–25. doi: 10.1016/j.bpj.2010.02.002
48. Fedosov DA, Caswell B, Karniadakis GE. Systematic coarse-graining of spectrin-level red blood cell models. *Comput Meth Appl Mech Eng*. (2010) 199:1937–48. doi: 10.1016/j.cma.2010.02.001
49. Helfrich W. Elastic properties of lipid bilayers: theory and possible experiments. *Z Naturforschung C*. (1973) 28:693–703. doi: 10.1515/znc-1973-11-1209
50. Gompper G, Kroll DM. Random surface discretizations and the renormalization of the bending rigidity. *J Phys I France*. (1996) 6:1305–20. doi: 10.1051/jp1:1996246
51. Guckenberger A, Gekle S. Theory and algorithms to compute Helfrich bending forces: a review. *J Phys*. (2017) 29:203001. doi: 10.1088/1361-648X/aa6313
52. Español P, Revenga M. Smoothed dissipative particle dynamics. *Phys Rev E*. (2003) 67:026705. doi: 10.1103/PhysRevE.67.026705
53. Müller K, Fedosov DA, Gompper G. Smoothed dissipative particle dynamics with angular momentum conservation. *J Comp Phys*. (2015) 281:301–15. doi: 10.1016/j.jcp.2014.10.017
54. Lucy LB. A numerical approach to the testing the fission hypothesis. *Astronom J*. (1977) 82:1013–24. doi: 10.1086/112164
55. Alizadehrad D, Fedosov DA. Static and dynamic properties of smoothed dissipative particle dynamics. *J Comp Phys*. (2018) 356:303–18. doi: 10.1016/j.jcp.2017.12.009
56. Fedosov DA, Karniadakis GE. Triple-decker: interfacing atomistic-mesoscopic-continuum flow regimes. *J Comp Phys*. (2009) 228:1157–71. doi: 10.1016/j.jcp.2008.10.024
57. Evans EA. Bending elastic modulus of red blood cell membrane derived from buckling instability in micropipet aspiration tests. *Biophys J*. (1983) 43:27–30. doi: 10.1016/S0006-3495(83)84319-7
58. Dao M, Lim CT, Suresh S. Mechanics of the human red blood cell deformed by optical tweezers. *J Mech Phys Solids*. (2003) 51:2259–80. doi: 10.1016/j.jmps.2003.09.019
59. Yoon YZ, Kotar J, Yoon G, Cicuta P. The nonlinear mechanical response of the red blood cell. *Phys Biol*. (2008) 5:036007. doi: 10.1088/1478-3975/5/3/036007
60. Goldsmith HL, Marlow J. Flow behaviour of erythrocytes. I. Rotation and deformation in dilute suspensions. *Proc R Soc Lond B*. (1972) 182:351–84. doi: 10.1098/rspb.1972.0084
61. Fischer TM, Stöhr-Liesen M, Schmid-Schönbein H. The red cell as a fluid droplet: tank tread-like motion of the human erythrocyte membrane in shear flow. *Science*. (1978) 202:894–6. doi: 10.1126/science.715448
62. Dasanna AK, Fedosov DA, Gompper G, Schwarz US. State diagram for wall adhesion of red blood cells in shear flow: from crawling to flipping. *Soft Matter*. (2019) 15:5511–20. doi: 10.1039/C9SM00677J
63. Noguchi H, Gompper G. Dynamics of fluid vesicles in shear flow: effect of the membrane viscosity and thermal fluctuations. *Phys Rev E*. (2005) 72:011901. doi: 10.1103/PhysRevE.72.011901
64. Kaoui B, Krüger T, Harting J. How does confinement affect the dynamics of viscous vesicles and red blood cells? *Soft Matter*. (2012) 8:9246–52. doi: 10.1039/c2sm26289d
65. Coste B, Mathur J, Schmidt M, Earley TJ, Ranade S, Petrus MJ, et al. Piezo1 and Piezo2 are essential components of distinct mechanically activated cation channels. *Science*. (2010) 330:55–60. doi: 10.1126/science.1193270
66. Zarychanski R, Schulz VP, Houston BL, Maksimova Y, Houston DS, Smith B, et al. Mutations in the mechanotransduction protein PIEZO1 are associated with hereditary xerocytosis. *Blood*. (2012) 120:1908–15. doi: 10.1182/blood-2012-04-422253
67. Omori T, Ishikawa T, Barthés-Biesel D, Salsac AV, Imai Y, Yamaguchi T. Tension of red blood cell membrane in simple shear flow. *Phys Rev E*. (2012) 86:056321. doi: 10.1103/PhysRevE.86.056321
68. Vutukuri HR, Hoore M, Abaurrea-Velasco C, van Buren L, Dutto A, Auth T, et al. Active particles induce large shape deformations in giant lipid vesicles. *Nature*. (2020) 586:52–6. doi: 10.1038/s41586-020-2730-x
69. Wan J, Ristenpart WD, Stone HA. Dynamics of shear-induced ATP release from red blood cells. *Proc Natl Acad Sci USA*. (2008) 105:16432–7. doi: 10.1073/pnas.0805779105
70. Forsyth AM, Wan J, Owrutsky PD, Abkarian M, Stone HA. Multiscale approach to link red blood cell dynamics, shear viscosity, and ATP release. *Proc Natl Acad Sci USA*. (2011) 108:10986–91. doi: 10.1073/pnas.1101315108
71. Danielczok JG, Terriac E, Hertz L, Petkova-Kirova P, Lautenschläger F, Laschke MW, et al. Red blood cell passage of small capillaries is associated with transient Ca^{2+}-mediated adaptations. *Front Physiol*. (2017) 8:979.
72. Kariuki SN, Marin-Menendez A, Introini V, Ravenhill BJ, Lin YC, Macharia A, et al. Red blood cell tension protects against severe malaria in the Dantu blood group. *Nature*. (2020) 585:579–83. doi: 10.1038/s41586-020-2726-6

Conflict of Interest: The authors declare that the research was conducted in the absence of any commercial or financial relationships that could be construed as a potential conflict of interest.

frontiers in Physics

ORIGINAL RESEARCH
published: 13 May 2021
doi: 10.3389/fphy.2021.674958

Effect of F-Actin Organization in Lamellipodium on Viscoelasticity and Migration of Huh-7 Cells Under pH Microenvironments Using AM-FM Atomic Force Microscopy

Miao Chen[1,2,3], *Wenpeng Zhu*[1,2,3]*, *Zhihua Liang*[1,2,3], *Songyou Yao*[1,2,3], *Xiaoyue Zhang*[1,2,3]* *and Yue Zheng*[1,2,3]

[1]School of Physics, Sun Yat-sen University, Guangzhou, China, [2]State Key Laboratory of Optoelectronic Materials and Technologies, Sun Yat-sen University, Guangzhou, China, [3]Centre for Physical Mechanics and Biophysics, School of Physics, Sun Yat-sen University, Guangzhou, China

OPEN ACCESS

Edited by:
Ying Li,
University of Connecticut, United States

Reviewed by:
Zhao Qin,
Syracuse University, United States
Lei Tao,
University of Connecticut, United States

***Correspondence:**
Wenpeng Zhu
zhuwp3@mail.sysu.edu.cn
Xiaoyue Zhang
zhangxy26@mail.sysu.edu.cn

Specialty section:
This article was submitted to Biophysics, a section of the journal Frontiers in Physics

Received: *02 March 2021*
Accepted: *29 April 2021*
Published: *13 May 2021*

Citation:
Chen M, Zhu W, Liang Z, Yao S, Zhang X and Zheng Y (2021) Effect of F-Actin Organization in Lamellipodium on Viscoelasticity and Migration of Huh-7 Cells Under pH Microenvironments Using AM-FM Atomic Force Microscopy. Front. Phys. 9:674958. doi: 10.3389/fphy.2021.674958

Cytoskeleton is responsible for fundamental cellular processes and functions. The filamentous actin (F-actin) is a key constituent of the cytoskeleton system which is intrinsically viscoelastic and greatly determines the mechanical properties of cells. The organization and polymerization of F-actin are relevant to the viscoelasticity distribution and the migration of living cells responding to pH microenvironments. Recently, progression in various diseases such as cancers have been found that cellular migration is related to the alterations in the viscoelasticity of lamellipodium. However, the correlation among F-actin organization, viscoelastic properties and cellular migration of living cancer cells under different pH microenvironments are still poorly understood. Conventional experimental methods of optical microscopy and atomic force microscopy (AFM) can neither break the trade-off between resolution and rate in cytoskeleton imaging, nor achieve the structural characterization and the mechanical measurement simultaneously. Although multifrequency AFM with amplitude modulation-frequency modulation (AM–FM) enables us to probe both the surface topography and the viscoelasticity distribution of cells, it is difficult to image the cytoskeletal filaments with the diameter down to the scale of tens of nanometers. Here, we have improved the AM-FM AFM by employing the high damping of cell culture medium to increase the signal-to-noise ratio and achieve a stable imaging of F-actin with the resolution down to 50 nm under *in situ* microenvironment. The approach that can successfully visualize the structures of cytoskeletal filaments and measure the distribution of mechanical properties simultaneously enable us to understand the relationship between the organization of F-actin and the viscoelasticity of living Huh-7 cancer cells under different pH values. Our experimental results have demonstrated that, unlike the randomly distributed F-actin and the homogeneous viscoelasticity at the normal pH level of 7.4, the living Huh-7 cancer cells with the reduced pH level of 6.5 show highly oriented and organized F-actin along the lamellipodium direction associated with the significant gradient increase both in elasticity and viscosity, which are confirmed by immunofluorescence confocal microscopy. The F-actin organization and the gradient

viscoelasticity of lamellipodium provide structural and mechanical understanding on the adhesion and migration of living cancer cells that undergo metastasis and malignant transformation.

Keywords: amplitude modulation-frequency modulation atomic force microscopy, living cancer cells, viscoelasticity gradient, F-actin cytoskeleton, lamellipodium, pH microenvironments, migration

INTRODUCTION

Living cells, as the smallest unit in biological systems, plays a pivotal role in human life and disease processes [1]. Changes in the viscoelastic properties of cells are relevant to the fundamental cellular physiological behaviors and functions, such as cell migration [2], adhesion [3], differentiation [4] and absorption [5]. Cytoskeleton that is an essential structural component of cells, is intrinsically viscoelastic and responsible for the cell viscoelasticity [6], controlling the cellular development and maintenance [7]. In the cytoskeleton system, the filamentous actin (F-actin) (**Figure 1**) is one of the most major constituent building up many higher order structures in cells (e.g., stress fibers, lamellipodia, and filopodia) [8]. The arrangement and distribution of F-actin greatly dominates the mechanical properties of cells including viscoelasticity [9–13]. For example, the actin cortex is a thin layer that lies beneath the plasma membrane, maintaining and regulating cell topography [10]. Oberleithner et al. found that the depolymerization of cortical actin induced by altering the local microenvironment reduces the elasticity of cells, thus modulating the deformation of the plasma membrane [11]. The stress fibers are arranged in parallel by F-actin, connecting the cytoskeleton to the extracellular matrix via focal adhesions [12]. Wang et al. reported that viscosity of F-actin can significantly increase stability of the cell adhesion [13]. The cellular protrusions including lamellipodium and filopodium located at the edge of cells is involved with the cell migration [14, 15]. Lamellipodia are sheet-like structures, from which filopodia usually grow out [16]. Lamellipodial branched actin network not only generates a pushing force by actin polymerization but also provides crucial mechanical support for cell migration through the extracellular matrix or adjacent cells [17, 18]. Laurent et al. revealed that cells migrates toward the more rigidity side of the lamellipodia [19]. Moreover, lamellipodia-based cell migration plays a crucial role in cancer metastasis [20]. The malignant degree of cancer cells is related to their migration speed, that is, the metastasis and invasiveness of cancer cells [21]. In particular, in the complex microenvironment of tumor tissues [22, 23], the cancer cells will change the structure and topography of lamellipodia at an acid pH level, and then accelerate their metastasis [24, 25]. However, the organization of the F-actin in lamellipodia under different pH microenvironments associated with the underlying relationship with the viscoelasticity and migration of living cancer cells remain unclear and is in urgent need to be fully interpreted. The nanomechanical mechanism revealing the effects of F-actin in lamellipodia on the cell viscoelasticity and migration represents a meaningful approach to understand the physical nature in the malignant metastasis of cancer cell response to the change of pH microenvironments.

To understand the correlation among F-actin organization, viscoelastic properties and cellular migration of living cancer cells under different pH microenvironments, it is the key issue to simultaneously obtain the high-resolution *in situ* images of the cytoskeleton topography and viscoelastic properties of cells. For the soft matter of cells that are heterogeneous with intrinsically

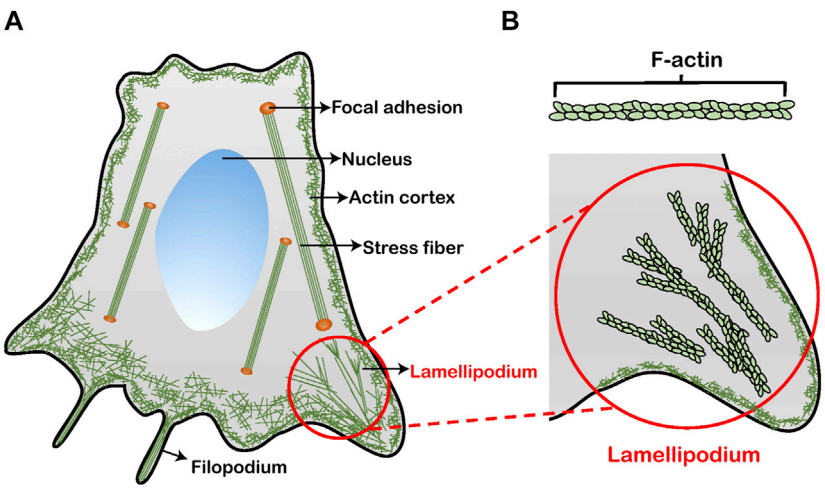

FIGURE 1 | Schematics of a cell with F-actin architectures. **(A)** Four primary types of F-actin structures in the cytoskeleton: actin cortex, stress fiber, filopodium, and lamellipodium. **(B)** A magnified view of the lamellipodium. The formation of lamellipodium is facilitated by the organization of F-actin.

viscoelastic cytoskeletons and undergo large deformation [26, 27], the structural organization and mechanical properties are highly coupled [28]. A wide variety of experimental work has been performed in order to assess the relationship between cell mechanics and microstructures [29, 30], focusing on the changes in either cytoskeletal structure [29] or elasticity [30]. However, these experiments have been limited by the characterization methods of cells and cytoskeletons. Although the fluorescence imaging techniques have the advantage in the fast *in situ* identification of subcellular structures, it is difficult for the optical resolution to be smaller than the diffraction limit around hundreds of nanometers and capture the details of cytoskeletal structures [31]. The transmission electron microscopy is usually adopted to observe the cells and cytoskeletons [32]. Nevertheless, the sample preparation process is complicated with fixation, dehydration, infiltration and staining, which will cause the loss of cell activity [33]. Furthermore, the imaging of transmission electron microscopy is slow and commonly conducted under vacuum condition, which make it unable for the fast *in situ* identification of cells and cytoskeletons under different microenvironments. For studying cellular mechanics, a number of experimental methodologies have been developed, including micropipette aspiration [34], traction force microscope [35], optical tweezers [36], and magnetic twisting cytometry [37]. Atomic force microscopy (AFM) is one of the most major and reliable methods for probing the mechanical properties of cells [38, 39]. Conventional AFM imaging based on contact mode force curve measurement has been introduced to measure the cellular viscoelasticity [40, 41]. And yet the poor resolution and long acquisition time prevent it from fast high-resolution characterization of subcellular microstructures and mechanical properties. It is a key challenge to not only break the trade-off between resolution and rate in cytoskeleton imaging, but also achieve the structural characterization and the mechanical measurement simultaneously.

In this work, we use amplitude modulation–frequency modulation (AM–FM) AFM to characterize the topography and viscoelasticity of living Huh-7 cancer cells at the same time. We have improved the AM-FM AFM by using the high damping of cell culture medium, instead of original damping materials that cannot be used in liquid, to dissipate unnecessary vibration that deviates from the standard resonance of the AFM cantilever. The efficient stabilization of the cantilever oscillation enables us to increase the signal-to-noise ratio, achieving a fast imaging and mapping simultaneously of F-actin structures, cellular topography and viscoelasticity with the ultrahigh resolution down to 50 nm under *in situ* pH microenvironment. Moreover, the capability of AM–FM AFM to capture the F-actin microstructures are validated by immunofluorescence confocal microscopy. By using AM–FM AFM, we study the effect of pH level on the organization of F-actin in lamellipodium and the change in the topography and viscoelasticity of living Huh-7 cancer cells. The experimental results demonstrate that the F-actin in lamellipodium under normal culture medium (pH 7.4) is short, thin and dispersed, associated with the homogeneous distribution of cell viscoelasticity. On the contrary, in acid culture medium (pH 6.5), the F-actin cytoskeletons polymerize and are woven into a long and thick bundle-like structure directed to the protruding direction of lamellipodium. Both the elasticity and viscosity show a significant gradient increase along the protruding direction, which can facilitate the adhesion and migration of living cancer cells. These results have significant implications for understanding the significance of F-actin structures and viscoelasticity in changing cell topography and behaviors, and opening a new paradigm of nanomechanical mechanisms for the metastasis of cancer cells under pH microenvironments.

MATERIALS AND METHODS

Cells Culture and Treatment

The cells used in this study are the human hepatoma cell lines Huh-7 cells, obtained from the Type Culture Collection of the Chinese Academy of Sciences, Shanghai, China. The cells were cultured in Dulbecco's Modified Eagle Medium (Gibco, Life Technologies, China) supplemented with 10% fetal bovine serum (Gibco, Life Technologies, Australia) and 1% penicillin-streptomycin (Gibco, Life Technologies, United States), at 37°C and 5% CO_2 in humid conditions. The pH level of normal culture medium is set as 7.4. One day prior to the AFM experiments, the cells were seeded onto 25 mm × 25 mm glass slides. After the cells had enough time to adhere to the substrate, the existing medium was replaced with the fresh medium to remove dead and loosely attached cells every 2 h. The fresh medium was prepared in the normal or acid condition to mimic microenvironments at different pH levels. HCl (0.5 mol/L) was added precisely to the normal culture medium for the acid culture medium (pH 6.5) by using a pH meter measurement to verify the targeted pH value of 6.5. Phosphate buffer saline (PBS) solution was used to rinse the substrate every time before adding and changing the culture medium. The cells were cultured with either pH microenvironment for at least 6 h in CO_2 incubator for subsequent characterization and measurement in AFM experiments. To maintain the pH level in the cell cultivation, the new acid culture medium of pH 6.5 was replaced every 2 h. By pH monitoring, we found that the acid culture medium of pH 6.5 in the CO_2 incubator can be kept well within 2 h. The time of AM-FM AFM measurement was limited to a maximum of 2 h. During the AM-FM AFM measurement, the pH monitoring was employed constantly and the acid culture medium of pH 6.5 was added when needed.

Atomic Force Microscopy

AFM experiments were performed with an Asylum Research MFP-3D Infinity AFM system. The AM-FM bimodal imaging mode was performed by using BL-AC40TS cantilever (Olympus, Japan) with 0.11 nN/nm nominal force constant (k_1). The spring constant for the first eigenmode k_1 of the cantilever was obtained by force constant calibration. In AM-FM method that employs the tapping mode, the cantilever is excited near the first and second resonant frequencies simultaneously. To ensure the physiological conditions of cells, the cantilever was completely

immersed in the liquid of culture medium during the experiments. The cantilever tuning was conducted in liquid by which the first cantilever eigenmode was excited to the resonant frequency ($f_1 \approx 30$ kHz) by the AFM software (Asylum Research) and the second eigenmode to the second-order resonant frequency ($f_2 \approx 110$ kHz). And the spring constant for the second eigenmode k_2 of the cantilever can be calculated by $k_2 = \left(\frac{f_2}{f_1}\right)^2 k_1$.

During the scanning, the first order amplitude A_1 is adjusts to maintain constant that is equal to amplitude setpoint $A_{1,\text{set}}$, so that the displacement of scanner in z-direction can be used for living cell topography tracking. Meanwhile, the cantilever is also excited at the second resonant frequency f_2. Here, a frequency feedback loop adjusts the frequency by a small amount Δf_2 to maintain the second eigenmode on resonance as the AFM tip interacts with the cell. The AM-FM signals were recorded by the lock-in and feedback system and can be used to extract the effective storage modulus E_{storage} for elastic property [42]:

$$E_{\text{storage}} = \frac{\pi}{R}\sqrt{\frac{1}{6}}\left(\frac{k_1}{Q_1}\frac{A_{1,\text{free}}}{A_{1,\text{set}}}\cos\varnothing_1\right)^{-\frac{1}{2}}\left(\frac{2k_2\Delta f_2}{f_2}\right)^{\frac{3}{2}},$$

where Q_1 are the quality factor, $A_{1,\text{free}}$ (4.0 V) is the free amplitude tuned for the first eigenmode in liquid, $A_{1,\text{set}}$ (2.0 V) is the setpoint used for imaging, and R (~10 nm) is the radius of AFM tip provided by the manufacturer. As described in details [43], the mapping of loss tangent E_{loss} can be derived by the amplitude (A_1) and phase signals ($\varnothing_1$) in the first resonance mode:

$$E_{\text{loss}} = \frac{\pi\left(\frac{A_{1,\text{set}}}{A_{1,\text{free}}} - \sin\varnothing_1\right)}{\cos\varnothing_1}.$$

The loss tangent is equivalent to the ratio of the dissipated energy to stored energy:

$$\text{Loss tangent} = \frac{E_{\text{loss}}}{E_{\text{storage}}},$$

which allows us to calculate the loss modulus for viscous property. Correlated topography and viscoelastic images were generated with a resolution of 256 × 256 pixels. And the scan speed was set at 0.5 line/s. As the modulus of the AFM tip used defers greatly from that of the glass substrate, the mechanical signal from the background part of glass substrate is meaningless and not considered, and is shown as the gray background in **Figures 4**, **5**. The same AFM tip and imaging configuration were used for all samples to maintain consistency between measurements of cell viscoelasticity. Repetitions of experiments with more living Huh-7 cancer cells under different pH states are performed to verify the robustness of results and mechanisms in our work.

Confocal Fluorescence Microscopy

Confocal fluorescence microscopy was used to observe the F-actin microstructures and validate the AFM imaging. The cells for the imaging by confocal fluorescence microscopy were seeded onto 20 mm cell slides and incubated with the same culture conditions as for AFM measurements. The cells were washed with PBS, fixed with 4% paraformaldehyde in PBS and kept at 4°C for around 15 min. Afterwards the cells were permeabilized with 0.5% Triton X-100 in PBS at room temperature for 15 min and rinsed with PBS. The nucleus of cells was stained with DAPI (Solarbio, China) for 15 min in dark. The F-actin cytoskeleton of cells was stained in dark using Alexa-Fluor 488 Phalloidin (Solarbio, China) for 30 min. Finally, the slides were mounted with the DAPI mounting medium (Solarbio, China). The stained cells were examined by using a confocal microscope setup (Leica SP8X, Germany) to visualize the F-actin microstructures. The fluorescent F-actin cytoskeleton images were acquired with a 63x/1.40 oil immersion objective lens (Leica Microsystems, Germany).

RESULTS AND DISCUSSION

Improved Amplitude Modulation-Frequency Modulation Atomic Force Microscopy for Mapping Topography and Viscoelasticity of Living Cells

To simultaneously obtain the images of topography and viscoelastic properties of living cells under physiological conditions, we have improved the original AM-FM AFM assembly. In the AM-FM method, two driving signals with different frequencies (black and red signals) are superposed to excite two independent vertical oscillation modes of the cantilever (**Figure 2A**). The first resonance operates in normal tapping mode (AM mode). The amplitude A_1 controls the vertical feedback loop of the standard tapping mode for topography, and the phase $\varnothing_1$ gives the values for the loss tangent (black box). The second resonance operates in the FM mode. The change in resonance frequency f_2 determines the elasticity, while the change in the amplitude A_2 gives the dissipation information (red box). Therefore, the AM-FM method strictly relies on the resonance information of the cantilever, and the stability of the first-order and second-order resonance peaks limits the signal-to-noise. Although AFM with AM-FM mode is competent for the simultaneous mapping of topography and viscoelasticity, the original AM-FM AFM of MFP-3D Infinity AFM system is inappropriate for the *in situ* environment of cell culture medium, as the build-in high damping material that is required to optimize the resonance of the cantilever cannot work in the liquid of culture medium. Without the high damping material, it is difficult for AM-FM AFM to achieve high-resolution imaging of F-actin microstructures [44]. In our work of *in situ* AM-FM AFM imaging, we unloaded the original high damping material and naturally used the liquid of cell culture medium as the high damping to dissipate unnecessary vibration in the oscillation process of AFM cantilever that deviates from the standard resonance. **Figure 2B** shows the first resonance signal of the cantilever without high damping in air, while **Figure 2C** shows the first resonance signal of the cantilever with the high damping in liquid. The introduction of

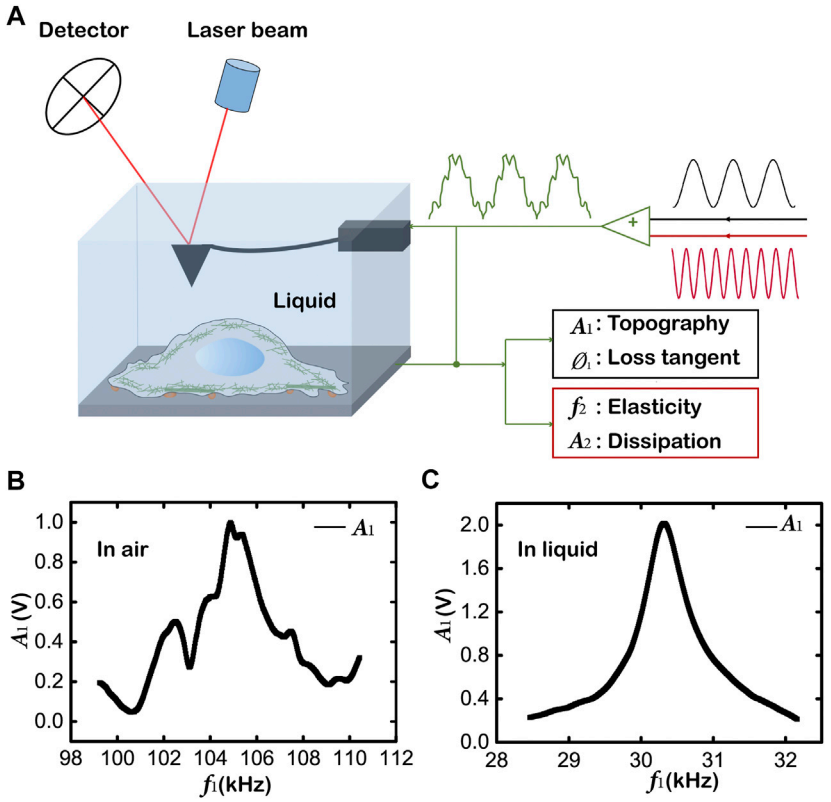

FIGURE 2 | Mapping topography and viscoelasticity of living cells by AM-FM AFM. **(A)** Schematics of the AM-FM AFM showing the experimental setup and the working principle. The AFM tip and the whole cantilever are immersed in the liquid of culture medium for *in situ* measurement of living cells in physiological condition. Two separate excitation signals are combined to excite the cantilever resonances. The cantilever deflection when probing the sample is analyzed to evaluate the offsets of the two resonances for the mapping of topography and viscoelasticity. **(B)** The first resonance signal of the cantilever without high damping in air. **(C)** The first resonance signal of the cantilever in liquid.

the high damping eliminates spurious peaks of the vibration information from unnecessary media and optimizes the resonance of the cantilever to form a clean standard peak in liquid. Similarly, the cluttered signal of the second-order resonance is greatly reduced due to the presence of high damping in liquid (see **Supplementary Figure S1**).

In addition, the ratio $A_{1,\mathrm{set}}/A_{1,\mathrm{free}}$ is set in the range of 0.3–0.5 which ensures the optimal tracking of surface topography for living cell imaging in AM-FM AFM. By introducing the high damping and setting the appropriate parameters, we successfully stabilize the cantilever oscillation, efficiently increase the signal-to-noise ratio, and achieve a high-resolution mapping in AM-FM AFM. As shown in **Figure 3**, we are able to simultaneously measure the cell topography (**Figures 3A,B**), associated with the distributions of storage modulus E_{storage} (**Figure 3C**), loss modulus E_{loss} (**Figure 3D**), and loss tangent (**Figure 3E**) of living cancer cells under physiological conditions. By taking advantage of the high contrast in the mapping of loss tangent, we have achieved an ultrahigh resolution down to 50 nm (**Figure 3F**) and captured cytoskeleton microstructures under *in situ* microenvironment.

Figure 3 shows the topography and viscoelasticity of living cells. It is important to note that the string microstructure observed in the images of viscoelasticity (**Figures 3C–E**) are highly correlated to the features observed in the topography image (**Figures 3A,B**). The widths of the strings are tens of nanometers. The storage moduli E_{storage} of the strings are higher than the gaps in between as shown in **Figure 3C**, while the loss tangents of the strings in **Figure 3E** are lower. These results show that the string microstructure takes the elasticity as the dominant property, which may correspond to the mechanical characteristics of cytoskeletons reported in previous study [45]. Hence, the same topography and viscoelasticity give us a strong implication that the microstructures shown by AM-FM AFM are cytoskeletons, which will be confirmed as F-actin by the latter section of immunofluorescence confocal microscopy. This AM-FM AFM method allows a direct observation in correlation of cytoskeletal structure with both topography and viscoelasticity for living cells, which shows better capability and application than the optical microscope that is limited by the diffraction limit resolution [31], the transmission electron microscope that cannot maintain the physiological state of living cells [32], and other methods for measuring mechanical properties of cells including the traction force microscope, optical tweezers and magnetic twisting cytometry that cannot obtain the topography simultaneously [35–37]. Our improvement of AM-FM AFM

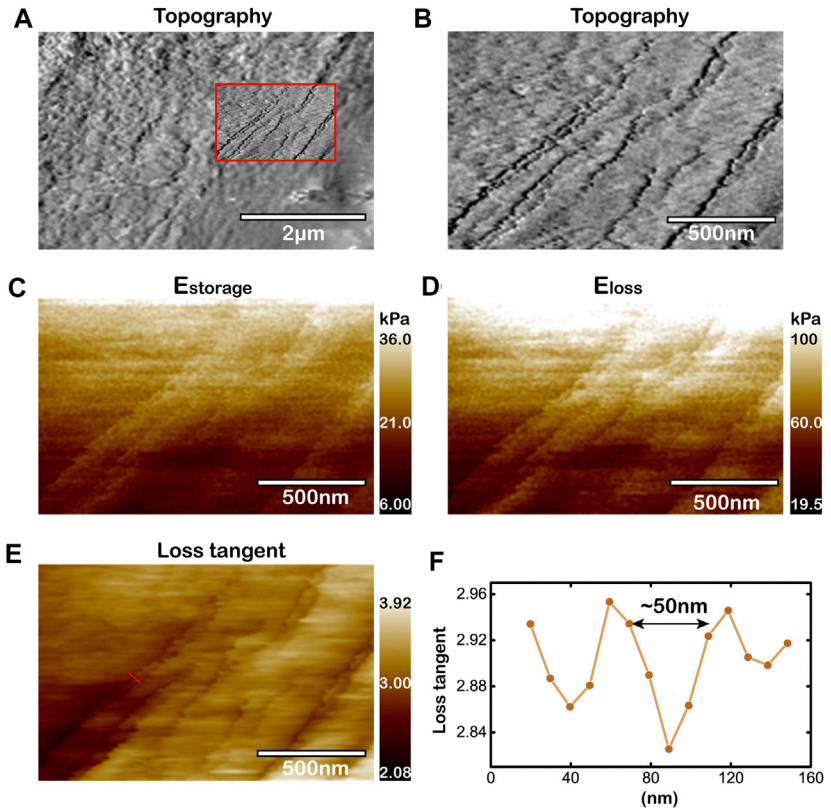

FIGURE 3 | Capability to image cytoskeleton microstructures of living cells by improved AM-FM AFM. **(A,B)** Topography of microregion near the periphery of living cancer cell. The view of **(B)** magnifies the rectangular region within the red box in **(A)**. Topography of the red box in **(A)**. **(C–E)** Mapping of $E_{storage}$ **(C)**, E_{loss} **(D)**, and loss tangent **(E)** simultaneously obtained by AM-FM AFM. **(F)** Cross-section profiles for the loss tangent along the red solid line in **(E)**.

has increased the resolution of cell mechanical imaging, and achieved simultaneously characterization of cytoskeleton topography, viscoelasticity, which are crucial for studying the relationship between the organization of cytoskeleton microstructure and the distribution of mechanical properties associated with their effects on cellular behaviors and functions.

Topography and Viscoelasticity of Cytoskeletons in Lamellipodium at pH 7.4

Based on the *in situ* AM-FM AFM method we improved for simultaneous mapping topography and viscoelasticity of living cells, it is feasible to study the relationship between the organization of cytoskeleton microstructures and the distribution of viscoelastic properties under different pH microenvironments. The microenvironment of cancer cells in tumor tissue is constantly acidified [23], with a lower extracellular pH value (~6.5) than the basic value (~7.4) in normal tissue [22]. The acid microenvironment enables the progression of cancer cells by promoting proliferation, the evasion of apoptosis, metabolic adaptation, migration and invasion that are involved with the malignant transformation and metastasis [46]. During this stage, the F-actin and the lamellipodium are the two crucial media linking the cellular behaviors and the mechanical properties. It has been reported that the acid extracellular pH induces the reorganization of F-actin cytoskeleton and facilitates the formation of lamellipodial protrusion [25], which can modulate the morphology and rigidity against the forces needed for cell migration [47]. It would be a key challenge and a great significance to study the correlation between the organization of F-actin structures and the viscoelasticity distribution in lamellipodium of living cancer cells under normal (pH 7.4) and acid (pH 6.5) microenvironments for revealing the nanomechanical mechanism of the cellular migration in metastasis.

In the normal microenvironment (pH 7.4), we use the improved AM-FM AFM method to characterize the topography and the viscoelasticity of living Huh-7 cells as shown in **Figure 4**. **Figure 4A** shows an overall topography of the cell edge, with the region of lamellipodium in the red box measured by larger contact force and scanning density for higher resolution in topography (**Figure 4B**), storage modulus $E_{storage}$ (**Figures 4C,D**), loss modulus E_{loss} (**Figures 4E,F**), and loss tangent (**Figures 4G,H**). The topography image of **Figure 4B** represents the shot and thin cytoskeletal structures randomly dispersed in lamellipodium, which is also reflected by the

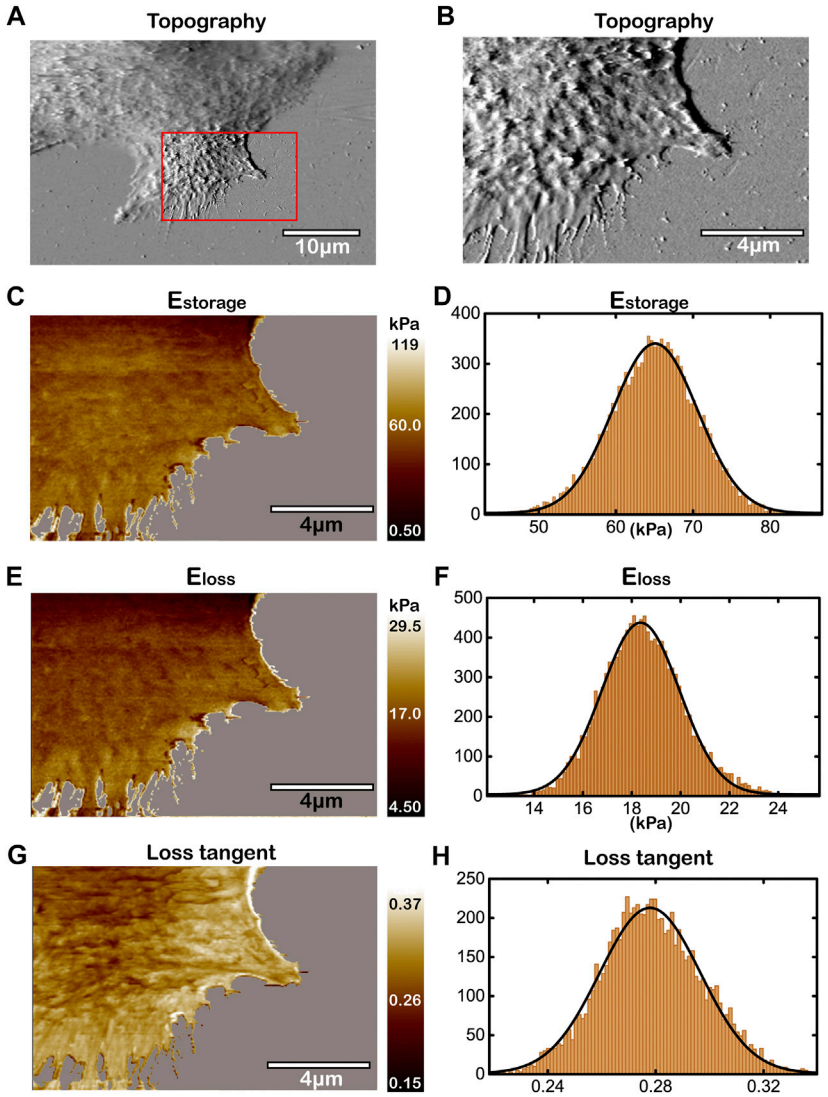

FIGURE 4 | Topography and the viscoelasticity of Huh-7 cells at pH 7.4. **(A)** Topography of cell edge. **(B)** High-resolution topography of lamellipodium region within the red box in **(A)**. **(C**,**E**,**G)** Mapping of $E_{storage}$ **(C)**, E_{loss} **(E)**, and loss tangent **(G)** simultaneously obtained by AM-FM AFM. **(D**,**F**,**H)** Histogram analyses of the measured $E_{storage}$, E_{loss}, and loss tangent in **(C)**, **(E)** and **(G)**, respectively.

homogeneous patterns of viscoelasticity (**Figures 4C,E,G** and **Supplementary Figure S2**). The histogram analyses of storage modulus, loss modulus and loss tangent for **Figures 4C,E,G** were performed as shown in **Figures 4D,F,H**, respectively. The storage modulus in the lamellipodium region (**Figure 4D**) indicates a single Gaussian peak for elasticity with the main range of 50–80 kPa and the mean value of ~65 kPa, which are in good agreement with previous studies [29, 48]. Similarly, the viscous properties measured by loss modulus and loss tangent exhibit monomodal Gaussian peaks, which further indicates the homogeneous distribution of cytoskeletons (**Figures 4F,H**). The Gaussian peak of loss modulus has a mean value of ~18 kPa with the range varying from 14 to 24 kPa, while that of the loss tangent has a mean value of ~0.28. The mappings of storage modulus and loss modulus demonstrate that the cytoskeletons have slightly higher elasticity and viscosity than the background of intracellular fluid or other organelles (**Figures 4C,E**) [48]. Note that the greater difference between the cytoskeletons and the intracellular background is shown in the mapping of loss tangent (**Figure 4G**), owing to the dominant elasticity of cytoskeletal filaments [28, 29]. As a result, the mapping of loss tangent can show higher contrast and resolution with the patterns greatly corelated to the cytoskeletal structures in the topography image, which further proves the capability in characterizing the detailed organization of cytoskeletal structures by the improved AM-FM AFM. Repetitions of experiments for more living Huh-7 cancer cells at pH 7.4 (**Supplementary Figure S2**) show similar cytoskeleton

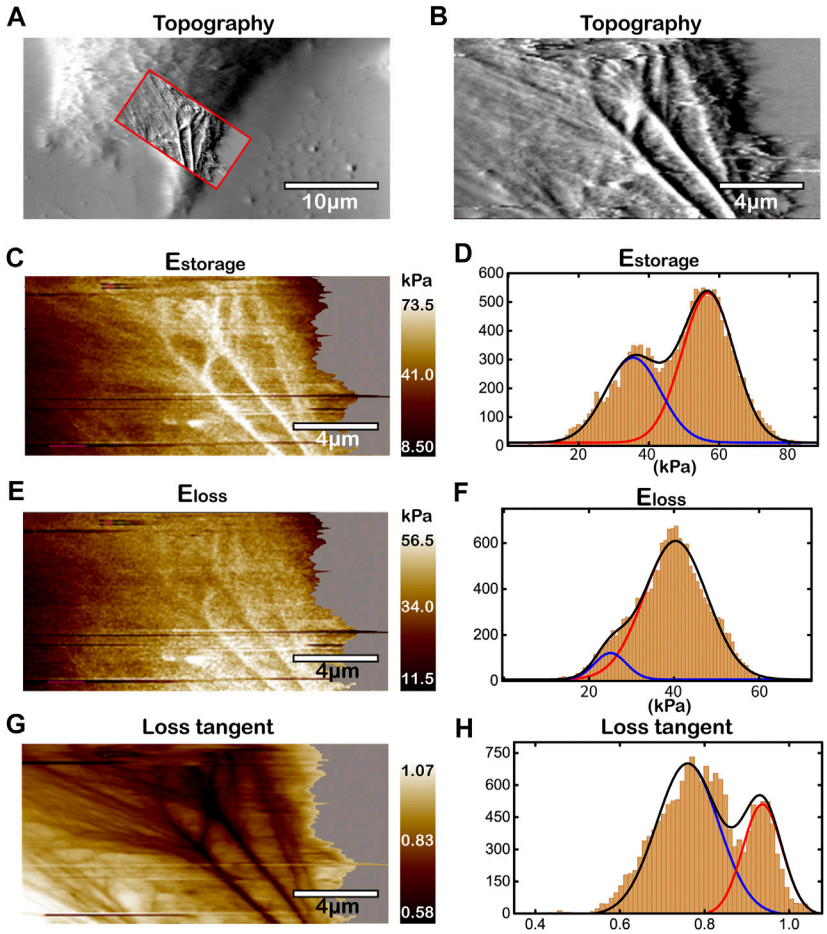

FIGURE 5 | Topography and the viscoelasticity of Huh-7 cells at pH 6.5. **(A)** Topography of cell edge. **(B)** High-resolution topography of lamellipodium region within the red box in **(A)**. **(C**,**E**,**G)** Mapping of $E_{storage}$ **(C)**, E_{loss} **(E)**, and loss tangent **(G)** simultaneously obtained by AM-FM AFM. **(D**,**F**,**H)** Histogram analyses of the measured $E_{storage}$, E_{loss}, and loss tangent in **(C)**, **(E)** and **(G)**, respectively.

organization and cell viscoelasticity, which verify the robustness of our results.

Topography and Viscoelasticity of Cytoskeletons in Lamellipodium at pH 6.5

To study the effect of acid microenvironment on living cancer cells, we change pH value of the culture medium to pH 6.5 [22], and measure the topography and the viscoelasticity of Huh-7 cells by the improved AM-FM AFM as shown in **Figure 5** and **Supplementary Figure S3**. Unlike the homogeneous dispersion of cytoskeletons in lamellipodium at pH 7.4, the topography of **Figures 5A,B** show highly oriented and organized patterns of cytoskeletal structures at pH 6.5. The cytoskeletons are polymerized to long filaments and woven into thick bundle-like structures directed to the protruding direction of lamellipodium. The viscoelasticity, including storage modulus, loss modulus and loss tangent, of the same lamellipodium region in Huh-7 cells are measured and analyzed in **Figures 5C–H** in which the polymerized filaments and bundles are visible. The strings that have higher storage modulus, higher loss modulus and lower loss tangent than the intracellular background indicate the cytoskeletal filaments in **Figures 5C,E,G**, respectively. Interestingly, along with the convergence of cytoskeletal filaments towards the protruded lamellipodium, the storage modulus and loss modulus increase while the loss tangent decreases. The gradient of viscoelasticity in the lamellipodium region with the relationship to the cellular migration will be discussed in details in the latter section.

The histogram analyses of storage modulus, loss modulus and loss tangent were also performed as shown in **Figures 5D,F,H**, respectively. Unlike monomodal Gaussian peaks at pH 7.4, all of the storage modulus, loss modulus and loss tangent show bimodal distributions at pH 6.5, corresponding to the heterogeneous organization of cytoskeletons. In **Figure 5D** for elasticity, the lower peak of storage modulus with the mean value of ~35 kPa represents the thin and unwoven cytoskeletal filaments, while the higher peak (~60 kPa) the thick cytoskeletal filaments that have been bundled together. These results of elasticity distribution are consistent with the previous studies that the increased density of

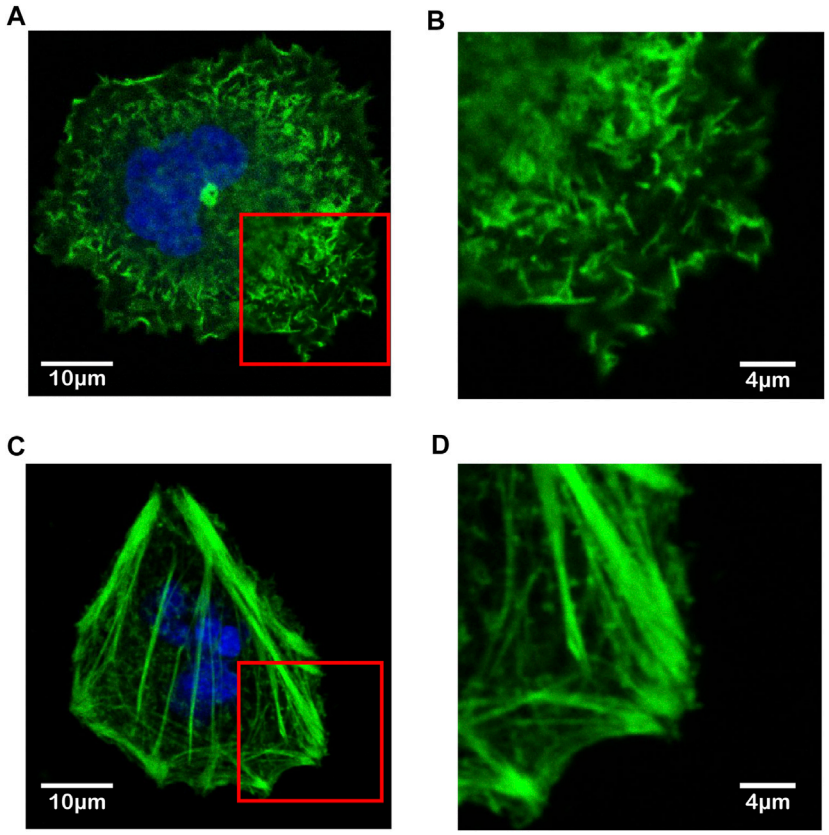

FIGURE 6 | Immunofluorescence confocal microscopy images of F-actin filaments in living Huh-7 cells under different pH microenvironments. **(A,B)** F-actin in Huh-7 cell at pH 7.4. **(C,D)** F-actin in Huh-7 cell at pH 6.5. The F-actin filaments are highlighted by green and the cell nuclei by blue. The view of **(B)** and **(D)** magnifies the rectangular region near the periphery of cell within the red box in **(A)** and **(C)**, respectively.

actin filaments can lead to the stiffening of cells [28, 29, 49]. The bundled actin filaments are bound by crosslinking proteins and molecular motor, such as fascin and myosin-X, providing strong viscosity [50, 51], which results in an elevated loss modulus as the higher peak (~40 kPa) in **Figure 5F**. Our work visualizes the organization of cytoskeletal filaments and reveals the structural origins of the viscoelasticity distribution in the lamellipodium region of living cancer cells under acid microenvironment. Repetitions of experiments for more living Huh-7 cancer cells at pH 6.5 (**Supplementary Figure S3**) show similar cytoskeleton organization and cell viscoelasticity, which verify the robustness of our results. We also performed the experiments at the pH level within the range from 6.5 to 7.4, and found that the more cells with F-actin polymerization and viscoelasticity gradient can be seen at the lower pH state.

Validation of F-Actin Cytoskeletons by Immunofluorescence Confocal Microscopy

To identify the type of cytoskeletal structures shown by the improved AM-FM AFM as in **Figures 4**, **5**, the immunofluorescence confocal microscopy was adopted and the fluorescent phalloidin that can selectively bind to F-actin was used to image the distribution of F-actin in the living Huh-7 cells (**Figure 6**) [52]. The Huh-7 cells were cultured in the two different pH environments (pH 7.4 and pH 6.5) as in AFM experiments and stained with Alexa-Fluor 488 Phalloidin and DAPI. The imaging of confocal microscopy shows that the F-actin filaments dyed by green are short, thin and randomly dispersed within the whole Huh-7 cell at pH 7.4 (**Figure 6A**). Although becoming slightly thicker near the periphery, the F-actin filaments are loosely arranged with the same homogeneous feature observed in AFM experiments (**Figure 6B**). On the contrary, at pH 6.5, the F-actin filaments that are much thicker and longer form highly oriented bundle-like structures (**Figure 6C**) and converge toward the front of lamellipodium (**Figure 6D**), which is in good agreement with the AFM imaging as well. The consistency of intercellular structures confirms that the cytoskeletal filaments visualized by the improved AM-FM AFM are the F-actin.

Viscoelasticity Gradient Facilitates Cell Adhesion and Migration

In previous sections, by using the improved AM-FM AFM, we have successfully characterized the viscoelasticity distribution of the lamellipodium regions in living Huh-7 cells at pH 7.4 and 6.5 (**Figures 4**, **5**). To compare them quantitatively, we rescale the

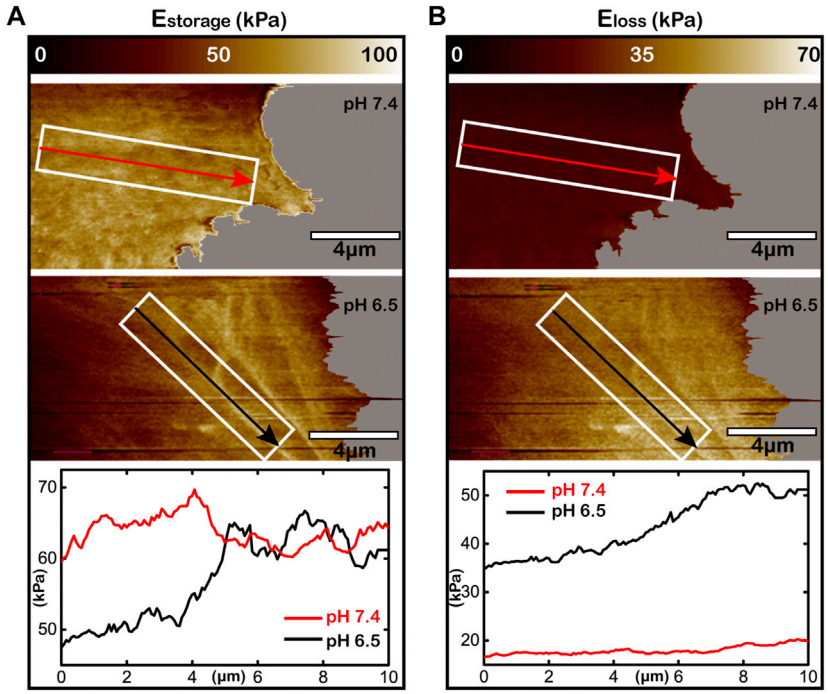

FIGURE 7 | Acid microenvironment inducing viscoelasticity gradient in the lamellipodium of living Huh-7 cells. **(A,B)** The storage modulus for elasticity **(A)** and the loss modulus for viscosity **(B)** of the lamellipodium under different pH environments. The upper panels are at pH 7.4, the middle panels are at pH 6.5, and the lower curves analyze the storage modulus or the loss modulus within the white rectangular boxes along the arrows directed to lamellipodium protrusion. The white rectangular boxes with the directions of arrows are the same for each pH value.

mapping of storage modulus (**Figure 7A**) and loss modulus (**Figure 7B**) to the same color range for studying the effect of viscoelasticity distribution on cell adhesion and migration. **Figure 7A** shows that along the direction of lamellipodium protrusion (as the arrows), the storage modulus of cell elasticity increases from ~50 kPa to over 60 kPa at the acid microenvironment and maintains at a plateau (~60 kPa) at the normal microenvironment. For cell viscosity following the same arrows, the loss modulus increases from 35 to over 50 kPa at pH 6.5, while staying at a low level of ~10 kPa at pH 7.4 (**Figure 7B**). Combining the AFM images of cytoskeletons, we can conclude that the acid microenvironment may result in the organization of F-actin filaments and the gradient of both elasticity and viscosity in living cancer cells.

Recent researches of cell migration and cancer metastasis have reported that the living cancer cells prefer to migrate toward the substrate with higher stiffness [19, 53]. However, few studies focus on the distribution and alteration of cell viscoelasticity during migration associated with the effects of cell viscoelasticity on migration. According to literatures, the higher elasticity and viscosity enable stronger adhesion to substrate [13, 54]. In our work, by using the improved AM-FM AFM, we found that the F-actin cytoskeleton aggregate and form the thick bundle-like filaments directed to the protruding direction of lamellipodium, leading to gradient increases in elasticity and viscosity. The gradient of viscoelasticity suggests a gradient of adhesion strength, which means that the lamellipodium can achieve stable adhesion at the front but have high possibility to detach the substrate at the back, resulting in the driving force for cell migration towards the direction of lamellipodium protrusion. Moreover, the aggregation and the stiffening of F-actin cytoskeleton allow focal adhesions to enhance cell adhesion, and provide sufficient cell rigidity against the forces needed for migration [55, 56]. In all, the homogeneity of F-actin cytoskeleton and viscoelasticity in the lamellipodium at pH 7.4 suppresses the migration of cancer cells, which consistent with the fact of uneasy malignant transformation of cancer cells under normal environment [47, 57]. Conversely, the aggregation of F-actin cytoskeleton and the gradient of viscoelasticity at pH 6.5 facilitate cell adhesion and migration, which explains the strong tendency in migration and metastasis of cancer cells under the acidified microenvironment in tumor tissues [47, 58]. These findings may help us to understand the structural and nanomechanical mechanism of malignant behavior of cancer cells under different pH microenvironments.

CONCLUSIONS

In summary, we have improved the original AM-FM AFM assembly, achieved the simultaneous mappings of topography and viscoelasticity of living cells under physiological conditions, and reached an ultrahigh resolution down to 50 nm for the imaging of F-actin cytoskeletons. By using the improved AM-

FM AFM, we were able to study the effect of pH microenvironment on organization of F-actin cytoskeletons and the distribution of viscoelasticity in lamellipodia of living Huh-7 cancer cells correlated with the cell adhesion and migration. The acidified environment can transform the short, thin and dispersed F-actin structures to the long, thick and oriented bundle-like structure converged along the protruding direction of lamellipodium. The conformation of F-actin cytoskeletons leads to the gradient increases of both elasticity and viscosity directed to the lamellipodium front, which provides sufficient driving force and rigidity that can facilitate cell adhesion and migration. Our work has paved the avenue for the *in situ* characterization of the F-actin microstructures and cell viscoelasticity, and contributed insights into the structural origins and nanomechanical mechanism of the migration and metastasis of living cancer cells under the acidified microenvironment.

DATA AVAILABILITY STATEMENT

The original contributions presented in the study are included in the article/**Supplementary Material**, further inquiries can be directed to the corresponding authors.

AUTHOR CONTRIBUTIONS

WZ, XZ, and YZ conceived the research. MC, WZ, XZ, ZL, and SY designed, performed, and analyzed the experiments. WZ supervised the project. MC, WZ, XZ, and YZ wrote the manuscript. All authors discussed the results and commented on the manuscript.

FUNDING

This study was supported by the National Natural Science Foundation of China (Grants 11972383 and 81827802) to WZ, by the National Natural Science Foundation of China (Grant 11672339) to YZ, by the Fundamental Research Funds for the Central Universities (Grant 19LGPY258) to WZ, and by the Natural Science Foundation of Guangdong Province, China (Grant 2021A1515010348) to WZ. The funders had no influence on study design, data collection and analysis, decision to publish or preparation of the manuscript.

ACKNOWLEDGMENTS

The experiments reported were conducted on the Physical Research Platform in School of Physics, Sun Yat-sen University (PRPSP, SYSU) and the Instrumental Analysis and Research Center, Sun Yat-sen University. We thank Teaching Center of Biology Experiment, Sun Yat-sen University for assistance with confocal fluorescence microscopy imaging.

SUPPLEMENTARY MATERIAL

The Supplementary Material for this article can be found online at: https://www.frontiersin.org/articles/10.3389/fphy.2021.674958/full#supplementary-material

REFERENCES

1. Ellinger I, and Ellinger A. Smallest Unit of Life: Cell Biology. In: E Jensen-Jarolim, editor. *Comparative Medicine Anatomy and Physiology*. Germany: Springer Press (2014). p. 19–33. doi:10.1007/978-3-7091-1559-6_2
2. Lange JR, and Fabry B. Cell and Tissue Mechanics in Cell Migration. *Exp Cel Res* (2013) 319(16):2418–23. doi:10.1016/j.yexcr.2013.04.023
3. Khalili A, and Ahmad M. A Review of Cell Adhesion Studies for Biomedical and Biological Applications. *Int J Mol Sci* (2015) 16:18149–84. doi:10.3390/ijms160818149
4. Engler AJ, Sen S, Sweeney HL, and Discher DE. Matrix Elasticity Directs Stem Cell Lineage Specification. *Cell* (2006) 126(4):677–89. doi:10.1016/j.cell.2006.06.044
5. Wei Q, Huang C, Zhang Y, Zhao T, Zhao P, Butler P, et al. Mechanotargeting: Mechanics-dependent Cellular Uptake of Nanoparticles. *Adv Mater* (2018) 30(27):1707464. doi:10.1002/adma.201707464
6. Fletcher DA, and Mullins RD. Cell Mechanics and the Cytoskeleton. *Nature* (2010) 463(7280):485–92. doi:10.1038/nature08908
7. Pollard TD, and Cooper JA. Actin, a Central Player in Cell Shape and Movement. *Science* (2009) 326(5957):1208–12. doi:10.1126/science.1175862
8. Blanchoin L, Boujemaa-Paterski R, Sykes C, and Plastino J. Actin Dynamics, Architecture, and Mechanics in Cell Motility. *Physiol Rev* (2014) 94(1):235–63. doi:10.1152/physrev.00018.2013
9. Fritzsche M, Erlenkämper C, Moeendarbary E, Charras G, and Kruse K. Actin Kinetics Shapes Cortical Network Structure and Mechanics. *Sci Adv* (2016) 2(4):e1501337. doi:10.1126/sciadv.1501337
10. Chugh P, and Paluch EK. The Actin Cortex at a Glance. *J Cel Sci* (2018) 131(14). doi:10.1242/jcs.186254
11. Oberleithner H, Callies C, Kusche-Vihrog K, Schillers H, Shahin V, Riethmüller C, et al. Potassium Softens Vascular Endothelium and Increases Nitric Oxide Release. *Proc Natl Acad Sci U S A* (2009) 106(8):2829–34. doi:10.1073/pnas.0813069106
12. Tojkander S, Gateva G, and Lappalainen P. Actin Stress Fibers - Assembly, Dynamics and Biological Roles. *J Cel Sci* (2012) 125(8):1855–64. doi:10.1242/jcs.098087
13. Li L, Zhang W, and Wang J. A Viscoelastic-Stochastic Model of the Effects of Cytoskeleton Remodelling on Cell Adhesion. *R Soc Open Sci* (2016) 3(10):160539. doi:10.1098/rsos.160539
14. Jacquemet G, Hamidi H, and Ivaska J. Filopodia in Cell Adhesion, 3D Migration and Cancer Cell Invasion. *Curr Opin Cel Biol* (2015) 36:23–31. doi:10.1016/j.ceb.2015.06.007
15. Bergert M, Chandradoss SD, Desai RA, and Paluch E. Cell Mechanics Control Rapid Transitions between Blebs and Lamellipodia during Migration. *Proc Natl Acad Sci* (2012) 109(36):14434–9. doi:10.1073/pnas.1207968109
16. Nemethova M, Auinger S, and Small JV. Building the Actin Cytoskeleton: Filopodia Contribute to the Construction of Contractile Bundles in the Lamella. *J Cel Biol* (2008) 180(6):1233–44. doi:10.1083/jcb.200709134
17. Mueller J, Szep G, Nemethova M, De Vries I, Lieber AD, Winkler C, et al. Load Adaptation of Lamellipodial Actin Networks. *Cell* (2017) 171(1):188–200. doi:10.1016/j.cell.2017.07.051
18. Bieling P, Li T-D, Weichsel J, McGorty R, Jreij P, Huang B, et al. Force Feedback Controls Motor Activity and Mechanical Properties of Self-Assembling Branched Actin Networks. *Cell* (2016) 164(1-2):115–27. doi:10.1016/j.cell.2015.11.057
19. Laurent VM, Kasas S, Yersin A, Schäffer TE, Catsicas S, Dietler G, et al. Gradient of Rigidity in the Lamellipodia of Migrating Cells Revealed by Atomic Force Microscopy. *Biophysical J* (2005) 89(1):667–75. doi:10.1529/biophysj.104.052316

20. Friedl P, and Alexander S. Cancer Invasion and the Microenvironment: Plasticity and Reciprocity. *Cell* (2011) 147(5):992–1009. doi:10.1016/j.cell.2011.11.016
21. Rofstad EK, Mathiesen B, Kindem K, and Galappathi K. Acidic Extracellular pH Promotes Experimental Metastasis of Human Melanoma Cells in Athymic Nude Mice. *Cancer Res* (2006) 66(13):6699–707. doi:10.1158/0008-5472.can-06-0983
22. Estrella V, Chen T, Lloyd M, Wojtkowiak J, Cornnell HH, Ibrahim-Hashim A, et al. Acidity Generated by the Tumor Microenvironment Drives Local Invasion. *Cancer Res* (2013) 73(5):1524–35. doi:10.1158/0008-5472.can-12-2796
23. Corbet C, and Feron O. Tumour Acidosis: from the Passenger to the Driver's Seat. *Nat Rev Cancer* (2017) 17(10):577–93. doi:10.1038/nrc.2017.77
24. Suzuki A, Maeda T, Baba Y, Shimamura K, and Kato Y. Acidic Extracellular pH Promotes Epithelial Mesenchymal Transition in Lewis Lung Carcinoma Model. *Cancer Cel Int* (2014) 14(1):1–11. doi:10.1186/s12935-014-0129-1
25. Li S, Xiong N, Peng Y, Tang K, Bai H, Lv X, et al. Acidic pHe Regulates Cytoskeletal Dynamics through Conformational Integrin β1 Activation and Promotes Membrane Protrusion. *Biochim Biophys Acta Mol Basis Dis* (2018) 1864(7):2395–408. doi:10.1016/j.bbadis.2018.04.019
26. Efremov YM, Velay-Lizancos M, Weaver CJ, Athamneh AI, Zavattieri PD, Suter DM, et al. Anisotropy vs Isotropy in Living Cell Indentation with AFM. *Sci Rep* (2019) 9(1):1–12. doi:10.1038/s41598-019-42077-1
27. Brückner BR, Nöding H, and Janshoff A. Viscoelastic Properties of Confluent MDCK II Cells Obtained from Force Cycle Experiments. *Biophysical J* (2017) 112(4):724–35. doi:10.1016/j.bpj.2016.12.032
28. Rianna C, Ventre M, Cavalli S, Radmacher M, and Netti PA. Micropatterned Azopolymer Surfaces Modulate Cell Mechanics and Cytoskeleton Structure. *ACS Appl Mater Inter* (2015) 7(38):21503–10. doi:10.1021/acsami.5b06693
29. Calzado-Martín A, Encinar M, Tamayo J, Calleja M, and San Paulo A. Effect of Actin Organization on the Stiffness of Living Breast Cancer Cells Revealed by Peak-Force Modulation Atomic Force Microscopy. *ACS Nano* (2016) 10(3):3365–74. doi:10.1021/acsnano.5b07162
30. Wang N, Zhang M, Chang Y, Niu N, Guan Y, Ye M, et al. Directly Observing Alterations of Morphology and Mechanical Properties of Living Cancer Cells with Atomic Force Microscopy. *Talanta* (2019) 191:461–8. doi:10.1016/j.talanta.2018.09.008
31. Zheludev NI. What Diffraction Limit? *Nat Mater* (2008) 7(6):420–2. doi:10.1038/nmat2163
32. Henson JH, Yeterian M, Weeks RM, Medrano AE, Brown BL, Geist HL, et al. Arp2/3 Complex Inhibition Radically Alters Lamellipodial Actin Architecture, Suspended Cell Shape, and the Cell Spreading Process. *Mol Biol Cel* (2015) 26(5):887–900. doi:10.1091/mbc.e14-07-1244
33. Svitkina TM. Platinum Replica Electron Microscopy: Imaging the Cytoskeleton Globally and Locally. *Int J Biochem Cel Biol* (2017) 86:37–41. doi:10.1016/j.biocel.2017.03.009
34. Hochmuth RM. Micropipette Aspiration of Living Cells. *J Biomech* (2000) 33(1):15–22. doi:10.1016/S0021-9290(99)00175-X
35. Peschetola V, Laurent VM, Duperray A, Michel R, Ambrosi D, Preziosi L, et al. Time-dependent Traction Force Microscopy for Cancer Cells as a Measure of Invasiveness. *Cytoskeleton* (2013) 70(4):201–14. doi:10.1002/cm.21100
36. Ayala YA, Pontes B, Ether DS, Pires LB, Araujo GR, Frases S, et al. Rheological Properties of Cells Measured by Optical Tweezers. *BMC Biophys* (2016) 9(1):1–11. doi:10.1186/s13628-016-0031-4
37. Hu S, Eberhard L, Chen J, Love JC, Butler JP, Fredberg JJ, et al. Mechanical Anisotropy of Adherent Cells Probed by a Three-Dimensional Magnetic Twisting Device. *Am J Physiol Cel Physiol* (2004) 287(5):C1184–C1191. doi:10.1152/ajpcell.00224.2004
38. Krieg M, Fläschner G, Alsteens D, Gaub BM, Roos WH, Wuite GJL, et al. Atomic Force Microscopy-Based Mechanobiology. *Nat Rev Phys* (2019) 1(1):41–57. doi:10.1038/s42254-018-0001-7
39. Haase K, and Pelling AE. Investigating Cell Mechanics with Atomic Force Microscopy. *J R Soc Interf* (2015) 12(104):20140970. doi:10.1098/rsif.2014.0970
40. Iyer S, Gaikwad RM, Subba-Rao V, Woodworth CD, and Sokolov I. Atomic Force Microscopy Detects Differences in the Surface Brush of Normal and Cancerous Cells. *Nat Nanotech* (2009) 4(6):389–93. doi:10.1038/nnano.2009.77
41. Efremov YM, Dokrunova AA, Bagrov DV, Kudryashova KS, Sokolova OS, and Shaitan KV. The Effects of Confluency on Cell Mechanical Properties. *J Biomech* (2013) 46(6):1081–7. doi:10.1016/j.jbiomech.2013.01.022
42. Kocun M, Labuda A, Meinhold W, Revenko I, and Proksch R. Fast, High Resolution, and Wide Modulus Range Nanomechanical Mapping with Bimodal Tapping Mode. *ACS Nano* (2017) 11(10):10097–105. doi:10.1021/acsnano.7b04530
43. Proksch R, and Yablon DG. Loss Tangent Imaging: Theory and Simulations of Repulsive-Mode Tapping Atomic Force Microscopy. *Appl Phys Lett* (2012) 100(7):073106. doi:10.1063/1.3675836
44. Guan D, Charlaix E, Qi RZ, and Tong P. Noncontact Viscoelastic Imaging of Living Cells Using a Long-Needle Atomic Force Microscope with Dual-Frequency Modulation. *Phys Rev Appl* (2017) 8(4):044010. doi:10.1103/PhysRevApplied.8.044010
45. Haga H, Sasaki S, Kawabata K, Ito E, Ushiki T, and Sambongi T. Elasticity Mapping of Living Fibroblasts by AFM and Immunofluorescence Observation of the Cytoskeleton. *Ultramicroscopy* (2000) 82(1-4):253–8. doi:10.1016/S0304-3991(99)00157-6
46. Webb BA, Chimenti M, Jacobson MP, and Barber DL. Dysregulated pH: a Perfect Storm for Cancer Progression. *Nat Rev Cancer* (2011) 11(9):671–7. doi:10.1038/nrc3110
47. Mogilner A, and Rubinstein B. The Physics of Filopodial Protrusion. *Biophysical J* (2005) 89(2):782–95. doi:10.1529/biophysj.104.056515
48. Guerrero CR, Garcia PD, and Garcia R. Subsurface Imaging of Cell Organelles by Force Microscopy. *ACS Nano* (2019) 13(8):9629–37. doi:10.1021/acsnano.9b04808
49. Gardel ML, Shin JH, MacKintosh FC, Mahadevan L, Matsudaira P, and Weitz DA. Elastic Behavior of Cross-Linked and Bundled Actin Networks. *Science* (2004) 304(5675):1301–5. doi:10.1126/science.1095087
50. Mattila PK, and Lappalainen P. Filopodia: Molecular Architecture and Cellular Functions. *Nat Rev Mol Cel Biol* (2008) 9(6):446–54. doi:10.1038/nrm2406
51. Rigato A, Miyagi A, Scheuring S, and Rico F. High-frequency Microrheology Reveals Cytoskeleton Dynamics in Living Cells. *Nat Phys* (2017) 13(8):771–5. doi:10.1038/nphys4104
52. Dancker P, Löw I, Hasselbach W, and Wieland T. Interaction of Actin with Phalloidin: Polymerization and Stabilization of F-Actin. *Biochim Biophys Acta* (1975) 400(2):407–14. doi:10.1016/0005-2795(75)90196-8
53. Ponti A, Machacek M, Gupton SL, Waterman-Storer CM, and Danuser G. Two Distinct Actin Networks Drive the Protrusion of Migrating Cells. *Science* (2004) 305(5691):1782–6. doi:10.1126/science.1100533
54. Yao H, and Gao H. Mechanics of Robust and Releasable Adhesion in Biology: Bottom-Up Designed Hierarchical Structures of Gecko. *J Mech Phys Sol* (2006) 54(6):1120–46. doi:10.1016/j.jmps.2006.01.002
55. Natale CF, Ventre M, and Netti PA. Tuning the Material-Cytoskeleton Crosstalk via Nanoconfinement of Focal Adhesions. *Biomaterials* (2014) 35(9):2743–51. doi:10.1016/j.biomaterials.2013.12.023
56. Qian J, Wang J, Lin Y, and Gao H. Lifetime and Strength of Periodic Bond Clusters between Elastic Media under Inclined Loading. *Biophysical J* (2009) 97(9):2438–45. doi:10.1016/j.bpj.2009.08.027
57. White KA, Grillo-Hill BK, and Barber DL. Cancer Cell Behaviors Mediated by Dysregulated pH Dynamics at a Glance. *J Cel Sci* (2017) 130(4):663–9. doi:10.1242/jcs.195297
58. Petrie RJ, Doyle AD, and Yamada KM. Random versus Directionally Persistent Cell Migration. *Nat Rev Mol Cel Biol* (2009) 10(8):538–49. doi:10.1038/nrm2729

Conflict of Interest: The authors declare that the research was conducted in the absence of any commercial or financial relationships that could be construed as a potential conflict of interest.

frontiers in Physics

MINI REVIEW
published: 27 May 2021
doi: 10.3389/fphy.2021.675885

Regulation of Actin Bundle Mechanics and Structure by Intracellular Environmental Factors

Nicholas Castaneda[1,2†], *Jinho Park*[1,3†] *and Ellen Hyeran Kang*[1,3,4*]

[1] NanoScience Technology Center, University of Central Florida, Orlando, FL, United States, [2] Burnett School of Biomedical Sciences, College of Medicine, University of Central Florida, Orlando, FL, United States, [3] Department of Materials Science and Engineering, University of Central Florida, Orlando, FL, United States, [4] Department of Physics, University of Central Florida, Orlando, FL, United States

The mechanical and structural properties of actin cytoskeleton drive various cellular processes, including structural support of the plasma membrane and cellular motility. Actin monomers assemble into double-stranded helical filaments as well as higher-ordered structures such as bundles and networks. Cells incorporate macromolecular crowding, cation interactions, and actin-crosslinking proteins to regulate the organization of actin bundles. Although the roles of each of these factors in actin bundling have been well-known individually, how combined factors contribute to actin bundle assembly, organization, and mechanics is not fully understood. Here, we describe recent studies that have investigated the mechanisms of how intracellular environmental factors influence actin bundling. This review highlights the effects of macromolecular crowding, cation interactions, and actin-crosslinking proteins on actin bundle organization, structure, and mechanics. Understanding these mechanisms is important in determining *in vivo* actin biophysics and providing insights into cell physiology.

Keywords: actin bundles, macromolecular crowding, cation interactions, actin crosslinker, bending stiffness

OPEN ACCESS

Edited by:
Yuan Lin,
The University of Hong Kong, Hong Kong

Reviewed by:
Naomi Courtemanche, University of Minnesota Twin Cities, United States
Yashar Bashirzadeh, University of Michigan, United States

***Correspondence:**
Ellen Hyeran Kang
ellen.kang@ucf.edu

†These authors have contributed equally to this work

Specialty section:
This article was submitted to Biophysics, a section of the journal Frontiers in Physics

Received: *04 March 2021*
Accepted: *13 April 2021*
Published: *27 May 2021*

Citation:
Castaneda N, Park J and Kang EH (2021) Regulation of Actin Bundle Mechanics and Structure by Intracellular Environmental Factors. Front. Phys. 9:675885. doi: 10.3389/fphy.2021.675885

INTRODUCTION

The dynamic assembly of actin monomers into higher-ordered structures such as bundles and networks is vital to many eukaryotic cell functions. Actin bundle mechanics and structure play essential roles in the formation of filopodia [1, 2], structural support of plasma membrane [3], force generation [4], cell division, and cell motility [2, 5, 6]. Recent studies demonstrate that actin bundles can function as mechanosensors displaying mechanical responses to external stimuli and mechanical deformation [7, 8]. Bundle assembly dynamics are tightly regulated by intracellular environmental factors, contributing to changes in cell mechanics as well as physiology.

Actin bundle formation can be achieved by macromolecular crowding, electrostatic interactions, and various actin-crosslinking and/or bundling proteins (**Figure 1A**) [10–17]. Bundles are formed in highly crowded intracellular environments consisting of various macromolecules and ions that limit available cytoplasmic space [18–20]. The presence of macromolecular crowding promotes steric exclusion ("hard") and/or non-specific ("soft") effects [21, 22]. Depletion forces induced by macromolecular crowding lead to bundle formation through excluded volume effects, which can overcome repulsive interaction between negatively charged actin filaments [10, 23, 24]. In comparison, cation interactions result in actin bundle formation through counterion condensation

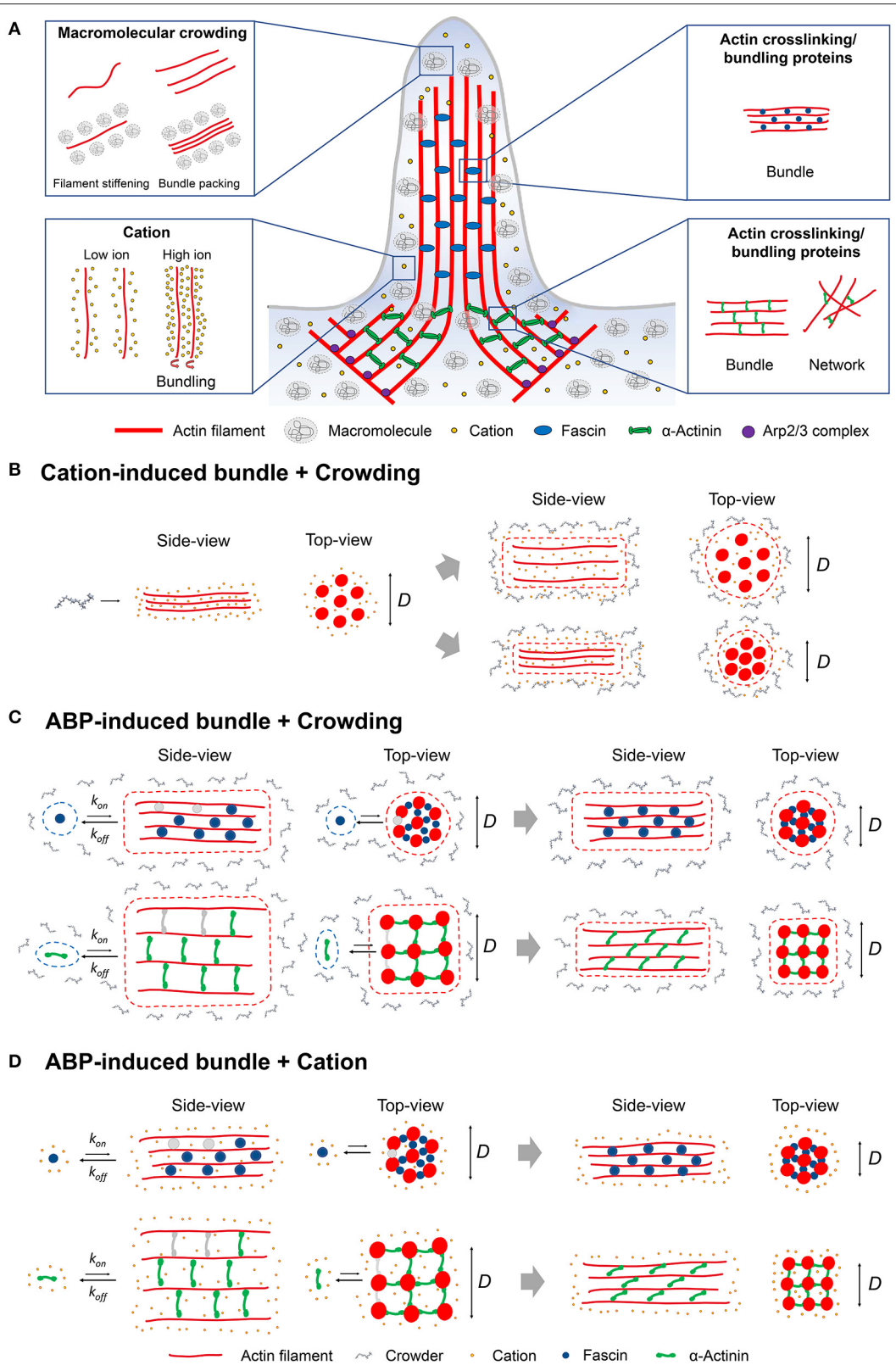

FIGURE 1 | (A) Schematic representation of the various intracellular factors such as macromolecular crowding, cation interactions, and actin-crosslinking/bundling proteins (fascin or α-actinin) that can induce actin bundling at the leading edge of a cell. **(B)** Cation-induced actin bundle formation in the presence of macromolecular crowding. Potential interactions between cations and crowding may affect the organization of bundles with a different bundle diameter (*D*). **(C)** Bundles induced

(Continued)

FIGURE 1 | by actin-crosslinking proteins [actin-binding proteins (ABPs)] in crowded environments. Potential competitive interactions between ABPs and crowding may affect the binding of ABPs to filaments as well as bundle organization. Actin bundling proteins bind to actin filament (gray; unbound state, blue and green; bound state) during bundle formation with k_{on}, which is slower than k_{off} due to reduced bundling interactions between actin filament and bundling proteins. Compared with small crosslinkers (e.g., fascin; blue), longer crosslinkers (e.g., α-actinin; green) yield a significant decrease in *D* since their orientation switches from perpendicular to angled on filament, affecting bundle compactness [9]. **(D)** ABP-induced bundle formation in the presence of cations can result in modulations to association/dissociation constant k_{on} and k_{off} by cations influencing bundle organization.

[11, 25], similar to DNA condensation [26]. In addition to depletion and electrostatic interactions, cells utilize various actin-crosslinking proteins to form crosslinked bundles or networks [2]. These actin-crosslinking proteins bind actin filaments with different on- and off-rates, influencing the dynamic organization of bundles [15, 27, 28].

The main goal of this review is to summarize major findings on how macromolecular crowding, cation interactions, and actin-crosslinking proteins influence the assembly, organization, and mechanics of actin bundles. In the first part, we describe the effects of depletion and cation interactions on bundle mechanics and structure. In the second part, we introduce the influence of both crowding and cation interactions on the organization and mechanics of bundles crosslinked by actin-binding proteins (ABPs). While the effects of either crowding, cations, or ABPs on actin bundle assembly and mechanics are well-characterized individually, we mainly focus on recent studies demonstrating the potential interplay between these factors on actin-bundling mechanisms.

EFFECTS OF DEPLETION AND CATION INTERACTIONS ON ACTIN BUNDLE MECHANICS AND STRUCTURE

Macromolecular crowding induces actin bundle assembly by generating depletion interactions [10, 12, 29, 30] through excluded volume effects [31]. Macromolecular crowding promotes attractive interactions between filaments by reducing the free energy required for bundle formation [10, 32, 33]. Depletion forces maximize the overlap between filaments by minimizing the system free energy [33] and generating sliding of filaments [34]. Crowding has been demonstrated to affect actin filament assembly kinetics [35–37], and filament stability has been evidenced by altered critical concentration of actin [38]. A recent study indicates that crowding enhances filament bending stiffness and alters filament conformations, including filament helical twist [39]. Although the effects of crowding on actin filament assembly are known, how crowding modulates bundle assembly kinetics is not well-understood. Changes to bundle assembly by crowding can potentially influence the mechanical properties of actin bundles.

The mechanical properties of depletion-induced actin bundles have been determined by measuring bundle bending stiffness, elastic moduli, and force between filaments (summarized in **Table 1**) [12, 50]. Previous *in vitro* studies have demonstrated that non-specific depletion forces can function as effective crosslinkers [10, 12, 40]. Bundle bending stiffness depends on the number of filaments per bundle and crosslinker effectiveness demonstrated by mechanical modeling as well as previous experimental evidence [12, 51]. Bundle bending stiffness was shown to quadratically scale with the number of filaments within the bundle [12]. Increasing polyethylene glycol (PEG) concentrations result in enhanced local elastic moduli of actin bundles and networks as well as an increase in bundle diameter, which were determined by microrheological analysis (**Table 1**) [40]. A recent study using optical tweezers determined the force exerted on two bundling filaments [23] by PEG, resulting in weaker bundling ($\sim$0.07 $\pm$ 0.006 pN) as compared to divalent cations (Mg^{2+}) ($\sim$0.20 $\pm$ 0.094 pN) (**Table 1**). Bundles induced by depletion interactions display distinct elastic responses to external forces, such as bending deformations, with minimal evidence of permanent damage [52]. Recently, *in vitro* motility assay and mathematical modeling have demonstrated that depletion-induced bundles exhibit a critical buckling length, which affects the bundle structure and is dependent on the bundle rigidity and the number of filaments in bundles [53]. Martiel et al. [53] demonstrated that as depletion-induced bundles increase in length, they reach a boundary transition that allows for bundle deformations (i.e., loops) although this boundary can be extended depending on bundle stiffness [53]. The relationship displayed between critical buckling length and persistence length as well as the number of filaments in a bundle is a key determinant in bundle deformation [53].

Cation interactions (non-specific electrostatic and/or specific ion binding) promote bundling of actin filaments, which are linear polyelectrolytes, through a reduction in electrostatic repulsion between filaments above a threshold cation concentration required for actin polymerization [17, 25, 54, 55]. High concentrations of divalent cations (e.g., Mg^{2+} and Ca^{2+}) were shown to condense actin filaments to bundles and induce over twisting of filaments in bundles, increasing bundle bending persistence length ranging from $\sim$15 to 45 μm (**Table 1**) [16]. Cation binding modulates the mechanics and structure of actin filaments, potentially affecting bundle mechanics and structure. Hocky et al. [56]. demonstrated, through molecular dynamics (MD) simulations that binding of divalent cations at the "stiffness cation site [57]," along an actin filament, induced the reorganization of the DNase-I binding loop (D-loop). Cation binding at the stiffness site generates a tighter twist angle distribution and affects filament torsional stiffness [56]. The addition of counterions further alters the structure of bundled filaments by changing the contact angle per monomer of the filament helices, obtaining an additional twist of $\sim$3.8° [25]. Recently, Gurmessa et al. [41] have shown the effects of varying concentrations of Mg^{2+} on the stiffness and elasticity of bundled networks

TABLE 1 | The geometric and mechanical properties of actin bundles induced by crowding, cations, and actin-crosslinking proteins.

Bundle-inducing factor	*D* (nm)	*L* (μm)	*N*	L_p (μm) or κ (pN· μm^2)	*G′* (Pa)	*F* (pN)	References
Polyethylene glycol (PEG)	∼ 2–20	N/A	∼ 6–20	$\kappa = \sim 1$–10	∼ 0.1–1	0.07 ± 0.006	[12, 23, 40]
Mg^{2+}	∼ 10–350	∼ 2–6	∼ 4–28	$L_p = \sim 15$–45	∼ 0.01–0.1	0.2 ± 0.094	[16, 23, 41]
Ca^{2+}	∼ 10–300	∼ 4–5	∼ 4–15	$L_p = \sim 12$–25	N/A	N/A	[16]
Fascin	∼ 10–140	∼ 5.4–7.7	∼ 3–30	$L_p = \sim 35$–170 $\kappa = \sim 0.4$–10	∼ 8.5 ± 0.8	N/A	[13, 14, 42–47]
α-Actinin	∼ 94–114	∼ 2.0–2.5	∼ 3–30	$L_p = \sim 18$ $\kappa = \sim 0.2$–10	∼ 44 ± 2	N/A	[42, 48, 49]
Fascin + crowding	∼ 108–173	∼ 2.3–2.7	∼7–13	$L_p = \sim 25$–95	N/A	N/A	[9]
α-Actinin + crowding	∼ 52–130	∼ 3–12	∼8–15	$L_p = \sim 10$	N/A	N/A	[9]

D, bundle diameter; L, bundle length; N, No. of filaments per bundle; L_p, persistence length; κ, bending stiffness; G', Elastic modulus; F, forces between filaments within a bundle.

using optical tweezers microrheology and confocal microscopy imaging. They demonstrated that the stiffness, elasticity, and non-linear force response of the actin network increase with increasing concentration of Mg^{2+} (≥10 mM) (**Table 1**) [41]. Cation binding at discrete sites along actin filaments can lead to bundle formation and promote modulations to bundle structural properties, such as helical twist [16, 25, 41, 58, 59]. Small-angle x-ray scattering (SAXS) showed that actin filaments condensed into bundles display an over twisting of filaments within the bundles [25]. The observed helical twisting of bundles due to cation interactions was corroborated in a recent study that showed cations specifically bind between filaments at key amino acid residues promoting helical twist of bundles [16]. Cation-induced bundles were shown to retain their secondary structures under high pressures (up to ∼5 kbar) and temperatures (up to ∼60°C), evidenced by Fourier transform infrared (FTIR) spectroscopy [36].

Although investigations into the effects of cations and crowding on actin bundling have been individually shown, the interplay of both factors together has not been well-established. A previous study demonstrated that the onset of bundling promoted by depletion (PEG) and electrostatic interactions exhibits opposite dependence on cation (K^+) concentrations [29]. A possible competition between electrostatic and depletion interactions can modulate the assembly and organization of actin bundles (**Figure 1B**). Experimental evidence has demonstrated the individual impacts of both crowding and ionic interactions on actin filament or bundle structure [16, 25]. For example, high divalent cation concentrations condense actin filaments to form bundles, resulting in changes to filament helical symmetry [25]. A potential competition between the bending energy of helical filaments and the binding energy of crosslinkers can contribute to finite bundle sizes [60]. We speculate that the concentrations, types, and size of crowding agents and cations contribute to alterations in actin bundle structure by changes in bending and/or binding energy. A recent study on PEG-induced microtubule bundling indicated that cohesive interactions between microtubules depend on the attractive depletion interactions and electrostatic repulsion [61]. Investigations into the opposite effects of depletion and cation interactions have been performed with DNA [62]. Krotova et al. [62] demonstrated competition, upon an increase in salt concentration between entropy and ionic interactions, of DNA undergoing an unfolding transition in crowded environments. These studies illustrate the counteracting effects of crowding and cation interactions on bundling of cytoskeletal biopolymers as well as DNA condensation. Further studies on the combined effects of both crowding and cation interactions are necessary to determine their impacts on actin bundle mechanics and structures.

THE INFLUENCE OF CROWDING AND CATION INTERACTIONS ON THE ORGANIZATION AND MECHANICS OF ACTIN BUNDLES CROSSLINKED BY ACTIN-BINDING PROTEINS

Actin-crosslinking and bundling proteins can assemble filaments into higher-ordered structures such as bundles and networks [2, 4, 63]. The size of the crosslinker size, the kinetics of crosslinkers, and the binding affinity of crosslinkers, along with competitive or cooperative interaction between crosslinkers can influence the architecture as well as mechanical properties of actin bundles [15, 27, 28, 42, 51]. The size of actin-crosslinking proteins determines the architecture and compactness of bundles. For example, fascin is an crosslinking protein (diameter ∼6 nm), which forms tightly packed bundles, whereas α-actinin is a larger-sized crosslinker (diameter ∼35 nm) inducing widely spaced bundles and/or networks [12, 15]. The bending stiffness of fascin- and α-actinin-induced bundles depends on interfilament spacing, supporting an important role of bundle architecture and compactness in bending mechanics of ABP-crosslinked bundles (**Table 1**) [12, 51]. Binding kinetics (on- and off-rates) and binding affinity of both fascin and α-actinin to filaments have been shown to affect actin bundle assembly and architecture [27, 28]. Competitive interactions between fascin and α-actinin have been shown in a recent study, where fascin-induced bundles, in the presence of α-actinin, were observed to have a reduction in bundle stiffness and filopodia protrusions with varying concentrations of α-actinin [43]. In comparison, combining α-actinin and filamin results in more enhanced elastic moduli of

actin filament networks formed by each crosslinker, supporting their cooperative interactions [64].

In a living cell, actin bundles induced by ABPs are formed in a crowded cytoplasm; therefore, it is important to understand how crowding modulates ABP-induced bundling. Changes in filament bending stiffness and conformations in crowded environments [39] can influence interactions between filaments and ABPs, including actin-crosslinking proteins (e.g., fascin and α-actinin) [9] and severing proteins (e.g., gelsolin) [65]. Crowders with different sizes and concentrations [PEG and methylcellulose (MC)] have been shown to affect the organization patterns and potentially nucleation/growth of microtubule bundles crosslinked with microtubule-associated protein (MAP65) [66]. Potential competitive interactions between crowding (PEG, sucrose, and Ficoll) and actin-crosslinking proteins, fascin, and α-actinin, have recently begun to be explored [9]. Macromolecular crowding influences the organization of either fascin or α-actinin bundles by reducing binding interactions between actin filaments and crosslinking proteins (**Figure 1C** and **Table 1**), evidenced by fluorescence microscopy and atomic force microscopy imaging along with MD simulations [9]. MD simulations indicated that macromolecular crowding increases interaction energy between fascin or α-actinin and filaments, and reduces the number of hydrogen bonds [9].

Competitive binding of actin-crosslinking proteins, such as fascin and α-actinin, affects their sorting in a size-dependent manner, thereby influencing the actin bundle structure [15]. Furthermore, recent studies suggest that physical confinement has a significant impact on the mechanics and structure of bundles induced by these actin-crosslinking proteins [43, 67]. Giant unilamellar vesicles (GUVs) were used to demonstrate the impacts of enclosed boundary conditions on self-assembly of actin networks and competition between fascin and α-actinin [43]. The physical confinement has a drastic impact on the formation of actin networks, where larger-diameter ($>16\,\mu m$) GUV resulted in a greater probability of actin network/aster formation and reductions in ring formation, directly driving the sorting of fascin [43] and α-actinin [67]. Live cells can introduce a boundary of lipid bilayers that potentially interact with the formation of networks by ABPs [42, 43, 68]. The effects of macromolecular crowding on the self-organization of actin rings by heavy meromyosin (HMM) and α-actinin in confinement have been previously investigated [69]. Crowding agent MC was shown to hinder the contraction of actin rings formed by either α-actinin or HMM in GUVs [69]. Overall, the encapsulation of the actin cytoskeleton can be a regulatory mechanism that facilitates the reorganization of actin bundled networks and potential interactions with lipid membranes.

Cation interactions impact the conformations of actin-crosslinking proteins as well as actin filaments, potentially influencing the mechanics and structure of ABP-induced bundles and/or networks (**Figure 1D**). The actin filament-binding domain, calponin-homology (CH) domain, is found in various types of actin-crosslinking proteins such as α-actinin and filamin [70]. Divalent cation binding has been shown to induce structural transitioning of the CH domain, impacting actin bundle formation by ABPs. For example, Pinotsis et al. demonstrated that Ca^{2+} binding to α-actinin increases the rigidity of α-actinin, leading to the hindrance of actin bundle formation [71]. Cation binding modulates the bending stiffness of actin filaments [57] and the rheological properties of actin networks [72]. Bidone et al. [72] showed that changes in filament rigidity incurred by specific cation binding result in different strain-stiffening responses of actin networks that depend on the flexibility of actin crosslinkers. Overall, these studies indicate that cation interactions with actin filaments and crosslinking proteins are key modulators in bundle formation as well as mechanics.

SUMMARY AND OUTLOOK

In this review, we gave an overview of the growing body of work demonstrating how intracellular environmental factors, specifically macromolecular crowding and cation interactions, modulate the assembly, mechanics, and structure of both non-crosslinked actin bundles and ABP-induced bundles. Studies highlighted that both depletion and cation interactions are key players in the tight regulation of actin bundling. Given that actin bundles respond to changes in intracellular environmental factors, it is important to understand (1) whether combined environmental factors act synergistically or competitively to control bundle assembly and (2) how the interactions between actin crosslinkers and crowding and/or cation binding modulate bundle mechanics and structure. Knowledge gained from *in vitro* studies on actin-bundling mechanisms will enhance our understanding of how complex cellular environments influence actin cytoskeleton organization and mechanics. Future studies will benefit from investigating how the actin cytoskeleton actively responds to local changes in intracellular environments as well as external stimuli shaping its architecture, organization, function, and mechanical properties.

AUTHOR CONTRIBUTIONS

All authors contributed to the analysis, organizing, writing of the manuscript, commented on, and approved the submitted version.

ACKNOWLEDGMENTS

The authors would like to thank the financial support provided by the National Science Foundation under Grant No. 1943266 (to EHK) and the National Institute of Allergy and Infectious Diseases of the National Institutes of Health under Award Number R01AI139242, as well as the funds from the University of Central Florida (UCF) awarded to EHK.

REFERENCES

1. Mogilner A, Rubinstein B. The physics of filopodial protrusion. *Biophys J*. (2005) 89:782–95. doi: 10.1529/biophysj.104.056515
2. Blanchoin L, Boujemaa-Paterski R, Sykes C, Plastino J. Actin dynamics, architecture, and mechanics in cell motility. *Physiol Rev*. (2014) 94:235–63. doi: 10.1152/physrev.00018.2013
3. Zsolnay V, Katkar HH, Chou SZ, Pollard TD, Voth GA. Structural basis for polarized elongation of actin filaments. *Proc Natl Acad Sci USA*. (2020) 117:30458–64. doi: 10.1073/pnas.2011128117
4. De La Cruz EM, Gardel ML. Actin mechanics and fragmentation. *J Biol Chem*. (2015) 290:17137–44. doi: 10.1074/jbc.R115.636472
5. Mitchison TJ, Cramer LP. Actin-based cell motility and cell locomotion. *Cell*. (1996) 84:371–9. doi: 10.1016/S0092-8674(00)81281-7
6. Pollard TD, Cooper JA. Actin, a central player in cell shape and movement. *Science*. (2009) 326:1208–12. doi: 10.1126/science.1175862
7. Narayanan P, Chatterton P, Ikeda A, Ikeda S, Corey DP, Ervasti JM, et al. Length regulation of mechanosensitive stereocilia depends on very slow actin dynamics and filament-severing proteins. *Nat Commun*. (2015) 6:6855. doi: 10.1038/ncomms7855
8. Rückerl F, Lenz M, Betz T, Manzi J, Martiel J-L, Safouane M, et al. Adaptive response of actin bundles under mechanical stress. *Biophys J*. (2017) 113:1072–9. doi: 10.1016/j.bpj.2017.07.017
9. Park J, Lee M, Lee B, Castaneda N, Tetard L, Kang EH. Crowding tunes the organization and mechanics of actin bundles formed by crosslinking proteins. *FEBS Lett*. (2021) 595:26–40. doi: 10.1002/1873-3468.13949
10. Hosek M, Tang JX. Polymer-induced bundling of F-actin and the depletion force. *Phys Rev E Stat Nonlin Soft Matter Phys*. (2004) 69:051907. doi: 10.1103/PhysRevE.69.051907
11. Angelini TE, Sanders LK, Liang H, Wriggers W, Tang JX, Wong GC. Structure and dynamics of condensed multivalent ions within polyelectrolyte bundles: a combined x-ray diffraction and solid-state NMR study. *J Phys Condens Matter*. (2005) 17:S1123–35. doi: 10.1088/0953-8984/17/14/001
12. Claessens MM, Bathe M, Frey E, Bausch AR. Actin-binding proteins sensitively mediate F-actin bundle stiffness. *Nat Mater*. (2006) 5:748–53. doi: 10.1038/nmat1718
13. Jansen S, Collins A, Yang C, Rebowski G, Svitkina T, Dominguez R. Mechanism of actin filament bundling by fascin. *J Biol Chem*. (2011) 286:30087–96. doi: 10.1074/jbc.M111.251439
14. Takatsuki H, Bengtsson E, Mansson A. Persistence length of fascin-cross-linked actin filament bundles in solution and the *in vitro* motility assay. *Biochim Biophys Acta*. (2014) 1840:1933–42. doi: 10.1016/j.bbagen.2014.01.012
15. Winkelman JD, Suarez C, Hocky GM, Harker AJ, Morganthaler AN, Christensen JR, et al. Fascin-and α-actinin-bundled networks contain intrinsic structural features that drive protein sorting. *Curr Biol*. (2016) 26:2697–706. doi: 10.1016/j.cub.2016.07.080
16. Castaneda N, Zheng T, Rivera-Jacquez HJ, Lee H-J, Hyun J, Balaeff A, et al. Cations modulate actin bundle mechanics, assembly dynamics, and structure. *J Phys Chem B*. (2018) 122:3826–35. doi: 10.1021/acs.jpcb.8b00663
17. Schnauß, J., Händler T, Käs JA. Semiflexible biopolymers in bundled arrangements. *Polymers*. (2016) 8:274. doi: 10.3390/polym8080274
18. Minton AP. Implications of macromolecular crowding for protein assembly. *Curr Opin Struct Biol*. (2000) 10:34–9. doi: 10.1016/S0959-440X(99)00045-7
19. Kuznetsova IM, Turoverov KK, Uversky VN. What macromolecular crowding can do to a protein. *Int J Mol Sci*. (2014) 15:23090–140. doi: 10.3390/ijms151223090
20. Shahid S, Hassan MI, Islam A, Ahmad F. Size-dependent studies of macromolecular crowding on the thermodynamic stability, structure and functional activity of proteins: *in vitro* and *in silico* approaches. *Biochim Biophys Acta General Subjects*. (2017) 1861:178–97. doi: 10.1016/j.bbagen.2016.11.014
21. Sarkar M, Li C, Pielak GJ. Soft interactions and crowding. *Biophys Rev*. (2013) 5:187–94. doi: 10.1007/s12551-013-0104-4
22. Sarkar M, Lu J, Pielak GJ. Protein crowder charge and protein stability. *Biochemistry*. (2014) 53:1601–6. doi: 10.1021/bi4016346
23. Streichfuss M, Erbs F, Uhrig K, Kurre R, Clemen AE, Bohm CH, et al. Measuring forces between two single actin filaments during bundle formation. *Nano Lett*. (2011) 11:3676–80. doi: 10.1021/nl201630y
24. Huber F, Strehle D, Schnauß J, Käs J. Formation of regularly spaced networks as a general feature of actin bundle condensation by entropic forces. *New J Phys*. (2015) 17:043029. doi: 10.1088/1367-2630/17/4/043029
25. Angelini TE, Liang H, Wriggers W, Wong GC. Like-charge attraction between polyelectrolytes induced by counterion charge density waves. *Proc Natl Acad Sci USA*. (2003) 100:8634–37. doi: 10.1073/pnas.1533355100
26. Manning GS. Counterion binding in polyelectrolyte theory. *Acc Chem Res*. (1979) 12:443–9. doi: 10.1021/ar50144a004
27. Courson DS, Rock RS. Actin cross-link assembly and disassembly mechanics for alpha-Actinin and fascin. *J Biol Chem*. (2010) 285:26350–7. doi: 10.1074/jbc.M110.123117
28. Falzone TT, Lenz M, Kovar DR, Gardel ML. Assembly kinetics determine the architecture of α-actinin crosslinked F-actin networks. *Nat Commun*. (2012) 3:1–9. doi: 10.1038/ncomms1862
29. Tang JX, Ito T, Tao T, Traub P, Janmey PA. Opposite effects of electrostatics and steric exclusion on bundle formation by F-actin and other filamentous polyelectrolytes. *Biochemistry*. (1997) 36:12600–7. doi: 10.1021/bi9711386
30. Köhler S, Lieleg O, Bausch AR. Rheological characterization of the bundling transition in F-actin solutions induced by methylcellulose. *PLoS ONE*. (2008) 3:2736. doi: 10.1371/journal.pone.0002736
31. Minton AP. The influence of macromolecular crowding and macromolecular confinement on biochemical reactions in physiological media. *J Biol Chem*. (2001) 276:10577–80. doi: 10.1074/jbc.R100005200
32. Lau AW. C., Prasad A, Dogic Z. Condensation of isolated semi-flexible filaments driven by depletion interactions. *Europhys Lett*. (2009) 87:48006. doi: 10.1209/0295-5075/87/48006
33. Braun M, Lansky Z, Hilitski F, Dogic Z, Diez S. Entropic forces drive contraction of cytoskeletal networks. *BioEssays*. (2016) 38:474–81. doi: 10.1002/bies.201500183
34. Ward A, Hilitski F, Schwenger W, Welch D, Lau AW, Vitelli V, et al. Solid friction between soft filaments. *Nat Mater*. (2015) 14:583–8. doi: 10.1038/nmat4222
35. Drenckhahn D, Pollard TD. Elongation of actin filaments is a diffusion-limited reaction at the barbed end and is accelerated by inert macromolecules. *J Biol Chem*. (1986) 261:12754–8. doi: 10.1016/S0021-9258(18)67157-1
36. Rosin C, Erlkamp M, Ecken JV, Raunser S, Winter R. (2014). Exploring the stability limits of actin and its suprastructures. *Biophys. J*. 107:2982–92. doi: 10.1016/j.bpj.2014.11.006
37. Rosin C, Estel K, Halker J, Winter R. Combined effects of temperature, pressure, and co-solvents on the polymerization kinetics of actin. *ChemPhysChem*. (2015) 16:1379–85. doi: 10.1002/cphc.201500083
38. Frederick KB, Sept D, De La Cruz EM. Effects of solution crowding on actin polymerization reveal the energetic basis for nucleotide-dependent filament stability. *J Mol Biol*. (2008) 378:540–50. doi: 10.1016/j.jmb.2008.02.022
39. Castaneda N, Lee M, Rivera-Jacquez HJ, Marracino RR, Merlino TR, Kang H. Actin filament mechanics and structure in crowded environments. *J Phys Chem B*. (2019) 123:2770–9. doi: 10.1021/acs.jpcb.8b12320
40. Tharmann R, Claessens M, Bausch A. Micro-and macrorheological properties of actin networks effectively cross-linked by depletion forces. *Biophys J*. (2006) 90:2622–7. doi: 10.1529/biophysj.105.070458
41. Gurmessa B, Francis M, Rust MJ, Das M, Ross JL, Robertson-Anderson RM. Counterion crossbridges enable robust multiscale elasticity in actin networks. *Phys Rev Res*. (2019) 1:013016. doi: 10.1103/PhysRevResearch.1.013016
42. Tseng Y, Kole TP, Lee JS, Fedorov E, Almo SC, Schafer BW, et al. How actin crosslinking and bundling proteins cooperate to generate an enhanced cell mechanical response. *Biochem Biophys Res Commun*. (2005) 334:183–92. doi: 10.1016/j.bbrc.2005.05.205
43. Bashirzadeh Y, Wubshet NH, Liu AP. Confinement geometry tunes fascin-actin bundle structures and consequently the shape of a lipid bilayer vesicle. *Front Molec Biosci*. (2020) 7:610277. doi: 10.3389/fmolb.2020.610277
44. Lieleg O, Claessens MM, Heussinger C, Frey E, Bausch AR. Mechanics of bundled semiflexible polymer networks. *Phys Rev Lett*. (2007) 99:088102. doi: 10.1103/PhysRevLett.99.088102

45. Claessens MM, Semmrich C, Ramos L, Bausch AR. Helical twist controls the thickness of F-actin bundles. *Proc Natl Acad Sci USA*. (2008) 105:8819–22. doi: 10.1073/pnas.0711149105
46. Ishikawa R, Sakamoto T, Ando T, Higashi-Fujime S, Kohama K. Polarized actin bundles formed by human fascin-1: their sliding and disassembly on myosin II and myosin V *in vitro*. *J Neurochem*. (2003) 87:676–85. doi: 10.1046/j.1471-4159.2003.02058.x
47. Haviv L, Gov N, Ideses Y, Bernheim-Groswasser A. Thickness distribution of actin bundles *in vitro*. *Eur Biophys J*. (2008) 37:447–54. doi: 10.1007/s00249-007-0236-1
48. Ghosh S, Park J, Thomas M, Cruz E, Cardona O, Kang H, et al. Biophysical characterization of actin bundles generated by the *Chlamydia trachomatis* Tarp effector. *Biochem Biophys Res Commun*. (2018) 500:423–8. doi: 10.1016/j.bbrc.2018.04.093
49. Kang B, Jo S, Baek J, Nakamura F, Hwang W, Lee H. Role of mechanical flow for actin network organization. *Acta Biomater*. (2019) 90:217–24. doi: 10.1016/j.actbio.2019.03.054
50. Schnauß J, Golde T, Schuldt C, Schmidt BS, Glaser M, Strehle D, et al. Transition from a linear to a harmonic potential in collective dynamics of a multifilament actin bundle. *Phys Rev Lett*. (2016) 116:108102. doi: 10.1103/PhysRevLett.116.108102
51. Bathe M, Heussinger C, Claessens MM, Bausch AR, Frey E. Cytoskeletal bundle mechanics. *Biophys J*. (2008) 94:2955–64. doi: 10.1529/biophysj.107.119743
52. Strehle D, Mollenkopf P, Glaser M, Golde T, Schuldt C, Käs JA, et al. Single actin bundle rheology. *Molecules*. (2017) 22:1804. doi: 10.3390/molecules22101804
53. Martiel J-L, Michelot A, Boujemaa-Paterski R, Blanchoin L, Berro J. Force production by a bundle of growing actin filaments is limited by its mechanical properties. *Biophys J*. (2020) 118:182–92. doi: 10.1016/j.bpj.2019.10.039
54. Tang JX, Wong S, Tran PT, Janmey PA. Counterion induced bundle formation of rodlike polyelectrolytes. *Ber Bunsenges Phys Chem*. (1996) 100:796–806. doi: 10.1002/bbpc.19961000620
55. Kang H, Bradley MJ, Elam WA, De La Cruz EM. Regulation of actin by ion-linked equilibria. *Biophys J*. (2013) 105:2621–8. doi: 10.1016/j.bpj.2013.10.032
56. Hocky GM, Baker JL, Bradley MJ, Sinitskiy AV, De La Cruz EM, Voth GA. Cations stiffen actin filaments by adhering a key structural element to adjacent subunits. *J Phys Chem B*. (2016) 120:4558–67. doi: 10.1021/acs.jpcb.6b02741
57. Kang H, Bradley MJ, Mccullough BR, Pierre A, Grintsevich EE, Reisler E, et al. Identification of cation-binding sites on actin that drive polymerization and modulate bending stiffness. *Proc Natl Acad Sci USA*. (2012) 109:16923–7. doi: 10.1073/pnas.1211078109
58. Gao M, Berghaus M, Von Der Ecken J, Raunser S, Winter R. Condensation agents determine the temperature–pressure stability of F-actin bundles. *Angewandte Chem Int Ed*. (2015) 54:11088–92. doi: 10.1002/anie.201504247
59. Ricketts S, Khanal P, Rust M, Das M, Ross J, Robertson-Anderson R. Triggering cation-induced contraction of cytoskeleton networks *via* microfluidics. *J Front Phys*. (2020) 2020:596699. doi: 10.3389/fphy.2020.596699
60. Gov NS. Packing defects and the width of biopolymer bundles. *Phys Rev E Stat Nonlin Soft Matter Phys*. (2008) 78:011916. doi: 10.1103/PhysRevE.78.011916
61. Hilitski F, Ward AR, Cajamarca L, Hagan MF, Grason GM, Dogic Z. Measuring cohesion between macromolecular filaments one pair at a time: depletion-induced microtubule bundling. *Phys Rev Lett*. (2015) 114:138102. doi: 10.1103/PhysRevLett.114.138102
62. Krotova M, Vasilevskaya V, Makita N, Yoshikawa K, Khokhlov A. DNA compaction in a crowded environment with negatively charged proteins. *Phys Rev Lett*. (2010) 105:128302. doi: 10.1103/PhysRevLett.105.128302
63. Pollard TD. Actin and actin-binding proteins. *Cold Spring Harb Perspect Biol*. (2016) 8:a018226. doi: 10.1101/cshperspect.a018226
64. Esue O, Tseng Y, Wirtz D. Alpha-actinin and filamin cooperatively enhance the stiffness of actin filament networks. *PLoS ONE*. (2009) 4:e4411. doi: 10.1371/journal.pone.0004411
65. Heidings JB, Demosthene B, Merlino TR, Castaneda N, Kang EH. Gelsolin-mediated actin filament severing in crowded environments. *Biochem Biophys Res Commun*. (2020) 532:548–54. doi: 10.1016/j.bbrc.2020.08.041
66. Sahu S, Herbst L, Quinn R, Ross JL. Crowder and surface effects on self-organization of microtubules. *arXiv preprint arXiv, 2009.04669*. (2020) 7.
67. Bashirzadeh Y, Redford SA, Lorpaiboon C, Groaz A, Litschel T, Schwille P, et al. Actin crosslinker competition and sorting drive emergent GUV size-dependent actin network architecture. *bioRxiv*. (2020). doi: 10.1101/2020.10.03.322354
68. Liu AP, Fletcher DA. Actin polymerization serves as a membrane domain switch in model lipid bilayers. *Biophys J*. (2006) 91:4064–70. doi: 10.1529/biophysj.106.090852
69. Miyazaki M, Chiba M, Eguchi H, Ohki T, Ishiwata S. Cell-sized spherical confinement induces the spontaneous formation of contractile actomyosin rings *in vitro*. *Nat Cell Biol*. (2015) 17:480–9. doi: 10.1038/ncb3142
70. Korenbaum E, Rivero F. Calponin homology domains at a glance. *J Cell Sci*. (2002) 115:3543–5. doi: 10.1242/jcs.00003
71. Pinotsis N, Zielinska K, Babuta M, Arolas JL, Kostan J, Khan MB, et al. Calcium modulates the domain flexibility and function of an α-actinin similar to the ancestral α-actinin. *Proc Natl Acad Sci USA*. (2020) 117:22101–12. doi: 10.1073/pnas.1917269117
72. Bidone TC, Kim T, Deriu MA, Morbiducci U, Kamm RD. Multiscale impact of nucleotides and cations on the conformational equilibrium, elasticity and rheology of actin filaments and crosslinked networks. *Biomech Model Mechanobiol*. (2015) 14:1143–55. doi: 10.1007/s10237-015-0660-6

Conflict of Interest: The authors declare that the research was conducted in the absence of any commercial or financial relationships that could be construed as a potential conflict of interest.

frontiers in Physics

ORIGINAL RESEARCH
published: 28 May 2021
doi: 10.3389/fphy.2021.673875

Chemomechanical Simulation of Microtubule Dynamics With Explicit Lateral Bond Dynamics

*Matthias Schmidt and Jan Kierfeld**

Department of Physics, TU Dortmund University, Dortmund, Germany

We introduce and parameterize a chemomechanical model of microtubule dynamics on the dimer level, which is based on the allosteric tubulin model and includes attachment, detachment and hydrolysis of tubulin dimers as well as stretching of lateral bonds, bending at longitudinal junctions, and the possibility of lateral bond rupture and formation. The model is computationally efficient such that we reach sufficiently long simulation times to observe repeated catastrophe and rescue events at realistic tubulin concentrations and hydrolysis rates, which allows us to deduce catastrophe and rescue rates. The chemomechanical model also allows us to gain insight into microscopic features of the GTP-tubulin cap structure and microscopic structural features triggering microtubule catastrophes and rescues. Dilution simulations show qualitative agreement with experiments. We also explore the consequences of a possible feedback of mechanical forces onto the hydrolysis process and the GTP-tubulin cap structure.

Keywords: microtubule dynamics, dynamic instability, chemomechanical model, catastrophes, hydrolysis, microtubule, cytoskeleton

OPEN ACCESS

Edited by:
Yuan Lin,
The University of Hong Kong, China

Reviewed by:
Chao Fang,
The University of Hong Kong, China
Jin Qian,
Zhejiang University, China

****Correspondence:***
Jan Kierfeld
jan.kierfeld@tu-dortmund.de

Specialty section:
This article was submitted to Biophysics, a section of the journal Frontiers in Physics

Received: *28 February 2021*
Accepted: *26 April 2021*
Published: *28 May 2021*

Citation:
Schmidt M and Kierfeld J (2021) Chemomechanical Simulation of Microtubule Dynamics With Explicit Lateral Bond Dynamics. Front. Phys. 9:673875. doi: 10.3389/fphy.2021.673875

1. INTRODUCTION

Microtubule (MT) dynamics is essential for many cellular processes, such as the positioning and separation of chromosomes in mitosis [1], or maintenance of cell polarity and cell shape [2]. An important feature, which enables MTs to exert pulling and pushing forces in these cellular processes, is their dynamic instability, which is the stochastic switching of MTs between states of growth by polymerization and states of fast shrinkage by depolymerization [3].

Switching from growth into shrinkage happens in catastrophe events, whose mechanism and triggers are not completely understood on the molecular level, but they are associated with a loss of the GTP-cap by hydrolysis within the MT [4, 5] (see references [6, 7] for reviews). Hydrolysis is strongly coupled to mechanics of the MT, as is clearly seen in the curling of MT protofilaments into a "ram's horn" conformation after the catastrophe and during the shrinking phase [8]. The loss of the stabilizing GTP-cap triggers a release of binding energy and stored mechanical energy in the tubular MT structure. Therefore, shrinkage following a catastrophe is more than simple depolymerization of the MT; it is rather a rupture or crack propagation process between protofilaments, which releases chemical and mechanical energy while it propagates toward the minus end. The energy released during shrinking has biological functions and can be employed to exert pulling forces onto kinetochores during separation of MTs in mitosis [9].

The curling of hydrolyzed protofilaments into a ram's horn structure shows that GDP-tubulin dimers have a bent conformation [8, 10–12]. Tubulin dimers assembled within the MT body are in a straight conformation, on the other hand [13]. Hydrolysis of tubulin dimers embedded in a straight MT causes mechanical strains in the tubular structure because the surrounding MT lattice prevents these GDP-tubulin dimers from assuming their preferred bent conformation. This mechanical strain is released in a catastrophe via the rupture of lateral bonds.

There are different models explaining how the mechanical strain is increased by hydrolysis or how lateral bonds are weakened by hydrolysis such that the strained MT becomes more prone for catastrophes. The first cryo-electron microscopy (EM) studies showed blunt tips for growing MTs but curved tips for shrinking MTs [8] suggesting that GTP-protofilaments are straight while GDP-protofilaments are curved. Later evidence from cryo-EM showed that GTP-protofilaments are also curved, but significantly less than GDP-protofilaments [10]. The *allosteric model* is based on the assumption that hydrolysis of a tubulin dimer changes the dimer conformation from a rather straight GTP-conformation to a bent GDP-conformation. Hydrolysis of tubulin dimers embedded in a straight MT causes mechanical strain in the tubular structure because the surrounding MT lattice prevents these GDP-tubulin dimers from assuming their preferred bent conformation. This model was employed in almost all previous MT simulation models that consider MT mechanics [14–19]. The *lattice model*, on the other hand, is based on evidence from X-ray and cryo-EM structures [20–23] and simulations [24, 25] that also GTP-tubulin dimers assume a bent conformation and that hydrolysis rather affects the lateral and longitudinal dimer interaction energies. It is supported by recent experimental observations that both growing and shrinking MTs have bent protofilament ends [26]. Reference [26] also presents first simulation results with a lattice model. But there is also recent evidence from molecular dynamics (MD) simulation pointing in a different direction and supporting an intermediate model, where hydrolysis affects interactions but also lowers GDP-tubulin flexibility [27]. If hydrolysis weakens lateral interaction energies, hydrolysis makes the MT structure more prone for a catastrophe. While in the allosteric model, the mechanical strain in the structure is increased by hydrolysis, in the lattice model, the mechanical strain that the MT structure can tolerate is reduced by hydrolysis. In both models, the result is an increased propensity for lateral bonds to rupture. Therefore, chemomechanical MT models with explicit bond rupture are a necessity to reproduce catastrophes. We build on existing modeling approaches based on the allosteric model [14–19] and include lateral bond rupture as explicit stochastic events with force-dependent rates, which can give important clues about how catastrophes are triggered in the MT structure.

The influence of tubulin dimer hydrolysis onto the mechanics of the MT lattice suggests that, vice versa, mechanical forces and torques acting on tubulin dimers via strains in the tubular structure could also affect hydrolysis rates, an effect which has been explored only in reference [17] previously. Although this interplay is plausible from a mechanochemistry point of view, experimental verification on the dimer level is extremely difficult and not possible yet, but we can employ chemomechanical MT models to explore and suggest possible implications for the dynamic instability.

The coupling between chemical events—namely polymerization events, dimer hydrolysis, bond rupture—and mechanical forces because of conformational changes due to these chemical events, is a characteristic of MTs and requires chemomechanical MT models on the dimer level in order to develop a microscopic understanding of their dynamic instability including catastrophe and rescue events [28]. In this respect, chemomechanical models go beyond a phenomenological description of MT dynamics in a four-parameter model based on growth and shrinking velocities and phenomenological catastrophe and rescue rates [29]. The challenge for microscopic chemomechanical models is to include all chemical events as stochastic processes, to perform conformational relaxation governed by MT mechanics following each chemical event, and, eventually, to also include the feedback of mechanical forces within the MT onto reaction rates of the chemical events.

We present a stochastic chemomechanical MT model on the dimer level. Our model includes (i) a mechanical model of the MT containing lateral elastic bonds between tubulin monomers in neighboring protofilaments and a harmonic bending energy between tubulin monomers with a non-zero equilibrium angle after hydrolysis (allosteric model), (ii) stochastic addition and removal of tubulin dimers, (iii) explicit stochastic lateral bond rupture and bond formation; the bond rupture rate is coupled to the mechanical stress state of the bond and thus via elastic interactions within the MT lattice also to the other bonds, (iv) stochastic hydrolysis of dimers with a rate that can also couple to the mechanical bending stress in the dimer. The stochastic kinetics (ii)–(iv) is handled by a Gillespie algorithm and after each stochastic event, a mechanical energy minimization mimicking the relaxational dynamics of the structure is applied to the MT.

In order to parameterize our model, we will focus on the simplified scenarios of a growing MT consisting of GTP-tubulin only and a shrinking MT consisting of GDP-tubulin only. In both cases, we can neglect hydrolysis (iv); in the growing GTP-MT, we can also neglect mechanics, which is generated by hydrolysis. In the presence of mechanics and hydrolysis, repeated catastrophe and rescue events are obtained and will be described and analyzed. One problem in chemomechanical MT models is the computational effort associated with the mechanical relaxation. We investigate in detail, which level of computational effort is necessary in our model to obtain a sufficient mechanical relaxation following each chemical event, on the one hand, and which simplifications can be taken to assure a finite simulation time for growing MTs, on the other hand. This will allow us to simulate arbitrarily long growing MTs at fixed computational speed.

Our chemomechanical model has to be compared to previous modeling approaches, which include the mechanics of the MT [14–19]:

- References [15, 16] employ the allosteric model for dimer bending and include stochastic addition and removal of dimers. Hydrolysis is random. Mechanical energy

minimization is performed only locally on randomly selected dimers. Lateral bond rupture is not implemented as explicit stochastic process but only included using a threshold energy criterion.

- The models in references [14, 19] focus on mechanics and do not include dimer addition and removal. They are also based on the allosteric model but consider fixed hydrolysis states. In reference [14], the lateral bond energy landscape is harmonic around a minimum but includes an energy barrier and a dissociated, i.e., ruptured state. Global energy minimization gives the final state of the static structure.
- In reference [18], the stochastic kinetics is added to a mechanical model similar to Molodtsov et al. [14]. Here, the mechanical relaxation and lateral bond rupture is performed using Brownian dynamics (which include thermal fluctuations) with small time steps (equivalent to 2×10^7 minimization steps), which is only applied to 300 tubulin dimers at the plus end. Stochastic addition of dimers and removal by rupture of lateral and longitudinal bonds is included. The rupture of lateral bonds happens by activation over the bond energy barrier, the longitudinal rupture by a threshold criterion. Hydrolysis is random and stochastic with a rate that is independent of mechanics.
- Reference [17] is also based on the allosteric model. Lateral bond rupture is possible using a threshold criterion. Mechanical energy minimization was performed globally. There is no addition or removal of dimers, but hydrolysis is included. In a first attempt to include a coupling of the hydrolysis rate to mechanical forces, the hydrolysis kinetics remained deterministic, however, with the most probable hydrolysis event determined by mechanical forces. In the present paper, we will add addition and removal of dimers and a fully stochastic hydrolysis kinetics.

Our chemomechanical model has also to be compared to previous purely chemical modeling approaches on the dimer level but without explicit mechanical model [30–34]. These models include attachment and detachment of tubulin dimers; some of these models [32–34] also include lateral bond rupture and are thus able to produce crack-like catastrophe events. Crack-like catastrophe events are, however, triggered by adjusting chemical rupture rates rather than including MT mechanics. The model by Margolin et al. [33] has successfully reproduced features of the experimentally observed MT dynamic instability [35] but relies on a heuristic tuning of simulation parameters.

2. MATERIALS AND METHODS

2.1. Microtubule Structure and Energy

Our MT model is formulated on the dimer level. The base units of the model are alpha- and beta-tubulin monomers. In our model, we represent each monomer as cylinder with radius $r_t = 2\,nm$ and height $\ell_t = 4\,nm$ (see **Table 1**). Alpha- and beta-tubulin monomers form unbreakable tubulin dimers, which are arranged head-to-tail into protofilaments. Thirteen protofilaments form a 13_3 MT, i.e., a MT with a helical shift of three tubulin monomer lengths per turn.

TABLE 1 | Geometric parameters of our MT model.

Parameter	Symbol	Value
Mean MT radius	R_{MT}	10.5 nm
Tubulin monomer radius	r_t	2 nm
Tubulin monomer length	ℓ_t	4 nm
Helical shift between protofilaments	Δz_h	0.92 nm
Rest length of lateral springs	s_0	1.47 nm
Straight equilibrium bending angle	$\Delta\theta_0$	0°
Curved equilibrium bending angle	$\Delta\theta_0$	11°

For the remainder of this paper, we will use triples (p, d, t) to address specific tubulin monomers within the MT with $p \in \{1, 2, \ldots, 13\}$ as the protofilament number, $d \in \{1, 2, \ldots, d(p)\}$ as the tubulin layer [with $d = 1$ denoting the minus end and $d = d(p)$ denoting the plus end of the protofilament p], and $t \in \{1, 2\}$ denoting the tubulin monomer within the dimer with $t = 1$ for the alpha- and $t = 2$ for the beta-tubulin monomers. For simplicity, we assume periodicity in p (i.e., $p = 0 \equiv 13$ and $p = 14 \equiv 1$) and combined periodicity in d and t [i.e., $(p, d, 3) \equiv (p, d + 1, 1)$ and $(p, d, 0) \equiv (p, d - 1, 2)$]. We will also generally refer to the lateral neighbors of tubulin monomer (p, d, t) using $(p \pm 1, d, t)$ even though at the seam, lateral neighbors differ in all three indices.

The MT is straight and oriented along the z-axis with the positive z-direction pointing to the plus end. Vectors $\vec{m}(p, d, t)$ and $\vec{p}(p, d, t)$ point to the to the lower (minus end) and upper (plus end) circular base of the tubulin monomer (p, d, t). The direction vector

$$\vec{d}(p, d, t) = \vec{p}(p, d, t) - \vec{m}(p, d, t) = \ell_t \begin{pmatrix} \cos\phi(p) \sin\theta(p, d, t) \\ -\sin\phi(p) \sin\theta(p, d, t) \\ \cos\theta(p, d, t) \end{pmatrix} \tag{1}$$

with length $\ell_t = 4\,nm$ points from $\vec{m}(p, d, t)$ to $\vec{p}(p, d, t)$ and is specified using spherical coordinates, i.e., azimuthal and polar angles (see **Figure 1A**). The polar angle $\theta(p, d, t)$ is the only degree of freedom of each monomer, because we assume that monomers can only be displaced in radial direction, i.e., all azimuthal angles are fixed to $\phi(p) = 2\pi(p-1)/13$. As both alpha- and beta-tubulin have their polar angles as a degree of freedom, the model supports intra- and inter-dimer curling [36].

At the minus end of the MT each protofilament p starts with an alpha-tubulin arranged in a circle with mean MT radius $R_{MT} = 10.5\,nm$ and with an offset $z(p, 1, 1) = 3\ell_t(p - 1)/13$ in z-direction, such that the seam is between the 13th and the 1st protofilament. The protofilament length that will be used to calculate the growth and shrinkage velocities is the maximum z-coordinate $\ell_{max}(p)$ of all tubulin monomers within the protofilament (see **Supplementary Material** for more details). The MT length is given by the average

$$\ell_{MT} = \frac{1}{13} \sum_{p=1}^{13} \ell_{max}(p). \tag{2}$$

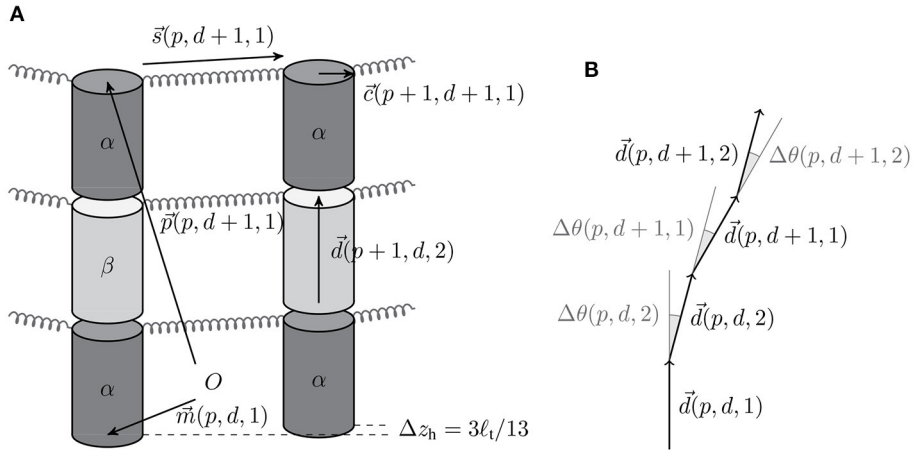

FIGURE 1 | (A) Schematic illustration of the different vectors with the origin O (The vertical gaps between tubulin cylinders are for illustration purposes only). **(B)** Bending angles between the tubulin monomer direction vectors.

Every tubulin monomer has four interaction points: two in longitudinal direction and two in lateral direction. The longitudinal bond between alpha- and beta-tubulin monomers of the same dimer is considered unbreakable but the orientation of this junction can change via the beta-tubulin's polar angle $\theta(p,d,2)$. In contrast, the longitudinal bond between adjacent tubulin monomers of different dimers can break and is modeled via the bond energy $\Delta G^{0*}_{\mathrm{long}}$ (where the "0" refers to it being a standard energy [37] and the asterisk to the fact that it also includes the entropic cost of "immobilization" [30]). The lateral interaction points are located at the edge of the upper base (see **Figure 1A**). If there is a lateral bond between tubulin monomer (p,d,t) and its neighbor in the $(p+1)$-th protofilament, the bond is modeled as a harmonic spring with base energy $\Delta G^{0}_{\mathrm{lat}}$:

$$E_{\mathrm{lat}}(p,d,t) = \Delta G^{0}_{\mathrm{lat}} + \frac{1}{2}k_{\mathrm{lat}}\left(|\vec{s}(p,d,t)| - s_0\right)^2 \qquad (3)$$

with the spring constant k_{lat} of the bond and the vector $\vec{s}(p,d,t)$ connecting the lateral interaction points; $s_0 \simeq 1.47\,nm$ is the rest length of the spring (see [17] and also consider the helical shift between two neighboring tubulin monomers of $3\ell_\mathrm{t}/13$). Lateral bonds at the seam are assumed to have identical mechanical properties as other lateral bonds based on evidence that they do not constitute a weaker bond [22, 38]. Additionally, there is a lateral repulsion term between neighboring tubulin monomers (regardless of whether they are bonded or not) to ensure a cylindrical form [17]:

$$E_{\mathrm{rep}}(p,d,t) = k_{\mathrm{rep}}\left(|\vec{p}(p,d,t) - \vec{p}(p+1,d,t)| - 2r_\mathrm{t}\right)^{-12}. \qquad (4)$$

The bending of monomer junctions is described by a harmonic potential with bending constant κ:

$$E_{\mathrm{bend}}(p,d,t) = \frac{1}{2}\kappa\left(\Delta\theta(p,d,t) - \Delta\theta_0(p,d,t)\right)^2. \qquad (5)$$

The bending angle $\Delta\theta(p,d,t) = \theta(p,d,t) - \theta(p,d,t-1)$ (see **Figure 1B**) is calculated with the neighboring monomer in the minus direction [using the periodicity convention in d and t, $(p,d,0) \equiv (p,d-1,2)$], and $\Delta\theta_0(p,d,t)$ is its equilibrium value. For hydrolyzed beta-tubulin monomers and for alpha-tubulin monomers on top of a hydrolyzed beta-tubulin (and for the first alpha-tubulin monomers of each protofilament if the beta-tubulin in the same dimer is hydrolyzed), we use a rest angle $\Delta\theta_0(p,d,t) = 11^\circ$ in order to reproduce the experimentally measured radius of curvature of 21 nm corresponding to an angle of 22° per dimer for a GDP-protofilament curling into the ram's horn configuration [10, 39]. Otherwise (for an unhydrolyzed beta-tubulin monomer or an alpha-tubulin monomer on top of an unhydrolyzed beta-tubulin monomer), we assume a straight equilibrium configuration with $\Delta\theta_0(p,d,t) = 0^\circ$. This choice of rest angles implements the allosteric model, where GTP-hydrolysis leads to bending of tubulin dimers.

Our mechanical MT model is defined by the total energy

$$E_{\mathrm{MT}} = \sum_{p=1}^{13}\sum_{d=1}^{d(p)}\left(\Delta G^{0*}_{\mathrm{long}} + \sum_{t=1}^{2}\Big[E_{\mathrm{lat}}(p,d,t) + E_{\mathrm{rep}}(p,d,t) + E_{\mathrm{bend}}(p,d,t)\Big]\right), \qquad (6)$$

where $E_{\mathrm{lat}}(p,d,t)$ only contributes if there is a lateral bond between tubulin monomers (p,d,t) and $(p+1,d,t)$ and $E_{\mathrm{rep}}(p,d,t)$ only contributes if tubulin monomer (p,d,t) has a lateral partner $(p+1,d,t)$.

There are four free parameters in our mechanical MT model (see **Table 2**): the longitudinal bond energy $\Delta G^{0*}_{\mathrm{long}}$, the lateral bond energy $\Delta G^{0}_{\mathrm{lat}}$, the lateral spring constant k_{lat}, and the bending constant κ. For the repulsion constant k_{rep}, we use the same value $k_{\mathrm{rep}} = 10^{-6}\,rad^2\,nm^{12}\kappa$ that has been found previously to ensure the overall cylindrical shape of the MT and only contributes a small portion to the MT energy [17].

TABLE 2 | Free parameters of our MT model and the "standard set" of their values that we will focus on in the rest of the paper.

Parameter	Symbol	Standard set of values
Longitudinal bond energy	$\Delta G^{0*}_{\text{long}}$	$-9.3\,k_BT$
Lateral bond energy	$\Delta G^{0}_{\text{lat}}$	$-1.58\,k_BT$
Lateral spring constant	k_{lat}	$100\,k_BT/\text{nm}^2$
Bending constant	κ	$149\,k_BT/\text{rad}^2$
Pseudo-first-order polymerization rate	k_+	$4\,\mu\text{M}^{-1}\,\text{s}^{-1}$
Lateral bond formation attempt rate	k_{att}	$258\,\text{s}^{-1}$
Constant hydrolysis rate	k_{hydr}	$0.1–0.5\,\text{s}^{-1}$
Base hydrolysis rate	k^0_{hydr}	$1–5\,\text{s}^{-1}$

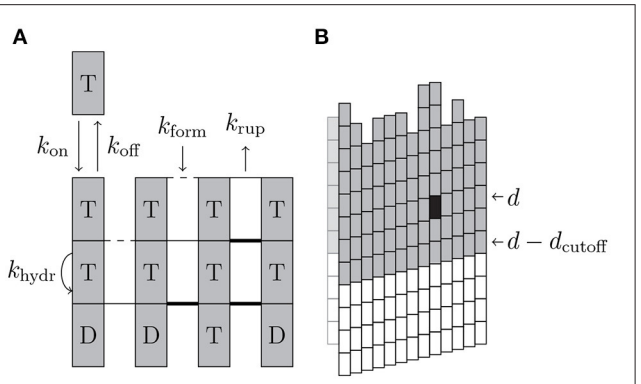

FIGURE 2 | (A) Schematic illustration of the different simulation events with their rates. Dashed lateral bonds can be formed with rate k_{form}, thin solid lateral bonds can rupture with rate k_{rup}, and thick bond cannot rupture. "T" and "D" correspond to the hydrolysis state of beta-tubulin of the dimers. **(B)** If the black tubulin dimer in layer d is affected by an event and $d_{\text{cutoff}} = 2$ was used, all of the gray (and the black) tubulin dimers are used for energy minimization.

In the simulation model, we do not use this mechanical energy to calculate forces for a microscopic dynamics, such as Brownian dynamics on the dimer level (as opposed to [18]). We rather assume that mechanical relaxation dynamics is fast compared to chemical changes in the MT due to tubulin attachment and detachment, bond rupture and formation, or hydrolysis. The slowest mechanical process is relaxation of bending modes of protofilaments governed by small restoring bending moments. The basic time scale for this process can be estimated as $\tau \sim \eta \ell_t^3/\kappa$ [40], where $\eta \sim 10^{-3}\,Pa\,s$ is the viscosity of water. This gives $\tau \sim 10^{-10}\,s$, which is orders of magnitude smaller than typical time scales of seconds for chemical events. Therefore, even longer protofilaments relax fast compared to chemical changes. There is additional evidence from Brownian dynamics that bending mode relaxation is also much faster than immobilization in cryo-EM [41]. Therefore, we perform a quasi-instantaneous energy minimization of (6) between these chemical simulation steps. This is the computationally more efficient strategy to achieve mechanical relaxation. The rates of all chemical simulation events themselves determine the dynamics of the MT and are handled by a Gillespie algorithm as explained in more detail below.

2.2. Chemical Simulation Events

To simulate the dynamics of MTs, we include attachment of individual GTP-tubulin dimers and detachment of (laterally unbonded) tubulin dimers or whole (laterally unbonded) protofilament segments at the plus end, as well as lateral bond rupture and formation, and hydrolysis of tubulin dimers as stochastic chemical events into the simulation; **Figure 2A** summarizes the different possible events and the associated rates.

2.2.1. Attachment and Detachment

At the plus end of each protofilament, a GTP-tubulin dimer can attach with an on-rate

$$k_{\text{on}} = k_+ c_{\text{tub}} \tag{7}$$

where k_+ is the pseudo-first-order polymerization rate and c_{tub} is the concentration of free GTP-tubulin dimers. The on-rate is assumed to be independent of the hydrolysis state of the protofilament end.

For depolymerization, we assume that a tubulin dimer at the plus end can only detach if it has no lateral bonds. We also allow for detachment of whole protofilament segments starting from an interior dimer [$d < d(p)$] if the whole segment has no lateral bonds. Laterally unbounded dimers or segments can detach with a rate

$$k_{\text{off}} = k_+ c_0 \exp\left(\Delta G^{0*}_{\text{long}}\right) \tag{8}$$

as given by Kramers theory with the longitudinal standard bond energy $\Delta G^{0*}_{\text{long}}$ (including the entropic cost of "immobilization") and the standard concentration $c_0 = 1\,M$ [37].

This approach differs from other models [15, 30, 42], where tubulin dimers can detach regardless of whether they have lateral bonds or not. In such models, if a tubulin dimer still has lateral bonds, its detachment rate decreases exponentially with the additional lateral bond energies. In our model, we rather include lateral bond rupture and formation as separate stochastic events into the simulation (similarly to the purely chemical models in [32–34]); bond rupture can then be followed by detachment of laterally unbounded dimers or protofilament segments. Bond rupture enables dimer detachment and is necessary prior to a catastrophe; vice versa, bond reformation is necessary for a rescue event. Therefore, it is essential to also include the process of bond formation into the model. Moreover, it has been observed in MD simulations in Kononova et al. [43] that lateral tubulin bonds can easily reform. The restriction that only laterally unbonded dimers can detach also causes an indirect increase of the effective off-rate if the last dimers of a protofilament are hydrolyzed because this tends to create stretched bonds, which rupture more easily.

2.2.2. Zipper-Like Lateral Bond Rupture and Bond Formation

We assume that bond rupture between protofilaments starts from the plus end and proceeds by a rupture front monomer by monomer toward the minus end; likewise, bonds can be reformed

only monomer by monomer toward the plus end in a zipper-like fashion. As a result, we always have a rupture front between two neighboring protofilaments such that all monomers on top of the front toward the plus end are ruptured and all monomers below toward the minus end are intact. If tubulin monomer $(p, d, t-1)$ has a lateral bond with its neighbor in protofilament $p+1$ but the tubulin monomer on top of it, (p, d, t), has no lateral bond with this neighbor, the rupture front can recede toward the plus end, and tubulin monomer (p, d, t) can form a bond with rate

$$k_{\text{form}} = k_{\text{att}} \tag{9}$$

with the attempt rate k_{att}. Vice versa, if the bond at (p, d, t) is intact and bond $(p, d, t+1)$ is broken, the rupture front can advance toward the minus end by rupturing this bond with a rate

$$k_{\text{rup}} = k_{\text{att}} \exp\left(\Delta G^0_{\text{lat}} + \Delta G_{\text{mech}}\right) \tag{10}$$

which contains the chemical lateral bond energy ΔG^0_{lat} and a mechanical energy ΔG_{mech}, which accounts for the weakening of the lateral bond due to mechanical strain in the bond and enters according to Bell theory [44, 45]. In our model, ΔG_{mech} is due to the stretching of the Hookean springs representing the lateral bonds so that $\Delta G_{\text{mech}} = F_{\text{lat}} \ell_{\text{rup}}$, where $F_{\text{lat}} = -\partial E_{\text{lat}}/\partial |\vec{s}(p, d, t)|$ is the force currently acting on the lateral bond and ℓ_{rup} is the characteristic bond rupture length. We define ℓ_{rup} as the length increase of the lateral bond from its rest length s_0 at which the stretching energy of the spring cancels the bond energy:

$$\ell_{\text{rup}} = \sqrt{\frac{-2\Delta G^0_{\text{lat}}}{k_{\text{lat}}}}. \tag{11}$$

2.2.3. Hydrolysis Without and With Mechanical Feedback

Lastly, GTP in beta-tubulin monomers can hydrolyze into GDP via a random (or scalar) hydrolysis rule meaning that almost every GTP-tubulin dimer in the MT can hydrolyze with a fixed rate k_{hydr} regardless of the hydrolysis state of its longitudinal neighbor (which would be a vectorial hydrolysis rule). The "almost" in the previous sentence refers to the finding that the polymerization of the tubulin dimer (p, d) and thus the formation of a longitudinal bond between beta-tubulin $(p, d-1, 2)$ and alpha-tubulin $(p, d, 1)$ catalyzes the hydrolysis reaction in beta-tubulin $(p, d-1, 2)$ [13]. As a consequence, only GTP-tubulin dimers that ever had another tubulin dimer on top of them can be hydrolyzed in our model.

We also consider the possibility that hydrolysis is mechanochemically coupled to the bending strain [17]. Then, the hydrolysis rate

$$k_{\text{hydr}}(p, d) = k^0_{\text{hydr}} \exp\left(-\Delta E_{\text{hydr}}(p, d)\right) \tag{12}$$

is modulated with a dimer-specific change $\Delta E_{\text{hydr}}(p, d)$ in the energy barrier height of the hydrolysis reaction, which depends on the bending state of dimer (p, d). Because this bending state also depends via lateral bonds on the bending states in all neighboring dimers, and because the bending state of all neighboring dimers strongly depends on their hydrolysis state, the hydrolysis dynamics becomes effectively non-random but depends on the hydrolysis state of the neighbors.

The basis for our assumption of a tubulin dimer-specific mechanochemical hydrolysis rate is to view the equilibrium bending angle $\Delta\theta_0$ of a dimer as the reaction coordinate for hydrolysis which can be described by an energy profile $F_{\text{hydr}}(\Delta\theta_0)$. $F_{\text{hydr}}(\Delta\theta_0)$ has two local minima corresponding to the straight conformation with $\Delta\theta_0 = 0^\circ$ and the curved conformation with $\Delta\theta_0 = 11^\circ$ and a rate-limiting energy barrier of unknown height $\Delta F^{\text{barrier}}_{\text{hydr}}$ in between. We propose that hydrolysis of a tubulin dimer is eased if its actual bending angle $\Delta\theta$ is closer to the equilibrium angle $\Delta\theta_0 = 11^\circ$ in the hydrolyzed state. We model this dependency by adding a dimer-specific bending energy contribution $E_{\text{hydr}}(\Delta\theta_0)$ to $F_{\text{hydr}}(\Delta\theta_0)$, which changes the energy barrier height from $\Delta F^{\text{barrier}}_{\text{hydr}}$ to $\Delta F^{\text{barrier}}_{\text{hydr}} + \Delta E_{\text{hydr}}(p, d)$ (see **Figure 3**). $\Delta F^{\text{barrier}}_{\text{hydr}}$ can be absorbed into the constant rate k^0_{hydr} so that only $\Delta E_{\text{hydr}}(p, d)$ remains in the Arrhenius factor in (12).

To calculate the change in the energy barrier height $\Delta E_{\text{hydr}}(p, d)$, we now consider the total MT energy in (6) as a function of the hydrolysis reaction coordinate $\Delta\theta_0$ while keeping all polar angles $\{\theta(p, d, t)\}$ fixed. We simply assume that the energy barrier is centered between the minima at $\Delta\theta_0^{\text{barrier}} = 5.5^\circ$ resulting in

$$\Delta E_{\text{hydr}} = E_{\text{MT}}(\Delta\theta_0 = 5.5^\circ) - E_{\text{MT}}(\Delta\theta_0 = 0^\circ). \tag{13}$$

Because hydrolysis of tubulin dimer (p, d) affects the rest bending angles of beta-tubulin monomer $(p, d, 2)$ and alpha-tubulin monomer $(p, d+1, 1)$ and the rest bending angles only affect the

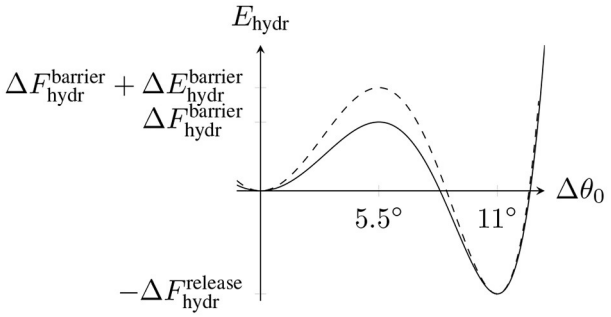

FIGURE 3 | Schematic hydrolysis energy landscape with two local minima corresponding to the straight conformation ($\Delta\theta_0 = 0^\circ$) and the bent conformation ($\Delta\theta_0 = 11^\circ$) and an energy barrier $\Delta F^{\text{barrier}}_{\text{hydr}}$ at $\Delta\theta_0 = 5.5^\circ$ between them. $\Delta F^{\text{release}}_{\text{hydr}}$ is the energy released by hydrolysis. The dashed line represents the modified energy landscape due to the dimer-dependent contribution $E_{\text{hydr}}(\Delta\theta_0)$.

bending energies (5), we finally obtain

$$\begin{aligned}\Delta E_{\mathrm{hydr}}(p,d) &= \frac{1}{2}\kappa\Big[(\Delta\theta(p,d,2)-5.5^\circ)^2-\Delta\theta^2(p,d,2)\\ &\quad+(\Delta\theta(p,d+1,1)-5.5^\circ)^2-\Delta\theta^2(p,d+1,1)\Big]\\ &= \frac{1}{2}\kappa\Big[-(\Delta\theta(p,d,2)+\Delta\theta(p,d+1,1))\cdot 11^\circ\\ &\quad+2\cdot(5.5^\circ)^2\Big] \end{aligned} \tag{14}$$

so that only a local bending energy change has to be calculated. As a result, tubulin monomers in the MT lattice with larger bending angles $\Delta\theta(p,d,t)$ tend to hydrolyze preferentially. For the terminal tubulin dimer of a protofilament $(p,d(p))$, the $d+1$-term in (14) is missing because tubulin monomer $(p,d(p)+1,1)$ does not exist. This results in an overall smaller energy barrier and, thus, a higher hydrolysis rate of the terminal tubulin dimer.

We also see that the base hydrolysis rate k^0_{hydr} in (12) is not the hydrolysis rate for a perfectly straight MT [$\Delta\theta(p,d,t)=0^\circ$ for all tubulin monomers] because there is still the constant contribution $\kappa(5.5^\circ)^2$ to the energy barrier in (14) that reduces the hydrolysis rate. As these terms are proportional to the bending constant κ, we cannot simply absorb them into the constant factor k^0_{hydr}.

We note that for almost all GTP-tubulin dimers in the GDP-body of the MT, we will typically find *negative* bending angles; these dimers bend inward in order to allow the longitudinal GDP-dimer neighbors to further bend outwards. For such negative bending angles the hydrolysis rate is reduced according to (14).

In addition to the previous four free parameters from the MT energy, the simulation events add three additional free parameters: the pseudo-first-order polymerization rate k_+, the attempt rate k_{att}, and the hydrolysis rate k_{hydr} (or k^0_{hydr}). In total, there are now seven free parameters, which are listed in **Table 2**.

2.3. Simulation and Parameter Determination

The actual MT simulation (implemented in C++) works as follows:

1. Initially, a MT with N_{GDP} GDP-tubulin dimers followed by N_{GTP} GTP-tubulin dimers per protofilament is constructed with $\theta(p,d,t)=0^\circ$ for all (p,d,t).
2. Using the tubulin monomers' polar angles $\{\theta(p,d,t)\}$, the MT's actual initial configuration is determined by minimizing its mechanical energy. Details on the minimization procedure will be discussed in the next section.
3. For all of the events described in the previous section, a list of possible events is determined and based on their rates k_i, a "tentative" event time t_i is calculated using Gillespie's first reaction method [46]:

$$t_i = \frac{1}{k_i}\ln\frac{1}{r} \tag{15}$$

   where r is a uniformly distributed random number from 0 to 1. The event i with the shortest event time t_i is executed and the simulation time is increased by t_i.
4. Assuming fast mechanical relaxation the MT's energy is minimized after any event.
5. The simulation terminates if a protofilament is shorter than two tubulin dimers.[1] Otherwise we go back to the third step to determine the next event.

There is a general agreement between different experiments [3, 47–52] that the MT growth velocity v_{gro} increases linearly with the tubulin dimer concentration c_{tub} and that the shrinkage velocity v_{shr} is independent of c_{tub}. We will use the results by Walker et al. [47], which were measured for $c_{\mathrm{tub}}\in[7.7, 15.5\,\mu M]$,

$$v_{\mathrm{gro}}(c_{\mathrm{tub}}) = (0.33\pm0.01)\,\frac{\mu m}{min\,\mu M}c_{\mathrm{tub}} - (1.59\pm0.50)\,\frac{\mu m}{min}, \tag{16}$$

$$v_{\mathrm{shr}} = (-27\pm1)\,\frac{\mu m}{min}, \tag{17}$$

and lead to an individual critical concentration $c_{\mathrm{tub,c}}\simeq 5\,\mu M$ (below which $v_{\mathrm{gro}}<0$).

To determine the values of the model parameters, we use a "divide and conquer" approach [15, 30]. First, we consider MT growth, where mechanics are assumed not to play a significant role as protofilaments are not curling outward so that $\Delta G_{\mathrm{mech}}=0$. Thus, we use a GTP-only MT ($N_{\mathrm{GDP}}=0$) and set $k_{\mathrm{lat}}=0$ and $\kappa=0$ so that the only free parameters left are k_+, $\Delta G^{0*}_{\mathrm{long}}$, $\Delta G^0_{\mathrm{lat}}$, and k_{att}. The goal of these simulations is to reproduce the measured growth velocity in (16) as function of the free tubulin dimer concentration c_{tub}. Secondly, we consider MT shrinkage, where mechanics are now assumed to play a significant role, i.e., $k_{\mathrm{lat}}>0$ and $\kappa>0$. For a shrinking MT, we use $N_{\mathrm{GTP}}=0$, $N_{\mathrm{GDP}}>0$, and the parameter values already determined by the growth simulations to reproduce the shrinkage velocity in (17). In both cases, hydrolysis is ignored. A schematic overview of the entire parameter determination procedure can be found in **Figure S7** in the Supplementary Material.

Comparing the number of free parameters and the amount of experimental data, we can already predict that we will not be able to determine one set of fixed parameter values but only restrict some parameter values to specific values if other parameter values are set to (arbitrarily but reasonably) chosen values. We will discuss this issue in more detail in the conclusion.

2.4. Energy Minimization

In previous three-dimensional models, different energy minimization approaches have been used. VanBuren et al. [15] used a local minimization approach in which they randomly selected individual tubulin dimers and then only locally

[1] To calculate shrinkage velocities of shrinkage simulations via a simple linear fit, it has proven to be easier to stop simulations if a protofilament still contains one tubulin dimer instead of zero tubulin dimers as the last tubulin dimer requires more time to depolymerize creating a "tail" in the length-vs.-time plot. This time increase is due to lateral springs being stretched less because there is no additional tubulin dimer below the terminal tubulin dimer that would exert an additional bending moment. In practice, for determining parameters and when running full simulations, this first layer at the minus end is irrelevant and could be regarded as a "seed" on which the MT grows.

minimized with respect to the parameters of this dimer. On average, each tubulin dimer was visited three times for minimization. Zakharov et al. [18] employed a completely different approach by explicitly modeling the stochastic motion of tubulin monomers in space using Brownian dynamics (applied to the first 300 tubulin dimers at the plus end). They solve Langevin equations every 2×10^{-10} s while using 10^{-3} s as the time step for the events in their simulation resulting in $\mathcal{O}(10^7)$ dynamics steps between actual events. Using a parallel implementation run on a supercomputer, their simulation took more than a day to simulate 1 s of MT dynamics. There are drawbacks for both approaches: a local energy minimization scheme might not come close enough to a mechanically relaxed configuration, whereas a full Brownian dynamics simulation is computationally very costly. In this paper, we employ a systematic mechanical energy minimization between each stochastic chemical simulation event. We try to achieve a better mechanical energy relaxation than VanBuren et al. [15] with significantly less computational steps than Zakharov et al. [18].

In our simulation, we use the Broyden–Fletcher–Goldfarb–Shanno (BFGS) algorithm, a quasi-Newton method, provided by the GNU Scientific Library (GSL) [53] to minimize the total mechanical MT energy in (6) as a function of the polar angles $\{\theta(p, d, t)\}$. If each protofilament in the simulated MT contains $N_{\mathrm{GDP}} + N_{\mathrm{GTP}}$ tubulin dimers, there are a total of $26(N_{\mathrm{GDP}} + N_{\mathrm{GTP}})$ polar angles and thus the same number of minimization parameters. In realistic simulations, MTs can stay in the growing phase for a very long time resulting in an unbounded increase in the number of minimization parameters drastically slowing down the simulation. In essence, the average time for one minimization step increases with the MT length in this scenario making long-running simulations impossible.

To overcome this limitation, we will explore two possibilities to avoid having a MT length-dependent number of minimization parameters:

1. restricting the number of minimization steps per energy minimization to a small value but still considering all minimization parameters (this approach is similar to the strategy in [15]),
2. restricting the number of minimization parameters by only considering the tip of the MT but not restricting the number of minimization steps.

While the first strategy is easy to understand and implement, the second needs further specifications in terms of how we define the tip of the MT here. If a certain event is executed that affects tubulin dimer (p, d), we include all layers starting from $\min(0, d - d_{\mathrm{cutoff}})$ in the mechanical energy minimization because mechanical interactions within the MT have a certain range; d_{cutoff} is a cutoff *layer* distance (see **Figure 2B**).

Below, we will compare these approaches of restricted minimization with respect to accuracy and speed and find that we obtain accurate energy minimization at a high simulation speed by using the second approach and restricting the number of minimization parameters with $d_{\mathrm{cutoff}} = 10$. We can compare with the approaches of Zakharov et al. [18] and VanBuren et al. [15] in terms of the average number of minimization steps between chemical events.

Zakharov et al. [18] use $\mathcal{O}(10^7)$ Brownian dynamics steps between events and restrict the number of simulation parameters to 300 tubulin dimers at the plus end. With $d_{\mathrm{cutoff}} = 10$ we minimize on average with respect to a comparable number of 150 tubulin dimers at the plus end. To compare the efficiency, we consider a single quasi-Newton minimization step in our simulation to be equivalent to one time step of their Brownian dynamics (if we ignore the random thermal fluctuations in their Langevin equations, they are basically using a gradient descent method). We compare our event time t_i divided by the number of minimization steps after the execution of that event to their Brownian dynamics time step of 2×10^{-10} s. For shrinking MTs, one minimization step takes $\mathcal{O}(10^{-5}\, s)$ after polymerization events, $\mathcal{O}(10^{-4}\, s)$ after depolymerization events, and $\mathcal{O}(10^{-7}\, s)$ after lateral bond events; all of these time steps are orders of magnitude larger than 2×10^{-10} s and, thus, the simulation proceeds orders of magnitude faster, while we still achieve an accurate energy minimization. As a comparison with the 1 s of MT dynamics simulated in more than a day in a parallel computation in reference [18], we generally do not require more than a few hours for 1 min of MT dynamics (for a constant hydrolysis rate) using just a single CPU core.

VanBuren et al. [15] apply a local minimization procedure and restrict minimization to, on average, three minimizations with respect to the parameters of each dimer. Because one step of their algorithm minimizes with respect to the parameters of a single tubulin dimer, a comparison to our quasi-Newton minimization steps which minimize the MT energy with respect to the parameters of, on average, $\mathcal{O}(150)$ tubulin dimers is not straightforward. In addition, VanBuren et al.'s model also contains longitudinal springs so that outward bending of single tubulin dimers as a consequence of local minimization can be compensated by stretching the next longitudinal spring. As our model does not contain such longitudinal springs, bending one tubulin dimer causes the whole protofilament part above the tubulin dimer to also bend outwards creating an effectively non-local, far-reaching interaction. Consequently, we are not able to also implement a local minimization procedure for comparison. To make a qualitative comparison between the two approaches, we assume that one minimization step of our BFGS algorithm, which acts on average on 300 parameters, i.e., 150 tubulin dimers, corresponds to 100 single tubulin dimer minimizations in the model of reference [15] as they consider three parameters per tubulin dimer. Between chemical events, we perform on average 150 BFGS minimization steps, which corresponds to 1.5×10^4 single tubulin dimer minimizations in reference [15]. Therefore, we apply the equivalent of $15,000/150 = 100$ single tubulin minimizations to each of the 150 tubulin dimers close to the plus tip on average as compared to three single tubulin dimer minimizations in the simulation model of reference [15]. Accordingly, we should achieve a more accurate mechanical energy relaxation.

We also compared our chosen minimization method, the BFGS algorithm, against the other multidimensional minimization algorithms using derivatives provided by GSL [53],

including the conjugate gradient method, and found the BFGS algorithm to perform better. In particular, to fully minimize the initial configuration of a MT with $N_{GDP} = 20$ and $N_{GTP} = 0$, BFGS only required about a third of the time compared to the next best algorithm, a conjugate gradient method.

3. RESULTS

3.1. GTP-Microtubule Growth and Model Parameterization

MT growth mainly depends on the four parameters k_+, ΔG^{0*}_{long}, ΔG^{0}_{lat}, and k_{att}, because the growing MT tip mainly consists of straight GTP-tubulin dimers. Therefore, we consider growth of a GTP-only MT ($N_{GDP} = 0$) in the absence of hydrolysis and set $k_{lat} = 0$ and $\kappa = 0$ so that the only free parameters left are k_+, ΔG^{0*}_{long}, ΔG^{0}_{lat}, and k_{att}. For $k_+ = 2\,\mu M^{-1}\,s^{-1}$ and $k_+ = 4\,\mu M^{-1}\,s^{-1}$, we scanned the parameter space $(\Delta G^{0*}_{long}, \Delta G^{0}_{lat}, k_{att})$ in steps $\Delta\Delta G^{0*}_{long} = 0.2\,k_BT$ to find parameter values that reproduce the experimental growth velocity data of Walker et al. in (16). The growth velocity v_{gro} for each simulation was determined by fitting $\ell_{MT}(t_{sim})$ with a linear function. Experiments on MT growth show a linear dependence $v_{gro}(c_{tub}) = a_{gro}c_{tub} + b_{gro}$ characterized by two parameters a_{gro} and b_{gro} from (16). If simulations reproduce a linear dependence of v_{gro} as a function of c_{tub}, we can determine two of the three model parameters $(\Delta G^{0*}_{long}, \Delta G^{0}_{lat}, k_{att})$ by fitting to the experimental data (16) for a_{gro} and b_{gro}, i.e., two experimental constraints fix two model parameters as a function of the third parameter. This will allow us to parameterize a one-dimensional sub-manifold (a line) within the three-dimensional parameter space $(\Delta G^{0*}_{long}, \Delta G^{0}_{lat}, k_{att})$ where our model agrees with experimental growth data. This procedure is conceptually analogous to the approach of VanBuren et al. [30], but we work in a higher-dimensional (three-dimensional) space of model parameters.

As a result, we obtain a line in the three-dimensional parameter space, which we parameterize by ΔG^{0*}_{long}, i.e., for a given value of ΔG^{0*}_{long}, a value of ΔG^{0}_{lat} (see **Figure 4A**) and a value of k_{att} (see **Figure 4B**) is determined by the experimental growth data.

Afterwards, we will fix a particular value of ΔG^{0*}_{long} by the additional requirement that the simulation should exhibit an as linear as possible concentration dependence of the growth velocity v_{gro} over a certain range of tubulin concentrations c_{tub} (see **Figure 4D**) such that we arrive at parameter sets

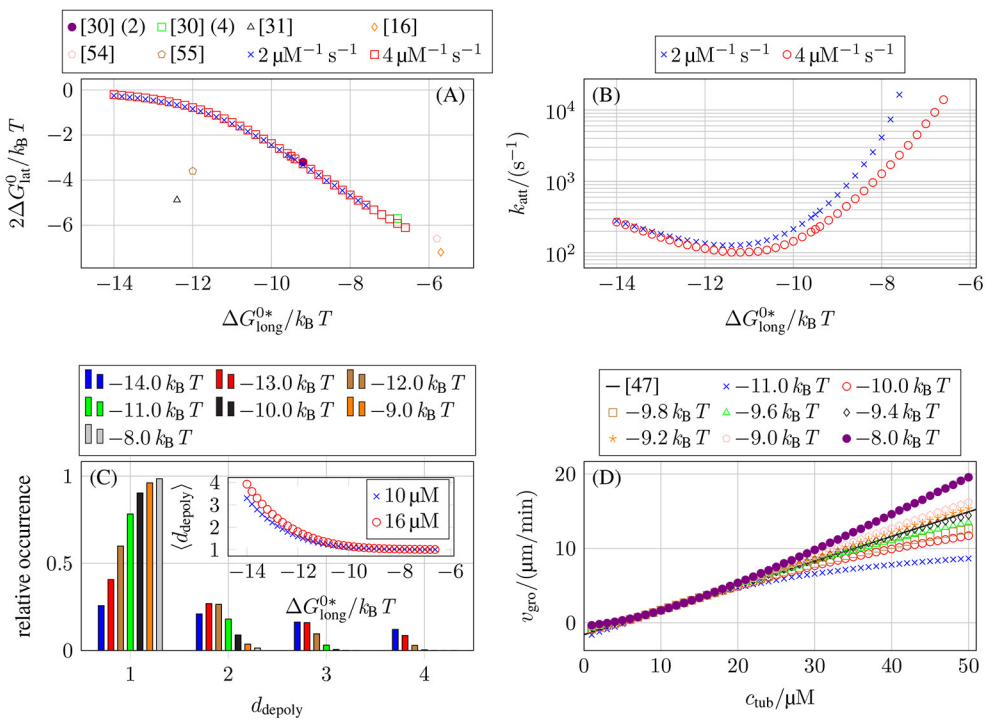

FIGURE 4 | (A) Lateral bond energy ΔG^{0}_{lat} as a function of the longitudinal bond energy ΔG^{0*}_{long} from matching the concentration-dependent growth velocity data from Walker et al. [47], see (16). To compare our lateral bond energies (per tubulin monomer) to other publications (lateral bond energy per tubulin *dimer*), the *y*-axis shows $2\Delta G^{0}_{lat}$. (The numbers behind reference [30] refer to their value of k_+.) **(B)** Lateral bond attempt rate k_{att} as a function of the longitudinal bond energy ΔG^{0*}_{long} for our two values of k_+ from matching the concentration-dependent growth velocity data from Walker et al. [47], see (16). **(C)** Relative occurrence of different d_{depoly} values for MT growth with $k_+ = 4\,\mu M^{-1}\,s^{-1}$ and $c_{tub} = 10\,\mu M$. The inset shows the average d_{depoly} as a function of ΔG^{0*}_{long} for $k_+ = 4\,\mu M^{-1}\,s^{-1}$ and $c_{tub} = 10\,\mu M$ and also for $c_{tub} = 16\,\mu M$. **(D)** MT growth velocity v_{gro} as a function of a larger interval of free tubulin dimer concentration values c_{tub} for $k_+ = 4\,\mu M^{-1}\,s^{-1}$ and different longitudinal bond energies ΔG^{0*}_{long}. We also plot (16) from the growth velocity data from Walker et al. [47] over the larger concentration interval.

$(\Delta G^{0*}_{\text{long}}, \Delta G^{0}_{\text{lat}}, k_{\text{att}})$ for $k_+ = 2\,\mu M^{-1}\,s^{-1}$ and $k_+ = 4\,\mu M^{-1}\,s^{-1}$ (see **Table 3**).

The results in **Figure 4A** show that the values of $\Delta G^{0*}_{\text{long}}$ and $\Delta G^{0}_{\text{lat}}$ depend only weakly on our chosen k_+ values. **Figure 4A** also shows that our data matches results obtained in [30] (this data was later re-used in [15, 16, 54]) but also differs from other results [31, 55], which were all obtained by the same approach of fitting growth velocity data from Walker et al. [47] (or their own growth data in [55]). Kononova et al. [43] obtained bond energies from MD simulations of nano-indentation experiments; the values from Kononova et al. [43] are much larger for both types of bonds ($\Delta G^{0*}_{\text{long}} \sim 2\Delta G^{0}_{\text{lat}} \sim 25 k_B T$) and, thus, not shown in **Figure 4A**.

Qualitatively, the measured dependencies of $\Delta G^{0}_{\text{lat}}$ and k_{att} on $\Delta G^{0*}_{\text{long}}$ can be understood as follows: the weaker longitudinal bonds are, the more likely it is that a tubulin dimer will depolymerize. To get the same growth velocity, this decrease in "longitudinal stability" has to be compensated by an increase in "lateral stability" by stronger lateral bonds (making it less likely that lateral bonds break and, thus, enabling depolymerization) or faster formation of lateral bonds (to stabilize newly polymerized tubulin dimers). **Figure 4C** shows the number of tubulin dimers d_{depoly} that detach at once during depolymerization events. For increasingly stronger longitudinal bonds and, thus, weaker lateral bonds, multi-dimer depolymerization becomes more relevant. The data in the inset in **Figure 4C** is also compatible with results in reference [33] obtained with a purely chemical model.

Until now, we only considered free tubulin dimer concentrations $c_{\text{tub}} \in [7, 16\,\mu M]$ to use similar values as Walker et al. [47], but there have also been other measurements with a larger range of c_{tub} values [3, 48, 51, 52]. In general, it is assumed that the growth velocity v_{gro} increases linearly with c_{tub} for the whole MT just as the polymerization rate in (7) increases linearly with c_{tub} for individual protofilaments. Theoretically, it has been shown that, for multistranded polymers, lateral interactions give rise to a non-linear relation between growth velocity on monomer concentration [56]. For MT growth, a non-linear dependence on tubulin concentration was found in reference [31] using a two-dimensional model based on reference [30]. Over a larger range of c_{tub} values, our simulations also exhibit a non-linear relation between v_{gro} and c_{tub} depending on the value of $\Delta G^{0*}_{\text{long}}$, as shown in **Figure 4D**. Data for different values of $\Delta G^{0*}_{\text{long}}$ (and correspondingly adjusted values of $\Delta G^{0}_{\text{lat}}$ and k_{att}, see **Figures 4A,B**) and the same value of k_+ that was previously overlapping in the interval $c_{\text{tub}} \in [7, 16\,\mu M]$ start to differentiate in a larger concentration interval. While possible non-linear relations have been predicted theoretically, the available experimental data show a linear $v_{\text{gro}}(c_{\text{tub}})$ dependence over a large range of c_{tub} values [3, 48, 51, 52]. Therefore, we determined the remaining free parameter value of $\Delta G^{0*}_{\text{long}}$ for the two k_+ values from the condition that the concentration dependence of v_{gro} is as linear as possible up to 50 µM. To determine these values of $\Delta G^{0*}_{\text{long}}$, we ignored concentrations c_{tub} below the individual critical concentration (for which $v_{\text{gro}} < 0$) which violate our fundamental assumption of a growing MT.

In summary, we find a triple $(\Delta G^{0*}_{\text{long}}, \Delta G^{0}_{\text{lat}}, k_{\text{att}})$ that fits the growth velocity data from Walker et al. [47] and that gives a linear concentration dependence over a wide tubulin concentration range for two representative values of k_+. **Table 3** lists these parameter triples for $k_+ = 2\,\mu M^{-1}\,s^{-1}$ and $k_+ = 4\,\mu M^{-1}\,s^{-1}$. For a given k_+, these results fix four of the seven model parameters in **Table 2** using experimental data on MT growth. To address the parameters κ and k_{lat}, we now turn to MT shrinkage.

TABLE 3 | Growth parameter values that generate the most linear dependence $v_{\text{gro}}(c_{\text{tub}})$.

k_+ (µM^{-1} s^{-1})	2	4
$\Delta G^{0*}_{\text{long}}$ ($k_B T$)	−9.7	−9.3
$\Delta G^{0}_{\text{lat}}$ ($k_B T$)	−1.38	−1.58
k_{att} (s^{-1})	281	258

3.2. GDP-Microtubule Shrinkage and Model Parameterization

As opposed to MT growth, MT shrinkage also depends on the bending constant κ and spring constant k_{lat} as protofilament curling and bond rupture become relevant processes for a shrinking MT. We consider a shrinking MT that initially only consists of GDP-tubulin dimers ($N_{\text{GTP}} = 0$, $N_{\text{GDP}} > 0$) with parameter values k_+, $\Delta G^{0*}_{\text{long}}$, $\Delta G^{0}_{\text{lat}}$, and k_{att} as already determined by the growth simulations and in the absence of hydrolysis (a shrinking, initially GDP-only MT acquires some GTP-dimers by attachment but remains GDP-dominated). To investigate shrinkage, MTs with $N_{\text{GDP}} = 20$ and $N_{\text{GTP}} = 0$ were used. For each parameter set, 20 simulations were run to get an average shrinkage velocity v_{shr}. Experimental data on shrinking MTs show a shrinkage speed v_{shr} that is independent of the tubulin dimer concentration. For each value of k_+, we should be able to determine one of the two parameters (κ, k_{lat}) as a function of the other parameter by fitting such that the experimental value of the shrinkage velocity is reproduced in simulations (for parameters $\Delta G^{0*}_{\text{long}}$, $\Delta G^{0}_{\text{lat}}$, and k_{att} fixed by the growth velocity data). We use the experimental shrinkage velocity of Walker et al., see (17), for this fitting procedure.

Figures 5A,B show the values of k_{lat} and κ for $k_+ = 2\,\mu M^{-1}\,s^{-1}$ and $k_+ = 4\,\mu M^{-1}\,s^{-1}$ and different values of $\Delta G^{0*}_{\text{long}}$ that reproduce the experimentally measured shrinkage velocity in (17). All data points for each $\Delta G^{0*}_{\text{long}}$ fall on square root functions

$$\kappa(k_{\text{lat}}) = a_{\text{shr}}\sqrt{k_{\text{lat}}} + b_{\text{shr}}. \tag{18}$$

This functional dependence can be understood qualitatively by considering the mechanical contribution to the bond rupture rate (10), $\exp(F_{\text{lat}}\ell_{\text{rup}})$, which, on average, should have the same value for all mechanical parameter combinations to produce the same shrinkage velocity. As the characteristic bond rupture length in (11) depends on k_{lat} as $\ell_{\text{rup}} \sim \sqrt{k_{\text{lat}}}^{-1}$, the average lateral bond force at rupture should depend on k_{lat} like $F_{\text{rup}} \sim k_{\text{lat}}\ell_{\text{rup}} \sim$

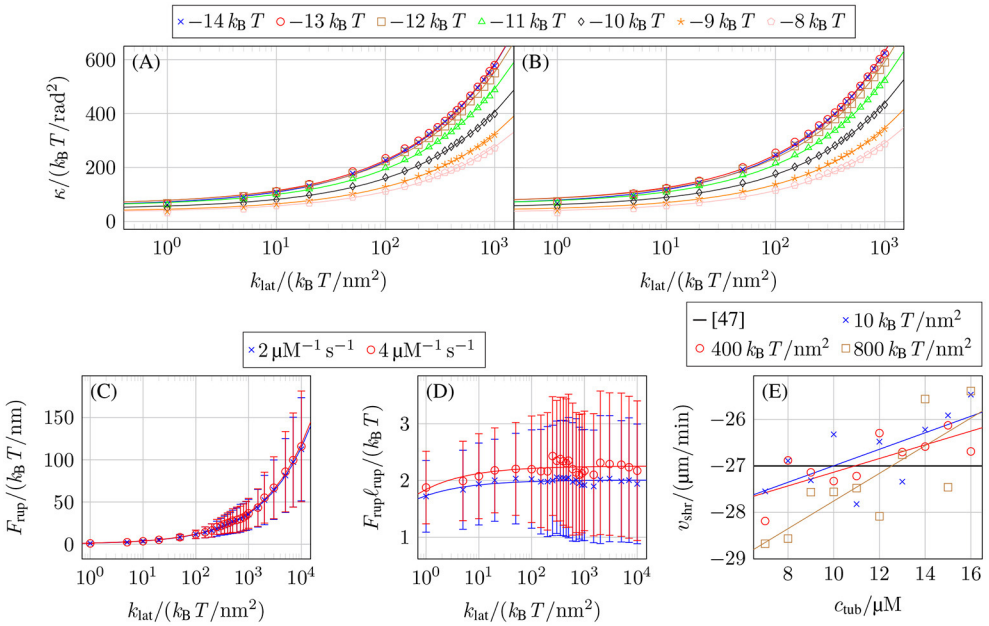

FIGURE 5 | Mechanical parameter values reproducing the experimentally measured shrinkage velocity in (17) for **(A)** $k_+ = 2\,\mu\mathrm{M}^{-1}\,\mathrm{s}^{-1}$ and **(B)** $k_+ = 4\,\mu\mathrm{M}^{-1}\,\mathrm{s}^{-1}$ and different values of $\Delta G^{0*}_{\mathrm{long}}$. **(C)** Force on lateral bonds at rupture F_{rup} as a function of k_{lat} for $k_+ = 2\,\mu\mathrm{M}^{-1}\,\mathrm{s}^{-1}$ with $\Delta G^{0*}_{\mathrm{long}} = -9.5\,k_B T$ and $k_+ = 4\,\mu\mathrm{M}^{-1}\,\mathrm{s}^{-1}$ with $\Delta G^{0*}_{\mathrm{long}} = -9.0\,k_B T$, both at $c_{\mathrm{tub}} = 10\,\mu\mathrm{M}$. **(D)** Rupture energy $F_{\mathrm{rup}}\ell_{\mathrm{rup}}$ of lateral bonds as a function of k_{lat} for the same parameters as in **(C)**. **(E)** Shrinkage velocity v_{shr} as a function of the free tubulin dimer concentration c_{tub} for $k_+ = 4\,\mu\mathrm{M}^{-1}\,\mathrm{s}^{-1}$, $\Delta G^{0*}_{\mathrm{long}} = -9.3\,k_B T$, and different values of k_{lat} and linear fits $v_{\mathrm{shr}}(c_{\mathrm{tub}})$.

$\sqrt{k_{\mathrm{lat}}}$. The lateral bond force F_{lat} is a consequence of the lateral bonds stretching as the tubulin monomers curl outward to decrease the bending force $F_{\mathrm{bend}} = \kappa\left(\Delta\theta(p,d,t) - \Delta\theta_0(p,d,t)\right)$, which leads to $F_{\mathrm{rup}} \sim F_{\mathrm{bend}} \sim \kappa$ resulting in $\kappa \sim \sqrt{k_{\mathrm{lat}}}$ in accordance with **Figures 5A,B**.

Figure 5C confirms that the average force on lateral bonds at rupture $\langle F_{\mathrm{rup}}\rangle$ has the functional dependence $\langle F_{\mathrm{rup}}\rangle \sim \sqrt{k_{\mathrm{lat}}}$ predicted by our above qualitative argument ($\langle F_{\mathrm{rup}}\rangle$ and error bars $\sigma_{F_{\mathrm{rup}}}$ were determined by fitting normal distributions to the histogram of the lateral bond rupture forces collected for 20 shrinkage simulations per parameter set with $N_{\mathrm{GDP}} = 20$). Also, the resulting mechanical contribution $F_{\mathrm{rup}}\ell_{\mathrm{rup}}$ for the exponential function of the lateral bond rupture rate in **Figure 5D** is approximately constant as expected from our above argument.

As the experimentally measured shrinkage velocity v_{shr} does not depend on the free tubulin dimer concentration c_{tub}, we used constants to fit our $v_{\mathrm{shr}}(c_{\mathrm{tub}})$ data. In reality, however, our data shows a linear dependence between v_{shr} and c_{tub} as shown in **Figure 5E** corresponding to a slowing down of depolymerization. This is caused by an increased probability for intermediate addition of tubulin dimers and lateral bond formation between them; these lateral bonds require additional time to rupture. While this dependency of v_{shr} on c_{tub} will have a small influence on the concrete value of the shrinkage velocity, we expect it to not have any qualitative effect on the overall MT dynamics. At higher tubulin concentrations, where the decrease of $|v_{\mathrm{shr}}(c_{\mathrm{tub}})|$ would become significant, the catastrophe rates decrease dramatically so that shrinking will rarely occur.

Comparing our results from **Figures 5A,B** to other results is not always directly possible due to different modeling approaches but most find that $k_{\mathrm{lat}} \ll 1.000\,k_B T/nm^2$ and $\kappa \ll 1.000\,k_B T/rad^2$ [15, 57, 58], with some exceptions [43, 59]. Previously, we used MD simulation data from Grafmüller et al. [60] to calculate the bending constant κ [17]. Compared to reference [17], we have to adjust the calculation to consider both inter-dimer and intra-dimer bending resulting in $\kappa \simeq 50\,k_B T/rad^2$. MD simulation in Kononova et al. [43], on the other hand, give a persistence length of individual protofilaments of $L_p \simeq 6\,\mu m$, which corresponds to a significantly larger value of $\kappa \simeq 1.500\,k_B T/rad^2$ for the bending constant. This discrepancy cannot be resolved at present. We use $\kappa = 149\,k_B T/rad^2$ in the following together with the corresponding value of $k_{\mathrm{lat}} = 100\,k_B T/nm^2$ according to **Figure 5B** which are values close to the ones used by VanBuren et al. [15].

3.3. Restricted Energy Minimization for Efficient Simulation

Until now, energy minimization was not restricted by either a maximum number of minimization steps or by only considering a subset of tubulin dimers at the MT tip so that we will consider this unrestricted minimization as the "gold standard" to which we will compare the two restricted energy minimization approaches described in section 2.4. We use the shrinkage velocity v_{shr} as the observable by which we judge the relevant cutoff values in the two approaches.

For restricting the number of quasi-Newton minimization steps, **Figure 6A** shows that an acceptable maximum number of

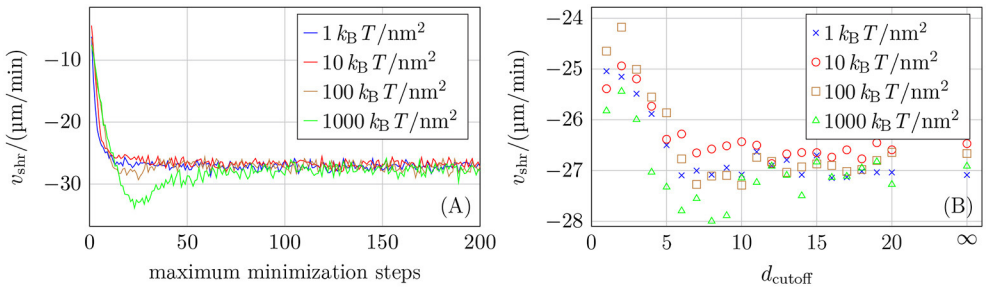

FIGURE 6 | (A) Shrinkage velocity v_{shr} as a function of the maximum number of minimization steps. **(B)** Shrinkage velocity v_{shr} as a function of the layer cutoff distance d_{cutoff} (where $d_{cutoff} = \infty$ means that no cutoff was used). Twenty simulations for each parameter set were run for both plots and both used $k_+ = 4\,\mu M^{-1}\,s^{-1}$, $\Delta G^{0*}_{long} = -9.3\,k_BT$, $c_{tub} = 10\,\mu M$, $N_{GDP} = 20$, and different values of k_{lat}.

minimization steps reproducing $v_{shr} = -27\,\mu m/min$ depends on the chosen mechanical parameters as the higher their values are, the greater the energy and its gradient. A maximum number of minimization steps of around 100 should be an appropriate value according to the results shown in **Figure 6A**. The results in **Figure 6A** also show that reducing the number of minimization steps by a factor of 10 can lead to deviating growth velocities. Therefore, the improved energy relaxation that we obtain in comparison to reference [15] by applying the equivalent of one order of magnitude more minimization steps should be relevant.

If minimization is restricted to a subset of minimization parameters at the tip of the simulated MT, this subset is defined by the cutoff distance d_{cutoff}. To have a maximum improvement in simulation speed, d_{cutoff} should be as small as possible. It is evident from the data shown in **Figure 6B** that values $d_{cutoff} < 5$ have a detectable influence on the shrinkage velocity. We also ran some simulations with $N_{GDP} = 50$ and also for $k_+ = 2\,\mu M^{-1}\,s^{-1}$ (see **Figure S8** in the Supplementary Material) and based on all data, we choose $d_{cutoff} = 10$ as a conservative value for the cutoff distance.

In summary, we are more confident in the second approach to only minimize the MT tip where actual conformational changes happen, because for this subset, the restricted energy is fully minimized. Additionally, the first approach still has the issue of slowing down with an increasing number of minimization parameters as all minimization parameters are considered. The second approach ensures that the number of minimization parameters does not scale with the MT length but remains bounded, which assures that we can simulate arbitrarily long growing MTs at a fixed minimal computational speed. In the first approach, the quality of the minimization will probably also decline because the number of minimization parameters increases while the number of minimization steps is kept constant. Lastly, the first approach, in contrast to the second approach, does not guarantee that the upper, i.e., the dynamic part of the MT is properly minimized.

We also note that in the presence of mechanical feedback onto hydrolysis, simulations take longer because minimizations after hydrolysis events need to consider more tubulin dimers if the hydrolyzed tubulin dimer is relatively deep in the MT lattice (see **Supplementary Material** for more details).

3.4. Full Simulations Exhibit Repeated Catastrophe and Rescue Events

Based on the previous section on energy minimization, we use $d_{cutoff} = 10$ for full simulations in which the initial MTs have both a GDP-body and a GTP-cap, thus $N_{GDP} > 0$ and $N_{GTP} > 0$. We now aim for realistic MT dynamics with repeated phases of growth and shrinkage in the same simulation and catastrophe and rescue events in between. First, we only consider strictly random hydrolysis with a hydrolysis rate k_{hydr} that is independent of tubulin dimers' position or mechanical forces and which is another unknown free parameter in our model. Hydrolysis coupled to mechanics via (12) will be considered later.

It poses a computational challenge for chemomechanical MT models to reach time scales of MT dynamics where repeated catastrophe events occur at realistic hydrolysis rates k_{hydr} and tubulin dimer concentrations c_{tub}. In reference [18], where mechanics was implemented via full Brownian dynamics, only short times scales could be reached (although the Brownian dynamics was applied to only 300 tubulin dimers at the plus end). Therefore, they increased the hydrolysis rate from their "normal" value of $0.5\,s^{-1}$ (based on the 2 s delay between polymerization and phosphate release measured by [61], which is also used by [62]) into a range of $3–11\,s^{-1}$ in order to trigger catastrophe events within computationally accessible time scales. They found a linear scaling of catastrophe rate with k_{hydr} and employed a linear extrapolation to obtain catastrophe rates for realistic hydrolysis rates (see their Figure 3A). In our simulations, we observe that increasing k_{hydr} beyond a certain (c_{tub}-dependent) value leads to immediate MT shrinkage because the initial cap quickly hydrolyzes; this can be interpreted as an instantaneous catastrophe. In such cases (like in **Figure 7** for $c_{tub} = 7\,\mu M$ and $k_{hydr} = 0.5\,s^{-1}$), there is no real growth phase based on which a catastrophe frequency could be determined. For these hydrolysis rates, the individual critical concentration $c_{tub,c}$ (where $v_{gro} = 0$ is reached) has apparently increased above the given tubulin concentration.

The experimental data on the hydrolysis rate is limited, so that many publications determine the hydrolysis rate themselves by matching simulation results with experimental data [16, 30–33, 63–65]. There are, however, more direct measurements in

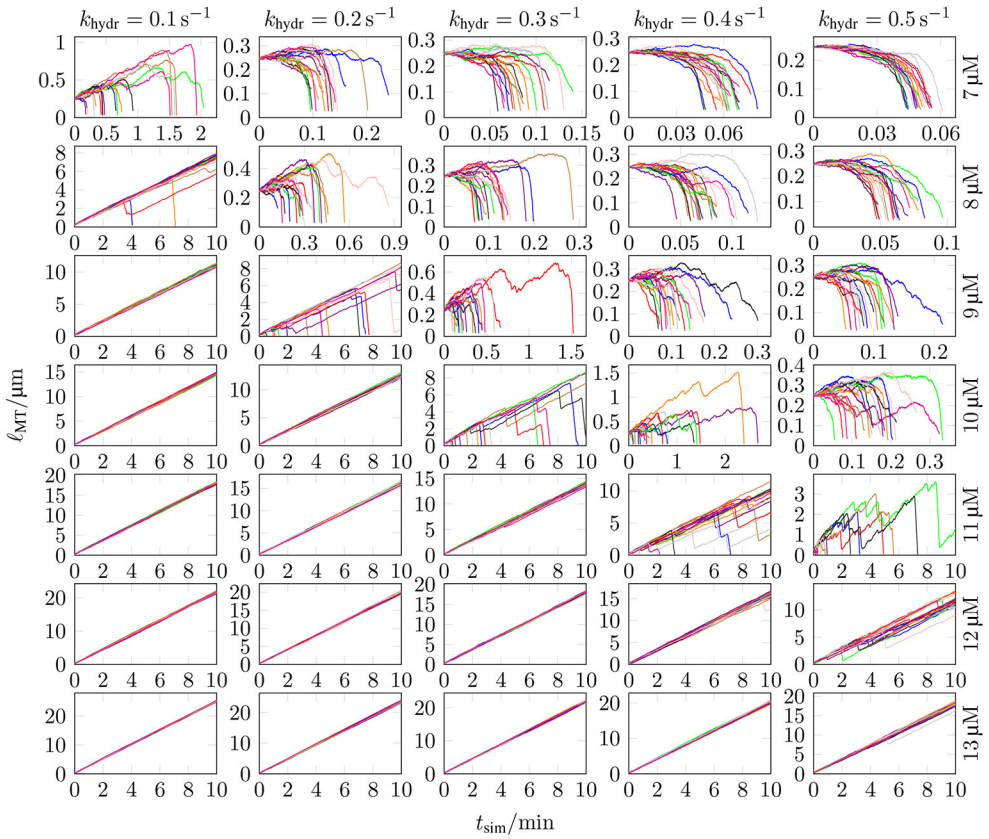

FIGURE 7 | The MT length ℓ_{MT} was measured as a function of the simulation time t_{sim} for 20 different simulations with $k_+ = 4\,\mu M^{-1}\,s^{-1}$, $\Delta G^{0*}_{long} = -9.3\,k_BT$, $k_{lat} = 100\,k_BT/nm^2$, seven different values of c_{tub}, and five different values of k_{hydr}. MT growth trajectories for three additional c_{tub} values can be found in **Figure S9** in the Supplementary Material.

Melki et al. [61]. In most models and also in measurements from Melki et al. [61], the (random) hydrolysis rate is in the range of 0.1–0.5 s^{-1} (reference [30] use a relatively high value of 0.95 s^{-1}). We explore exactly this range of hydrolysis rates, see **Figure 7**.

Figure 7 shows MT growth curves (length vs. time) over simulation times up to $t_{sim} = 10$ min for several representative tubulin concentrations and realistic hydrolysis rates. MT growth trajectories as in **Figure 7** for other k_{lat} values can be found in **Figures S10–13** in the Supplementary Material. Simulations in **Figure 7** were started with $N_{GTP} = 10$ and $N_{GDP} = 20$, but results are largely independent of the initial ratio N_{GTP}/N_{GDP} (see, e.g., **Figure S11** in the Supplementary Material).

Our chemomechanical MT model is computationally efficient such that we can determine catastrophe and rescue rates as inverse average growth and shrinking times between repeated catastrophe and rescue events. In the **Supplementary Material**, we explain the algorithm that we used to identify catastrophe and rescue events and, thus, growth and shrinking times from MT simulation trajectories in detail. The results are shown in **Figure 8**. In comparison to typical experimental data [47, 67], the decrease of the catastrophe rate with tubulin concentration seems too steep. Current phenomenological models for the MT catastrophe rate as a function of tubulin concentration can be found in Flyvbjerg et al. [68] and Zelinski and Kierfeld [69], experimental data in Walker et al. [47] and Janson et al. [66]; the decrease of the catastrophe rate with GTP-tubulin concentration c_{tub} appears steeper in the simulation for all hydrolysis rates $k_{hydr} = 0.1$–$0.5\,s^{-1}$.

In the following, we will discuss two aspects of MT growth and catastrophes in more detail, namely the dependence of growth velocity on hydrolysis rate and the detailed dynamics within single catastrophe events, which become accessible within a computational model and are impossible to address experimentally.

3.5. Growth Velocity Reduces Linearly With Hydrolysis Rate Because of Cap Structure

So far, we parameterized the model by fitting the growth velocity of GTP-only MTs, i.e., in the absence of hydrolysis to the experimentally measured velocity in (16). Hydrolysis reduces this growth velocity by increasing the probability of GDP-dimers at the plus end. This increases the rate of bond rupture because hydrolyzed dimers tend to create stretched bonds which rupture more easily (there is no direct increase of the off-rate

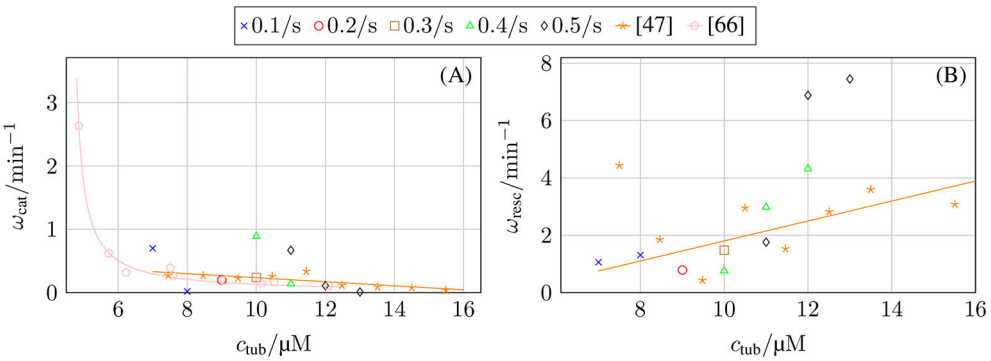

FIGURE 8 | (A) Catastrophe rate ω_{cat} and **(B)** rescue rate ω_{res} as a function of GTP-tubulin concentration c_{tub} and in comparison with experimental data from Walker et al. [47] and Janson et al. [66].

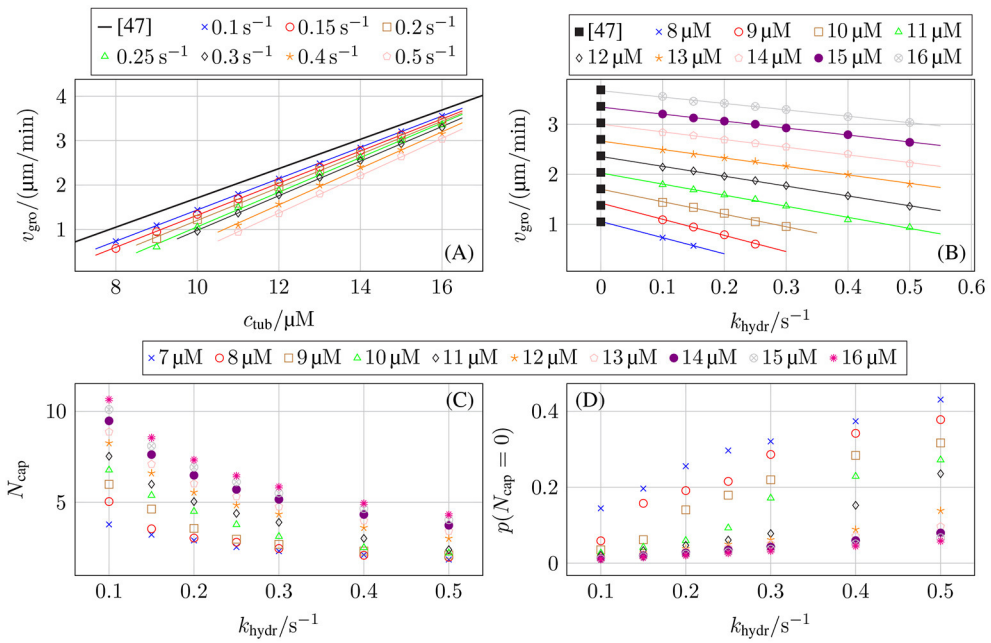

FIGURE 9 | Growth velocity v_{gro} as a function of **(A)** the free tubulin dimer concentration c_{tub} for different hydrolysis rates k_{hydr} and as a function of **(B)** the hydrolysis rate k_{hydr} for different free tubulin dimer concentrations c_{tub} in comparison to the experimental data from Walker et al. [47]. **(C)** Average GTP-tubulin cap length $\langle N_{cap} \rangle$ of protofilaments and **(D)** fraction of protofilaments without a GTP-cap as a function of the hydrolysis rate k_{hydr}. The standard set of parameters from **Table 2** was used.

for hydrolyzed GDP-dimers in our model). As only laterally unbounded dimers can detach, hydrolyzed GDP-dimers at the plus end have an effectively higher detachment rate.

The last row of **Figure 7** indicates and **Figure 9B** shows explicitly that increasing the hydrolysis rate decreases the growth velocity linearly although the growth reduction mechanism is indirect via the increased probability of bond rupture for hydrolyzed GDP-dimers. Our model parameterization was such that we obtain the experimentally measured growth velocities by Walker et al. [47] at $k_{hydr} = 0\,s^{-1}$ in **Figure 9B**. Nevertheless, **Figure 9A** shows that there is still a linear relation between the free tubulin dimer concentration c_{tub} and the growth velocity v_{gro} so that it is possible to re-adjust parameters to reproduce the growth velocity in the presence of hydrolysis, once a particular hydrolysis rate can be reliably selected.

Because both the dependence on tubulin concentration in **Figure 9A** remains linear and the reduction by the hydrolysis rate in **Figure 9B** is linear, we also expect that the individual critical concentration (where $v_{gro} = 0$ is reached) increases linearly with the hydrolysis rate beyond the value $c_{tub,c} \simeq 5\,\mu M$ of Walker et al. [47]. **Figure 7** clearly shows that increasing k_{hydr} actually increases the individual critical concentration $c_{tub,c}$.[2]

[2]The individual critical concentration can be read off from **Figure 7** as the concentration below which immediate MT shrinkage sets in.

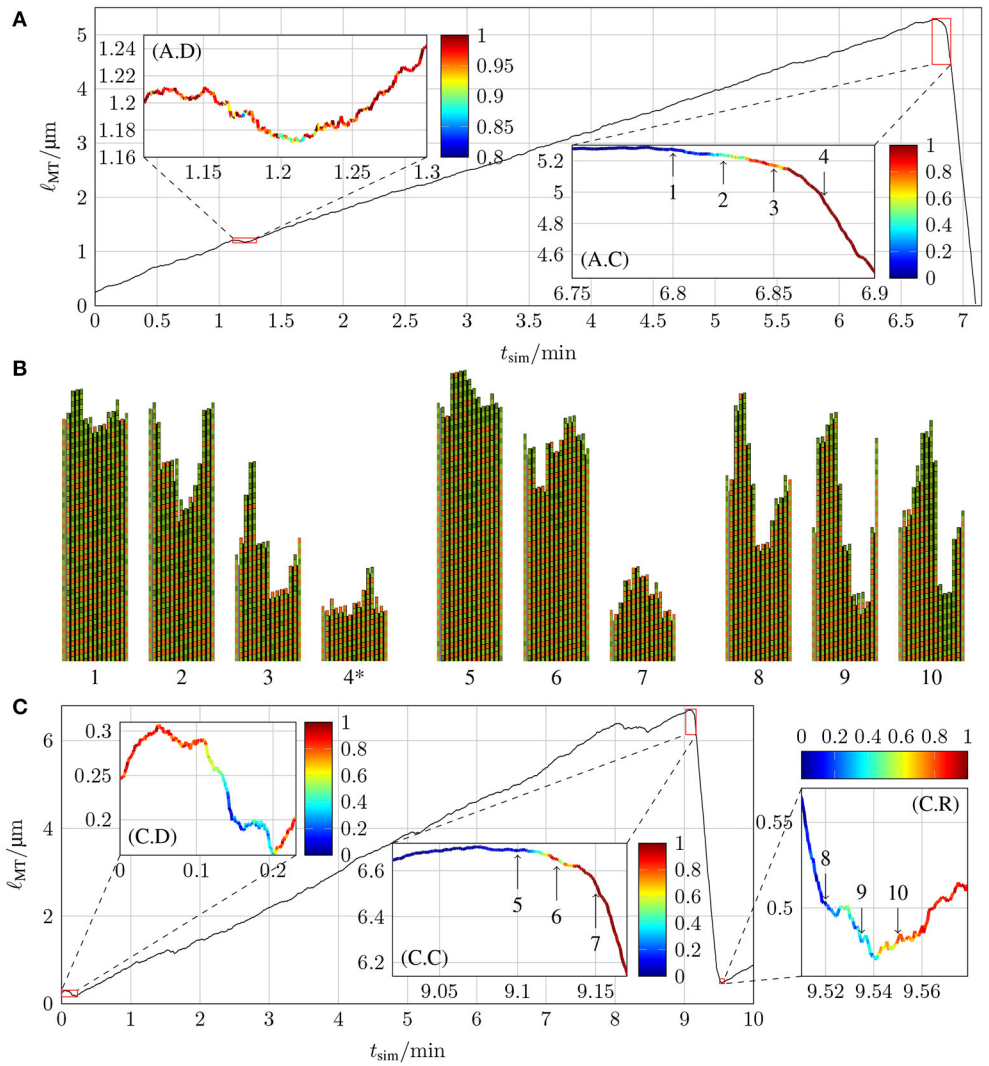

FIGURE 10 | Lengths of two MTs as a function of simulation time t_{sim} with $k_+ = 4\,\mu M^{-1}\,s^{-1}$, $\Delta G^{0*}_{long} = -9.3\,k_BT$, $k_{lat} = 100\,k_BT/nm^2$, and **(A)** $c_{tub} = 8\,\mu M$ and $k_{hydr} = 0.1\,s^{-1}$ and **(C)** $c_{tub} = 9\,\mu M$ and $k_{hydr} = 0.2\,s^{-1}$. The insets highlight parts of the trajectories of interest for the dynamics and color-code the probability of the $\ell_{MT}(t_{sim})$ curve to stay quantitatively the same at the relevant point in time if new simulations are started with the relevant configuration as the initial configuration (for more details, refer to the text). **(B)** shows the two-dimensional representations of certain MT tip configurations that are marked by arrows in the insets of **(A,C)** (configuration 4* has been shifted toward the MT tip by 24 tubulin dimer lengths). The first protofilament is the periodic image of $p = 13$ and the last protofilament is the periodic image of $p = 1$. Lateral bonds are represented by the thick black line between protofilaments.

The mechanism of growth velocity reduction by hydrolysis can be further elucidated by comparing the average GTP-tubulin cap length $\langle N_{cap}\rangle$ of protofilaments (see **Figure 9C**), and the fraction of protofilaments without a GTP-cap (see **Figure 9D**): The higher the hydrolysis rate is, the smaller the GTP-cap and the higher the fraction of cap-less protofilaments is.[3] The increase in GDP-tubulin dimers depolymerizing from the protofilament tips for higher hydrolysis rates is due to an increase in the probability of uncapped protofilaments with the hydrolysis rate as shown in **Figure 9D**. In reference [70], dependencies $\langle N_{cap}\rangle \propto \sqrt{c_{tub}/k_{hydr}}$ and $p(N_{cap} = 0) \propto k_{hydr}/c_{tub}$ have been predicted, which are in agreement with **Figures 9C,D**.

3.6. Detailed Dynamics Within Single Catastrophe and Rescue Events

The chemomechanical model reproduces realistic MT dynamics including catastrophe and rescue events. **Figure 10** shows typical MT growth paths featuring two catastrophe events and a rescue event in subfigure (C). Moreover, we observe "dips" in the growth path where a short phase of shrinking appears, which are

[3] As the cap lengths shown in **Figure 9C** are averaged over the whole duration of the simulations, these cap lengths also average over growth and shrinkage phases. As cap lengths are shorter during shrinkage than growth, the cap lengths in **Figure 9C** can be regarded as a lower limit on the average cap length during MT growth.

similar to "stutter" events that have been observed in reference [35]. Videos of these two simulations with two- and three-dimensional representations of the MT structure can be found in the **Supplementary Material**.

Using our computational model, we can systematically identify the point in a MT growth path, where a catastrophe becomes structurally unavoidable. This allows us to search for typical catastrophe-triggering features in MT growth. To analyze how probable it is at specific points in the simulation of MT dynamics that the MT continues a certain growth path, we chose two simulations with at least one significant event (meaning a catastrophe, rescue, or a "dip"/"stutter") and took configurations around such events as starting points for new simulations (similar to [33]). In these new simulations, MTs were allowed to grow (or shrink) for a maximum of 60 s, a sufficient amount of time to check if the new simulations show dynamics similar to the original simulation around the significant event.

The MT growth trajectory shown in **Figure 10A** has two significant events: a dip at $t_{\rm sim} = 1.2\,min$ and a catastrophe at $t_{\rm sim} = 6.85\,min$; the trajectory in **Figure 10C** contains three significant events: a dip at the very beginning, a catastrophe at $t_{\rm sim} = 9.15\,min$, and a rescue at $t_{\rm sim} = 9.54\,min$. To determine whether newly run simulations with starting points from the initial simulation qualitatively follow the original simulation, we need criteria to identify dips, catastrophes, or rescue events. The exact criteria for these events in **Figures 10A,C** are stated in the **Supplementary Material**. In short, in order to identify whether a new simulation reproduces a catastrophe, we check after a time of 10–15 s whether the MT is sufficiently short that a catastrophe must have happened; for a dip, we check whether the MT continued to grow without entering a catastrophe; for a rescue, we check that the MT did not completely vanish because it continued to shrink. For each initial configuration, we ran 20 new simulations and calculated the fraction of simulations that fulfilled these criteria. These fractions are the probabilities for the original growth path at different points in time, and they are shown color-coded in all the insets in **Figure 10**.

Both catastrophes and the rescue show that the transition from a high probability to stay in the current dynamic state to a high probability to switch into the other dynamic state occurs within a few seconds. In **Figures 10A,C**, we first observe that catastrophes become practically unavoidable [red color code in (A.C) and (C.C)] after a phase of relatively slow shrinking by 50–100 nm; similar "transitional catastrophe" behavior has been observed in reference [35]. A dip, on the other hand, can only evade a catastrophe [yellow to red color code in (A.D) and (C.D)] if the MT length shrinks by significantly $< 50\,nm$.

Because hydrolysis followed by straining and rupture of the lateral bonds is required before a laterally unbonded dimer can detach, MT shrinking by $50\,nm$ suggests that roughly 6 dimer layers must hydrolyze in a row to trigger a catastrophe. This is, however, not sufficient to remove the entire GTP-cap. The GTP-cap length averaged over all protofilaments is still > 1 when the catastrophe becomes unavoidable (at points 3 in **Figure 10A** and 6 in **Figure 10C**, see also **Figure S1** in the Supplementary Material). As the corresponding MT snapshot insets 3 and 6 reveal, the reason for this discrepancy is the average over all protofilaments: it appears that typically only a "nucleus" of three neighboring protofilaments shrinks by more than 6 dimers, such that its GTP-cap is removed and its ends reach into the GDP-body of the MT, when a catastrophe is triggered. The MT snapshots in **Figure 10B** also suggest that rescue events require formation of a GTP-cap on almost all 13 protofilaments (with an average cap length ~ 4) such that nuclei of three neighboring uncapped GDP-protofilaments are avoided. Further investigation of more catastrophe events will be necessary to definitely deduce catastrophe- and rescue-triggering structural MT features.

3.7. Hydrolysis Coupled to Mechanics Changes the Cap Structure

We also test how a mechanical feedback onto the hydrolysis rate as introduced in (12) and (14) changes the cap structure and dynamic behavior. In the presence of this mechanical feedback, tubulin dimers in the MT lattice with larger bending angles tend to hydrolyze preferentially.

Overall, we find a linear relation between $k^0_{\rm hydr}$ and the average hydrolysis rate $\langle k_{\rm hydr}\rangle$ (see **Figure 11A**) with $k^0_{\rm hydr} \gg \langle k_{\rm hydr}\rangle$. When comparing MT growth with hydrolysis coupled to mechanics with average hydrolysis rate $\langle k_{\rm hydr}\rangle$ to MT growth with constant hydrolysis rate $k_{\rm hydr}$ (for example in **Figures 11D–F**), we use **Figure 11A** to choose the base hydrolysis rate $k^0_{\rm hydr}$ such that $\langle k_{\rm hydr}\rangle \approx k_{\rm hydr}$.

Figure 11B shows the average hydrolysis rate $\langle k_{\rm hydr}\rangle$ as a function of the free tubulin dimer concentration $c_{\rm tub}$ for $k^0_{\rm hydr} = 1.5\,s^{-1}$. Here, we observe a pronounced non-linear concentration dependence with a decrease around the individual critical tubulin concentration $c_{\rm tub} \simeq 10\,\mu M$. At the same concentration, also the porous cap length $N_{\rm pcap}$ (see **Figure 11C**), which is defined as the difference between the number of tubulin dimers in a protofilament and the value of d of the first GTP-tubulin dimer counted from the minus end, starts to increase. As a result, the porous cap length for hydrolysis coupled to mechanics is much longer compared to a constant hydrolysis rate, even if the average effective hydrolysis rate is roughly the same. In the following, we argue that the reason for this increase in porous cap length is a decrease of the hydrolysis rate for GTP-dimers away from the tip. Mechanical feedback gives rise to preferential hydrolysis at the tip, i.e., the average hydrolysis rate $\langle k_{\rm hydr}(x)\rangle$ (over all actually executed hydrolysis events) is larger for small layer distances $x \equiv d(p) - d$ from the tip, as can be seen in **Figure 11G**. This is in line with previous results in reference [17] from a much simpler version of our model with a deterministic hydrolysis kinetics and without dimer attachment and detachment.

According to (14), GTP-tubulin dimers with larger bending angles tend to hydrolyze preferentially. If a straight GTP-dimer is bent inward ($\Delta\theta < 0^\circ$), its hydrolysis rate is reduced according to (14); if it is bent outwards ($\Delta\theta > 0^\circ$) the rate is increased. From the hydrolysis rates shown in **Figure 11G**, it is possible to calculate the average bending angles using (12) and (14),

$$\langle \Delta\tilde{\theta}(p,d)\rangle = \frac{1}{11^\circ}\left[\frac{1+\delta_{d,d(p)}}{\kappa}\ln\left(\frac{k_{\rm hydr}(p,d)}{k^0_{\rm hydr}}\right) + (5.5^\circ)^2\right]. \tag{19}$$

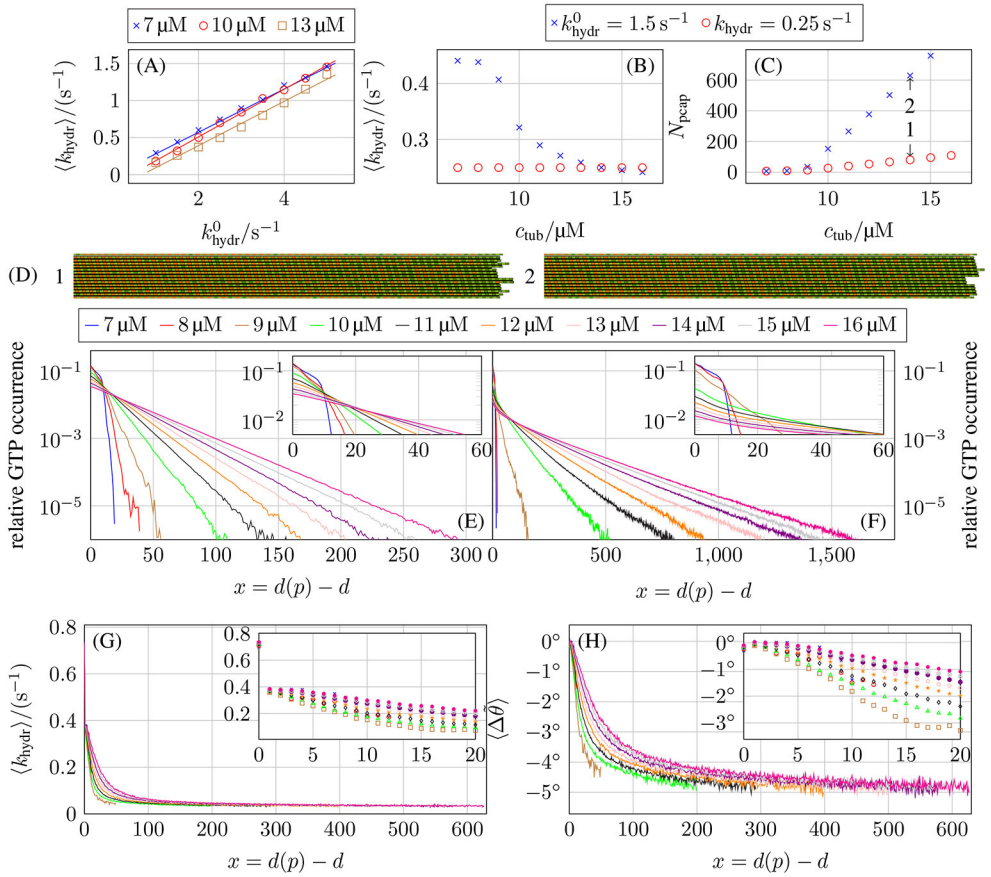

FIGURE 11 | (A) Average actual hydrolysis rate $\langle k_{\text{hydr}} \rangle$ as a function of the constant base hydrolysis rate k^0_{hydr}. Comparison of **(B)** the average actual hydrolysis rate $\langle k_{\text{hydr}} \rangle$ and **(C)** the porous cap length N_{pcap} as a function of the free tubulin dimer concentration c_{tub} for hydrolysis coupled to mechanics with $k^0_{\text{hydr}} = 1.5\,\text{s}^{-1}$ and a constant hydrolysis rate of $k_{\text{hydr}} = 0.25\,\text{s}^{-1}$. **(D)** Shows the two-dimensional representations of two MT tip configurations that are marked by arrows in **(C)** at $t_{\text{sim}} = 5\,\text{min}$. The top and bottom protofilaments are periodic images of $p = 13$ and $p = 1$, respectively. Relative occurrence of GTP-tubulin dimers as a function of the dimer-based distance from the protofilament tip $d(p) - d$ for **(E)** a constant hydrolysis rate of $k_{\text{hydr}} = 0.25\,\text{s}^{-1}$ and **(F)** hydrolysis being coupled to mechanics and $k^0_{\text{hydr}} = 1.5\,\text{s}^{-1}$. **(G)** Average hydrolysis rate as a function of distance $d(p) - d$ from the tip and **(H)** the associated average bending angle $\langle \Delta\tilde{\theta} \rangle$ for hydrolysis coupled to mechanics and $k^0_{\text{hydr}} = 1.5\,\text{s}^{-1}$. All plots are for $k_+ = 4\,\mu\text{M}^{-1}\,\text{s}^{-1}$, $\Delta G^{0*}_{\text{long}} = -9.3\,k_{\text{B}}T$, and $k_{\text{lat}} = 100\,k_{\text{B}}T/\text{nm}^2$.

The results for these bending angles as a function of the distance x from the top are shown in **Figure 11H**. Surprisingly, almost all GTP-tubulin dimers are bent inwards ($\Delta\theta < 0°$) on average prior to hydrolysis apart from dimers close to the tip. We will interpret these results in the following.

An isolated GTP-dimer within the GDP-body can alleviate the bending stress of GDP-dimers by bending inward ($\Delta\theta < 0°$), which allows longitudinally neighboring GDP-dimers to bend outwards (such that $\Delta\theta > 0°$) resulting in an overall decrease of the MT energy (see **Figures S14, S15** in the Supplementary Material). Therefore, isolated GTP-dimers deep in the GDP-body hydrolyze with a reduced asymptotic rate $\langle k_{\text{hydr}} \rangle_\infty \ll k_{\text{hydr}}$.

We also find that, for several consecutive GTP-dimers in the same protofilament, GTP-dimers curl inward directly at the GDP/GTP interface resulting in a reduced hydrolysis rate (see **Figure S15**), while GTP-dimers in the center of a GTP-island are straight so that they have a higher hydrolysis rate than at the GDP/GTP interfaces. Effectively, this hydrolysis rate distribution within a GTP-island results in a "anti-vectorial" hydrolysis mechanism with which GTP-islands are hydrolyzed from the interior in contrast to vectorial hydrolysis where hydrolysis happens at the GTP/GDP interfaces.

Also for GTP-dimers in layers closer to the MT tip, other longitudinally close-by GTP-dimers cooperate in alleviating bending stresses; then inward bending is still preferred, but the inward bending angle becomes smaller. This decrease in inward bending corresponds to an increase of the average hydrolysis rates $\langle k_{\text{hydr}}(x) \rangle$ for GTP-dimers in these layers compared to GTP-dimers buried deeper in the MT body (see **Figures 11G,H**). For terminal tubulin dimers ($x = 0$), we observe a hydrolysis rate $\langle k_{\text{hydr}}(x) \rangle$ *higher* than k_{hydr} (while it is equal or lower than k_{hydr} for all other layers $x > 0$). Hydrolysis in the first layer is enhanced because there are no tubulin dimers on top, such that hydrolysis has to overcome a smaller energy barrier as pointed out previously [the $d + 1$-term in (14) is missing corresponding to the $\delta_{d,d(p)}$-contribution in (19)].

As a result of the hydrolysis bias toward the tip, the spatial GTP-tubulin dimer distribution also differs. For concentrations where the MTs are growing only on time scales of several minutes ($c_{\mathrm{tub}} \geq 11\,\mu M$) for the chosen parameters, a constant hydrolysis rate leads to the expected exponential distribution of GTP-dimers shown in **Figure 11E** as observed in *in vivo* experiments [71]. Using an effective one-dimensional (or single protofilament) model similar to Padinhateeri et al. [63] to calculate the probability of tubulin dimers being GTP-tubulin dimers as a function of the polymerization rate k_{on}, effective depolymerization rate $\tilde{k}_{\mathrm{off}}$, and hydrolysis rate k_{hydr} matches the simulation results for concentrations at which the MTs can be considered in a steady state of growth (see section 4 in the **Supplementary Material**). We use an effective depolymerization rate $\tilde{k}_{\mathrm{off}}$ instead of k_{off}, because we map onto the depolymerization process of a one-dimensional model so that $\tilde{k}_{\mathrm{off}}$ includes all effects from lateral bond formation and rupture and the actual depolymerization process in the full model.

If hydrolysis is coupled to mechanics, the spatial distribution is only exponential in its tail, has larger values at the MT tip, and GTP-tubulin dimers can be found much deeper in the GDP-body (see **Figure 11F**). These results reflect that the average hydrolysis rate $\langle k_{\mathrm{hydr}}(x)\rangle$ is decreasing toward the GDP-body and reaches a small limiting value $\langle k_{\mathrm{hydr}}\rangle_\infty \ll k_{\mathrm{hydr}}$ for distances $x = d(p) - d > 500$ away from the tip, which governs the exponential tail (see **Figure 11G**). This can be rationalized by considering the probability $p_{\mathrm{GTP}}(x)$ to find a GTP-dimer at distance x from the tip in a single protofilament and continuum approximation. The balance between attachment/detachment and hydrolysis leads to

$$0 = -(k_{\mathrm{on}} - \tilde{k}_{\mathrm{off}})\frac{\mathrm{d}p_{\mathrm{GTP}}}{\mathrm{d}x} - \langle k_{\mathrm{hydr}}(x)\rangle\, p_{\mathrm{GTP}}(x) \qquad (20)$$

in the stationary state, which results in a sharp initial decrease of $p_{\mathrm{GTP}}(x)$ because $\langle k_{\mathrm{hydr}}(0)\rangle$ is large at the tip but a much slower asymptotic exponential decrease when $\langle k_{\mathrm{hydr}}(x)\rangle \approx \langle k_{\mathrm{hydr}}\rangle_\infty \ll k_{\mathrm{hydr}}$, which explains the main features in **Figure 11F**. In section 4 in the **Supplementary Material**, we show that (20) describes simulations with a constant hydrolysis and with hydrolysis coupled to mechanics equally well. With $p_{\mathrm{GTP}}(x)$, we can define an "average cap length" as $\bar{\ell}_{\mathrm{cap}} = \int_0^\infty \mathrm{d}x\, p_{\mathrm{GTP}}(x)x$. This average cap length $\bar{\ell}_{\mathrm{cap}}$ is longer if hydrolysis is coupled to mechanics compared to a constant hydrolysis rate because $p_{\mathrm{GTP}}(x)$ is much greater for larger x (see **Figures 11E,F**). As $\bar{\ell}_{\mathrm{cap}} < N_{\mathrm{pcap}}$, this increase in average cap length also explains the increased porous cap length if hydrolysis is coupled to mechanics.

The relative increase of hydrolyzed GDP-dimers at the tip could make MTs more prone for catastrophes and give rise to an increased catastrophe rate and, eventually, a more realistic concentration dependence of catastrophe rates. **Figure 12**,

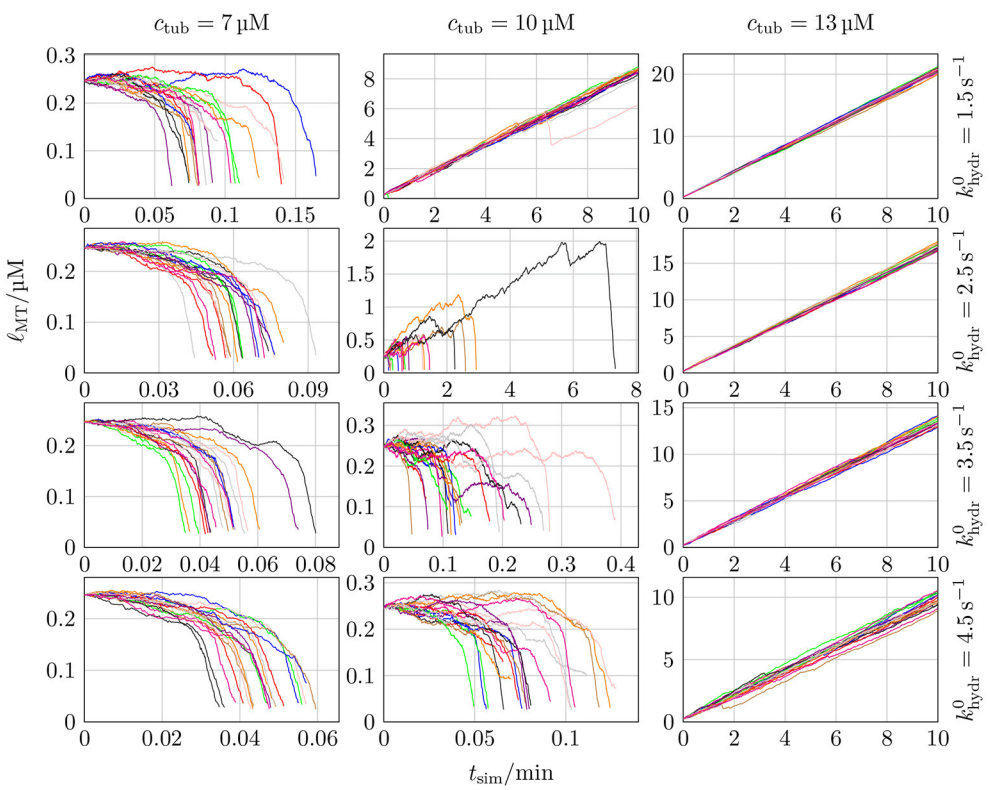

FIGURE 12 | MT length ℓ_{MT} as a function of the simulation time t_{sim} for 20 different simulations with $k_+ = 4\,\mu\mathrm{M}^{-1}\,\mathrm{s}^{-1}$, $\Delta G^{0*}_{\mathrm{long}} = -9.3\,k_{\mathrm{B}}T$, $k_{\mathrm{lat}} = 100\,k_{\mathrm{B}}T/\mathrm{nm}^2$, three different values of c_{tub}, and four different values of k^0_{hydr}.

however, shows that this is not the case. Instead, the same steep dependence on the (base) hydrolysis rate as in **Figure 7** persists.

In comparison to the MT growth trajectories with a constant hydrolysis rate shown in **Figures 10**, **13** shows an example of a MT simulation in which the hydrolysis rate is coupled to mechanics. To calculate the probabilities shown in the insets, the same criteria as for **Figure 10A** were used. At first sight, these trajectories look similar to the corresponding trajectories for a constant hydrolysis rate (**Figure 10A**). There is, however, a significantly increased roughness of the trajectory during the growth phase, which could be interpreted as increased occurrence of "dips" or "stutter" events. A high probability of stutter events has also been observed in reference [35], which supports the existence of a mechanochemical coupling in hydrolysis. The catastrophe-triggering configuration of a "nucleus" of several neighboring protofilaments shrinking by more than 6 dimers is also similar as snapshots 4 and 5 in **Figure 13B** show.

3.8. Dilution Experiments

In dilution experiments, the free tubulin dimer concentration c_{tub} is reduced to $c_{\mathrm{dil}} \ll c_{\mathrm{tub}}$ at a certain point in time [5, 72, 73]. If the diluted concentration is sufficiently small or zero, the GTP-cap stops growing by polymerization (and depolymerizes) but continues to hydrolyze; after a characteristic delay time $\Delta t_{\mathrm{delay}}$, the GTP-cap has vanished, a catastrophe is initiated, and the MT shrinks. Thus, dilution experiments and their comparison to corresponding dilution simulations can give information on the hydrolysis rate. Simulation results for the delay time are shown in **Figure 14**. In the **Supplementary Material**, we explain the algorithm that we used to determine the delay time $\Delta t_{\mathrm{delay}}$ from MT simulation trajectories in detail.

We expect the delay time to be proportional to the GTP-cap length, $\Delta t_{\mathrm{delay}} \propto \langle N_{\mathrm{cap}} \rangle$, as corroborated by **Figure 14C** and $\langle N_{\mathrm{cap}} \rangle \propto \sqrt{c_{\mathrm{tub}}/k_{\mathrm{hydr}}}$ according to section 3.5 (see **Figures 9C,D**) [70]. This results in $\Delta t_{\mathrm{delay}} \propto \sqrt{c_{\mathrm{tub}}/k_{\mathrm{hydr}}}$, which is in qualitative

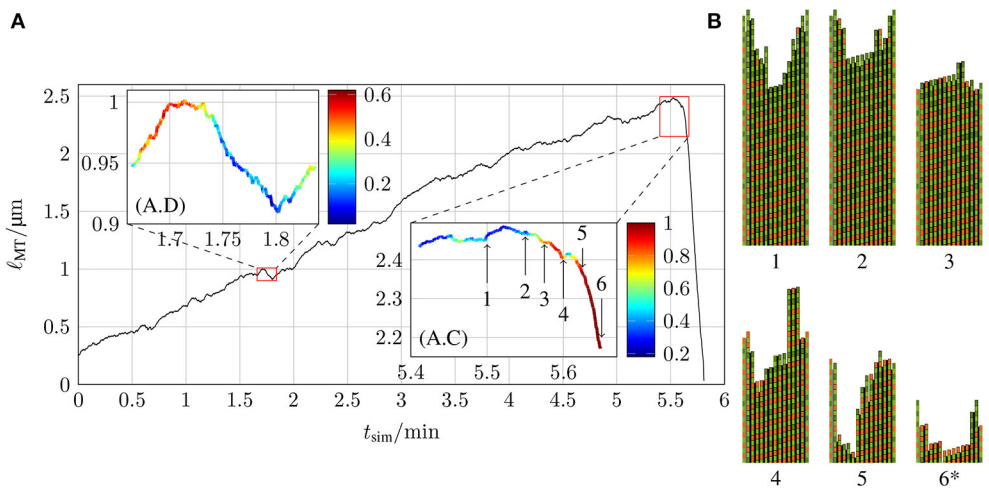

FIGURE 13 | (A) Length of a MT ℓ_{MT} as a function of the simulation time t_{sim} with $k_+ = 4\,\mu\mathrm{M}^{-1}\,\mathrm{s}^{-1}$, $\Delta G^{0*}_{\mathrm{long}} = -9.3\,k_{\mathrm{B}}T$, $k_{\mathrm{lat}} = 100\,k_{\mathrm{B}}T/\mathrm{nm}^2$, $c_{\mathrm{tub}} = 9\,\mu\mathrm{M}$ and $k^0_{\mathrm{hydr}} = 1.5\,\mathrm{s}^{-1}$ with hydrolysis being coupled to mechanics and **(B)** the two-dimensional representations of certain MT tip configurations that are marked by arrows in the inset (A.C) (configuration 6* has been shifted toward the MT tip by 21 tubulin dimer lengths).

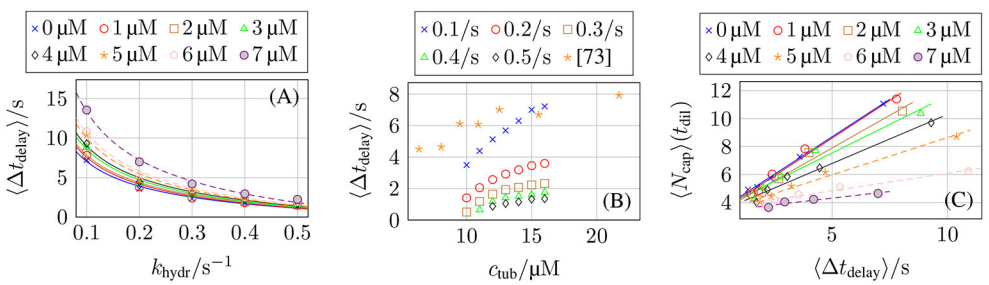

FIGURE 14 | Average post-dilution delay time $\langle \Delta t_{\mathrm{delay}} \rangle$ as a function of **(A)** the hydrolysis rate k_{hydr} for $c_{\mathrm{tub}} = 16\,\mu\mathrm{M}$ and different post-dilution GTP-tubulin dimer concentrations c_{dil} and **(B)** the pre-dilution GTP-tubulin dimer concentration c_{tub} for $c_{\mathrm{dil}} = 0\,\mu\mathrm{M}$ and different hydrolysis rates k_{hydr}. The averaged data from Duellberg et al. [73] specified the pre-dilution growth velocity, which was converted to c_{tub} for this plot. **(C)** Average GTP-cap length $\langle N_{\mathrm{cap}} \rangle$ at the time of dilution t_{dil} as a function of the delay time $\langle \Delta t_{\mathrm{delay}} \rangle$ for $c_{\mathrm{tub}} = 16\,\mu\mathrm{M}$ and different values of c_{dil}.

agreement with our simulation data in **Figures 14A,B**. The comparison with the experimental dilution data from reference [73] in **Figure 14B** shows that delay times for a hydrolysis rate $k_{\mathrm{hydr}} = 0.1\,s^{-1}$ come close to the experimental data but appear to depend too steeply on c_{tub}.

4. DISCUSSION

We introduced, parameterized, and analyzed a chemomechanical model for MT dynamics in which, in addition to polymerization (attachment of dimers), depolymerization (detachment of dimers), and hydrolysis of dimers, the rupture of lateral bonds between monomers in neighboring protofilaments is explicitly modeled and coupled to the mechanics of the MT. The basis for this coupling is the allosteric model according to which a hydrolyzed dimer acquires a more bent configuration, which builds up mechanical stress in the MT tubular structure via lateral bonds between dimers.

As many model parameters as possible have been determined from the experimentally measured MT growth and shrinkage velocities measured by Walker et al. [47]. To determine the values of the model parameters, we use a "divide and conquer" approach [15, 30]. We used simulations of growing GTP-only MTs to parameterize longitudinal and lateral bond energies $\Delta G^{0*}_{\mathrm{long}}$ and $\Delta G^{0}_{\mathrm{lat}}$ and the attempt rate k_{att} for lateral bond formation. By requiring a linear concentration dependence of growth velocity, we can fix all three parameter values for a given value of k_+. We used simulations of shrinking GDP-only MTs to parameterize the bending constant κ and the spring constant k_{lat} of the lateral bonds. Here, we can only fix one of the two parameters. Moreover, the hydrolysis rate k_{hydr} is still a free parameter, for which we use values in the range 0.1–0.5 s^{-1} known from experiments [61].

The general philosophy of a divide-and-conquer approach is the successive fixation of simulation parameters by using first GTP-only growth, then GDP-only shrinkage and, eventually, catastrophe frequencies or dilution to fix the hydrolysis rate. This successive fixation is, however, problematic, as the corresponding experimental data is influenced by all simulation parameters in general. The problem becomes apparent when considering the hydrolysis rate: changes in the hydrolysis rate also affect the growth rate over a wide concentration range because hydrolyzed dimers have an effectively higher detachment rate, see **Figure 9B**. Strictly speaking, all simulation parameters in **Table 2** must be determined at once by fitting several experimental results simultaneously instead of the successive fixation in the divide-and-conquer approach or to apply the divide-and-conquer approach iteratively several times until a self-consistent parameter set is found. A simultaneous fixation of all parameters has been performed, for example, in reference [31] on a chemical model without bond rupture and, thus, with only four parameters (on-rate, bond energies, and hydrolysis rate). Future work on our model should include at least a re-adjustment of the parameters once a hydrolysis rate is selected such that the growth velocity of Walker et al. [47] is reproduced in the presence of hydrolysis. If mechanical feedback onto hydrolysis is included, the model has to be re-parameterized again, in principle.

Our simulation model handles all chemical events, i.e., dimer attachment and detachment, bond rupture and formation, and hydrolysis using a Gillespie algorithm. After each chemical event, we relax the resulting MT structure mechanically by energy minimization based on the assumption that the microscopic mechanical dynamics is much faster than the chemical steps. Therefore, mechanical energy minimization is the computationally most demanding step in the simulation. This is a common problem in all dimer-based chemomechanical MT models [15, 16, 18]. We address this problem by restricting the mechanical energy minimization to bounded number MT degrees of freedom near the plus end. We showed that restricting energy minimization to a depth of $d_{\mathrm{cutoff}} = 10$ additional layers into the MT (in minus end direction) from the point of the last chemical event is an accurate and efficient choice. Computational efficiency of this procedure is better than performing a dedicated microscopic Brownian dynamics simulation [18] and better than random local energy minimization [15, 16] (for the same accuracy in energy minimization). The restricted energy minimization strategy also ensures that the number of minimization parameters does not scale with the MT length but remains bounded, which assures that we can simulate arbitrarily long growing MTs at a fixed minimal computational speed using our approach.

Simulations do not require more than a few hours for 1 min of MT dynamics (for a constant hydrolysis rate) using just a single CPU core. Therefore, we can reach time scales of several minutes of MT dynamics which is the time scale for repeated catastrophe events for concentrations above the individual critical concentration, where the dynamic instability can occur. We performed a first systematic analysis of catastrophe and rescue rates in **Figure 8**, which indicates that the decrease of the catastrophe rate with tubulin concentration is too steep compared to experimental data [47, 66]. It is also much steeper than simulation results of reference [18] but these results for the catastrophe rate relied on linear extrapolation from unrealistically high hydrolysis rates (3–11 s^{-1}) down to realistic values (0.1–0.5 s^{-1}). In the future, our computational model can also be used to measure the dependence of catastrophe rates on MT lifetime [67].

Within our model, we could also study single catastrophe and rescue events in detail (see **Figure 10**). The growth paths appear very similar to experimentally observed catastrophe and rescue events. Catastrophes typically feature an initial "transitional" phase of slow shrinking by 50–100 nm as also observed in reference [35]. Moreover, we observe "dips" in the growth paths resembling the "stutter" events from reference [35].

The most interesting results of chemomechanical models are possible statements about the typical catastrophe-triggering configurations. In this respect, our simulations indicate that a catastrophe could be triggered by a "nucleus" of three neighboring protofilaments shrinking by more than 6 dimers, such that its GTP-cap is removed and its ends reach into the GDP-body of the MT. To rescue a shrinking MT the GTP-cap has to be re-established on almost all 13 protofilaments such that

nuclei of three neighboring uncapped GDP-protofilaments are avoided. This shows that mechanical correlations in the dynamics of protofilaments are important in triggering catastrophe events. This is an aspect which is absent in the calculation of catastrophe frequencies based on simplified purely chemical models, such as in reference [68], where protofilaments are regarded as effectively independent and uncorrelated.

Our model can achieve qualitative agreement with experimental data on dilution experiments (see **Figure 14C**) from reference [73] for relatively low hydrolysis rates of $k_{\mathrm{hydr}} = 0.1\,s^{-1}$, which is an indication that the catastrophe mechanism is correctly captured by our chemomechanical model. This also constrains the hydrolysis rate, which is still a free parameter in our model, to lower values around $k_{\mathrm{hydr}} = 0.1\,s^{-1}$.

Finally, we explored the consequences of a mechanochemical coupling in the hydrolysis of tubulin dimers. Because hydrolysis gives rise to bending of the GTP-dimers, we argue that mechanical forces on a dimer that increase its bending angle should also lead to higher hydrolysis rates, see (12) and (14). In the presence of mechanical feedback, hydrolysis gets a bias toward the MT plus end which, in turn, also causes an increase in porous cap length. At the same average hydrolysis rate, hydrolysis in the immediate tip of the GTP-cap is more likely while it is less likely in the remaining part of the cap such that GTP-tubulin dimers can be found much deeper in the GDP-body (see **Figure 11**). Individual catastrophe and rescue events (see **Figure 13**) look qualitatively similar in the presence of mechanical feedback but the probability of "dips" or "stutter" events is increased in agreement with reference [35]. The coupling of hydrolysis to mechanics does not increase catastrophe rates significantly such that the steep decrease of the catastrophe rate with tubulin concentration persists.

The main problem of our model appears to be the steep decrease of catastrophe rate with tubulin concentration, which could hint to a failure of basic assumptions. One possibility is that a direct effect of the hydrolysis state of the dimer onto the off-rate (as also suggested by atomistic simulations [74]) is relevant and not included in the model. Another possibility is a failure of allosteric models in general. The steep decline of catastrophe rates with the tubulin concentration gives a hint that MTs are structurally too stable for GTP-rich caps. This might provide evidence for a shortcoming of the underlying allosteric model, which inserts GTP-dimers in a straight configuration that is more prone to form stable lateral bonds than a curved configuration. An alternative are so-called lattice models [20, 21], according to which dimers are always bent but hydrolysis affects lateral and longitudinal dimer interaction energies. A systematic comparison of allosteric and lattice models toward the resulting concentration dependence of catastrophe rates within the framework provided here could help decide which class of models is more appropriate.

So far, almost all chemomechanical modeling approaches were based on the allosteric model [14–19] but recent experimental advancements in the analysis of the structure of MT tips [26] demonstrated that both growing and shrinking MTs have bent protofilament ends supporting similar earlier results [75–78]. Additionally, calculations using MT structures with different nucleotide content in the beta-tubulin [23] and all-atom MD simulations of GTP- and GDP-only MTs [24, 25] revealed that hydrolysis weakens lateral bonds and strengthens longitudinal bonds. Both aspects support the lattice model for the influence of hydrolysis on MT mechanics. There is, however, also evidence from MD simulations for intermediate models, where hydrolysis affects interactions and also leads to a much lower GDP-tubulin flexibility [27]. Independent of these findings, our study based on the allosteric model is valuable for the following reasons: (i) In both the allosteric and the lattice model, catastrophes are cascades of lateral bond rupture and in both models, the bent shape of GDP-dimers is the dominating cause of mechanical strain in the MT structure. In the allosteric model, bending and mechanical strain is directly generated by the hydrolysis of GTP-dimers, whereas in the lattice model, the tubulin dimers are always bent but hydrolysis weakens lateral bonds. In both models, the result is an increased lateral bond rupture rate of mechanically strained bonds after hydrolysis. Therefore, an explicit modeling approach for lateral bond rupture as a stochastic process under force generated by the bending of GDP-dimers will also be important in all future chemomechanical models based on the lattice model. So far explicit stochastic models of lateral bond rupture have only been included into two-dimensional models lacking explicit mechanics [32–34] or with heavy computational cost by explicitly simulating the Brownian dynamics of dimers and bonds [18]. (ii) The importance of lateral bond rupture becomes particularly clear for shrinking MTs or MTs entering a catastrophe. In these phases of the dynamic instability, GDP-tubulin dimers are significantly more relevant than GTP-tubulin dimers. As GDP-dimers are bent in both models and this bending gives rise to lateral bond stretching, we believe that both types of models will display a very similar behavior in these phases. The only difference in this scenario is that in the lattice model, the lateral bond energy $\Delta G^0_{\mathrm{lat}}$ in the rupture rate (10) will depend on the nucleotide type of the bonded tubulin monomers, which also makes k_{rup} an explicit function of the nucleotide state. Because the nucleotide state is predominantly GDP during shrinkage, the results for properly parameterized models will be very similar. (iii) We also introduced a computationally efficient scheme to relax the mechanical energy between chemical events, which can also be employed in future chemomechanical lattice models. Within the allosteric model, we achieve a better mechanical energy relaxation than previous models [15] with significantly less computational steps than a full Brownian dynamics simulation requires [18]. (iv) The idea of a feedback of mechanical forces onto the hydrolysis rate can also be applied in future chemomechanical lattice models: if hydrolysis leads to a weakening of lateral bonds, one could expect mechanical strains that favor weakening of lateral bonds also to favor hydrolysis.

In the future, our model could be extended to also include regulating TIP+ proteins [79] for which different mechanisms of how they influence MTs could be implemented. Comparing the results of such simulations with experimental data could help to develop a mechanistic picture of the action of these proteins. Another future extension is MT polymerization under force [80, 81]. So far, polymerization under force has been investigated using chemical models [56, 82–85]; the influence

of an external force on the microscopic level, in particular the detailed dynamics of catastrophe events and the catastrophe-triggering configurations is unknown.

DATA AVAILABILITY STATEMENT

The raw data supporting the conclusions of this article will be made available by the authors, without undue reservation.

AUTHOR CONTRIBUTIONS

MS performed the simulations and theoretical analysis, evaluated the data, wrote, and revised the manuscript. JK conceived the research, wrote, and revised the manuscript. Both authors contributed to the article and approved the submitted version.

FUNDING

We acknowledge funding from the German Research Foundation (DFG, www.dfg.de) through Grant number KI 662/9-1. The authors gratefully acknowledge computing time provided on the Linux HPC cluster at Technical University Dortmund (LiDO3), partially funded in the course of the Large-Scale Equipment Initiative by the German Research Foundation (DFG) as project 271512359.

SUPPLEMENTARY MATERIAL

The Supplementary Material for this article can be found online at: https://www.frontiersin.org/articles/10.3389/fphy.2021.673875/full#supplementary-material

REFERENCES

1. McIntosh JR, Grishchuk EL, West RR. Chromosome-microtubule interactions during mitosis. *Annu Rev Cell Dev Biol*. (2002) 18:193–219. doi: 10.1146/annurev.cellbio.18.032002.132412
2. Siegrist SE, Doe CQ. Microtubule-induced cortical cell polarity. *Genes Dev*. (2007) 21:483–96. doi: 10.1101/gad.1511207
3. Mitchison T, Kirschner M. Dynamic instability of microtubule growth. *Nature*. (1984) 312:237–42. doi: 10.1038/312237a0
4. Carlier MF, Hill TL, Chen Yd. Interference of GTP hydrolysis in the mechanism of microtubule assembly: an experimental study. *Proc Natl Acad Sci USA*. (1984) 81:771–5. doi: 10.1073/pnas.81.3.771
5. Walker RA, Pryer NK, Salmon ED. Dilution of individual microtubules observed in real time *in vitro*: evidence that cap size is small and independent of elongation rate. *J Cell Biol*. (1991) 114:73–81. doi: 10.1083/jcb.114.1.73
6. Howard J, Hyman AA. Growth, fluctuation and switching at microtubule plus ends. *Nat Rev Mol Cell Biol*. (2009) 10:569–74. doi: 10.1038/nrm2713
7. van Haren J, Wittmann T. Microtubule plus end dynamics-do we know how microtubules grow? *Bioessays*. (2019) 41:1800194. doi: 10.1002/bies.201800194
8. Mandelkow EM, Mandelkow E, Milligan RA. Microtubule dynamics and microtubule caps: a time-resolved cryo-electron microscopy study. *J Cell Biol*. (1991) 114:977–91. doi: 10.1083/jcb.114.5.977
9. McIntosh JR, Volkov V, Ataullakhanov FI, Grishchuk EL. Tubulin depolymerization may be an ancient biological motor. *J Cell Sci*. (2010) 123:3425–34. doi: 10.1242/jcs.067611
10. Müller-Reichert T, Chrétien D, Severin F, Hyman AA. Structural changes at microtubule ends accompanying GTP hydrolysis: Information from a slowly hydrolyzable analogue of GTP, guanylyl (α,β) methylenediphosphonate. *Proc Natl Acad Sci USA*. (1998) 95:3661–6. doi: 10.1073/pnas.95.7.3661
11. Downing KH, Eva N. Tubulin and microtubule structure. *Curr Opin Cell Biol*. (1998) 10:16–22. doi: 10.1016/S0955-0674(98)80082-3
12. Nogales E, Wang HW. Structural mechanisms underlying nucleotide-dependent self-assembly of tubulin and its relatives. *Curr Opin Struct Biol*. (2006) 16:221–9. doi: 10.1016/j.sbi.2006.03.005
13. Nogales E, Whittaker M, Milligan RA, Downing KH. High-resolution model of the microtubule. *Cell*. (1999) 96:79–88. doi: 10.1016/S0092-8674(00)80961-7
14. Molodtsov MI, Ermakova EA, Shnol EE, Grishchuk EL, McIntosh JR, Ataullakhanov FI. A molecular-mechanical model of the microtubule. *Biophys J*. (2005) 88:3167–79. doi: 10.1529/biophysj.104.051789
15. VanBuren V, Cassimeris L, Odde DJ. Mechanochemical model of microtubule structure and self-assembly kinetics. *Biophys J*. (2005) 89:2911–26. doi: 10.1529/biophysj.105.060913
16. Coombes C, Yamamoto A, Kenzie M, Odde D, Gardner M. Evolving tip structures can explain age-dependent microtubule catastrophe. *Curr Biol*. (2013) 23:1342–8. doi: 10.1016/j.cub.2013.05.059
17. Müller N, Kierfeld J. Effects of microtubule mechanics on hydrolysis and catastrophes. *Phys Biol*. (2014) 11:046001. doi: 10.1088/1478-3975/11/4/046001
18. Zakharov P, Gudimchuk N, Voevodin V, Tikhonravov A, Ataullakhanov F, Grishchuk E. Molecular and mechanical causes of microtubule catastrophe and aging. *Biophys J*. (2015) 109:2574–91. doi: 10.1016/j.bpj.2015.10.048
19. Jain I, Inamdar MM, Padinhateeri R. Statistical mechanics provides novel insights into microtubule stability and mechanism of shrinkage. *PLoS Comput Biol*. (2015) 11:e1004099. doi: 10.1371/journal.pcbi.1004099
20. Buey RM, Díaz JF, Andreu JM. The nucleotide switch of tubulin and microtubule assembly: a polymerization-driven structural change. *Biochemistry*. (2006) 45:5933–8. doi: 10.1021/bi060334m
21. Rice LM, Montabana EA, Agard DA. The lattice as allosteric effector: structural studies of $\alpha\beta$- and γ-tubulin clarify the role of GTP in microtubule assembly. *Proc Natl Acad Sci USA*. (2008) 105:5378–83. doi: 10.1073/pnas.0801155105
22. Alushin GM, Lander GC, Kellogg EH, Zhang R, Baker D, Nogales E. High-resolution microtubule structures reveal the structural transitions in $\alpha\beta$-tubulin upon GTP hydrolysis. *Cell*. (2014) 157:1117–29. doi: 10.1016/j.cell.2014.03.053
23. Manka SW, Moores CA. The role of tubulin–tubulin lattice contacts in the mechanism of microtubule dynamic instability. *Nat Struct Mol Biol*. (2018) 25:607–15. doi: 10.1038/s41594-018-0087-8
24. Ayoub AT, Klobukowski M, Tuszynski JA. Detailed per-residue energetic analysis explains the driving force for microtubule disassembly. *PLoS Comput Biol*. (2015) 11:e1004313. doi: 10.1371/journal.pcbi.1004313
25. Fedorov VA, Orekhov PS, Kholina EG, Zhmurov AA, Ataullakhanov FI, Kovalenko IB, et al. Mechanical properties of tubulin intra- and inter-dimer interfaces and their implications for microtubule dynamic instability. *PLoS Comput Biol*. (2019) 15:e1007327. doi: 10.1371/journal.pcbi.1007327
26. McIntosh JR, O'Toole E, Morgan G, Austin J, Ulyanov E, Ataullakhanov F, et al. Microtubules grow by the addition of bent guanosine triphosphate tubulin to the tips of curved protofilaments. *J Cell Biol*. (2018) 217:2691–708. doi: 10.1083/jcb.201802138
27. Igaev M, Grubmüller H. Microtubule assembly governed by tubulin allosteric gain in flexibility and lattice induced fit. *Elife*. (2018) 7:e34353. doi: 10.7554/eLife.34353.041
28. Zakharov PN, Arzhanik VK, Ulyanov EV, Gudimchuk NB, Ataullakhanov FI. Microtubules: dynamically unstable stochastic phase-switching polymers. *Phys Uspekhi*. (2016) 59:773–86. doi: 10.3367/UFNe.2016.04.037779
29. Dogterom M, Leibler S. Physical aspects of the growth and regulation of microtubule structures. *Phys Rev Lett*. (1993) 70:1347–50. doi: 10.1103/PhysRevLett.70.1347

30. VanBuren V, Odde DJ, Cassimeris L. Estimates of lateral and longitudinal bond energies within the microtubule lattice. *Proc Natl Acad Sci USA*. (2002) 99:6035–40. doi: 10.1073/pnas.092504999
31. Piette BMAG, Liu J, Peeters K, Smertenko A, Hawkins T, Deeks M, et al. A thermodynamic model of microtubule assembly and disassembly. *PLoS ONE*. (2009) 4:e6378. doi: 10.1371/journal.pone.0006378
32. Margolin G, Goodson HV, Alber MS. Mean-field study of the role of lateral cracks in microtubule dynamics. *Phys Rev E*. (2011) 83:041905. doi: 10.1103/PhysRevE.83.041905
33. Margolin G, Gregoretti IV, Cickovski TM, Li C, Shi W, Alber MS, et al. The mechanisms of microtubule catastrophe and rescue: implications from analysis of a dimer-scale computational model. *Mol Biol Cell*. (2012) 23:642–56. doi: 10.1091/mbc.e11-08-0688
34. Li C, Li J, Goodson HV, Alber MS. Microtubule dynamic instability: the role of cracks between protofilaments. *Soft Matter*. (2014) 10:2069–80. doi: 10.1039/C3SM52892H
35. Mahserejian SM, Scripture JP, Mauro AJ, Lawrence EJ, Jonasson EM, Murray KS, et al. Stutter: a transient dynamic instability phase that is strongly associated with catastrophe. *bioRxiv*. (2019). doi: 10.1101/2019.12.16.878603
36. Wang HW, Nogales E. Nucleotide-dependent bending flexibility of tubulin regulates microtubule assembly. *Nature*. (2005) 435:911–5. doi: 10.1038/nature03606
37. VanBuren V, Odde DJ, Cassimeris L. Errata for VanBuren et al., Estimates of lateral and longitudinal bond energies within the microtubule lattice, PNAS 2002 99:6035–6040. *Proc Natl Acad Sci USA*. (2004) 101:14989. doi: 10.1073/pnas.0406393101
38. Harris BJ, Ross JL, Hawkins TL. Microtubule seams are not mechanically weak defects. *Phys Rev E*. (2018) 97:062408. doi: 10.1103/PhysRevE.97.062408
39. Elie-Caille C, Severin F, Helenius J, Howard J, Muller DJ, Hyman AA. Straight GDP-tubulin protofilaments form in the presence of taxol. *Curr Biol*. (2007) 17:1765–70. doi: 10.1016/j.cub.2007.08.063
40. Kroy K, Frey E. Dynamic scattering from solutions of semiflexible polymers. *Phys Rev E*. (1997) 55:3092–101. doi: 10.1103/PhysRevE.55.3092
41. Ulyanov EV, Vinogradov DS, McIntosh JR, Gudimchuk NB. Brownian dynamics simulation of protofilament relaxation during rapid freezing. *PLoS ONE*. (2021) 16:e0247022. doi: 10.1371/journal.pone.0247022
42. Gardner M, Charlebois B, Jánosi I, Howard J, Hunt A, Odde D. Rapid microtubule self-assembly kinetics. *Cell*. (2011) 146:582–92. doi: 10.1016/j.cell.2011.06.053
43. Kononova O, Kholodov Y, Theisen KE, Marx KA, Dima RI, Ataullakhanov FI, et al. Tubulin bond energies and microtubule biomechanics determined from nanoindentation *in silico*. *J Am Chem Soc*. (2014) 136:17036–45. doi: 10.1021/ja506385p
44. Bell GI. Models for the specific adhesion of cells to cells. *Science*. (1978) 200:618–27. doi: 10.1126/science.347575
45. Evans E, Ritchie K. Dynamic strength of molecular adhesion bonds. *Biophys J*. (1997) 72:1541–55. doi: 10.1016/S0006-3495(97)78802-7
46. Gillespie DT. A general method for numerically simulating the stochastic time evolution of coupled chemical reactions. *J Comput Phys*. (1976) 22:403–34. doi: 10.1016/0021-9991(76)90041-3
47. Walker RA, O'Brien ET, Pryer NK, Soboeiro MF, Voter WA, Erickson HP, et al. Dynamic instability of individual microtubules analyzed by video light microscopy: rate constants and transition frequencies. *J Cell Biol*. (1988) 107:1437–48. doi: 10.1083/jcb.107.4.1437
48. O'Brien ET, Salmon ED, Walker RA, Erickson HP. Effects of magnesium on the dynamic instability of individual microtubules. *Biochemistry*. (1990) 29:6648–56. doi: 10.1021/bi00480a014
49. Drechsel DN, Hyman AA, Cobb MH, Kirschner MW. Modulation of the dynamic instability of tubulin assembly by the microtubule-associated protein tau. *Mol Biol Cell*. (1992) 3:1141–54. doi: 10.1091/mbc.3.10.1141
50. Trinczek B, Marx A, Mandelkow EM, Murphy DB, Mandelkow E. Dynamics of microtubules from erythrocyte marginal bands. *Mol Biol Cell*. (1993) 4:323–35. doi: 10.1091/mbc.4.3.323
51. Chrétien D, Fuller SD, Karsenti E. Structure of growing microtubule ends: two-dimensional sheets close into tubes at variable rates. *J Cell Biol*. (1995) 129:1311–28. doi: 10.1083/jcb.129.5.1311
52. Pedigo S, Williams RC Jr. Concentration dependence of variability in growth rates of microtubules. *Biophys J*. (2002) 83:1809–19. doi: 10.1016/S0006-3495(02)73946-5
53. Galassi M, Davies J, Theiler J, Gough B, Jungman G, Alken P, et al. *GNU Scientific Library Reference Manual*. Available online at: https://www.gnu.org/software/gsl/
54. Ayaz P, Munyoki S, Geyer EA, Piedra FA, Vu ES, Bromberg R, et al. A tethered delivery mechanism explains the catalytic action of a microtubule polymerase. *eLife*. (2014) 3:e03069. doi: 10.7554/eLife.03069.014
55. Mickolajczyk KJ, Geyer EA, Kim T, Rice LM, Hancock WO. Direct observation of individual tubulin dimers binding to growing microtubules. *Proc Natl Acad Sci USA*. (2019) 116:7314–22. doi: 10.1073/pnas.1815823116
56. Stukalin EB, Kolomeisky AB. Simple growth models of rigid multifilament biopolymers. *J Chem Phys*. (2004) 121:1097–104. doi: 10.1063/1.1759316
57. Sim H, Sept D. Properties of microtubules with isotropic and anisotropic mechanics. *Cell Mol Bioeng*. (2013) 6:361–8. doi: 10.1007/s12195-013-0302-y
58. Driver JW, Geyer EA, Bailey ME, Rice LM, Asbury CL. Direct measurement of conformational strain energy in protofilaments curling outward from disassembling microtubule tips. *eLife*. (2017) 6:e28433. doi: 10.7554/eLife.28433.023
59. Deriu MA, Enemark S, Soncini M, Montevecchi FM, Redaelli A. Tubulin: from atomistic structure to supramolecular mechanical properties. *J Mater Sci*. (2007) 42:8864–72. doi: 10.1007/s10853-007-1784-6
60. Grafmüller A, Voth G. Intrinsic bending of microtubule protofilaments. *Structure*. (2011) 19:409–17. doi: 10.1016/j.str.2010.12.020
61. Melki R, Fievez S, Carlier MF. Continuous monitoring of P_i release following nucleotide hydrolysis in actin or tubulin assembly using 2-amino-6-mer-capto-7-methylpurine ribonucleoside and purine-nucleoside phosphorylase as an enzyme-linked assay. *Biochemistry*. (1996) 35:12038–45. doi: 10.1021/bi961325o
62. Aparna JS, Padinhateeri R, Das D. Signatures of a macroscopic switching transition for a dynamic microtubule. *Sci Rep*. (2017) 7:45747. doi: 10.1038/srep45747
63. Padinhateeri R, Kolomeisky A, Lacoste D. Random hydrolysis controls the dynamic instability of microtubules. *Biophys J*. (2012) 102:1274–83. doi: 10.1016/j.bpj.2011.12.059
64. Bowne-Anderson H, Zanic M, Kauer M, Howard J. Microtubule dynamic instability: a new model with coupled GTP hydrolysis and multistep catastrophe. *Bioessays*. (2013) 35:452–61. doi: 10.1002/bies.201200131
65. Piedra FA, Kim T, Garza ES, Geyer EA, Burns A, Ye X, et al. GDP-to-GTP exchange on the microtubule end can contribute to the frequency of catastrophe. *Mol Biol Cell*. (2016) 27:3515–25. doi: 10.1091/mbc.e16-03-0199
66. Janson ME, de Dood ME, Dogterom M. Dynamic instability of microtubules is regulated by force. *J Cell Biol*. (2003) 161:1029–34. doi: 10.1083/jcb.200301147
67. Gardner M, Zanic M, Gell C, Bormuth V, Howard J. Depolymerizing kinesins Kip3 and MCAK shape cellular microtubule architecture by differential control of catastrophe. *Cell*. (2011) 147:1092–103. doi: 10.1016/j.cell.2011.10.037
68. Flyvbjerg H, Holy TE, Leibler S. Microtubule dynamics: caps, catastrophes, and coupled hydrolysis. *Phys Rev E*. (1996) 54:5538–60. doi: 10.1103/PhysRevE.54.5538
69. Zelinski B, Kierfeld J. Cooperative dynamics of microtubule ensembles: polymerization forces and rescue-induced oscillations. *Phys Rev E*. (2013) 87:012703. doi: 10.1103/PhysRevE.87.012703
70. Li X, Lipowsky R, Kierfeld J. Coupling of actin hydrolysis and polymerization: reduced description with two nucleotide states. *Europhys Lett*. (2011) 89:38010. doi: 10.1209/0295-5075/89/38010
71. Seetapun D, Castle B, McIntyre A, Tran P, Odde D. Estimating the microtubule GTP cap size *in vivo*. *Curr Biol*. (2012) 22:1681–7. doi: 10.1016/j.cub.2012.06.068
72. Voter WA, O'Brien ET, Erickson HP. Dilution-induced disassembly of microtubules: relation to dynamic instability and the GTP cap. *Cell Motil Cytoskeleton*. (1991) 18:55–62. doi: 10.1002/cm.970180106
73. Duellberg C, Cade NI, Holmes D, Surrey T. The size of the EB cap determines instantaneous microtubule stability. *eLife*. (2016) 5:e13470. doi: 10.7554/eLife.13470.023
74. Grafmüller A, Noya EG, Voth GA. Nucleotide-dependent lateral and longitudinal interactions in microtubules. *J Mol Biol*. (2013) 425:2232–46. doi: 10.1016/j.jmb.2013.03.029
75. Höög JL, Huisman SM, Sebö-Lemke Z, Sandblad L, McIntosh JR, Antony C, et al. Electron tomography reveals a flared morphology on

growing microtubule ends. *J Cell Sci*. (2011) 124:693–8. doi: 10.1242/jcs.072967
76. Kukulski W, Schorb M, Welsch S, Picco A, Kaksonen M, Briggs JAG. Correlated fluorescence and 3D electron microscopy with high sensitivity and spatial precision. *J Cell Biol*. (2011) 192:111–9. doi: 10.1083/jcb.201009037
77. Nawrotek A, Knossow M, Gigant B. The determinants that govern microtubule assembly from the atomic structure of GTP-tubulin. *J Mol Biol*. (2011) 412:35–42. doi: 10.1016/j.jmb.2011.07.029
78. Pecqueur L, Duellberg C, Dreier B, Jiang Q, Wang C, Plückthun A, et al. A designed ankyrin repeat protein selected to bind to tubulin caps the microtubule plus end. *Proc Natl Acad Sci USA*. (2012) 109:12011–16. doi: 10.1073/pnas.1204129109
79. Akhmanova A, Steinmetz MO. Tracking the ends: a dynamic protein network controls the fate of microtubule tips. *Nat Rev Mol Cell Biol*. (2008) 9:309–22. doi: 10.1038/nrm2369
80. Dogterom M, Yurke B. Measurement of the force-velocity relation for growing microtubules. *Science*. (1997) 278:856–60. doi: 10.1126/science.278.5339.856
81. Dogterom M, Kerssemakers JWJ, Romet-Lemonne G, Janson ME. Force generation by dynamic microtubules. *Curr Opin Cell Biol*. (2005) 17:67–74. doi: 10.1016/j.ceb.2004.12.011
82. van Doorn GS, Tănase C, Mulder BM, Dogterom M. On the stall force for growing microtubules. *Eur Biophys J*. (2000) 29:2–6. doi: 10.1007/s002490050245
83. Kolomeisky AB, Fisher ME. Force-velocity relation for growing microtubules. *Biophys J*. (2001) 80:149–54. doi: 10.1016/S0006-3495(01)76002-X
84. Ranjith P, Lacoste D, Mallick K, Joanny JF. Nonequilibrium self-assembly of a filament coupled to ATP/GTP hydrolysis. *Biophys J*. (2009) 96:2146–59. doi: 10.1016/j.bpj.2008.12.3920
85. Krawczyk J, Kierfeld J. Stall force of polymerizing microtubules and filament bundles. *Europhys Lett*. (2011) 93:28006. doi: 10.1209/0295-5075/93/28006

Conflict of Interest: The authors declare that the research was conducted in the absence of any commercial or financial relationships that could be construed as a potential conflict of interest.

frontiers in Physics

ORIGINAL RESEARCH
published: 04 June 2021
doi: 10.3389/fphy.2021.680983

Coarse-Grained Modeling of Coronavirus Spike Proteins and ACE2 Receptors

*Timothy Leong, Chandhana Voleti and Zhangli Peng**

Richard and Loan Hill Department of Bioengineering, University of Illinois at Chicago, Chicago, IL, United States

We developed coarse-grained models of spike proteins in SARS-CoV-2 coronavirus and angiotensin-converting enzyme 2 (ACE2) receptor proteins to study the endocytosis of a whole coronavirus under physiologically relevant spatial and temporal scales. We first conducted all-atom explicit-solvent molecular dynamics simulations of the recently characterized structures of spike and ACE2 proteins. We then established coarse-grained models using the shape-based coarse-graining approach based on the protein crystal structures and extracted the force field parameters from the all-atom simulation trajectories. To further analyze the coarse-grained models, we carried out normal mode analysis of the coarse-grained models to refine the force field parameters by matching the fluctuations of the internal coordinates with the original all-atom simulations. Finally, we demonstrated the capability of these coarse-grained models by simulating the endocytosis of a whole coronavirus through the host cell membrane. We embedded the coarse-grained models of spikes on the surface of the virus envelope and anchored ACE2 receptors on the host cell membrane, which is modeled using a one-particle-thick lipid bilayer model. The coarse-grained simulations show the spike proteins adopt bent configurations due to their unique flexibility during their interaction with the ACE2 receptors, which makes it easier for them to attach to the host cell membrane than rigid spikes.

Keywords: multiscale modeling, endocytosis, SARS-CoV-2, cell membrane, coarse-graining

OPEN ACCESS

Edited by:
Ying Li,
University of Connecticut,
United States

Reviewed by:
Baofu Qiao,
Northwestern University,
United States
Zhiqiang Shen,
Oak Ridge National Laboratory (DOE),
United States

****Correspondence:***
Zhangli Peng
zhpeng@uic.edu

Specialty section:
This article was submitted to Biophysics, a section of the journal Frontiers in Physics

Received: *15 March 2021*
Accepted: *18 May 2021*
Published: *04 June 2021*

Citation:
Leong T, Voleti C and Peng Z (2021) Coarse-Grained Modeling of Coronavirus Spike Proteins and ACE2 Receptors. Front. Phys. 9:680983. doi: 10.3389/fphy.2021.680983

INTRODUCTION

Although a significant amount of research effort has been conducted to understand the SARS-CoV-2 coronaviruses and vaccines have been developed the exact infection mechanisms remain unclear [1]. Coronaviruses are spherical viruses with unique surface spikes [2]. The average diameter is about 80–120 nm. The virus is protected by the envelope and nucleocapsid when it is outside the host cell [3]. The RNAs of the virus are enclosed in an envelope with a diameter of roughly 85 nm [1]. The envelope consists of a lipid bilayer and the membrane (M), envelope (E), and spike (S) structural proteins embedded in the bilayer. While membrane proteins, envelope proteins, and the lipid bilayer shape the viral envelope and maintain its size, spike proteins interact with the host cells by binding with surface receptors such as angiotensin-converting enzyme 2 (ACE2) receptors. Cryo-electron microscopy (cryo-EM) and x-ray crystallographic techniques have been applied to reveal the new structures of viral proteins [4–16]. Due to their significance, computational modeling was employed alongside experimental studies to investigate the properties of these proteins [17], but most of these existing computational studies are limited to atomistic length and time scales. In this study, we will

investigate the endocytosis of the whole virus under physiologically relevant spatial and temporal scales by constructing coarse-grained models of the spike proteins and ACE2 receptors.

On the one hand, multiscale coarse-grained models of the whole coronavirus have been developed [15], but they have not been applied to study the endocytosis. In addition, to build a minimal model with enough molecular details, we adopted a more aggressive coarse-graining approach than that used in [15] for both proteins and membranes. On the other hand, the endocytosis of nanoparticles has been extensively studied by computational modeling [18–24], but the endocytosis of coronavirus has not been explored computationally with sufficient molecular details. In the current study, we will explicitly take into account the detailed molecular structures of the spikes and ACE2 rather than modeling them as abstract binding points.

We will focus on establishing the coarse-grained models of the spike proteins and ACE2 receptors. The spikes are unique structures of coronaviruses and are responsible for their distinguishing halo-like surface. A coronavirus particle typically has about 70 spikes on its surface [25]. Each spike consists of three spike proteins (a trimer) and its length is about 20 nm. Each spike protein is made of an S1 head subunit and an S2 stem subunit. The S1 head subunit includes the receptor-binding domain (RBD). Although one spike has three RBDs, only one of them is in the up position for binding [26]. The S2 stem subunit anchors the spike in the viral envelope. Recently, the crystal structure of the SARS-CoV-2 spike protein has been characterized using cryo-EM [PDB ID: 6Vestigial sideband (VSB)] [6], which is responsible for binding to the cell membrane *via* the extracellular domain of the ACE2 receptor (PDB ID: 6M17) [27]. ACE2 receptor is a membrane-bound carboxypeptidase that forms a dimer and serves as the cellular receptor for SARS-CoV-2 [27]. Molecular dynamics (MD) simulations revealed that the spike protein polybasic cleavage sites, which are distributed approximately 10 nm away from the RBD, can enhance the binding affinity between the SARS-CoV-2 RBD and ACE2 [28]. We took this into consideration by using the enhanced binding energy (−177 kcal/mol) between RBD and ACE2 among the predicted values of −50 kcal/mol ∼ −177 kcal/mol [28–32].

During the infection, the viral spike proteins first attach to their complementary host cell receptors such as ACE2. Then the host cell protease activates the receptor-attached spike proteins. The virus enters the host cell by either endocytosis or membrane fusion of the viral envelope with the host membrane, depending on the availability of the host cell proteases [33]. One of our goals is to simulate the endocytosis by coarse-grained modeling and explicit consideration of the structures of spike and receptor proteins. We will focus on the endocytosis simulation in this study and extend the model to study membrane fusion in the future.

Since the coronavirus is more than 80 nm, all-atom molecular dynamics simulation is prohibitively expensive, not to mention the long-time scale of the endocytosis. Instead, we will apply a multiscale modeling approach. We will conduct all-atom MD simulations of the spike protein and the ACE2 receptors based on their recently characterized crystal structures. Then we will build coarse-grained models of these proteins using the all-atom simulation trajectories. After we demonstrate that the coarse-grained model share similar structural properties with the original all-atom proteins by matching fluctuations, we will construct a whole virus model with a realistic number of spike proteins, and conduct simulations of the endocytosis process of the virus to investigate the cell entry mechanisms. In addition, we developed automated scripts and MATLAB code for establishing these CG models and conducting normal mode analysis. We made them publicly available so that other users can repeat and modify these models.

MATERIALS AND METHODS

All-Atom Molecular Dynamics Simulations

All-atom MD simulations of the spike protein and ACE2 receptor were conducted using Nanoscale Molecular Dynamics (NAMD) [34]. Explicit solvent is used in order to capture the accurate fluctuations of the structure in equilibrium. A standard protocol is applied. Minimization and annealing processes were carried out first and then equilibrium simulation with the backbone fixed were done before production MD simulations were run. Both the fully-glycosylated full-length spike protein model (**Supplementary Figure S1** in the Supplementary Material) and spike protein head S1 subunit model (**Figure 1A**) were conducted by following the procedure described in [35]. The simulation of the S1 subunit model is used to extract the force field parameters of the bonds and angles in the S1 subunit, and the simulation of the full-length spike protein model is used to estimate the bond and angle coefficients for the stem S2 subunit. A typical simulation box is 25 by 25 by 38 nm and about 2.3 million atoms were simulated for 20 ns. All-atom MD and CG simulations were conducted on the supercomputer Theta in Argonne Leadership Computing Facility (ALCF) in the Argonne National Lab.

Shape-Based Coarse-Graining and Coarse Grained Simulations

We utilized a technique called the Shape-Based Coarse Graining (SBCG) approach to develop the CG models, where large-scale motions of organic/biological molecules are represented using as few spherical CG sites (beads) as possible [36]. This decreases computational demand significantly when performing molecular dynamics simulations. When it comes to the force-field equation, atoms are substituted with CG beads. “Intramolecular” bonds between CG beads are established if the CG beads are within a certain distance of each other, or if the all-atom domains that comprise the CG beads are contiguously connected by intramolecular bonds.

We applied the SBCG tool in Visual Molecular Dynamics (VMD) to construct the coarse-grained model [37]. First, the CG sites and bonded interactions (bonds and angles) were established based on the original all-atom structures. The coefficients of

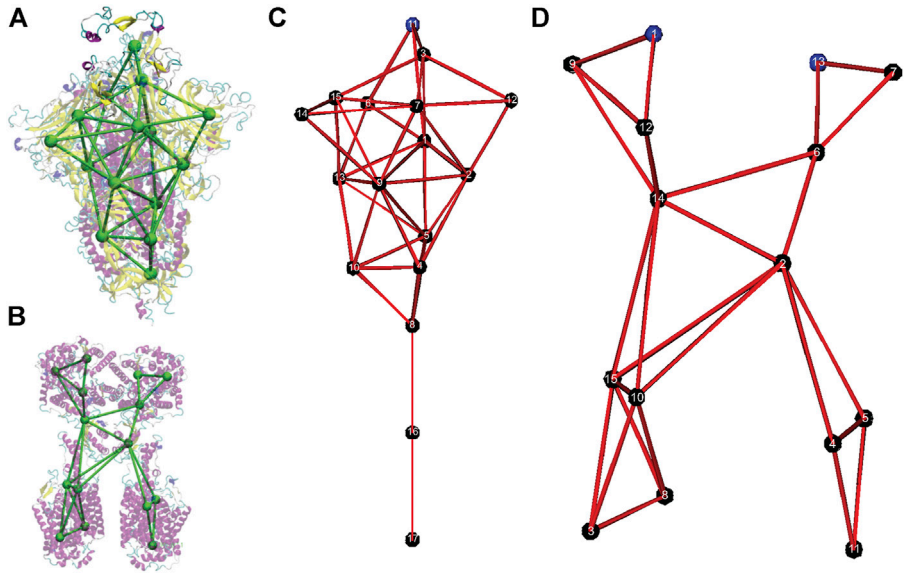

FIGURE 1 | Coarse-grained models of the spike protein and the Angiotensin-Converting Enzyme 2 (ACE2) receptor. **(A)** Overlap of the original all-atom structure of the head unit of spike protein (PDB ID: 6VSB) with the CG model. **(B)** Overlap of the original all-atom structure of the head unit of ACE2 protein (PDB ID: 6M18) with the CG model. **(C)** Numbering of CG sites of the spike CG model. **(D)** Numbering of CG sites of the ACE2 CG model.

Lennard-Jones (LJ) potential and the bonded interactions were extracted based on all-atom MD simulation trajectories. Specifically, an initial guess of the coefficients of bonded interactions was made by matching the root mean square displacement (RMSD) of internal coordinates, such as bond lengths and angles. Then iterations of refinements were made through CGMD simulations and normal mode analysis [38]. Detailed steps are shown in the **Supplementary Material**. In addition, we also developed an automated Tool Command Language (TCL) script for this procedure ("To-CG-File.tcl") within the **Supplementary Material**. The following classical intramolecular and intermolecular interactions without dihedrals were used

$$V = \sum_{bonds\ k} \frac{K_{b,k}}{2}(R_k - R_{0,k})^2 + \sum_{angles\ k} \frac{K_{\theta,k}}{2}(\theta_k - \theta_{0,k})^2 + \sum_{beads\ i,j} 4E_{ij}\left[\left(\frac{\sigma_{ij}}{r_{ij}}\right)^{12} - \left(\frac{\sigma_{ij}}{r_{ij}}\right)^{6}\right] + \sum_{beads\ i,j} \frac{q_i q_j}{4\pi\epsilon\epsilon_0 r_{i,j}} \quad (1)$$

where $E_{ij} = (E_i \times E_j)^{1/2}$, $\sigma_{ij} = (\sigma_i + \sigma_j)/2.0$. The first term in **Eq. 1** represents the energy associated with the harmonic oscillation of a bond connecting two beads. $K_{b,k}$ is the proportionality constant for the harmonic oscillator, and $R_{0,k}$ is the equilibrium distance of the bond, or, the distance where the elastic force is zero for bond k. The 2nd term represents the energy associated with the harmonic oscillation of an angle between the position vectors of two beads that are bonded to a common bead. $K_{\theta,k}$ is the proportionality constant, and $\theta_{0,k}$ is the equilibrium angle between the three beads for angle k. Energy arising from electrostatic interactions is modeled through Coulombic potential energy and the Van der Waals interaction is modeled using the 6–12 LJ potential. r_{ij} is the distance between beads i and j, and q_i and q_j are the charges of beads i and j, respectively. ε_0 is the vacuum permittivity constant and ε is the relative permittivity of the medium that beads i and j exist in. σ_{ij} represents the Van der Waals radius of the pair of beads i and j, or, the distance where the LJ potential is zero. E_{ij} is a proportionality constant representing the minima of the LJ potential energy graph for the paired beads i and j, and is proportional to the maximum strength of the attraction between beads i and j. LJ potentials prevent the overlapping or penetrating of neighboring CG sites. The equation sums up all of the individual energies obtained from every intramolecular bond, intramolecular bond angle, and every combinatorial pair of beads that exist in the molecule. In addition to the force field approximations, the following Langevin equation is used to describe the motions of the CG beads

$$m\frac{\partial^2 \boldsymbol{r}}{\partial \boldsymbol{t}^2} = F - m\gamma\frac{\partial \boldsymbol{r}}{\partial \boldsymbol{t}} + \chi\psi(t) \quad (2)$$

where F is the force imparted on the bead by other beads in the system, r is the position of the bead, m is the mass of the bead, γ is the damping coefficient of the solvent the bead is in, and χ is a fluctuation-dissipation theorem function of the form $\chi = (2\gamma k_B T/m)^{1/2}$, where k_B is the Boltzmann constant. $\psi(t)$ is a Gaussian process used to simulate Brownian motion. As $\partial^2 r/\partial t^2$ would represent the acceleration of the bead, then this Langevin equation describes the motion of the bead after accounting for fluid viscous friction and thermal fluctuations.

The CG simulations of individual spike proteins and ACE2 receptors were carried out in NAMD for refinement of the force field parameters.

The detailed procedure is given in the **Supplementary Material** for building the CG model based on all-atom MD simulations in VMD and converting it to the format of molecule files that can be used in CG simulations of endocytosis using Large-scale Atomic/Molecular Massively Parallel Simulator (LAMMPS) [39].

Normal Mode Analysis

We also wrote a Matlab code to conduct the normal mode analysis (NMA) [38] of the two CG models. We constructed the Hessian matrix $\nabla^2 E$ (E is the total energy) based on bond and angle interactions

$$\left|\nabla^2 E - \lambda \boldsymbol{M}\right| = 0 \tag{3}$$

where $\boldsymbol{M}$ is the mass matrix and $\lambda = \omega^2$ is the eigenvalue (ω is the vibration frequency). We diagonalized the mass weighted Hessian matrix to obtain eigenvalues and eigenvectors. The fluctuations of the CG bead coordinates are given as

$$\langle \Delta x_k^2 \rangle = \sum_{i=1}^{3N-6} \frac{k_B T}{M_k \omega^2} \left| y_{ki} \right|^2 \tag{4}$$

The mean square displacement (MSD) of the internal coordinates can be written as function of eigenvalues and eigenvectors as [38].

$$\langle \Delta \phi_j^2 \rangle = \sum_{i=1}^{3N-6} \frac{k_B T}{\omega^2} \sum_{k=1}^{3N} \left| B_{jk} M_k^{-1/2} y_{kj} \right|^2 \tag{5}$$

where $\omega^2 = \lambda$ and $\boldsymbol{y}$ is the eigenvector and $\boldsymbol{B}$ is the Wilson matrix relating the CG bead coordinates to the internal coordinate as $\boldsymbol{\Delta\phi} = \boldsymbol{B\Delta x}$[38].

Setup of Endocytosis Coarse-Grained Simulations

We modeled the envelope of the virus as a rigid sphere with a diameter of 85 nm. Seventy-two spikes are embedded in the envelope in our model. The end CG sites (CG site 17 in **Figure 1C**) of the spike stems are anchored to the envelope. Morse bonds are formed between the receptor binding site (CG site 11 **Figure 1C**) of the spike and the binding sites (CG sites 1 and 13 in **Figure 1D**) of the ACE2 protein when they get close to each other. Only one receptor binding site is modeled on each spike, as the crystal structure of the spike has only one receptor binding site up [26]. Two binding sites on each ACE2 receptor were modeled. The virus is given an initial small velocity towards the cell membrane to initiate the endocytosis process. Body temperature is used for all simulations, and a simulation box of 800 by 800 by 1600 nm is applied with the periodic boundary condition. While there is no direct measurement of absolute ACE2 surface densities and only relative ACE2 expressions were measured [40, 41], Chen et al. measured a density of 480–640/μm^2 for receptors of various species [42]. We used a surface density of 300/μm^2 which is about 1/10 of the surface density of the spike on the envelope (3,260/μm^2). This value was also used in a recent study to quantify the adhesive strength between the SARS-CoV-2 spike proteins and the human receptor ACE2 [43].

We applied the one-particle-thick lipid bilayer model [44], which we developed as a LAMMPS package [45], to simulate a flat cell membrane patch with ACE2 proteins embedded. It gives a bending rigidity of 50 k_BT, and ACE2 proteins can diffuse freely on the surface of the fluctuating cell membrane. All the CG simulations of endocytosis were carried out in LAMMPS.

We used the Berendsen thermostat and barostat to control the temperature and membrane tension. The temperature is set to T = 0.23 $\boldsymbol{\varepsilon/k_B}$ for all the particles in the simulations, where $\boldsymbol{\varepsilon}$ is the energy depth in the one-particle-thick lipid bilayer. We controlled the membrane tension to zero by setting the coupled XYZ pressure to zero. Because the out-of-plane stress of the membrane is always zero, and the membrane is curved in 3D due to deformation, the coupled XYZ pressure is linearly proportional to the membrane tension.

The binding energy between the spike RBD and ACE2 is modeled using the Morse breakable bond as

$$E = D\left[1 - e^{-\alpha(r-r_0)}\right]^2 \tag{6}$$

with an energy well depth of D = 68 $\boldsymbol{\varepsilon}$, which gives a physical value of 177 kcal/mol obtained from all-atom simulations [28], and $\alpha = 1.0$, $r_0 = 1$ nm. We used Morse breakable bonds instead of Morse pair interactions because pair interactions can cause clustering of ACE2 receptors, as many ACE2 receptors can bind to the same spike at the same time [18]. This unphysical problem can be solved by using LAMMPS commands "fix bond/create" and "fix bond/break". We set the maximum number of bonds that can be formed for the spike RBD from ACE2 to be one. The cutoff for Morse bond formation in "fix bond/create" is set to 20 nm, and the cutoff for Morse bond break in "fix bond/break" is set to 28 nm. By using the command "fix bond/break", we not only make the simulation of binding/unbinding more realistic, but also avoid numerical instability due to excessive bond stretch. Because the attraction branch of Morse potential near the cutoff distance is weak, after the bond is formed the bond can be stretched beyond the ghost atom cutoff length in LAMMPS in some cases, leading to errors of missing atoms in multiple CPU simulations. With "fix_bond/break", the bond will break if it is longer than 28 nm before it reaches the ghost atom cutoff length, which is set to 30 nm in the simulations.

RESULTS

Overview of the Coarse-Grained Models

Although different resolutions of coarse-graining can be developed by using the SBCG approach, we focused on the minimal model with a small number of CG sites. The CG models for the SARS-CoV-2 spike protein and the ACE2 receptor are shown in **Figure 1B**. In **Figure 1A** and **Figure 2B**, the CG models are superimposed on top of their respective all-atom structures, and only the head S1 subunit is

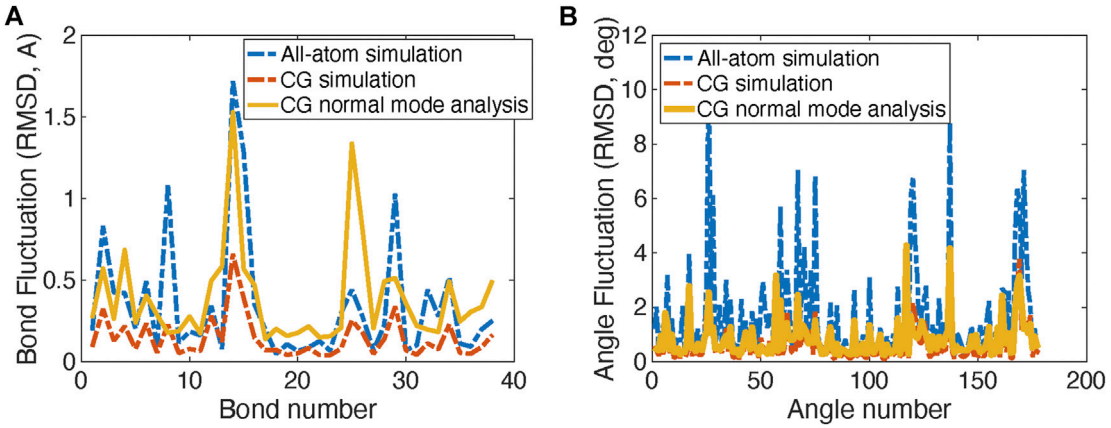

FIGURE 2 | Comparison of Root Mean Square Displacement (RMSD) fluctuations of bond lengths **(A)** and angles **(B)** obtained from the original all-atom simulations, the CG simulations, and the normal mode analysis of the CG model of the spike protein head S1 unit.

shown for the spike protein. The all-atom systems are colored based on their secondary structures.

The CG model of the spike protein has 17 CG sites. Sites 1–15 represent the S1 head subunit and sites 16 and 17 present the S2 stem subunit. Within the S1 subunit, CG site 11 represents the receptor binding domain (RBD) in the original crystal structure (PDB: 6VSB), and CG sites 3 and 15 present the hidden RBDs. CG sites 6, 12, and 14 represent the outer beta sheets domains of each spike protein in the trimer. In the S2 subunit, CG site 17 is anchored in the viral envelope, and CG site eight is the connecting region between S1 and S2 subunits.

The CG model of the ACE2 receptor has 15 CG sites. CG sites 3, 4, 5, 8, 10, 11, and 15 represent the transmembrane domains, while CG sites 1 and 13 represent two binding sites for the spike protein.

Parameters of the Coarse-Grained Model

The CG parameters in **Eq. 1**, such as bond coefficients and initial lengths, are listed as **Supplementary Tables S1–S8** in the Supplementary Material for the SARS-CoV-2 spike protein and the ACE2 receptor. Note that only bond and angle interactions are used as shown in **Eq. 1**, while dihedral angles are not included in this shape-based coarse-graining approach.

Note that the bonded coefficients of the S1 head subunit are obtained from the all-atom simulations of the S1 head subunit, while the bonded coefficients of S2 subunits are obtained from the fully-glycosylated full-length spike protein model (**Supplementary Figure S1** in the Supplementary Material).

The comparison RMSDs of the original all-atom simulations with the CG models for bond length and angles are shown in **Figure 2A**. **Figure 2B** shows the fluctuation magnitudes of the CG model match well with the original all-atom model.

Normal mode analysis of the coarse-grained model

Normal mode analysis (NMA) is also applied to calculate the fluctuations and vibration modes of the CG models. In **Figure 2B**, the fluctuations (yellow curves) obtained by NMA match well with the all-atom model. The fluctuations calculated from NMA are different from the fluctuations obtained from direction CG simulation of the same model due to the anharmonic effect in the direct CG simulations. In addition, the first three vibration modes of the spike S1 head unit are shown in **Figure 3**. The 1st and 2nd modes involve the motions of the RBD site in two horizontal directions, respectively, and the 3rd mode involves the motion of one of the three exterior beta sheet domains.

Modeling of the Endocytosis of the Coronavirus.

After we established the CG models of the spike protein and ACE2 protein, we applied them to simulate the endocytosis of a whole coronavirus. As shown in **Figure 4A**, we modeled the virus envelope as a rigid sphere with a diameter of 85 nm. The CG models of the spike proteins (red) are distributed on the surface of the virus with the stems embedded in the viral envelope (grey). The RBD binding sites of the spike proteins (CG site 11 in **Figure 1A**) are highlighted as blue. The transmembrane domain CG sites of the ACE2 proteins (green) are embedded in the host cell membrane (orange). The host cell membrane is modeled by using the one-particle-thick bilayer model [44, 45]. The same interaction is applied between the cell membrane particles and the CG particles of the transmembrane domains of ACE2 so that the ACE2 proteins are anchored in the cell membrane with the right orientation as shown in **Figure 4A**. The binding sites of the ACE2 proteins are also shown as blue. The depth of the energy well $\boldsymbol{\varepsilon}$ of the pair interaction in the one-particle-thick model is set to about 5.0 times thermal energy (k_B T) and the characteristic length and the cutoff length are set to 4 and 10.4 nm so that the membrane self-assembled into a one-particle-thick layer with the fluid behavior and bending rigidity of 50 k_B T. The attraction and repulsive parameters $\eta = 2$ and $\zeta = 4$, and the bending parameter $\mu = 3$ (see Fu et al. [45]).

As shown in **Figures 4C,D**, the ACE2 proteins can diffuse on the fluctuating cell membrane with the correct orientations. The

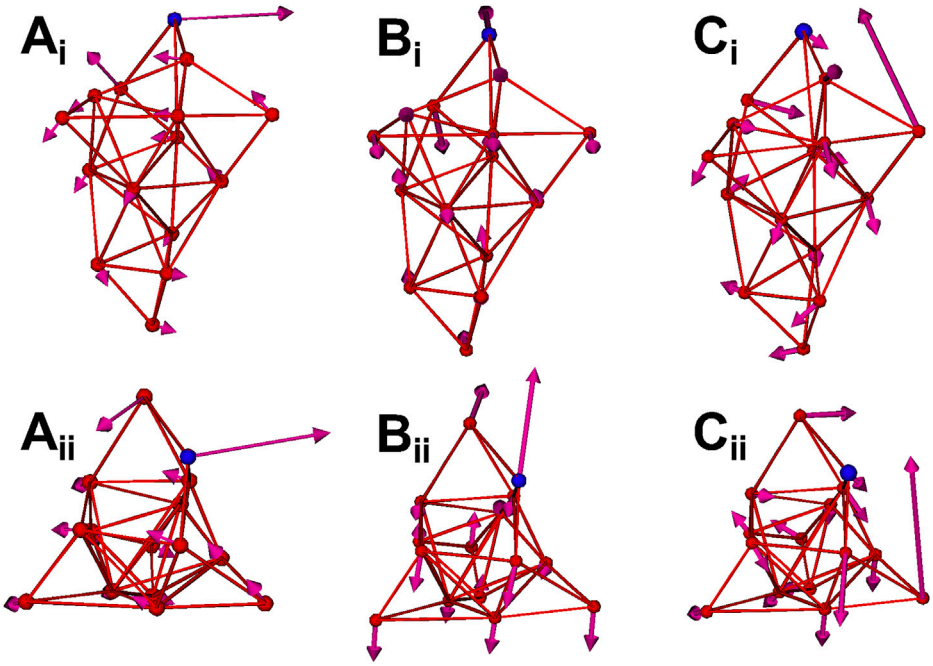

FIGURE 3 | The first three normal modes of the spike CG model. **(Ai)** 1st mode (**side view**). **(Aii)** 1st mode (**top view**). **(Bi)** 2nd mode (**side view**). **(Bii)** 2nd mode (**top view**). **(Ci)** 3rd mode (**side view**). **(Cii)** 3rd mode **(top view**). The RBD site (CG site 11) is highlighted as blue.

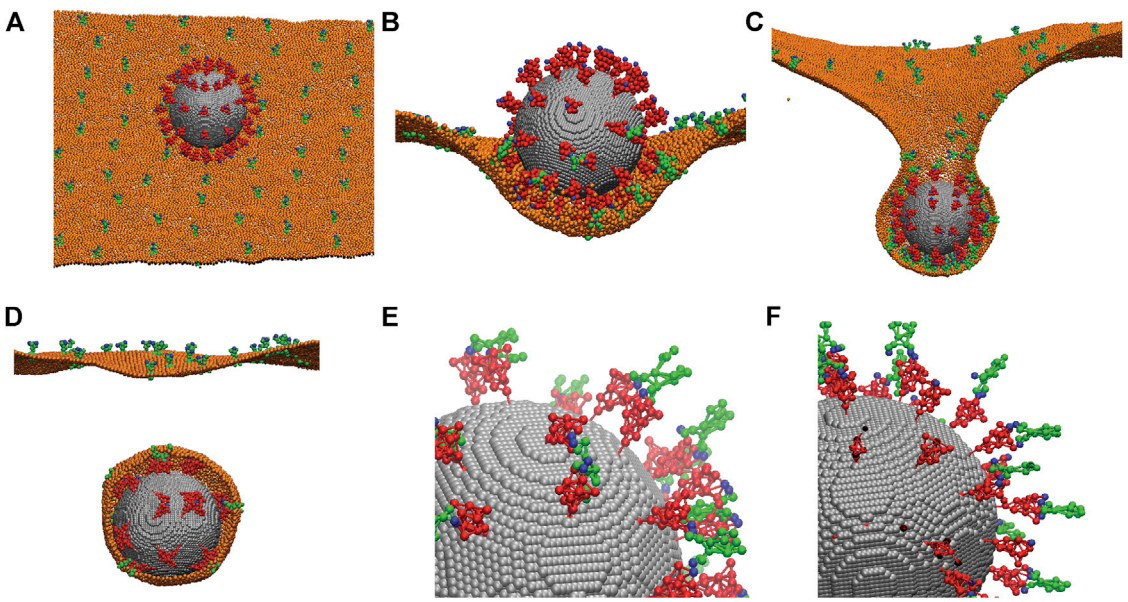

FIGURE 4 | Simulations of the endocytosis of a whole virus by incorporating the CG models of the spike protein and the ACE2 receptor. **(A)** A CG model of the whole virus with 72 distributed spike proteins (red) anchored on its viral envelope (grey). The spike proteins are modeled using the CG model described in **Figure 1**. ACE2 proteins (green) are anchored in the host cell membrane (orange). Both the binding sites of the spike proteins and ACE2 proteins are marked as blue. **(B)** The initial attachment of the virus to the fluctuating cell membrane. **(C)** The progress of the endocytosis due to spike-ACE2 interaction. **(D)** Separation of the membrane-bounded virus from the host cell membrane. Only half of the cell membrane is shown in **(B, C, D)** for revealing the interior virus and interactions. **(E)** A close view of the interactions between the spike proteins (red) and ACE2 receptors (green) through their binding sites (blue). Most ACE2 receptors bind to two spikes. Membrane is not shown. **(F)** The same as **(E)** except the ACE2 receptors and spikes are modeled as rigid bodies without flexibility. All ACE2 bind to one spike only. Membrane is not shown.

Berendsen thermostat and barostat are used to maintain a constant membrane temperature and zero membrane tension. The rigid body dynamics in LAMMPS is employed for the viral envelope, and the NVE integrator with Langevin thermostats is employed for the dynamics of spike and ACE2 proteins under the same temperature as the membrane. The interaction between the spike RBD sites and the ACE2 binding sites is simulated by breakable Morse bonds. The binding energy between the spike and ACE2 is set to −177 kcal/mol, obtained from the literature for spike-ACE2 interaction [28–32].

When the virus is initially attached to the cell membrane, the spike proteins at the bottom surface of the virus bind to the ACE2 proteins and are deformed due to their structure flexibility as shown in **Figure 4B**, while the spike proteins on the top surface remain much less deformed, although they vibrate due to thermal fluctuations. After more ACE2 proteins bind to the spikes, the virus is engulfed by the cell membrane. This eventually leads to the necking and rupture of the cell membrane as shown in **Figures 4C,D**. Our simulations show that due to the flexibility of the spike proteins and their actual surface density, it is possible for the two spikes to bend significantly to bind to the same ACE2 receptor as shown in **Figure 4E**. Our simulations show that this is not possible if the spike and ACE2 proteins are modeled as rigid structures, and one spike can only bind to one ACE2 as shown in **Figure 4F**. Therefore, it is critical to consider the realistic flexibility of the spike and ACE2 proteins in the simulations, as also demonstrated in all-atom MD simulations [46–48].

CONCLUSIONS AND DISCUSSIONS

We developed the CG models of the spike proteins and ACE2 receptors using the shape-based coarse-graining approach. The force field parameters are obtained from the all-atom simulations by matching the fluctuations. Then these CG models are incorporated into LAMMPS to simulate the binding of the spike proteins with the ACE2 receptors during the endocytosis of a whole virus. We found that the realistic structure flexibility of the spike proteins and ACE2 proteins is critical for better interaction between these two proteins. For example, our results showed that two spike proteins can easily bind to one ACE2 receptor due to significant bending deformation.

Besides endocytosis, the coronavirus can enter the host cell by membrane fusion. To model the membrane fusion process in a future study, we will need to consider the viral envelope as a flexible membrane using the one-particle-thick lipid bilayer model. As the connection between the S1 and S2 subunits is cleaved and the S1 head subunit is removed from the virus during the membrane fusion process, we also need to refine the CG model to incorporate this breakable bond mechanism.

In summary, we simulated the endocytosis of the whole coronavirus with minimal atomistic details of its spike proteins and corresponding ACE2 receptors. Although the resolution is coarse and the coarse-graining is aggressive, it can help us understand the biophysical behavior of the coronavirus at large temporal and spatial scales beyond typical atomistic simulations. Furthermore, the CG resolutions can be refined if needed through the same procedure by using the scripts provided in the **Supplementary Material**.

DATA AVAILABILITY STATEMENT

The original contributions presented in the study are included in the article/**Supplementary Material**, further inquiries can be directed to the corresponding author.

AUTHOR CONTRIBUTIONS

ZP constructed the cell membrane CG model, the CG virus using the SARS-CoV-2 and ACE2 CG models, and performed MD simulations with the aforementioned CG models in LAMMPS. TL designed the coarse-graining program to convert the all-atom SARS-CoV-2 and ACE2 proteins into their CG models, and designed the program to extract the bonding parameters from the CG models and convert them into a LAMMPS-compatible format. TL was also responsible for patching a technical issue that impeded CG model creation. CV designed the normal mode analysis program and performed normal mode analyses on all aforementioned CG models.

FUNDING

ZP acknowledge the funding support from NSF Grant No. CBET-1948347. TL is supported through the Research Experiences for Undergraduates (REU) supplement of NSF CBET-1948347. CV is supported by the Guaranteed Paid Internship Program (GPIP) from University of Illinois at Chicago. This research used resources of the Argonne Leadership Computing Facility, which is a DOE Office of Science User Facility supported under Contract DE-AC02-06CH11357.

ACKNOWLEDGMENTS

All-atom MD and CG simulations were conducted on the supercomputer Theta in Argonne Leadership Computing Facility (ALCF) in the Argonne National Lab under Director's Discretionary (DD) allocation Modeling Corona Virus.

SUPPLEMENTARY MATERIAL

The Supplementary Material for this article can be found online at: https://www.frontiersin.org/articles/10.3389/fphy.2021.680983/full#supplementary-material

REFERENCES

1. He F, Deng Y, and Li W. Coronavirus Disease 2019: What We Know? *J Med Virol* (2020). 92(7):719–25. doi:10.1002/jmv.25766
2. Goldsmith CS, Tatti KM, Ksiazek TG, Rollin PE, Comer JA, Lee WW, et al. Ultrastructural Characterization of SARS Coronavirus. *Emerg Infect Dis* (2004). 10(2):320–6. doi:10.3201/eid1002.030913
3. Godet M, L'Haridon R, Vautherot J-F, and Laude H. TGEV corona Virus ORF4 Encodes a Membrane Protein that Is Incorporated into Virions. *Virology* (1992). 188(2):666–75. doi:10.1016/0042-6822(92)90521-p
4. Andersson R. University Decentralization as Regional Policy: the Swedish experiment. *J Econ Geogr* (2004). 4(4):371–88. doi:10.1093/jeg/4.4.371
5. Berman H, Henrick K, and Nakamura H. Announcing the Worldwide Protein Data Bank. *Nat Struct Mol Biol* (2003). 10(12):980. doi:10.1038/nsb1203-980
6. Berman HM. The Protein Data Bank. *Nucleic Acids Res* (2000) 28(1):235–42. doi:10.1093/nar/28.1.235
7. Frick DN, Virdi RS, Vuksanovic N, Dahal N, and Silvaggi NR. Molecular Basis for ADP-Ribose Binding to the Mac1 Domain of SARS-CoV-2 Nsp3. *Biochemistry* (2020) 59(28):2608–15. doi:10.1021/acs.biochem.0c00309
8. Hillen HS, Kokic G, Farnung L, Dienemann C, Tegunov D, and Cramer P. Structure of Replicating SARS-CoV-2 Polymerase. *Nature* (2020) 584(7819): 154–6. doi:10.1038/s41586-020-2368-8
9. Kern DM, Sorum B, Mali SS, Hoel CM, Sridharan S, Remis JP, et al. *Cryo-EM Structure of the SARS-CoV-2 3a Ion Channel in Lipid Nanodiscs. bioRxiv* (2020) [Preprint]. doi:10.1101/2020.06.17.156554
10. Rut W, Lv Z, Zmudzinski M, Patchett S, Nayak D, Snipas SJ, et al. *Activity Profiling and Structures of Inhibitor-Bound SARS-CoV-2-PLpro Protease Provides a Framework for Anti-COVID-19 Drug Design. bioRxiv* (2020) [Preprint]. doi:10.1101/2020.04.29.068890
11. Shang J, Ye G, Shi K, Wan Y, Luo C, Aihara H, et al. Structural Basis of Receptor Recognition by SARS-CoV-2. *Nature* (2020) 581(7807):221–4. doi:10.1038/s41586-020-2179-y
12. Yan R, Zhang Y, Li Y, Xia L, Guo Y, and Zhou Q. Structural basis for the recognition of SARS-CoV-2 by full-length human ACE2. *Science* (2020) 367(6485):1444–1448. doi:10.1126/science.abb2762
13. Surya W, Li Y, and Torres J. Structural Model of the SARS Coronavirus E Channel in LMPG Micelles. *Biochim Biophys Acta (Bba) - Biomembranes* (2018) 1860(6):1309–17. doi:10.1016/j.bbamem.2018.02.017
14. Walls AC, Park Y-J, Tortorici MA, Wall A, McGuire AT, and Veesler D. Structure, Function, and Antigenicity of the SARS-CoV-2 Spike Glycoprotein. *Cell* (2020) 183(6):1735. doi:10.1016/j.cell.2020.11.032
15. Yu A, Pak AJ, He P, Monje-Galvan V, Casalino L, Gaieb Z, et al. A Multiscale Coarse-Grained Model of the SARS-CoV-2 Virion. *Biophys J* (2021) 120(6): 1097–1104. doi:10.1016/j.bpj.2020.10.048
16. Zhang L, Lin D, Sun X, Curth U, Drosten C, Sauerhering L, et al. Crystal Structure of SARS-CoV-2 Main Protease Provides a Basis for Design of Improved α-ketoamide Inhibitors. *Science* (2020) 368(6489):409–12. doi:10.1126/science.abb3405
17. Jaimes JA, André NM, Chappie JS, Millet JK, and Whittaker GR. Phylogenetic Analysis and Structural Modeling of SARS-CoV-2 Spike Protein Reveals an Evolutionary Distinct and Proteolytically Sensitive Activation Loop. *J Mol Biol* (2020) 432(10):3309–25. doi:10.1016/j.jmb.2020.04.009
18. Shen Z, Ye H, Yi X, and Li Y. Membrane Wrapping Efficiency of Elastic Nanoparticles during Endocytosis: Size and Shape Matter. *ACS Nano* (2018) 13(1):215–28. doi:10.1021/acsnano.8b05340
19. Shen Z, Ye H, and Li Y. Understanding Receptor-Mediated Endocytosis of Elastic Nanoparticles through Coarse Grained Molecular Dynamic Simulation. *Phys Chem Chem Phys* (2018) 20(24):16372–85. doi:10.1039/c7cp08644j
20. Shen Z, Ye H, Kröger M, and Li Y. Aggregation of Polyethylene Glycol Polymers Suppresses Receptor-Mediated Endocytosis of PEGylated Liposomes. *Nanoscale* (2018) 10(9):4545–60. doi:10.1039/c7nr09011k
21. Richards DM, and Endres RG. Target Shape Dependence in a Simple Model of Receptor-Mediated Endocytosis and Phagocytosis. *Proc Natl Acad Sci USA* (2016) 113(22):6113–8. doi:10.1073/pnas.1521974113
22. Li Y, Kröger M, and Liu WK. Endocytosis of PEGylated Nanoparticles Accompanied by Structural and Free Energy Changes of the Grafted Polyethylene Glycol. *Biomaterials* (2014) 35(30):8467–78. doi:10.1016/j.biomaterials.2014.06.032
23. Gao H, Shi W, and Freund LB. From the Cover: Mechanics of Receptor-Mediated Endocytosis. *Proc Natl Acad Sci* (2005) 102(27):9469–74. doi:10.1073/pnas.0503879102
24. Doherty GJ, and McMahon HT. Mechanisms of Endocytosis. *Annu Rev Biochem* (2009) 78(1):857–902. doi:10.1146/annurev.biochem.78.081307.110540
25. Neuman BW, Kiss G, Kunding AH, Bhella D, Baksh MF, Connelly S, et al. A Structural Analysis of M Protein in Coronavirus Assembly and Morphology. *J Struct Biol* (2011) 174(1):11–22. doi:10.1016/j.jsb.2010.11.021
26. Wrapp D, Wang N, Corbett KS, Goldsmith JA, Hsieh C-L, Abiona O, et al. Cryo-EM Structure of the 2019-nCoV Spike in the Prefusion Conformation. *Science* (2020) 367(6483):1260–3. doi:10.1126/science.abb2507
27. Yan R, Zhang Y, Li Y, Xia L, Guo Y, and Zhou Q. Structural Basis for the Recognition of SARS-CoV-2 by Full-Length Human ACE2. *Science* (2020) 367(6485):1444–8. doi:10.1126/science.abb2762
28. Qiao B, and Olvera de la Cruz M. Enhanced Binding of SARS-CoV-2 Spike Protein to Receptor by Distal Polybasic Cleavage Sites. *ACS Nano* (2020) 14(8): 10616–23. doi:10.1021/acsnano.0c04798
29. Ali A, and Vijayan R. Dynamics of the ACE2–SARS-CoV-2/sars-CoV Spike Protein Interface Reveal Unique Mechanisms. *Scientific Rep* (2020) 10(1). doi:10.1038/s41598-020-71188-3
30. He J, Tao H, Yan Y, Huang S-Y, and Xiao Y. Molecular Mechanism of Evolution and Human Infection with SARS-CoV-2. *Viruses* (2020) 12(4):428. doi:10.3390/v12040428
31. Mercurio I, Tragni V, Busto F, De Grassi A, and Pierri CL. Protein Structure Analysis of the Interactions between SARS-CoV-2 Spike Protein and the Human ACE2 Receptor: from Conformational Changes to Novel Neutralizing Antibodies. *Cell. Mol. Life Sci.* (2020) 78(4):1501–22. doi:10.1007/s00018-020-03580-1
32. Spinello A, Saltalamacchia A, and Magistrato A. Is the Rigidity of SARS-CoV-2 Spike Receptor-Binding Motif the Hallmark for Its Enhanced Infectivity? Insights from All-Atom Simulations. *J Phys Chem Lett* (2020)11(12): 4785–4790. doi:10.1021/acs.jpclett.0c01148
33. Simmons G, Zmora P, Gierer S, Heurich A, and Pöhlmann S. Proteolytic Activation of the SARS-Coronavirus Spike Protein: Cutting Enzymes at the Cutting Edge of Antiviral Research. *Antiviral Res* (2013) 100(3):605–14. doi:10.1016/j.antiviral.2013.09.028
34. Phillips JC, Hardy DJ, Maia JDC, Stone JE, Ribeiro JV, Bernardi RC, et al. Scalable Molecular Dynamics on CPU and GPU Architectures with NAMD. *J Chem Phys* (2020) 153(4):044130. doi:10.1063/5.0014475
35. Woo H, Park S-J, Choi YK, Park T, Tanveer M, Cao Y, et al. Developing a Fully Glycosylated Full-Length SARS-CoV-2 Spike Protein Model in a Viral Membrane. *J Phys Chem B* (2020) 124(33):7128–37. doi:10.1021/acs.jpcb.0c04553
36. Arkhipov A, Schulten K, Freddolino P, Ying Y, Shih A, and Chen Z. *Coarse-Graining of Condensed Phase and Biomolecular Systems*. Boca Raton, FL: CRC Press (2008). p. 299–315. doi:10.1201/9781420059564 ch20 Application of Residue-Based and Shape-Based Coarse-Graining to Biomolecular Simulations.
37. Humphrey W, Dalke A, and Schulten K. VMD: Visual Molecular Dynamics. *J Mol Graphics* (1996) 14(1):33–8. doi:10.1016/0263-7855(96)00018-5
38. Brooks BR, Jane?i? Da., and Karplus M. Harmonic Analysis of Large Systems. I. Methodology. *J Comput Chem* (1995) 16(12):1522–42. doi:10.1002/jcc.540161209
39. Plimpton S. Fast Parallel Algorithms for Short-Range Molecular Dynamics. *J Comput Phys* (1995) 117(1):1–19. doi:10.1006/jcph.1995.1039
40. Al-Benna S. Association of High Level Gene Expression of ACE2 in Adipose Tissue with Mortality of COVID-19 Infection in Obese Patients. *Obes Med* (2020) 19:100283. doi:10.1016/j.obmed.2020.100283
41. Zhang L, Han X, and Shi Y. Comparative Analysis of SARS-CoV-2 Receptor ACE2 Expression in Multiple Solid Tumors and Matched Non-diseased Tissues. *Infect Genet Evol* (2020) 85:104428. doi:10.1016/j.meegid.2020.104428
42. Chen Y, Munteanu AC, Huang Y-F, Phillips J, Zhu Z, Mavros M, et al. Mapping Receptor Density on Live Cells by Using Fluorescence Correlation Spectroscopy. *Chem Eur J* (2009) 15(21):5327–36. doi:10.1002/chem.200802305
43. Ponga M. Quantifying the Adhesive Strength between the SARS-CoV-2 S-Proteins and Human Receptor and its Effect in Therapeutics. *Scientific Rep* (2020) 10(1). doi:10.1038/s41598-020-74189-4

44. Yuan H, Huang C, Li J, Lykotrafitis G, and Zhang S. One-particle-thick, Solvent-free, Coarse-Grained Model for Biological and Biomimetic Fluid Membranes. *Phys Rev E* (2010) 82(1). doi:10.1103/physreve.82.011905
45. Fu S-P, Peng Z, Yuan H, Kfoury R, and Young Y-N. Lennard-Jones Type Pair-Potential Method for Coarse-Grained Lipid Bilayer Membrane Simulations in LAMMPS. *Computer Phys Commun* (2017) 210:193–203. doi:10.1016/j.cpc.2016.09.018
46. Barros EP, Casalino L, Gaieb Z, Dommer AC, Wang Y, Fallon L, et al. The Flexibility of ACE2 in the Context of SARS-CoV-2 Infection. *Biophys J* (2020) 120(6):1072–1084. doi:10.1101/2020.09.16.300459
47. Pierri CL. SARS-CoV-2 Spike Protein: Flexibility as a New Target for Fighting Infection. *Signal Transduction Targeted Ther* (2020) 5(1). doi:10.1038/s41392-020-00369-3
48. Römer RA, Römer NS, and Wallis AK. Flexibility and Mobility of SARS-CoV-2-Related Protein Structures. *Scientific Rep* (2021) 11(1). doi:10.1038/s41598-021-82849-2

Conflict of Interest: The authors declare that the research was conducted in the absence of any commercial or financial relationships that could be construed as a potential conflict of interest.

frontiers in Physics

REVIEW
published: 20 October 2021
doi: 10.3389/fphy.2021.749830

Bidirectional Mechanical Response Between Cells and Their Microenvironment

*Claudia Tanja Mierke**

Faculty of Physics and Earth Science, Peter Debye Institute of Soft Matter Physics, Biological Physics Division, University of Leipzig, Leipzig, Germany

Cell migration and invasion play a role in many physiological and pathological processes and are therefore subject of intensive research efforts. Despite of the intensively investigated biochemical processes associated with the migration and invasion of cells, such as cancer cells, the contribution of mechanobiological processes to the migratory capacity of cells as well as the role of physical polymeric phase transitions is not yet clearly understood. Unfortunately, these experiments are not very informative because they completely disregard the influence of the three-dimensional cell environment. Despite this data situation, it was possible to adequately demonstrate that there exists a direct mechanical interplay between cells and their microenvironment in both directions, where both elements can be mechanically altered by one another. In line with these results, it has turned out that the mechanobiological molecular processes through which cells interact with each other and additionally sense their nearby microenvironment have an impact on cellular functions such as cellular motility. The mechanotransduction processes have become the major focus of biophysical research and thereby, diverse biophysical approaches have been developed and improved to analyze the mechanical properties of individual cells and extracellular matrix environments. Both, the cell mechanics and matrix environment mechanics regulate the cell migration types in confined microenvironments and hence it seems to be suitable to identify and subsequently present a common bidirectional interplay between cells and their matrix environment. Moreover, hallmarks of the mechanophenotype of invasive cells and extracellular matrices can be defined. This review will point out how on the one hand the intracellular cytoskeletal architecture and on the other hand the matrix architecture contribute to cellular stiffness or contractility and thereby determines the migratory phenotype and subsequently the emergence of a distinct migration mode. Finally, in this review it is discussed whether universal hallmarks of the migratory phenotype can be defined.

OPEN ACCESS

Edited by:
Yuan Lin,
The University of Hong Kong, Hong Kong, SAR China

Reviewed by:
Youhua Tan,
Hong Kong Polytechnic University, Hong Kong, SAR China
Andrey Cherstvy,
University of Potsdam, Germany

***Correspondence:**
Claudia Tanja Mierke
claudia.mierke@uni-leipzig.de

Specialty section:
This article was submitted to Biophysics, a section of the journal Frontiers in Physics

Received: *30 July 2021*
Accepted: *30 September 2021*
Published: *20 October 2021*

Citation:
Mierke CT (2021) Bidirectional Mechanical Response Between Cells and Their Microenvironment. Front. Phys. 9:749830. doi: 10.3389/fphy.2021.749830

Abbreviations: 3D, three-dimensional; ADAMs, A Disintegrin And Metalloproteinases; CT, cytoplasmic tail; DHT, dehydrothermal treatment; EDC-NHS, 1-ethyl-3-(3-dimethylaminopropyl) carbodiimide-N-hydroxysuccinimide; EMT, Epithelial-to-mesenchymal; FAK, focal adhesion kinase; FGF, fibroblast growth factor; GFP, Green fluorescent protein; GPI, glycosylphosphatidylinositol; LOX, lysyl oxidase; MIDAS, metal ion dependent adhesion site; MMPs, matrix metallo-proteinases; NMHC II, non-muscle myosin heavy chain II; PAA, polyacrylamide; PDGF, platelet-derived growth factor; PDMS, polydimethyalsiloxane; PSGL-1, P-selectin glycoprotein ligand-1; TEPIC, tris (2,3-Epoxy propyl) isocyanurate; TG2, transglutaminase 2; TGF-β, transforming growth factor-β; TNF, tumor necrosis factor; UV, ultraviolet radiation; VCAM-1, vascular cell adhesion molecule-1.

Keywords: cytoskeletal mechanics, confinement, extracellular matrix, homogeneities, cancer cell, fibroblast, matrix degradation, forces

1 INTRODUCTION TO CELLS AND THEIR ENVIRONMENT

Specific migratory phenotypes are exhibited by cells and the speed of migration and invasion can be dynamically adapted to the physical characteristics of their microenvironment [1,2]. Thereby the physical constraints, cell adhesion, matrix rigidity and topology are key issues of the extracellular matrix environment that consequently impact the migratory capacity of cells [3,4]. It has been seen that the mechanical properties of cells contribute to their migratory capacity and seem to determine their migration mode. The mechanical properties of cells define their overall mechanophenotype. Similar to cells, the extracellular matrix mechanical properties can also define the matrix mechanophenotype of the microenvironment of cells and tissues. Since mechanophenotypes may be addressed in a more quantitative and comparable manner compared to shape or structural phenotypes, they seem to be more suitable to determine the migratory capacity of cells or collections of cells. However, it is still unclear whether the mechanophenotype of the cell relies on the mechanophenotype of the matrix and adapts accordingly to changes in the mechanophenotype in the environment. Eukaryotic cells promote the migration and invasion through linkage of the intracellular force and the actin cytoskeleton toward the microenvironment. Whereas the force coupling mechanics employed by mesenchymal migrating cells is generally conducted through transmembrane adhesion receptors, such as primarily those of the well-known integrin family, amoeboid cells, such as leukocytes can manage to move with highspeed, since there exists very weak cell-matrix adhesion forces [5,6]. Living organisms are subjected to a broad array of mechanical stimuli on different length scales, which cover universal forces, such as gravity, and microscopically localized forces, such as fluid shear stress within blood vessels [7], compression through adjacent tissues [8,9] or the rigidity of the extracellular matrix scaffold [10]. Specifically, it can be inferred that the displacement of the balance equilibrium among actin protrusion, actomyosin contraction, and adhesion to the extracellular substrate can account for the diverse modes of amoeboid locomotion, and the fact that blebbing and gliding are scarcely extreme varieties of a commonly adopted migratory pattern [5].

When enclosed in three-dimensional (3D) environments, cells exploit the topographic characteristics of the subsurface to move around. In particular, the retrograde flow of the actin cytoskeleton tends to have a pattern that closely matches the texture of the substrate, generating retrograde shear forces that are adequate to propel the cell body onward. It is noteworthy that adhesion-dependent and adhesion-independent migration are not necessarily contradictory, and instead are versions of the identical principle of linkage of retrograde actin flow to the surroundings, and thus can operate prospectively and interchangeably at the same time [6]. Univariate maps and phase diagrams provide an insight into how physical characteristics impact cell migration. Moreover, the phase transition may offer a simple explanation for a phase shift within cell populations, such as the unjamming-jamming phase transition or epithelial-mesenchymal transition [11]. Computational modeling allows systematic reconnaissance of the phase space to emphasize strategies for experimental investigations [1]. The phase transition may serve as a mechanical hallmark for cancer and its malignant progression.

2 CELLS IMPACT THEIR MICROENVIRONMENT

There are commonly physiological and pathological processes where the migration and invasion of cells plays a crucial role. Cancers develop to handle environmental stress or face and overcome all kinds of challenges, including nutrient deficiencies, lack of survival factors, and out-of-balance mechanical forces. The runaway growth and anomalous deregulation of central homeostatic cellular tracts resulting from genetic mutations establishes a stressful milieu [11]. Adjustments of cancers to the evolving surroundings can cause alterations in the motility engine of cells that impact migration, invasion, and metastasis. Cancer cells may enter singly or in groups, or may be ejected out of surrounding epithelium. These mechanisms are assumed to represent modulations of normal events that arise either in the course of development or tissue repair or in inflammatory responses [3,11]. The Plausibility of Life [12], which posits that every system in a cell or organism has developed to incorporate built-in distinct moduli of variability that can be triggered under stress or in the light of new capabilities, seems to be applicable for cells that need to adapt to the environmental cues. In turn, cells can alter the extracellular matrix surroundings, which may represent one such mechanism of adaption. Thereby, the cells can either secrete matrix metalloproteinases (MMPs), such as MT1-MMP toward their local environment [13], expresses sheddases on their cell surface or release matrix crosslinking molecules or secrete growth factors, cytokine or matrix-degrading enzymes regulatory molecules that are stored within the microenvironmental cavities.

Cancer cells overcome steric obstacles that represent enormous tissue barriers through the exertion of small actin-rich membrane protrusions, which are referred to as invadopodia. These invadopodia play a role in many steps of the metastatic cascade (**Figure 1**). The full maturation of invadopodia relies on extrusion and elongation of protrusions and the timed release of the matrix metalloproteinase MT1-MMP through endosomal trafficking involving unidentified mechanisms. The endoplasmatic reticulum (ER) protein protrudin can be demonstrated to foster the maturation and function of invadopodia. Protrudin assembles interaction sites for MT1-

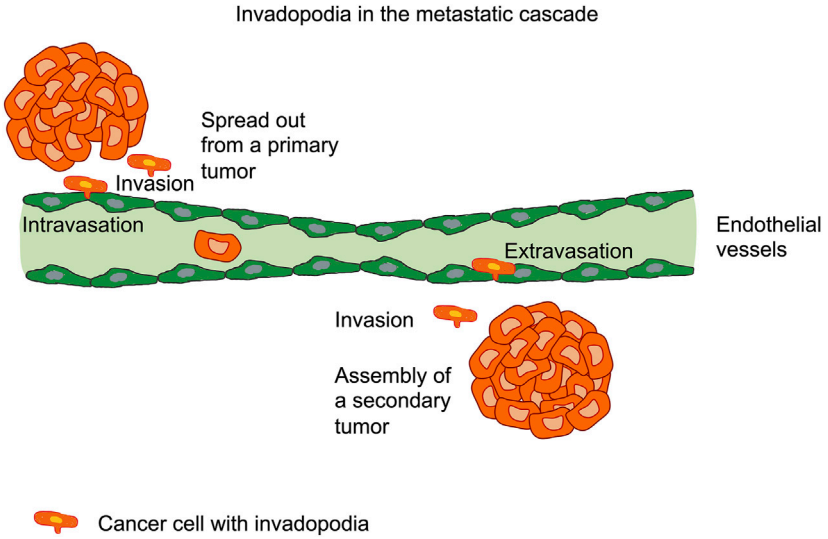

FIGURE 1 | Cancer cells form invadopodia in many steps of the metastatic cascade, such as the spreading out of cancer cells from the primary tumor, the invasion through the extracellular matrix tissue environment, the intravasation through the endothelial cell layer into vessels, such as blood or lymphoid vessels, the extravasation of cancer cells through the endothelium and subsequent invasion through the extracellular matrix of targeted tissue. Finally, secondary tumors can be assembled and the metastasis cascade is completed.

MMP-positive endosomes that are filled with the RAB7-binding kinesin-1 adaptor FYCO1 [14]. However, the lack of RAB7, FYCO1, or protrudin impaired the MT1-MMP-dependent extracellular matrix break-down and consequently, the invasion of cancer cells through blockage of the anterograde translocation and the release MT1-MMP through exocytosis [14]. In the event that endosome translocation or exocytosis has been hindered through depletion of protrudin or synaptotagmin VII, respectively, the invadopodia failed to extend and lengthen. In contrast, when protrudin has been overexpressed, noncancerous cells exhibited prominent invadopodia-like protrusions and displayed enhanced levels of matrix breakdown and elevated invasion.

Stabilization of progenitors promotes the maturation of invadopodia, which proceeds by a dual-track mechanism. On the one hand, actin polymerization and cortactin-dependent ramification permit the extension and elongation of the invadopodium. There is on the other hand fusion of MMP-containing vesicles with the plasma membrane of invadopodia, which results in the breakdown of the extracellular matrix. Curiously, both stages of invadopodia maturation abide on membrane plasticity and vesicle trafficking. While lysosomes have been proposed to act as membrane feeders for invadopodium outgrowth [15], late endosomes and lysosomes (henceforth collectively designated LE/Lys) have an well-established function in the supply of transmembrane (MT)1-MMP, synonymously referred to as MMP14, to the plasma membrane of invadopodia [16]. Thus, protrudin-facilitated ER-endosome contact sites encourage the invasion of cells through driving the translocation of MT1-MMP-laden endosomes toward the plasma membrane, which then fosters the outgrowth of invadopodia outgrowth and the exocytosis of MT1-MMPs.

Evidence suggests that invasive cancer cells overcome these tissue barriers producing specialized F-actin-based protrusions referred to as invadopodia, which focally breakdown the extracellular matrix to accommodate cell invasion [17–19]. In light of this, MT1-MMP is highly expressed within invadopodia and is found to be a key component of pericellular matrix breakdown, which labels the invasion of carcinoma cells across the basement membrane and through dense, collagen-rich tissue confinements [20–24]. While by definition all invadopodia types break down the matrix and are dependent on the catalytic activity of MT1-MMP, their composition and activity may vary according to the molecular composition and mechanical characteristics of the matrix microenvironment [25–27]. In the conventional model employed to examine invadopodia assembly, cancer cells are seeded atop a thin quasi-2D substrate of denatured collagen, such as gelatin, where deterioration activity is focused within 0.5–1 μm-sized, actin-rich spots [18]. In contrary, when confronted with a truer physiological matrix construction of collagen type I fibers [24,28], cancer cells form cortactin/F-actin-positive constructs that continue to mature into breakdown-competent invadopodia, together with focal MT1-MMP shedding and aggregating in conjunction with the subjacent matrix of collagen fibers [16,26,29,30]. Typically, these structures, extended in the plane of the plasma membrane, may be multiple micrometers long [26,29,30]. It has been seen that cancer cells penetrating through the collagen gel with a nucleus-at-the-back conformation [31,32], favorably develop prolonged invadopodia at the advance level of the invasive protrusion in front of the nucleus and dismantle the

matrix-constricting fibers to aid in invasive pathway formation [24,28,33].

However, another more common mechanism of cell adaption may either alter their own mechanical characteristics or induce a phase separation due to modified assemblies of proteins.

Fundamental concepts of cell locomotion have been first uncovered in the 1970s [34–36]. Specifically, the 2D locomotion of fibroblasts that migrate over a flat substratum have been examined. Nevertheless, cell migration on the 2D surface insufficiently mirrors cell migration *in vivo*, as the cells are permanently subjected to the physical restraints of the extracellular matrix [13]. The fundamental stages of cell migration through the extracellular matrix can be identified by the three-stage model of invasion [37]. According to this theory, during migration, cells first acknowledge the extracellular matrix and adhere to it by adhesion molecules such as integrins [37]. Subsequently, proteinases are conscripted to induce local breakdown of the extracellular matrix. Ultimately, the cell body relocates to the deteriorated extracellular matrix cavity [37]. Repeating the three steps effectively empowers the cells to traverse over the extracellular matrix. This type of migration is termed mesenchymal type and demands the harmonious orchestration of integrin-facilitated cell adhesion, cytoskeletal rearrangement, and proteinase activity [13]. In reaction to the presence of sufficiently large, porous matrices, cells can also embrace a protease-independent regime of movement commonly referred to as amoeboid locomotion [38]. However, when cells break down extracellular matrix moieties and need to find a pathway to migrate, they engage MMPs, a set of proteinases that feature prominently in the breakdown of the extracellular matrix [39,40].

2.1 Cells Act on the Extracellular Matrix

Apart from biochemical signal transduction processes, cellular functionality and fate critically rely on the mechanophenotype of the surrounding extracellular matrix environment [2,3,41]. The extracellular matrix represents an acellular element of tissues that builds a matrix scaffold for the adhesion of cells and fosters multiple mechanotransduction events, which play a role in physiological processes encompassing morphogenesis and homeostasis [42]. Alterations of the mechanical characteristics of the extracellular matrix in *in vivo* and *in vitro* models through reimplanting tissues or alterations of the rigidity of the adherent substrate seem to be relevant in the reversion of the aging process [43], enhance developmental events [8] or modify the malignancy of cancers [44,45].

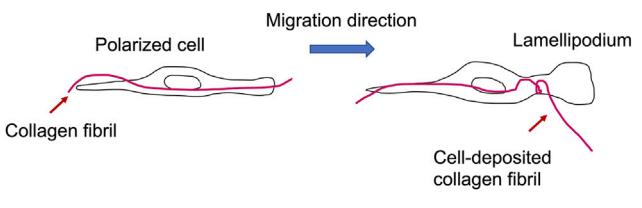

FIGURE 2 | Migrating cells can bend and deposit a collagen fibril during the formation of lamellipodia in the course of cell migration.

Restructuring of extracellular matrix scaffold and their compositional proteins seems to be relevant for the organization of entire tissues and organs. In this light, it is essential to gain an insight into the cellular and molecular stages that occur when individual collagen fibers move [46]. The movement of single collagen fibers may be either a cause of cell movement in 3D confinement or a prerequisite for the cell movement by deposition of misplaced collagen fibers (**Figure 2**).

2.1.1 Effects of the Dimensionality Affects Transportation of Collagen Fibers

The dimensionality of the cell culture systems impacts the mechanism of collagen fiber transportation. In specific detail, cell propagation on glass and other flat 2D substrates seems not to be strictly involved in the motion of fibers in 3D matrices. A limited level of crossover is seen between proteins resident at 3D matrix interfaces and those incident at 2D adhesions [47,48]. Specifically, the shape of fibroblasts in a 3D collagen matrix shares scant similarity with their morphology on a 2D collagen-coated interface [49,50]. Therefore, an essentially alternative mode of motility exists on 3D fibers in comparison to 2D surfaces [4,51,52]. Precisely regulated motions of actin and myosin filaments form the basement of multiple migration events of cells [53–55]. In line with this, it has been proposed that the cell locomotion system creates the cortical cytoskeleton. Due to coupling with extracellular matrix proteins, integrin receptors trigger an intricate signal transduction cascade leading to the activation of contraction through motor proteins empowering cell migration [56]. Thereby, the integrin–extracellular matrix interferences connect physically the extracellular microenvironment with the cell's actin cytoskeleton and consequently couples it to microtubules and intermediate filaments. It has been explored what type of myosin and signal transduction pathways are engaged. In general, non-muscle myosin II (NM II) represents an actin-binding protein that can crosslink actin filaments and obeys contractile characteristics and its regulation is performed through the phosphorylation of its light and heavy chains. Specifically, myosin molecules are capable of moving longitudinally along actin filaments, driving their sliding or creating tension on them. While this demands energy supplied through the hydrolysis of ATP, it also necessitates that myosins contain catalytic sites possessing ATPase activity.

Apart from the linkage through integrins and the extracellular matrix scaffold, zyxin can localize to and dissociate from focal adhesions due to forces imposed by the extracellular matrix scaffold [57]. In contrast, the focal adhesion kinase (FAK), a prominent adhesion-associated tyrosine kinase, is required for durotaxis, which is based on the tendency of cells to move toward more rigid substrates [58]. Hence, these two molecules play also a crucial role in the process of cell migration and force generation [59–61].

Lack of non-muscle myosin heavy chain II (NMHC II) in cells does not impact numerous motile events, such as 2D migration on glass, however, it causes a reduction of the cell's capacity to generate large forces [62,63]. Since large forces are commonly

associated with the restructuring of collagen scaffolds, NMHC II seems to play a role in this process [64,65].

The remodeling of collagen carried out by fibroblasts fulfills a prominent function in the optimization of tissue architecture, which is fundamental for motility in the course of wound healing, developmental processes and the control of cell growth. Nevertheless, the mechanism of collagen fiber locomotion in 3D matrices has not been fully elucidated. Fibroblast lamellipodia project along retained collagen fibers, engage them, and retract them in a "hand-over-hand" cycle engaging α2β1-integrin [46]. Wild-type fibroblasts propel collagen fibers three to four times farther in each cycle than fibroblasts deficient in myosin II-B, referred to as myosin II-B$^{-/-}$. In a similar manner, myosin II-B$^{-/-}$ fibroblasts shrink 3D collagen gels threefold less compared to controls. Nevertheless, on 2D substrates, the propagation rates of collagen beads and cells are not influenced by loss of myosin II-B. Green fluorescent protein (GFP)-labeled myosin II-B, while not myosin II-A, re-establishes the normal function in knockout cells and becomes locally distributed at cell processes, whereas myosin II-A is distributed rather at a central location. In this regard, GFP myosin II-B travels to the peripheral region and returns to the central region during hand-over-hand fiber locomotion, while on 2D collagen, myosin II-B tends to be more centrally dispersed. Consequently, it has been hypothesized that a cyclic formation of myosin II-B and contraction within lamellipodia foster the locomotion of 3D fibers [46].

NMHC II is instrumental in the contractility of actin upon migration, cytokinesis, and formation/sustainment of the cell shape. There exist three isoforms of NMHC II in mice and humans, NMHC II-A, II-B and II-C [66–68] that exhibit various expression profiles [67]. Even though NMHC II-A and NMHC II-B exhibit 85% amino acid sequence identity within the motor domain, they seem to have nonoverlapping distinct functions [69–71]. Ablation of NMHC II-B is embryonically fatal in mice due to serious defects in the heart and brain [72,73]. NMHC II-B$^{-/-}$ fibroblasts that express NMHC II-A but not II-C have normal appearance on tissue culture plastic and other 2D supports, although they display more haphazard locomotion and marginally elevated on-momentum motion rates [46,74,75].

NMIIA is linked to complement receptor-driven but not FcγR-driven phagocytosis, which has been suggested to engage the polymerization of actin [76]. NMIIA filaments may also coordinate phagocytosis [77] through either fostering the depolymerization of cortical actin [78] or its fluidization [79]. NMIIA filaments resemble exactly toward collagen adhesion sites and are needed for interference and capture of the small GTPase Rap1 within focal adhesions [80,81], which is critical for governing the activation of β1 integrins [82] and, correspondingly, for the phagocytosis of collagen. All of which has been revealed through siRNA-knock-down of NMIIA [81]. Apart from collagen remodeling through phagocytosis, there exists another collagen remodeling process that seems to be based on collagen transportation.

To enlighten the last process of collagen remodeling, single fibers of Cy5-labelled or TAMRA-labelled collagen type I can be positioned on top of the apical plasma membrane of adherent cells. The labeling of collagen fibers provided the opportunity to monitor individual cells that interfere with individual collagen fibers, and record the local collagen displacement or transport, whereby the capacity of cells to adhere to or act on fluorescent collagen fibers is not altered [46,83]. It has been reported that the displacements of individual collagen fibers are subject to the cycles of cell elongation, retraction, and liberation at the anterior surface of a polarized cell [46].

When examining the movement of the cell edge and the fiber displacement over time, it has been seen that the fiber is stalled upon the cell extension at the cell's leading edge. When the lamellipodium expanded parallel to the fiber, the contact is maintained and no motions in any other direction can be seen. After the extension phase in the range of 20–40 s, the lamellipodium pulled back; concurrently with this contraction, the fiber traveled inwards at the identical velocity as the leading edge. After the fiber has been carried into the endoplasmic region, it became liberated from the cell. While this behavioral rhythm pattern of motility in 3D is akin to the cycles of cell motility observed in 2D models [53], it is distinct from 2D motions [46]. The behavioral pattern of fiber motions through the cell is intermittent; the lamellipodium stretches along a retained fiber, attaches, and pulls backward in a set of distinctive steps that is what is referred to as an event. Several events appear hand in hand and produce large fiber dislocations. Therefore, the main mechanism for collagen remodeling entails a sequence of elongation/retraction events propelled through lamellipodia. To quantify fiber motion, the frequency of remodeling events for each cell, the speed and duration can be determined. The location of the fibers has been monitored over time that leads to displacement over time curves, which can be subdivided into distinct individual events, The events start when the fibers initiate their movements, and are terminated when the movements are stalled. From the collagen fiber displacements, it can be deduced that wild-type cells exhibit multiple high velocity phases and display long duration periods.

Since the fiber motion seem to rely on NMHC II-B, the fiber movements have been determined in NMHC II-B$^{-/-}$ fibroblasts and wild-type controls, whereby the knock-out cells exhibited less motion. Employing a more precise quantitative examination of the events pointed out that the duration and velocity of fiber motion is reduced that leads to the reduction of displacements for each event appearing subsequently at a lower frequency in NMHC II-B$^{-/-}$ compared to NMHC II-B$^{+/+}$ cells. Restoration of NMHC II-B content in NMHC II-B$^{-/-}$ cells through transient or stable transfection with GFP-NMHC II-B [84] augmented fiber shift per event; however, expression of GFP-NMHC II-A failed to increase the fiber shift per event.

To assess whether reduced fiber motion at the single-cell level mirrors the capacity of 3D collagen matrix remodeling, the contraction of collagen matrices through a suspension of a standard amounts of fibroblasts has been determined. Wild-type cells can contract the matrix to about 25% of the original area, whereby NMHC II-B$^{-/-}$ cells solely to about 75% original area. Stable transfection of GFP–NMHC II-B is able to rescue capability of the NMHC II-B$^{-/-}$ cells to contract the matrix, while

transfection of GFP–NMHC II-A cannot restore it. This finding indicates that NMHC II-B is necessary for the contraction of collagen matrices, while NMHC II-A is not required. However, NMHC II-A possesses a different distribution from NMHC II-B with merely little colocalization of both.

To move collagen fibers, cells must bend them, which necessitates a pronounced force [70], and fibers under tension experience the same type of movement. The high force demand and failure of NMHC II-A to balance the loss of II-B is in accordance with the higher pulse duty cycle of NMHC II-B (F. [71]). Consequently, the reduction of fiber trafficking through the hand-over-hand cycle and 3D matrix contraction in NMHC II-B$^{-/-}$ cells seems to directly rely on the lack of NMHC II-B. Thereby, it has been ruled out that the divergent effects of the two cell types are based on different adhesion strength toward collagen matrices through the binding to the α2β1 integrin [49,85]. Moreover, the expression of α2β1 integrin is not challenged in the two cell types. Therefore, NMHC II-B is intimately affiliated with collagen contact points in 3D matrices, traveling into the extending lamellipodia and migrating posteriorly in concert with actin back transport [53–55] as the fiber contracts.

Finally, the process of collagen fiber motility has been shown to entail repeated hand-to-hand retraction of the fiber by parts of the cell lamellipodia. Lamellipodia elongate whereas the fiber is steady-state, and fiber trafficking tends to substantially correspond to lamellipodia retraction. Even though this is parallel in multiple ways to the process of cell movement on glass [86], the two processes differ significantly in their reliance on NMHC II-B.

It has been figured out that contractility of cells may be related with specific localization of NMHC II-B, which is almost distinct from the localization of NMHC II-A [87–89]. This discrepancy in their specific localizations may be attributable to their different behavior within various organisms or cell types that possess different integrin types, undergo different phases of motility or are either cultured in a 2D environment or within a 3D matrix. There is an increasingly agreement on the fact that cellular interplay inside 3D matrices is pronouncedly diverse compared to traditional cell cultures on top of 2D substrates. In specific, when cells are seeded on pure coverslips for 18 h, NMHC II-A can be found at the edges of polarized cells, while NMHC II-B is located farther at the rear end of the cell [89]. However, when cells spread and polarize for solely 1.5 h on a dense 2D collagen matrix, the localizations are reversed. NMHC II-B$^{-/-}$ cells cannot compensate for defect of II-B through re-localizing II-A toward the periphery. Instead, II-A is located in the endoplasm. In line with this finding, transfected GFP–NMHC II-A and II-B proteins can be found to the identical regions as endogenous proteins. Finally, these results strongly point out toward a NMHC II-B-driven mechanism of collagen remodeling process.

When cells in 3D collagen matrices are grown, NMHC II-B can be detected in the periphery of the cell, and most prominent when thin, dendritic protrusions alongside collagen fiber interactions are exerted. However, NMHC II-A is still centrally focused. These findings further contribute the hypothesis that dimensionality impacts strongly the localization of NMHC II. Hence, it can be hypothesized that NMHC II-B is targeted toward cell–collagen adhesion sites through a process involving integrin activation via collagen.

Moreover, NMHC II-B dynamic response activity is found to be accompanied by episodes of cellular expansion and contraction. As the leading edge extended, NMHC II-B translocalizes in the lamellipodia. Directly before membrane retraction, ripples of NMHC II-B traveled posteriorly, while the collagen fiber underwent posterior traction. The process persisted all the way until the lamellipodia became fully retracted, at which point NMHC II-B started to be carried forwards back into the freshly expanded lamellipodia. Conversely, the dynamics of NMHC II-B in cells that moved on non-treated substrates appeared to be distinct. Cells plated on non-treated 2D glass substrates expanded and contracted lamellipodia ordinarily, but GFP-NMHC II-B remained invariably lacking in the expanding or contracting lamellipodia. The same pattern of GFP-NMHC II-B locus formation has been consistently seen in cells migrating within a 3D collagen matrix; however, cells migrating on 2D collagen fail to obey this type of pattern [46].

These findings provide evidence that NMHC II-B plays a dedicated, immediate role in the trafficking of collagen fibers through fibroblasts in the 3D matrix that it is distinctly dissimilar to its involvement in 2D substrate motility. A number of alternative explanations for the decline in fiber movement have been examined. To begin with, there has been no change in NMHC II-B$^{-/-}$ cell migration on 2D substrates [90,91] or in the rate of cell spreading on fibronectin. In addition, the existence of a collagen fiber on the top surface in no way modified the migration levels of NMHC II-B$^{-/-}$ and NMHC II-B$^{+/+}$ cells on the medium. Lastly, the speed of the collagen-coated beads on the lamellipodia on control and NMHC II-B$^{-/-}$ cells remained the identical. Thus, the lack of collagen fiber and 3D cell motility in NMHC II-B$^{-/-}$ cells is by no means the consequence of a variation in 2D migration speed, backward transport of actin, or the spreading of lamellipodia on interfaces.

Motility in 3D collagen matrices has been found to be heavily reliant on NMHC II-B, while motion on 2D surfaces is unaffected. Because NMHC II-B$^{-/-}$ cells can move collagen spheres posteriorly on a 2D surface while not moving collagen fibers, the fiber architecture appears to be indicative of NMHC II-B engagement. These findings imply that NMHC II-B is substantial for correct cellular rearrangement of collagen matrices *in vivo*, which is in accordance with the aberrant cardiac performance in the knockout mouse [71]. While transfection of GFP-NMHC II-B into NMHC II-B$^{-/-}$ cells resembled and rescued the wild-type phenotype, which failed to do so when GFP-NMHC II-A has been expressed in these cells. This outcome offers complementary circumstantial support that NMHC II-A and II-B perform nonredundant functions in the production of contractile forces throughout the reorganization of the collagen matrix. The cycling of NMHC II-B motion into the lamellipodia, contraction, and breakdown to fuel the locomotion of collagen fibers is subject to a sophisticated, stepwise process to generate whole-cell motion in three dimensions.

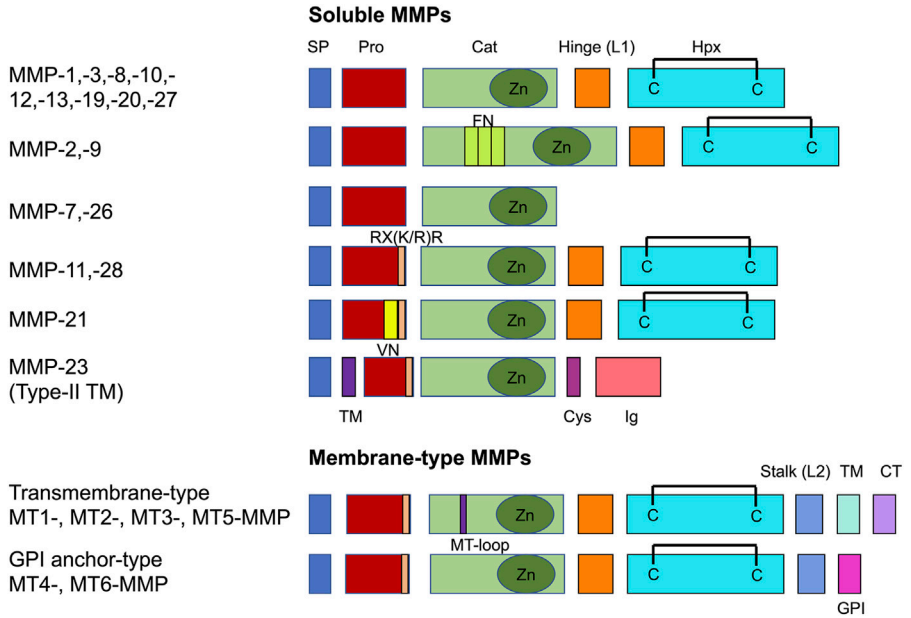

FIGURE 3 | Common domain structure of the MMP family. There are two major classes, such as soluble MMPs and membrane-bound membrane-type MMPs. Catalytic domain (Cat), cysteine-rich domain (Cys), cytoplasmic tail (CT), fibronectin type II repeats (FN), GPI-anchor signal sequence (GPI), hemopexin domain with a C-C disulfide bond (Hpx), immunoglobulin-like domain (Ig), linker 1 (L1), linker 2 (L2), MT-loop = eight-amino acid insertion characteristic to TM-type MT-MMPs, pro-domain (Pro), RX(K/R)R = PC recognition sequence, signal peptide (SP), transmembrane domain (TM), vitronectin-type domain (VN).

2.1.2 Degradation of Collagen Fibers and Networks

A Disintegrin And Metalloproteinases (ADAMs) are a transmembrane protease family that function in the regulation of inflammatory reactions [92]. Emerging in their role in cardiovascular disease/atherosclerosis is that ADAM10 regulates the assembly of atherosclerotic plaques [93], whereas ADAM15 participates in plaque lesion evolution [94] and ADAM17 is linked to atherosclerosis resistance [95,96]. Of multiple members of this family, ADAM8 possesses sheddase activity that facilitates the scission of cell surface proteins related to atherosclerosis, such as the inflammatory adhesion receptor molecules L-selectin, P-selectin glycoprotein ligand-1 (PSGL-1), vascular cell adhesion molecule 1 (VCAM-1), tumor necrosis factor (TNF) and TNF receptor 1 [97,98]. ADAM8 is strongly expressed in the majority of cells of hematopoietic origin and also in brain, bone, lung and thymus [99–104]. Although ADAM8 expression is widespread, mice lacking ADAM8 have a normal evolution with no conspicuous phenotype [103]. In terms of pathologies, ADAM8 expression is raised in cancer and inflammatory diseases of the lung, central nervous system, bone, and joints, and its expression correlates strongly with the seriousness of disease [97,100,105,106].

Membrane type 1 matrix metalloproteinase (MT1-MMP) represents a type I transmembrane proteinase that is part of the matrix metalloproteinase (MMP) family. In fact, MT1-MMP is a powerful cellular microenvironment remodeler and enhances cell migration and invasion of a broad range of cell types under both physiological and pathological circumstances. Therefore, it encourages cell migration through breaking down the extracellular matrix on the cell surface and establishing a migration trail, through altering the characteristic of cell adhesion through shedding cell adhesion molecules to improve cell motility, and through modifying cellular consumption metabolism. Consequently, MT1-MMP is a multipurpose cell motility amplifier [107].

MMPs comprise a set of zinc-dependent metalloproteases that are capable of breaking down all constituents of the extracellular matrix. In humans, a total of 23 MMPs are available, and they can be categorized on the grounds of substrate sensitivity or domain architecture [108]. Optionally, they can be divided into soluble MMPs or membrane-type MMPs (MT-MMPs) (**Figure 3**). The characteristic domain structure of MMPs is composed of a signal peptide, a pro-domain, a domain of catalytic activity, a coupling peptide, also referred to as a hinge region, and a hemopexin domain [108] (**Figure 3**). The soluble MMPs are frequently released as inactive zymogens and have to be activated extracellularly by additional proteinases. MT-MMPs have a domain structure in common with other MMPs, but they are bound to the plasma membrane either by a transmembrane domain trailed with a small cytoplasmic tail (CT) (MT1-, MT2-, MT3-, and MT5-MMPs) or a glycosylphosphatidylinositol (GPI) anchor (MT4-, MT6-MMPs) at their C-terminus [109] (**Figure 3**). Intracellularly, all MT-MMPs are being activated through proprotein convertases such as furin and expressed as active species on the cell surface. The proprotein convertases identify and subsequently scission a basic amino acid motif of RX(K/R)R at the C-terminus of the pro-domain, which is shared between all

MT-MMPs and some soluble MMPs such as MMP-11, -21, -23, and -28 [109]. Transmembrane-type MT-MMPs can also be identified as having an eight-amino-acid loop in their catalytic domain, referred to as MT-loop [109].

Membrane type I MMP (MT1-MMP) has been found to be the unique MMP among these that enhances cell migration in a collagen-rich setting [21]. MT1-MMP-facilitated the migration and invasion of cells and hence have been associated with various disease processes, encompassing inflammation [110], atherosclerosis [111], rheumatoid arthritis [112], invasion of cancer and malignant progression of cancer, such as metastasis [113]. Consequently, insight into the mechanisms of MT1-MMP-directed cell migration/invasion is critical to gain an appreciation of the pathogenesis of various diseases. There is ample evidence that MT1-MMP enhances cellular invasion both in response to and independently of proteolytic activity [107]. In the following the three different mechanisms for the migration modes of MT1-MMP-dependent cell migration/invasion are presented and discussed. These three mechanisms comprise direct proteolytic extracellular matrix degradation, indirect extracellular matrix proteolysis and modification of cell adhesion molecules.

2.1.3 Cross-Linking of Fibers

The extracellular matrix contains primarily collagen type I fibers. Collagen-made scaffolds have turned out to function as ideal biomaterial for the purpose of tissue engineering and development of *in vivo* implants. For multiple biomedical techniques, collagen can be crosslinked to strengthen the strength, rigidity and stability of the overall mechanical construct. This can be done by chemical, biomaterial and cell-derived cross-linkers, however, for the *in vivo* situation, the cell-derived cross-linkers are relevant. The other cross-linkers, such as chemical substances, biophysical techniques and biomolecules from other species than the cells or tissues under investigation can solely be employed to mimic the *in vivo* situation in *in vitro* cell or tissue culture assays.

Collagen is omnipresent, self in tissues that are biologically and structurally diverse. The natural layering and positioning of cells in the body is controlled through biochemical and biomechanical indications of the extracellular matrix and the physiological circumstances at the location of the tissue. Whereas some of these indications can be customized in a framework through the use of additive fabrication, some changes result in a natural way from the decisions encountered during the process of synthesizing the nucleus of a framework. Therefore, the structural and property alterations imparted by the underlying manufacturing processes over the length scales simply are not possible to oversee. Specifically, the networking process not merely enhances the mechanical characteristics of a collagen skeleton, however, it also leads to additional alterations in the molecular framework. In the following seven most frequently employed substances for the cross-linking of collagen type I fibers are presented and discussed. There are three major classes of collagen cross-linkers, such as chemical, biomaterial and cell-derived cross-linkers. A special focus is placed on cell-derived cross-linkers, since they are present *in vivo* and possess no potential toxic effects on cells and tissues. However, for experimentalists the chemical cross-linkers and the techniques to cross-link extracellular matrices are important for future studies and are mentioned below. The biological cross-linkers may have the advantage that they are less toxic for the cells and tissues and hence they are included in this part.

2.1.3.1 Chemical Cross-Linkers

The basic goal of chemical crosslinking is to enhance the mechanical characteristics and stability of the processed collagen end product. The choice of a suitable cross-linker, by contrast, may vary according to a number of factors. Collagen is commonly utilized in biomedical implementations to mimic the biochemical environment encountered *in vivo*, so amine-based cross-linkers [114–118] are frequently selected to imitate the lysine-based linkages inherently occurring in collagen [119]. The mode of selection and mechanism of crosslinking may also unintentionally alter different structural properties and the relevant biological reaction. Chemical cross-linkers, for example, can be roughly categorized according to their ability to integrate the cross-linker straight into the protein. This yields the "zero-length" cross-linkers, where they do not stay within the protein structure after crosslinking, or the "non-zero-length" cross-linkers, where a portion or the entire cross-linker is built-in (**Figure 4**). Whereas zero-length cross-linkers can alter the local chemical composition, leading to non-native such as cellular interactions [120], it also raises some issues of concern regarding the specific nature of the potential for non-zero-length crosslinked collagen profiles to liberate cytotoxic compounds when subject to metabolism [121]. The main cross-linkers in use, most of which are amine-based and span a variety of cross-linkers with and without zero length [122]. Among them are conventional cross-linkers including glutaraldehyde, which is a non-zero length cross-linker, and 1-ethyl-3-(3-dimethylaminopropyl) carbodiimide-N-hydroxysuccinimide (EDC-NHS), ultraviolet radiation (UV), dehydrothermal treatment (DHT), that are zero length cross-linkers. New and upcoming crosslinking techniques involve the utilization of genipin as a non-zero length cross-linker, and riboflavin and tissue transglutaminase 2 (TG2) as zero length cross-linkers.

2.1.3.1.1 Glutaraldehyde Glutaraldehyde represents a chemical cross-linker that is frequently investigated in tissue engineering due to its exceptional capacity to increase the elastic modulus of scaffolds [123]. Glutaraldehyde utilizes the generation of imide as a mechanism to crosslink collagen fibers (**Figure 4**). As evident from the collagen interaction mechanism, glutaraldehyde is not a zero-length cross-linker and the final crosslinked collagen includes portions of the linker molecule in the resulting structure. Glutaraldehyde has also proven capable of attaining an unusually high level of crosslinking, with full (amine-based) crosslinking exceeding 0.12 wt% obtained in porcine dermal telocollagen-depleted collagen gels [124]. The concern with this, nonetheless, is that crosslinks can be formed both within and across collagen fibrils, and that an advance in crosslink density is not necessarily accompanied with a comparable rise in mechanical characteristics [116]. Glutaraldehyde

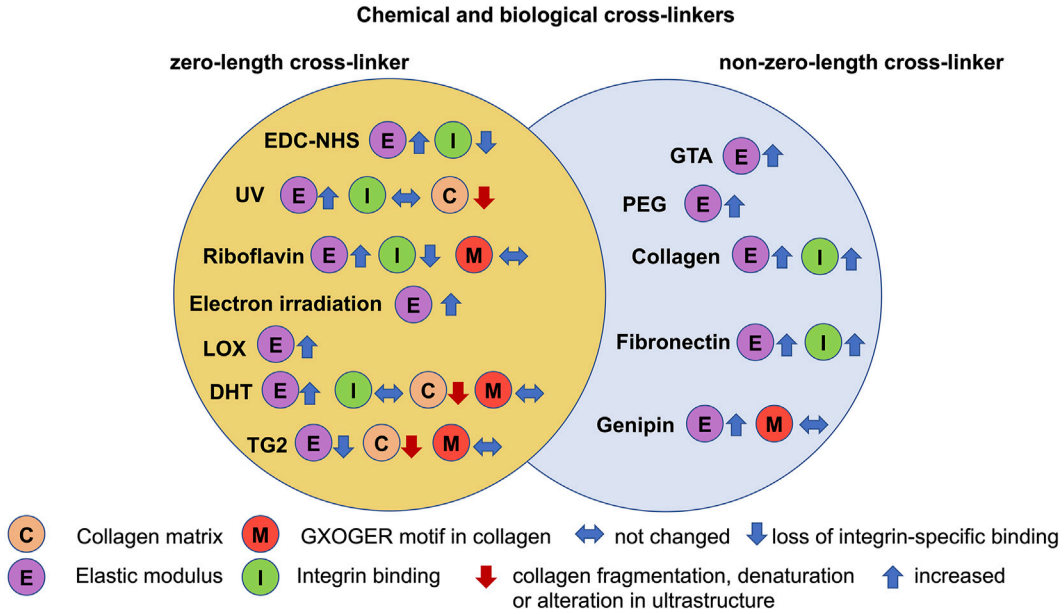

FIGURE 4 | Chemical and biological cross-linkers serve as modifiers for 3D collagen matrices. Among them are zero-length (yellow circle), including 1-ethyl-3-(3-dimethylamino propyl) carbodiimide hydrochloride (EDC)-N-hydroxysuccinimide (NHS), ultraviolet radiation (UV), riboflavin, electron irradiation, dehydrothermal treatment (DHT), lysyl oxidase (LOX) and transglutaminase 2 (TG2) and non-zero-length cross-linkers (blue circle), such as glutaraldehyde (GTA), polyethyleneglycol (PEG), collagen, fibronectin and genipin.

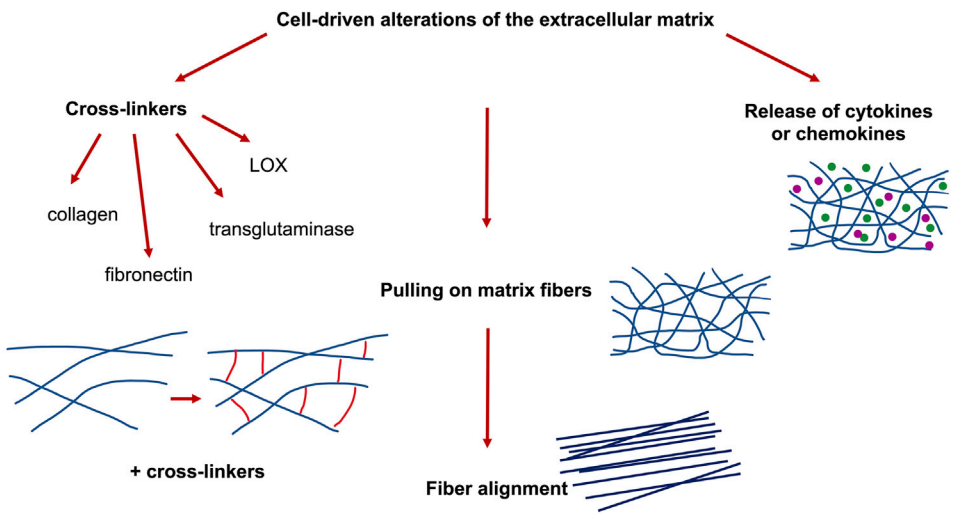

FIGURE 5 | Cell-driven alterations of 3D extracellular matrix scaffolds, such as cross-linking of cell-derived molecules, cellular pulling on collagen fibers and cell-released cytokines or chemokines.

crosslinking of dermal sheep collagen has been determined to raise the modulus at low strain due to crosslinking from 1.7 to 3.5 MPa at 0.5 wt/wt%, even though the modulus at high strain drops slightly from 32.7 to 21.0 MPa with rising crosslinking concentration [116]. In addition, cell sowing and proliferation has been found to be enhanced by glutaraldehyde crosslinking through hindering cell-mediated contraction of a rat tail atelocollagen-derived type I scaffold, whereas differentiation was markedly impeded compared with the noncrosslinked scaffolds [125]. The byproducts of breakdown in subsequent metabolic pathways also led to the cellular cytotoxicity seen, even though there is no indication of carcinogenicity or mutagenicity associated with the usage of glutaraldehyde [121].

2.1.3.1.2 1-ethyl-3-(3-dimethylaminopropyl) carbodiimide-N-hydroxysuccinimide (EDC-NHS)

EDC-NHS represents a general collagen cross-linker which has a non-cytotoxic, zero-length crosslinking alternative to glutaraldehyde. Zero-length cross-linking leads to restricted access to "adjacent" free amines [126], which obeys a reaction mechanism (**Figure 4**). The cross-links are between glutamates and arginines/lysines and in each case involve the GXOGER sequence detected by integrins acting to intercede cell binding on collagen, where the amino acid X is usually phenylalanine (F). The EDC-NHS is referred to as the standard concentration of 100% [117,127] and is frequently written as a precise molar ratio of 5:2:1 EDC:NHS:COO^{-}, where COO^{-} denotes the carboxylate groups in the protein.

EDC-NHS crosslinking provides a lower density of the crosslinks compared to classical cross-linkers such as glutaraldehyde. However, it delivers a more hydrophilic surface, which is favorable for fibronectin activity and enables a higher degree of swelling than traditional cross-linkers on type I bovine dermal swollen gel-derived collagen fibers, such as those exhibiting chondroitin-6-sulfate additives [126]. In addition, EDC-NHS has been demonstrated to trigger self-assembly of collagen bundles with a width of approximately 300 nm with both acid-soluble and insoluble type I bovine dermal collagen, implying the feasibility of both intra-fibril and inter-fibril binding, although it is a zero-length cross-linker. The non-soluble collagen fragments exhibited amplification and localization of the piezoelectric response alongside these self-assembled fiber bundles [128].

In the past, cross-linking of collagen up to 200%, synonymously referred to as 10:4:1 EDC:NHS:COO- of the standard composition, however, substantial research on EDC-NHS constitution and its impact on cell migration and mechanics [127,129–132] indicate that far lower concentrations (10–100%) can maintain the enhancements in mechanical characteristics imparted by crosslinking. Extruded collagen fibers, such as bovine dermal acid-swollen gel collagen type I, have been analyzed after crosslinking at three specific EDC-NHS concentrations (0.02 w/w EDC%-0.006 w/w% NHS, 0.002 w/w EDC%-0.0006 w/w% NHS and 0.0002 w/w EDC %-0.00006 w/w% NHS) [129] for alteration of the ultimate tensile strengths, which revealed to be not impacted through the levels of EDC-NHS cross-linker. Human tenocytes of the anterior cruciate ligaments can adhere to these extruded collagen fibers at lower levels, when these fibers are strongly crosslinked after 1 day [129]. After 3 weeks of culturing, the tenocyte proliferation on the heavily crosslinked fibers has been decreased. The results implicate that the crosslinking conditions can be lowered by roughly two orders of magnitude with no impact on the tensile characteristics [129].

Similar results of impaired attachment of C2C12 mouse cardiomyocytes, platelets and HT1080 fibrosarcoma cells have been obtained with the EDC-NHS cross-linker for collagen films, such as type I microfibrillar bovine dermal and Achilles tendon, whereas there is not effect for crosslinked gelatin films of bovine dermal sources [127,130]. The hypothesis connected the perceived decrease in cellular attachment to the ablation of GXOGER motifs in collagen by the carbodiimide crosslinking procedure. Based on the access of RGD motifs for cell binding in gelatin that is cryptic in collagen, similar reductions in cell attachment are not seen with crosslinked gelatin.

The impact of EDC-NHS crosslinking on integrin binding has been explored to obtain a mechanistic comprehension how the cross-linkers alter the collagen skeleton to generate the drop in cell adhesion [120]. Moreover, biochemical receptors involved in binding with the crosslinked type I collagen substrates of bovine Achilles tendon have been identified by analyzing the binding of two integrin I domains (α1 and α2) and classifying four different model cell lines, such as platelets, HT1080 human fibrosarcomas, Rugli rat glioma cells, and C2C12 mouse fibroblasts with transfected integrin I domains that express distinct collagen-binding integrins. Through isolated integrin domain binding and cellular attachment experiments to collagen, it has been revealed that four collagen integrins, such α1β1, α2β1, α10β1, and α11β1, are impacted through the EDC-NHS crosslinking. Thus, the mechanism has been proposed to delineate the inhibition of integrin binding through the engagement of glutamic acids in the crosslinks created by EDC-NHS. Because I-domain binding in an integrin relies on pairing with a divalent cation aided by metal ion dependent adhesion site (MIDAS) motifs, depletion of glutamates upon EDC-NHS cross-linking is hypothesized to ablate GXOGER motifs on collagen. At high EDC-NHS crosslinking (≥10%), the extent of GXOGER ablation evoked through the carbodiimide seems to facilitate non-native cellular interferences with the substrate [120].

2.1.3.1.3 Dehydrothermal Treatment

DHT utilizes LeChatelier's principle of advancing a reaction accomplished through the removal of the crosslinking by-product, water, using heat and vacuum (**Figure 4**). The impact of DHT sustained at a variety of temperatures (110, 120, 140, 160, 160, 180°C) at 30–50 Torr for 24 h after a 1-h ramp has been examined on scaffolds of bovine type I dermal collagen. It can be seen that the compressive elastic modulus of DHT-treated films rose with the employed DHT temperature, in accordance with the interlacing density of the films [133]. The treated collagen films have also been prone to denaturation in the process, exhibiting a significant denaturation (57.84%), crumbling, and embrittlement at elevated temperatures (180°C) [133]. The crosslink density of DHT-treated collagen obtained from cow skin has been observed to rise with temperature from 105 to 125°C, although not with time beyond 3 days [134]. Even though some denaturation of collagen is claimed to enhance crosslink density by providing physical adhesion to hidden groups, beyond 145°C or 5 days, a significant amount of denaturation and diminished mechanical characteristics have been noted [134].

An *in vivo* evaluation of DHT-treated microfibrillar type I collagen-chondrotin-6-sulfate scaffolds has been performed within transected peripheral rat nerves [135]. Thereby, the treatments at higher times and temperatures aided nerve regeneration more effectively, offering an optimal time frame for breakdown that corresponded to the tissue regeneration

speed. In addition, an examination of the *in vitro* cell reaction of DHT-treated type I collagen-choindroitin-6-sulfate collagen scaffolds has been performed employing MC3T3-E1 mouse preosteoblasts at higher temperatures. Specifically, these scaffolds have been modified with four temperatures, such as 105, 120, 150 and 180°C, under a vacuum of 37.5 Torr. DHT-treated scaffolds exhibited both extreme priming and proliferation of preosteoblasts when compared to EDC-NHS or glutaraldehyd-cross-linked scaffolds, which is especially seen at the higher temperature of 150°C [131]. Although the findings of an *in vivo* and an *in vitro* assay cannot be directly matched, it is reasonable to assume that the utilization of DHT treatment to evoke high cellular activity can be restricted to lower temperature regimens at which the chance of denaturation is low.

2.1.3.1.4 Ultraviolet Radiation

The utilization of UV to crosslink collagen is a fairly new technique that is based on the generation of highly reactive radicals to assist in the creation of crosslinks throughout the microstructure (**Figure 4**). Due to the nonspecificity of radical-based reactions, no rigorous chemical mechanism exists, although amino acid analyses indicate cross-links through aromatic residues, such as phenylalanine and tyrosine [127,136], which may act to stabilize the radicals inside their delocalized π-systems.

UV-irradiated films of acid-soluble rat tail tendon collagen exhibit a decrease in thermal stability and generate of surface flaws, such as wrinkles and micro-cracks upon UV crosslinking at $\lambda = 254$ nm, 0.196 J $cm^{-2}min^{-1}$, for 2, 4 and 8 h [137]. It was hypothesized that the applied UV radiation breaks the hydrogen bonds within and transverse to the collagen in these samples, initiating the liberation of water and the creation of collagen fragments [137]. The UV-dependent fragmentation of collagen has been demonstrated to be restricted through the addition of glucose that impairs the unwrapping of the triple helices in bovine insoluble dermal and Achilles tendon collagen polymers [138].

An evaluation of the physical characteristics of UV-irradiated collagen films and scaffolds in the presence and absence of glucose has been carried out [127]. Bovine type I skin scaffolds and bovine Achilles tendon collagen scaffolds and films have been prepared and subsequently exposed to various UV treatments, such as $\lambda = 254$ nm for 30 min with a defined spectrum of intensities ranging from 0.06 to 0.96 J cm^{-2} for scaffolds and either 0.42 or 0.96 J cm^{-2} for films. The crosslink strengths attained remained extremely low regardless of the extended exposure times, resulting in a maximum Young's modulus of less than 2 kPa for the glucose-treated tendon collagen, and 0.5 kPa in the absence of any supplements [138]. In addition, the effect of UV crosslinking on breakdown resistance in water has been determined to be related to the collagen source. UV cross-linking enhanced tendon collagen strength and exhibited no relationship to irradiation level, while dermal collagen strength strengthened at the lowest intensity and deteriorated at higher intensities. All this became balanced through the rival actions of collagen crosslinking and collagen breakdown encountered throughout UV exposure [138].

However, what type of *in vitro* cellular integrin-driven response is expected after UV cross-linking? Specifically, α2β1-integrin, which facilitates HT1080 cell and platelet binding to collagen, and HT1080 spreading and proliferation have been shown to be not impaired upon UV cross-linking, indicating that GXOGER sequences remained intact upon UV treatment [138]. On the basis of these findings, the synergistic crosstalk effects of UV crosslinking and EDC-NHS crosslinking on insoluble bovine Achilles tendon collagen type I have been examined. UV irradiation has been determined to restrain adhesion of α2-I domains beyond the anticipated impact of EDC-NHS on its own, with EDC-NHS concentration-dependent hindrance of HT1080 cell adhesion and cell coverage. It has been theorized that this is due to the engagement of phenylalanine (F) in UV crosslinking, leading to the depletion of GFOGER crosslinking motifs, which is the tightest tethering of the GXOGER motifs. Consequently, tethering is counterbalanced through the GLOGER motifs, wherein L stands for leucine, being compensatory for the attachment of the α1-I domain, but having a weak affiliation for α2-I domains [139].

2.1.3.1.5 Electron Irradiation Crosslinking

High-energy electron-induced crosslinking techniques have been revealed to be useful for accurately tuning collagen characteristics for extracellular matrix schemes [140]. Due to the procedure's minimally invasive nature, collagen remnants stay intact when exposed to high-energy electrons (**Figure 4**). Specifically, a collagen network 3D pore size analysis as a matter of irradiation dosage indicates an enhancement in density resulting in a reduction in pore size. In addition, mechanical characterization of these scaffolds by rheological techniques reveals increased storage and loss moduli that correspond to an enhancement in crosslink density. Collagen gels can be modified to adapt specific features, such as structural or mechanical cues, to mimic natural and physiological extracellular matrices. These biomimetic scaffold systems need to exhibit a designed and engineered scaffold architecture, distinct mechanical characteristics, distinct thermal stability and display a specific swelling phenotype, precise and non-cytotoxic crosslinking techniques are demanded [141]. Since conventional techniques use compounds such as aldehydes [116,142], tris (2,3-Epoxy propyl) isocyanurate (TEPIC) [143], or enzyme-based cross-linkers [144], which can negatively impact cell performance, reagent-free techniques are of great advantage. Electron irradiation is very efficient among them to network polymeric hydrogels [145]. In this process, macro- and radical ·OH radicals are generated due to homolytic scission of bonds on the polymer chain and radiolysis of water molecules [146]. The radical ·OH radicals continue to target the polymer chains, generating additional macroradicals. The macroradicals are extremely reactive and self-recombine to establish covalent bonds that build cross-links inside the polymer matrix. By comparison with chemical crosslinking techniques, electron irradiation at 5–20 kGy holds the prospect of high effectiveness and accurate and rapid crosslinking without causing cytotoxicity of gelatin gels [147,148]. It also instantly sterilizes the media, thereby guaranteeing biomedical usage [149]. Inside the class of ionizing irradiation, electron irradiation is very beneficial for the hydrogel alteration owing to its high penetration depth [150] and

high dosage rates [151], which facilitates homogeneous crosslinking. Moreover, it provides accurate global as well as on-site meshing through the utilization of a highly centered electron beam, thereby paving the way for a variety of uses spanning from mechanical texturing to actuators [147,152]. Rather, for future biomedical applications including extracellular matrix models, a characterization of electron beam crosslinked collagen gels with respect to network structure, such as pore size, rheological features, and cytocompatibility, has been performed [140]. Fourier-transform-infrared spectroscopic observations demonstrate that electron beam-assisted crosslinking causes only small alterations, whereas the distinctive polymeric architecture of the collagen is maintained across doses of 50–100 kGy. Electron irradiated collagen possesses high cytocompatibility and can be combined with other isolation techniques of tissue-based scaffolds that comprise a high content of collagen type I, such as decellularized matrices of tissue biopsies or specimen. Consequently, these collagen-rich tissue scaffold samples can be mechanically tailored. Decellularized scaffolds and 3D-printed scaffolds utilizing biomaterials can become nature-like tissue scaffolds.

2.1.3.2 Biological Cross-Linkers

2.1.3.2.1 Genipin

Genipin, a substance derived out of the fruits of Gardenia jasminoides Ellis, has proven to be an alternative biomaterial crosslinking agent in view of the cytotoxicity of crosslinking agents, including glutaraldehyde and formaldehyde [153]. Based on the firmly entrenched food safety of genipin, the crosslinking technique has been proposed for applications in collagen-, gelatin-, and chitosan-based scaffolds and drug-delivery schemes [153]. Genipin has been implicated as a cross-linker in chitosan-based frameworks and is assumed to obey the same two-step mechanistic route in both chitosan and collagen (**Figure 4**). One of the crosslinking steps has been mapped to incorporate a secondary amide bond of a free amine to the genipin through a nucleophilic SN2 substitution [154,155], and more recently it has been delineated that the second crosslink develops via two additional pathways to accomplish crosslinking to collagen, either through two imide crosslinks or two amide crosslinks [155]. Genipin crosslinks gelatin via lysine and arginine moieties and is anticipated to pursue a resembling mechanistic route in collagen [156]. The cross-links established with genipin provide collagen scaffolds that raise the elastic modulus by almost an order of magnitude. Collagen scaffolds derived from rat tail tendon type I with a porosity of 92% have been shown to be most efficacious when subjected to high crosslinking concentrations (0.7812 wt/wt%) and temperatures (20–37°C), yielding a compressive modulus of elasticity of 30 kPa relative to a noncrosslinked reference control at 5 kPa [157].

However, there seems to be cytotoxicity of genipin at very large concentrations above 5 mM, when crosslinking collagen type I matrices [156]. In addition, neurocompatibility and long-term large animal research trials have proven that genipin, when injected directly into the spine of individuals, relieves their chronic low back pain through enhancing the mechanical characteristics of the annulus [158].

Another examination of the mechanical characteristics of genipin involving bovine type I dermal insoluble collagen indicated that at the highest crosslinking concentrations (1.5624 wt% at room temperature), genipin can function as an alternative for the intermediate crosslinking constraints of EDC-NHS, enhancing both the Young's modulus and the stress to rupture [159]. Integrin-specific binding has also been seen to be not impaired by genipin crosslinking, leading to high proliferation levels in human dermal fibroblasts and minimal cellular toxicity [159].

2.1.3.2.2 Riboflavin

Riboflavin, synonymously referred to as vitamin B2, has also found to be biocompatible in terms of achieving crosslinking of collagen matrices with blue light. Riboflavin crosslinking of collagen is of specific concern due to the short application times, such as 15 min, needed to obtain pronounced enhancements in mechanical characteristics, such as a 2.5-fold raise in modulus of elasticity [122].

Riboflavin has been used to generate crosslinks in a collagen matrix, such as type I insoluble, bovine Achilles tendon membranes, in specific, through arginine, histidine and lysine amino acids (**Figure 4**). Even though lack of arginines can lead to impediment of integrin-mediated adhesion, it has been postulated that arginines are not as functional for stabilization of a divalent cation in GFOGER motifs as are glutamines, that are being lost upon EDC-NHS crosslinking [122,160]. However, cell adhesion assays verified that only α2β1-integrin-mediated binding has been impacted, as assessed with HT1080 fibrosarcomas, while integrin binding has been left undisturbed in human dermal fibroblasts expressing a variety of integrins. However, in contrast to EDC-NHS-crosslinked films, riboflavin-crosslinked films failed to induce an enhancement of nonspecific binding while exhibiting similar ultimate tensile strengths compared to EDC-NHS-crosslinked collagen membranes [122,160]. In an investigation of plastically compacted collagen scaffolds, a decline in oxygen diffusivity and viability of human dermal neonatal fibroblasts has been seen after crosslinking of a compacted rat tail collagen type I scaffold [161]. Nevertheless, this cytotoxicity could result from an interplay of compression and crosslinking, as higher levels of plastic compression led to a more pronounced reduction in cell viability compared with riboflavin crosslinking.

2.1.3.2.3 Polyethylene Glycol

The impact of polyethylene glycol polymers with varies molecular weights (**Figure 4**), degree of branching, and specific terminal groups have been largely analyzed in terms of cross-linking and functionalization of 3D collagen matrices [162–166]. Branched cross-linkers increase the amount of fibers converging at every junction of the scaffold, which is referred to as local connectivity or junction points of the network and additionally enhances the mechanical strength of the hydrogel [167,168].

2.1.3.3 Cell-Derived Cross-Linkers

Cell-derived cross-linkers are undoubtedly the most important class of cross-linkers, and thus greater research efforts need to be devoted to them in the future, as they have the potential to be non-toxic to cells and may also affect the mechanophenotype of the extracellular matrix environment, which in turn may alter the cellular mechanophenotype. In specific, cell-based cross-linkers play a pivotal role in the characterization of organoid and therefore special attention must be paid to them.

2.1.3.3.1 Transglutaminase

Transglutaminases pertain to a family of transferase enzymes that network proteins through the establishment of a bond between an ε-amine (lysine) and γ-carboxyl in glutamines (**Figure 5**). Many types of transglutaminases exist, among them microbial transglutaminase, factor XII, epidermal, keratinocyte, and tissue transglutaminases, which are frequently encountered as cross-linking reagents in skin, hair, and blood clots *in vivo*. Within these enzymes, tissue transglutaminase 2 (TG2) is a calcium-dependent enzyme that has exhibited an exceptionally high cellular contribution, encompassing an enhancement in the number of osteoblast adhesions following TG2 crosslinking of freeze-dried type I calfskin collagen scaffolds [169].

Transglutaminases attach to glutamines in the polypeptide chain and engage them for subsequent reactions [170]. In the vicinity of water, this leads to the conversion of the glutamine into a glutamate residue, while in the presence of a suitable amine, an amide bond is produced at the location of the activated glutamine [170]. Therefore, TG2 may serve either as an amide cross-linker that avoids preexisting aspartic or glutamic acids (E and D) in the generation of crosslinks or, conversely, may help to reintegrate glutamates (E) into the substrate, thereby enhancing the number of MIDAS motifs that can be accessed on the substrate for integrin sensing.

The analysis of mechanical properties of TG2 revealed global characteristics, such as the tensile modulus, plasticity and failure strength of TG2-treated films, that are increased compared to non-crosslinked type I bovine dermal insoluble collagen films [122]. TG2 treatment has been not observed to hamper the spreading, attachment, cytotoxicity and proliferation rate of human dermal fibroblasts to their substrate.

2.1.3.3.2 Lysyl Oxidase

Lysyl oxidase (LOX) represents an amine oxidase that is copper-dependent and fulfills a prominent function in the course of connective tissue matrix through crosslinking the extracellular matrix proteins, such as collagen and elastin (**Figure 5**). LOX promotes the catalysis of the oxidative deamination of specific lysyl and hydroxylysyl residues within collagens and elastin, which represents the initial step of the covalent crosslinking of these extracellular matrix components [171,172]. Therefore, it acts as a key regulator for collagen homeostasis. LOX concentrations rise in numerous fibrotic diseases, in contrast to the reduced expression of the enzyme in specific diseases with disturbed copper metabolism. LOX is produced as a preprotein that is liberated by secretion as a 50 kDa N-glycosylated proenzyme and subsequently undergo proteolytic cutting to the 32 kDa catalytically active mature enzyme. Effectors or conditions that regulate LOX expression comprise transforming growth factor (TGF)-β, platelet-derived growth factor (PDGF), angiotensin II, retinoic acid, fibroblast growth factor (FGF), altered serum conditions, and shear stress. As new LOX-like genes have been discovered, a multigene family may be in question. There is also growing awareness that LOX can have additional important biological roles in parallel to its function in cross-linking elastin and collagen in the extracellular matrix [118].

2.1.4 Collagen and/or Fibronectin Secretion (Altering the Composition of Fibers)

Apart from the cell-derived cross-linkers, the secretion of extracellular matrix proteins by cells and tissues can alter the structural and mechanical properties of the extracellular matrix environment. Currently, 29 types of collagen are known, grouped into types I, II, III, IV, and IX, and are more prevalent in humans [173–175]. *In vivo*, fibril-forming collagen promotes the creation of fibers, and the fibers are intertwined in a specific manner due to the specific tissue characteristics [176]. The self-assembly of collagen into fibers represents a gradual process [177,178], which is impacted through parameters including initial concentration, ionic strength, temperature and pH [179–181]. The presence of potassium ions causes the formation of the banding pattern, referred to as "D" period patter, of collagen fibers [182]. Moreover, collagen fibers fulfill a largely irreplaceable role in the proper functioning and structure of tissues. On the cellular scale, cells serve as one of the main components of the extracellular matrix, the achievement of multiple functions of cells is highly reliant on the availability of fibers, such as cell adhesion, motility, proliferation and metabolism [183–188]. On the organic scale, collagen fibers provide a fundamental basis for the shape of tissues [189–191], mechanical characteristics [192–194] and tissue repair mechanisms during the process of wound healing [195,196]. In addition, cell-secreted collagen, such as type I or type IV, or fibronectin molecules can crosslink the collagen matrix, both of which enhances the elastic modulus of the collagen matrices (**Figure 5**).

2.1.5 "Pulling" on Fibers

A scalable technique has been presented to determine how multicellular clusters rely on their capacity to locally pull, push, and even twist the neighboring extracellular matrix. Therefore, they probed their technique by applying biochemical treatments toward cell clusters in order to perturb cell–cell and cell–matrix interferences, which cause subsequently a remodeling of the overall cell cluster and consequently lead to a dissemination with specific mechanical signatures of matrix deformation [197]. These mechano-signatures can alter the mechanophenotype of the microenvironment and specific tractions, encompassing spatially heterogeneous contractile, protrusive, and circumferential types. Multicellular clusters in diverse phases of the epithelial–mesenchymal transition exhibit a successive decrease of protrusive and circumferential tractions, and the generation of localized contractile tractions due to elongated shapes of the cell cluster, all of which has been

characterized. Consequently, the mechanical probing of collagen fibers can lead to aligned and hence oriented collagen fiber architectures (**Figure 5**). Thereby, oriented collagen fiber scaffolds foster the migration of cells [75,198], differentiation [199], wound repair mechanics [200], and the assembly of vascular framework [201]. These results point out to the usefulness of oriented collagen fiber matrices during tissue repair, regeneration, and other functions that deal with the repair and regeneration of bearing tissues with distinct fiber orientation, including discs, cartilage, ligaments, and fibers.

In specific detail, through placement of collagen type I matrices within prestrained (0, 10, 25, 50% strain), poly(dimethylsiloxane) (PDMS)-based microcavities and liberating the mold strain after matrix polymerization, collagen gels have been polymerized with diverse fiber alignment. Endothelial cells incorporated within the various matrices reacted to the elevated collagen fiber orientation with formation of 3D vascular reticulations consisting of thicker, directional branching that promoted collagen IV deposition and lumen creation compared with control conditions. These substrate-dependent variations in microvascular meshwork assembly have been linked to modified cell division and migration modes and have been linked to augmented mechanotransduction pathways [201]. These results suggest that collagen fiber alignment can provide a direct modulation of vascular reticular assembly and that culture systems containing aligned collagen can be employed to explore the underpinning mechanisms, thereby advancing finally the understanding of disease, tissue evolution, and homeostasis.

When subjected to the mechanical force, the buckling sites in the fibers and molecules are initially extended [202], and the buckling sites accumulate a portion of the energy produced due to the stress in the shape of elastic potential energy in a spring-like fashion. Afterwards, when the tensile force progressively grows, the fibers and the molecules slip with respect to one another, and the sliding among the fibers results in the energy continuing to dissipate. In the course of this, the slippage releases energy in a damper-like fashion and maintains a fairly slow rate of variation of the structure under stress [203,204]. The emergence of fiber rearrangement leads to the stress-strain characteristic of the tendon becoming nonlinear, which means that under lower stress, the fiber experiences a large degree of deformation [205–207]. The linear area in the mechanical curve is the action of elongating the fiber. Ultimately, the fiber is extended until it ruptures under loading.

2.1.6 Fiber Alignment Theory

Collagen fibers have been detected in the compartments of fibroblasts when monitoring chicken embryonic corneal cuts [208] and subsequently the same effect has been seen in chicken embryonic tendons [209]. Specifically, it seemed that microfibers are formed in the compartments and that the microfibers increase in density due to side-to-side fusion of the compartments into a dense bundle. Based on experimental findings in embryonic chicken and rat tail tendon, the theory of "fibripositor" has been formulated, that is, the fibers are sequestered into the extracellular matrix through the pores created by the merging of microtubule carriers for the microfiber trafficking and cell protrusion. The alignment of the fibers throughout this process is in accordance to the alignment of fibripositor [177]. The theory has been advanced by the idea that fibripositor are able to apply an inward pulling force on fibers and combine with tissue tension to reorganize the fibers [210]. A schematic model of the fibripositor has been provided in **Figure 6**. Mechanics has then been determined to have a major impact in the mechanism of aligned fiber generation via the development of a suggested model that accounts for the nature and mode of tendon growth during tensile loads [211]. In this regard, there is also an assumption that the generation of oriented fibers is related to the mechanism of collagen liquid crystal [212], which means that the collagen monomer in highly concentrated liquid solution self-composes into oriented fibers in some restricted environments. Nevertheless, the theory of liquid crystal orientation is not able to fully clarify the generation of mature fibers. Thus, the theory of fibripositor seems to be more suitable to provide an appropriate mechanism of fiber alignment, and the mechanical microenvironment may fulfill an additional task in the alignment process of the fibers.

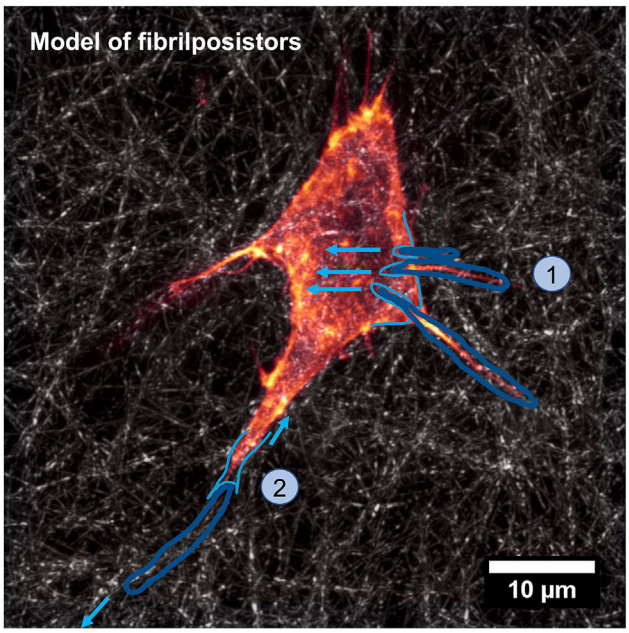

FIGURE 6 | Model of the fibripositor. A single fiber is stretched inward due to the tension of the fibripositor (step 1), which is drawn out of the fibripositor because of the tension of the extracellular environment (step 2).

2.1.7 Release of Cytokines or Chemokines

Infiltration of immune cells into solid cancers, their locomotion within the tumor microenvironment, and engagement with other immune cells are governed by their directional movement in the upward direction of chemokine gradients. Deregulated chemokine signal transduction pathways in the tumor microenvironment foster growth of cancers, efflux of effector immune cells, and plethora of immunosuppressive cells. Within physiological settings, the movement of cells within the organ is

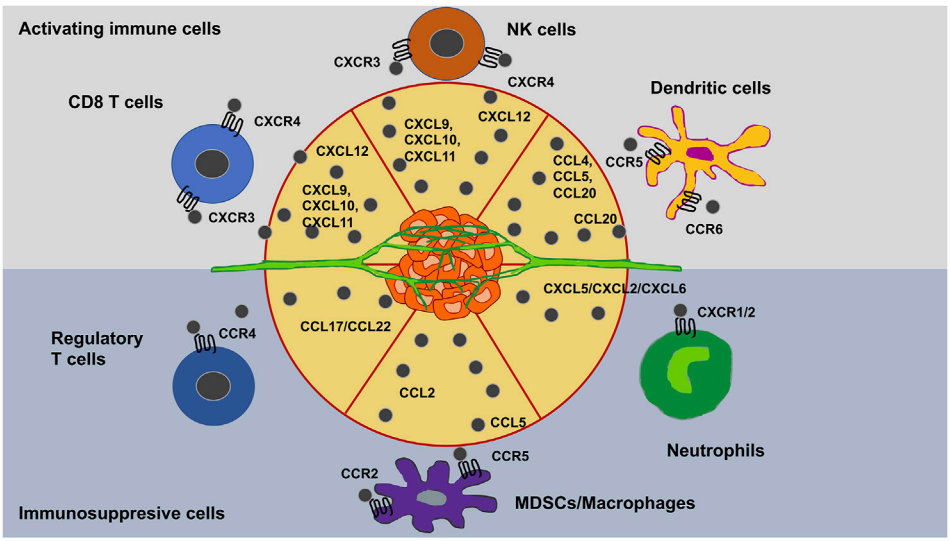

FIGURE 7 | Chemokines trigger the infiltration of immune cells in solid cancers microenvironments.

decisive and governing for the outcomes of the immune system [213,214]. Thus, the inter- and intraorganic locomotion of immune cells is directed through a set of secreted molecules known as chemokines. Immune cells which express the cognate chemokine receptor translocate in response to gradients of the respective cognate ligands in a signaling mechanism referred to as chemotaxis [215].

To date, 50 chemokine ligands and 20 chemokine receptors have been characterized, and all but six chemokine receptors are sensitive to more than one chemokine. Chemokines are classified into four principal classes, according to the position of the first two cysteine (C) residues in their protein sequence: specifically, CC, CXC, C, and CX3C chemokines. The majority of chemokine receptors are cross-membrane heterotrimeric G protein-coupled receptors [214]. Chemokine receptor binding initiates G-protein linkage and consequent activation of subsequent signaling proteins implicated in cell migration, including Rac, Rho, and Cdc42. The overall impact is a motion of the cells in the same direction as the chemotactic slope [214].

Influx of immune cells into the cancer microenvironment remains a pivotal determinant of cancer prognosis, and chemokines serve an integral purpose in guiding the directional migration of both activating and suppressive immune cell types [216–219]. Immune cell movement into cancer tissues is less foreseeable than homeostatic migration of immune cells into lymphoid organs since solid cancers are ectopic and heterogeneous and have no well-defined anatomy. Among even same-type cancers, immune cell migratory profiles differ with time and individual cases. Nevertheless, insight into the chemotactic milieu of solid cancers and recognition of chemokines that govern immune cell entrance into solid cancers is vital for enhancing contemporary immunotherapeutic therapies, encompassing immune checkpoint blockade (**Figure 7**).

Landmarks that govern this migratory response include soluble signals such as chemotaxis [220] and tethered chemo-attractants/repellents, such as haptotaxis [221]. Moreover, the latter is linked to the durotaxis response of the cells. Chemokines comprise chemotactic cytokines that direct the migration and placement of immune cells within tissues and are crucial for the proper functionality of the innate immune system. Moreover, they play a role in cancer disease, such as malignant progression of cancer. Deregulated chemokine signal transduction in the cancer microenvironment favors growth of cancers, efflux of effector immune cells, and plethora of immunosuppressive cells. Key chemokines that govern immune cell migration into cancer tissues have been pinpointed.

Various investigations have emphasized how chemotactic agent cues, and in specific chemokines, can function as the natural antagonists or act to trigger synergistic actions on selective receptors through the generation of heterocomplexes, thus affecting the migratory immune cell replies. Different chemokines may also mutually interfere with one another and display antagonistic or synergistic behavior at targeted chemokine receptors. They can simultaneously elicit distinct receptors, leading to either arrest or amplification of intracellular cell signals [222,223], or a single receptor can be engaged through a heterocomplex of two chemokines, leading to a more robust cellular answer [223,224]. A number of chemokines have been characterized to generate heterocomplexes both *in vitro* and *in vivo* under both inflammatory and regenerative circumstances (G. [223,225,226]), but little is yet appreciated about the existence and pertinence of heterocomplexes in the cancer microenvironment [227]. In this regard, chemokines may also mutually interfere with inflammatory substances liberated in the microenvironment, thus enhancing cellular reactions triggered by chemokine receptors [228,229]. It has been delineated that the alarmin high-mobility group box protein 1 (HMGB1), capable of massive liberation in the microsurroundings of the cancers, creates a complex with the chemokine CXCL12 that augments CXCR4-driven signal transduction, thereby adding to the modulation of the

activity of the chemokine network [230]. However, there is still an ongoing debate whether all *in vitro* heterocomplexes are relevant for *in vivo* situations.

3 EXTRACELLULAR MATRIX ACTS ON CELLS AND CELL CLUSTERS

In the past, the majority of cell culture assays has been performed in a simple 2D environment, where the cells or collections of cells were cultured on a flat surface treated for tissue culture. For this reason, the focus of this review is slightly shifted to the cellular side acting on their microenvironment. However, in more advanced approaches, the surface is modulated by several coatings with commonly employed extracellular matrix proteins, such as fibronectin, collagen, vitronectin or laminin. The motility of cells has been assessed employing these flat surfaces on which mainly the cell adhesion to the substrate is the rate-limiting factor of cell migration and a gradient either of the coating or in the culture liquid can determine the directionality of the movement. Thereby, 2D and 3D environments as well as the *in vitro* and *in vivo* cell migration situations need to be taken into account, since these data may point in opposite directions [231].

The architecture of tissues is based on the extracellular matrix that serves as its major contributor. The extracellular matrix assembles a 3D scaffold and is mostly secreted by nearby stromal cells, which contains a broad range of fibrous and non-fibrous elements. Additionally, the extracellular matrix stores non-structural elements, such as polysaccharides [232]. Consequently, multiple *in vitro* cell culture scaffolds that can imitate the characteristics of the extracellular matrix have been developed to examine tumor biology, such as various 3D cell culture models. Various implementations of 3D culture scaffolds have arisen incorporating prominent hydrogels [233,234], such as collagen [235–237] and Matrigel [238], non-adhesive surfaces [239,240] and artificial frameworks [241–244].

In principle, 3D culture systems are expected to more closely match the physiological extracellular milieu *in vivo* than conventional 2D cell culture systems. While these cell culture tools assist in resolving some key concerns, they may be coupled with multidisciplinary intricacies. For instance, the non-uniform largeness of spheroids accounts for the low repeatability of cell responsiveness to cytotoxic pharmaceuticals [245,246]. In addition, large spheroids do not have a vasculature in the center, so the potential inability to supply drug to the entire multicellular spheroid is likely to be an influential contributor to reduced chemosensitivity rather than cellular resistance to pharmaceuticals [247]. Cell culture requirements can cause the expression of certain genes to shift, which in turn results in altered cellular behaviors [248,249]. Consequently, to a certain degree, *in vitro* cell reactions do not actually reproduce the response of cancer cells *in situ*, but show cell behavior linked to the prevailing experimental circumstances [250–253]. Based on this finding, it is important to cautiously conceive the selected cell culture model in order to explore the specified hypotheses.

3.1 Benefits of 3D Extracellular Matrix Environments Over 2D Substrates

Since drug screenings have been less efficient, there is a need for new oncology drug candidates to be successfully identified for testing in clinical trials. The bad outcome of the predictive capacity of artificial monolayers based on 2D culture assays has contributed to a large amount to this urgent demand. Monolayer assays fail to consider the natural 3D microenvironment of the cells. Consequently, false positives frequently get into clinical investigations, resulting in high attrition rates and a huge amount of wasted time and resources. During the last two decades, a wide range of 3D *in vitro* cultivation instruments have been created by both tissue engineers and cell biologists to improve the depiction of cell biology *in vivo*. These instruments maintain the 3D architecture of the cells and can be leveraged to forecast the toxicity of and resistance to antitumor compounds. Advances in tissue engineering further enhance 3D cell models by incorporating the tumor microenvironment, which is essential for metastatic spread progression and the formation of blood vessels. Nevertheless, the pervasive adoption of 3D cell culture in cell-based drug discovery applications has been constrained by multiple factors, among which are their expense and replicability. Moreover, different 3D cell culture methods often yield spheroids of varying size and shape, which can greatly impact drug potency and toxicity. Therefore, it is essential to morphometrically classify multicellular spheroids to circumvent confounding assumptions between distinct spheroid types. Standardized 3D culturing techniques may decrease data variation even further and increase biological pertinence.

3.2 Structural Characteristics of the Matrix Environment: Composition, Such as Structural Elements and Storage of Non-structural Molecules

The components of the extracellular matrix combine to create a structurally robust compound and provide a key input to the mechanical characteristics of the tissue. The extracellular matrix is also a repository of growth factors and bioactive molecules. It is a very dynamic unit that is of crucial importance as it defines and monitors the most basic functions and properties of cells, including proliferation, adhesion, migration, invasion, polarity, differentiation, and apoptosis. The extracellular matrix environment can influence the migratory behavior of cells therein by altering the matrix composition and the storage of non-structural elements, such as growth factors, cytokines, chemokines, enzymes or matrix cross-linkers.

The extracellular matrix environment can be termed “core matrisome” [254] and includes more than 300 proteins. Among them are collagens, elastin, fibronectin, proteoglycans, and cell-binding glycoproteins, each of which possesses specific physical and biochemical characteristics. The two major components are presented briefly in the following.

Collagen is made of three polypeptide α chains that build a triple helical structure. In vertebrates, 46 different collagen chains combine to generate 28 collagen types [174,255] that can be

divided into fibril-forming collagens, such as types I, II, III, fibril-associated collagens with interruptions in their triple helices, or FACITs, such as types IX, XII, network-forming collagens, such as the basement membrane collagen type IV and others, including type VI. The fibril-associated collagens comprise uninterrupted triple-helix-forming domains accompanied by amino- and carboxyl-terminal non-collagenous domains. These non-collagenous domains undergo proteolytic excision, and the triple helices produced are laterally attached to produce fibrils. Non-fibrillar supramolecular structures, exemplified by the reticular nets of collagen IV in basement membranes and pearly filaments, are constituted by non-fibrillar collagens. FACITs are not self-assembling into fibrils, but are instead accompanied by collagen fibrils.

Proteoglycans are composed of a core protein with side chains of glycosaminoglycans appended to it. Glycosaminoglycans are linear, anionic polysaccharides consisting of repetitive disaccharide entities. Four groups of glycosaminoglycans exist, such as hyaluronic acid, keratan sulfate, chondroitin/dermatan sulfate, and heparan sulfate with the latter covering heparin. All are sulfated apart from hyaluronic acid. The highly negatively charged GAG chains enable proteoglycans to bind water and divalent cations, giving them room-filling and smearing properties. Secreted proteoglycans comprise large proteoglycans including aggrecan and versican, small leucine-rich proteoglycans such as decorin and lumican, and basement membrane proteoglycans like perlecan. Syndecans have a cell surface connection, whereas serglycine represents an intracellular proteoglycan.

Certain proline residues present in collagens are hydroxylated through prolyl 4-hydroxylase and prolyl 3-hydroxylase. LOX additionally hydroxylates certain selected lysine residues. After processing, the fibrillar procollagens are sequestered into the extracellular compartment, where their propeptides are excised. The evolved collagens subsequently combine to form fibrils through covalent cross-links established between the lysine residues of two collagen chains through a process catalyzed by LOX. The basic collagenous framework determines the architecture, shape, and organizational structure of tissues. Proteoglycans also are known to cross-talk with growth factors and growth factor receptors and are involved in cell signaling [256] and biological functions, including angiogenesis.

The aforementioned components of extracellular matrix networks are just major constituents that pronouncedly impact the mechanical characteristics and non-structural components of the matrix that both serve as signaling reservoir for cells and tissues. Considerable evidence points to the extracellular matrix as an essential niche for stem cells, as ordinary stem cells are reliant on signal transduction across extracellular matrix receptors including the laminin receptor, α6β1 integrin [257], the vitronectin receptor αVβ3 [258], and collagen receptors, such as α1β1, α2β1, α10β1 and α11β1 integrins [259] and new indications that the cancer-associated extracellular matrix is an integral feature of the cancer stem cell niche [260]. Thereby, apart from the composition of the extracellular matrix environment, the architecture and the mechanical cues play a crucial role in creating an environment that supports a niche for cancer stem cells. In specific detail, the structural parameters, such as pore-size, fiber-size, matrix-alignment, fiber length and fiber nodes affect the mechanical characteristics of the matrix scaffold, such as stiffness, viscosity and poroelasticity. Consequently, there are increased efforts to precisely characterize the structural elements of extracellular matrix environments [167,261–263].

3.3 Mechanical Constraints of the Environment

Most of the investigations on the reaction of cells to mechanical pacing, nevertheless, are performed on planar 2D substrates, which are unable to resemble the natural mechanical microsurroundings of 3D cells. There is growing body of evidence that cell performance in 2D and 3D microenvironments is markedly divergent. Within the group of materials employed for engineering the mechanical microenvironment of 3D cells, hydrogels have become progressively more relevant due to their tunable characteristics such as chemical and mechanical attributes.

The relevance of the mechanical constraint in cancer has in fact been emphasized through experiments that change the composition and rigidity of the extracellular matrix [264]. Tumor growth has also been demonstrated to be regulated through mechanical compression induced through the tumor on its own as it grows in a constrained space [265,266]. Pressure-induced patho-physiological outgrowth of this type has also been examined *in vitro*. The growth of multicellular aggregates is significantly diminished when they are entrapped within soft gels [267–269] or subjected to mild osmotic compression [270,271]. Evidence has been obtained that the cell cytoskeleton is engaged in the reaction to compression and can induce growth inhibition through cell cycle stoppage [269,272]. Moreover, it has recently been suggested that cell volume is a pivotal factor in the mechanosensitive response tract [272]. However, it is not clear how such modest global compression is imparted to the single cells of the assemblage to modify their proliferation.

In this case, the cells are assumed to respond primarily to the mechanical stress transmitted through the extracellular matrix when the aggregate is under pressure [273]. The hypothesis is based on two experimental findings. Firstly, an aggregate is a compound substance comprising cells, extracellular matrix, and interstitial liquid. The existence of hydrated extracellular matrix is attested through the richness of fibronectin within the interstitial cavity (**Figure 8**). Because the extracellular matrix is 100–1000 times capable of compaction relative to the cells, it accommodates the majority of the deformation, while still imparting the mechanical stress to the cells. Secondly, while an osmotic pressure of a few kPa severely diminishes cell proliferation inside multicellular assemblies, an equivalent pressure has no apparent impact on individual cells cultured on a Petri dish, in the complete absence of extracellular matrix [271]. Moreover, the utilization of pharmaceuticals that influence the architecture of the cytoskeleton exerts a marginal impact on the actual compressibility of multicellular assemblies. This characteristic pattern suggests that the volume loss under compression is primarily attributable to the dehydration of the extracellular matrix [273].

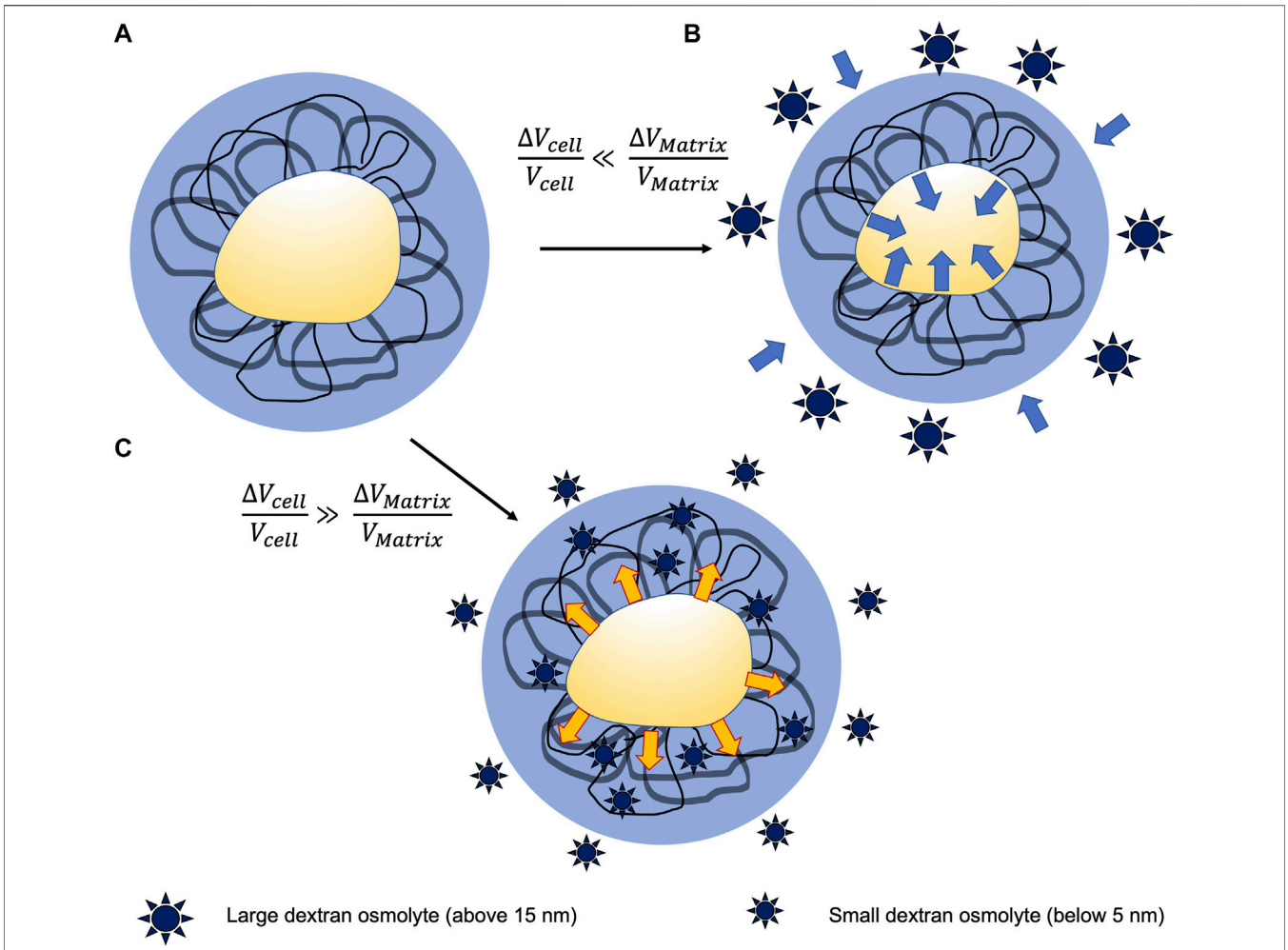

FIGURE 8 | Interplay between cell aggregates and their matrix surrounding modeled through a selective compression technique. **(A)** Schematic drawing of a cell surrounded by the extracellular matrix filaments and permeated through the interstitial liquid. **(B)** Large osmolytes cannot penetrate the extracellular matrix scaffold and thereby a bulk compression is imposed toward the cell. Since the extracellular matrix is more compressible compared to the incorporated cells, the extracellular matrix effectively soaks up the majority of the deformation and imposes a positive stress on the cell. **(C)** Small osmolytes can penetrate the extracellular matrix scaffold in the absence of any osmotic pressure. However, they compress the cell that, in turn, transmits tension toward the extracellular matrix scaffold.

The significance of the mechanical environment in cancer has long been emphasized through experiments that change the constitution and rigidity of the extracellular matrix [264]. Tumor growth has also been found to be regulated through mechanical compression imposed directly through the tumor by its own extension in a constrained setting [265,266]. Pressure-induced patho-physiological growth of this kind has also been examined *in vitro*. However, when multicellular assemblies are entrapped through soft gels [267–269] or undergo mild osmotic compression [271,273,274], their rate of growth is markedly diminished. The presence of the intracellular cytoskeleton has been implicated in the reaction to compression and has been demonstrated to elicit growth arrest due to cell cycle blockage [269,272]. Moreover, it has also been proposed lately that cell volume is a pivotal factor in the mechanosensory response [272,275]. However, it is not clear how such gentle overall compression is imparted to the individual cells of the assembly to modify their proliferation.

3.4 Extracellular Matrix Fiber Reassembly Encourages the Mechanosensing of Distant Cells

Cells perceive the intrinsic mechanical features of the extracellular matrix by exerting tensile forces. The capacity of cells to react to external forces, to sense and translate the mechanical nature of the extracellular matrix, and to both synthesize and restructure it, has an essential part to fill in multiple domains of cellular performance [276]. For instance, extracellular matrix stiffening in the course of advancing disease states, including cancer and fibrosis [277], signal reservoir of non-structural elements [278] or the ongoing cell and tissue aging [279] may have a detrimental effect on cell migration,

growth, differentiation and proliferation. In the alternative, abnormalities in intracellular signaling pathways that impair the capacity of cells to recognize and react to extracellular mechanical cues may also account for diseases such as cancer [277]. The capacity of cells to perceive and react to mechanical cues is referred to as mechanotransduction. Mechanotransduction involves sensing of external forces or biomechanical features and relaying this kind of input, which initiates a specified intracellular signaling answer. The cytoskeleton serves a vital purpose in mechanotransduction by connecting cellular compartments such as other cytoskeletal components and the nucleus to the force-sensing machinery [280].

The intricacy of the mechanical characteristics of the extracellular is placed in the focus and it is pointed out that cells sensing the mechanical characteristics of the matrix can in turn be impacted by them. While cells harbor multiple force sensors, including as the force sensitive channels TRPV4 and PIEZO1-2 [281,282] and intercellular adhesions [283], the focus of the current effort has been on mechanotransduction events at integrin-associated complexes. These link the extracellular matrix directly to the actin cytoskeleton and are key contributors to mechanotransduction. Thus, an important research focus is to investigate and discuss the functional role of protein dynamics of integrin-associated complexes in the context of their function in mechanosensing and signaling.

Elasticity has been seen to govern multiple cellular functions, such as the motility of various cells, cell growth, proliferation and differentiation [284,285]. Nevertheless, it is not merely the elastic characteristics that matter in stimulating modulation of cell performance, and in contrast to purely elastic polyacrylamide gels, tissues exhibit stress relaxation properties [286]. In fact, the proliferation of fibroblasts on soft surfaces is improved when the capacity to remodel the extracellular matrix is augmented by imposing stress relaxation in the subjacent surface or raising its viscous characteristics [287]. Moreover, hydrogels with greater or lower stress relaxation can control stem cell fate regardless of other known variables such as elasticity or ligand density [286]. The pairing of elasticity and viscous characteristics, or viscoelasticity, may be especially relevant to "in vivo-like" settings such as collagen nets, which exhibit significant viscous characteristics on time scales pertinent to cells [288].

It gets more complex when looking at the mechanical characteristics of extracellular matrix structures, because they offer more than just a stiffness coefficient: they have a tendency to rigidify when subjected to external forces [289]. This phenomenon is referred to as strain-stiffening of extracellular matrix networks that can also occur when cellular forces are applied, causing the entire network to become stiffer [4,290]. Stiffening by stretch can induce cells to gauge a stiffer ambient than would be expected due to initial polymerization constraints *in vitro*, and can establish a positive feedback circuit for achieving cellular force production [291]. Therefore, the final stiffness of the surrounding environment can be characterized as the aggregate of multiple determinants including the mechanics of the extracellular matrix meshwork, the cell density, and the capacity of these cells to react and apply tensile forces. In fact, cells that generate low traction, such as neuronal cells, rigidify the extracellular matrix meshwork through this stiffening mechanism considerably inferior to cells that produce high traction force potential, such as fibroblasts.

A major difference to 2D traction force analysis assays, such as those based on conventional polyacrylamide or PDMS substrates, and 3D traction force assays is that forces propagate further in the extracellular matrix scaffold. This characteristic feature of extracellular matrixes is highly similar to the *in vivo* situation, where the fibrous nature of the connective tissue microenvironment is present [292,293]. Subsequently, the distances over which cells can interact in a mechanical sense with each other are allowed to lengthen [294,295].

3.5 Classical Cancer Hallmarks Heavily Omit the Role of the Extracellular Matrix in Cell Migration

Since the first classic cancer features have been proposed over two decades ago [296] and more of them have been presented more than a decade ago [297], there is a new discussion about whether these features are still appropriate or need to be redefined. More challenging arguments have questioned not only the incorporation of specific characteristics, but also the question: what exactly is it that truly defines a cancer characteristic feature? The term cancer is commonly referred as a malignant tumor [298]. In this sense, a "hallmark" is a distinctive characteristic. However, it needs to be mentioned that five of the six initial hallmarks, but not the hallmark of invasion and metastasis are present in both benign and malignant neoplasms. Therefore it is difficult to distinguish benign from malignant cancers. It may be necessary to supplement that even invasion and spreading are characteristics of certain non-malignant diseases. An instance of this is endometriosis, a relatively frequent disease in women in which endometrial cells migrate to extraanatomical locations and infiltrate new tissue while retaining a benign histologic phenotype [299].

However, it can be argued that the purpose of hallmarks is to establish an organizational setting for cellular features that are exposed throughout the transformation (phenotypically) of normal cells - regardless of whether such transformation ends in a benign growth stage or further develops toward a more advanced and menacing malignancy. Thus, an evolutionary approach to mutation theory can be selected, wherein carcinogenesis represents a dynamic process that can begin (and end) within the lifespan of cells, with cancer characteristics becoming evident during this trajectory [300].

Criticism has also been leveled at the reductionist assumption of somatic mutation theory-the so-called bottom-up perspective on the examination of carcinogenesis that views cancer simply as a disease in which "genes are out-of control," whereas more organismic, systems- or tissue-disorganizing perspectives have been proposed [301–303]. It is evident that even the original hallmarks list includes tissue-relevant rather than cancer cell-specific moieties, such as angiogenesis [296] and the hallmarks II manuscript contains a part addressing the importance of the

tumor microenvironment [297]. Most recently, phenotypically normal cells have been demonstrated to have a high load of nonsilent somatic mutations that are positively targeted in the absence of cancer [304–306]. Consequently, the usefulness of hallmarks of cancer is under question. Additionally, the stromal element of cancers has been identified as an incidental catalyst [307,308] and imperative accessory [305] of the carcinogenic progression.

While the concept of hallmarks brings similarities, it is nevertheless critical to remember that cancer is not a uniform disease and that reliance on common pathways-and the implications of their use-vary across cancer types. For instance, vascularization is an essential hallmark of cancer, but several cancers are poorly vascularized and may rely somewhat less on one such hallmark [309]. Another instance is the tissue-specific usage of branched-chain amino acids in cancer cells that exhibit the identical driving mutation [310]. Consequently, cancer can be considered to be a multitude of diseases, each with a distinct agenda, utilizing features to varying degrees, and consequently demanding customized therapy.

4 CELL MECHANOPHENOTYPE

The migration of cells is fundamental to basic stages of development and adulthood, encompassing embryogenesis, wound healing, and inflammatory reactions [311]. The migratory capacity results broadly from the active momentum of its intracellular constituents-primarily the cytoskeleton-which produces propulsive forces and defines the anterior-posterior polarity of cells [1,312]. The spatiotemporal dynamics of the cytoskeleton are governed through intricate regulatory reticulations [313], and can be typified through both deterministic and stochastic moieties [314–316]. The temporal incorporation of these intricate intracellular dynamics dictates the large-scale characteristics of cell trajectories, which for their part can be employed as accessible metrics to deduce intracellular characteristics [317–319], as well as cell interactions with the surrounding area [320–322] or with adjacent cells [323,324]. Cells interoperate *in vivo* with various extracellular settings with a broad range of biochemical and biomechanical characteristics [1]. These exchanges have been demonstrated to be bidirectional: ambient stimuli directly impact cell form, migration, and polarity [325–327], and reciprocally, cells participate in active ways to reshape their surroundings [328,329]. However, to date, both pathways have been characterized separately, and the feedback of cell-induced reshaping of the environment on the large-scale attributes of cell migration has largely eluded investigation [330].

To surmount the intrinsic challenges of assaying cell migration in 3D conditions *in vivo*, the engineering of micropatterned surfaces has emerged as a high-performance strategy [331–333]. Within these types of *in vitro* settings, and especially in 1D settings, the decreased dimensionality of the cellular surroundings permits a comprehensive quantitative analysis of the phase space traversed by the traveling cells. Notably, while such 1D assays have unveiled noticeable deterministic characteristics in cell movement profiles, cell pathways in higher dimensions appear to remain arbitrary [315,323,328,334,335]. In addition, a lot of the characteristics of cell migration on a 1D substrate can imitate cell performance in a 3D matrix [328].

4.1 Single Cell Mechanophenotype

Components of the cytoskeleton are readily identified as epithelial-mesenchymal transition (EMT) biomarkers, especially intermediate filaments such as keratin (within epithelial cells) and vimentin (within mesenchymal cells) [336]. Hence, it seems to be likely that these dramatic cytoskeletal scaffold alterations affect the overall cell mechanophenotype of individual cells. It is still a question whether these structural alterations occur first or whether the mechanophenotype of the cells emerges first and secondarily cause the well-known cytoskeletal challenges of cells undergoing a EMT or MET. Intermediary phases may also occur and render this phenomenon even more intricate.

To bridge the gaps in cancer screening and surveillance, one exciting line of research is cellular mechanophenotyping. To persist and prosper, cancer cells face many challenges related to extrinsic forces from adjacent cells, the extracellular matrix, and the vasculature. The process of identifying and gaining an intimate knowledge of their mechanical response to these forces ultimately appears to be advancing the knowledge of cancer. Additionally, mechanophenotyping, alongside the conventional approaches of immunostaining and genetic mapping, has the potential to deliver a complete portrait of a heterogeneous cancer. In future applications and experiments, the focus needs to be on the advancement of techniques and the development of new technologies that provide single-cell mechanophenotyping. Single cell analysis is critical because mechanical cues from the surroundings can mask the intrinsic mechanical characteristics of a cell, which can vary in the course of time. Phenotypic heterogeneity and plasticity are both defining characteristics of cancer cells and continue to be a difficulty when examining bulk end point assessments [337]. EMT seems to take place as a rare event within a small subfraction of cells, which can be overseen when solely conducting bulk measurement. Instead, comprehensive single cell measurements need to be performed. New knowledge of molecular and cellular length scale dynamics can be gained through live cell imaging on the basis of high spatial and temporal resolution in the course of invasion and EMT [338]. In specific, cytoskeletal protrusions are especially essential for directional migration, and cells can noticeably reshape their ambient extracellular matrix [339]. Conversely, cells can experience considerable deformation to pass through the extracellular matrix, a process that can be eased through a pliable (more compliant) cytoskeleton. Moreover, it has been postulated that cancer cells are considerably softer than their non-transformed equivalents, especially in the setting of stem-like states expressing vimentin [340].

This leads to the hypothesis about the universality of both the usage of migratory phenotypes by cells and mechanophenotypes of cells. It seems to be a rather simple view on the migratory phenotype of cells, when hypothesizing

that all diverse cell types behave universal and hence exhibit the identical migratory phenotype with a specific and universal mechanophenotype. There are so many differences between the cell types or among the diverse differential stages of cells under physiological conditions that it seems to be not conclusive to state that they all acquire the exact same mechanophenotype when migrating through a dense extracellular matrix environment. Instead, it seems to be more accurate or intuitive to hypothesize that cells can adapt several diverse mechanophenotypes in order to migrate through their extracellular matrix tissue environment [2,341].

However, there is still debate on whether the aggressive cancer cells all employ the same mechanophenotype or whether they can adapt even a more elastic (stiffer cytoskeleton) to migrate and invade dense extracellular matrix confinements [236,341].

Finally, there is increased focus on the subcellular resolution of cell-matrix adhesions [342], and on collective responses conveyed through cell-cell connections [343]. Consequently, bulk studies conceal heterogeneity in the mechanistic characteristics of individual cells, particularly those infrequent subsets that aggressively result in cancer progression or resistance to treatment. The technologies on which the focus should be placed on encompass atomic force microscopy, hydrodynamic and optical stretching, suspended microchannel resonators, and mechano-node pore sensing [344].

Traditionally, EMT has been conceived as a multilayered regimen of phenotypic alterations that result in an epithelial cell gaining mesenchymal characteristics, incorporating changed polarity and cytoskeletal architecture [345]. EMT programs can be triggered through inflammatory cues, which include growth factors such as TGF-β, HGF, EGF, and WNT, hypoxia, and extracellular matrix components such as collagen I, which function via developmental transcription factors such as SNAIL, SLUG, TWIST, and ZEB1/2, as well as E2A proteins, E12/E47, to attenuate E-cadherin expression and trigger mesenchymal gene expression (**Figure 9**) [346]. Small, non-coding single-stranded RNAs (microRNAs or miRNAs) function collaboratively with transcription factors to modulate the facilitation or attenuation of EMT signaling pathway profiles in a sensitive, contextual fashion [346]. For example, the well-known miR-34 and miR-200 miRNA families serve dual functions as both tumor and EMT suppressors through establishment of double-negative feedback circuits with SNAIL and ZEB1/2, respectively [347]. EMT is capable of being excited to different degrees, resulting in a multifaceted array of intermediate stages referred to as partial EMT ([341,348,349,350,351]), and can be reverse-engaged through

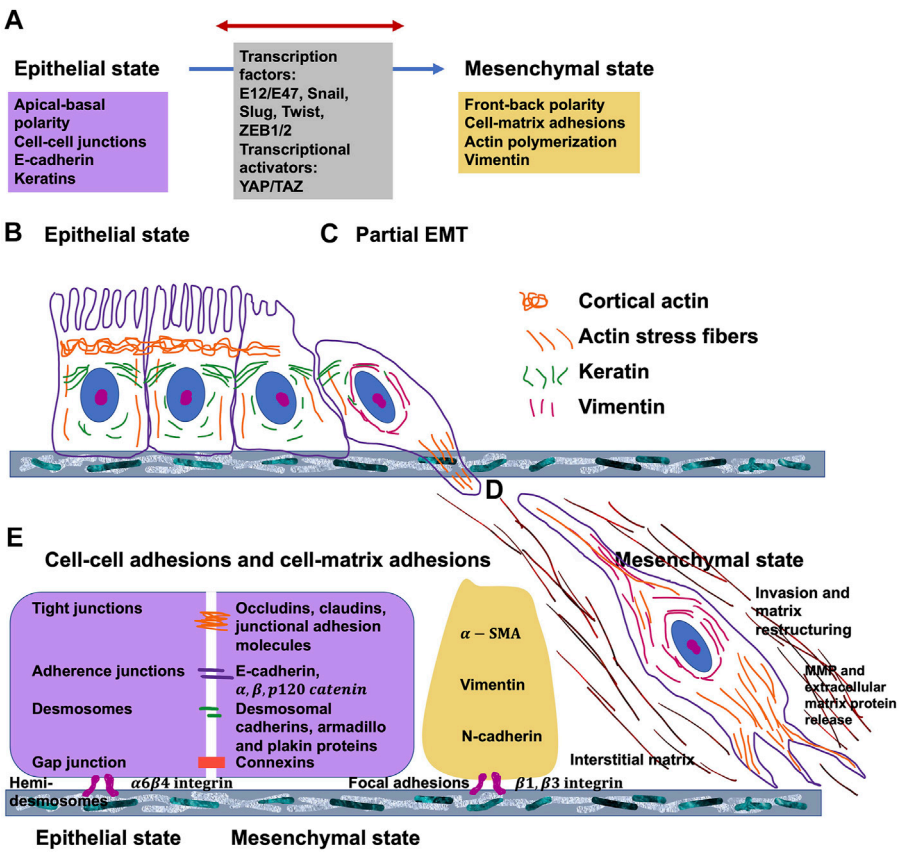

FIGURE 9 | Epithelial-to-mesenchymal (EMT) progression. **(A)** General characteristics of epithelial and mesenchymal phenotypes and transcription factors that govern EMT. Cell shape and cytoskeletal structure of **(B)** epithelial stage, **(C)** partial EMT stage and **(D)** mesenchymal stage. **(E)** Cell-cell and cell matrix adhesions.

mesenchymal-epithelial transitions (MET). Collectively, these dynamic events have been more widely characterized as so-called epithelial-mesenchymal plasticity [352].

4.2 Bulk Cell Mechanophenotype

Insight into the contribution of the mechanophenotype to the competitive attachment of cells to other cells or to subjacent carriers may provide insight into mechanisms such as tissue evolution, progression of cancer, and injury healing. The purpose of this investigation is to determine how the mechanophenotype, characterized by entire-cell elastic/viscoelastic characteristics for the perinuclear area, and the cellular organization are entangled through the mechanosensing mechanism [353].

The whole cell mechanophenotype impacts a number of crucial features, manifold of which encompass proliferation, differentiation, motility, shaping, and multicellular connectivity [354]. Thus, gaining an appreciation of how the mechanophenotype affects cell performance in terms of the local, mechanical microsurroundings, is crucial to governing and guiding an outcome of achieving successful cellular architecture in regenerating tissues. The capacity of cells to accumulate or expand singly relies not alone on cell type, extracellular matrix ligands, and substrate rigidity, yet more notably on the intrinsic mechanophenotype [63,355].

The cells retained a signature perinuclear, entire-cell mechanophenotype on all supports, irrespective of their stiffness and throughout all cluster forms and assemblies generated by the cells. Non-transfected WI-38 cells achieved a steady mechanical condition 1 day after out-plating and retained this mechanophenotype for the remaining 3 days of the experiment. Mechanically diverse GFP-, dnRhoA-, and β-actin-transfected cells also exhibited intrinsic entire-cell mechanical characteristics that largely seemed to be disconnected to the external microenvironment. Specifically, in the presence of a polyacrylamide (PAA) substrate, the findings of this investigation further imply that cells have the capacity to mechanosensitively grasp their surroundings and electively attach and propagate to any material, PAA substrate or adjacent cells, that is more rigid than their intrinsic mechanophenotype (atomic force microscopy with 5 μm bead). The most compliant cell type displayed the lowest quantity of nodulation across all three gels, indicating that it tends to prefer to attach to the more rigid substrate rather than soft, adjacent cells. Moreover, meaningfully larger nodule development for all cell types has been noted on 0.3 and 0.5 kPa PAA gels compared to 1.4 kPa gels, where cells could expand and evolve a more patterned actin cytoskeleton [353].

The intrinsic mechanophenotype of WI-38 cells differed throughout the initial adhesion to a substrate, although it maintained a broadly stable pattern over time. The various cellular assemblies in place also started to build during the first day, suggesting that the cells are able to respond rapidly to their surrounding microenvironment. Because the mechanical properties of WI-38 cells do not change with time, single time point comparisons between the transfected cell lines have been made. Mechanically diverse transfected WI-38 cell lines also retained their intrinsic entire-cell mechanophenotypes on carriers of different rigidity. These findings are corroborated by other investigations that have also noted a stable, intrinsic mechanophenotype regardless of alterations in the cellular microsurroundings. Embryonic stem cells did not enhance their apical cell rigidity on surfaces of varying rigidity, whereas basal tensile forces at the border of cell-substrate interactions on PAA gels are in the spectrum of 0.35–8 kPa [356].

Oligodendrocyte progenitor cells have been revealed to be more compliant compared to differentiated oligodendrocytes. Moreover, the stiffness of both progenitor and differentiated cells appeared to be unaffected by the elasticity of the PAA gel and varied between 0.1 and 70 kPa [357]. It is relevant to remark that alterations in cell survival, proliferation, migration and other biological determinants emerged which remained autonomous from the cellular mechanophenotype, underlining that this indicator is not merely a secondary marker of normal cellular function [357]. However, other investigations have proposed that the mechanophenotype is a pliable property that adapts to the elasticity of the surface to which the cell is adhered [356–360]. Nevertheless, these experimental designs vary markedly in the mechanical assay strategies employed, such as atomic force microscopy with sharp pyramidal apices over the cytoplasm/cytoskeleton instead of spherical beads over the perinuclear region, the range of PAA gel stiffness examined, encompassing 0.5–40 kPa, which are several times higher than the WI-38 mechanophenotype, and the cell type examined, such as fibroblasts vs glioma cells vs endothelial cells. The focus is placed on whole-cell characteristics to yield an average measurement of a cell's mechanical behavior, rather than nanometer-scale point measurements, which can differ widely according to what undergirding cellular constituent it is contacted. Gel elasticity has also been narrowly constrained to stiffnesses immediately above and below those of the cells, instead of involving elasticities orders of magnitude higher. In this way, the focus is on the competitive attachment of cells to a soft interface due to their elasticity [353].

4.3 BULK CELL SPHEROID PHENOTYPE

Macroscale tools like tissue surface tensiometry and micropipette aspiration technique are not be employed to reveal local variation of around cells within the center of the spheroid. Instead, they can only provide results from bulk measurement from the outside of the spheroid. Cavitation rheology seems to be a suitable biophysical technique to determine the elastic modulus of spheroids from the inside, since the technique relates the knowledge of bubble formation to the spheroid deformation [361,362]. In particular, a spheroid is soaked partly into a glass capillary, whereafter a micron-sized glass needle, which is accurately controlled by a micromanipulator, is placed within the spheroid. Injection of a cavitation agent (air or water) creates an elastic instability in the shape of a void by applying pressure slowly. The pressure-growth correlation for this forced spherical bubble is based on the spheroid's modulus of elasticity [207,363]. Specifically, matching the energy involved in bubble generation with the bond energies of the cell surface proteins yields an

approximation of the cortical tension of the cells comprising the spheroid [361]. Spheroids are retained in the culture medium throughout the measurements, which presents a technical difficulty as they can swim away from the needle upon insertion. Besides, the elastic modulus values obtained are of validity under the "thick-shell" regime alone, where the forced voids are sufficiently small so as not to interfere with the outer diameter of the spheroid.

The local tissue mechanical characteristics can be assessed through the usage of hydrogels that serve as mechanosensors [270,364]. In specific, mechanically precisely determined elastic polyacrylamide (PAA) microbeads act as internal cell-like sensors, which have been embedded inside the spheroids that are cultured under mechanical stress [364]. These beads are fluorescently labeled for tracking properties and functionalized for serving as an adhesive substrate for the cells that exhibits total elastic characteristics. An advantage of the PAA material is that it is inert and the cell can solely interact through the linkage of the ligand coated to the beads and the cell surface receptor. The local pressure within the spheroid can be determined by detecting the strain of the hydrogels, which is reflected in volume alterations. The bulk modulus of the bead can be revealed by osmotic compression before the experiment start employing higher weight dextran solution. At relatively small compressions, which are observed at low dextran concentrations, the stress/strain relationship is purely linear and the bulk modulus of the beads can be derived from the inclination of the curve. Aside the linear regime, the empirical polynomial Mooney-Rivlin model can be employed. Thereafter, the pressure pattern of the spheroid can be analyzed before and after the osmotic compression of the entire spheroid with randomly distributed microbeads. These PAA gels can be fine-tuned in mechanics through alteration of the ratio between acrylamide and bisacrylamide [365]. To overcome a foreign body reaction, the microbeads can be coated with elevated levels of extracellular matrix proteins [366]. An alternative technique are hydrogels that can be tuned by temperature, such as PNiPAAM beads. These beads stay in a compact state under tissue culture temperatures, but expand when they are chilled down a couple of degrees. They can be envisioned as springs that are prestressed through thermodynamic driving out of water prior to their installation in the tissue. Reducing the temperature relaxes this preload and places the beads back into a new steady-state volume determined on the basis of the stiffness of the ambient tissue. The volume variation pertains to the elasticity of the tissue after the creep process. These samples can be injected in *in vivo* mouse cancers without causing additional fibrosis or inflammation over a timespan of 3 weeks, which indicates that they possess a suitable biocompatibility [270]. The calibration of the PNiPAAM beads can be performed by the encapsulation in PAA gels with fine-tunable stiffness that display linear elastic characteristics. In specific, through the alteration of the radii of the beads after releasing the pre-strain, the mechanical characteristics can be obtained. Nevertheless, it needs to be pointed out that these hydrogel mechanosensors exhibit at least four specific limitations. Firstly, the analysis of the tissue bulk modulus or elasticity following creep miss a time-dependent part. Secondly, PNiPAAM can be dependent on local surrounding parameters, including pH, which may be not homogeneous within spheroids [367]. Thirdly, the change in temperature required to carry out the analysis may impact the stiffness of the tissue, however, it has been demonstrated that cellular stiffness is not severely altered in the range of 21°C and 37°C [368]. Fourthly, hydrogel sensors can have an impact on cellular functions, as they represent foreign objects and trigger a foreign body reaction [366,369]. However, the functionalization of the hydrogel surface with suitable extracellular matrix molecules can aid to circumvent this effect. A major advantage of these beads is that they can be utilized directly for *in situ* mechanical probing within spheroids and living tissues.

Another alternative biophysical technique to investigate spheroid mechanics are optical tweezers. They permit the analysis of mechanics at a subcellular length scale inside spheroids that have been embedded within an extracellular matrix scaffold. Optical tweezers have been broadly employed, such as in physics, in soft matter [370] and in biology, including biological physics [371]. Moreover, the optical tweezer technique has been coupled to nano- and microfluids. The technique utilizes a highly strongly focused laser beam to optically trap a refractive object (bead) in the focal point [372], which offers excellent resolution in positioning (±1 nm) of micron-sized beads and in non-contact analysis of forces (±50 fN) [373]. Optical tweezers have recently been employed to carry out active microrheology on migrating cells in the circumference of a spheroid enveloped in a collagen matrix [275]. The mechanical characteristics of the cytoplasm within the peripheral cells have been gauged through the incorporation of tiny latex beads into the gel, which have been subjected to endocytosis. The force-displacement curve obtained when pulling the beads with the optical tweezers reveals the cytoplasmic stiffness. Most importantly, the technique is insensitive to the mechanics of the actin cortex, which lies underneath the membrane and is a major contributor to cell surface tension. Moreover, the interior of a cell is inherently heterogeneous, thus requires carefulness in identifying which cellular moieties govern the reaction. Nonetheless, this technique provides the closest to insights into sub-cellular mechanics within cell spheroids.

5 MATRIX MECHANOPHENOTYPE

What about local inhomogeneities? What about non-linearity of mechanical properties of the extracellular matrix? What about the dynamic nature of the mechanophenotype? There exists large inhomogeneities in hydrogels based on biopolymers, such as collagen matrices [167]. These inhomogeneities rely mainly on the different sources of collagen and may subsequently be based on extraction techniques of collagen type I from tissues of different organisms.

Apart from the capability to restructure the extracellular matrix through proteolytic break-down, cancer cells can employ alternatively cellular force to mechanically remodulate the extracellular matrix environment, when these cells migrate

across barriers of tissue [325–327]. Although it has been revealed that the assembly of invadopodia and their activity can be governed through the rigidity of the extracellular matrix [328,329,331,332], it is currently unclear whether invadopodial structures assembled in concert with collagen fibers are imbued with matrix-deforming activity that imparts forces to the ambient extracellular matrix. Moreover, the mechanisms through which invasive cells orchestrate topological and mechanical inputs from the 3D extracellular matrix milieu with the organization and operation of invadopodia throughout matrix break-down and invasion are still mostly unclear. To elucidate this issue, the ultrastructural arrangement, dynamics, and mechanical features of invadopodia arising at the boundary layer between breast cancer cells and fibrillar type I collagen require assessment. Employing a combination of platinum replica electron microscopy, collagen type I fiber tracking and laser-based scission of collagen fibrils, there exists a protease-independent function for MT1-MMP in guiding the polymerization of actin and the generation of force at the leading edge of invadopodia [31]. These results strongly endorse a paradigm shift in invasion in which self-assembling force-generating proteolytic cell-matrix contacts encourage expansion of matrix pores to favor cancer cell invasion.

5.1 Perlecan

Perlecan constitutes a large multiplex multipurpose heparan sulfate proteoglycan abundant in vascularized tissues, however, it is also prevalent in low- and non-vascularized connective tissues including articular cartilage, intervertebral disc, meniscus, ligament, and in tendon in the form of a hybrid in which at least one of its heparan sulfate glycosaminoglycan chains is substituted with a chondroitin sulfate chain [374,375]. Smooth muscle cells (SMCs) produce a chondroitin sulfate/heparan sulfate hybrid version of perlecan, while keratinocytes in epithelial tissues produce a version comprising chondroitin sulfate, heparan sulfate, and keratan sulfate [376], and endothelial cells-perlecan has been found monosubstituted with heparan sulfate. Mast cells generate perlecan specimens with reduced molecular weight nuclear proteins [377] which appear to be caused through alternative splicing and/or protease scission in immunoglobulin-rich domain IV.

Perlecan acts to coordinate tropoelastin and aids in the assembly of elastic microfibrils into translamellar transverse bridges that, along with fibrillin and elastin, work to stabilize the extracellular matrix of the annulus fibrosus of the intervertebral disc. Pericellular perlecan interfaces with collagen VI and XI to delineate and solidify this matrix partition, which assumes a strategic location that facilitates two-way cell-matrix communication linking the cell to its broader extracellular matrix. Evidence from the extracellular matrix is transmitted through this pericellular matrix all the way down to the chondrocyte, so that it can sense and react to subsequent subtle alterations in the microenvironment in an effort to adjust tissue homeostasis. Therefore, perlecan has a crucial modulatory function in chondrocyte metabolism and differentiation. Perlecan functions as a carrier proteoglycan that transports low soluble lipid-modified proteins including the Wnt or Hedgehog family and aids in the formation of tissue morphogen gradients that propel tissue embryogenesis. Cell surface perlecan on endothelial cells or osteocytes serves as a flow detector within the blood [378] and lacunar duct fluid, supplying responses to smooth muscle cells that adjust vascular tone and blood pressure, and the regulation of bone turnover through osteocytes, illustrating the multiple functions of perlecan in load-bearing connective tissues [379]. Cell-assembled extracellular matrix frameworks composed of perlecan-elastin and perlecan-elastin-collagen type VI are both firm and compliant and account for the viscoelastic material characteristics of tension- and load-bearing connective tissues.

5.2 Heparansulfate Proteoglycan

Heparan sulfate/hyaluronan proteoglycans are engaged in numerous tasks spanning from the development and maintenance of microstructure to the organization of the extracellular matrix and basement membrane through attachment to matrix molecules including collagen IV, laminin and fibronectin [380,381]. In specific detail, heparan sulphate alters cell-cell interplay through serving as a co-receptor for various cell surface receptors and impacting cell-extracellular matrix interactions. In addition, heparan sulfate can promote the sequestration of several growth factors, chemokines, cytokines, morphogens, and enzymes that create a sheltered pool that, when liberated, can foster receptor-ligand signaling compounds to impart key regulatory actions in cellular events to sustain tissue homeostasis [382]. Structural alteration of heparan sulfate can result posttranslationally through the function of sulfotransferases, sulfatases, and heparanase. MMPs and other proteolytic enzymes, such as plasminogen, can change the core of heparan sulphate proteoglycans and hence, can govern heparan sulphate proteoglycan-dependent signal transduction processes [383,384]. They play a role in cancer progression [385].

6 HALLMARKS OF THE MECHANOPHENOTYPE TRANSITION

How solid tumors gain the capacity to metastasize at distant locations is not well comprehended. A driver of metastasis by the enemy microenvironment may be that it provokes the stress reactions itself, which leads to hypervariability of ordinary routines that govern cell migration, nutrient absorption, and the tissue organization [11]. The habit variability may impart survival benefits and permit flexibility to accommodate fairly major program adjustments under stress. Imagining a solid tumor as not just a haphazardly altering tumbling ball of cells, but as an evolving system that is subject to adaptation to survive in the body through kidnapping and merging of intrinsic diversity programs, gives rise to a different way of conceiving of what is behind complicated phenomena such as cancer metastasis. Several cellular processes could be susceptible to such selection and hypervariability induction under stress, though the focus is set on tissue organization, cell migration, and nutrient acquisition through macropinocytosis, that utilizes the cellular migration machinery [11].

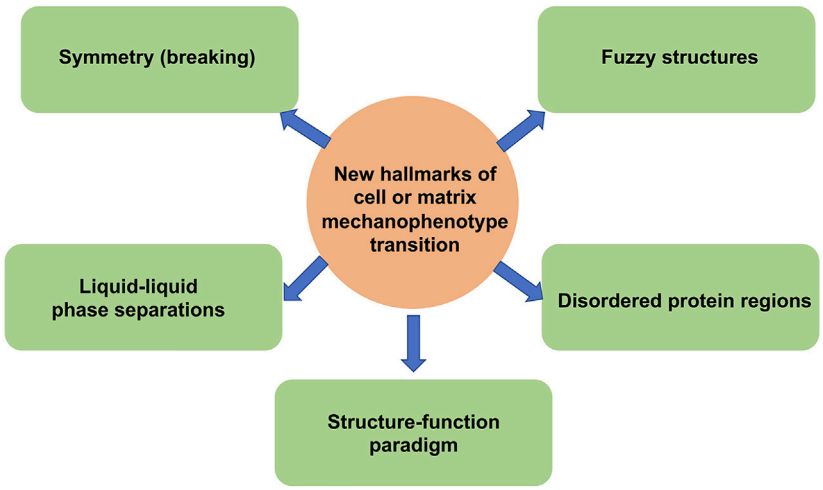

FIGURE 10 | New hallmarks of the mechanophenotype transition.

Cells can evade primary cancers in either an individual or a collective fashion. Single cells produce protrusions, regulate their adhesion, and exploit their actomyosin cytoskeleton to generate forces, propel themselves through physical restraints and traverse the extracellular matrix. Specifically, cells characteristically institute an anterior-posterior polarization through positive and negative loopback mechanisms that establish master sites of actin assembly, adhesion, or contractile force production. The Rho GTPase family of proteins has a key function in controlling single-cell migration through coordinating the activation and dynamics of a number of actin cytoskeleton-regulating proteins. While the regulatory nature of the interconnected webs is intricate, Rac1 is characteristically assumed to primarily regulate actin-based protrusions [52], RhoA primarily conveys actomyosin contractility and Cdc42 orchestrates the polarity of adhesion, contractility, and cell protrusion [386]. Cell polarity emerges from asymmetry in the allocation and arrangement of cell constituents (**Figure 10**). The polarity is an essential characteristic of all living organisms, and a lot of energy is spent on breaking the symmetry and creating the polarity. There are parallels between planar cell polarity and apical-basal polarity in epithelial tissues and face-back polarity in motile cells.

6.1 Phase Separation as a Hallmark

The route of signal transduction in the course of innate and adaptive immunity are critical for the defense of pathogen and especially in their identification and the overall functional roles of immune cells. Assemblies of higher order have evolved lately as a core operating mechanism that governs immune signaling and, consequently, cellular intercommunication in more general terms. Primarily, higher-order assemblies exist in two types: on the one hand, ordered, solid-like large supramolecular aggregates generated through stable and rigid protein-protein interactions, and on the other hand, liquid-like phase-separated condensates generated through softer and more dynamic intermolecular interactions (**Figure 10**) [387].

The structure and dynamics of a variety of higher-order assemblies, among them amyloids, several types of signalosomes, and intracellular granules. It has been hypothesized that the synergy between folded domains, linear motifs, and regions of intrinsic disorganization governs the creation and intrinsic uncertainty of all higher-order assemblies, generating a textural and dynamic continuum [387].

With the acquisition of the initial protein crystal patterns, the structure-function paradigm emerged, where a folded protein structure dictates the proper operation of a protein. Which has been recently further refined by the MeshCODE theory [388]. Growing evidence from different areas of structural biology revealed that protein function also emanates from their intrinsically disordered regions that do not exhibit a coherently well-defined conformation, extending the classical view of how structure dictates function [389,390]. Some sequences in intrinsically disordered regions are repeats and carry little content of information in comparison to folded proteins. Such domains are often termed low complexity domains [391]. Intrinsically disordered regions can wrinkle into a singular conformation when bound to another protein or during oligomerization to carry out their designated purpose. Alternatively, these can convolve into sets of structured conformations or stay extensively disordered and demonstrate a fast swapping of conformations even in the intricate regime, both of those have been termed fuzzy structures [392].

6.2 Fuzzy Structures as a Hallmark of Transition of Cellular Functions

In tandem with growing structural abundance, higher-order intricacies have arisen over a wide array of the biological scene, comprising amyloids and prions [393], several types of signaling complexes commonly referred to as signalosomes [394,395], and nuclear and cytoplasmic granules [396–398].

For instance, signalosomes possess elevated local concentrations of protein-binding sites, and thereby offer a high avidity for low-affinity ligands, which then foster the signal transduction processes [394]. Consequently, signalosomes have serially shifted the manner in which the entire field views cellular assembly and signal transduction in a collective manner [395,399].

Intracellular organelles consist of membrane-bound vesicles or membrane-free compositions made up of proteins and RNA. These organelles perform pivotal biological functions to compartmentalize the cell for spatial and temporal organization of biological actions. Emerging evidence indicates that membrane-free intracellular compartments are multiphase viscous fluid droplets that develop through phase separation. Proteins with an intrinsic propensity to be conformally heterogeneous tend to be the principal carriers of liquid-liquid phase separation inside the cell. These results illustrate the pertinence of traditional ideas from the physics of polymer phase transitions for gaining an in-depth insight into the structure of intracellular membrane-free compartments [399].

These complexes are distinct from the majority of conventional macromolecular complexes in that their constituent proteins frequently polymerize or interconnect, which leads to diverse stoichiometries and heterogeneous conformational features. There is a fundamental question to be answered: are there shared biophysical principles at stake in the various kinds of higher-order structures? Because insights from one type of structure can influence the functional mechanisms of the other, they were therefore surveyed jointly for mechanistic evidence. Folded domains, linear motifs, and intrinsically unordered domains have been found to be synergistic with one another in higher-order assemblies, creating integrally fuzzy structures. These complexes may share a common critical concentration for their assemblage, however, they display distinct structural and dynamic characteristics as a function of the basic underlying assembly machinery and regulatory regime (**Figure 10**).

6.3 Mechanics-Induced Invadopodia Formation

Live cell imaging revealed that Tks5GFP-positive invadopodia at the ventral cell surface appeared to be highly dynamic, with a mean lifespan of approximately 41 ± 1.7 min, and that they expanded alongside the subjacent collagen fiber at a speed of 0.15 ± 0.02 μm/min, forming characteristic arc-shaped or circular structures [31]. Temporal sequences revealed that invadopodia/collagen fiber assemblages homothetically elongate over time, with an overall mean radial speed of 0.16 ± 0.02 μm/min [31]. Supplementing this type of activity, in many cases there has been seen proteolytic breakage and pushback of the assembly of invadopodia and collagen fibers. The fiber relaxation analysis plotted as a function of time yielded a characteristic viscoelastic performance of the invadopodia/fiber complex that exhibits an initial speed of $V_0 = 3.1 \pm 0.22$ μm/min, typifying the relationship of stress to resistance of the fiber [400]. Collectively, these findings indicate a powerful rearrangement ability of collagenolytic invadopodia on the basis of MMP activity and demonstrate that collagen fibers affiliated with invadopodia maintain mechanical tension and bending moment that unwind during proteolytic breakage, revealing that cells at the level of invadopodia generate and transmit force toward the fibers.

7 MIGRATORY PHENOTYPE

Cell migration is a basic mechanism in multicellular organisms and is characterized by a concerted motion of individual or multiple cells in a certain direction and to a specific location. Embryo development, healing of wounds, and proper operation of the immune system all demand cell movement in multicellular organisms, underscoring their essential contribution to life. Routes fueling migratory activity can be switched on or off according to prevailing conditions, nevertheless adult epithelia, the source of numerous solid cancers or carcinomas, exhibit restricted migration and are prone to stick to adjacent cells in an organized fashion.

7.1 Single Cell Migration

Single cell migration is regulated through the Rho GTPase Rac1, which interfaces with the Scar/WAVE complex, leading to activation of Arp2/3 and exploding nucleation of ramified actin filaments [401]. As the earliest *de novo* actin nucleator to be detected, the Arp2/3 complex is a key actor within protrusive force production models through the dynamic actin meshwork. Actin nucleation centers agglomerate with receptors and associated signaling scaffold proteins owing to multivalent binding interactions, producing domains that are similar to phase separations [402,403]. Transmembrane receptors at the cell membrane surface frequently cluster at nanometer to micrometer scales to engage in signal transduction in reaction to environmental stimuli. Extracellular ligand oligomerization, domain-domain interferences, and binding to multivalent proteins are all factors conducive to cluster development. There are specific mechanisms that foster the assembly of clusters in several prominent receptor systems, encompassing glycosylated receptors, cell adhesion receptors, immune receptors, receptor tyrosine kinases and Wnt receptors. These clusters have been proposed to share characteristics of systems that perform a liquid-liquid phase separation and therefore can be analyzed in this regard (**Figure 10**) [402]. These clusters facilitate persistent local actin polymerization and can initiate crosstalk with other signaling molecules, permitting cells to outwardly extrude the plasma membrane and generate outgrowths including lamellipodia, filopodia, and invadopodia.

7.1.1 Phase Separation in the Cytoplasm

Biomolecular condensates congregate macromolecules in mounts lacking a circumferential membrane. Multiple multivalent exchanges occur in most condensates, leading to a phase separation of the liquid and the fluid. The liquid-liquid phase separation enhances the intrinsic activity of actin-regulatory proteins for the assembly of actin through the Arp2/3 complex. This elevation has been observed to occur due to the liquid-liquid

phase separation of the Nephrin-Nck-N-WASP signal transduction route on lipid bilayers. Thereby, the membrane dwell time of N-WASP and Arp2/3 complex is raised, which subsequently enhances the assembly of actin structures [403]. The residence time depends on the relative stoichiometry of the signaling proteins in the phase-separated clusters, resulting in stoichiometry-dependent N-WASP and Arp2/3 activity. This mechanism for governing protein activity is facilitated due to the stoichiometrically indeterminate character of the biomolecular condensates. Such control should be a common attribute of signaling schemes that are constituted via multivalent exchanges and yield non-equilibrium outcomes [403].

Biomolecular condensates are membrane-free cellular subcompartments that frequently arise from liquid-liquid phase partitioning fueled through intermolecular multivalent cross-talk. Phase separation of liquid from liquid has been identified in processes as divergent as gene regulation, autophagy, and signal transduction at membrane receptors. Precisely how the generation of biomolecular condensates governs these processes is not clear. Two recent investigations revealed that biomolecular 2D condensates of membrane-associated signaling compounds enhance the dwell time of signaling compounds within these complexes at the membrane, which is termed membrane dwell time, and thus control their activity ([403,404]).

Analysis of the local assembly of F-actin at membrane-associated biomolecular 2D condensates revealed that the generation of these condensates is based on specific interactions resembling those of the LAT-GRB2-SOS system, albeit with a different group of proteins participating, including phosphorylated nephrin (membrane receptor), NCK (adaptor protein), and N-WASP (NCK-interacting protein and activator of the actin nucleation factor Arp2/3 complex). Arp2/3-driven actin polymerization has been identified to be increased within condensates compared to levels outside of condensates, which has been inferred to be due to elevated N-WASP activity present within condensates. Resembling SOS, this upregulation of N-WASP activity actually directly covariates with enhanced membrane residence time of N-WASP (and also Arp2/3) inside the condensates. Significantly, the retention time of the N-WASP membrane responded sensitively to NCK concentration: as the NCK concentration increases, the residence time initially lengthened but subsequently declined beyond a saturation point. This saturation point presumably mirrors the depletion of phosphorylated sites on nephrin with consequent loss of multivalent connectivity, leaving N-WASP garnished with free NCK that is not linked to phospho-nephrin. Hence, the relative stoichiometry of the condensate constituents - through mutually influencing multivalent reactions inside the condensate - finely tunes their activity and regulates their dwell time within the signaling compounds. Since multivalent interactions and multistep reaction cascades are prevalent in signal transduction paths, these tenets of signal regulation through biomolecular condensates are probably universally valid. Subsequently, it can be concluded that the mechanophenotype of cells can be altered by phase-separation of cytoplasmic liquid components.

7.1.2 Phase Separation in the Nucleus

Besides the phase separation in the cytoskeleton, there exist a liquid-liquid phase separation in the nucleus [405]. In the majority of previous experimental setups, the nuclear-scale phase separation between chromatin and aqueous phase in the nucleus has not been accounted. Nevertheless, recent super-resolution microscopy indicates a pool of chromatin and aqueous phase with a non-uniform dispersion of chromatin at the submicron length scale [406]. In a different investigation, greater phase separation of chromatin and the aqueous phase has been noticed in early development, with chromatin situated at the nuclear periphery [407]. Theoretically, chromatin can be located near the lamina layer of the nuclear envelope, occupy the nucleus in a traditional fashion, be arranged in the center, or be available as wetting droplets. These transitions are governed through alterations in nuclear volume and the engagement of chromatin with the lamina, which is part of the nuclear envelope at the nuclear periphery. On the basis of a simple polymer model that encompasses the main characteristics of chromatin self-attraction and its attachment to the lamina, it can be theoretically demonstrated that the type of chromatin partitioning is governed by the rivalry of these two actions [408]. Chromatin is an intricate, linear macromolecule composed of DNA and histone proteins that is resident in the nucleus of eukaryotic cells, where it is dissolved by water, salts, and other small molecules [409]. In multiple investigations, the organization of chromatin in interphase cells appears to be homogeneous at nuclear length scale. According to this traditional view, the chromatin and its aqueous diluent fill the nucleus homogeneously as a single phase [410]. In fact, even the context of the conventional screen exhibits a phase separation resembling that of soluble AB-block copolymers [411], with areas of transcriptionally active euchromatin (A-block) divided from areas of relatively inactive heterochromatin (B-block), both of which are abundant in equal amounts.

7.2 Collective Cell Migration

Cells that form a tissue migrate as members of a collective. To coordinate collective multicellular navigation, each individual cell assimilates local input, incorporating chemical cues and mechanical stresses [264]. The border between a component cell and its immediate adjacent cells comprises cell-cell junctions and cryptic lamellipodia [412], however, the condition of local mechanical stress applied at this interface is not amenable to experimentation. It is therefore not evident how collective mechanical events can be orchestrated over length scales that encompass large multicellular assemblies. Within the cell layer, for instance, a cell monolayer, there are unpredictable fluctuations of the mechanical stress, which are strong, occur instantaneously and propagate across the monolayer. These fluctuations clearly delineate a fractured stress scene that grows more heterogeneous, inertial, and cohesive as the density of the whole system grows. Local cell migrations move alongside local alignments of the maximum principal stress inside this sustained fractured stress scene. Therefore, it can be postulated that collective migration is

guided through a straightforward but standardizing physiological rationale: neighboring cells converge to transfer a noticeable intercellular normal stress through local cell-cell junctions, while migrating down alignments with minimal intercellular shear stress.

High-throughput genomic approaches have pinpointed molecular actors and depicted their engagement in broad signaling pathways [413]. However, in spite of receiving in-depth signaling and structural insights, the role of intercellular adhesion in collective migration is controversial [414], and a lack of predictive power is inherent in what is known about collective cell migration, leaving it largely descriptive.

A major reason for these constraints is the lack of a physical picture linking cell movement to mechanical stresses occurring within the cell body and at cell-cell interfaces; these stresses have never been gauged. A high-resolution card of these stress constituents inside a moving monolayer has been presented, which acts as a basic experimental model scheme [415]. These stress patterns indicate that the regional cellular trajectory tracks local stress fields that are highly heterogeneous and interact drastically over ranges that span across multiple cell bodies. In combination, these results point to an unexpected but standardizing physiological principle, specifically, that every cell is prone to migrate and rearrange in a manner that minimizes local intercellular shear stress. In-depth familiarity with the biology of the cell-cell junction, the cryptic lamellipodium, or a particular molecular occurrence could certainly not ever anticipate such a standardizing principle, as it is an emergent characteristic of a multicellular collective framework. By comparison with the familiar single-cell guided mechanisms of chemotaxis, durotaxis, and haptotaxis, this disparate but inherently collective mechanism is termed plithotaxis [415].

Monolayer Stress Microscopy has been designed to quantify the local stress level inside a monolayer. Using an inverted optical microscope, it is possible to record the cell-generated shifts of fluorescent markers incorporated near the surface of a collagen-coated PAA gel support to that the cells adhere. Based on these dislocations, a chart of the tensile forces acting on the gel exerted by the monolayer is obtained [343]. Ultimately, on the basis of these tensile forces determined locally at the cell-substrate boundary, a simple equilibrium of forces, as required by Newton's laws, can be employed to evaluate the distribution of mechanical stresses throughout the cell layer. The slope of these stresses across the cell layer results from the accumulation of tensile forces acting on the undersurface of the cells. The recorded stresses in the single-layer film reflect the average values over the entire cell layer thickness. At any point within the patch, the local coordinate system can be flipped in the cell plane to locate the specific alignments along which the local normal stress is maximum and minimum, respectively, thereby delineating the two principal stress elements, such as maximum and minimum stress items, and the two corresponding principal alignments that are orthogonal to one another. Therefore, the accompanying monolayer stress microscopy output shows every single component of the stress tensor in the layer in high resolution and images them individually.

Since cells spread cryptic lamellipodia [412] and move forward across the monolayer, stresses need to be in mechanical equilibrium at all points and at all times. However, there is not yet a mechanistic setting or physical framework that ties these stresses to cellular reorientation, restructuring, or migration. In contrast, in the instance of an isolated single cell, uniaxial strain typically results in the cell realigning at a certain angle based on the amount of applied stress, ranging from parallel to vertical, based on the time scale of the mechanical perturbation. At this point, in the instance of monolayers, a question is to what extent intercellular tensions are biologically reasonable and beneficial for forecasting. The response to this question is implied from two pieces of experimental proof. Firstly, because phase contrast images and stress maps are unrelated measurements, the correspondence between the alignment of the cell body and the orientation of the maximum principal stress is remarkable. There are more tensile stress and zero shear stresses. Secondly, cells may not merely align themselves with the maximal principal orientation, however, they additionally move alongside that orientation. However, it seems to be not attributable to inhomogeneous stresses, since the stress field is more or less isotropic.

Cooperative movements arise in a natural way in inert particle systems that feature tight packing, structural disorganization, and glassy dynamics, such as colloidal glasses [416]. A key characteristic that identifies these schemes as glassy is the deceleration of internal structural reordering with increasing system density. As the system density grows, each participant is progressively enclosed by its surrounding particles, so that many adjacent particles need to be relocated in a cooperative manner in order to be capable of being relocated at all [417]. Therefore, the size of the cooperative system clusters grows as system density rises. In addition, the number of possible structural rearrangements diminishes with increasing cluster size, so that the time required for cooperative relocations jumps until the system ultimately gets effectively frozen or stalled [417]. Could the monolayer cell layer reveal such evidence of glassy dynamics? Even though a mechanistic relationship between particle-to-particle forces and spatially heterogeneous dynamical behavior in glassy systems continues to be ambiguous [418], the results are in line with the convergence towards a glass transition [415].

A pivotal question in morphogenesis and disease is of how distinct structures arise from uniform populations of cells [285]. Differentiation and pattering in multicellular systems is presently accounted for by the presence of morphogenetic gradients and through local variability in the constitution, topology, and rigidity of the extracellular matrix [419]. Moreover, the spontaneously generated, fractured stress landscape referred to here, when transmitted through the sensory scheme of the individual cell [420], is anticipated to induce uneven release of soluble or insoluble proteins, thereby changing the local cellular microenvironment, resulting in cytoskeletal reinforcement [421] or fluidization of the cytoskeleton [422], and activate stress-dependent genetic programs in a highly nonuniform fashion, yielding differentiated tissues.

8 CONCLUSION AND FUTURE DIRECTIONS

Although there have been many efforts to analyze mechanotransduction within cells, one was still at the beginning of understanding the entities complex play. Although cellular responses and their mechanophenotype are altered by changes in the mechanophenotype of their microenvironment, it has been found that the matrix mechanophenotype is also altered by the cells. This bidirectional response interaction has just begun to be incorporated into cell and tissue models and, in particular, the effects of cells on the mechanophenotype of extracellular matrices has been increasingly studied. In addition, the initial mechanical analyses were mostly time point dependent in a 2D microenvironment, which is now changing to studies in a 3D microenvironment and is a tremendous advantage. Similarly, time point measurements are rather outdated. In the future, the focus should be on dynamic analysis of mechanical properties, with the addition of another 4-dimensionality, time. Fluctuations in mechanophenotype can thus be translated, and changes in the amplitude of these fluctuations can also provide insights into the overall regulatory scheme. This includes a particular focus on phase transitions in the cytoplasm and nucleus. Moreover, thereby play also hydrogel-based 3D scaffolds a crucial role that can be easily and reproducibly mechanical probed by using chemical, natural or physical techniques. Moreover, the embedment of immune and stromal cells provides an additional crucial element to explore the effect of cell-derived factors, such as matrix-embedded by-stander cells or cells under investigation, such as cancer cells.

A recognized gap in scientific knowledge is the mechanism by which cells, such as non-tumorigenic epithelial cells and cancer cells, respond to and integrate acute mechanical stress. It should be noted that certain mechanical stresses can be more severe and dynamic than others. New biophysical techniques to examine the effects of mechanical stress in normal and malignant epithelial cells may yield new glimpses into the prospective contribution of fast mechano-chemical signaling, which has been shown to be effective in a number of different cell types.

To change the mechanophenotype in a precisely controlled manner, it seems necessary to alter the crosslinking efficiency, which affects multiple hydrogel characteristics, comprising pore size, rigidity, and sensitivity of the hydrogel to enzymatic break-down and matrix deposition. Specifically, more dedicated molecules implicated need to be identified that regulate the process of signal transduction from the outer extracellular matrix environment to the interior of the cell. Thereby, signaling directly or indirectly into the nucleus, where transcription of genes in affected in order to respond to the mechanical constraints evoked by the local surrounding microenvironment. Consequently, the cellular investigation levels need to be on different length scales, such as organoid, cellular, cytoskeletal and nuclear length scales including the alteration of gene transcription.

Frequently, architecture, mechanotransduction, and cellular performance are tightly coupled. The present difficulty is to discriminate the multiple target labels in the process of interplay between microenvironment and cellular functions. In this regard, it is still not clear, in part, how the current components generate and translate the physical force to alter cytoskeletal rearrangement and cellular functionalities. Another major challenge is the lack of available techniques to quantify the specific mechanical pressure in the course of perturbation of the mechanophenotype of the extracellular matrix environment. Moreover, knowledge of the fundamental mechanisms of the mechanical characteristics of the microenvironment contributes to advances in the treatment of injuries, malignancies, and diseases associated with alterations in the mechanophenotype of the extracellular matrix. A recently developed biophysical technique is a method that paves the way for monitoring both extracellular stiffness and dynamic mechanical stress by cladding cells on substrates of varying stiffness in conjunction with transient stretching of the substrate or "tugging" by magnetic manipulations [423].

Beyond the development of biophysical techniques, it needs to be clarified whether there exist universal hallmarks of the migratory behavior of cells that can be defined on the basis of the mechanophenotype. This appears to be the most complicated question to address and is likely to require the greatest future effort.

Another, less important, concern is that most synthetic hydrogel systems employed in this research discipline are nanoporous and lack the fibrillarity and ligand appearance of native extracellular matrices. Integrating collagen fibers into synthetic hydrogels [424,425], or employing synthetic approaches to engineer collagen-like fibers [426], has the potential to aid in overcoming this critical restriction. Integrating advancements in chemical synthesis pathways that enable a more explicit level of control over the constitution, structure, and accurate placement of functional moieties [427,428] may further help to overcome these concerns. In addition, RAFT or DNA origami [429] and noninvasive tailoring of characteristics in real time [430], with adaptive fabrication techniques that are capable of programming material constitution and architectural design over multiple length scales [431] are expected to afford new material frameworks for examining the effects of viscoelasticity and viscoplasticity in both *in vitro* and *in vivo* settings. Thereby, also theoretical models need to be addressed, modified and newly developed.

Finally, there are prosperous future directions that can be envisioned for the field of cell migration and invasion, when the microenvironment is taken into account. Overall, the utilization of spheroids has been identified as a feasible vehicle for the assessment of nanomedicines under circumstances that more accurately mirror the *in vivo* tumor microenvironment than conventional monolayer studies [240]. By customizing conventional cell-based assays, spheroids have the inherent capability to act as a middleman between conventional *in vitro* and *in vivo* testing models for high-throughput assessment of therapeutic contenders. These spheroids or organoids also allow the application of biophysical methods.

A future research avenue is that these interactions of extracellular matrix composition, influenced by target cells or neighboring cells, are implicated in the generation of supramolecular assemblies such as collagen fibrils and elastic fibers, in tissue architecture, and in cell-matrix interactions that in turn govern cell growth and behavior. Consequently, the emphasis is on interdisciplinary research, the development of new biophysical techniques, and the discovery of key principles of cellular constituents, the mechanoduction process and the directional interplay between cells and their microenvironment.

AUTHOR CONTRIBUTIONS

CTM designed and wrote the manuscript and prepared all figures.

ACKNOWLEDGMENTS

The author acknowledges support from the German Research Foundation (DFG) and Universität Leipzig within the program of Open Access Publishing, and Thomas M. L. Mierke for critical proof reading of the manuscript.

REFERENCES

1. Charras G, and Sahai E. Physical Influences of the Extracellular Environment on Cell Migration. *Nat Rev Mol Cel Biol* (2014) 15(12):813–24. doi:10.1038/nrm3897
2. Mierke CT. The Matrix Environmental and Cell Mechanical Properties Regulate Cell Migration and Contribute to the Invasive Phenotype of Cancer Cells. *Rep Prog Phys* (2019) 82(6):064602. doi:10.1088/1361-6633/ab1628
3. Mierke CT. The Fundamental Role of Mechanical Properties in the Progression of Cancer Disease and Inflammation. *Rep Prog Phys* (2014) 77(7):076602. doi:10.1088/0034-4885/77/7/076602
4. Mierke CT, Kollmannsberger P, Zitterbart DP, Diez G, Koch TM, Marg S, et al.Vinculin Facilitates Cell Invasion into Three-Dimensional Collagen Matrices. *J Biol Chem* (2010) 285(17):13121–30. doi:10.1074/jbc.M109.087171
5. Lämmermann T, and Sixt M. Mechanical Modes of 'amoeboid' Cell Migration. *Curr Opin Cel Biol* (2009) 21(5):636–44. doi:10.1016/j.ceb.2009.05.003
6. Reversat A, Gaertner F, Merrin J, Stopp J, Tasciyan S, Aguilera J, et al. Cellular Locomotion Using Environmental Topography. *Nature* (2020) 582(7813):582–5. doi:10.1038/s41586-020-2283-z
7. Lu D, and Kassab GS. Role of Shear Stress and Stretch in Vascular Mechanobiology. *J R Soc Interf* (2011) 8(63):1379–85. doi:10.1098/rsif.2011.0177
8. Barriga EH, Franze K, Charras G, and Mayor R. Tissue Stiffening Coordinates Morphogenesis by Triggering Collective Cell Migration *In Vivo*. *Nature* (2018) 554(7693):523–7. doi:10.1038/nature25742
9. Kim BG, Gao M-Q, Kang S, Choi YP, Lee JH, Kim JE, et al. Mechanical Compression Induces VEGFA Overexpression in Breast Cancer via DNMT3A-dependent miR-9 Downregulation. *Cell Death Dis* (2017) 8(3):e2646. doi:10.1038/cddis.2017.73
10. Chaudhuri O, Cooper-White J, Janmey PA, Mooney DJ, and Shenoy VB. Effects of Extracellular Matrix Viscoelasticity on Cellular Behaviour. *Nature* (2020) 584(7822):535–46. doi:10.1038/s41586-020-2612-2
11. Nikolaou S, and Machesky LM. The Stressful Tumour Environment Drives Plasticity of Cell Migration Programmes, Contributing to Metastasis. *J Pathol* (2020) 250(5):612–23. doi:10.1002/path.5395
12. JC Gerhart and J Norton, editors. *The Plausibility of Life: Resolving Darwin's Dilemma*. London, England: Yale University Press (2008).
13. Friedl P, and Wolf K. Proteolytic Interstitial Cell Migration: A Five-step Process. *Cancer Metastasis Rev* (2009) 28(1–2):129–35. doi:10.1007/s10555-008-9174-3
14. Pedersen NM, Wenzel EM, Wang L, Antoine S, Chavrier P, Stenmark H, et al. Protrudin-mediated ER-Endosome Contact Sites Promote MT1-MMP Exocytosis and Cell Invasion. *J Cel Biol* (2020) 219(8):e202003063. doi:10.1083/jcb.202003063
15. Naegeli KM, Hastie E, Garde A, Wang Z, Keeley DP, Gordon KL, et al. Cell Invasion *In Vivo* via Rapid Exocytosis of a Transient Lysosome-Derived Membrane Domain. *Develop Cel* (2017) 43(4):403–17.e10. doi:10.1016/j.devcel.2017.10.024
16. Castro-Castro A, Marchesin V, Monteiro P, Lodillinsky C, Rossé C, and Chavrier P. Cellular and Molecular Mechanisms of MT1-MMP-Dependent Cancer Cell Invasion. *Annu Rev Cel Dev. Biol.* (2016) 32(1):555–76. doi:10.1146/annurev-cellbio-111315-125227
17. Eddy RJ, Weidmann MD, Sharma VP, and Condeelis JS. Tumor Cell Invadopodia: Invasive Protrusions that Orchestrate Metastasis. *Trends Cel Biol* (2017) 27(8):595–607. doi:10.1016/j.tcb.2017.03.003
18. Linder S, Wiesner C, and Himmel M. Degrading Devices: Invadosomes in Proteolytic Cell Invasion. *Annu Rev Cel Dev. Biol.* (2011) 27(1):185–211. doi:10.1146/annurev-cellbio-092910-154216
19. Murphy DA, and Courtneidge SA. The 'ins' and 'outs' of Podosomes and Invadopodia: Characteristics, Formation and Function. *Nat Rev Mol Cel Biol* (2011) 12(7):413–26. doi:10.1038/nrm3141
20. Feinberg TY, Zheng H, Liu R, Wicha MS, Yu SM, and Weiss SJ. Divergent Matrix-Remodeling Strategies Distinguish Developmental from Neoplastic Mammary Epithelial Cell Invasion Programs. *Develop Cel* (2018) 47(2):145–60.e6. doi:10.1016/j.devcel.2018.08.025
21. Hotary K, Allen E, Punturieri A, Yana I, and Weiss SJ. Regulation of Cell Invasion and Morphogenesis in a Three-Dimensional Type I Collagen Matrix by Membrane-type Matrix Metalloproteinases 1, 2, and 3. *J Cel Biol* (2000) 149(6):1309–23. doi:10.1083/jcb.149.6.1309
22. Lodillinsky C, Infante E, Guichard A, Chaligné R, Fuhrmann L, Cyrta J, et al. P63/MT1-MMP axis Is Required for *In Situ* to Invasive Transition in Basal-like Breast Cancer. *Oncogene* (2016) 35(3):344–57. doi:10.1038/onc.2015.87
23. Sabeh F, Shimizu-Hirota R, and Weiss SJ. Protease-dependent versus -independent Cancer Cell Invasion Programs: Three-Dimensional Amoeboid Movement Revisited. *J Cel Biol* (2009) 185(1):11–9. doi:10.1083/jcb.200807195
24. Wolf K, Wu YI, Liu Y, Geiger J, Tam E, Overall C, et al. Multi-step Pericellular Proteolysis Controls the Transition from Individual to Collective Cancer Cell Invasion. *Nat Cel Biol* (2007) 9(8):893–904. doi:10.1038/ncb1616
25. Artym VV, Swatkoski S, Matsumoto K, Campbell CB, Petrie RJ, Dimitriadis EK, et al. Dense Fibrillar Collagen Is a Potent Inducer of Invadopodia via a Specific Signaling Network. *J Cel Biol* (2015) 208(3):331–50. doi:10.1083/jcb.201405099
26. Juin A, Billottet C, Moreau V, Destaing O, Albiges-Rizo C, Rosenbaum J, et al. Physiological Type I Collagen Organization Induces the Formation of a Novel Class of Linear Invadosomes. *Mol Biol Cel* (2012) 23(2):297–309. doi:10.1091/mbc.e11-07-0594
27. Parekh A, Ruppender NS, Branch KM, Sewell-Loftin MK, Lin J, Boyer PD, et al.Sensing and Modulation of Invadopodia across a Wide Range of Rigidities. *Biophysical J* (2011) 100(3):573–82. doi:10.1016/j.bpj.2010.12.3733
28. Wolf K, te Lindert M, Krause M, Alexander S, te Riet J, Willis AL, et al.Physical Limits of Cell Migration: Control by ECM Space and Nuclear Deformation and Tuning by Proteolysis and Traction Force. *J Cel Biol* (2013) 201(7):1069–84. doi:10.1083/jcb.201210152
29. Castagnino A, Castro-Castro A, Irondelle M, Guichard A, Lodillinsky C, Fuhrmann L, et al. Coronin 1C Promotes Triple-Negative Breast Cancer Invasiveness through Regulation of MT1-MMP Traffic and Invadopodia Function. *Oncogene* (2018) 37(50):6425–41. doi:10.1038/s41388-018-0422-x
30. Monteiro P, Rossé C, Castro-Castro A, Irondelle M, Lagoutte E, Paul-Gilloteaux P, et al. Endosomal WASH and Exocyst Complexes Control Exocytosis of MT1-MMP at Invadopodia. *J Cel Biol* (2013) 203(6):1063–79. doi:10.1083/jcb.201306162

31. Ferrari R, Martin G, Tagit O, Guichard A, Cambi A, Voituriez R, et al. MT1-MMP Directs Force-Producing Proteolytic Contacts that Drive Tumor Cell Invasion. *Nat Commun* (2019) 10(1):4886. doi:10.1038/s41467-019-12930-y
32. Petersen NO, McConnaughey WB, and Elson EL. Dependence of Locally Measured Cellular Deformability on Position on the Cell, Temperature, and Cytochalasin B. *Proc Natl Acad Sci* (1982) 79(17):5327–31. doi:10.1073/pnas.79.17.5327
33. Infante E, Castagnino A, Ferrari R, Monteiro P, Agüera-Gonza´lez S, Paul-Gilloteaux P, et al. LINC Complex-Lis1 Interplay Controls MT1-MMP Matrix Digest-On-Demand Response for Confined Tumor Cell Migration. *Nat Commun* (2018) 9(1):2443. doi:10.1038/s41467-018-04865-7
34. Abercrombie M, Heaysman JEM, and Pegrum SM. The Locomotion of Fibroblasts in Culture I. Movements of the Leading Edge. *Exp Cel Res* (1970) 59(3):393–8. doi:10.1016/0014-4827(70)90646-4
35. Abercrombie M, Heaysman JE, and Pegrum SM. The Locomotion of Fibroblasts in Culture. I. Movements of the Leading Edge. *Exp Cel Res* (1970) 59(2–3):393–8. doi:10.1016/0014-4827(70)90646-4
36. Abercrombie M, Joan E, Heaysman M, and Pegrum SM. The Locomotion of Fibroblasts in Culture. *Exp Cel Res* (1970) 60(3):437–44. doi:10.1016/0014-4827(70)90537-9
37. Liotta LA. Tumor Invasion and Metastases-Rrole of the Extracellular Matrix: Rhoads Memorial Award Lecture. *Cancer Res* (1986) 46(1):1–7.
38. Friedl P, and Wolf K. Plasticity of Cell Migration: A Multiscale Tuning Model. *J Cel Biol* (2010) 188(1):11–9. doi:10.1083/jcb.200909003
39. Page-McCaw A, Ewald AJ, and Werb Z. Matrix Metalloproteinases and the Regulation of Tissue Remodelling. *Nat Rev Mol Cel Biol* (2007) 8(3):221–33. doi:10.1038/nrm2125
40. Sato H, Takino T, and Miyamori H. Roles of Membrane-type Matrix Metalloproteinase-1 in Tumor Invasion and Metastasis. *Cancer Sci* (2005) 96(4):212–7. doi:10.1111/j.1349-7006.2005.00039.x
41. Humphrey JD, Dufresne ER, and Schwartz MA. Mechanotransduction and Extracellular Matrix Homeostasis. *Nat Rev Mol Cel Biol* (2014) 15(12):802–12. doi:10.1038/nrm3896
42. Vogel V. Unraveling the Mechanobiology of Extracellular Matrix. *Annu Rev Physiol* (2018) 80(1):353–87. doi:10.1146/annurev-physiol-021317-121312
43. Segel M, Neumann B, Hill MFE, Weber IP, Viscomi C, Zhao C, et al.Niche Stiffness Underlies the Ageing of central Nervous System Progenitor Cells. *Nature* (2019) 573(7772):130–4. doi:10.1038/s41586-019-1484-9
44. Paszek MJ, Zahir N, Johnson KR, Lakins JN, Rozenberg GI, Gefen A, et al.Tensional Homeostasis and the Malignant Phenotype. *Cancer Cell* (2005) 8(3):241–54. doi:10.1016/j.ccr.2005.08.010
45. Tanner K, Mori H, Mroue R, Bruni-Cardoso A, and Bissell MJ. Coherent Angular Motion in the Establishment of Multicellular Architecture of Glandular Tissues. *Proc Natl Acad Sci* (2012) 109(6):1973–8. doi:10.1073/pnas.1119578109
46. Meshel AS, Wei Q, Adelstein RS, and Sheetz MP. Basic Mechanism of Three-Dimensional Collagen Fibre Transport by Fibroblasts. *Nat Cel Biol* (2005) 7(2):157–64. doi:10.1038/ncb1216
47. Cukierman E. Taking Cell-Matrix Adhesions to the Third Dimension. *Science* (2001) 294(5547):1708–12. doi:10.1126/science.1064829
48. Maaser K, Wolf K, Klein CE, Niggemann B, Zänker KS, Bröcker E-B, et al. Functional Hierarchy of Simultaneously Expressed Adhesion Receptors: Integrin α2β1 but Not CD44 Mediates MV3 Melanoma Cell Migration and Matrix Reorganization within Three-Dimensional Hyaluronan-Containing Collagen Matrices. *Mol Biol Cel* (1999) 10(10):3067–79. doi:10.1091/mbc.10.10.3067
49. Friedl P. Prespecification and Plasticity: Shifting Mechanisms of Cell Migration. *Curr Opin Cel Biol* (2004) 16(1):14–23. doi:10.1016/j.ceb.2003.11.001
50. Grinnell F, Ho C-H, Tamariz E, Lee DJ, and Skuta G. Dendritic Fibroblasts in Three-Dimensional Collagen Matrices. *MBoC* (2003) 14(2):384–95. doi:10.1091/mbc.e02-08-0493
51. Friedl P, and Bröcker E-B. The Biology of Cell Locomotion within Three-Dimensional Extracellular Matrix. *Cell Mol Life Sci (Cmls)* (2000) 57(1):41–64. doi:10.1007/s000180050498
52. Kunschmann T, Puder S, Fischer T, Steffen A, Rottner K, and Mierke CT. The Small GTPase Rac1 Increases Cell Surface Stiffness and Enhances 3D Migration into Extracellular Matrices. *Sci Rep* (2019) 9(1):7675. doi:10.1038/s41598-019-43975-0
53. Giannone G, Dubin-Thaler BJ, Döbereiner H-G, Kieffer N, Bresnick AR, and Sheetz MP. Periodic Lamellipodial Contractions Correlate with Rearward Actin Waves. *Cell* (2004) 116(3):431–43. doi:10.1016/S0092-8674(04)00058-3
54. Mitchison TJ, and Cramer LP. Actin-Based Cell Motility and Cell Locomotion. *Cell* (1996) 84(3):371–9. doi:10.1016/S0092-8674(00)81281-7
55. Ridley AJ. Cell Migration: Integrating Signals from Front to Back. *Science* (2003) 302(5651):1704–9. doi:10.1126/science.1092053
56. Defilippi P, Olivo C, Venturino M, Dolce L, Silengo L, and Tarone G. Actin Cytoskeleton Organization in Response to Integrin-Mediated Adhesion. *Microsc Res Tech* (1999) 47(1):67–78. doi:10.1002/(SICI)1097-0029(19991001)47:1<67::AID-JEMT7>3.0.CO;2-P
57. Yoshigi M, Hoffman LM, Jensen CC, Yost HJ, and Beckerle MC. Mechanical Force Mobilizes Zyxin from Focal Adhesions to Actin Filaments and Regulates Cytoskeletal Reinforcement. *J Cel Biol* (2005) 171(2):209–15. doi:10.1083/jcb.200505018
58. Wang R, Wang Z, Millet L, Gillette MU, Levine AJ, and Popescu G. Dispersion-relation Phase Spectroscopy of Intracellular Transport. *Opt Express* (2011) 19(21):20571. doi:10.1364/OE.19.020571
59. Ghosh S, Kollar B, Nahar T, Suresh Babu S, Wojtowicz A, Sticht C, et al. Loss of the Mechanotransducer Zyxin Promotes a Synthetic Phenotype of Vascular Smooth Muscle Cells. *J Am Heart Assoc* (2015) 4(6):e001712. doi:10.1161/JAHA.114.001712
60. Hirata H, Tatsumi H, and Sokabe M. Zyxin Emerges as a Key Player in the Mechanotransduction at Cell Adhesive Structures. *Communicative Integr Biol* (2008) 1(2):192–5. doi:10.4161/cib.1.2.7001
61. Mierke CT, Fischer T, Puder S, Kunschmann T, Soetje B, and Ziegler WH. Focal Adhesion Kinase Activity Is Required for Actomyosin Contractility-Based Invasion of Cells into Dense 3D Matrices. *Sci Rep* (2017) 7(1):42780. doi:10.1038/srep42780
62. Jay PY, Pham PA, Wong SA, and Elson EL. A Mechanical Function of Myosin II in Cell Motility. *J Cel Sci* (1995) 108(Pt 1):387–93. doi:10.1242/jcs.108.1.387
63. Yeung T, Georges PC, Flanagan LA, Marg B, Ortiz M, Funaki M, et al. Effects of Substrate Stiffness on Cell Morphology, Cytoskeletal Structure, and Adhesion. *Cell Motil. Cytoskeleton* (2005) 60(1):24–34. doi:10.1002/cm.20041
64. Eastwood M, McGrouther D, and Brown R. A Culture Force Monitor for Measurement of Contraction Forces Generated in Human Dermal Fibroblast Cultures: Evidence for Cell-Matrix Mechanical Signalling. *Biochim Biophys Acta* (1994) 1201(2):186–92. doi:10.1016/0304-4165(94)90040-x
65. Lee GM, and Loeser RF. Cell Surface Receptors Transmit Sufficient Force to bend Collagen Fibrils. *Exp Cel Res* (1999) 248(1):294–305. doi:10.1006/excr.1999.4418
66. Golomb E, Ma X, Jana SS, Preston YA, Kawamoto S, Shoham NG, et al. Identification and Characterization of Nonmuscle Myosin II-C, a New Member of the Myosin II Family. *J Biol Chem* (2004) 279(4):2800–8. doi:10.1074/jbc.M309981200
67. Shohet RV, Conti MA, Kawamoto S, Preston YA, Brill DA, and Adelstein RS. Cloning of the cDNA Encoding the Myosin Heavy Chain of a Vertebrate Cellular Myosin. *Proc Natl Acad Sci* (1989) 86(20):7726–30. doi:10.1073/pnas.86.20.7726
68. Simons M, Wang M, McBride OW, Kawamoto S, Yamakawa K, Gdula D, et al. Human Nonmuscle Myosin Heavy Chains Are Encoded by Two Genes Located on Different Chromosomes. *Circ Res* (1991) 69(2):530–9. doi:10.1161/01.RES.69.2.530
69. Bresnick AR. Molecular Mechanisms of Nonmuscle Myosin-II Regulation. *Curr Opin Cel Biol* (1999) 11(1):26–33. doi:10.1016/s0955-0674(99)80004-0
70. Kovács M, Wang F, Hu A, Zhang Y, and Sellers JR. Functional Divergence of Human Cytoplasmic Myosin II. *J Biol Chem* (2003) 278(40):38132–40. doi:10.1074/jbc.M305453200
71. Wang F, Kovács M, Hu A, Limouze J, Harvey EV, and Sellers JR. Kinetic Mechanism of Non-muscle Myosin IIB. *J Biol Chem* (2003) 278(30):27439–48. doi:10.1074/jbc.M302510200
72. Tullio AN, Accili D, Ferrans VJ, Yu Z-X, Takeda K, Grinberg A, et al. Nonmuscle Myosin II-B Is Required for normal Development of the Mouse Heart. *Proc Natl Acad Sci* (1997) 94(23):12407–12. doi:10.1073/pnas.94.23.12407

73. Üren D, Hwang H-K, Hara Y, Takeda K, Kawamoto S, Tullio AN, et al. Gene Dosage Affects the Cardiac and Brain Phenotype in Nonmuscle Myosin II-B-Depleted Mice. *J Clin Invest* (2000) 105(5):663–71. doi:10.1172/JCI8199
74. Kuragano M, Murakami Y, and Takahashi M. Nonmuscle Myosin IIA and IIB Differentially Contribute to Intrinsic and Directed Migration of Human Embryonic Lung Fibroblasts. *Biochem Biophysical Res Commun* (2018) 498(1):25–31. doi:10.1016/j.bbrc.2018.02.171
75. Lee P, Lin R, Moon J, and Lee LP. Microfluidic Alignment of Collagen Fibers for *In Vitro* Cell Culture. *Biomed Microdevices* (2006) 8(1):35–41. doi:10.1007/s10544-006-6380-z
76. Olazabal IM, Caron E, May RC, Schilling K, Knecht DA, and Machesky LM. Rho-Kinase and Myosin-II Control Phagocytic Cup Formation during CR, but Not FcγR, Phagocytosis. *Curr Biol* (2002) 12(16):1413–8. doi:10.1016/S0960-9822(02)01069-2
77. Isik N, Brzostowski JA, and Jin T. An Elmo-like Protein Associated with Myosin II Restricts Spurious F-Actin Events to Coordinate Phagocytosis and Chemotaxis. *Develop Cel* (2008) 15(4):590–602. doi:10.1016/j.devcel.2008.08.006
78. Haviv L, Gillo D, Backouche F, and Bernheim-Groswasser A. A Cytoskeletal Demolition Worker: Myosin II Acts as an Actin Depolymerization Agent. *J Mol Biol* (2008) 375(2):325–30. doi:10.1016/j.jmb.2007.09.066
79. Humphrey D, Duggan C, Saha D, Smith D, and Käs J. Active Fluidization of Polymer Networks through Molecular Motors. *Nature* (2002) 416(6879):413–6. doi:10.1038/416413a
80. Arora PD, Conti MA, Ravid S, Sacks DB, Kapus A, Adelstein RS, et al. Rap1 Activation in Collagen Phagocytosis Is Dependent on Nonmuscle Myosin II-A. *MBoC* (2008) 19(12):5032–46. doi:10.1091/mbc.e08-04-0430
81. Arora PD, Wang Y, Janmey PA, Bresnick A, Yin HL, and McCulloch CA. Gelsolin and Non-muscle Myosin IIA Interact to Mediate Calcium-Regulated Collagen Phagocytosis. *J Biol Chem* (2011) 286(39):34184–98. doi:10.1074/jbc.M111.247783
82. Bos JL, de Bruyn K, Enserink J, Kuiperij B, Rangarajan S, Rehmann H, et al. The Role of Rap1 in Integrin-Mediated Cell Adhesion. *Biochem Soc Trans* (2003) 31(1):83–6. doi:10.1042/bst0310083
83. Fischer T, Wilharm N, Hayn A, and Mierke CT. Matrix and Cellular Mechanical Properties Are the Driving Factors for Facilitating Human Cancer Cell Motility into 3D Engineered Matrices. *Converg Sci Phys Oncol* (2017) 3(4):044003. doi:10.1088/2057-1739/aa8bbb
84. Wei Q, and Adelstein RS. Conditional Expression of a Truncated Fragment of Nonmuscle Myosin II-A Alters Cell Shape but Not Cytokinesis in HeLa Cells. *Mol Biol Cel* (2000) 11(10):3617–27. doi:10.1091/mbc.11.10.3617
85. Schiro JA, Chan BMC, Roswit WT, Kassner PD, Pentland AP, Hemler ME, et al. Integrin α2β1 (VLA-2) Mediates Reorganization and Contraction of Collagen Matrices by Human Cells. *Cell* (1991) 67(2):403–10. doi:10.1016/0092-8674(91)90191-Z
86. Nishizaka T, Shi Q, and Sheetz MP. Position-dependent Linkages of Fibronectin- Integrin-Cytoskeleton. *Proc Natl Acad Sci* (2000) 97(2):692–7. doi:10.1073/pnas.97.2.692
87. Kelley CA, Sellers JR, Gard DL, Bui D, Adelstein RS, and Baines IC. Xenopus Nonmuscle Myosin Heavy Chain Isoforms Have Different Subcellular Localizations and Enzymatic Activities. *J Cel Biol* (1996) 134(3):675–87. doi:10.1083/jcb.134.3.675
88. Kolega J. Asymmetric Distribution of Myosin IIB in Migrating Endothelial Cells Is Regulated by a Rho-dependent Kinase and Contributes to Tail Retraction. *Mol Biol Cel* (2003) 14(12):4745–57. doi:10.1091/mbc.e03-04-0205
89. Saitoh T, Takemura S, Ueda K, Hosoya H, Nagayama M, Haga H, et al. Differential Localization of Non-muscle Myosin II Isoforms and Phosphorylated Regulatory Light Chains in Human MRC-5 Fibroblasts. *FEBS Lett* (2001) 509(3):365–9. doi:10.1016/S0014-5793(01)03186-6
90. Brown ME, and Bridgman PC. Retrograde Flow Rate Is Increased in Growth Cones from Myosin IIB Knockout Mice. *J Cel Sci* (2003) 116(6):1087–94. doi:10.1242/jcs.00335
91. Lo C-M, Buxton DB, Chua GCH, Dembo M, Adelstein RS, and Wang Y-L. Nonmuscle Myosin IIB Is Involved in the Guidance of Fibroblast Migration. *Mol Biol Cel* (2004) 15(3):982–9. doi:10.1091/mbc.e03-06-0359
92. Dreymueller D, Pruessmeyer J, Groth E, and Ludwig A. The Role of ADAM-Mediated Shedding in Vascular Biology. *Eur J Cel Biol* (2012) 91(6–7):472–85. doi:10.1016/j.ejcb.2011.09.003
93. van der Vorst EPC, Jeurissen M, Wolfs IMJ, Keijbeck A, Theodorou K, Wijnands E, et al. Myeloid A Disintegrin and Metalloproteinase Domain 10 Deficiency Modulates Atherosclerotic Plaque Composition by Shifting the Balance from Inflammation toward Fibrosis. *Am J Pathol* (2015) 185(4):1145–55. doi:10.1016/j.ajpath.2014.11.028
94. Sun C, Wu MH, Lee ES, and Yuan SY. A Disintegrin and Metalloproteinase 15 Contributes to Atherosclerosis by Mediating Endothelial Barrier Dysfunction via Src Family Kinase Activity. *Arterioscler Thromb Vasc Biol* (2012) 32(10):2444–51. doi:10.1161/ATVBAHA.112.252205
95. Holdt LM, Thiery J, Breslow JL, and Teupser D. Increased ADAM17 mRNA Expression and Activity Is Associated with Atherosclerosis Resistance in LDL-Receptor Deficient Mice. *Arterioscler Thromb Vasc Biol* (2008) 28(6):1097–103. doi:10.1161/ATVBAHA.108.165654
96. Nicolaou A, Zhao Z, Northoff BH, Sass K, Herbst A, Kohlmaier A, et al. *Adam17* Deficiency Promotes Atherosclerosis by Enhanced TNFR2 Signaling in Mice. *Arterioscler Thromb Vasc Biol* (2017) 37(2):247–57. doi:10.1161/ATVBAHA.116.308682
97. Schlomann U, Rathke-Hartlieb S, Yamamoto S, Jockusch H, and Bartsch JW. Tumor Necrosis Factor α Induces a Metalloprotease-Disintegrin, ADAM8 (CD 156): Implications for Neuron-Glia Interactions during Neurodegeneration. *J Neurosci* (2000) 20(21):7964–71. doi:10.1523/JNEUROSCI.20-21-07964.2000
98. van der Vorst EPC, Keijbeck AA, de Winther MPJ, and Donners MMPC. A Disintegrin and Metalloproteases: Molecular Scissors in Angiogenesis, Inflammation and Atherosclerosis. *Atherosclerosis* (2012) 224(2):302–8. doi:10.1016/j.atherosclerosis.2012.04.023
99. Ainola M, Li T-F, Mandelin J, Hukkanen M, Choi SJ, Salo J, et al. Involvement of a Disintegrin and a Metalloproteinase 8 (ADAM8) in Osteoclastogenesis and Pathological Bone Destruction. *Ann Rheum Dis* (2009) 68(3):427–34. doi:10.1136/ard.2008.088260
100. Foley SC, Mogas AK, Olivenstein R, Fiset PO, Chakir J, Bourbeau J, et al.Increased Expression of ADAM33 and ADAM8 with Disease Progression in Asthma. *J Allergy Clin Immunol* (2007) 119(4):863–71. doi:10.1016/j.jaci.2006.12.665
101. Gossens K, Naus S, Holländer GA, and Ziltener HJ. Deficiency of the Metalloproteinase-Disintegrin ADAM8 Is Associated with Thymic Hyper-Cellularity. *PLoS ONE* (2010) 5(9):e12766. doi:10.1371/journal.pone.0012766
102. Johansson MW, Lye MH, Barthel SR, Duffy AK, Annis DS, and Mosher DF. Eosinophils Adhere to Vascular Cell Adhesion Molecule-1 via Podosomes. *Am J Respir Cel Mol Biol* (2004) 31(4):413–22. doi:10.1165/rcmb.2004-0099OC
103. Kelly K, Hutchinson G, Nebenius-Oosthuizen D, Smith AJH, Bartsch Jr. W, Horiuchi K, et al. Metalloprotease-disintegrin ADAM8: Expression Analysis and Targeted Deletion in Mice. *Dev Dyn* (2005) 232(1):221–31. doi:10.1002/dvdy.20221
104. Richens J, Fairclough L, Ghaemmaghami A, Mahdavi J, Shakib F, and Sewell H. The Detection of ADAM8 Protein on Cells of the Human Immune System and the Demonstration of its Expression on Peripheral Blood B Cells, Dendritic Cells and Monocyte Subsets. *Immunobiology* (2007) 212(1):29–38. doi:10.1016/j.imbio.2006.06.012
105. Oreo KM, Gibson PG, Simpson JL, Wood LG, McDonald VM, and Baines KJ. Sputum ADAM8 Expression Is Increased in Severe Asthma and COPD. *Clin Exp Allergy* (2014) 44(3):342–52. doi:10.1111/cea.12223
106. Valkovskaya N, Kayed H, Felix K, Hartmann D, Giese NA, Osinsky SP, et al. ADAM8 Expression Is Associated with Increased Invasiveness and Reduced Patient Survival in Pancreatic Cancer. *J Cell. Mol Med* (2007) 11(5):1162–74. doi:10.1111/j.1582-4934.2007.00082.x
107. Gifford V, and Itoh Y. MT1-MMP-dependent Cell Migration: Proteolytic and Non-proteolytic Mechanisms. *Biochem Soc Trans* (2019) 47(3):811–26. doi:10.1042/BST20180363
108. Nagase H, Visse R, and Murphy G. Structure and Function of Matrix Metalloproteinases and TIMPs. *Cardiovasc Res* (2006) 69(3):562–73. doi:10.1016/j.cardiores.2005.12.002
109. Itoh Y. Membrane-type Matrix Metalloproteinases: Their Functions and Regulations. *Matrix Biol* (2015) 44-46(46):207–23. doi:10.1016/j.matbio.2015.03.004
110. Pap T, Shigeyama Y, Kuchen S, Fernihough JK, Simmen B, Gay RE, et al. Differential Expression Pattern of Membrane-type Matrix Metalloproteinases

in Rheumatoid Arthritis. *Arthritis Rheum* (2000) 43(6):1226–32. doi:10.1002/1529-0131(200006)43:6<1226::AID-ANR5>3.0.CO;2-4
111. Ohkawara H, Ikeda K, Ogawa K, and Takeishi Y. Membrane Type 1-matrix Metalloproteinase (Mt1-mmp) Identified as a Multifunctional Regulator of Vascular Responses. *Fukushima J Med Sci* (2015) 61(2):91–100. doi:10.5387/fms.2015-15
112. Miller M-C, Manning HB, Jain A, Troeberg L, Dudhia J, Essex D, et al. Membrane Type 1 Matrix Metalloproteinase Is a Crucial Promoter of Synovial Invasion in Human Rheumatoid Arthritis. *Arthritis Rheum* (2009) 60(3):686–97. doi:10.1002/art.24331
113. Seiki M. Membrane-type 1 Matrix Metalloproteinase: A Key Enzyme for Tumor Invasion. *Cancer Lett* (2003) 194(1):1–11. doi:10.1016/S0304-3835(02)00699-7
114. Fortunati D, Chau DYS, Wang Z, Collighan RJ, and Griffin M. Cross-linking of Collagen I by Tissue Transglutaminase Provides a Promising Biomaterial for Promoting Bone Healing. *Amino Acids* (2014) 46(7):1751–61. doi:10.1007/s00726-014-1732-0
115. Mekhail M, Wong KKH, Padavan DT, Wu Y, O'Gorman DB, and Wan W. Genipin-Cross-linked Electrospun Collagen Fibers. *J Biomater Sci Polym Edition* (2011) 22(17):2241–59. doi:10.1163/092050610X538209
116. Olde Damink LHH, Dijkstra PJ, Van Luyn MJA, Van Wachem PB, Nieuwenhuis P, and Feijen J. Glutaraldehyde as a Crosslinking Agent for Collagen-Based Biomaterials. *J Mater Sci Mater Med* (1995) 6(8):460–72. doi:10.1007/BF00123371
117. Olde Damink LHH, Dijkstra PJ, van Luyn MJA, van Wachem PB, Nieuwenhuis P, and Feijen J. Cross-linking of Dermal Sheep Collagen Using a Water-Soluble Carbodiimide. *Biomaterials* (1996) 17(8):765–73. doi:10.1016/0142-9612(96)81413-X
118. Smith-Mungo LI, and Kagan HM. Lysyl Oxidase: Properties, Regulation and Multiple Functions in Biology. *Matrix Biol* (1998) 16(7):387–98. doi:10.1016/S0945-053X(98)90012-9
119. Mouw JK, Ou G, and Weaver VM. Extracellular Matrix Assembly: A Multiscale Deconstruction. *Nat Rev Mol Cel Biol* (2014) 15(12):771–85. doi:10.1038/nrm3902
120. Bax DV, Davidenko N, Gullberg D, Hamaia SW, Farndale RW, Best SM, et al. Fundamental Insight into the Effect of Carbodiimide Crosslinking on Cellular Recognition of Collagen-Based Scaffolds. *Acta Biomater* (2017) 49:218–34. doi:10.1016/j.actbio.2016.11.059
121. Takigawa T, and Endo Y. Effects of Glutaraldehyde Exposure on Human Health. *J Occup Health* (2006) 48(2):75–87. doi:10.1539/joh.48.75
122. Nair M, Best SM, and Cameron RE. Crosslinking Collagen Constructs: Achieving Cellular Selectivity through Modifications of Physical and Chemical Properties. *Appl Sci* (2020) 10(19):6911. doi:10.3390/app10196911
123. Schmidt CE, and Baier JM. Acellular Vascular Tissues: Natural Biomaterials for Tissue Repair and Tissue Engineering. *Biomaterials* (2000) 21(22):2215–31. doi:10.1016/S0142-9612(00)00148-4
124. Sheu M-T, Huang J-C, Yeh G-C, and Ho H-O. Characterization of Collagen Gel Solutions and Collagen Matrices for Cell Culture. *Biomaterials* (2001) 22(13):1713–9. doi:10.1016/S0142-9612(00)00315-X
125. Chen D-C, Lai Y-L, Lee S-Y, Hung S-L, and Chen H-L. Osteoblastic Response to Collagen Scaffolds Varied in Freezing Temperature and Glutaraldehyde Crosslinking. *J Biomed Mater Res* (2007) 80A(2):399–409. doi:10.1002/jbm.a.30932
126. Shepherd JH, Ghose S, Kew SJ, Moavenian A, Best SM, and Cameron RE. Effect of Fiber Crosslinking on Collagen-Fiber Reinforced Collagen-Chondroitin-6-Sulfate Materials for Regenerating Load-Bearing Soft Tissues. *J Biomed Mater Res* (2013) 101A(1):176–84. doi:10.1002/jbm.a.34317
127. Davidenko N, Schuster CF, Bax DV, Raynal N, Farndale RW, Best SM, et al. Control of Crosslinking for Tailoring Collagen-Based Scaffolds Stability and Mechanics. *Acta Biomater* (2015) 25:131–42. doi:10.1016/j.actbio.2015.07.034
128. Nair M, Calahorra Y, Kar-Narayan S, Best SM, and Cameron RE. Self-assembly of Collagen Bundles and Enhanced Piezoelectricity Induced by Chemical Crosslinking. *Nanoscale* (2019) 11(32):15120–30. doi:10.1039/C9NR04750F
129. Ahmad Z, Shepherd JH, Shepherd DV, Ghose S, Kew SJ, Cameron RE, et al. Effect of 1-Ethyl-3-(3-Dimethylaminopropyl) Carbodiimide and N-Hydroxysuccinimide Concentrations on the Mechanical and Biological Characteristics of Cross-Linked Collagen Fibres for Tendon Repair. *Regenerative Biomater* (2015) 2(2):77–85. doi:10.1093/rb/rbv005
130. Grover CN, Gwynne JH, Pugh N, Hamaia S, Farndale RW, Best SM, et al. Crosslinking and Composition Influence the Surface Properties, Mechanical Stiffness and Cell Reactivity of Collagen-Based Films. *Acta Biomater* (2012) 8(8):3080–90. doi:10.1016/j.actbio.2012.05.006
131. Haugh MG, Murphy CM, McKiernan RC, Altenbuchner C, and O'Brien FJ. Crosslinking and Mechanical Properties Significantly Influence Cell Attachment, Proliferation, and Migration within Collagen Glycosaminoglycan Scaffolds. *Tissue Eng A* (2011) 17(9–10):1201–8. doi:10.1089/ten.tea.2010.0590
132. Shepherd DV, Shepherd JH, Ghose S, Kew SJ, Cameron RE, and Best SM. The Process of EDC-NHS Cross-Linking of Reconstituted Collagen Fibres Increases Collagen Fibrillar Order and Alignment. *APL Mater* (2015) 3(1):014902. doi:10.1063/1.4900887
133. Madaghiele M, Calò E, Salvatore L, Bonfrate V, Pedone D, Frigione M, et al. Assessment of Collagen Crosslinking and Denaturation for the Design of Regenerative Scaffolds. *J Biomed Mater Res* (2016) 104(1):186–94. doi:10.1002/jbm.a.35554
134. Chen X, Zhou L, Xu H, Yamamoto M, Shinoda M, Kishimoto M, et al. Effect of the Application of a Dehydrothermal Treatment on the Structure and the Mechanical Properties of Collagen Film. *Materials* (2020) 13(2):377. doi:10.3390/ma13020377
135. Soller EC, Tzeranis DS, Miu K, So PTC, and Yannas IV. Common Features of Optimal Collagen Scaffolds that Disrupt Wound Contraction and Enhance Regeneration Both in Peripheral Nerves and in Skin. *Biomaterials* (2012) 33(19):4783–91. doi:10.1016/j.biomaterials.2012.03.068
136. Kato Y, Nishikawa T, and Kawakishi S. Formation of Protein-Bound 3,4-dihydroxyphenylalanine in Collagen Types I and IV Exposed to Ultraviolet Light. *Photochem Photobiol* (1995) 61(4):367–72. doi:10.1111/j.1751-1097.1995.tb08624.x
137. Sionkowska A. Modification of Collagen Films by Ultraviolet Irradiation. *Polym Degrad Stab* (2000) 68(2):147–51. doi:10.1016/S0141-3910(99)00176-7
138. Davidenko N, Bax DV, Schuster CF, Farndale RW, Hamaia SW, Best SM, et al. Optimisation of UV Irradiation as a Binding Site Conserving Method for Crosslinking Collagen-Based Scaffolds. *J Mater Sci Mater Med* (2016) 27(1):14. doi:10.1007/s10856-015-5627-8
139. Bax DV, Davidenko N, Hamaia SW, Farndale RW, Best SM, and Cameron RE. Impact of UV- and Carbodiimide-Based Crosslinking on the Integrin-Binding Properties of Collagen-Based Materials. *Acta Biomater* (2019) 100:280–91. doi:10.1016/j.actbio.2019.09.046
140. Riedel S, Hietschold P, Krömmelbein C, Kunschmann T, Konieczny R, Knolle W, et al. Design of Biomimetic Collagen Matrices by Reagent-free Electron Beam Induced Crosslinking: Structure-Property Relationships and Cellular Response. *Mater Des* (2019) 168:107606. doi:10.1016/j.matdes.2019.107606
141. Weadock K, Olson RM, and Silver FH. Evaluation of Collagen Crosslinking Techniques. *Biomater Med Devices, Artif Organs* (1983) 11(4):293–318. doi:10.3109/10731198309118815
142. Ruijgrok JM, de Wijn JR, and Boon ME. Glutaraldehyde Crosslinking of Collagen: Effects of Time, Temperature, Concentration and Presoaking as Measured by Shrinkage Temperature. *Clin Mater* (1994) 17(1):23–7. doi:10.1016/0267-6605(94)90044-2
143. Di Y, and Heath RJ. Collagen Stabilization and Modification Using a Polyepoxide, Triglycidyl Isocyanurate. *Polym Degrad Stab* (2009) 94(10):1684–92. doi:10.1016/j.polymdegradstab.2009.06.019
144. Reiser K, McCormick RJ, and Rucker RB. Enzymatic and Nonenzymatic Cross-linking of Collagen and Elastin. *FASEB j.* (1992) 6(7):2439–49. doi:10.1096/fasebj.6.7.1348714
145. E Reichmanis, CW Frank, and JH O'Donnell, editors. *Irradiation of Polymeric Materials: Processes, Mechanisms, and Applications*, Vol. 527. Washington, United States: American Chemical Society (1993). doi:10.1021/bk-1993-0527
146. Hennink WE, and van Nostrum CF. Novel Crosslinking Methods to Design Hydrogels. *Adv Drug Deliv Rev* (2012) 64:223–36. doi:10.1016/j.addr.2012.09.009

147. Riedel S, Bela K, Wisotzki EI, Suckfüll C, Zajadacz J, and Mayr SG. Reagent-free Mechanical Patterning of Gelatin Surfaces by Two-step Electron Irradiation Treatment. *Mater Des* (2018) 153:80–5. doi:10.1016/j.matdes.2018.04.076
148. Wisotzki EI, Friedrich RP, Weidt A, Alexiou C, Mayr SG, and Zink M. Cellular Response to Reagent-free Electron-Irradiated Gelatin Hydrogels. *Macromol Biosci* (2016) 16(6):914–24. doi:10.1002/mabi.201500408
149. Monaco G, Cholas R, Salvatore L, Madaghiele M, and Sannino A. Sterilization of Collagen Scaffolds Designed for Peripheral Nerve Regeneration: Effect on Microstructure, Degradation and Cellular Colonization. *Mater Sci Eng C* (2017) 71:335–44. doi:10.1016/j.msec.2016.10.030
150. Hara M. Various Cross-Linking Methods for Collagens: Merit and Demerit of Methods by Radiation. *Jpn Assoc Regenerative Dentistry* (2006). doi:10.11223/jarde.3.118
151. Vieira FF, and Del Mastro NL. Comparison of γ-radiation and Electron Beam Irradiation Effects on Gelatin. *Radiat Phys Chem* (2002) 63(3–6):331–2. doi:10.1016/S0969-806X(01)00522-9
152. Riedel S, Heyart B, Apel KS, and Mayr SG. Programing Stimuli-Responsiveness of Gelatin with Electron Beams: Basic Effects and Development of a Hydration-Controlled Biocompatible Demonstrator. *Sci Rep* (2017) 7(1):17436. doi:10.1038/s41598-017-17734-y
153. Manickam B, Sreedharan R, and Elumalai M. 'Genipin' - the Natural Water Soluble Cross-Linking Agent and its Importance in the Modified Drug Delivery Systems: An Overview. *Curr Drug Deliv* (2014) 11(1):139–45. doi:10.2174/15672018113106660059
154. Butler MF, Ng Y-F, and Pudney PDA. Mechanism and Kinetics of the Crosslinking Reaction between Biopolymers Containing Primary Amine Groups and Genipin. *J Polym Sci A Polym Chem* (2003) 41(24):3941–53. doi:10.1002/pola.10960
155. Tambe N, Di J, Zhang Z, Bernacki S, El-Shafei A, and King MW. Novel Genipin-Collagen Immobilization of Polylactic Acid (PLA) Fibers for Use as Tissue Engineering Scaffolds. *J Biomed Mater Res* (2015) 103(6):1188–97. doi:10.1002/jbm.b.33285
156. Sundararaghavan HG, Monteiro GA, Lapin NA, Chabal YJ, Miksan JR, and Shreiber DI. Genipin-induced Changes in Collagen Gels: Correlation of Mechanical Properties to Fluorescence. *J Biomed Mater Res* (2008) 87A(2):308–20. doi:10.1002/jbm.a.31715
157. Zhang X, Chen X, Yang T, Zhang N, Dong L, Ma S, et al. The Effects of Different Crossing-Linking Conditions of Genipin on Type I Collagen Scaffolds: An *In Vitro* Evaluation. *Cell Tissue Bank* (2014) 15(4):531–41. doi:10.1007/s10561-014-9423-3
158. Singh H, Racadio J, Brown M, and Hedman T. Six-Month Safety and Efficacy of Genipin Crosslinking Treatment for Chronic Low Back Pain. *Spine J* (2017) 17(10):S206. doi:10.1016/j.spinee.2017.08.069
159. Nair M, Johal RK, Hamaia SW, Best SM, and Cameron RE. Tunable Bioactivity and Mechanics of Collagen-Based Tissue Engineering Constructs: A Comparison of EDC-NHS, Genipin and TG2 Cross-linkers. *Biomaterials* (2020) 254:120109. doi:10.1016/j.biomaterials.2020.120109
160. Tirella A, Liberto T, and Ahluwalia A. Riboflavin and Collagen: New Crosslinking Methods to Tailor the Stiffness of Hydrogels. *Mater Lett* (2012) 74:58–61. doi:10.1016/j.matlet.2012.01.036
161. Cheema U, Rong Z, Kirresh O, MacRobert AJ, Vadgama P, and Brown RA. Oxygen Diffusion through Collagen Scaffolds at Defined Densities: Implications for Cell Survival in Tissue Models. *J Tissue Eng Regen Med* (2012) 6(1):77–84. doi:10.1002/term.402
162. Collin EC, Grad S, Zeugolis DI, Vinatier CS, Clouet JR, Guicheux JJ, et al. An Injectable Vehicle for Nucleus Pulposus Cell-Based Therapy. *Biomaterials* (2011) 32(11):2862–70. doi:10.1016/j.biomaterials.2011.01.018
163. Cosgriff-Hernandez E, Hahn MS, Russell B, Wilems T, Munoz-Pinto D, Browning MB, et al. Bioactive Hydrogels Based on Designer Collagens. *Acta Biomater* (2010) 6(10):3969–77. doi:10.1016/j.actbio.2010.05.002
164. Sarrigiannidis SO, Rey JM, Dobre O, González-García C, Dalby MJ, and Salmeron-Sanchez M. A Tough Act to Follow: Collagen Hydrogel Modifications to Improve Mechanical and Growth Factor Loading Capabilities. *Mater Today Bio* (2021) 10:100098. doi:10.1016/j.mtbio.2021.100098
165. Taguchi T, Xu L, Kobayashi H, Taniguchi A, Kataoka K, and Tanaka J. Encapsulation of Chondrocytes in Injectable Alkali-Treated Collagen Gels Prepared Using Poly(ethylene Glycol)-Based 4-armed star Polymer. *Biomaterials* (2005) 26(11):1247–52. doi:10.1016/j.biomaterials.2004.04.029
166. Ward J, Kelly J, Wang W, Zeugolis DI, and Pandit A. Amine Functionalization of Collagen Matrices with Multifunctional Polyethylene Glycol Systems. *Biomacromolecules* (2010) 11(11):3093–101. doi:10.1021/bm100898p
167. Hayn A, Fischer T, and Mierke CT. Inhomogeneities in 3D Collagen Matrices Impact Matrix Mechanics and Cancer Cell Migration. *Front Cel Dev. Biol.* (2020) 8:593879. doi:10.3389/fcell.2020.593879
168. Jansen KA, Licup AJ, Sharma A, Rens R, MacKintosh FC, and Koenderink GH. The Role of Network Architecture in Collagen Mechanics. *Biophysical J* (2018) 114(11):2665–78. doi:10.1016/j.bpj.2018.04.043
169. Chau DYS, Collighan RJ, Verderio EAM, Addy VL, and Griffin M. The Cellular Response to Transglutaminase-Cross-Linked Collagen. *Biomaterials* (2005) 26(33):6518–29. doi:10.1016/j.biomaterials.2005.04.017
170. Keillor JW, Clouthier CM, Apperley KYP, Akbar A, and Mulani A. Acyl Transfer Mechanisms of Tissue Transglutaminase. *Bioorg Chem* (2014) 57:186–97. doi:10.1016/j.bioorg.2014.06.003
171. Mäki JM. Lysyl Oxidases in Mammalian Development and Certain Pathological Conditions. *Histol Histopathol* (2009) 24:651–60. doi:10.14670/HH-24.651
172. Trackman PC. Enzymatic and Non-enzymatic Functions of the Lysyl Oxidase Family in Bone. *Matrix Biol* (2016) 52-54(54):7–18. doi:10.1016/j.matbio.2016.01.001
173. Gelse K. Collagens-structure, Function, and Biosynthesis. *Adv Drug Deliv Rev* (2003) 55(12):1531–46. doi:10.1016/j.addr.2003.08.002
174. Ricard-Blum S. The Collagen Family. *Cold Spring Harbor Perspect Biol* (2011) 3(1):a004978. doi:10.1101/cshperspect.a004978
175. Söderhäll C, Marenholz I, Kerscher T, Rüschendorf F, Esparza-Gordillo J, Worm M, et al. Variants in a Novel Epidermal Collagen Gene (COL29A1) Are Associated with Atopic Dermatitis. *Plos Biol* (2007) 5(9):e242. doi:10.1371/journal.pbio.0050242
176. Lin J, Shi Y, Men Y, Wang X, Ye J, and Zhang C. Mechanical Roles in Formation of Oriented Collagen Fibers. *Tissue Eng B: Rev* (2020) 26(2):116–28. doi:10.1089/ten.teb.2019.0243
177. Canty EG, Lu Y, Meadows RS, Shaw MK, Holmes DF, and Kadler KE. Coalignment of Plasma Membrane Channels and Protrusions (Fibripositors) Specifies the Parallelism of Tendon. *J Cel Biol* (2004) 165(4):553–63. doi:10.1083/jcb.200312071
178. Kadler KE, Holmes DF, Trotter JA, and Chapman JA. Collagen Fibril Formation. *Biochem J* (1996) 316(1):1–11. doi:10.1042/bj3160001
179. Noitup P, Morrissey MT, and Garnjanagoonchorn W. *In Vitro* self-assembly of Silver-Line Grunt Type I Collagen: Effects of Collagen Concentrations, pH and Temperatures on Collagen Self-Assembly. *J Food Biochem* (2006) 30(5):547–55. doi:10.1111/j.1745-4514.2006.00081.x
180. Wood GC, and Keech MK. The Formation of Fibrils from Collagen Solutions 1. The Effect of Experimental Conditions: Kinetic and Electron-Microscope Studies*. *Biochem J* (1960) 75(3):588–98. doi:10.1042/bj0750588
181. Yan M, Li B, Zhao X, and Qin S. Effect of Concentration, pH and Ionic Strength on the Kinetic Self-Assembly of Acid-Soluble Collagen from Walleye pollock (*Theragra chalcogramma*) Skin. *Food Hydrocolloids* (2012) 29(1):199–204. doi:10.1016/j.foodhyd.2012.02.014
182. Cisneros DA, Friedrichs J, Taubenberger A, Franz CM, and Muller DJ. Creating Ultrathin Nanoscopic Collagen Matrices for Biological and Biotechnological Applications. *Small* (2007) 3(6):956–63. doi:10.1002/smll.200600598
183. Hauschka SD, and Konigsberg IR. The Influence of Collagen on the Development of Muscle Clones. *Proc Natl Acad Sci* (1966) 55(1):119–26. doi:10.1073/pnas.55.1.119
184. Kleinman HK, Luckenbill-Edds L, Cannon FW, and Sephel GC. Use of Extracellular Matrix Components for Cell Culture. *Anal Biochem* (1987) 166(1):1–13. doi:10.1016/0003-2697(87)90538-0
185. Martin GR, and Kleinman HK. Extracellular Matrix Proteins Give New Life to Cell Culture. *Hepatology* (1981) 1(3):264–6. doi:10.1002/hep.1840010312
186. Mogilner A, and Oster G. Cell Motility Driven by Actin Polymerization. *Biophysical J* (1996) 71(6):3030–45. doi:10.1016/S0006-3495(96)79496-1
187. Vicker MG. F-actin Assembly in *Dictyostelium* Cell Locomotion and Shape Oscillations Propagates as a Self-Organized Reaction-Diffusion Wave. *FEBS Lett* (2002) 510(1–2):5–9. doi:10.1016/S0014-5793(01)03207-0

188. Vicker MG. Eukaryotic Cell Locomotion Depends on the Propagation of Self-Organized Reaction-Diffusion Waves and Oscillations of Actin Filament Assembly☆. *Exp Cel Res* (2002) 275(1):54–66. doi:10.1006/excr.2001.5466
189. Cowin SC. How Is a Tissue Built?1. *J Biomechanical Eng* (2000) 122(6):553–69. doi:10.1115/1.1324665
190. Cowin SC. Tissue Growth and Remodeling. *Annu Rev Biomed Eng* (2004) 6(1):77–107. doi:10.1146/annurev.bioeng.6.040803.140250
191. Silver FH, Freeman JW, and Seehra GP. Collagen Self-Assembly and the Development of Tendon Mechanical Properties. *J Biomech* (2003) 36(10):1529–53. doi:10.1016/S0021-9290(03)00135-0
192. Amiel D, Ishizue KK, Harwood FL, Kitabayashi L, and Akeson WH. Injury of the Anterior Cruciate Ligament: The Role of Collagenase in Ligament Degeneration. *J Orthop Res* (1989) 7(4):486–93. doi:10.1002/jor.1100070405
193. Elliott DH. Structure and Function of Mammalian Tendon. *Biol Rev* (1965) 40(3):392–421. doi:10.1111/j.1469-185X.1965.tb00808.x
194. Kjær M. Role of Extracellular Matrix in Adaptation of Tendon and Skeletal Muscle to Mechanical Loading. *Physiol Rev* (2004) 84(2):649–98. doi:10.1152/physrev.00031.2003
195. Mosesson MW, Siebenlist KR, and Meh DA. The Structure and Biological Features of Fibrinogen and Fibrin. *Ann N Y Acad Sci* (2006) 936(1):11–30. doi:10.1111/j.1749-6632.2001.tb03491.x
196. Welch MP, Odland GF, and Clark RA. Temporal Relationships of F-Actin Bundle Formation, Collagen and Fibronectin Matrix Assembly, and Fibronectin Receptor Expression to Wound Contraction. *J Cel Biol* (1990) 110(1):133–45. doi:10.1083/jcb.110.1.133
197. Leggett SE, Patel M, Valentin TM, Gamboa L, Khoo AS, Williams EK, et al. Mechanophenotyping of 3D Multicellular Clusters Using Displacement Arrays of Rendered Tractions. *Proc Natl Acad Sci USA* (2020) 117(11):5655–63. doi:10.1073/pnas.1918296117
198. Torbet J, Malbouyres M, Builles N, Justin V, Roulet M, Damour O, et al. Orthogonal Scaffold of Magnetically Aligned Collagen Lamellae for Corneal Stroma Reconstruction. *Biomaterials* (2007) 28(29):4268–76. doi:10.1016/j.biomaterials.2007.05.024
199. Yang S, Shi X, Li X, Wang J, Wang Y, and Luo Y. Oriented Collagen Fiber Membranes Formed through Counter-rotating Extrusion and Their Application in Tendon Regeneration. *Biomaterials* (2019) 207:61–75. doi:10.1016/j.biomaterials.2019.03.041
200. Chen J, Gao K, Liu S, Wang S, Elango J, Bao B, et al. Fish Collagen Surgical Compress Repairing Characteristics on Wound Healing Process *In Vivo*. *Mar Drugs* (2019) 17(1):33. doi:10.3390/md17010033
201. McCoy MG, Wei JM, Choi S, Goerger JP, Zipfel W, and Fischbach C. Collagen Fiber Orientation Regulates 3D Vascular Network Formation and Alignment. *ACS Biomater Sci Eng* (2018) 4(8):2967–76. doi:10.1021/acsbiomaterials.8b00384
202. Fratzl P, Misof K, Zizak I, Rapp G, Amenitsch H, and Bernstorff S. Fibrillar Structure and Mechanical Properties of Collagen. *J Struct Biol* (1998) 122(1–2):119–22. doi:10.1006/jsbi.1998.3966
203. Lidén M, Movin T, Ejerhed L, Papadogiannakis N, Blomén E, Hultenby K, et al. A Histological and Ultrastructural Evaluation of the Patellar Tendon 10 Years after Reharvesting its Central Third. *Am J Sports Med* (2008) 36(4):781–8. doi:10.1177/0363546507311092
204. Screen HRC, Berk DE, Kadler KE, Ramirez F, and Young MF. Tendon Functional Extracellular Matrix. *J Orthop Res* (2015) 33(6):793–9. doi:10.1002/jor.22818
205. Fang F, and Lake SP. Experimental Evaluation of Multiscale Tendon Mechanics. *J Orthop Res* (2017) 35(7):1353–65. doi:10.1002/jor.23488
206. Lake SP, Miller KS, Elliott DM, and Soslowsky LJ. Effect of Fiber Distribution and Realignment on the Nonlinear and Inhomogeneous Mechanical Properties of Human Supraspinatus Tendon under Longitudinal Tensile Loading. *J Orthop Res* (2009) 27(12):1596–602. doi:10.1002/jor.20938
207. Lake SP, Miller KS, Elliott DM, and Soslowsky LJ. Tensile Properties and Fiber Alignment of Human Supraspinatus Tendon in the Transverse Direction Demonstrate Inhomogeneity, Nonlinearity, and Regional Isotropy. *J Biomech* (2010) 43(4):727–32. doi:10.1016/j.jbiomech.2009.10.017
208. Birk DE, and Trelstad RL. Extracellular Compartments in Matrix Morphogenesis: Collagen Fibril, Bundle, and Lamellar Formation by Corneal Fibroblasts. *J Cel Biol* (1984) 99(6):2024–33. doi:10.1083/jcb.99.6.2024
209. Birk DE, and Trelstad RL. Extracellular Compartments in Tendon Morphogenesis: Collagen Fibril, Bundle, and Macroaggregate Formation. *J Cel Biol* (1986) 103(1):231–40. doi:10.1083/jcb.103.1.231
210. Kalson NS, Starborg T, Lu Y, Mironov A, Humphries SM, Holmes DF, et al. Nonmuscle Myosin II Powered Transport of Newly Formed Collagen Fibrils at the Plasma Membrane. *Proc Natl Acad Sci* (2013) 110(49):E4743–E4752. doi:10.1073/pnas.1314348110
211. Paten JA, Siadat SM, Susilo ME, Ismail EN, Stoner JL, Rothstein JP, et al. Flow-Induced Crystallization of Collagen: A Potentially Critical Mechanism in Early Tissue Formation. *ACS Nano* (2016) 10(5):5027–40. doi:10.1021/acsnano.5b07756
212. Giraud-Guille MM, Mosser G, and Belamie E. Liquid Crystallinity in Collagen Systems *In Vitro* and *In Vivo*. *Curr Opin Colloid Interf Sci* (2008) 13(4):303–13. doi:10.1016/j.cocis.2008.03.002
213. Griffith JW, Sokol CL, and Luster AD. Chemokines and Chemokine Receptors: Positioning Cells for Host Defense and Immunity. *Annu Rev Immunol* (2014) 32(1):659–702. doi:10.1146/annurev-immunol-032713-120145
214. Schulz O, Hammerschmidt SI, Moschovakis GL, and Förster R. Chemokines and Chemokine Receptors in Lymphoid Tissue Dynamics. *Annu Rev Immunol* (2016) 34(1):203–42. doi:10.1146/annurev-immunol-041015-055649
215. Kohli K, Pillarisetty VG, and Kim TS. Key Chemokines Direct Migration of Immune Cells in Solid Tumors. *Cancer Gene Ther* (2021). doi:10.1038/s41417-021-00303-x
216. Barnes TA, and Amir E. HYPE or HOPE: The Prognostic Value of Infiltrating Immune Cells in Cancer. *Br J Cancer* (2017) 117(4):451–60. doi:10.1038/bjc.2017.220
217. Burugu S, Asleh-Aburaya K, and Nielsen TO. Immune Infiltrates in the Breast Cancer Microenvironment: Detection, Characterization and Clinical Implication. *Breast Cancer* (2017) 24(1):3–15. doi:10.1007/s12282-016-0698-z
218. Di Caro G, Marchesi F, Laghi L, and Grizzi F. Immune Cells: Plastic Players along Colorectal Cancer Progression. *J Cel Mol. Med.* (2013) 17(9):1088–95. doi:10.1111/jcmm.12117
219. Ladányi A. Prognostic and Predictive Significance of Immune Cells Infiltrating Cutaneous Melanoma. *Pigment Cel Melanoma Res* (2015) 28(5):490–500. doi:10.1111/pcmr.12371
220. Roussos ET, Condeelis JS, and Patsialou A. Chemotaxis in Cancer. *Nat Rev Cancer* (2011) 11(8):573–87. doi:10.1038/nrc3078
221. Oudin MJ, and Weaver VM. Physical and Chemical Gradients in the Tumor Microenvironment Regulate Tumor Cell Invasion, Migration, and Metastasis. *Cold Spring Harb Symp Quant Biol* (2016) 81:189–205. doi:10.1101/sqb.2016.81.030817
222. De Buck M, Gouwy M, Berghmans N, Opdenakker G, Proost P, Struyf S, et al. COOH-terminal SAA1 Peptides Fail to Induce Chemokines but Synergize with CXCL8 and CCL3 to Recruit Leukocytes via FPR2. *Blood* (2017) 131:439–49. doi:10.1182/blood-2017-06-788554
223. Proudfoot AEI, and Uguccioni M. Modulation of Chemokine Responses: Synergy and Cooperativity. *Front Immunol* (2016) 7. doi:10.3389/fimmu.2016.00183
224. Gouwy M, Schiraldi M, Struyf S, Van Damme J, and Uguccioni M. Possible Mechanisms Involved in Chemokine Synergy fine Tuning the Inflammatory Response. *Immunol Lett* (2012) 145(1–2):10–4. doi:10.1016/j.imlet.2012.04.005
225. Lee G, Espirito Santo AI, Zwingenberger S, Cai L, Vogl T, Feldmann M, et al. Fully Reduced HMGB1 Accelerates the Regeneration of Multiple Tissues by Transitioning Stem Cells to GAlert. *Proc Natl Acad Sci USA* (2018) 115(19):E4463–E4472. doi:10.1073/pnas.1802893115
226. Tirone M, Tran NL, Ceriotti C, Gorzanelli A, Canepari M, Bottinelli R, et al. High Mobility Group Box 1 Orchestrates Tissue Regeneration via CXCR4. *J Exp Med* (2018) 215(1):303–18. doi:10.1084/jem.20160217
227. Venetz D, Ponzoni M, Schiraldi M, Ferreri AJM, Bertoni F, Doglioni C, et al. Perivascular Expression of CXCL9 and CXCL12 in Primary central Nervous System Lymphoma: T-Cell Infiltration and Positioning of Malignant B Cells. *Int J Cancer* (2010) 127(10):2300–12. doi:10.1002/ijc.25236

228. Cecchinato V, D'Agostino G, Raeli L, and Uguccioni M. Chemokine Interaction with Synergy-Inducing Molecules: Fine Tuning Modulation of Cell Trafficking. *J Leukoc Biol* (2016) 99(6):851–5. doi:10.1189/jlb.1MR1015-457R
229. Schiraldi M, Raucci A, Muñoz LM, Livoti E, Celona B, Venereau E, et al. HMGB1 Promotes Recruitment of Inflammatory Cells to Damaged Tissues by Forming a Complex with CXCL12 and Signaling via CXCR4. *J Exp Med* (2012) 209(3):551–63. doi:10.1084/jem.20111739
230. D'Agostino G, Cecchinato V, and Uguccioni M. Chemokine Heterocomplexes and Cancer: A Novel Chapter to Be Written in Tumor Immunity. *Front Immunol* (2018) 9:2185. doi:10.3389/fimmu.2018.02185
231. Mierke CT, Zitterbart DP, Kollmannsberger P, Raupach C, Schlötzer-Schrehardt U, Goecke TW, et al. Breakdown of the Endothelial Barrier Function in Tumor Cell Transmigration. *Biophysical J* (2008) 94(7):2832–46. doi:10.1529/biophysj.107.113613
232. Sarwar M, and Evans JJ. Bioimprinting: Bringing Together 2D and 3D in Dissecting Cancer Biology. *BioTechniques* (2021). doi:10.2144/btn-2021-0058
233. Dhandayuthapani B, Yoshida Y, Maekawa T, and Kumar DS. Polymeric Scaffolds in Tissue Engineering Application: A Review. *Int J Polym Sci* (2011) 2011:1–19. doi:10.1155/2011/290602
234. Huang G, Wang L, Wang S, Han Y, Wu J, Zhang Q, et al. Engineering Three-Dimensional Cell Mechanical Microenvironment with Hydrogels. *Biofabrication* (2012) 4(4):042001. doi:10.1088/1758-5082/4/4/042001
235. Gille J, Kunow J, Boisch L, Behrens P, Bos I, Hoffmann C, et al. Cell-Laden and Cell-free Matrix-Induced Chondrogenesis versus Microfracture for the Treatment of Articular Cartilage Defects. *CARTILAGE* (2010) 1(1):29–42. doi:10.1177/1947603509358721
236. Mierke CT, Frey B, Fellner M, Herrmann M, and Fabry B. Integrin α5β1 Facilitates Cancer Cell Invasion through Enhanced Contractile Forces. *J Cel Sci* (2011) 124(3):369–83. doi:10.1242/jcs.071985
237. Patil VA, and Masters KS. Engineered Collagen Matrices. *Bioengineering* (2020) 7(4):163. doi:10.3390/bioengineering7040163
238. Vinci M, Gowan S, Boxall F, Patterson L, Zimmermann M, Court W, et al. Advances in Establishment and Analysis of Three-Dimensional Tumor Spheroid-Based Functional Assays for Target Validation and Drug Evaluation. *BMC Biol* (2012) 10(1):29. doi:10.1186/1741-7007-10-29
239. Breslin S, and O'Driscoll L. The Relevance of Using 3D Cell Cultures, in Addition to 2D Monolayer Cultures, when Evaluating Breast Cancer Drug Sensitivity and Resistance. *Oncotarget* (2016) 7(29):45745–56. doi:10.18632/oncotarget.9935
240. Mikhail AS, Eetezadi S, and Allen C. Multicellular Tumor Spheroids for Evaluation of Cytotoxicity and Tumor Growth Inhibitory Effects of Nanomedicines *In Vitro*: A Comparison of Docetaxel-Loaded Block Copolymer Micelles and Taxotere. *PLoS ONE* (2013) 8(4):e62630. doi:10.1371/journal.pone.0062630
241. Carrow JK, Di Luca A, Dolatshahi-Pirouz A, Moroni L, and Gaharwar AK. 3D-printed Bioactive Scaffolds from Nanosilicates and PEOT/PBT for Bone Tissue Engineering. *Regenerative Biomater* (2019) 6(1):29–37. doi:10.1093/rb/rby024
242. Grant R, Hay D, and Callanan A. From Scaffold to Structure: The Synthetic Production of Cell Derived Extracellular Matrix for Liver Tissue Engineering. *Biomed Phys Eng Express* (2018) 4(6):065015. doi:10.1088/2057-1976/aacbe1
243. Hippler M, Lemma ED, Bertels S, Blasco E, Barner-Kowollik C, Wegener M, et al. 3D Scaffolds to Study Basic Cell Biology. *Adv Mater* (2019) 31(26):1808110. doi:10.1002/adma.201808110
244. Langer EM, Allen-Petersen BL, King SM, Kendsersky ND, Turnidge MA, Kuziel GM, et al. Modeling Tumor Phenotypes *In Vitro* with Three-Dimensional Bioprinting. *Cel Rep* (2019) 26(3):608–23.e6. doi:10.1016/j.celrep.2018.12.090
245. Eguchi H, Akizuki R, Maruhashi R, Tsukimoto M, Furuta T, Matsunaga T, et al. Increase in Resistance to Anticancer Drugs Involves Occludin in Spheroid Culture Model of Lung Adenocarcinoma A549 Cells. *Sci Rep* (2018) 8(1):15157. doi:10.1038/s41598-018-33566-w
246. Gong X, Lin C, Cheng J, Su J, Zhao H, Liu T, et al. Generation of Multicellular Tumor Spheroids with Microwell-Based Agarose Scaffolds for Drug Testing. *PLOS ONE* (2015) 10(6):e0130348. doi:10.1371/journal.pone.0130348
247. Mehta G, Hsiao AY, Ingram M, Luker GD, and Takayama S. Opportunities and Challenges for Use of Tumor Spheroids as Models to Test Drug Delivery and Efficacy. *J Controlled Release* (2012) 164(2):192–204. doi:10.1016/j.jconrel.2012.04.045
248. Ghosh S, Spagnoli GC, Martin I, Ploegert S, Demougin P, Heberer M, et al. Three-dimensional Culture of Melanoma Cells Profoundly Affects Gene Expression Profile: A High Density Oligonucleotide Array Study. *J Cel Physiol.* (2005) 204(2):522–31. doi:10.1002/jcp.20320
249. Zietarska M, Maugard CM, Filali-Mouhim A, Alam-Fahmy M, Tonin PN, Provencher DM, et al. Molecular Description of a 3D *In Vitro* Model for the Study of Epithelial Ovarian Cancer (EOC). *Mol Carcinog* (2007) 46(10):872–85. doi:10.1002/mc.20315
250. Belanger MH, Dolman L, Arcand SL, Shen Z, Chong G, Mes-Masson A-M, et al. A Targeted Analysis Identifies a High Frequency of BRCA1 and BRCA2 Mutation Carriers in Women with Ovarian Cancer from a Founder Population. *J Ovarian Res* (2015) 8(1):1. doi:10.1186/s13048-015-0124-8
251. Kapałczyńska M, Kolenda T, Przybyła W, Zajączkowska M, Teresiak A, Filas V, et al. 2D and 3D Cell Cultures - a Comparison of Different Types of Cancer Cell Cultures. *Arch Med Sci* (2016) 14:910. doi:10.5114/aoms.2016.63743
252. Karlsson H, Fryknäs M, Larsson R, and Nygren P. Loss of Cancer Drug Activity in colon Cancer HCT-116 Cells during Spheroid Formation in a New 3-D Spheroid Cell Culture System. *Exp Cel Res* (2012) 318(13):1577–85. doi:10.1016/j.yexcr.2012.03.026
253. Sieh S, Taubenberger AV, Rizzi SC, Sadowski M, Lehman ML, Rockstroh A, et al. Phenotypic Characterization of Prostate Cancer LNCaP Cells Cultured within a Bioengineered Microenvironment. *PLoS ONE* (2012) 7(9):e40217. doi:10.1371/journal.pone.0040217
254. Hynes RO, and Naba A. Overview of the Matrisome--An Inventory of Extracellular Matrix Constituents and Functions. *Cold Spring Harbor Perspect Biol* (2012) 4(1):a004903. doi:10.1101/cshperspect.a004903
255. Mecham RP. Overview of Extracellular Matrix. *Curr Protoc Cel Biol* (2012) 57(1). doi:10.1002/0471143030.cb1001s57
256. A Varki, RD Cummings, JD Esko, P Stanley, GW Hart, M Aebi, et al. editors. *Essentials of Glycobiology*. 3rd ed. Cold Spring Harbor, New York: Cold Spring Harbor Laboratory Press (2015). Available from: http://www.ncbi.nlm.nih.gov/books/NBK310274/ (Accessed July 20, 2021).
257. Villa-Diaz LG, Kim JK, Laperle A, Palecek SP, and Krebsbach PH. Inhibition of Focal Adhesion Kinase Signaling by Integrin α6β1 Supports Human Pluripotent Stem Cell Self-Renewal. *Stem Cells* (2016) 34(7):1753–64. doi:10.1002/stem.2349
258. Cattavarayane S, Palovuori R, Tanjore Ramanathan J, and Manninen A. α6β1- and αV-integrins Are Required for Long-Term Self-Renewal of Murine Embryonic Stem Cells in the Absence of LIF. *BMC Cel Biol* (2015) 16(1):3. doi:10.1186/s12860-015-0051-y
259. Popov C, Radic T, Haasters F, Prall WC, Aszodi A, Gullberg D, et al. Integrins α2β1 and α11β1 Regulate the Survival of Mesenchymal Stem Cells on Collagen I. *Cel Death Dis* (2011) 2(7):e186. doi:10.1038/cddis.2011.71
260. Plaks V, Kong N, and Werb Z. The Cancer Stem Cell Niche: How Essential Is the Niche in Regulating Stemness of Tumor Cells?. *Cell Stem Cell* (2015) 16(3):225–38. doi:10.1016/j.stem.2015.02.015
261. Fischer T, Hayn A, and Mierke CT. Fast and Reliable Advanced Two-step Pore-Size Analysis of Biomimetic 3D Extracellular Matrix Scaffolds. *Sci Rep* (2019) 9(1):8352. doi:10.1038/s41598-019-44764-5
262. Park S, Lim S, Siriviriyakul P, and Jeon JS. Three-dimensional Pore Network Characterization of Reconstructed Extracellular Matrix. *Phys Rev E* (2020) 101(5):052414. doi:10.1103/PhysRevE.101.052414
263. Shimshoni E, Adir I, Afik R, Solomonov I, Shenoy A, Adler M, et al. Distinct Extracellular-Matrix Remodeling Events Precede Symptoms of Inflammation. *Matrix Biol* (2019) 96:47. doi:10.1016/j.matbio.2020.11.001
264. Levental KR, Yu H, Kass L, Lakins JN, Egeblad M, Erler JT, et al. Matrix Crosslinking Forces Tumor Progression by Enhancing Integrin Signaling. *Cell* (2009) 139(5):891–906. doi:10.1016/j.cell.2009.10.027
265. Fernández-Sánchez ME, Barbier S, Whitehead J, Béalle G, Michel A, Latorre-Ossa H, et al. Mechanical Induction of the Tumorigenic β-catenin Pathway by Tumour Growth Pressure. *Nature* (2015) 523(7558):92–5. doi:10.1038/nature14329

266. Nia HT, Liu H, Seano G, Datta M, Jones D, Rahbari N, et al. Solid Stress and Elastic Energy as Measures of Tumour Mechanopathology. *Nat Biomed Eng* (2017) 1(1):0004. doi:10.1038/s41551-016-0004
267. Alessandri K, Sarangi BR, Gurchenkov VV, Sinha B, Kiessling TR, Fetler L, et al. Cellular Capsules as a Tool for Multicellular Spheroid Production and for Investigating the Mechanics of Tumor Progression *In Vitro*. *Proc Natl Acad Sci* (2013) 110(37):14843–8. doi:10.1073/pnas.1309482110
268. Helmlinger G, Netti PA, Lichtenbeld HC, Melder RJ, and Jain RK. Solid Stress Inhibits the Growth of Multicellular Tumor Spheroids. *Nat Biotechnol* (1997) 15(8):778–83. doi:10.1038/nbt0897-778
269. Taubenberger AV, Girardo S, Träber N, Fischer-Friedrich E, Kräter M, Wagner K, et al. 3D Microenvironment Stiffness Regulates Tumor Spheroid Growth and Mechanics via P21 and ROCK. *Adv Biosys* (2019) 3(9):1900128. doi:10.1002/adbi.201900128
270. Dolega ME, Delarue M, Ingremeau F, Prost J, Delon A, and Cappello G. Cell-like Pressure Sensors Reveal Increase of Mechanical Stress towards the Core of Multicellular Spheroids under Compression. *Nat Commun* (2017) 8(1):14056. doi:10.1038/ncomms14056
271. Montel F, Delarue M, Elgeti J, Malaquin L, Basan M, Risler T, et al. Stress Clamp Experiments on Multicellular Tumor Spheroids. *Phys Rev Lett* (2011) 107(18):188102. doi:10.1103/PhysRevLett.107.188102
272. Delarue M, Montel F, Vignjevic D, Prost J, Joanny J-F, and Cappello G. Compressive Stress Inhibits Proliferation in Tumor Spheroids through a Volume Limitation. *Biophysical J* (2014) 107(8):1821–8. doi:10.1016/j.bpj.2014.08.031
273. Dolega ME, Monnier S, Brunel B, Joanny J-F, Recho P, and Cappello G. Extracellular Matrix in Multicellular Aggregates Acts as a Pressure Sensor Controlling Cell Proliferation and Motility. *ELife* (2021) 10:e63258. doi:10.7554/eLife.63258
274. Dolega M, Zurlo G, Goff ML, Greda M, Verdier C, Joanny J-F, et al. Mechanical Behavior of Multi-Cellular Spheroids under Osmotic Compression. *J Mech Phys Sol* (2021) 147:104205. doi:10.1016/j.jmps.2020.104205
275. Han YL, Pegoraro AF, Li H, Li K, Yuan Y, Xu G, et al. Cell Swelling, Softening and Invasion in a Three-Dimensional Breast Cancer Model. *Nat Phys* (2020) 16(1):101–8. doi:10.1038/s41567-019-0680-8
276. Jansen KA, Atherton P, and Ballestrem C. Mechanotransduction at the Cell-Matrix Interface. *Semin Cel Develop Biol* (2017) 71:75–83. doi:10.1016/j.semcdb.2017.07.027
277. Jaalouk DE, and Lammerding J. Mechanotransduction Gone Awry. *Nat Rev Mol Cel Biol* (2009) 10(1):63–73. doi:10.1038/nrm2597
278. Lu P, Weaver VM, and Werb Z. The Extracellular Matrix: A Dynamic Niche in Cancer Progression. *J Cel Biol* (2012) 196(4):395–406. doi:10.1083/jcb.201102147
279. Snedeker JG, and Gautieri A. The Role of Collagen Crosslinks in Ageing and Diabetes - the Good, the Bad, and the Ugly. *Muscles Ligaments Tendons J* (2014) 4(3):303–8. doi:10.11138/mltj/2014.4.3.303
280. Cho S, Irianto J, and Discher DE. Mechanosensing by the Nucleus: From Pathways to Scaling Relationships. *J Cel Biol* (2017) 216(2):305–15. doi:10.1083/jcb.201610042
281. Moroni M, Servin-Vences MR, Fleischer R, Sánchez-Carranza O, and Lewin GR. Voltage Gating of Mechanosensitive PIEZO Channels. *Nat Commun* (2018) 9(1):1096. doi:10.1038/s41467-018-03502-7
282. Rocio Servin-Vences M, Moroni M, Lewin GR, and Poole K. Direct Measurement of TRPV4 and PIEZO1 Activity Reveals Multiple Mechanotransduction Pathways in Chondrocytes. *ELife* (2017) 6:e21074. doi:10.7554/eLife.21074
283. Pontani L-L, Jorjadze I, Viasnoff V, and Brujic J. Biomimetic Emulsions Reveal the Effect of Mechanical Forces on Cell-Cell Adhesion. *Proc Natl Acad Sci* (2012) 109(25):9839–44. doi:10.1073/pnas.1201499109
284. Engler AJ, Sen S, Sweeney HL, and Discher DE. Matrix Elasticity Directs Stem Cell Lineage Specification. *Cell* (2006) 126(4):677–89. doi:10.1016/j.cell.2006.06.044
285. Engler AJ, Humbert PO, Wehrle-Haller B, and Weaver VM. Multiscale Modeling of Form and Function. *Science* (2009) 324(5924):208–12. doi:10.1126/science.1170107
286. Chaudhuri O, Gu L, Klumpers D, Darnell M, Bencherif SA, Weaver JC, et al. Hydrogels with Tunable Stress Relaxation Regulate Stem Cell Fate and Activity. *Nat Mater* (2016) 15(3):326–34. doi:10.1038/nmat4489
287. Chaudhuri O, Gu L, Darnell M, Klumpers D, Bencherif SA, Weaver JC, et al. Substrate Stress Relaxation Regulates Cell Spreading. *Nat Commun* (2015) 6(1):6365. doi:10.1038/ncomms7365
288. Mohammadi H, and McCulloch CA. Impact of Elastic and Inelastic Substrate Behaviors on Mechanosensation. *Soft Matter* (2014) 10(3):408–20. doi:10.1039/C3SM52729H
289. Storm C, Pastore JJ, MacKintosh FC, Lubensky TC, and Janmey PA. Nonlinear Elasticity in Biological Gels. *Nature* (2005) 435(7039):191–4. doi:10.1038/nature03521
290. Jansen KA, Bacabac RG, Piechocka IK, and Koenderink GH. Cells Actively Stiffen Fibrin Networks by Generating Contractile Stress. *Biophysical J* (2013) 105(10):2240–51. doi:10.1016/j.bpj.2013.10.008
291. Hall MS, Alisafaei F, Ban E, Feng X, Hui C-Y, Shenoy VB, et al. Fibrous Nonlinear Elasticity Enables Positive Mechanical Feedback between Cells and ECMs. *Proc Natl Acad Sci USA* (2016) 113(49):14043–8. doi:10.1073/pnas.1613058113
292. Ma X, Schickel ME, Stevenson MD, Sarang-Sieminski AL, Gooch KJ, Ghadiali SN, et al. Fibers in the Extracellular Matrix Enable Long-Range Stress Transmission between Cells. *Biophysical J* (2013) 104(7):1410–8. doi:10.1016/j.bpj.2013.02.017
293. Rudnicki MS, Cirka HA, Aghvami M, Sander EA, Wen Q, and Billiar KL. Nonlinear Strain Stiffening Is Not Sufficient to Explain How Far Cells Can Feel on Fibrous Protein Gels. *Biophysical J* (2013) 105(1):11–20. doi:10.1016/j.bpj.2013.05.032
294. Reinhart-King CA, Dembo M, and Hammer DA. Cell-Cell Mechanical Communication through Compliant Substrates. *Biophysical J* (2008) 95(12):6044–51. doi:10.1529/biophysj.107.127662
295. Sapir L, and Tzlil S. Talking over the Extracellular Matrix: How Do Cells Communicate Mechanically? *Semin Cel Develop Biol* (2017) 71:99–105. doi:10.1016/j.semcdb.2017.06.010
296. Hanahan D, and Weinberg RA. The Hallmarks of Cancer. *Cell* (2000) 100(1):57–70. doi:10.1016/S0092-8674(00)81683-9
297. Hanahan D, and Weinberg RA. Hallmarks of Cancer: The Next Generation. *Cell* (2011) 144(5):646–74. doi:10.1016/j.cell.2011.02.013
298. Lazebnik Y. What Are the Hallmarks of Cancer?. *Nat Rev Cancer* (2010) 10(4):232–3. doi:10.1038/nrc2827
299. Wilbur M, Shih I-M, Segars J, and Fader A. Cancer Implications for Patients with Endometriosis. *Semin Reprod Med* (2017) 35(01):110–6. doi:10.1055/s-0036-1597120
300. Horne SD, Pollick SA, and Heng HHQ. Evolutionary Mechanism Unifies the Hallmarks of Cancer. *Int J Cancer* (2015) 136(9):2012–21. doi:10.1002/ijc.29031
301. Bizzarri M, Cucina A, Conti F, and D'Anselmi F. Beyond the Oncogene Paradigm: Understanding Complexity in Cancerogenesis. *Acta Biotheor* (2008) 56(3):173–96. doi:10.1007/s10441-008-9047-8
302. Sonnenschein C, Soto AM, Rangarajan A, and Kulkarni P. Competing Views on Cancer. *J Biosci* (2014) 39(2):281–302. doi:10.1007/s12038-013-9403-y
303. Sonnenschein C, and Soto AM. The Aging of the 2000 and 2011 Hallmarks of Cancer Reviews: A Critique. *J Biosci* (2013) 38(3):651–63. doi:10.1007/s12038-013-9335-6
304. Busque L, Patel JP, Figueroa ME, Vasanthakumar A, Provost S, Hamilou Z, et al. Recurrent Somatic TET2 Mutations in normal Elderly Individuals with Clonal Hematopoiesis. *Nat Genet* (2012) 44(11):1179–81. doi:10.1038/ng.2413
305. Martincorena I, Roshan A, Gerstung M, Ellis P, Van Loo P, McLaren S, et al. High burden and Pervasive Positive Selection of Somatic Mutations in normal Human Skin. *Science* (2015) 348(6237):880–6. doi:10.1126/science.aaa6806
306. Xie M, Lu C, Wang J, McLellan MD, Johnson KJ, Wendl MC, et al. Age-related Mutations Associated with Clonal Hematopoietic Expansion and Malignancies. *Nat Med* (2014) 20(12):1472–8. doi:10.1038/nm.3733
307. Kode A, Manavalan JS, Mosialou I, Bhagat G, Rathinam CV, Luo N, et al. Leukaemogenesis Induced by an Activating β-catenin Mutation in Osteoblasts. *Nature* (2014) 506(7487):240–4. doi:10.1038/nature12883

308. Raaijmakers MHGP. Myelodysplastic Syndromes: Revisiting the Role of the Bone Marrow Microenvironment in Disease Pathogenesis. *Int J Hematol* (2012) 95(1):17–25. doi:10.1007/s12185-011-1001-x
309. Carmeliet P, and Jain RK. Angiogenesis in Cancer and Other Diseases. *Nature* (2000) 407(6801):249–57. doi:10.1038/35025220
310. Mayers JR, Torrence ME, Danai LV, Papagiannakopoulos T, Davidson SM, Bauer MR, et al. Tissue of Origin Dictates Branched-Chain Amino Acid Metabolism in Mutant Kras-Driven Cancers. *Science* (2016) 353(6304): 1161–5. doi:10.1126/science.aaf5171
311. Ladoux B, and Mège R-M. Mechanobiology of Collective Cell Behaviours. *Nat Rev Mol Cel Biol* (2017) 18(12):743–57. doi:10.1038/nrm.2017.98
312. Ladoux B, Mège R-M, and Trepat X. Front-Rear Polarization by Mechanical Cues: From Single Cells to Tissues. *Trends Cel Biol* (2016) 26(6):420–33. doi:10.1016/j.tcb.2016.02.002
313. Parsons JT, Horwitz AR, and Schwartz MA. Cell Adhesion: Integrating Cytoskeletal Dynamics and Cellular Tension. *Nat Rev Mol Cel Biol* (2010) 11(9):633–43. doi:10.1038/nrm2957
314. Bödeker HU, Beta C, Frank TD, and Bodenschatz E. Quantitative Analysis of Random Ameboid Motion. *EPL (Europhysics Letters)* (2010) 90(2):28005. doi:10.1209/0295-5075/90/28005
315. Brückner DB, Fink A, Schreiber C, Röttgermann PJF, Rädler JO, and Broedersz CP. Stochastic Nonlinear Dynamics of Confined Cell Migration in Two-State Systems. *Nat Phys* (2019) 15(6):595–601. doi:10.1038/s41567-019-0445-4
316. Selmeczi D, Mosler S, Hagedorn PH, Larsen NB, and Flyvbjerg H. Cell Motility as Persistent Random Motion: Theories from Experiments. *Biophysical J* (2005) 89(2):912–31. doi:10.1529/biophysj.105.061150
317. Bosgraaf L, and Van Haastert PJM. The Ordered Extension of Pseudopodia by Amoeboid Cells in the Absence of External Cues. *PLoS ONE* (2009) 4(4): e5253. doi:10.1371/journal.pone.0005253
318. Callan-Jones AC, and Voituriez R. Actin Flows in Cell Migration: From Locomotion and Polarity to Trajectories. *Curr Opin Cel Biol* (2016) 38:12–7. doi:10.1016/j.ceb.2016.01.003
319. Maiuri P, Rupprecht J-F, Wieser S, Ruprecht V, Bénichou O, Carpi N, et al. Actin Flows Mediate a Universal Coupling between Cell Speed and Cell Persistence. *Cell* (2015) 161(2):374–86. doi:10.1016/j.cell.2015.01.056
320. Bagorda A, and Parent CA. Eukaryotic Chemotaxis at a Glance. *J Cel Sci* (2008) 121(16):2621–4. doi:10.1242/jcs.018077
321. Metzner C, Mark C, Steinwachs J, Lautscham L, Stadler F, and Fabry B. Superstatistical Analysis and Modelling of Heterogeneous Random Walks. *Nat Commun* (2015) 6(1):7516. doi:10.1038/ncomms8516
322. Nakajima A, Ishihara S, Imoto D, and Sawai S. Rectified Directional Sensing in Long-Range Cell Migration. *Nat Commun* (2014) 5(1):5367. doi:10.1038/ncomms6367
323. Brückner DB, Arlt N, Fink A, Ronceray P, Rädler JO, and Broedersz CP. Learning the Dynamics of Cell-Cell Interactions in Confined Cell Migration. *Proc Natl Acad Sci USA* (2021) 118(7):e2016602118. doi:10.1073/pnas.2016602118
324. Dumortier JG, Martin S, Meyer D, Rosa FM, and David NB. Collective Mesendoderm Migration Relies on an Intrinsic Directionality Signal Transmitted through Cell Contacts. *Proc Natl Acad Sci* (2012) 109(42): 16945–50. doi:10.1073/pnas.1205870109
325. Gupta M, Sarangi BR, Deschamps J, Nematbakhsh Y, Callan-Jones A, Margadant F, et al. Adaptive Rheology and Ordering of Cell Cytoskeleton Govern Matrix Rigidity Sensing. *Nat Commun* (2015) 6(1):7525. doi:10.1038/ncomms8525
326. Liu Y-J, Berre ML, Lautenschlaeger F, Maiuri P, Callan-Jones A, Heuzé M, et al. Confinement and Low Adhesion Induce Fast Amoeboid Migration of Slow Mesenchymal Cells. *Cell* (2015) 160(4):659–72. doi:10.1016/j.cell.2015.01.007
327. Petrie RJ, and Yamada KM. Multiple Mechanisms of 3D Migration: The Origins of Plasticity. *Curr Opin Cel Biol* (2016) 42:7–12. doi:10.1016/j.ceb.2016.03.025
328. Petrie RJ, Gavara N, Chadwick RS, and Yamada KM. Nonpolarized Signaling Reveals Two Distinct Modes of 3D Cell Migration. *J Cel Biol* (2012) 197(3): 439–55. doi:10.1083/jcb.201201124
329. Yamada KM, Collins JW, Cruz Walma DA, Doyle AD, Morales SG, Lu J, et al. Extracellular Matrix Dynamics in Cell Migration, Invasion and Tissue Morphogenesis. *Int J Exp Path* (2019) 100(3):144–52. doi:10.1111/iep.12329
330. d'Alessandro J, Barbier–Chebbah A, Cellerin V, Benichou O, Mège RM, Voituriez R, et al. Cell Migration Guided by Long-Lived Spatial Memory. *Nat Commun* (2021) 12(1):4118. doi:10.1038/s41467-021-24249-8
331. Caballero D, Voituriez R, and Riveline D. Protrusion Fluctuations Direct Cell Motion. *Biophysical J* (2014) 107(1):34–42. doi:10.1016/j.bpj.2014.05.002
332. Jain S, Cachoux VML, Narayana GHNS, de Beco S, D'Alessandro J, Cellerin V, et al. The Role of Single-Cell Mechanical Behaviour and Polarity in Driving Collective Cell Migration. *Nat Phys* (2020) 16(7):802–9. doi:10.1038/s41567-020-0875-z
333. Mohammed D, Charras G, Vercruysse E, Versaevel M, Lantoine J, Alaimo L, et al. Substrate Area Confinement Is a Key Determinant of Cell Velocity in Collective Migration. *Nat Phys* (2019) 15(8):858–66. doi:10.1038/s41567-019-0543-3
334. Hennig K, Wang I, Moreau P, Valon L, DeBeco S, Coppey M, et al. Stick-slip Dynamics of Cell Adhesion Triggers Spontaneous Symmetry Breaking and Directional Migration of Mesenchymal Cells on One-Dimensional Lines. *Sci Adv* (2020) 6(1):eaau5670. doi:10.1126/sciadv.aau5670
335. Lavi I, Piel M, Lennon-Duménil A-M, Voituriez R, and Gov NS. Deterministic Patterns in Cell Motility. *Nat Phys* (2016) 12(12):1146–52. doi:10.1038/nphys3836
336. Eriksson JE, Dechat T, Grin B, Helfand B, Mendez M, Pallari H-M, et al. Introducing Intermediate Filaments: From Discovery to Disease. *J Clin Invest* (2009) 119(7):1763–71. doi:10.1172/JCI38339
337. Marusyk A, Janiszewska M, and Polyak K. Intratumor Heterogeneity: The Rosetta Stone of Therapy Resistance. *Cancer Cell* (2020) 37(4):471–84. doi:10.1016/j.ccell.2020.03.007
338. Skylaki S, Hilsenbeck O, and Schroeder T. Challenges in Long-Term Imaging and Quantification of Single-Cell Dynamics. *Nat Biotechnol* (2016) 34(11): 1137–44. doi:10.1038/nbt.3713
339. Fletcher DA, and Mullins RD. Cell Mechanics and the Cytoskeleton. *Nature* (2010) 463(7280):485–92. doi:10.1038/nature08908
340. Alibert C, Goud B, and Manneville J-B. Are Cancer Cells Really Softer Than normal Cells?. *Biol Cel* (2017) 109(5):167–89. doi:10.1111/boc.201600078
341. Mierke CT. Mechanical Cues Affect Migration and Invasion of Cells from Three Different Directions. *Front Cel Dev. Biol.* (2020) 8:583226. doi:10.3389/fcell.2020.583226
342. Polacheck WJ, and Chen CS. Measuring Cell-Generated Forces: A Guide to the Available Tools. *Nat Methods* (2016) 13(5):415–23. doi:10.1038/nmeth.3834
343. Trepat X, Wasserman MR, Angelini TE, Millet E, Weitz DA, Butler JP, et al. Physical Forces during Collective Cell Migration. *Nat Phys* (2009) 5(6): 426–30. doi:10.1038/nphys1269
344. Kozminsky M, and Sohn LL. The Promise of Single-Cell Mechanophenotyping for Clinical Applications. *Biomicrofluidics* (2020) 14(3):031301. doi:10.1063/5.0010800
345. Lamouille S, Xu J, and Derynck R. Molecular Mechanisms of Epithelial-Mesenchymal Transition. *Nat Rev Mol Cel Biol* (2014) 15(3):178–96. doi:10.1038/nrm3758
346. Nieto MA, Huang RY-J, Jackson RA, and Thiery JP. EMT: 2016. *Cell* (2016) 166(1):21–45. doi:10.1016/j.cell.2016.06.028
347. Zaravinos A. The Regulatory Role of MicroRNAs in EMT and Cancer. *J Oncol* (2015) 2015:1–13. doi:10.1155/2015/865816
348. Kariya Y, Oyama M, Suzuki T, and Kariya Y. αvβ3 Integrin Induces Partial EMT Independent of TGF-β Signaling. *Commun Biol* (2021) 4(1):490. doi:10.1038/s42003-021-02003-6
349. Pal A, Barrett TF, Paolini R, Parikh A, and Puram SV. Partial EMT in Head and Neck Cancer Biology: A Spectrum Instead of a Switch. *Oncogene* (2021) 40:5049–65. doi:10.1038/s41388-021-01868-5
350. Saitoh M. Involvement of Partial EMT in Cancer Progression. *J Biochem* (2018) 164(4):257–64. doi:10.1093/jb/mvy047
351. Saxena N, Mogha P, Dash S, Majumder A, Jadhav S, and Sen S. Matrix Elasticity Regulates Mesenchymal Stem Cell Chemotaxis. *J Cel Sci* (2018) 131: jcs211391. doi:10.1242/jcs.211391

352. Yang J, Antin P, Antin P, Berx G, Blanpain C, Brabletz T, et al. Guidelines and Definitions for Research on Epithelial-Mesenchymal Transition. *Nat Rev Mol Cel Biol* (2020) 21(6):341–52. doi:10.1038/s41580-020-0237-9
353. Shah MK, Garcia-Pak IH, and Darling EM. Influence of Inherent Mechanophenotype on Competitive Cellular Adherence. *Ann Biomed Eng* (2017) 45(8):2036–47. doi:10.1007/s10439-017-1841-5
354. Di Carlo D. A Mechanical Biomarker of Cell State in Medicine. *J Lab Autom* (2012) 17(1):32–42. doi:10.1177/2211068211431630
355. Gilchrist CL, Darling EM, Chen J, and Setton LA. Extracellular Matrix Ligand and Stiffness Modulate Immature Nucleus Pulposus Cell-Cell Interactions. *PLoS ONE* (2011) 6(11):e27170. doi:10.1371/journal.pone.0027170
356. Poh Y-C, Chen J, Hong Y, Yi H, Zhang S, Chen J, et al. Generation of Organized Germ Layers from a Single Mouse Embryonic Stem Cell. *Nat Commun* (2014) 5(1):4000. doi:10.1038/ncomms5000
357. Jagielska A, Norman AL, Whyte G, Vliet KJV, Guck J, and Franklin RJM. Mechanical Environment Modulates Biological Properties of Oligodendrocyte Progenitor Cells. *Stem Cell Develop* (2012) 21(16): 2905–14. doi:10.1089/scd.2012.0189
358. Sen S, Dong M, and Kumar S. Isoform-Specific Contributions of α-Actinin to Glioma Cell Mechanobiology. *PLoS ONE* (2009) 4(12):e8427. doi:10.1371/journal.pone.0008427
359. Sen S, Ng WP, and Kumar S. Contributions of Talin-1 to Glioma Cell-Matrix Tensional Homeostasis. *J R Soc Interf* (2012) 9(71):1311–7. doi:10.1098/rsif.2011.0567
360. Solon J, Levental I, Sengupta K, Georges PC, and Janmey PA. Fibroblast Adaptation and Stiffness Matching to Soft Elastic Substrates. *Biophysical J* (2007) 93(12):4453–61. doi:10.1529/biophysj.106.101386
361. Blumlein A, Williams N, and McManus JJ. The Mechanical Properties of Individual Cell Spheroids. *Sci Rep* (2017) 7(1):7346. doi:10.1038/s41598-017-07813-5
362. Zimberlin JA, McManus JJ, and Crosby AJ. Cavitation Rheology of the Vitreous: Mechanical Properties of Biological Tissue. *Soft Matter* (2010) 6(15):3632. doi:10.1039/b925407b
363. Zimberlin JA, Sanabria-DeLong N, Tew GN, and Crosby AJ. Cavitation Rheology for Soft Materials. *Soft Matter* (2007) 3(6):763. doi:10.1039/b617050a
364. Mok S, Al Habyan S, Ledoux C, Lee W, MacDonald KN, McCaffrey L, et al. Mapping Cellular-Scale Internal Mechanics in 3D Tissues with Thermally Responsive Hydrogel Probes. *Nat Commun* (2020) 11(1):4757. doi:10.1038/s41467-020-18469-7
365. Tse JR, and Engler AJ. Preparation of Hydrogel Substrates with Tunable Mechanical Properties. *Curr Protoc Cel Biol* (2010) 47(1). doi:10.1002/0471143030.cb1016s47
366. Morais JM, Papadimitrakopoulos F, and Burgess DJ. Biomaterials/Tissue Interactions: Possible Solutions to Overcome Foreign Body Response. *Aaps J* (2010) 12(2):188–96. doi:10.1208/s12248-010-9175-3
367. Pei Y, Chen J, Yang L, Shi L, Tao Q, Hui B, et al. The Effect of pH on the LCST of poly(N-Isopropylacrylamide) and poly(N-Isopropylacrylamide-Co-Acrylic Acid). *J Biomater Sci Polym Edition* (2004) 15(5):585–94. doi:10.1163/156856204323046852
368. Sunyer R, Conte V, Escribano J, Elosegui-Artola A, Labernadie A, Valon L, et al. Collective Cell Durotaxis Emerges from Long-Range Intercellular Force Transmission. *Science* (2016) 353(6304):1157–61. doi:10.1126/science.aaf7119
369. Mierke CT. Phagocytized Beads Reduce the α5β1 Integrin Facilitated Invasiveness of Cancer Cells by Regulating Cellular Stiffness. *Cell Biochem Biophys* (2013) 66(3):599–622. doi:10.1007/s12013-012-9506-3
370. Valentine MT, Dewalt LE, and Ou-Yang HD. Forces on a Colloidal Particle in a Polymer Solution: A Study Using Optical Tweezers. *J Phys Condens Matter* (1996) 8(47):9477–82. doi:10.1088/0953-8984/8/47/048
371. Bustamante C, Bryant Z, and Smith SB. Ten Years of Tension: Single-Molecule DNA Mechanics. *Nature* (2003) 421(6921):423–7. doi:10.1038/nature01405
372. Ashkin A. Optical Trapping and Manipulation of Neutral Particles Using Lasers. *Proc Natl Acad Sci* (1997) 94(10):4853–60. doi:10.1073/pnas.94.10.4853
373. Gutsche C, Elmahdy MM, Kegler K, Semenov I, Stangner T, Otto O, et al. Micro-rheology on (Polymer-grafted) Colloids Using Optical Tweezers. *J Phys Condens Matter* (2011) 23(18):184114. doi:10.1088/0953-8984/23/18/184114
374. Knox SM, and Whitelock JM. Perlecan: How Does One Molecule Do So many Things?. *Cell. Mol. Life Sci.* (2006) 63(21):2435–45. doi:10.1007/s00018-006-6162-z
375. Melrose J, Hayes AJ, Whitelock JM, and Little CB. Perlecan, the "jack of All Trades" Proteoglycan of Cartilaginous Weight-Bearing Connective Tissues. *BioEssays* (2008) 30(5):457–69. doi:10.1002/bies.20748
376. Knox S, Fosang AJ, Last K, Melrose J, and Whitelock J. Perlecan from Human Epithelial Cells Is a Hybrid Heparan/chondroitin/keratan Sulfate Proteoglycan. *FEBS Lett* (2005) 579(22):5019–23. doi:10.1016/j.febslet.2005.07.090
377. Jung M, Lord MS, Cheng B, Lyons JG, Alkhouri H, Hughes JM, et al. Mast Cells Produce Novel Shorter Forms of Perlecan that Contain Functional Endorepellin. *J Biol Chem* (2013) 288(5):3289–304. doi:10.1074/jbc.M112.387811
378. Siegel G, Malmsten M, and Ermilov E. Anionic Biopolyelectrolytes of the Syndecan/perlecan Superfamily: Physicochemical Properties and Medical Significance. *Adv Colloid Interf Sci* (2014) 205:275–318. doi:10.1016/j.cis.2014.01.009
379. Guilak F, Hayes AJ, and Melrose J. Perlecan in Pericellular Mechanosensory Cell-Matrix Communication, Extracellular Matrix Stabilisation and Mechanoregulation of Load-Bearing Connective Tissues. *Int J Mol Sci* (2021) 22(5):2716. doi:10.3390/ijms22052716
380. Iozzo RV. Basement Membrane Proteoglycans: From Cellar to Ceiling. *Nat Rev Mol Cel Biol* (2005) 6(8):646–56. doi:10.1038/nrm1702
381. Whitelock JM, and Iozzo RV. Heparan Sulfate: A Complex Polymer Charged with Biological Activity. *Chem Rev* (2005) 105(7):2745–64. doi:10.1021/cr010213m
382. Sarrazin S, Lamanna WC, and Esko JD. Heparan Sulfate Proteoglycans. *Cold Spring Harbor Perspect Biol* (2011) 3(7):a004952. doi:10.1101/cshperspect.a004952
383. Theocharis AD, Skandalis SS, Gialeli C, and Karamanos NK. Extracellular Matrix Structure. *Adv Drug Deliv Rev* (2016) 97:4–27. doi:10.1016/j.addr.2015.11.001
384. Whitelock JM, Murdoch AD, Iozzo RV, and Underwood PA. The Degradation of Human Endothelial Cell-Derived Perlecan and Release of Bound Basic Fibroblast Growth Factor by Stromelysin, Collagenase, Plasmin, and Heparanases. *J Biol Chem* (1996) 271(17):10079–86. doi:10.1074/jbc.271.17.10079
385. Elgundi Z, Papanicolaou M, Major G, Cox TR, Melrose J, Whitelock JM, et al. Cancer Metastasis: The Role of the Extracellular Matrix and the Heparan Sulfate Proteoglycan Perlecan. *Front Oncol* (2020) 9:1482. doi:10.3389/fonc.2019.01482
386. Woodham EF, and Machesky LM. Polarised Cell Migration: Intrinsic and Extrinsic Drivers. *Curr Opin Cel Biol* (2014) 30:25–32. doi:10.1016/j.ceb.2014.05.006
387. Xia S, Chen Z, Shen C, and Fu T-M. Higher-order Assemblies in Immune Signaling: Supramolecular Complexes and Phase Separation. *Protein Cell* (2021) 12:680–94. doi:10.1007/s13238-021-00839-6
388. Goult BT. The Mechanical Basis of Memory - the MeshCODE Theory. *Front Mol Neurosci* (2021) 14:592951. doi:10.3389/fnmol.2021.592951
389. Oldfield CJ, and Dunker AK. Intrinsically Disordered Proteins and Intrinsically Disordered Protein Regions. *Annu Rev Biochem* (2014) 83(1): 553–84. doi:10.1146/annurev-biochem-072711-164947
390. Wright PE, and Dyson HJ. Intrinsically Disordered Proteins in Cellular Signalling and Regulation. *Nat Rev Mol Cel Biol* (2015) 16(1):18–29. doi:10.1038/nrm3920
391. Huntley MA, and Golding GB. Simple Sequences Are Rare in the Protein Data Bank. *Proteins* (2002) 48(1):134–40. doi:10.1002/prot.10150
392. Tompa P, and Fuxreiter M. Fuzzy Complexes: Polymorphism and Structural Disorder in Protein-Protein Interactions. *Trends Biochem Sci* (2008) 33(1): 2–8. doi:10.1016/j.tibs.2007.10.003
393. Eisenberg D, and Jucker M. The Amyloid State of Proteins in Human Diseases. *Cell* (2012) 148(6):1188–203. doi:10.1016/j.cell.2012.02.022
394. Bienz M. Signalosome Assembly by Domains Undergoing Dynamic Head-To-Tail Polymerization. *Trends Biochem Sci* (2014) 39(10):487–95. doi:10.1016/j.tibs.2014.08.006

395. Wu J, Lewis AH, and Grandl J. Touch, Tension, and Transduction - the Function and Regulation of Piezo Ion Channels. *Trends Biochem Sci* (2017) 42(1):57–71. doi:10.1016/j.tibs.2016.09.004
396. Anderson P, Kedersha N, and Ivanov P. Stress Granules, P-Bodies and Cancer. *Biochim Biophys Acta* (2015) 1849(7):861–70. doi:10.1016/j.bbagrm.2014.11.009
397. Hyman AA, Weber CA, and Jülicher F. Liquid-Liquid Phase Separation in Biology. *Annu Rev Cel Dev. Biol.* (2014) 30(1):39–58. doi:10.1146/annurev-cellbio-100913-013325
398. Mitchell SF, and Parker R. Principles and Properties of Eukaryotic mRNPs. *Mol Cel* (2014) 54(4):547–58. doi:10.1016/j.molcel.2014.04.033
399. Brangwynne CP, Tompa P, and Pappu RV. Polymer Physics of Intracellular Phase Transitions. *Nat Phys* (2015) 11(11):899–904. doi:10.1038/nphys3532
400. Liang X, Michael M, and Gomez G. Measurement of Mechanical Tension at Cell-Cell Junctions Using Two-Photon Laser Ablation. *Bio Protoc* (2016) 6(24):e2068. doi:10.21769/BioProtoc.2068
401. Swaney KF, and Li R. Function and Regulation of the Arp2/3 Complex during Cell Migration in Diverse Environments. *Curr Opin Cel Biol* (2016) 42:63–72. doi:10.1016/j.ceb.2016.04.005
402. Case LB, Ditlev JA, and Rosen MK. Regulation of Transmembrane Signaling by Phase Separation. *Annu Rev Biophys* (2019) 48(1):465–94. doi:10.1146/annurev-biophys-052118-115534
403. Case LB, Zhang X, Ditlev JA, and Rosen MK. Stoichiometry Controls Activity of Phase-Separated Clusters of Actin Signaling Proteins. *Science* (2019) 363(6431):1093–7. doi:10.1126/science.aau6313 (
404. Huang WYC, Alvarez S, Kondo Y, Lee YK, Chung JK, Lam HYM, et al. A Molecular Assembly Phase Transition and Kinetic Proofreading Modulate Ras Activation by SOS. *Science* (2019) 363(6431):1098–103. doi:10.1126/science.aau5721
405. Cai D, Feliciano D, Dong P, Flores E, Gruebele M, Porat-Shliom N, et al. Phase Separation of YAP Reorganizes Genome Topology for Long-Term YAP Target Gene Expression. *Nat Cel Biol* (2019) 21(12):1578–89. doi:10.1038/s41556-019-0433-z
406. Cremer T, Cremer M, Hübner B, Strickfaden H, Smeets D, Popken J, et al. The 4D Nucleome: Evidence for a Dynamic Nuclear Landscape Based on Co-aligned Active and Inactive Nuclear Compartments. *FEBS Lett* (2015) 589(20 Pt A):2931–43. doi:10.1016/j.febslet.2015.05.037
407. Popken J, Brero A, Koehler D, Schmid VJ, Strauss A, Wuensch A, et al. Reprogramming of Fibroblast Nuclei in Cloned Bovine Embryos Involves Major Structural Remodeling with Both Striking Similarities and Differences to Nuclear Phenotypes Ofin Vitrofertilized Embryos. *Nucleus* (2014) 5(6):555–89. doi:10.4161/19491034.2014.979712
408. Bajpai G, Amiad Pavlov D, Lorber D, Volk T, and Safran S. Mesoscale Phase Separation of Chromatin in the Nucleus. *ELife* (2021) 10:e63976. doi:10.7554/eLife.63976
409. Bundschuh R. Physical Biology of the Cell Physical Biology of the Cell , Rob Phillips , Jané Kondev and Julie Theriot Garland Science, New York, 2009. $125.00 (807 pp). ISBN 978-0-8153-4163-5. *Phys Today* (2009) 62(8):44. doi:10.1063/1.3206095
410. Rosa S, and Shaw P. Insights into Chromatin Structure and Dynamics in Plants. *Biology* (2013) 2(4):1378–410. doi:10.3390/biology2041378
411. Meier DJ. Theory of Block Copolymers. I. Domain Formation in A-B Block Copolymers. *J Polym sci., C Polym Symp* (1969) 26(1):81–98. doi:10.1002/polc.5070260106
412. Farooqui R, and Fenteany G. Multiple Rows of Cells behind an Epithelial Wound Edge Extend Cryptic Lamellipodia to Collectively Drive Cell-Sheet Movement. *J Cel Sci* (2005) 118(1):51–63. doi:10.1242/jcs.01577
413. Simpson KJ, Selfors LM, Bui J, Reynolds A, Leake D, Khvorova A, et al. Identification of Genes that Regulate Epithelial Cell Migration Using an siRNA Screening Approach. *Nat Cel Biol* (2008) 10(9):1027–38. doi:10.1038/ncb1762
414. Bindschadler M, and McGrath JL. Sheet Migration by Wounded Monolayers as an Emergent Property of Single-Cell Dynamics. *J Cel Sci* (2007) 120(5):876–84. doi:10.1242/jcs.03395
415. Tambe DT, Corey Hardin C, Angelini TE, Rajendran K, Park CY, Serra-Picamal X, et al.Collective Cell Guidance by Cooperative Intercellular Forces. *Nat Mater* (2011) 10(6):469–75. doi:10.1038/nmat3025
416. Parisi G, and Zamponi F. Mean-field Theory of Hard Sphere Glasses and Jamming. *Rev Mod Phys* (2010) 82(1):789–845. doi:10.1103/RevModPhys.82.789
417. Weeks ER. Three-Dimensional Direct Imaging of Structural Relaxation Near the Colloidal Glass Transition. *Science* (2000) 287(5453):627–31. doi:10.1126/science.287.5453.627
418. Hall RW, and Wolynes PG. Intermolecular Forces and the Glass Transition. *J Phys Chem B* (2008) 112(2):301–12. doi:10.1021/jp075017j
419. Nelson CM, VanDuijn MM, Inman JL, Fletcher DA, and Bissell MJ. Tissue Geometry Determines Sites of Mammary Branching Morphogenesis in Organotypic Cultures. *Science* (2006) 314(5797):298–300. doi:10.1126/science.1131000
420. Geiger B, Spatz JP, and Bershadsky AD. Environmental Sensing through Focal Adhesions. *Nat Rev Mol Cel Biol* (2009) 10(1):21–33. doi:10.1038/nrm2593
421. Roca-Cusachs P, Gauthier NC, del Rio A, and Sheetz MP. Clustering of 5 1 Integrins Determines Adhesion Strength whereas V 3 and Talin Enable Mechanotransduction. *Proc Natl Acad Sci* (2009) 106(38):16245–50. doi:10.1073/pnas.0902818106
422. Krishnan R, Park CY, Lin Y-C, Mead J, Jaspers RT, Trepat X, et al. Reinforcement versus Fluidization in Cytoskeletal Mechanoresponsiveness. *PLoS ONE* (2009) 4(5):e5486. doi:10.1371/journal.pone.0005486
423. Indra I, Gasparski AN, and Beningo KA. An *In Vitro* Correlation of Metastatic Capacity and Dual Mechanostimulation. *PLOS ONE* (2018) 13(11):e0207490. doi:10.1371/journal.pone.0207490
424. Lou J, Stowers R, Nam S, Xia Y, and Chaudhuri O. Stress Relaxing Hyaluronic Acid-Collagen Hydrogels Promote Cell Spreading, Fiber Remodeling, and Focal Adhesion Formation in 3D Cell Culture. *Biomaterials* (2018) 154:213–22. doi:10.1016/j.biomaterials.2017.11.004
425. Vining KH, Stafford A, and Mooney DJ. Sequential Modes of Crosslinking Tune Viscoelasticity of Cell-Instructive Hydrogels. *Biomaterials* (2019) 188:187–97. doi:10.1016/j.biomaterials.2018.10.013
426. Baker BM, Trappmann B, Wang WY, Sakar MS, Kim IL, Shenoy VB, et al. Cell-mediated Fibre Recruitment Drives Extracellular Matrix Mechanosensing in Engineered Fibrillar Microenvironments. *Nat Mater* (2015) 14(12):1262–8. doi:10.1038/nmat4444
427. Braunecker WA, and Matyjaszewski K. Controlled/living Radical Polymerization: Features, Developments, and Perspectives. *Prog Polym Sci* (2007) 32(1):93–146. doi:10.1016/j.progpolymsci.2006.11.002
428. Ong LL, Hanikel N, Yaghi OK, Grun C, Strauss MT, Bron P, et al. Programmable Self-Assembly of Three-Dimensional Nanostructures from 10,000 Unique Components. *Nature* (2017) 552(7683):72–7. doi:10.1038/nature24648
429. Händler T, Tutmarc C, Glaser M, Freitag JS, Smith DM, and Schnauß J. Measuring Structural Parameters of Crosslinked and Entangled Semiflexible Polymer Networks with Single-Filament Tracing. *Phys Rev E* (2021) 103(6):062501. doi:10.1103/PhysRevE.103.062501
430. Rosales AM, and Anseth KS. The Design of Reversible Hydrogels to Capture Extracellular Matrix Dynamics. *Nat Rev Mater* (2016) 1(2):15012. doi:10.1038/natrevmats.2015.12
431. Truby RL, and Lewis JA. Printing Soft Matter in Three Dimensions. *Nature* (2016) 540(7633):371–8. doi:10.1038/nature21003

Conflict of Interest: The author declares that the research was conducted in the absence of any commercial or financial relationships that could be construed as a potential conflict of interest.

frontiers in Physics

ORIGINAL RESEARCH
published: 24 November 2021
doi: 10.3389/fphy.2021.775465

3D Computational Modeling of Bleb Initiation Dynamics

Wanda Strychalski *

Department of Mathematics, Applied Mathematics, and Statistics, Case Western Reserve University, Cleveland, OH, United States

Blebbing occurs in cells under high cortical tension when the membrane locally detaches from the actin cortex, resulting in pressure-driven flow of the cytosol and membrane expansion. Some cells use blebs as leading edge protrusions during cell migration, particularly in 3D environments such as a collagen matrix. Blebs can be initiated through either a localized loss of membrane-cortex adhesion or ablation of the cortex in a region. Bleb morphologies resulting from different initiation mechanisms have not been studied in detail, either experimentally or with theoretical models. Additionally, material properties of the cytoplasm, such as elasticity, have been shown to be important for limiting bleb size. A 3D dynamic computational model of the cell is presented that includes mechanics and the interactions of the cytoplasm, the actin cortex, the cell membrane, and the cytoskeleton. The model is used to quantify bleb expansion dynamics and shapes that result from simulations using different initiation mechanisms. The cytoplasm is modeled as a both viscous fluid and as a poroelastic material. Results from model simulations with a viscous fluid cytoplasm model show much broader blebs that expand faster when they are initiated via cortical ablation than when they are initiated by removing only membrane-cortex adhesion. Simulation results using the poroelastic model of the cytoplasm provide qualitatively similar bleb morphologies regardless of the initiation mechanism. Parameter studies on bleb expansion time, cytoplasmic stiffness, and permeability reveal different scaling properties, namely a smaller power-law exponent, in 3D simulations compared to 2D ones.

Keywords: cytoplasm, biomechanics, blebs, poroelasticity, fluid-structure interaction

OPEN ACCESS

Edited by:
Yuan Lin,
The University of Hong Kong, Hong Kong SAR, China

Reviewed by:
Chao Fang,
The University of Hong Kong, Hong Kong SAR, China
Thomas E. Woolley,
Cardiff University, United Kingdom

***Correspondence:**
Wanda Strychalski
wis6@case.edu

Specialty section:
This article was submitted to Biophysics, a section of the journal Frontiers in Physics

Received: *14 September 2021*
Accepted: *25 October 2021*
Published: *24 November 2021*

Citation:
Strychalski W (2021) 3D Computational Modeling of Bleb Initiation Dynamics. Front. Phys. 9:775465. doi: 10.3389/fphy.2021.775465

1 INTRODUCTION

Blebs are round membrane protrusions that are used in important cellular processes, such as migration [1] and cytokinesis [2, 3]. The hallmark of a bleb is a separation of the cell membrane from the cortex, a thin layer of actin cytoskeleton that is normally attached to the cell membrane by linker proteins. Cells that bleb typically have high intracellular pressure compared to outside the cell. The source of this pressure is attributed to cortical tension due to the myosin molecular motors that slide actin filaments with respect to each other [4]. A bleb is initiated in a localized region by either a loss of membrane-cortex adhesion or by a defect in the actin cortex caused by laser ablation [5] or myosin-driven contractility [1]. After a bleb is nucleated, contractile stresses within the cortex are no longer transmitted to the membrane in this localized region, resulting in a pressure gradient and cytoplasmic flow that expands the membrane to create a bleb. A bleb is fully expanded after about 30 s [1], but the timescale is considerably shorter for cells such as *Dictyostelium discoideum*, where bleb expansion can occur in as little as 0.2 s [6]. Cortical components such as actin and myosin

then diffuse into the bleb, the cortex reforms under the naked membrane, and the bleb retracts. During cell migration, the bleb may not retract because adhesion to the substrate (or ECM) may stabilize the bleb.

Theoretical modeling of blebbing has addressed various aspects of the process including expansion [7–10], retraction [11, 12], and migration [13–15]. One class of models is based on fluid-structure interaction, where the elastic membrane and cortex are immersed in fluid. Deformations of the elastic structures affect the fluid flow, and the fluid flow in turn influences the motion of the structures. First we summarize results from this approach using two-dimensional models. Using the framework of the immersed boundary (IB) method [16], simulation results from one model showed that cytoskeletal (cortical) drag, and not the viscosity of the cytoplasm, determined the timescale of bleb expansion [7]. When the cytoplasm was modeled as a poroelastic material, two bleb experiments from [5] were simulated. Results from these experiments found that the second bleb was approximately 30% smaller than the first bleb regardless of the location of the second bleb with respect to the first one. The authors found these experimental results could be explained by an initial fast time scale for pressure propagation across the cell combined with a slow timescale for pressure equilibration [9]. The models from [13, 17] follow a similar approach from [7, 9], but used a boundary integral method instead of the immersed boundary method. The authors simulated cell migration using blebs in confined and unconfined environments (swimming). A 2D agent-based model from [14, 18] was used to simulate blebbing-based migration. This model focused on interactions of the cell with different environments, and intracellular pressure was constant in simulations.

Several models consider membrane dynamics in blebbing cells [19–21]. These models assume a constant or specified intracellular pressure in the membrane energy. The 1D membrane model from [19] was used to find minimum conditions on pressure and membrane length for bleb nucleation, while the model from [20] found that membrane-cortex adhesion was critical in determining bleb initiation. The model from [19] was also used to quantify conditions for "circus" blebs that travel around the periphery of the cell. The 2D membrane model from [21] found conditions for circus bleb velocity in terms of biophysical parameters and was used to hypothesize that heterogeneity within the cell surface was necessary to maintain compact circus blebs.

Blebbing dynamics have been modeled in 3D for some simplified cases. The models in [8, 12, 15, 22] assume the cell is axisymmetric and intracellular pressure is constant. In the continuum mechanics model from [8], the membrane reference configuration was dynamically updated to maintain small increases in the area of the cell membrane. A similar approach that involved updating the membrane and cortical reference configuration to model bleb retraction was presented in [12]. In order to produce "small-necked" blebs observed in experiments, the authors in [22] needed to include either localized membrane growth or global cortical contraction. In a different approach, molecular dynamics simulations of a surface particle-based model were used to simulate bleb expansion in [23]. The authors determined that bleb formation

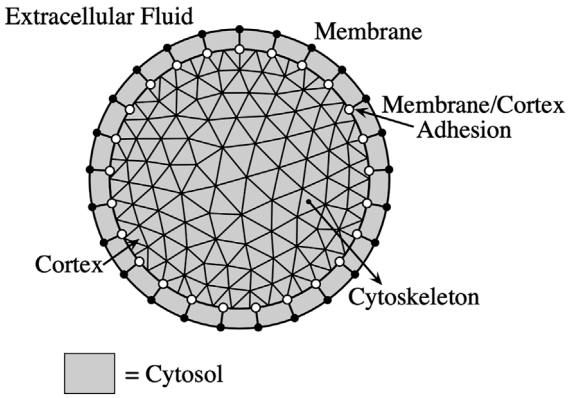

FIGURE 1 | Bleb model schematic. Circles indicate the discretized membrane and cortex. The triangular grid represents the discretized cytoskeletal network (cortex/cytoskeletal adhesion not shown).

is energetically favorable when the membrane area is larger than its attached cortical area. A membrane model of bleb expansion was simulated with a boundary integral method in [10]. Simulations showed conditions where either no bleb was nucleated, a bleb was nucleated without membrane peeling, and a bleb was nucleated with additional membrane peeling. Although this model included membrane-cortex adhesion dynamics, the membrane was assumed to be axisymmetric and the cortex was fixed in space. A model of bleb expansion that included reaction-diffusion of membrane-cortex adhesion proteins with limited membrane deformation was presented in [24]. Lastly, a full 3D model of bleb expansion with a viscous fluid cytoplasm (an extension of the model in [7]) was presented in [25] to illustrate a numerical method for computing forces on an elastic shell using the immersed boundary method [26].

All of the aforementioned studies highlight the importance of intracellular pressure and mechanics of different cellular components in blebbing dynamics. I consider blebs similar to those in experiments from [5], namely a single cell with one bleb without interactions to an extracellular matrix. These blebs expand on the order of 10 s. The contribution of this paper is a 3D dynamic model of bleb expansion that includes the mechanics of the membrane, cortex, and cytoplasm. In particular, the model presented here includes a dynamic cortex, different cytoplasmic models (viscous fluid and poroelastic material), and makes no *a priori* axisymmetric assumptions. I then use the model to simulate different bleb initiation using two different mechanisms: cortical ablation and loss of membrane-cortex adhesion. The 3D model with a poroelastic cytoplasm is then simulated to determine whether pressure dynamics follow the same behavior and scaling as described models in 1D [27] and 2D [9].

2 MATERIALS AND METHODS

2.1 Overview of Model

The mathematical model of the cell consists of the membrane, cortex, membrane-cortex adhesion, and cytoplasm (see **Figure 1**).

In particular, I consider two models of the cytoplasm: a viscous fluid model and a poroelastic model. In the poroelastic model, the cytoplasm includes a permeable elastic cytoskeleton. Detailed descriptions of the 2D models can be found in [7, 9]. The models are summarized here with detailed descriptions of notable differences between the 2D and 3D models.

The cell membrane is modeled as an impermeable elastic structure that moves with the velocity of the cytosol (fluid portion of the cytoplasm) while the cortex and the cytoskeleton (in the case of the poroelastic model) are modeled as permeable elastic materials. The model equations consist of force balances on the liquid cytosol, cell cortex, and cytoskeleton, constitutive equations, and equations of motion for the structures. The membrane and cortex are represented by continuous 2D infinitely thin shells immersed in a 3D fluid domain. The cytoskeleton is represented by a 3D structure immersed in the fluid.

The immersed boundary (IB) method is used to account for the interactions between the components of the cell and cytosol/cytoplasm [16]. In the IB method, structures such as the membrane are represented in a moving, Lagrangian coordinate system, while fluid variables such as cytosolic velocity and pressure are located on a fixed, Eulerian coordinate system. A surface force density on an immersed structure is communicated to the fluid coordinates as follows,

$$\boldsymbol{f} = \mathcal{S}\boldsymbol{F} = \int_{\Gamma} \boldsymbol{F}(\boldsymbol{s},t)\delta(\boldsymbol{x} - \boldsymbol{X}(\boldsymbol{s},t))\, d\boldsymbol{s}, \tag{1}$$

where $\boldsymbol{s} \in \Gamma$ is the material coordinate and $\boldsymbol{X}(\boldsymbol{s}, t)$ denotes the physical position of material point $\boldsymbol{s}$ at time t. The interpolation operator is given by

$$\boldsymbol{U} = \mathcal{S}^{*}\boldsymbol{u} = \int_{\Omega} \boldsymbol{u}(\boldsymbol{x},t)\delta(\boldsymbol{x} - \boldsymbol{X}(\boldsymbol{s},t))d\boldsymbol{x}, \tag{2}$$

where Ω represents the fluid domain. In this paper, capitalized letters represent Lagrangian variables and lower case letters indicate Eulerian variables.

2.1.1 Viscous Fluid Cytoplasm Model

The model of bleb expansion in [7] consisted of the cell membrane modeled as an impermeable elastic stucture, the actin cortex treated as a one-dimensional poroelastic structure attached to the membrane, and the cytoplasm modeled as a viscous fluid. A 3D extension of this model was published in [25] to demonstrate different methods for computing forces on a deforming surface. In this paper, I use the approach from [28] to compute forces due to elasticity on the cortex instead of the method in [25]. The fluid equation includes terms from the elastic membrane, membrane-cortex adhesion, and drag with cortex:

$$\mu\Delta\boldsymbol{u} - \nabla p + \boldsymbol{f}_{\text{elastic}}^{\text{mem}} + \boldsymbol{f}_{\text{adh}}^{\text{mem/cortex}} + \boldsymbol{f}_{\text{drag}}^{\text{cortex}} = \boldsymbol{0}, \tag{3}$$

$$\nabla \cdot \boldsymbol{u} = 0, \tag{4}$$

where $\boldsymbol{u}$ represents fluid velocity, p pressure, and $\boldsymbol{f}_i$ denotes force density on the fluid grid. Force densities due to membrane elasticity, membrane-cortex adhesion, and cortical drag are computed on their respective Lagrangian structures, then are spread onto the fluid grid using **Eq. 1**.

The drag force on the cortex is balanced by elastic forces within the cortex and adhesion to the membrane:

$$\boldsymbol{F}_{\text{drag}}^{\text{cortex}} + \boldsymbol{F}_{\text{elastic}}^{\text{cortex}} + \boldsymbol{F}_{\text{adh}}^{\text{cortex}} = \boldsymbol{0}. \tag{5}$$

The drag force density from the cortex moving through the fluid is explicitly given by

$$\boldsymbol{F}_{\text{drag}}^{\text{cortex}} = \xi\,(\mathcal{S}^{*}\boldsymbol{u} - \boldsymbol{U}_{\text{cortex}}), \tag{6}$$

and the drag force density on the fluid is related to the cortex drag force density by

$$\boldsymbol{f}_{\text{drag}}^{\text{cortex}} = -\mathcal{S}\boldsymbol{F}_{\text{drag}}^{\text{cortex}}. \tag{7}$$

The membrane and cortex are each modeled as a hyperelastic shell that experiences forces due to surface tension and stretching. This model is consistent with [29], where the surface area of membrane on a bleb was shown to increase during expansion. A hyperelastic material is characterized by an energy functional $E = \int_{\Gamma_0} W\, d\boldsymbol{q}$, where W is a given strain energy density and Γ_0 represents the reference configuration of the surface. In our model, the total membrane energy density is $E := E_{NH} + E_{ST}$, where E_{NH} represents the neo-Hookean strain energy density and E_{ST} represents the surface tension strain energy density. Bending forces are neglected because several studies have shown that they do not contribute significantly to blebbing mechanics [10, 30]. Following the formulation from [28], the neo-Hookean surface strain energy density is given by

$$\begin{aligned} E_{NH} :=& \frac{k_E}{2}\int_{\boldsymbol{s}} (J-1)^2\,(\det G_0)^{1/2}\, d\boldsymbol{s} \\ &+ \frac{\mu_E}{2}\int_{\boldsymbol{s}} \left(\operatorname{tr}(GG_0)^{-1}J^{-1} - 2\right)(\det G_0))^{1/2}\, d\boldsymbol{s}, \end{aligned} \tag{8}$$

where k_E is the bulk modulus, μ_E is the shear modulus and $\boldsymbol{s} = (s_1, s_2)$ represents the surface material coordinates. The following tensors G and G_0 are defined as

$$G: = \left(\frac{\partial \boldsymbol{X}}{\partial \boldsymbol{s}}\right)^{T}\left(\frac{\partial \boldsymbol{X}}{\partial \boldsymbol{s}}\right) \qquad G_0 := \left(\frac{\partial \boldsymbol{Z}}{\partial \boldsymbol{s}}\right)^{T}\left(\frac{\partial \boldsymbol{Z}}{\partial \boldsymbol{s}}\right), \tag{9}$$

where $\boldsymbol{X}(\boldsymbol{s})$ denotes the current surface position, $\boldsymbol{Z}(\boldsymbol{s})$ denotes the reference membrane position, and the scalar $J = (\det(GG_0^{-1}))^{-1}$. Energy due to surface tension is

$$E_{ST} := \gamma_i \int_{\boldsymbol{s}} (\det G)^{1/2}\, d\boldsymbol{s}, \tag{10}$$

where γ_i represents the parameter for surface tension on the membrane or cortex. The force density per unit reference configuration is then computed by

$$F_{\text{elastic}}^{i} = -\frac{\delta E}{\delta \boldsymbol{X}}(\boldsymbol{s},t), \tag{11}$$

where i indicates either the membrane or the cortex.

Membrane-cortex adhesion is modeled by elastic springs attaching the membrane to the cortex with force density

TABLE 1 | Default model parameters for the blebbing model. Values for the shear modulus were taken to be the same value as those listed for the bulk modulus for the membrane, cortex, and cytoskeleton, respectively.

Symbol	Quantity	Value	Source
r_{mem}	Cell radius	10 μm	[5]
r_{cortex}	Cortex radius	9.99 μm	[9]
γ_{mem}	Membrane surface tension	20 pN/μm	[5]
k_{mem}	Membrane bulk modulus	20–40 pN/μm	[9]
γ_{cortex}	Cortical tension	200 pN/μm	[5]
k_{cortex}	Cortical bulk modulus	1,000 pN/μm	
k_{cyto}	Cytoskeletal bulk modulus	2.5–10 $\cdot$ 10^2 Pa	[4, 9]
$k_{\text{adh}}^{\text{mem/cortex}}$	Membrane/cortex adhesion stiffness coefficient	4 $\cdot$ 10^3 pN/μm^3	
$k_{\text{adh}}^{\text{cortex/cyto}}$	Cortex-cytoskeleton adhesion	1 $\cdot$ 10^4 pN/μm^3	
μ	Cytosolic viscosity	0.01 Pa-s	[4, 5, 31]
ξ	Cortical drag coefficient	10 pN-s/μm^3	[7]
κ	Cytoskeletal permeability	0.5–2 $\cdot$ 10^{-3} μm^2	[4, 9]

$$\boldsymbol{F}_{\text{adh}}^{\text{mem/cortex}} = k_{\text{adh}}^{\text{mem/cortex}}\left(|\boldsymbol{X}_{\text{mem}} - \boldsymbol{X}_{\text{cortex}}|\right)\frac{\boldsymbol{X}_{\text{mem}} - \boldsymbol{X}_{\text{cortex}}}{|\boldsymbol{X}_{\text{mem}} - \boldsymbol{X}_{\text{cortex}}|}. \quad (12)$$

The membrane-cortex adhesion stiffness coefficient $k_{\text{adh}}^{\text{mem/cortex}}$ was chosen so that the cortex and membrane are within a computational grid cube of each other and velocity of the cortex is close to zero if no bleb is initiated. The adhesion force density on the membrane is the opposite of the corresponding force density on the cortex. The adhesion force densities satisfy the equation

$$\int_{\Omega} \mathcal{S}\boldsymbol{F}_{\text{adh}}^{\text{mem/cortex}}\, d\boldsymbol{x} + \int_{\Omega} \mathcal{S}\boldsymbol{F}_{\text{adh}}^{\text{cortex/mem}}\, d\boldsymbol{x} = 0. \quad (13)$$

Given the stiffness coefficient $k_{\text{adh}}^{\text{mem/cortex}}$, the corresponding stiffness coefficient for the cortex is obtained by $k_{\text{adh}}^{\text{cortex/mem}} = k_{\text{adh}}^{\text{mem/cortex}} dA_j^{\text{mem}}/dA_j^{\text{cortex}}$, where dA_j^i represents the surface area differential of the jth triangle of the membrane or cortex in reference coordinates.

Given a configuration of the membrane and cortex, the forces are computed, and the velocities of the fluid and cortex are obtained by solving **Eq. 3** and **Eq. 5** as described in **Section 2.2**. Then, the positions of the membrane and cortex are updated with their respective velocities.

$$\frac{d\boldsymbol{X}_{\text{mem}}}{dt} = \mathcal{S}^{\star}\boldsymbol{u} = \boldsymbol{U}, \quad (14)$$

$$\frac{d\boldsymbol{X}_{\text{cortex}}}{dt} = \frac{1}{\xi}\left(\boldsymbol{F}_{\text{elastic}}^{\text{cortex}} + \boldsymbol{F}_{\text{attach}}^{\text{cortex/mem}}\right) + \boldsymbol{U} = \boldsymbol{U}_{\text{cortex}}. \quad (15)$$

Table 1 lists the default parameters for blebbing simulations. The values for membrane and cortex surface tension were decreased by 50% compared to the values in [9] so that the initial pressure difference across the membrane matches the difference in the 2D model. The bulk modulus of the cortex was taken to be several orders of magnitude higher than the membrane to reflect stiffness due to the cross-linked cortical actin network.

2.1.2 Poroelastic Cytoplasm Model

The model formulation is the same as above with the addition of a poroelastic cytoplasm throughout the cell interior (a 2D version of the model is described in [9, 32]). The cytoskeleton is represented by a porous elastic network in **Figure 1**). The fluid equations have an additional term for cytoskeletal drag.

$$\mu\Delta\boldsymbol{u} - \nabla p + \boldsymbol{f}_{\text{elastic}}^{\text{mem}} + \boldsymbol{f}_{\text{adh}}^{\text{mem/cortex}} + \boldsymbol{f}_{\text{drag}}^{\text{cortex}} + \boldsymbol{f}_{\text{drag}}^{\text{cyto}} = \boldsymbol{0}, \quad (16)$$

$$\nabla \cdot \boldsymbol{u} = 0. \quad (17)$$

The force density balance on the cortex includes an additional adhesion term to link the cortex to the cytoskeleton,

$$\boldsymbol{F}_{\text{drag}}^{\text{cortex}} + \boldsymbol{F}_{\text{elastic}}^{\text{cortex}} + \boldsymbol{F}_{\text{adh}}^{\text{cortex/}mem} + \boldsymbol{F}_{\text{adh}}^{\text{cortex/cyto}} = \boldsymbol{0}. \quad (18)$$

Similarly, the force density balance on the cytoskeleton is

$$\boldsymbol{F}_{\text{drag}}^{\text{cyto}} + \boldsymbol{F}_{\text{elastic}}^{\text{cyto}} + \boldsymbol{F}_{\text{adh}}^{\text{cyto/cortex}} = \boldsymbol{0}, \quad (19)$$

where cytoskeletal drag is defined as

$$\boldsymbol{F}_{\text{drag}}^{\text{cyto}} = \frac{\mu}{\kappa}\left(\boldsymbol{U}_{\text{cyto}} - \mathcal{S}^{\star}\boldsymbol{u}\right), \quad (20)$$

where κ is the permeability of the cytoskeleton. In this formulation of poroelasticity, the volume fraction of the network (cytoskeleton) is negligible [32].

The cytoskeleton is modeled as a porous, neo-Hookean elastic structure. Elastic forces are computed using the energy functional-based version of the IB method proposed in [33]. The neo-Hookean strain energy is the same as given in **Eq. 8**, but the 2 $\times$ 2 tensors G and G_0 now have dimensions 3 $\times$ 3 for the solid cytoskeleton. The equivalence of the solid and surface neo-Hookean energy formulas is described in [28].

The force density for cortex-cytoskeleton adhesion is computed similarly to cortex-membrane adhesion in **Eq. 12** with the appropriate scaling of the force densities. Given the stiffness coefficient for cortex-cytoskeleton adhesion $k_{\text{adh}}^{\text{cortex/cyto}}$, we have $k_{\text{adh}}^{\text{cyto/cortex}} = k_{\text{adh}}^{\text{cortex/cyto}} dA_i^{\text{cortex}}/dV_i^{\text{cyto}}$, where dV_i^{cyto} represents the reference volume differential of the cytoskeleton at the ith point of a tetrahedron.

The structures are updated with their respective velocities.

$$\frac{d\boldsymbol{X}_{\text{mem}}}{dt} = \mathcal{S}^{\star}\boldsymbol{u} = \boldsymbol{U}, \quad (21)$$

$$\frac{d\boldsymbol{X}_{\text{cortex}}}{dt} = \frac{1}{\xi}\left(\boldsymbol{F}_{\text{elastic}}^{\text{cortex}} + \boldsymbol{F}_{\text{adh}}^{\text{cortex/mem}} + \boldsymbol{F}_{\text{adh}}^{\text{cortex/cyto}}\right) + \boldsymbol{U} = \boldsymbol{U}_{\text{cortex}}, \quad (22)$$

$$\frac{d\boldsymbol{X}_{\text{cyto}}}{dt} = \frac{\kappa}{\mu}\left(\boldsymbol{F}_{\text{elastic}}^{\text{cyto}} + \boldsymbol{F}_{\text{adh}}^{\text{cyto/cortex}}\right) + \boldsymbol{U} = \boldsymbol{U}_{\text{cyto}}. \quad (23)$$

Table 1 lists the values of parameters for blebbing simulations. Most simulations in the Results section use a value of 20 pN/μm for membrane stiffness, 500 Pa for k_{cyto}, and 1 $\cdot$ 10^{-2} μm^2 for permeabilty.

2.2 Numerical Formulation

Fluid variables (components of velocity and pressure) are discretized on an Eulerian grid of size $[0, 30] \times [0, 30] \times [0, 35]$ μm and spacing $h = 30/32$. The cytoskeleton is represented by an adaptive unstructured tetrahedral mesh with radius 9.99 μm. The mesh is more refined near the cortex with approximately two Lagrangian points per Eulerian grid cell and one Lagrangian point per Eulerian grid cell in the interior. The mesh consists of 28,153 points and 153,202 tetrahedra. The cortex is taken to be the boundary of the cytoskeleton, and membrane points are initialized to be the same as cortical points, except adjusted to have a radius of 10 μm. The membrane and cortex each consisted of 5,018 points and 10,032 triangles. The unstructured meshes were generated using distmesh [34].

To compute elastic forces on the membrane, cortex, and cytoskeleton, methods from [28, 33] are implemented. Elastic forces are computed directly from an energy functional without the use of stress tensors by taking the variational derivative of the energy (see **Eq. 11**). I assume the deformation map $\boldsymbol{X}(\boldsymbol{s}, t)$ is a piecewise linear function on each triangle of a discretized surface (tetrahedron in the cytoskeleton) so that the deformation gradient tensor and strain energy are constant on each triangle (or tetrahedron). This simplifies the integral of the strain energy density in **Eq. 8** and **Eq. 10**. The variational derivative in **Eq. 11** can then be computed analytically on each discretized element, and the force at each vertex i is the sum of all elements that contain i. Details for computing forces due to shell elasticity can be found in [28], and details for computing the forces due to the elasticity of a solid are located in [32, 33].

The time update follows [9, 32]. Given the current position of the structures (membrane, cortex, and cytoskeleton):

1. Compute elastic forces based on the current membrane, cortex, and cytoskeleton configuration ($\boldsymbol{X}_i^n = \boldsymbol{X}_i(\boldsymbol{s}, t^n)$, where i denotes the structure: membrane, cortex, or cytoskeleton) using the constitutive laws described in **Section 2.1**.
2. Spread the force densities onto nearby Eulerian points using **Eq. 1**.
3. Solve the forced Stokes equations to obtain the fluid velocity $\boldsymbol{u}$.
4. Interpolate the fluid velocity to the structure using **Eq. 2** to obtain $\boldsymbol{U}$.
5. Compute the porous structure velocities by **Eq. 15** and **Eq. 23**, and update the structure by

$$\boldsymbol{X}_i^{n+1} = \boldsymbol{X}_i^n + \Delta t\left(\frac{1}{\zeta_i}\sum_j \boldsymbol{F}_i^j + \boldsymbol{U}\right), \tag{24}$$

where ζ_i indicates the drag coefficient of the cortex or cytoskeleton, and the forces acting on the respective structure denoted by $\sum \boldsymbol{F}_i^j$ are in **Eq. 15** and **Eq. 23**. The membrane is updated by the fluid velocity.

The time step for simulations using a pure fluid cytoplasm is $\Delta t = 1 \cdot 10^{-4}$ (seconds). Cytoplasmic elasticity introduces significant stiffness in the model, and the time step is reduced to $\Delta t = 7.5 \cdot 10^{-6} - 3 \cdot 10^{-5}$. Small time steps are required for numerical stability when cytoplasmic permeability and/or elastic moduli are relatively large.

Velocity and pressure satisfy periodic boundary conditions on the Eulerian (fluid) domain. A Fourier-spectral method is used to solve the Stokes equations (**Eq. 3** and **Eq. 4**) for the viscous fluid model, **Eq. 16** and **Eq. 17** for the poroelastic fluid model).

The IB method involves approximate δ functions for the spreading and interpolating operators in **Eq. 1** and **Eq. 2** . Here, I use spectral delta functions as described in the Supporting Material of [9] to avoid unphysical velocities that occur in regions with a large pressure jump, such as across the cell membrane. The discretized spreading and interpolation integrals are approximated in Fourier space by a nonuniform fast Fourier transform (NUFFT) described in [35]. The result yields obtain a computationally efficient approximation of the Fourier transform of the spread force density. I use an mth order cardinal B-spline with compact support over $m + 1$ mesh points as a smoothing kernel [36]. In this paper, the oversampling factor is $r = 1.5$ and $m = 6$. The Fourier transform of the spread forces are filtered with a second-order raised cosine filter [37],

$$\sigma(k) = \frac{1}{2}\left(1 + \cos\left(\frac{2\pi k}{N}\right)\right), \tag{25}$$

to remove the Gibbs phenomenon in the numerical solution to the pressure field.

3 RESULTS

At the beginning of a simulation, the cell is pressurized due to membrane and cortical tension. According to Laplace's law, the change in pressure ΔP across a spherical membrane satisfies $\Delta P = \gamma/(2R)$, where γ represents surface tension and R is the radius of the cell. Here, $\Delta P \approx (\gamma_{\text{mem}} + \gamma_{\text{cortex}})/(2\ r_{\text{mem}}) = 44$ Pa.

A bleb is initiated by either removing membrane-cortex adhesion in a circular region at the top of the cell or by cortical ablation (see **Figure 2**). The initial radius of the circle is approximately 2.5 μm and centered at the point on the membrane with the highest z-coordinate. Numerically, $k_{\text{adh}}^{\text{mem/cortex}} = k_{\text{adh}}^{\text{cortex/mem}} = 0$ on surface triangles inside the region. The boundary between adjacent triangles on the surface where the membrane-cortex adhesion parameters change from nonzero to zero forms a round circular ring around the cell, referred to as the bleb ring. **Figure 2C**) shows a top down view of the cell with a dashed line indicating the bleb ring. When the cortex is ablated, the additional parameters $k_{\text{cortex}} = 0$, $k_{\text{adh}}^{\text{cortex/cyto}}$, and $k_{\text{adh}}^{\text{cyto/cortex}}$ are set to zero on triangles within the bleb ring.

For both initiation mechanisms, when cortical tension is no longer transmitted to the membrane, the resulting pressure gradient leads to fluid flow and membrane expansion in the localized region. Bleb expansion ceases when membrane tension balances intracellular pressure.

Parameter values for simulations are located in **Table 1**. Unless otherwise indicate, all simulations with a fluid cytoplasm use a value of 20 pN/μm for the membrane bulk modulus. Likewise, all simulations with a poroelastic

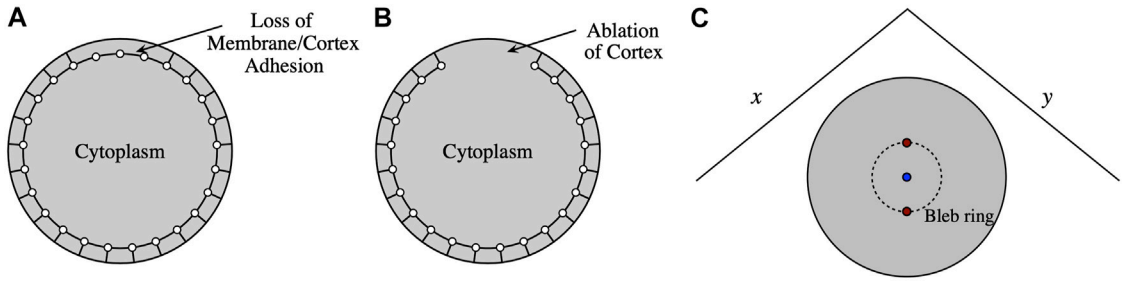

FIGURE 2 | A bleb is initiated by either **(A)** loss of membrane-cortex adhesion or **(B)** cortical ablation. **(C)** Top down view of the cell. For **(A)**, membrane-cortex adhesion parameters are set to zero within the bleb ring region, whereas for **(B)** cortical stiffness and cortex-cytoskeleton adhesion parameters are also set to zero within the bleb region (inside the dashed-line circle). The two red points are used to compute the relative change in bleb ring diameter. The blue circle shows the point with the largest *z*-coordinate on the cell that is used to compute bleb height.

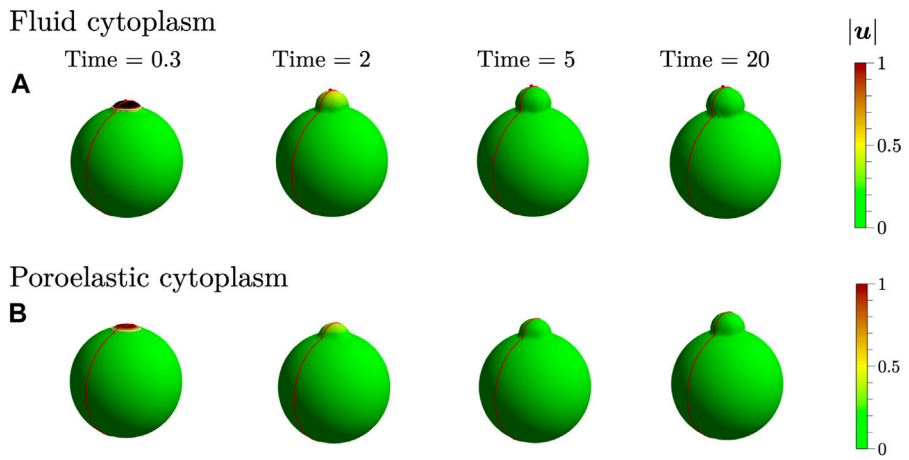

FIGURE 3 | A bleb is initiated by a loss of membrane-cortex adhesion within the bleb ring region using **(A)** a pure fluid cytoplasm and **(B)** a poroelastic cytoplasm. The colorbar indicates the speed of the cell membrane in μm/s. The white ring at the top of the cell at 0.3 s indicates the initial location of the bleb ring. The red curve indicates the *xz*-plane that intersects the cell membrane to generate 2D slices of the pressure field. The red point in **(A)** is used to define bleb height.

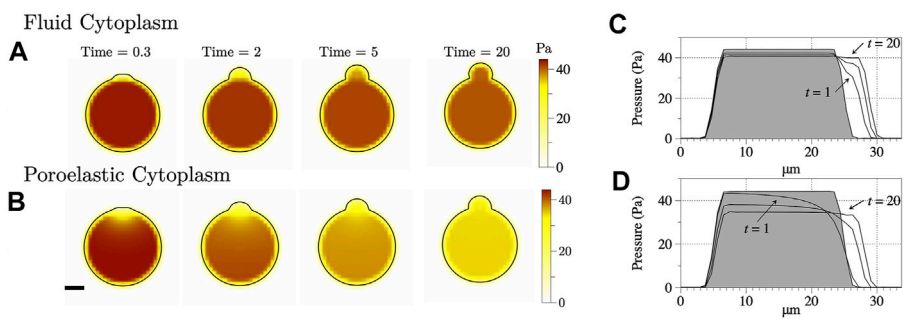

FIGURE 4 | (A–B) Intracellular pressure in the *xz*-plane ($y = 15$) for the simulations from **Figure 3**. The scale bar denotes 5 μm. **(C–D)** Pressure along the line $z = 0$ to 30 for x, $y = 15$. The intermediate time denotes pressure at $t = 2$ s.

cytoplasm use a value of 500 Pa for the bulk modulus of the cytoplasm and $1 \cdot 10^{-3}$ for the cytoskeletal permeability unless otherwise stated.

3.1 Bleb Initiation Dynamics

I begin by simulating bleb expansion by removing only membrane-cortex adhesion within the bleb ring region.

Figure 3 shows the cell membrane position and speed (magnitude of the velocity on the cell membrane) at several time values during bleb expansion. The speed is highest after removing membrane-cortex adhesion and decreases over time. Similar to 2D simulations from [9], the bleb appears smaller in simulations using a poroelastic cytoplasm model compared to the pure fluid model.

Intracellular pressure dynamics are shown in **Figure 4** for bleb simulations using fluid and poroelastic cytoplasm models. Intracellular pressure appears spatially uniform inside the cell body (outside of the bleb) for the simulation with a fluid cytoplasm (**Figures 4A,C**). The maximum pressure inside the cell decreases by about 4 Pa over 40 s of simulation time. For the poroelastic cytoplasm, a pressure gradient extends across the entire cell (**Figures 4B,D**). Pressure also equilibrates to a smaller value: 34 Pa for the poroelastic cytoplasm model compared to 41 Pa for the fluid cytoplasm model. Maximum pressure inside the cell decreases by approximately 10 Pa over 40 s of simulation time. The decrease in intracellular pressure results in decreased fluid speed and bleb size.

Decreased intracellular pressure in the poroelastic cytoplasm is a result of compression of the cytoskeleton as the bleb expands. The total volume of the cell is conserved so that as the bleb expands, the main cell body is compressed. In [9], the cytoskeletal pressure that acts against compressive stresses was given as $-k_{\text{cyto}}(J-1)$, where $J-1$ is the strain in **Eq. 11**. Cytoskeletal pressure at several time values is shown in **Supplementary Figure S1** when $k_{\text{cyto}} = 500$ Pa. Data show the cytoskeletal network is compressed near the nucleation site, and cytoskeletal pressure approaches a spatially nonuniform profile. Cytoskeletal pressure over time when $k_{\text{cyto}} = 250$, 500, and 1,000 Pa at the center of the cell is shown in **Supplementary Figure S2**. The pressure approaches a steady state value and increases with k_{cyto}.

Bleb size is quantified two ways, depending on how the bleb is initiated. When a bleb is initiated through a loss of membrane-cortex adhesion, I measure the relative bleb volume over time. The volume of the cortex is subtracted from the volume of the membrane, then divided by the initial volume of the membrane. Since there is an initial small volume between the membrane and cortex, this small initial volume is subtracted from the relative bleb volume equation, given by

$$\text{Vol}_{\text{bleb}}(t) = \frac{\text{Vol}_{\text{mem}}(t) - \text{Vol}_{\text{cortex}}(t) - (\text{Vol}_{\text{mem}}(0) - \text{Vol}_{\text{cortex}}(0))}{\text{Vol}_{\text{mem}}(0)}. \tag{26}$$

Note that the volume of the membrane is approximately the same value over time due to incompressibility of the fluid.

When a bleb is initiated through cortical ablation, the cortex is no longer a closed surface. I use bleb height as a measurement of bleb size and is defined as follows. The point on the membrane with the largest z-coordinate (see **Figure 3A**) and the point with the smallest z coordinate are identified. Initially, the difference between these z coordinates is the diameter of the cell, 20 μm. The difference between these z coordinates is measured over time. The initial distance is then subtracted from the difference between the z values,

$$\text{Height}_{\text{bleb}}(t) = z^{\text{mem}}_{\text{top}}(t) - z^{\text{mem}}_{\text{bottom}}(t) - \left(z^{\text{mem}}_{\text{top}}(0) - z^{\text{mem}}_{\text{bottom}}(0)\right). \tag{27}$$

Bleb height, relative bleb volume, and maximum intracellular pressure over time are shown in **Figure 5** for blebbing simulations using the viscous fluid and poroelastic cytoplasm models. Bleb height and volume initially increase after bleb nucleation, then approach a steady state value. In this paper, steady state is defined as a quantity having less than 5% relative change over 10 s of simulation time. Following [9], bleb expansion time is defined as 90% of the steady state value. White circles in **Figure 5A** indicate bleb expansion time using bleb height, and black circles in **Figure 5B** denote bleb expansion time defined as 90% of steady state relative bleb volume. Bleb height and volume are larger for the viscous fluid cytoplasm model compared to the poroelastic one. Bleb expansion time is also faster in simulations using the viscous fluid cytoplasm model.

Maximum intracellular pressure decreases over time as the bleb expands for simulations with fluid and poroelastic cytoplasm models, but significantly more pressure is relieved when bleb expansion is simulated using a poroelastic cytoplasm model (**Figures 4**, **5C**). To determine the time scale of pressure equilibration, the change in pressure from its initial value over 40 s is measured (approximately 4 Pa for a simulation with a fluid cytoplasm and 10 Pa for a simulation with a poroelastic cytoplasm). Pressure equilibration time is computed as the time when the maximum intracellular pressure equals the initial value minus 90% of the change in pressure over 40 s. **Figure 5C**) shows maximum intracellular pressure evaluated at pressure equilibration time, bleb expansion time using bleb height, and bleb expansion time using relative bleb volume. The data show close agreement between pressure equilibration time and bleb expansion time using relative bleb volume. Although bleb expansion time using bleb height is about 5 s faster than pressure equilibration time, 80% of the change in pressure is achieved by this time for simulations with both the fluid cytoplasm and poroelastic cytoplasm models. Therefore, bleb expansion time measured by using height or relative volume approximately correspond to pressure equilibration time.

3.2 Cortical Ablation

Bleb initiation by cortical ablation is simulated for several values of cortical elastic modulus, $k_{\text{cortex}} = 100$, 500, and 1,000 with both the fluid and poroelastic cytoplasm models. **Figure 6B** shows steady state membrane shape and mean curvature for simulations with cortical ablation. Membrane shape and curvature for bleb expansion by a loss of membrane-cortex adhesion with cortical elastic modulus $k_{\text{cortex}} = 1{,}000$ is shown in **Figure 6A** for comparison. The magnitude of mean curvature is computed along edges of triangles and assigned to vertices as described in [28, 38]. Following [25], the convex hull of the membrane is computed to determine the sign of mean curvature; points on the convex part of the surface are assigned negative mean curvature values, and other points on the membrane maintain their positive sign.

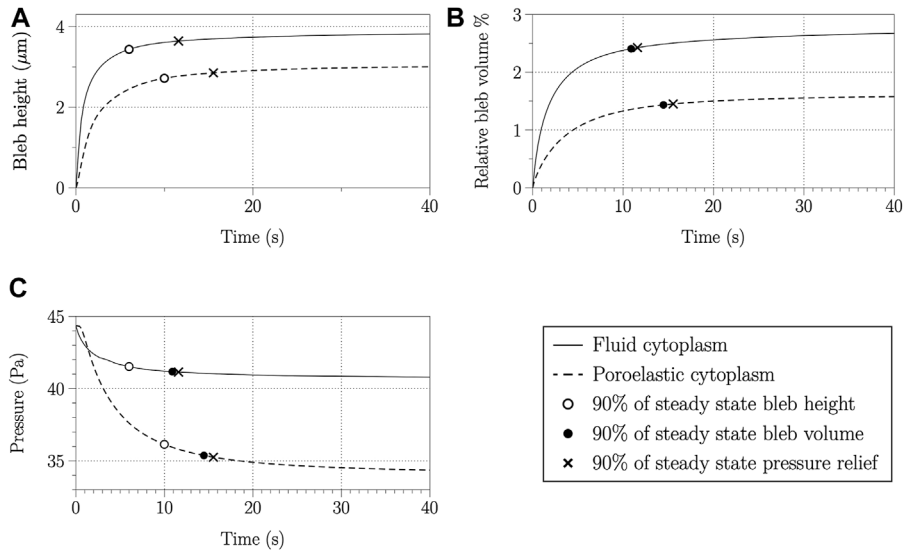

FIGURE 5 | Bleb height **(A)**, relative bleb volume **(B)**, and maximum pressure inside the cell **(C)** over time for a simulation using a fluid cytoplasm (solid lines) and poroelastic cytoplasm (dashed lines). The open circle, filled circle, and × denote the time value when bleb height, relative bleb volume, and maximum pressure, respectively, achieve 90% of their steady state values.

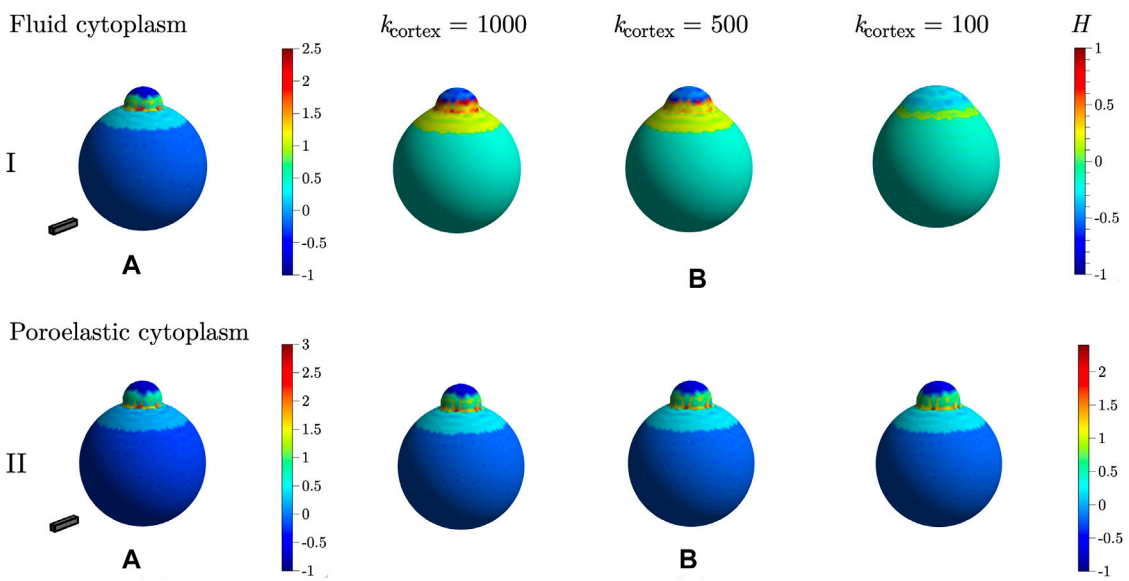

FIGURE 6 | Steady state bleb shapes and mean curvature when a bleb is initiated by **(A)** loss of membrane-cortex adhesion and **(B)** cortical ablation for different values of cortical elastic modulus k_{cortex}. Row I shows results from the fluid cytoplasm, and row II results are from simulations with a poroelastic cytoplasm. For the fluid cytoplasm model, the bulk modulus of the membrane was set to k_{mem} = 40 pN/μm. For the poroelastic cytoplasm model, k_{mem} = 20 pN/μm, k_{cyto} = 500 Pa, and $\kappa = 1 \cdot 10^{-3}$ μm^3. Other parameters are listed in **Table 1**. The scale bar has dimensions 5 × 1 × 1 μm. The colorbar indicates the value of mean curvature H over the surface of the membrane.

Data in **Figure 6** I show that steady state bleb shape is very sensitive to changes in cortical elastic modulus in the fluid cytoplasm model. As the values of cortical elastic modulus decrease, the bleb becomes more broad with a decrease in positive mean curvature near the bleb neck as compared to data when the bleb is initiated by only a loss in membrane-cortex adhesion (**Figure 6IA**). When blebbing is simulated using the poroelastic model, membrane shape and curvature do not change significantly as the cortical elastic modulus decreases. Data in **Figure 6IIB** show slightly broader blebs with a small

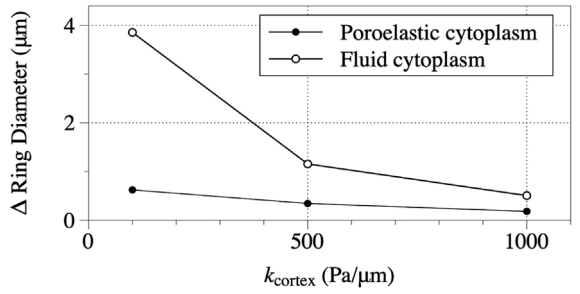

FIGURE 7 | Steady state change in bleb ring diameter for simulations with the fluid cytoplasm model and poroelastic cytoplasm model. Change in bleb ring diameter is defined as bleb ring diameter minus the steady state bleb ring diameter for simulations where blebs were initiated by removing only membrane-cortex adhesion. The bleb ring diameter for the fluid cytoplasm simulation where a bleb is initated by removing only membrane-cortex adhesion is 0.75 μm. The corresponding value for the poroelastic cytoplasm simulation is 0.97 μm. The parameters for the simulations are the same as described in the caption for **Figure 6**.

decrease in positive mean curvature near the bleb neck as compared to membrane shape and mean curvature in **Figure 6IIA**.

To quantity the broadness of the bleb, bleb ring diameter, defined as the distance between the point on the bleb ring closest to origin (in Euclidean distance) and the point furthest away from the origin as illustrated in **Figure 2C**, is computed. The change in bleb ring diameter for cortical ablation simulations is graphed in **Figure 7** for values of cortical elastic modulus, k_{cortex} = 100, 500, and 1,000 with both the fluid and poroelastic cytoplasm models. The change in bleb ring diameter is defined as steady state bleb ring diameter minus the steady state bleb ring diameter for a simulation when a bleb is initiated by a loss of membrane-cortex adhesion with cortical elastic modulus k_{cortex} = 1,000. Data in **Figure 7** show the diameter of the bleb ring increases as the cortical elastic modulus decreases, but the increase is relatively much larger for simulations with the fluid cytoplasm model than for simulations with the poroelastic model.

Bleb expansion time decreases when a bleb is initiated by cortical ablation compared to a loss of membrane-cortex adhesion. Expansion time is calculated by computing the time value when 90% of the steady state value of bleb height is reached. When blebbing is simulated with a fluid cytoplasm and a loss in membrane-cortex adhesion (**Figure 6IA**), bleb expansion time is 1.95 s. In comparison, bleb expansion time from cortical ablation simulations (**Figure 6IB**) is 0.016, 0.023, and 0.028 s for k_{cortex} = 100, 500, and 1,000 pN/μm, respectively. Bleb expansion time for the simulation with a poroelastic cytoplasm model initiated with loss of membrane-cortex adhesion (**Figure 6IIA**) is 10 s. When a bleb is initiated with cortical ablation, bleb expansion time decreases to 7.37, 6.96, and 6.60 s for k_{cortex} = 100, 500, and 1,000 pN/μm, respectively. Data from bleb simulations with a fluid cytoplasm show expansion time decreases by two orders of magnitude compared to simulations when blebbing is initiated by a loss in membrane-cortex adhesion. Simulations from the poroelastic cytoplasm model with cortical ablation show a decrease in bleb expansion time compared to initiation by a loss in membrane-cortex adhesion, but the relative decrease is approximately 30%.

3.3 Effect of Poroelasticity on Bleb Expansion Time

This section focuses on bleb expansion dynamics when the cytoplasm is modeled by poroelastic material, and a bleb is initiated by a loss in membrane-cortex adhesion. Several studies have used a poroelastic model of the cytoplasm to interpret experimental results. For example, when blebbing was locally inhibited by myosin-II-inhibiting drugs, blebbing was unaffected in other parts of the cell, suggesting that intracellular pressure is not equilibrated on the time scale of bleb expansion [27]. Using a simple 1D model, the authors in [27] showed that pressure diffuses over a length $x \sim \sqrt{Dt}$, where x is a characteristic length (10 μm, the radius of the cell), D is a diffusion coefficient proportional to both cytoplasmic permeability and stiffness. This scaling law can be expressed equivalently as bleb expansion time $t \sim x^2/D$. Since D is proportional to κ G, bleb expansion time is expected to scale like κ^{-1}. Simulations from the 2D version of the blebbing model with a poroelastic cytoplasm presented are in approximate agreement with the scaling $t \sim \kappa^{-1}$ [9].

Figure 8 shows bleb expansion time as a function of cytoplasmic permeability κ and bulk elastic modulus G. Expansion time is computed by both relative bleb volume using **Eq. 26** (**Figure 8A**) and bleb height **Eq. 27** (**Figure 8B**). The data show qualitative agreement with results from the 2D model in [9]. Expansion time decreases as cytoplasmic permeability and stiffness increase. Bleb height (and volume) decrease as cytoplasmic stiffness increase. Note that bleb height and volume each maintain the same value for different values of permeability, but change as a function of elastic modulus. One difference from 2D model results is that data in **Figure 8** show bleb expansion time scales slower than κ^{-1}. When relative bleb volume is the metric, expansion time scales like $\sim \kappa^{-0.65}$. If bleb height is used, the scaling is slightly larger, $\sim \kappa^{-0.69}$. These results suggest the cytoskeletal network does not obey a simple diffusion equation in 3D as described in [9, 27].

4 DISCUSSION

In this work, fully 3D simulations of bleb expansion with two different rheological descriptions of the cytoplasm, purely viscous fluid and poroelastic material, are presented. The model formulation follows [9], with significant extensions to model the elasticity of the membrane and cytoskeleton. It should be noted that no geometric simplifications, such as axisymmetry, were made. 3D models allow quantitative comparision to experimental data. For example, values for relative bleb volume reported in **Figure 5** match those computed from experimental data in [5].

3D simulations are necessary to simulate the dynamics of cortical ablation, rupturing the cortical actin shell, which has been performed

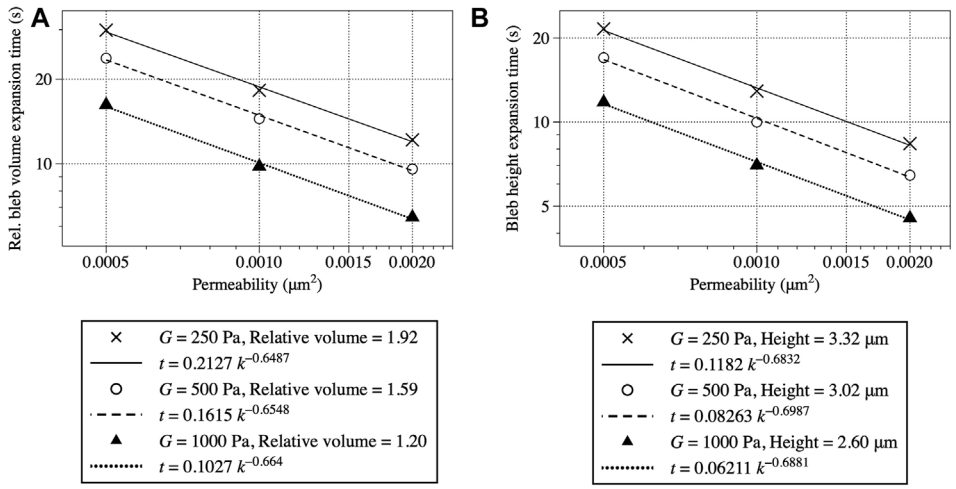

FIGURE 8 | Bleb expansion time in seconds as a function of cytoplasmic bulk modulus G and permeability κ. Bleb expansion is computed using relative bleb volume in **(A)** and bleb height in **(B)**. For both figures, the expansion time is 90% of the steady state value listed in the legend.

in experiments and has been hypothesized to occur due to localized regions of myosin-driven contractility. In a 2D model, the cortex can be thought of as a rubber band that quickly recoils after being cut. In the full 3D model, an additional line tension helps to maintain the structure of the elastic cortical shell. Simulations with a viscous fluid cytoplasm show much broader blebs that expand several orders of magnitude faster than expansion times from experiments. Bleb shape and expansion times in simulations with a poroelastic cytoplasm are qualitatively similar to those when blebbing was initiated with only removing membrane-cortex adhesion. It is energetically unfavorable for the membrane to maintain regions of high curvature, such as those observed in blebs, and these results suggest that the internal cytoskeleton along with attachments from the membrane to the cytoskeleton help maintain the shape of bleb-like protrusions.

In cortical ablation simulations with a viscous fluid cytoplasm, the timescale of bleb expansion is determined primarily by fluid viscosity in the absence of cortical drag [7]. Cytoplasm drag is still present during simulations with a poroelastic cytoplasm when blebs are initiated with cortical ablation. Although bleb expansion is slightly faster compared to the case when blebs are initiated by a loss of membrane-cortex adhesion, cytoplasmic drag dominates the timescale of bleb expansion, and biologically relevant values are obtained from these simulations. The decrease in bleb expansion time can be explained by a loss of cortical drag within the bleb ring region.

Pressure dynamics are quantified for both models of the cytoplasm with qualitatively similar behavior to 2D model simulations results from [9]. Pressure in the main cell body, i.e. the cell except the bleb, is approximately uniform for simulations with a viscous fluid cytoplasm, and diffuses across the cell body in simulations with a poroelastic cytoplasm. Instances of uncontrolled bleb growth for soft membranes were reported in [9] for simulations with a purely viscous cytoplasm. Although I observed large blebs in 3D simulations with a soft membrane (data not shown), I was unable to confirm the growth was actually uncontrolled. As the bleb expands, the spacing between the discretized nodes became too large to obtain reliable results from the simulation. Extending the numerical method to include mesh refinement within the bleb would be necessary to ascertain whether uncontrolled bleb growth can occur in 3D.

In a parameter study where bleb expansion is simulated with different values of permeability and cytoplasmic stiffness, I found that bleb expansion time follows a power law, where $t \sim \kappa^{-p}$, where $p = 0.65, 0.69$, depending on whether bleb volume or height was used to compute expansion time. These results are in contrast to the scaling law calculated from analyzing 2D simulations in [9] and 1D model analysis in [27]. If poroelasticity alone determines the time scale of bleb expansion, it can be shown that cytoskeletal displacement follows a diffusion equation after some simplifying model assumptions, i.e., deformation only in the radial direction and applying a small displacement in the radial direction (a reduced model in polar coordinates is located in [32]). Because the scaling of the diffusion equation remains the same in any dimension, my results point to the influence of other important contributing factors to limiting bleb expansion, such as stiffness of the cortex and membrane, and cortical permeability. The influence of these factors is a subject of future work.

The model presented here is limited in that I consider one cell and focus on the expansion of one bleb to focus on intracellular pressure dynamics with different models of the cytoplasm. Recent work on modeling blebbing-based migration involves simulations with multiple blebs and cycles of bleb expansion and retraction, but assume uniform cytoplasmic pressure [14, 15]. I have also neglected to include membrane-cortex adhesion dynamics [10, 19, 21]. Model extensions are currently underway to include these important effects into the current modeling framework.

Finally, I note that simulations of fully 3D models are computationally expensive; some simulations in this paper took weeks to run using parallelized C++ code on a cluster. Numerical methods for stiff fluid-structure interaction systems will need to be investigated and implemented in order to simulate multiple blebs and cell migration in 3D environments, particularly with an internal elastic cytoskeletal network.

DATA AVAILABILITY STATEMENT

The raw data supporting the conclusions of this article will be made available by the author, without undue reservation.

AUTHOR CONTRIBUTIONS

WS designed the research, developed the model, simulated and analyzed results, and wrote the article.

FUNDING

This work was supported in part by grant #429808 from the Simons Foundation to WS.

ACKNOWLEDGMENTS

This work made use of the High Performance Computing Resource in the Core Facility for Advanced Research Computing at Case Western Reserve University. The author would like to thank Calina A. Copos for providing code for computing elasticity of the cytoskeleton, Ondrej Maxian for providing code to compute membrane elasticity, and Robert D. Guy for helpful discussions.

SUPPLEMENTARY MATERIAL

The Supplementary Material for this article can be found online at: https://www.frontiersin.org/articles/10.3389/fphy.2021.775465/full#supplementary-material

REFERENCES

1. Charras G, Paluch E Blebs lead the Way: How to Migrate without Lamellipodia. *Nat Rev Mol Cel Biol.* (2008) 9:730–6. doi:10.1038/nrm2453
2. Sedzinski J, Biro M, Oswald A, Tinevez J-Y, Salbreux G, Paluch E Polar Actomyosin Contractility Destabilizes the Position of the Cytokinetic Furrow. *Nature* (2011) 476:462–6. doi:10.1038/nature10286
3. Wang X, Li L, Shao Y, Wei J, Song R, Zheng S, et al. Effects of the Laplace Pressure on the Cells during Cytokinesis. *iScience* (2021) 24:102945. doi:10.1016/j.isci.2021.102945
4. Charras GT, Coughlin M, Mitchison TJ, Mahadevan L Life and Times of a Cellular Bleb. *Biophysical J* (2008) 94:1836–53. doi:10.1529/biophysj.107.113605
5. Tinevez J-Y, Schulze U, Salbreux G, Roensch J, Joanny J-F, Paluch E Role of Cortical Tension in Bleb Growth. *Proc Natl Acad Sci* (2009) 106:18581–6. doi:10.1073/pnas.0903353106
6. Ibo M, Srivastava V, Robinson DN, Gagnon ZR. Cell Blebbing in Confined Microfluidic Environments. *PLOS One* (2016) 11:e0163866. doi:10.1371/journal.pone.0163866
7. Strychalski W, Guy RD A Computational Model of Bleb Formation. *Math Med Biol* (2013) 30:115–30. doi:10.1093/imammb/dqr030
8. Woolley TE, Gaffney EA, Oliver JM, Baker RE, Waters SL, Goriely A Cellular Blebs: Pressure-Driven, Axisymmetric, Membrane Protrusions. *Biomech Model Mechanobiol* (2014) 13:463–76. doi:10.1007/s10237-013-0509-9
9. Strychalski W, Guy RD Intracellular Pressure Dynamics in Blebbing Cells. *Biophysical J* (2016) 110:1168–79. doi:10.1016/j.bpj.2016.01.012
10. Fang C, Hui TH, Wei X, Shao X, Lin Y A Combined Experimental and Theoretical Investigation on Cellular Blebbing. *Sci Rep* (2017) 7:16666. doi:10.1038/s41598-017-16825-0
11. Young J, Mitran S A Numerical Model of Cellular Blebbing: a Volume-Conserving, Fluid-Structure Interaction Model of the Entire Cell. *J Biomech* (2010) 43:210–20. doi:10.1016/j.jbiomech.2009.09.025
12. Woolley TE, Gaffney EA, Goriely A Membrane Shrinkage and Cortex Remodelling Are Predicted to Work in harmony to Retract Blebs. *R Soc Open Sci* (2015) 2:150184. doi:10.1098/rsos.150184
13. Lim FY, Koon YL, Chiam K-H A Computational Model of Amoeboid Cell Migration. *Comp Methods Biomech Biomed Eng* (2013) 16:1085–95. doi:10.1080/10255842.2012.757598
14. Tozluoğlu M, Tournier AL, Jenkins RP, Hooper S, Bates PA, Sahai E Matrix Geometry Determines Optimal Cancer Cell Migration Strategy and Modulates Response to Interventions. *Nat Cel Biol.* (2013) 15:751–62. doi:10.1038/ncb2775
15. Woolley TE, Gaffney EA, Goriely A Random Blebbing Motion: A Simple Model Linking Cell Structural Properties to Migration Characteristics. *Phys Rev E* (2017) 96:012409. doi:10.1103/PhysRevE.96.012409
16. Peskin CS Numerical Analysis of Blood Flow in the Heart. *J Comput Phys* (1977) 25:220–52. doi:10.1016/0021-9991(77)90100-0
17. Yip AK, Chiam K-H, Matsudaira P Traction Stress Analysis and Modeling Reveal that Amoeboid Migration in Confined Spaces Is Accompanied by Expansive Forces and Requires the Structural Integrity of the Membrane-Cortex Interactions. *Integr Biol* (2015) 7:1196–211. doi:10.1039/C4IB00245H
18. Tozluoglu M, Mao Y, Bates PA, Sahai E Cost-benefit Analysis of the Mechanisms that Enable Migrating Cells to Sustain Motility upon Changes in Matrix Environments. *J R Soc Interf* (2015) 12:20141355. doi:10.1098/rsif.2014.1355
19. Lim FY, Chiam K-H, Mahadevan L The Size, Shape, and Dynamics of Cellular Blebs. *Epl* (2012) 100:28004. doi:10.1209/0295-5075/100/28004
20. Alert R, Casademunt J Bleb Nucleation through Membrane Peeling. *Phys Rev Lett* (2016) 116:068101. doi:10.1103/PhysRevLett.116.068101
21. Manakova K, Yan H, Lowengrub J, Allard J Cell Surface Mechanochemistry and the Determinants of Bleb Formation, Healing, and Travel Velocity. *Biophysical J* (2016) 110:1636–47. doi:10.1016/j.bpj.2016.03.008
22. Woolley TE, Gaffney EA, Oliver JM, Waters SL, Baker RE, Goriely A Global Contraction or Local Growth, Bleb Shape Depends on More Than Just Cell Structure. *J Theor Biol* (2015) 380:83–97. doi:10.1016/j.jtbi.2015.04.023
23. Spangler EJ, Harvey CW, Revalee JD, Kumar PBS, Laradji M Computer Simulation of Cytoskeleton-Induced Blebbing in Lipid Membranes. *Phys Rev E* (2011) 84:051906. doi:10.1103/PhysRevE.84.051906
24. Werner P, Burger M, Pietschmann J-F A PDE Model for Bleb Formation and Interaction with Linker Proteins. *Trans Maths Its Appl* (2020) 4:1–59. doi:10.1093/imatrm/tnaa001
25. Maxian O, Kassen AT, Strychalski W A Continuous Energy-Based Immersed Boundary Method for Elastic Shells. *J Comput Phys* (2018) 371:333–62. doi:10.1016/j.jcp.2018.05.045
26. Peskin CS The Immersed Boundary Method. *Acta Numerica* (2002) 11:479–517. doi:10.1017/S0962492902000077
27. Charras GT, Yarrow JC, Horton MA, Mahadevan L, Mitchison TJ Non-equilibration of Hydrostatic Pressure in Blebbing Cells. *Nature* (2005) 435:365–9. doi:10.1038/nature03550
28. Fai TG, Griffith BE, Mori Y, Peskin CS Immersed Boundary Method for Variable Viscosity and Variable Density Problems Using Fast Constant-Coefficient Linear Solvers I: Numerical Method and Results. *SIAM J Sci Comput* (2013) 35:B1132–B1161. doi:10.1137/120903038
29. Goudarzi M, Tarbashevich K, Mildner K, Begemann I, Garcia J, Paksa A, et al. Bleb Expansion in Migrating Cells Depends on Supply of Membrane from Cell Surface Invaginations. *Dev Cel* (2017) 43:577–87. e5. doi:10.1016/j.devcel.2017.10.030
30. Woolley TE, Gaffney EA, Waters SL, Oliver JM, Baker RE, Goriely A Three Mechanical Models for Blebbing and Multi-Blebbing. *IMA J Appl Maths* (2014) 79:636–60. doi:10.1093/imamat/hxu028
31. Moeendarbary E, Valon L, Fritzsche M, Harris AR, Moulding DA, Thrasher AJ, et al. The Cytoplasm of Living Cells Behaves as a Poroelastic Material. *Nat Mater* (2013) 12:253–61. doi:10.1038/nmat3517
32. Strychalski W, Copos CA, Lewis OL, Guy RD A Poroelastic Immersed Boundary Method with Applications to Cell Biology. *J Comput Phys* (2015) 282:77–97. doi:10.1016/j.jcp.2014.10.004

33. Devendran D, Peskin CS An Immersed Boundary Energy-Based Method for Incompressible Viscoelasticity. *J Comput Phys* (2012) 231:4613–42. doi:10.1016/j.jcp.2012.02.020
34. Persson P-O, Strang G A Simple Mesh Generator in MATLAB. *SIAM Rev* (2004) 46:329–45. doi:10.1137/S0036144503429121
35. Greengard L, Lee J-Y Accelerating the Nonuniform Fast Fourier Transform. *SIAM Rev* (2004) 46:443–54. doi:10.1137/S003614450343200X
36. Beylkin G On the Fast Fourier Transform of Functions with Singularities. *Appl Comput Harmonic Anal* (1995) 2:363–81. doi:10.1006/acha.1995.1026
37. Peyret R *Spectral Methods for Incompressible Viscous Flow*. New York: Springer (2002). doi:10.1007/978-1-4757-6557-1 Spectral Methods for Incompressible Viscous Flow
38. Sullivan JM. Curvatures of Smooth and Discrete Surfaces. In: AI Bobenko, JM Sullivan, P Schröder, GM Ziegler, editors. *Discrete Differential Geometry*, 38. Basel: Birkhäuser: Oberwolfach Seminars (2008). 175–88. doi:10.1007/978-3-7643-8621–49

Conflict of Interest: The author declares that the research was conducted in the absence of any commercial or financial relationships that could be construed as a potential conflict of interest.

Advantages of publishing in Frontiers

OPEN ACCESS
Articles are free to read for greatest visibility and readership

FAST PUBLICATION
Around 90 days from submission to decision

HIGH QUALITY PEER-REVIEW
Rigorous, collaborative, and constructive peer-review

TRANSPARENT PEER-REVIEW
Editors and reviewers acknowledged by name on published articles

Frontiers
Avenue du Tribunal-Fédéral 34
1005 Lausanne | Switzerland

Visit us: www.frontiersin.org
Contact us: frontiersin.org/about/contact

REPRODUCIBILITY OF RESEARCH
Support open data and methods to enhance research reproducibility

DIGITAL PUBLISHING
Articles designed for optimal readership across devices

FOLLOW US
@frontiersin

IMPACT METRICS
Advanced article metrics track visibility across digital media

EXTENSIVE PROMOTION
Marketing and promotion of impactful research

LOOP RESEARCH NETWORK
Our network increases your article's readership